frontiers | Research Topics

Invertebrate neurophysiology - of currents, cells, and circuits

Edited by
Edgar Buhl, James Newcomb and Krista Todd

Published in
Frontiers in Neuroscience
Frontiers in Physiology

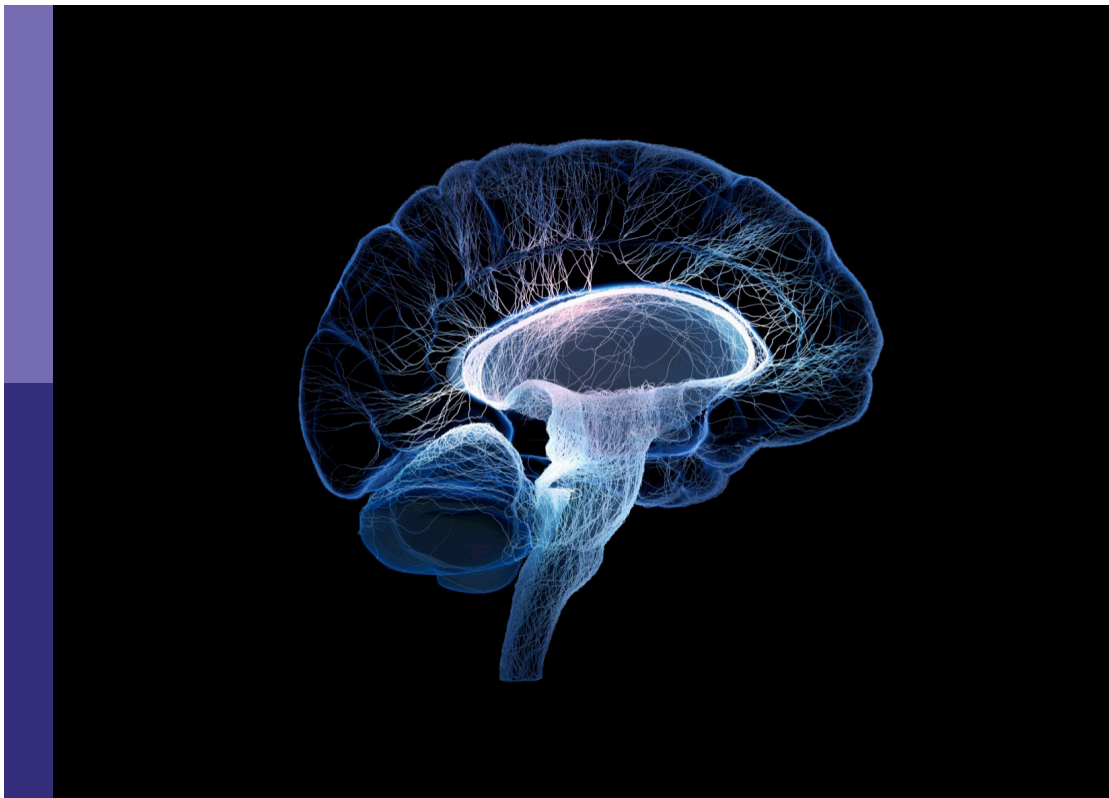

ISSN 1664-8714
ISBN 978-2-8325-3808-1
DOI 10.3389/978-2-8325-3808-1

About Frontiers

Frontiers is more than just an open access publisher of scholarly articles: it is a pioneering approach to the world of academia, radically improving the way scholarly research is managed. The grand vision of Frontiers is a world where all people have an equal opportunity to seek, share and generate knowledge. Frontiers provides immediate and permanent online open access to all its publications, but this alone is not enough to realize our grand goals.

Frontiers journal series

The Frontiers journal series is a multi-tier and interdisciplinary set of open-access, online journals, promising a paradigm shift from the current review, selection and dissemination processes in academic publishing. All Frontiers journals are driven by researchers for researchers; therefore, they constitute a service to the scholarly community. At the same time, the *Frontiers journal series* operates on a revolutionary invention, the tiered publishing system, initially addressing specific communities of scholars, and gradually climbing up to broader public understanding, thus serving the interests of the lay society, too.

Dedication to quality

Each Frontiers article is a landmark of the highest quality, thanks to genuinely collaborative interactions between authors and review editors, who include some of the world's best academicians. Research must be certified by peers before entering a stream of knowledge that may eventually reach the public - and shape society; therefore, Frontiers only applies the most rigorous and unbiased reviews. Frontiers revolutionizes research publishing by freely delivering the most outstanding research, evaluated with no bias from both the academic and social point of view. By applying the most advanced information technologies, Frontiers is catapulting scholarly publishing into a new generation.

What are Frontiers Research Topics?

Frontiers Research Topics are very popular trademarks of the *Frontiers journals series*: they are collections of at least ten articles, all centered on a particular subject. With their unique mix of varied contributions from Original Research to Review Articles, Frontiers Research Topics unify the most influential researchers, the latest key findings and historical advances in a hot research area.

Find out more on how to host your own Frontiers Research Topic or contribute to one as an author by contacting the Frontiers editorial office: frontiersin.org/about/contact

Invertebrate neurophysiology - of currents, cells, and circuits

Topic editors

Edgar Buhl — University of Bristol, United Kingdom
James Newcomb — New England College, United States
Krista Todd — Westminster College, United States

Citation

Buhl, E., Newcomb, J., Todd, K., eds. (2023). *Invertebrate neurophysiology - of currents, cells, and circuits*. Lausanne: Frontiers Media SA.
doi: 10.3389/978-2-8325-3808-1

Table of contents

frontiers | Frontiers in Neuroscience

TYPE Editorial
PUBLISHED 13 October 2023
DOI 10.3389/fnins.2023.1303574

OPEN ACCESS

EDITED AND REVIEWED BY
Laura Ballerini,
International School for Advanced Studies (SISSA), Italy

*CORRESPONDENCE
Edgar Buhl
✉ e.buhl@bristol.ac.uk

RECEIVED 28 September 2023
ACCEPTED 03 October 2023
PUBLISHED 13 October 2023

CITATION
Newcomb JM, Todd K and Buhl E (2023) Editorial: Invertebrate neurophysiology—of currents, cells, and circuits.
Front. Neurosci. 17:1303574.
doi: 10.3389/fnins.2023.1303574

Editorial: Invertebrate neurophysiology—of currents, cells, and circuits

James M. Newcomb[1], Krista Todd[2] and Edgar Buhl[3]*

[1]Department of Biology and Health Science, New England College, Henniker, NH, United States, [2]Neuroscience, Westminster University, Salt Lake City, UT, United States, [3]School of Physiology, Pharmacology and Neuroscience, University of Bristol, Bristol, United Kingdom

KEYWORDS

electrophysiological techniques, neuronal modeling, invertebrates, synapse, neural circuits

Editorial on the Research Topic
Invertebrate neurophysiology—of currents, cells, and circuits

Exploring the intricacies of the brain and comprehending how it gives rise to behavior, still stands as one of the foremost challenges for the scientific community. To investigate the functioning of the nervous system directly, researchers have often employed electrophysiological techniques. Nonetheless, the complexity and sheer abundance of neurons, along with their myriad connections, present significant obstacles. Consequently, scientists have turned to the study of simpler organisms with intricate behavioral patterns but a substantially lower number of neurons. Thus, over the years, invertebrates have been extensively employed in neuroscience research owing to their relative simplicity, accessibility, and lower ethical concerns compared to vertebrate models. Their significant contributions and pioneering role in advancing our understanding of neuroscience are evident through the numerous discoveries made using these organisms. As a result, the central neural circuits of worms, molluscs, insects, and crustaceans were characterized well before similar findings emerged from vertebrate preparations, highlighting the extensive and valuable history of invertebrate research in neuroscience (Clarac and Pearlstein, 2007). These ground-breaking achievements have unraveled numerous fundamental mechanisms underlying neuronal function and this Research Topic comprising nine original research articles and four reviews, emphasizes the continuing breakthroughs made by researchers investigating invertebrates like molluscs, insects, crustaceans, and others.

Invertebrate nervous systems offer several advantages over their vertebrate counterparts for trying to investigate and understand a range of different neurobiological phenomena. These advantages include large, individually identifiable neurons in some species, such as molluscs (Croll, 1987; Bullock, 2000). These relatively large neuronal somata facilitate intracellular electrophysiology, dynamic clamp, cell isolation and culture, DNA/RNA sequencing of individual neurons, and much more (Katz and Quinlan, 2019). In this Research Topic, Zhuo et al. review many of these techniques used in the infamous *Aplysia californica* nervous system, including focused ultrasound, optical recording and stimulation, and especially the more recent infrared neural inhibition, spearheaded by these authors over the last decade. Also in this topic, Lee and Watson use a molluscan nervous system to better understand the neural mechanisms underlying modulation of feeding behavior in the nudibranch, *Melibe leonina*. This work on feeding complements prior work in this species, on identified neurons involved in locomotion (Thompson and Watson, 2005; Sakurai et al., 2014).

Having access to identifiable neurons has facilitated the study of central pattern generators (CPGs) in numerous invertebrates, including crayfish swimmerets, feeding and swimming in gastropods, the leech heartbeat and swimming, the stomatogastric ganglion of crustaceans, and walking in stick insects (reviewed in Marder et al., 2005; Selverston, 2010). In this topic, Pirtle reviews over four decades of research on the CPG controlling locomotion in the pteropod *Clione limacina*, particularly mechanisms that contribute to acceleration of swimming, which is achieved through neuromodulation of the swim CPG. Blitz reviews neuromodulation in a number of invertebrate CPGs, especially the circuits in the crustacean stomatogastric ganglion that are responsible for regulating gastric activity. Both of these reviews highlight many of the neuromodulatory principles that have been learned from these invertebrate preparations, including co-transmitters, the roles of neuromodulatory projection neurons, state dependence, the role of sensory feedback, communication between CPG circuits, and many others.

Another advantage to invertebrates for unraveling elements of the nervous system, is that invertebrate taxa cover a far wider phylogenetic spread than vertebrates. Therefore, comparing the nervous systems of phylogenetically disparate invertebrates can be very informative in learning about conserved neurobiological principles and evolution of nervous systems. In this topic, there are articles on a wide array of bilaterian invertebrates, including ecdysozoans (Arthropoda—Au et al.; Cillov and Stumpner; Au et al.; Blitz; Megwa et al.; Powell et al.) and lophotrochozoans (Mollusca—Lee and Watson; Pirtle; Zhuo et al.; Gribkova et al.). However, research on cellular signaling and neurons in metazoans that diverged from bilaterians can provide additional understanding about the evolution of nervous systems. Moroz et al. and Norekian and Moroz investigate the use of various peptidergic and nitrergic signaling compounds in ctenophores, which may have independently evolved a nervous "system" (Moroz et al., 2014; Moroz and Kohn, 2016; Burkhardt et al., 2023). Going even further afield in the metazoan clade, Nikitin et al. report on the use of amino acids in nerveless placozoans, to integrate various behaviors, such as feeding and locomotion. Ultimately, one of the goals of this type of research in these invertebrate systems is to determine if certain principles can be applied to other organisms, such as mammals. Here, Gribkova et al. attempt to do just that, pointing out similar parallels in modular arrangement of nervous systems between soft-bodied invertebrates and vertebrates. These similarities in arrangement suggest that continued work in these simpler circuits may shed interesting light on vertebrate nervous systems.

Insect preparations with their simple nervous systems with well-defined neural circuits have been instrumental to study the neural basis of complex behaviors observed in their natural environments, providing valuable insights into general principles of neural processing and decision-making (e.g., Menzel, 2012). For example, crickets, bush crickets, and grasshoppers exhibit highly specialized auditory sensory systems and central circuits, allowing them to engage in acoustic communication (Huber et al., 1989). Their relatively larger and fewer identifiable neurons facilitate the consistent identification of individual homologous neurons across different animals and species. Exploiting this unique advantage, Cillov and Stumpner review and describe some novel elements in local prothoracic auditory neurons, investigating the evolution of nervous systems and deepening our understanding of their development and function.

The circadian clock is another well-researched behavior in insects, and the fruit fly *Drosophila melanogaster* has played a crucial role in understanding the molecular clock over the past five decades since the discovery of the first clock mutant (Konopka and Benzer, 1971), as recognized by the Nobel Prize in 2017. In addition to its small size, short generation time, rapid life cycle, and easy breeding at a low cost, *Drosophila*'s simple and well-characterized genetics have made it an invaluable and highly tractable tool for studying neural function and behavior as well as human disease (Bier, 2005). Researchers use heterologous gene expression, utilizing the binary GAL4/UAS system from yeast to introduce genes from different species (Brand and Perrimon, 1993). By exploiting this genetic flexibility and the significant genetic similarities to other insects, such as mosquitoes, Au et al. revealed that the Cryptochrome 1 proteins from nocturnal and diurnal mosquitos can mediate distinct physiological and behavioral responses to blue light in flies, aligning with the specific behaviors of the different mosquito species. Consequently, the authors were able to manipulate the behavior of the fruit flies based on the mosquito version of the protein expressed. More recently, fruit flies have also become accessible for electrophysiological studies, particularly patch clamp recordings, enabling researchers to understand and define the clock circuit responsible for the fly's time perception using just 150 neurons. Notably, the light input and arousal LNv neurons are well-studied, and here Au et al., using a similar experimental approach to above, showed that different photoreceptor systems are integrated in the LNvs to provide functional redundancy for wavelength-dependent light perception that triggers behavioral arousal in the flies.

Lastly, since the seminal work of Hodgkin and Huxley in the 1950s (Hodgkin and Huxley, 1952), computational modeling in neuroscience has become increasingly important and impactful, especially with the ever-increasing computational power available to researchers. In this collection, utilizing computational modeling, Megwa et al. study the mechanism of the sodium potassium ATPase ion pump affecting neuronal plasticity in the well-established larval fly motoneuron system. Accomplishing this task experimentally would have been exceedingly challenging; moreover, its application to vertebrate systems is facilitated by the models' universality.

The objective of this Research Topic was to emphasize and advocate the valuable role of invertebrate preparations for neuroscience research. We received a diverse array of contributions studying a range of different species and techniques and encompassing both original research studies and comprehensive reviews on invertebrate electrophysiology. Our aim is to inspire and motivate more researchers to embrace and study a broad range of invertebrate species using a wide spectrum of electrophysiological techniques once again.

Author contributions

JN: Conceptualization, Writing—original draft, review, and editing. KT: Writing—review and editing. EB: Conceptualization, Writing—original draft, review, and editing.

Funding

The author(s) declare that no financial support was received for the research, authorship, and/or publication of this article.

Conflict of interest

The authors declare that the research was conducted in the absence of any commercial or financial relationships that could be construed as a potential conflict of interest.

Publisher's note

All claims expressed in this article are solely those of the authors and do not necessarily represent those of their affiliated organizations, or those of the publisher, the editors and the reviewers. Any product that may be evaluated in this article, or claim that may be made by its manufacturer, is not guaranteed or endorsed by the publisher.

References

Bier, E. (2005). *Drosophila*, the golden bug, emerges as a tool for human genetics. *Nat. Rev. Genet.* 6, 9–23. doi: 10.1038/nrg1503

Brand, A. H., and Perrimon, N. (1993). Targeted gene expression as a means of altering cell fates and generating dominant phenotypes. *Development* 118, 401–415.

Bullock, T. H. (2000). Revisiting the concept of identifiable neurons. *Brain Behav. Evol.* 55, 236–240. doi: 10.1159/000006657

Burkhardt, P., Colgren, J., Medhus, A., Digel, L., Naumann, B., Soto-Angel, J. J., et al. (2023). Syncytial nerve net in a ctenophore adds insights on the evolution of nervous systems. *Science* 380, 293–297. doi: 10.1126/science.ade5645

Clarac, F., and Pearlstein, E. (2007). Invertebrate preparations and their contribution to neurobiology in the second half of the 20th century. *Brain Res. Rev.* 54, 113–161. doi: 10.1016/j.brainresrev.2006.12.007

Croll, R. P. (1987). "Identified neurons and cellular homologies," in *Nervous Systems in Invertebrates*, ed M. A. Ali (Boston, MA: Springer), 41–59.

Hodgkin, A. L., and Huxley, A. F. (1952). A quantitative description of membrane current and its application to conduction and excitation in nerve. *J. Physiol.* 117, 500–544.

Huber, F., Moore, T. E., and Loher, W. (1989). *Cricket Behavior and Neurobiology*. Ithaca, NY: Cornell University Press.

Katz, P. S., and Quinlan, P. D. (2019). The importance of identified neurons in gastropod molluscs to neuroscience. *Curr. Opin. Neurobiol.* 56, 1–7. doi: 10.1016/j.conb.2018.10.009

Konopka, R. J., and Benzer, S. (1971). Clock mutants of *Drosophila melanogaster*. *Proc. Natl. Acad. Sci. U.S.A.* 68, 2112–2116.

Marder, E., Bucher, D., Schulz, D. J., and Taylor, A. L. (2005). Invertebrate central pattern generation moves along. *Curr. Biol.* 15, R685–R699. doi: 10.1016/j.cub.2005.08.022

Menzel, R. (2012). The honeybee as a model for understanding the basis of cognition. *Nat. Rev. Neurosci.* 13, 758–768. doi: 10.1038/nrn3357

Moroz, L. L., Kocot, K. M., Citarella, M. R., Dosung, S., Norekian, T. P., Povolotskaya, I. S., et al. (2014). The ctenophore genome and the evolutionary origins of neural systems. *Nature* 510, 109–114. doi: 10.1038/nature13400

Moroz, L. L., and Kohn, A. B. (2016). Independent origins of neurons and synapses: insights from ctenophores. *Philos. Trans. R Soc. B* 371, 20150041. doi: 10.1098/rstb.2015.0041

Sakurai, A., Gunaratne, C. A., and Katz, P. S. (2014). Two interconnected kernels of reciprocally inhibitory interneurons underlie alternating left-right swim motor pattern generation in the mollusk *Melibe leonina*. *J. Neurophysiol.* 112, 1317–1328. doi: 10.1152/jn.00261.2014

Selverston, A. I. (2010). Invertebrate central pattern generator circuits. *Philos. Trans. R Soc. B* 365, 2329–2345. doi: 10.1098/rstb.2009.0270

Thompson, S., and Watson, W. H. III (2005). Central pattern generator for swimming in *Melibe*. *J. Exp. Biol.* 208, 1347–1361. doi: 10.1242/jeb.01500

frontiers | Frontiers in Physiology

TYPE Original Research
PUBLISHED 23 November 2022
DOI 10.3389/fphys.2022.1047106

OPEN ACCESS

EDITED BY
James Newcomb,
New England College, United States

REVIEWED BY
Akira Sakurai,
Georgia State University, United States
Roger P. Croll,
Dalhousie University, Canada

*CORRESPONDENCE
Colin Anthony Lee,
clee170@illinois.edu

SPECIALTY SECTION
This article was submitted to Invertebrate Physiology, a section of the journal Frontiers in Physiology

RECEIVED 20 September 2022
ACCEPTED 03 November 2022
PUBLISHED 23 November 2022

CITATION
Lee CA and Watson WH (2022), In the sea slug *Melibe leonina* the posterior nerves communicate stomach distention to inhibit feeding and modify oral hood movements.
Front. Physiol. 13:1047106.
doi: 10.3389/fphys.2022.1047106

In the sea slug *Melibe leonina* the posterior nerves communicate stomach distention to inhibit feeding and modify oral hood movements

Colin Anthony Lee[1,2]* and Winsor Hays Watson[1]

[1]Department of Biological Sciences, University of New Hampshire, Durham, NH, United States, [2]Neuroscience Program, University of Illinois at Urbana-Champaign, Urbana, IL, United States

The sea slug *Melibe leonina* is an excellent model system for the study of the neural basis of satiation, and previous studies have demonstrated that stomach distention attenuates feeding. Here we expanded on this work by examining the pathway communicating stomach distention to the central nervous system and the effects of distention on motor output. We found that the posterior nerves (PN), which extend posteriorly from the buccal ganglia and innervate the stomach, communicate stomach distention in Melibe. PN lesions led to increased feeding duration and food consumption, and PN activity increased in response to stomach distention. Additionally, the percentage of incomplete feeding movements increased with satiation, and PN stimulation had a similar impact in the nerves that innervate the oral hood. These incomplete movements may be functionally similar to the egestive, food rejecting motions seen in other gastropods and enable *Melibe* to remain responsive to food, yet adjust their behavior as they become satiated. Such flexibility would not be possible if the entire feeding network were inhibited.

KEYWORDS

gastropod, nudibranch, invertebrate, motivation, arousal, satiation, feeding, behavior

Introduction

In recent years the sea slug *Melibe leonina* has emerged as a promising species in which to study the neuronal regulation of behavioral state. It feeds using rhythmic movements of its oral hood to capture both planktonic prey (Watson and Trimarchi, 1992) and organisms on the kelp and sea grass on which it tends to reside (Watson et al., 2021), and it can feed while either stationary or crawling. Both its rhythmic feeding movements (Watson and Trimarchi, 1992) and locomotor activity (Newcomb et al., 2014)

Abbreviations: 5-HT, Serotonin; CNS, Central Nervous System; OHC, Oral Hood Closure; OHN, Oral Hood Nerve; PN, Posterior Nerve.

can be easily quantified, and the expression of these movements changes with time of day (Newcomb et al., 2014) or hunger state (Lee and Watson, 2016). Like all heterobranch gastropods, *Melibe* has a simple nervous system with a small number of large, individually identifiable neurons. However, unlike most heterobranchs *Melibe* lacks a buccal mass and complicated chewing mechanics, leading to an exceptionally simple (~30 neurons) buccal ganglion (Trimarchi and Watson, 1992). Finally, it is an organism about which we have transcriptomic (Cook et al., 2018) and peptidomic (Lee et al., 2021) information, and whose daily rhythms have been thoroughly documented (Newcomb et al., 2014).

Both time of day and hunger state influence behavioral arousal in *Melibe*, but our understanding of the neuronal mechanisms by which hunger does so remains limited. As a nocturnal animal, *Melibe* shows increased arousal during the night, with increased feeding and locomotion (Newcomb et al., 2014), and greater responsiveness to excitatory neurotransmitters (Watson et al., 2020). Its expression of key clock genes also peaks during this active period (Duback et al., 2018), consistent with what is seen across the metazoa (von Schantz and Archer, 2003; Nitabach and Taghert, 2008). A major regulator of hunger state in *Melibe* is stomach distention: as the volume in the stomach increases individuals become less likely to feed and move, until they are eventually satiated, and cease feeding altogether (Lee and Watson, 2016). This pattern has also been observed in other gastropods (e.g. *Pleurobranchaea californica* (Gillette et al., 2000), *Lymnaea stagnalis* (Dyakonova et al., 2015), and *Aplysia californica* (Kupfermann, 1974)) and other invertebrates (e.g. the fly *Phormia meigen* (Green, 1964) and the leech *Hirudo medicinalis* (Lent and Dickinson, 1987)). Stomach distention is conveyed by nerves that innervate the esophagus and stomach (Dethier and Gelperin, 1967; Kupfermann, 1974; Susswein and Kupfermann, 1975; Croll et al., 1987), and in several gastropods reductions in the motivation to feed are accompanied by reconfiguration of feeding networks to produce egestive, food rejecting motions (London and Gillette, 1986; Jing et al., 2007; Crossley et al., 2018). In *Melibe*, the most likely pathway for this signaling is *via* the posterior nerves (PN) of the buccal ganglia, which emanate from the buccal ganglia and innervate the esophagus and stomach (Figure 1 (Trimarchi and Watson, 1992)). The primary goal of this study was to test this hypothesis.

In this study we demonstrated that PN activity changes in response to stomach distention, and that PN signaling is necessary for normal satiation of feeding behavior. Additionally, we found that PN signaling attenuates feeding not merely by reducing the output from the feeding network, but by shortening feeding movements, so they do not cause consumption of food. These data demonstrate that the PNs are important regulators of the motivation to feed in *Melibe*.

Methods

Animals

Adult *Melibe leonina* (21.3 ± 2.69 g) were acquired from eelgrass beds near the University of Washington's Friday Harbor Laboratories (FHL) in the Puget Sound, WA and in Monterey Bay, California, and either maintained at FHL or shipped to the University of New Hampshire, Durham, NH. The subjects used

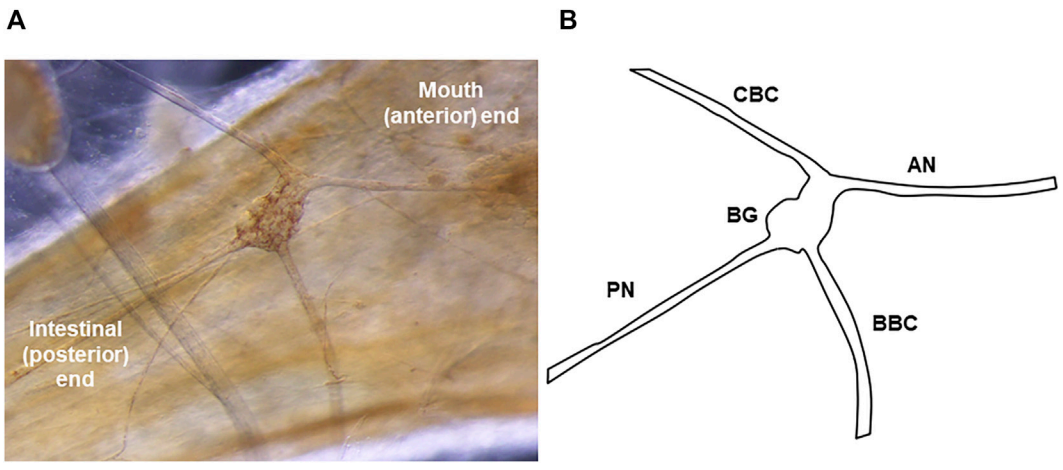

FIGURE 1
The *Melibe* buccal ganglion. **(A)** Picture of the buccal ganglion on the esophagus. A portion of the pedal ganglion, which is part of the fused cerebral-pleural-pedal complex, is visible in the top left. **(B)** Diagram of the ganglion and its nerves. The PN leaves the BG posteriorly and runs towards the stomach and intestines. In neurophysiological experiments examining the effect of stomach distention on activity, recordings were made from the severed distal end of the PN (conveying afferent signals from the stomach).

at FHL were housed in sea tables with flow through seawater, while those used at the University of New Hampshire were maintained in an aquarium with recirculating seawater, at approximately 13°C, until needed for experiments.

Feeding assays

To determine the effect of PN signaling on the motivation to feed, experiments were performed in which feeding rate over time was assessed for both *Melibe* with PN lesions (described in the next section) and control animals. Individual *Melibe* were placed in circular buckets (30 cm diameter) located within a larger tank of aerated seawater. The buckets had small mesh "windows" that allowed water exchange with the larger tank but prevented food from escaping. Tanks were located in a 13°C cold room that was kept on a 24-h light/dark cycle, with 10–14 h of light per day, depending on the season. After subjects acclimated to the buckets for 24 h, sufficient newly hatched *Artemia* spp. (brine shrimp) were added to the bucket to yield a density of approximately 3,000 *Artemia*/L. All trials began between 10 and 11 a.m. and *Melibe* were allowed to feed undisturbed for approximately 24 h. A black and white low light sensitive camera suspended directly above the buckets captured feeding activity, and recordings were obtained from approximately 1 hour before *Artemia* addition to 24 h post-addition. Camera outputs were digitized, time-stamped, and recorded on a Macintosh computer using the video capture software Gawker, which took one picture every second and streamed the images together at a rate of ten frames per second (Supplemental Video S1).

During the subsequent video analysis, the number of feeding motions performed per minute was counted for the entire experiment. *Melibe* feeds using rhythmic movements termed oral hood closures (OHCs), which consist of an oral hood closing phase (in which the hood comes forward and closes, capturing a bolus of water) and a tilt and squeeze swallowing phase (in which the closed hood is tilted back and the water is squeezed out through tentacles that are used to capture prey); see Watson and Trimarchi (Watson and Trimarchi, 1992) for a complete description of these phases. Subjects routinely produced incomplete feeding movements, performing only the oral hood closing phase, and likely not ingesting captured prey (Trimarchi and Watson, 1992). For comparisons between PN lesioned and control individuals these incomplete motions were ignored, and only the complete, ingestive OHCs were quantified. In a separate analysis of control individuals, both complete (Supplemental Video S2) and incomplete OHCs (Supplemental Video S3) were quantified.

PN lesions

Melibe were pinned out dorsally on a Sylgard-coated dish, with a single pin through the foot and two through the oral hood, and viewed under a dissecting microscope. A single incision was made in the skin directly above the central nervous system (CNS), exposing the fused cerebral, pedal, and pleural ganglia, the buccal ganglia, and PNs. Both PNs were then either cut with scissors or torn with tweezers. Incisions were sewn up with sterile sutures, and the subjects were given at least 5 days to recover. After this recovery period lesioned animals were fed as described in the previous section, and their feeding activity was compared to that of control animals. Half of the controls received sham operations, in which incisions were made and sutured, but PNs were left intact. There was no difference in the feeding activity between sham-operated (n = 4) and unoperated controls (n = 8). The baseline feeding rate for controls was 0.28 ± 0.12 OHC/min and 0.66 ± 0.22 OHC/min for sham-operated *Melibe* ($T(10) = 1.90$, $p = 0.087$). The maximum feeding rate was 2.15 ± 0.59 OHC/min for unoperated animals vs. 2.75 ± 0.17 OHC/min for those that were sham-operated ($T(10) = 0.76$, $p = 0.47$).

Quantification of food consumed during a satiating meal

Six lesioned and six control *Melibe* were fed to satiation with *Artemia*. After their feeding rate had returned to baseline, each individual's stomach was removed, and the number of *Artemia* in it was estimated. For estimates, the contents of the stomach were emptied into a known volume of seawater and stirred thoroughly to produce a homogenous concentration of *Artemia*. Three separate 1 ml aliquots were drawn up, and the number of *Artemia* in each aliquot was counted separately by two different people. Numbers were averaged between the measurements and used to estimate the total number of *Artemia* in the larger sample.

Neurophysiology

Extracellular neurophysiological recordings were carried out using both isolated CNS and semi-intact preparations. The semi-intact preparation was used to assess the effects of stomach distention on nervous system activity. For this preparation, the intact mouth, esophagus, stomach, intestine, and buccal ganglia were removed, pinned out in a Sylgard-coated dish, and continuously perfused with 13°C seawater. A cannula was inserted through the mouth and esophagus into the stomach, and a thread was used to tighten the junction of the mouth and esophagus to the cannula. Another thread was used to close the junction between the stomach and the intestine (Figure 2). Seawater was injected through the cannula to distend the stomach to one of four different diameters (1/4, 1/2, 3/4, maximum), and recordings were obtained from the PN (n = 6). To record the action potentials traveling *via* the PN from the stomach to the buccal ganglia, the nerve was severed near the

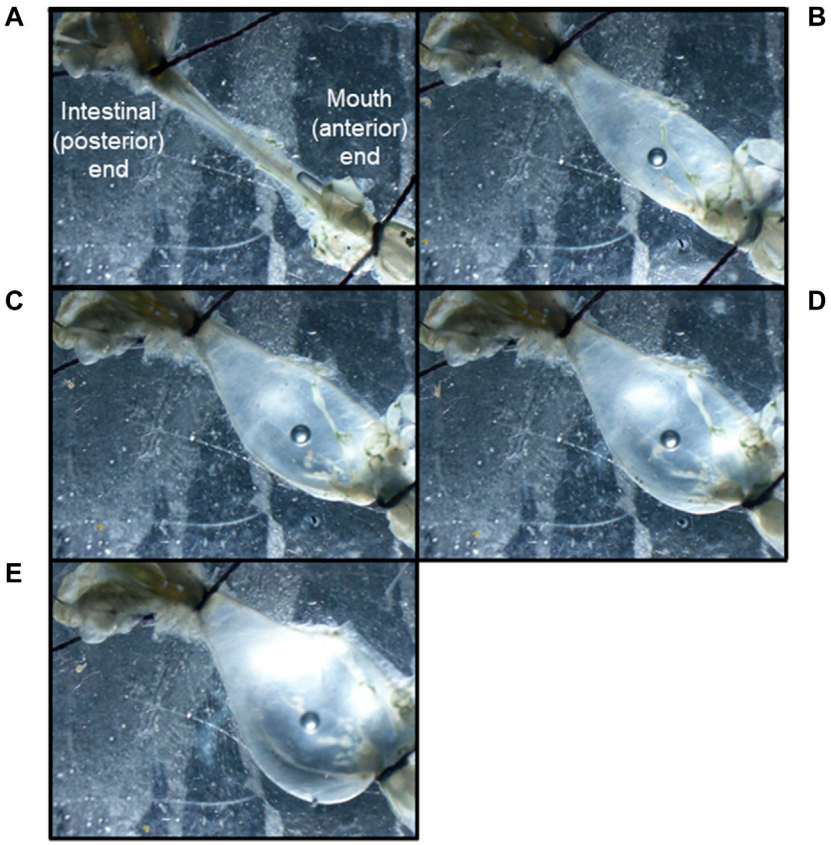

FIGURE 2
A *Melibe* mouth, esophagus and stomach preparation distended to the following degrees: **(A)** empty, **(B)** ¼ full, **(C)** ½ full, **(D)** ¾ full, **(E)** fully distended. Note the cannula held in place by a thread in the bottom right corner of image A, and the tied-off junctions between the stomach and intestines in all the images.

connection to the buccal ganglion and recordings were obtained from the cut distal end.

To assess the effects of PN activity on feeding motor output, extracellular recordings were obtained from the oral hood nerves (OHN) of the cerebral ganglion during sustained PN stimulation. For these recordings, the CNS was cut almost entirely away from the body, with only a piece of the esophagus retained to ensure that the buccal ganglia were not lost. The esophageal portion was pinned in a Sylgard-lined dish, and suction electrodes were attached to the PN and one to three OHNs. Recordings were carried out for several hours, alternating between ~30 min without PN stimulation and 20 min with PN stimulation. The PN was stimulated at 10 Hz 5 V. Fictive feeding can be identified in isolated *Melibe* brains by recording OHN bursts that have the same frequency as the oral hood movements of intact animals. Bursts identified using the following criteria: 1) at least 10 s in duration; 2) spiking at a rate of at least 5 Hz and at a rate that was at least twice that of the baseline spiking rate. For activity to be defined as a spike, it needed to be at least twice the voltage of the background noise.

Recordings were made with suction electrodes made of either pulled borosilicate capillaries or polyethylene tubing. Signals were amplified and filtered with an AM Systems Microelectrode AC Amplifier (AM-systems, Sequim, WA), digitized with an AD Instruments Powerlab 4/30 (AD Instruments, Dunedin, New Zealand), and displayed with Labchart software (AD Instruments, Dunedin, New Zealand). Stimuli were triggered using Labchart's Stimulator function. Changes in firing rate over time were determined by counting number of spikes/min using Labchart software.

Statistics

For the experiment comparing feeding rate over time in control and lesioned individuals, data were normalized by subtracting the baseline rate from the rate at a given time point. In all graphs, data are shown as the mean ± the standard error of means. All statistical tests were performed

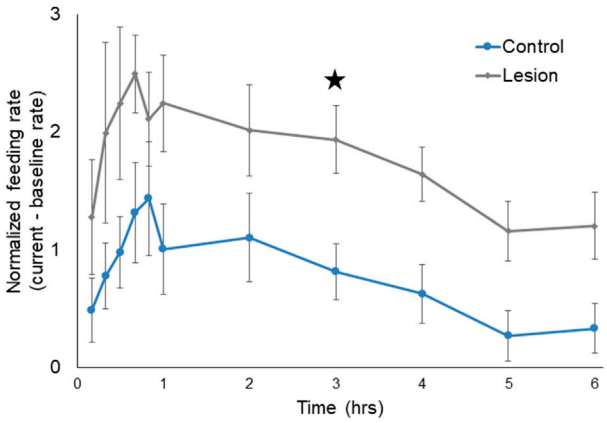

FIGURE 3
Normalized feeding rate over time for both control *Melibe* and individuals with PN lesions. For the graph rates were calculated in 10-min bins for the first hour, and for every hour thereafter; for statistical analysis rates were calculated for every hour. In the third hour the feeding rate was significantly elevated for lesioned individuals compared to controls (indicated by star).

with the software Prism (Graphpad, Boston, MA). A two-way repeated measures ANOVA with Sidak post-test was used to compare feeding rate over time between control and lesioned individuals. One-way repeated measures ANOVAs with Tukey post-tests were used to assess changes in complete vs. incomplete OHCs over time and PN responses to stomach distention. Changes in OHN activity were assessed using paired t-tests, and differences in the number of *Artemia* consumed between lesioned and control *Melibe* were assessed with unpaired t-tests.

Results

Posterior nerve lesions led to increases in feeding behavior

PN lesioned *Melibe* (n = 6) fed more than controls (n = 12) (Figure 3). The two groups displayed statistically significant differences in normalized feeding rate by both time ($F(5,80) = 6.96$, $p < 0.001$) and treatment group ($F(1,16) = 9.56$, $p = 0.0070$), although the interaction between the two variables was not significantly different ($F(5,80) = 0.13$, $p = 0.99$, two-way repeated measures ANOVA). Lesioned *Melibe* fed at a significantly greater rate in the third hour of their feeding bout (1.94 ± 0.29 OHC/min vs. 0.82 ± 0.24 OHC/min; $p = 0.042$, Sidak's Multiple Comparison Test). However, there was no significant difference in their maximum feeding rates (lesioned: 2.84 ± 0.30 OHC/min; controls: 1.94 ± 0.40 OHC/min; $T(16) = 1.64$, $p = 0.12$, unpaired *t*-test). Thus, PN lesions did not increase the initial or peak feeding intensity, but prolonged the duration of food arousal.

To verify that the lesioned *Melibe* consumed more prey, the stomachs of six lesioned and six control *Melibe* were removed after they had ceased feeding (8.9 h for lesioned individuals, 4.1 h for controls), and the *Artemia* in the stomachs were counted (Figure 4). Lesioned *Melibe* consumed significantly more *Artemia* (7323 ± 3278 *Artemia* for lesioned and 1358 ± 590 *Artemia* for controls; $p = 0.04$, *t*-test).

The frequency of complete, but not incomplete, OHCs decreased over time

Like many gastropods, *Melibe* can produce multiple feeding related movements, performing both complete OHCs, which lead to food ingestion, and incomplete ones, which likely do not lead to ingestion (Watson and Trimarchi, 1992; Wurstbaugh and Maciej Gliwicz, 2001; Crossley et al., 2018). To determine if the proportion of complete OHCs changes over the course of a feeding bout, we recorded incomplete vs. complete motions for a group of intact *Melibe* for 6 h (Figure 5, n = 8). While the rate of incomplete motions changed minimally over the course of the feeding period, the rate of complete motions dropped dramatically throughout the feeding bout, leading to a significantly increased ratio of incomplete motions for the final 2 hours of feeding compared to the first 3 h ($F(6,42) = 5.81$, $p < 0.001$, $p < 0.05$ for each comparison; one-way repeated measures ANOVA with Tukey post-test).

Stomach distention increases PN activity

To determine if the PNs communicate information about stomach fullness to the CNS, extracellular recordings were

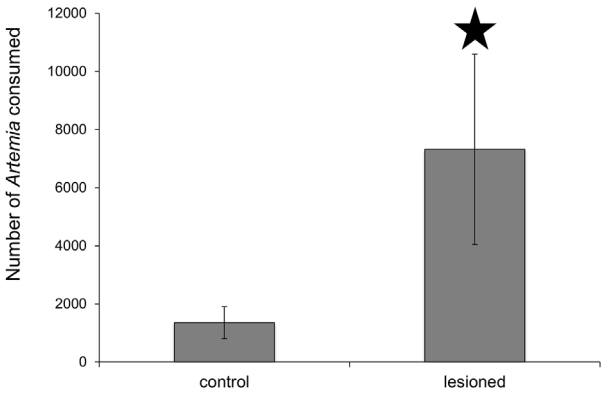

FIGURE 4
Assessment of stomach contents following feeding to satiation. *Melibe* with posterior nerve lesions consumed significantly more *Artemia* than controls. *Artemia* were less than 24 h old, and at this age are typically 500 μm in length (Wurstbaugh and Maciej Gliwicz, 2001).

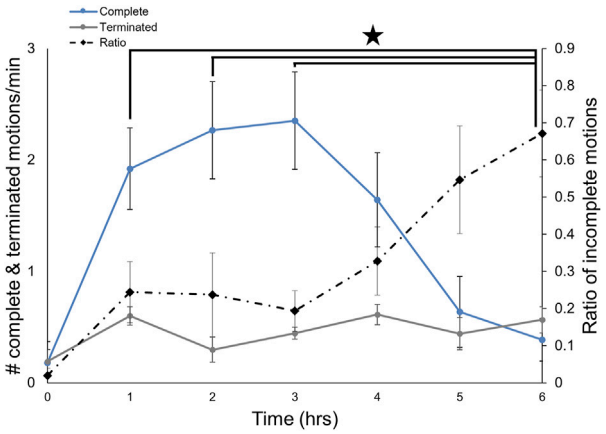

FIGURE 5
Changes in the types of OH movements during a feeding bout. The number of incomplete feeding motions remained constant over the course of a feeding bout, whereas the number of complete ones decreased after 3 hours. The frequency of incomplete movements was significantly greater at 6 h than for the first 3 hours.

obtained from the PN while the stomach was artificially inflated with seawater. Although there was activity in the PNs even when the stomach was empty, spike frequency changed in response to distention (Figures 6A, C) and was significantly increased compared to baseline rates 10–20 s after the start of distension (n = 5; F (11,44) = 2.39, $p < 0.021$; one-way repeated measures ANOVA with Tukey post-test). After the stomach was deflated PN activity showed a trend toward a decrease in firing rate (Figures 6B, D), although the decrease was not statistically significant (n = 6; F (11,55) = 1.853, $p = 0.067$; one-way repeated measures ANOVA).

To assess the effects of different levels of prolonged stomach distention on PN nerve activity we obtained PN recordings while the stomach was inflated to ¼, ½, ¾, and 100% of its maximum for at least 30 min at each distention level (Figure 7). During sustained distention multiple units burst rhythmically, and the overall firing rate increased (n = 6; F (4,25) = 5.98, $p = 0.0025$, one-way repeated measures ANOVA with Tukey post-test). Complete distention of the stomach caused a significant increase in posterior nerve firing compared to baseline, ½, and ¾ distention ($p < 0.05$ for each comparison) suggesting that partial stomach distention has a minimal impact on feeding behavior in *Melibe*.

PN signaling alters feeding-related activity in the CNS

Finally, we examined the effect of PN stimulation on patterns of OHN activity. These nerves emerge from the cerebral ganglion, cause contraction of the oral hood, the first phase of feeding behavior (Watson and Trimarchi, 1992), and produce spontaneous rhythmic bursts in isolated perparations (Figure 8A. 1.19 ± 0.21 OHCs/min, 21.70 ± 2.51 s duration). Long term recordings were performed during which we alternated between approximately 30 min without stimulation and 20 min with PN stimulation, and we found that stimulation significantly changed both the frequency (n = 4; F (2,6) = 60.24, $p < 0.001$, one-way repeated measures ANOVA with Tukey post-test) and duration of bursts F (2,6) = 9.74, $p = 0.013$, one-way repeated measures ANOVA with Tukey post-test). Specifically, stimulation of the PNs (Figure 8B) significantly reduced both the rate (0.56 ± 0.21 OHCs/min, 47.1% of baseline; $p < 0.001$) and duration (17.82 ± 2.12 s duration 82.1% of baseline; $p = 0.049$) of these bursts, with returns to baseline after stimulation ceased (Figure 8C; 1.08 ± 0.24 bursts/min, 90.8% of baseline; $p = 0.98$; 23.58 ± 2.44 s duration, 108.6% of baseline; $p = 0.49$). The shorter duration bursts that occurred during PN stimulation likely correspond to incomplete OHCs.

Discussion

This study demonstrates a clear role for the PNs in the regulation of *Melibe* feeding behavior. Both behavioral and neurophysiological data indicate that stomach distention, a key factor in *Melibe* satiation (Lee and Watson, 2016), is communicated to the CNS by the PNs. The data also indicate that this signaling leads to three changes in feeding related activity: 1) a decrease in the overall number of feeding

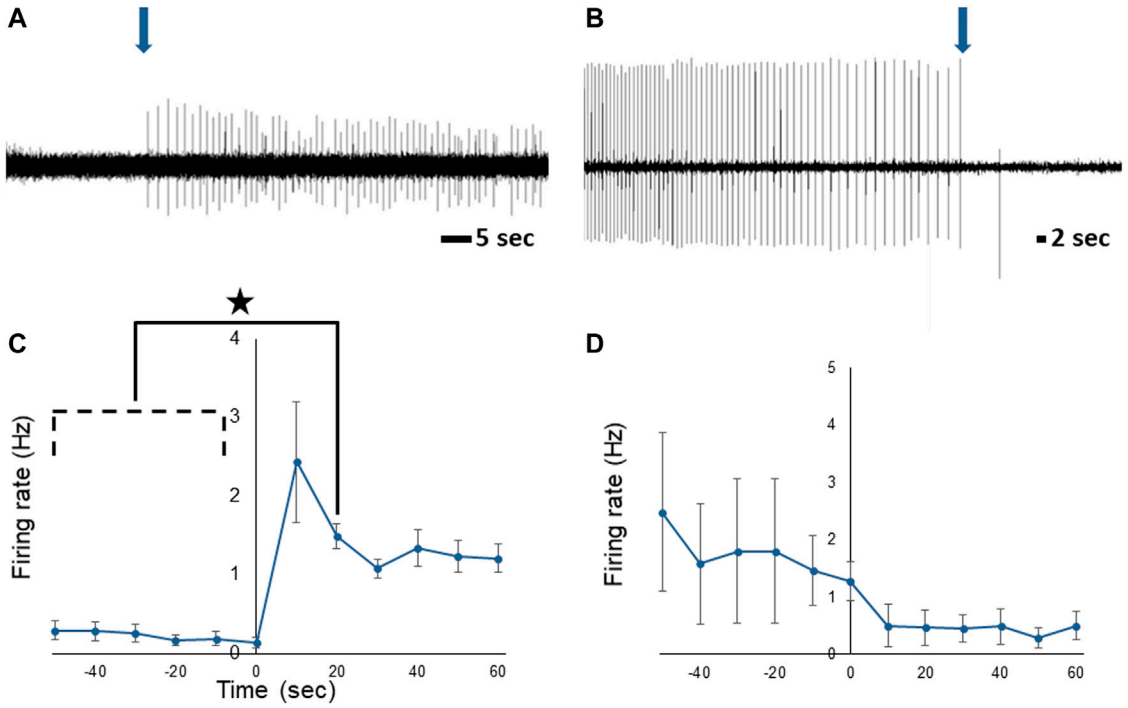

FIGURE 6
Response of the *Melibe* PN to stomach distention. **(A)** Representative neurophysiological recording showing the increase in spiking starting at the onset of distention (arrow). **(B)** Representative decrease in activity when the stomach was deflated (arrow). **(C)** Average spike frequency during the onset of distension, firing was significantly elevated compared to baseline at 10–20 s. **(D)** Average spike frequency before and after deflation of the stomach.

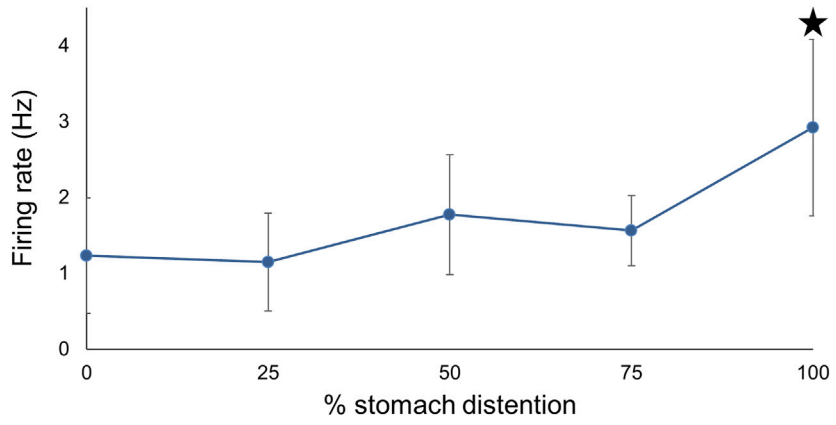

FIGURE 7
The relationship between PN firing rate and different levels of stomach distention. Maximal distention significantly increased firing compared to baseline, ¼, and ¾ distention.

movements; 2) an increase in the ratio of incomplete, non-ingestive movements to normal complete movements; 3) a decrease in the rhythmic movements of the esophagus associated with swallowing. This suggests that satiation in *Melibe* is more complex than simple inhibition of the feeding network.

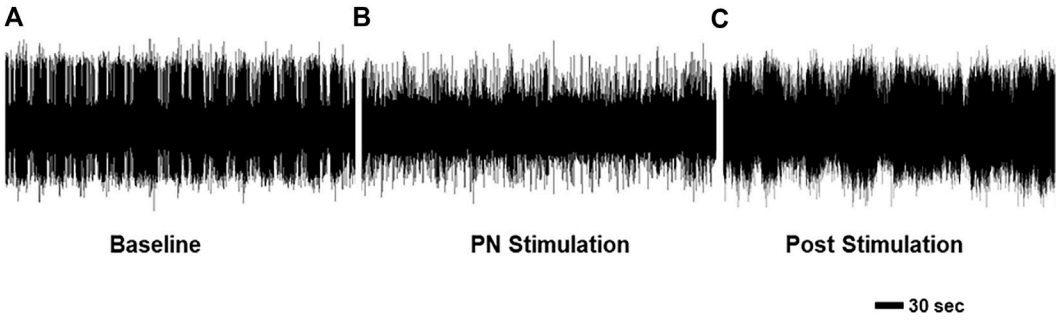

FIGURE 8
Recordings from an OHN showing activity **(A)** before, **(B)** during, and **(C)** after PN stimulation. Note the PN stimulation led to distinct bursting, which likely represents a change in the movements of the oral hood.

The PNs facilitate the inhibition of feeding by stomach distention

Loss of PN signaling, after they were lesioned, dramatically prolonged the duration of feeding-related arousal in *Melibe*. Lesions led to increases in both the duration of feeding bouts and the amount of food consumed. These results were very similar to those previously obtained when Melibe stomachs were lesioned, so food could not distend the stomach (Lee and Watson, 2016). The initial intensity of feeding did not increase in PN lesioned individuals, suggesting that they were not hungrier or experiencing greater food-induced arousal at the start of a meal. Rather, they simply took longer to satiate. This change did not appear to be due to behavioral deficits caused by the lesions, as individuals were fully healed from the surgery when experiments were performed, were still capable of consuming food, and consumed more than sham operated individuals. Additionally, in lesioned individuals, we observed defecation and transport of gut contents to the diverticuli that run throughout the body, indicating that the difference in final stomach volume was not a product of changes in the processing of stomach contents. Similar results have been obtained during studies involving the posterior stomatogastric nerve in *Pleurobranchaea* (Croll et al., 1987) and the esophageal nerve in *Aplysia* (Jing et al., 2007), suggesting a common function for the nerves that innervate the gut in gastropods.

Activity in the PNs signals the CNS that the stomach is filling with prey, and the information transmitted is proportional to the stimulus. Increases in stomach fullness cause immediate increases in PN activity, and deflation of the stomach causes an immediate cessation of activity. Additionally, the firing rate from the PNs during sustained (>30 min) distention roughly correlates with the degree of distention. However, a significant increase in the PN firing rate does not take place until the stomach is 100% distended, which suggests that *Melibe* will continue to feed until the stomach fills to this degree.

Satiation in Melibe is more complex than simple inhibition of feeding circuitry

Although satiation led to overall reductions in food-induced arousal, the feeding network still responded to food, but the response changed. Freely behaving *Melibe* continued to perform OHCs throughout a feeding bout, but the number of complete, ingestive ones decreased as their stomachs filled, whereas the incomplete, ineffective ones, remained unchanged. Similarly, the isolated CNS continued to produce rhythmic bursts during PN stimulation, but the duration of these bursts decreased. Therefore, as they start to become satiated, their feeding efforts become less effective and, while they do not start to egest prey, they also do not consume prey.

Other gastropods show a similar pattern as they satiate, producing egestive movements (Cropper et al., 2004; Wang et al., 2019), which are used to reject food in multiple contexts (e.g. (McManus et al., 2019)). It is unclear if these are homologous to *Melibe*'s incomplete OHCS, but they display functional similarities, as both are food-evoked movements of the feeding apparatus that do not result in consumption. *Aplysia* (Jing et al., 2007) and *Lymnaea* (Crossley et al., 2018) switch from ingestion to egestion as they satiate, and satiated *Pleurobranchaea* perform aversive behaviors in response to appetitive stimuli (Gillette et al., 2000). Mechanistic similarities also exist, as in *Aplysia* the shift to egestion is driven by the esophageal nerve, which, like the *Melibe* PN, innervates the gut and esophagus (Chiel et al., 1986). Studies in these species have also identified individual neurons involved in this shift. In both *Aplysia* (Jing et al., 2007) and *Lymnaea* (Crossley et al., 2018) an egestion specific interneuron becomes active, and in satiated *Aplysia* the multifunctional CBI2 interneuron, which can elicit both ingestive and egestive behaviors (Jing and Weiss, 2001), drives egestion. In *Pleurobranchaea* food avoidance conditioning biases individuals towards egestion, and this conditioning is accompanied by increases in the excitability of retraction

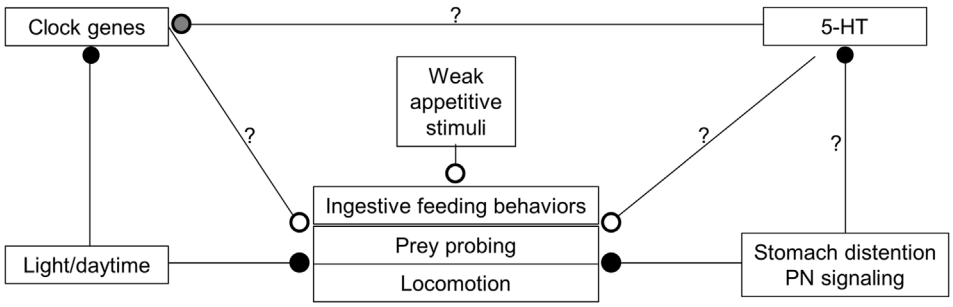

FIGURE 9
Model showing how various inputs might modulate *Melibe* feeding, locomotion, and overall arousal. Open circles are excitatory, closed circles are inhibitory. During the day, which is their quiescent period, 5-HT levels are reduced and light both inhibits active behaviors and reduces the expression of several clock genes. With the onset of darkness, clock genes are upregulated and 5-HT levels rise, leading to increased feeding, locomotion, and overall arousal. 5-HT may also have effects on clock gene expression (gray circle), perhaps serving to phase advance the circadian clock. When food is ingested it causes the stomach to distend, which is communicated to the NS by the PNs that innervate the stomach. This input reduces the motivation to feed, 5-HT levels, and locomotion. In the sea slug *Melibe leonina* the posterior nerves communicate stomach distention to inhibit feeding and modify oral hood movements.

phase neurons (London and Gillette, 1986), which in normal feeding behavior inhibit the protraction phase interneurons (London and Gillette, 1984). Similarly, in the land snail *Limax marginatus* feeding network oscillations increase following food avoidance conditioning (Kimura et al., 1998; Inoue et al., 2006). Thus, as gastropods satiate, they respond to palatable food in the same way they respond to unpalatable or toxic stimuli.

Why does satiation not merely manifest as simple inhibition of the feeding network, with no response of any type to food? Such inhibition can occur with defensive behaviors. In *Lymnaea* (Alania et al., 2004) and the nudibranch *Clione limacina* (Alania et al., 1999) the PlB neuron, which fires during defensive withdrawal, globally shuts down the feeding network, inhibiting neurons that act throughout the network, including the retraction phase ones that drive egestion. The answer likely lies in the complex and variable nature of the motivation to feed. Hunger state is not binary, but rather lies on a continuum (Susswein et al., 1976). On the hungry end of the continuum individuals feed robustly and primarily produce ingestive motions, whereas on the satiated end feeding responses are reduced and most movements are egestive or incomplete. Shifts away from ingestion allow individuals to flexibly move along this continuum. As they satiate, the number of non-ingestive movements decreases, but they can temporarily increase their feeding rate if food abundance or quality increases, in the same way that hungry individuals can temporarily perform egestive or incomplete feeding movements in response to an undesired food item.

This may be particularly important for *Melibe*, which filter feeds on patchy sources of planktonic prey, and which needs to be able to adaptively modify its feeding behavior in response to changes in food availability (Watson and Trimarchi, 1992). For example, a given bolus of seawater may hold toxic or unpalatable prey, so temporary expression of incomplete feeding motions allows individuals to clear undesirable material without ending a feeding bout. With inhibition as seen from the PlB neurons, feeding is inflexibly inhibited, and the feeding network cannot respond to changes in environmental condition. The existence of these separate mechanisms for feeding inhibition strongly indicates the utility of preserving some responsiveness within the feeding network, even with satiation.

How do stomach distention and circadian clocks interact to regulate the motivation to feed?

In *Melibe*, which are nocturnal animals, the onset of darkness initiates locomotion and bouts of feeding (Newcomb et al., 2014). This conflicts with satiation, which inhibits feeding behavior and has been shown in other species to inhibit overall activity. Studies in *Melibe* and other gastropods suggest that serotonin (5-HT) is involved in these processes. In gastropods it acts *via* the metacerebral cells and other 5-HT-ergic cerebral neurons to strongly potentiate feeding (Weiss et al., 1975; Weiss and Kupfermann, 1976; Gillette and Davis, 1977; Granzow and Kater, 1977; McCrohan and Benjamin, 1980; Delaney and Gelperin, 1990; Kobatake et al., 1992), and in *Pleurobranchaea* the 5-HT content of the metacerebral cells is reduced following satiation (Hatcher et al., 2008). Additionally, synaptically connected 5-HT-ergic neurons are embedded in each of the major locomotor networks (Gillette, 2006; Dyakonova et al., 2015), and act to regulate overall behavioral arousal; inhibition of 5-HT neurons in one circuit correlates with inhibition in another (Dyakonova et al., 2015). 5-HT mediates the effects of light in animals across the Metazoa (Morin, 1999; Itoh and Igarashi, 2000; Saifullah and Tomioka, 2002), including *Aplysia* (Koumenis and Eskin, 1992) and the marine snail *Bulla gouldiana* (Whitmore and Block, 1996), and is generally more abundant

during an animal's active period (Itoh and Igarashi, 2000). In *Melibe*, 5-HT-ergic processes project to the buccal ganglion *via* the cerebral-buccal connective (Newcomb et al., 2006).

Overall, hunger state, time of day, and the abundance of food act together to modulate the expression of feeding (Figure 9). During the day, 5-HT levels are likely lower, which combines with input from the circadian clock and inhibition from light, to reduce activity and responsiveness to the presence of prey in the water column. When night falls, 5-HT levels rise, circadian clock input changes, and it is dark, which leads to increased activity, and responsiveness to the same food-related stimuli that are present in the day. However, when individuals consume a satiating meal, even though they might still be in an active state, feeding is diminished.

Conclusion and future directions

This study demonstrates that stomach distension reduces the expression of rhythmic feeding behavior in *Melibe* and the state of distension is communicated to the NS *via* the posterior nerve. Satiating signals likely act alongside circadian clock cues to regulate overall behavioral arousal, and it is likely that 5-HT plays an important role. Further studies might eventually identify the neural circuits for feeding and swallowing and thus make it possible to determine how PN activity modifies their activity so there is a tendency for less feeding and more incomplete, likely egestive, movements. Additionally, although clear similarities in feeding behavior can be seen across gastropods, there is diversity in prey choice, feeding apparatus morphology, feeding mechanics, and gut morphology. Future work may also examine if these traits lead to interspecific variation in mechanisms of satiation.

Data availability statement

The raw data supporting the conclusions of this article will be made available by the authors, without undue reservation.

Author contributions

CL contributed to project and experimental design, data collection and analysis, and manuscript preparation. WW contributed to project and experimental design, and manuscript preparation.

Funding

This work was supported by the New Hampshire- INBRE through an Institutional Development Award (IDeA) from the National Institute of General Medical Sciences of the National Institutes of Health [grant number P20GM103506 to Jim Newcomb and WW]. CL was supported by the Conchologists of America through the grants to malacology program the University of New Hampshire Summer Teaching Assistant Fellowship Program, and the Friday Harbor Labs Summer Graduate Fellowship Program.

Acknowledgments

We thank Jim Newcomb, Leslie Curren and Megan Mahoney for their advice on this project, and Trevor Fay and Reyn Yoshioka for providing us with animals. Additionally, we thank Corey Collins for his help with video analysis and Maureen Raubach for her help with *Artemia* counts.

Conflict of interest

The authors declare that the research was conducted in the absence of any commercial or financial relationships that could be construed as a potential conflict of interest.

The handling editor JN declared a past co-authorship with the authors.

Publisher's note

Supplementary material

The Supplementary Material for this article can be found online at: https://www.frontiersin.org/articles/10.3389/fphys.2022.1047106/full#supplementary-material

References

Alania, M. A., Panchin, Y. V., and Sakharov, D. A. (1999). Pleural-buccal interneurons in the pteropod mollusc Clione limacina. *J. Comp. Physiology A Sens. Neural Behav. Physiology* 185, 267–275. doi:10.1007/s003590050386

Alania, M., Sakharov, D. A., and Elliott, C. J. H. (2004). Multilevel inhibition of feeding by a peptidergic pleural interneuron in the mollusc *Lymnaea stagnalis*. *J. Comp. Physiol. A Neuroethol. Sens. Neural Behav. Physiol.* 190, 379–390. doi:10.1007/s00359-004-0503-x

Chiel, H. J., Weiss, K. R., and Kupfermann, I. (1986). An identified histaminergic neuron modulates feeding motor circuitry in Aplysia. *J. Neurosci.* 6, 2427–2450. doi:10.1523/jneurosci.06-08-02427.1986

Cook, G. M., Gruen, A. E., Morris, J., Pankey, M. S., Senatore, A., Katz, P. S., et al. (2018). Sequences of circadian clock proteins in the nudibranch molluscs Hermissenda crassicornis, Melibe leonina, and Tritonia diomedea. *Biol. Bull.* 234, 207–218. doi:10.1086/698467

Croll, R. P., Albuquerque, T., and Fitzpatrick, L. (1987). Hyperphagia resulting from gut denervation in the sea slug, Pleurobranchaea. *Behav. Neural Biol.* 47, 212–218. doi:10.1016/s0163-1047(87)90341-4

Cropper, E. C., Evans, C. G., Hurwitz, I., Jing, J., Proekt, A., Romero, A., et al. (2004). Feeding neural networks in the mollusc Aplysia. *Neurosignals.* 13, 70–86. doi:10.1159/000076159

Crossley, M., Staras, K., and Kemenes, G. (2018). A central control circuit for encoding perceived food value. *Sci. Adv.* 4, eaau9180. doi:10.1126/sciadv.aau9180

Delaney, K., and Gelperin, A. (1990). Cerebral interneurons controlling fictive feeding in Limax maximus. *J. Comp. Physiol. A* 166, 311–326. doi:10.1007/bf00204805

Dethier, V. G., and Gelperin, A. (1967). Hyperphagia in the blowfly. *J. Exp. Biol.* 47, 191–200. doi:10.1242/jeb.47.1.191

Duback, V. E., Pankey, M. S., Thomas, R. I., Huyck, T. L., Mbarani, I. M., Bernier, K. R., et al. (2018). Localization and expression of putative circadian clock transcripts in the brain of the nudibranch Melibe leonina. *Comp. Biochem. Physiol. A Mol. Integr. Physiol.* 223, 52–59. doi:10.1016/j.cbpa.2018.05.002

Dyakonova, V. E., Hernadi, L., Ito, E., Dyakonova, T. L., Chistopolsky, I. A., Zakharov, I. S., et al. (2015). The activity of isolated neurons and the modulatory state of an isolated nervous system represent a recent behavioural state. *J. Exp. Biol.* 218, 1151–1158. doi:10.1242/jeb.111930

Gillette, R., and Davis, W. J. (1977). The role of the metacerebral giant neuron in the feeding behavior ofPleurobranchaea. *J. Comp. Physiol.* 116, 129–159. doi:10.1007/bf00605400

Gillette, R. (2006). Evolution and function in serotonergic systems. *Integr. Comp. Biol.* 46, 838–846. doi:10.1093/icb/icl024

Gillette, R., Huang, R. C., Hatcher, N., and Moroz, L. L. (2000). Cost-benefit analysis potential in feeding behavior of a predatory snail by integration of hunger, taste, and pain. *Proc. Natl. Acad. Sci. U. S. A.* 97, 3585–3590. doi:10.1073/pnas.97.7.3585

Granzow, B., and Kater, S. B. (1977). Identified higher-order neurons controlling the feeding motor program of Helisoma. *Neuroscience* 2, 1049–1063. doi:10.1016/0306-4522(77)90128-2

Green, G. W. (1964). The control of spontaneous locomotor activity in Phormia regina Meigen—II. Experiments to determine the mechanism involved. *J. Insect Physiology* 10, 727–752. doi:10.1016/0022-1910(64)90055-1

Hatcher, N. G., Zhang, X., Stuart, J. N., Moroz, L. L., Sweedler, J. V., and Gillette, R. (2008). 5–HT and 5–HT-SO 4 , but not tryptophan or 5-HIAA levels in single feeding neurons track animal hunger state. *J. Neurochem.* 104, 1358–1363. doi:10.1111/j.1471-4159.2007.05084.x

Inoue, T., Murakami, M., Watanabe, S., Inokuma, Y., and Kirino, Y. (2006). *In vitro* odor-aversion conditioning in a terrestrial mollusk. *J. Neurophysiol.* 95, 3898–3903. doi:10.1152/jn.00853.2005

Itoh, M. Y., and Igarashi, J. (2000). Circadian rhythm of serotonin levels in planarians. *Neuroreport* 11, 473–476. doi:10.1097/00001756-200002280-00009

Jing, J., Vilim, F. S., Horn, C. C., Alexeeva, V., Hatcher, N. G., Sasaki, K., et al. (2007). From hunger to satiety: Reconfiguration of a feeding network by Aplysia neuropeptide Y. *J. Neurosci.* 27, 3490–3502. doi:10.1523/JNEUROSCI.0334-07.2007

Jing, J., and Weiss, K. R. (2001). Neural mechanisms of motor program switching in Aplysia. *J. Neurosci.* 21, 7349–7362. doi:10.1523/jneurosci.21-18-07349.2001

Kimura, T., Toda, S., Sekiguchi, T., and Kirino, Y. (1998). Behavioral modulation induced by food odor aversive conditioning and its influence on the olfactory responses of an oscillatory brain network in the slug Limax marginatus. *Learn. Mem.* 4, 365–375. doi:10.1101/lm.4.5.365

Kobatake, E., Kawahara, S., Yano, M., and Shimizu, H. (1992). Control of feeding rhythm in the terrestrial slug Incilaria-bilineata. *Neurosci. Res.* 13, 257–265. doi:10.1016/0168-0102(92)90038-e

Koumenis, C., and Eskin, A. (1992). The hunt for mechanisms of circadian timing in the eye of Aplysia. *Chronobiol. Int.* 9, 201–221. doi:10.3109/07420529209064530

Kupfermann, I. (1974). Feeding behavior in Aplysia: A simple system for the study of motivation. *Behav. Biol.* 10, 1–26. doi:10.1016/s0091-6773(74)91644-7

Lee, C. A., and Watson, W. H. (2016). The influence of stomach distention on feeding in the nudibranch mollusk Melibe leonina. *Mar. Freshw. Behav. Physiology* 49, 277–290. doi:10.1080/10236244.2016.1192305

Lee, C. L. A., Romanova, E. V., Southey, B. R., Gillette, R., and Sweedler, J. V. (2021). Comparative analysis of neuropeptides in homologous interneurons and prohormone annotation in nudipleuran sea slugs. *Front. Physiol.* 12, 809529. doi:10.3389/fphys.2021.809529

Lent, C. M., and Dickinson, M. H. (1987). On the termination of ingestive behaviour by the medicinal leech. *J. Exp. Biol.* 131, 1–15. doi:10.1242/jeb.131.1.1

London, J. A., and Gillette, R. (1984). Functional roles and circuitry in an inhibitory pathway to feeding command neurones in Pleurobranchaea. *J. Exp. Biol.* 113, 423–446. doi:10.1242/jeb.113.1.423

London, J. A., and Gillette, R. (1986). Mechanism for food avoidance learning in the central pattern generator of feeding behavior of Pleurobranchae californica. *Proc. Natl. Acad. Sci. U. S. A.* 83, 4058–4062. doi:10.1073/pnas.83.11.4058

McCrohan, C. R., and Benjamin, P. R. (1980). Patterns of activity and axonal projections of the cerebral giant-cells of the snail, Lymnaea-stagnalis. *J. Exp. Biol.* 85, 149–168. doi:10.1242/jeb.85.1.149

McManus, J. M., Chiel, H. J., and Susswein, A. J. (2019). Successful and unsuccessful attempts to swallow in a reduced Aplysia preparation regulate feeding responses and produce memory at different neural sites. *Learn. Mem.* 26, 151–165. doi:10.1101/lm.048983.118

Morin, L. P. (1999). Serotonin and the regulation of mammalian circadian rhythmicity. *Ann. Med.* 31, 12–33. doi:10.3109/07853899909019259

Newcomb, J. M., Fickbohm, D. J., and Katz, P. S. (2006). Comparative mapping of serotonin-immunoreactive neurons in the central nervous systems of nudibranch molluscs. *J. Comp. Neurol.* 499, 485–505. doi:10.1002/cne.21111

Newcomb, J. M., Kirouac, L. E., Naimie, A. A., Bixby, K. A., Lee, C., Malanga, S., et al. (2014). Circadian rhythms of crawling and swimming in the nudibranch mollusc Melibe leonina. *Biol. Bull.* 227, 263–273. doi:10.1086/BBLv227n3p263

Nitabach, M. N., and Taghert, P. H. (2008). Organization of the Drosophila circadian control circuit. *Curr. Biol.* 18, R84–R93. doi:10.1016/j.cub.2007.11.061

Saifullah, A. S. M., and Tomioka, K. (2002). Serotonin sets the day state in the neurons that control coupling between the optic lobe circadian pacemakers in the cricket Gryllus bimaculatus. *J. Exp. Biol.* 205, 1305–1314. doi:10.1242/jeb.205.9.1305

Susswein, A. J., and Kupfermann, I. (1975). Bulk as a stimulus for satiation in Aplysia. *Behav. Biol.* 13, 203–209. doi:10.1016/s0091-6773(75)91903-3

Susswein, A. J., Kupfermann, I., and Weiss, K. R. (1976). The stimulus control of biting in Aplysia. *J. Comp. Physiol.* 108, 75–96. doi:10.1007/bf00625442

Trimarchi, J., and Watson, W. H. (1992). The role of the Melibe buccal ganglia in feeding-behavior. *Mar. Behav. Physiology* 19, 195–209. doi:10.1080/10236249209378808

von Schantz, M., and Archer, S. N. (2003). Clocks, genes and sleep. *J. R. Soc. Med.* 96, 486–489. doi:10.1258/jrsm.96.10.486

Wang, Y. Q., Weiss, K. R., and Cropper, E. C. (2019). Network degeneracy and the dynamics of task switching in the feeding circuit in Aplysia. *J. Neurosci.* 39, 8705–8716. doi:10.1523/JNEUROSCI.1454-19.2019

Watson, W. H., Bourque, K. M. F., Sullivan, J. R., Miller, M., Buell, A., Kallins, M. G., et al. (2021). The digestive diverticula in the carnivorous nudibranch, Melibe leonina, do not contain photosynthetic symbionts. *Integr. Org. Biol.* 3, 15. doi:10.1093/iob/obab015

Watson, W. H., Nash, A., Lee, C., Patz, M. D., and Newcomb, J. M. (2020). The distribution and possible roles of small cardioactive peptide in the nudibranch Melibe leonina. *Integr. Org. Biol.* 2, obaa016. doi:10.1093/iob/obaa016

Watson, W. H., and Trimarchi, J. (1992). A quantitative description of Melibe feeding-behavior and its modification by prey density. *Mar. Behav. Physiology* 19, 183–194. doi:10.1080/10236249209378807

Weiss, K. R., Cohen, J., and Kupfermann, I. (1975). Potentiation of muscle contraction: A possible modulatory function of an identified serotonergic cell in Aplysia. *Brain Res.* 99, 381–386. doi:10.1016/0006-8993(75)90041-4

Weiss, K. R., and Kupfermann, I. (1976). Homology of the giant serotonergic neurons (metacerebral cells) in Aplysia and pulmonate molluscs. *Brain Res.* 117, 33–49. doi:10.1016/0006-8993(76)90554-0

Whitmore, D., and Block, G. D. (1996). Cellular aspects of molluskan biochronometry. *Seminars Cell. & Dev. Biol.* 7, 781–789. doi:10.1006/scdb.1996.0096

Wurstbaugh, W. A., and Maciej Gliwicz, Z. (2001). Limnological control of brine shrimp population dynamics and cyst production in the Great Salt Lake, Utah. *Hydrobiologia* 466, 119–132. doi:10.1023/a:1014502510903

frontiers | Frontiers in Neuroscience

TYPE Original Research
PUBLISHED 30 November 2022
DOI 10.3389/fnins.2022.1042508

OPEN ACCESS

EDITED BY
Edgar Buhl,
University of Bristol, United Kingdom

REVIEWED BY
Masashi Tabuchi,
Case Western Reserve University, United States
Nara Ines Muraro,
CONICET Instituto de Investigación en Biomedicina de Buenos Aires (IBioBA), Argentina
Florencia Fernandez-Chiappe,
CONICET Instituto de Investigación en Biomedicina de Buenos Aires (IBioBA), Argentina, in collaboration with reviewer NM

*CORRESPONDENCE
Todd C. Holmes
tholmes@uci.edu

SPECIALTY SECTION
This article was submitted to Neural Technology, a section of the journal Frontiers in Neuroscience

RECEIVED 12 September 2022
ACCEPTED 04 November 2022
PUBLISHED 30 November 2022

CITATION
Au DD, Liu JC, Nguyen TH, Foden AJ, Park SJ, Dimalanta M, Yu Z and Holmes TC (2022) Nocturnal mosquito Cryptochrome 1 mediates greater electrophysiological and behavioral responses to blue light relative to diurnal mosquito Cryptochrome 1.
Front. Neurosci. 16:1042508.
doi: 10.3389/fnins.2022.1042508

Nocturnal mosquito Cryptochrome 1 mediates greater electrophysiological and behavioral responses to blue light relative to diurnal mosquito Cryptochrome 1

David D. Au[1], Jenny C. Liu[1], Thanh H. Nguyen[1], Alexander J. Foden[1], Soo Jee Park[1], Mia Dimalanta[1], Zhaoxia Yu[2,3] and Todd C. Holmes[1,3]*

[1]Department of Physiology and Biophysics, School of Medicine, University of California, Irvine, Irvine, CA, United States, [2]Department of Statistics, Donald Bren School of Information and Computer Sciences, University of California, Irvine, Irvine, CA, United States, [3]Center for Neural Circuit Mapping, School of Medicine, University of California, Irvine, Irvine, CA, United States

Nocturnal Anopheles mosquitoes exhibit strong behavioral avoidance to blue-light while diurnal Aedes mosquitoes are behaviorally attracted to blue-light and a wide range of other wavelengths of light. To determine the molecular mechanism of these effects, we expressed light-sensing Anopheles gambiae (AgCRY1) and Aedes aegypti (AeCRY1) Cryptochrome 1 (CRY) genes under a crypGAL4-24 driver line in a mutant Drosophila genetic background lacking native functional CRY, then tested behavioral and electrophysiological effects of mosquito CRY expression relative to positive and negative CRY control conditions. Neither mosquito CRY stops the circadian clock as shown by robust circadian behavioral rhythmicity in constant darkness in flies expressing either AgCRY1 or AeCRY1. AgCRY1 and AeCRY1 both mediate acute increases in large ventral lateral neuronal firing rate evoked by 450 nm blue-light, corresponding to CRY's peak absorbance in its base state, indicating that both mosquito CRYs are functional, however, AgCRY1 mediates significantly stronger sustained electrophysiological light-evoked depolarization in response to blue-light relative to AeCRY1. In contrast, neither AgCRY1 nor AeCRY1 expression mediates measurable increases in large ventral lateral neuronal firing rates in response to 405 nm violet-light, the peak of the Rhodopsin-7 photoreceptor that is co-expressed in the large lateral ventral neurons. These results are consistent with the known action spectra of type 1 CRYs and lack of response in cry-null controls. AgCRY1 and AeCRY1 expressing flies show behavioral attraction to low intensity blue-light, but

AgCRY1 expressing flies show behavioral avoidance to higher intensity blue-light. These results show that nocturnal and diurnal mosquito Cryptochrome 1 proteins mediate differential physiological and behavioral responses to blue-light that are consistent with species-specific mosquito behavior.

KEYWORDS

cryptochrome, non-image forming vision, electrophysiology, light-evoked behavior, mosquito sensory biology, *Drosophila melanogaster*, *Anopheles gambiae*, *Aedes aegypti*

Introduction

Many insect behaviors are modulated by short wavelength light (Coombe, 1982; Green and Cosens, 1983; Sumba et al., 2004; Das and Dimopoulos, 2008; Yamaguchi et al., 2010; Rund et al., 2012; Sawadogo et al., 2013; Tokushima et al., 2016; Knop et al., 2017; Sheppard et al., 2017; Farnesi et al., 2018; Padilha et al., 2018; Alonso San Alberto et al., 2022). It has been long assumed that insect behavioral light responses rely on image forming vision through eye photoreceptors that express opsins. However, insects additionally have non-image forming vision mediated by photoreceptors that are expressed directly in brain neurons (Fogle et al., 2011; Ni et al., 2017).

Insect non-imaging forming visual photoreceptors include ultraviolet, blue, and red-light activated Cryptochrome (CRY) that was first characterized as the primary circadian photoreceptor in *Drosophila* (Emery et al., 1998; Stanewsky et al., 1998) and violet-light activated Rhodopsin 7 (Rh7, Ni et al., 2017). Rh7 is an opsin photoreceptor expressed in central brain neurons that couples to G protein signaling pathways and also regulates light-evoked circadian photo-attraction/avoidance behaviors (Ni et al., 2017; Kistenpfennig et al., 2018; Baik et al., 2019b; Lazopulo et al., 2019). CRY is a riboflavin-based photoreceptor protein that uses flavin adenine dinucleotide (FAD) as its light sensing chromophore. In *Drosophila*, CRY is expressed in roughly half of all circadian neurons (Emery et al., 2000; Klarsfeld et al., 2004; Benito et al., 2008; Sheeba et al., 2008c; Yoshii et al., 2008; Fogle et al., 2011), which include all of the Pigment Dispersing Factor (PDF) expressing ventral lateral neurons (LNvs) that also mediate light-evoked behavioral arousal (Parisky et al., 2008; Shang et al., 2008; Sheeba et al., 2008c, 2010; Liu et al., 2014; Fogle et al., 2015; Muraro and Ceriani, 2015; Buhl et al., 2016; Potdar and Sheeba, 2018; Chaturvedi et al., 2022). While *Drosophila* only express light sensitive "type 1" CRYs, other insects also express light insensitive "type 2" CRYs similar to CRYs expressed in vertebrates that function as transcriptional repressors (Yuan et al., 2007; Gegear et al., 2010; Fogle et al., 2011; Damulewicz and Mazzotta, 2020). The best characterized function of CRYs in insects is the light activated initiation of the slow (~1 h) and irreversible process of circadian clock resetting that has been well characterized by molecular genetic analysis in *Drosophila*. This mechanism occurs by CRY mediated light activated protein degradation of the heteromultimeric clock protein complex consisting of TIMELESS (TIM), PERIOD (PER), and CRY itself, thus relieving repression of the transcriptional activators CLOCK and CYCLE at E-box promoter sequences upstream from the *tim* and *per* genes (Emery et al., 1998; Stanewsky et al., 1998; Busza et al., 2004; Koh et al., 2006; Peschel et al., 2009; Damulewicz and Mazzotta, 2020).

CRY photoactivation also evokes rapid and very long-lasting (30–40 s) neuronal depolarization and increased spontaneous action potential firing in large ventral lateral neurons (l-LNvs) and other CRY expressing neurons (Sheeba et al., 2008b; Fogle et al., 2011, 2015; Giachello et al., 2016; Baik et al., 2017, 2019a; Hong et al., 2018; Au et al., 2022). While light-evoked CRY mediated electrophysiological effects are acute and reversible in contrast to CRY mediated clock resetting, CRY on/off electrophysiological kinetic light responses are not as rapid as those mediated by image-forming opsins. Light-activated CRY couples to electrophysiological depolarization and clock resetting through multiple mechanisms including photoreduction electron transfer events along a chain of CRY tryptophan residues in close proximity to the FAD chromophore and CRY protein conformational changes, including the C terminal tail (Berndt et al., 2007; Bouly et al., 2007; Hoang et al., 2008; Öztürk et al., 2008; Liu et al., 2010; Ozturk et al., 2011, 2014; Vaidya et al., 2013; Fogle et al., 2015; Lin et al., 2018, 2022; Baik et al., 2019a; Chandrasekaran et al., 2021). In addition to circadian clock resetting, CRY phototransduction evokes acute behaviors in insects, including arousal (Sheeba et al., 2008a; Fogle et al., 2015) and short wavelength light attraction/avoidance behavior (Baik et al., 2017, 2018, 2019b, 2020; Au et al., 2022), which is under circadian modulation.

Light-activated CRY evoked behavioral changes are particularly interesting in mosquitoes as mosquito-spread diseases afflict hundreds of millions of people worldwide. Two medically important genera include nocturnal *Anopheline* and diurnal *Aedes* mosquitoes. *Anopheline* mosquitoes are responsible for over 200 million cases of malaria worldwide. *Aedes* mosquitoes are the principal vectors for Dengue virus (over 90 million cases worldwide) and yellow fever, West Nile

fever, chikungunya fever, Zika fever, and Japanese encephalitis (WHO website fact sheet). Insect control methods based on the sensory physiology of mosquitoes is very appealing as chemical pesticides are non-specific and environmentally harmful. The behavior of nocturnal *An. gambiae* (Ag) and diurnal *Ae. aegypti* (Ae) mosquitoes is subject to circadian regulation, thus enforcing their ecologically distinct temporal activity patterns (Jones et al., 1967; Taylor and Jones, 1969). Recently, we found that nocturnal *An. coluzzii* and diurnal *Ae. aegypti* mosquitoes display distinct innate circadian temporal attraction/avoidance behavioral responses to light. Nocturnal *Anopheles* mosquitoes behaviorally avoid short wavelength light during the day, while diurnal *Aedes*, particularly females, are behaviorally attracted to a broad range of light spectra during the day (Baik et al., 2020). Attraction/avoidance behavioral responses to light for both species change with time-of-day and show distinct sex differences that are consistent with predation and mate swarming activities of females vs. males. These distinct *Anopheles* and *Aedes* mosquito behavioral light responses appear to be mediated by light activated type 1 Cryptochrome signaling shown by disruption of these behaviors by prior exposure to constant light (Baik et al., 2020). Further, attraction/avoidance behavioral responses to light are mediated by ventral lateral neurons that are characterized by PDF and PER proteins co-expressed in *Drosophila melanogaster* and other insect species. We recently showed that *Ae. aegypti* and *An. coluzzii* mosquito female adult brains also display characteristics of large- (l-LNvs) and small-ventral lateral neurons (s-LNvs) marked by PDF and PER co-expression with similar morphology and projection patterning (Baik et al., 2020). Putative circadian dorsal neurons (DNs) are seen in both *Ae. aegypti* and *An. coluzzii* mosquito female adult brains, again identified by similar morphological projections in common with *Drosophila* (Baik et al., 2020). Therefore, we employed an "empty-neuron" model approach using transgenic *Drosophila* on a *cry-null* background to express AgCRY1 and AeCRY1. In that paper we show mosquito CRY electrophysiological and behavioral responses to UV and red-light and find by multiple assays that nocturnal AgCRY1 is significantly more light sensitive as compared with diurnal AeCRY1. In Au et al. (2022) we focused on those two light wavelengths because UV light is the most commonly used part of the light spectrum for insect control devices using light ("bug lights") to trap mosquitoes. We earlier characterized nocturnal and diurnal mosquito behavioral responses to UV light (Baik et al., 2020). Red light is of interest because we found distinctly different nocturnal and diurnal mosquito behavioral responses to red light (Baik et al., 2020). This followed our unexpected findings that insect CRYs functionally respond to red light (Baik et al., 2019a), in contrast to the lack of response of purified insect CRYs to red light for *in vitro* biophysical assays. In addition to CRYs which show spectral absorbance peaks in their base oxidized states to 365 nm UV light and 450 nm blue light, another photoreceptor, Rhodopsin 7 (Rh7) is expressed in the LNv and other brain neurons (Ni et al., 2017; Kistenpfennig et al., 2018; Baik et al., 2019b). Rh7 exhibits a comparatively broad spectral absorbance that peaks around 405 nm violet light. To compare the potential interactions between mosquito CRYs and Rh7, we tested AgCRY1 and AeCRY1 expressing transgenic flies for their responses to 450 nm blue light and 405 nm violet light.

Materials and methods

Experimental animals

Drosophila melanogaster flies were raised on standard media (yeast, cornmeal, agar) at 25 ± 1°C and 40–60% relative humidity in 12:12 h Light:Dark cycles. All flies used in experiments were first isogenized (backcrossed) to the w1118 genetic background for a minimum of six generations. All behavioral experiments used 3–4-day post-eclosion adult male flies. We generated pJFRC7 vectors containing cryptochrome 1 from *Drosophila melanogaster* (Dm), *An. gambiae* (Ag), and *Ae. aegypti* (Ae) in frame with eGFP. Use of the pJFRC7 vector allows for a controlled site-specific PhiC31 genomic insertion site. DNA constructs were then sent to the vendor Bestgene for fly embryonic injection and screening for successful transgenesis. Experimental transgenic flies backcrossed to the common wild-type w1118 background for a minimum of 6 generations. Genotyping primers were designed with the following sequences: AeCRY1 Forward: CGA GAA AGT GCA GGC CAA CAA TC, AeCRY1 Reverse: GT TCT TCA ACT CCG GCA GAT ATC, AgCRY1 Forward: CAG CCA GTT CAA GTA TCC GG, and AgCRY1 Reverse: CGG TTC GTG CAC AAA CTG TG. Experimental transgenic flies were crossed with a *cry-null* background (obtained from Jeff Hall, Brandeis University), then with a *crypGAL4-24* driver line for CRY-neuron specific expression of DmCRY or mosquito CRY1.

Locomotor activity behavioral assay

Adaptations to the behavioral assays from Nitabach et al. (2002), Chiu et al. (2010), and Nave et al. (2021) were made for testing constant dark conditions for circadian behavior following 12 h:12 h light:dark entrainment (LD:DD) tested under two light intensities of 1 lux and 400 lux white light. Adult male flies (2–4 days post-eclosion) were anesthetized over CO_2 and individually loaded into borosilicate activity tubes. The TriKinetics Locomotor Activity Monitoring System was used to track fly behavior over a protocol of: 12:12 h Light:Dark (LD) entrainment for 7 days, then 7 days of constant dark (DD) conditions. Actograms were generated using Clocklab software. Average activity education graphs and its statistics were

measured using FaasX software, then graphed using Microsoft Excel. Within FaasX, the CycleP analysis toolkit was used to calculate % rhythmicity from periodogram analysis with the following scoring criteria for flies in DD: minimum power ≥ 20, minimum width (h) ≥ 2, Chi-square significance ≥ 0.05 and calculation of tau. Data are reported as averages $\pm$ standard error mean. Anticipation index measurements during LD were adapted for the entrainment duration from Harrisingh et al. (2007) and Sheeba et al. (2010) taking the average activity in the 3 h preceding lights on (morning anticipation) or lights off (afternoon/evening anticipation) as a ratio over the average activity in the 6 h preceding lights on or off for individual flies over 5 days of LD entrainment. The reported values for anticipation index are an average of all the flies over the 5 days of LD entrainment.

Immunocytochemistry

Experimental transgenic flies were dissected for *ex vivo* brain preparations after 3–5 days of 12:12 h LD entrainment. Dissections began approximately 1 h before each ZT time point measured (ZT5, 11, 17, 23). Immunocytochemistry (ICC) experiments were performed for all genotypes in a given experiment, then repeated a minimum of 3 times to optimize statistical analysis and minimize experimental error. Dissected brains were placed in chilled 1X PBS, fixed in 4% paraformaldehyde (PFA) for 30 min, washed 3 × 10 min in PBS-Triton-X 1%, incubated in blocking buffer (10% Horse Serum-PBS-Triton-X 0.5%) at room temperature before incubation with rabbit α-TIM, polyclonal (1:1,000) antibodies overnight in 4°C. 3 rinse steps were performed at 10 min intervals with PBS-Triton-X 0.5% then incubated in goat α-rabbit-Alexa- 594 (1:1,000) secondary antibodies in blocking buffer overnight in 4°C. Brains were then rinsed 5 times at 15 min intervals in PBS-Triton-X 0.5% before mounting in Vectashield mounting media (Vector Laboratories). Sample slides were imaged using a Leica SP8 confocal microscope. We reproduced the TIM and CRY-GFP experiments published in Au et al. (2022), Current Biology and pooled the data with the earlier data for the results and updated total *n*'s reported in **Figures 1**, **2**. The *n*'s for the new data added to the earlier data are: for ZT 5: DmCRY: 7, AeCRY1: 4, AgCRY1: 9, *cry-null*: 7; for ZT 11: DmCRY: 10, AeCRY1: 4, AgCRY1: 7, *cry-null*: 7; for ZT 17: DmCRY: 4, AeCRY1: 16, AgCRY1: 15, *cry-null*: 12; for ZT 23: DmCRY: 10, AeCRY1: 14, AgCRY1: 22, *cry-null*: 18.

Confocal microscopy and image processing

For the data in **Figures 1**, **2**, brain samples were imaged with a Leica SP8 confocal microscope with 594 nm antibody fluorescence for TIM signal and 488 nm CRY-GFP signal. FIJI/ImageJ analysis software was utilized for quantification of ventral lateral neuronal. Maximum intensity projections were generated using the Z stack tool. Fluorescent quantification of TIM and CRY-GFP signal were obtained by marking regions-of-interest on LNv (small and large LNvs) soma identified by morphology and anatomical positioning within each brain sample. Fluorescent values for the total number of neurons in a brain are normalized to the background brain fluorescence, then measurements of all neurons from all brain samples are averaged together.

Light-evoked neuronal electrophysiology

Previously established whole-cell current-clamp protocols from Baik et al. (2019a) were modified to run our light-evoked potential electrophysiology experiments. Adult male fly brains were dissected in external recording solution consisting of: 122 mM NaCl, 3 mM KCl, 1.8 mM $CaCl_2$, 0.8 mM $MgCl_2$, 5 mM glucose, 10 mM HEPES, 7.2 pH, and calibrated to an osmolarity of 250–255 mOsm. The internal recording solution consists of: 102 mM Kgluconate, 17 mM NaCl, 0.085 mM $CaCl_2$, 1.7 mM $MgCl_2$ (hexahydrate), 8.5 mM HEPES, 0.94 mM EGTA, 7.2 pH, and is calibrated to an osmolarity of 232–235 mOsm. Custom multichannel LED source (Prizmatix/Stanford Photonics, Palo Alto, CA, United States) fitted to the Olympus BX51 WI microscope was used as the primary light source for our electrophysiology experiments. LED peak wavelengths are as follows: UV (365 nm), violet (405 nm), blue (450 nm), and red (635 nm), and all exposures were set to an intensity of 200 $\mu W/cm^2$ by use of a Newport 842-PE Power/Energy meter. Each LED was triggered on and off for each sweep with TTL pulses programmed by pClamp (Molecular Dynamics) data acquisition software. The light-evoked potential protocol is as follows: 50 s of dark for baseline recording, 5 s of colored-light stimulation, then 95 s of inter-pulse darkness for recovery back to baseline. The protocol repeats five times per recording. For analysis, sweeps are averaged, and baseline adjusted to pre-pulse signal, then low-pass noise filtered using Gaussian and Butterworth filters in the ClampFit 10 software (Molecular Dynamics). Our light-evoked potential protocol captures averaged light-evoked changes in membrane potential (Fogle et al., 2011; Baik et al., 2019a; Au et al., 2022), thus providing a kinetically robust light-evoked potential.

Light attraction/avoidance behavioral assay

Standard LD light choice assays were conducted using behavioral protocols developed in previous studies

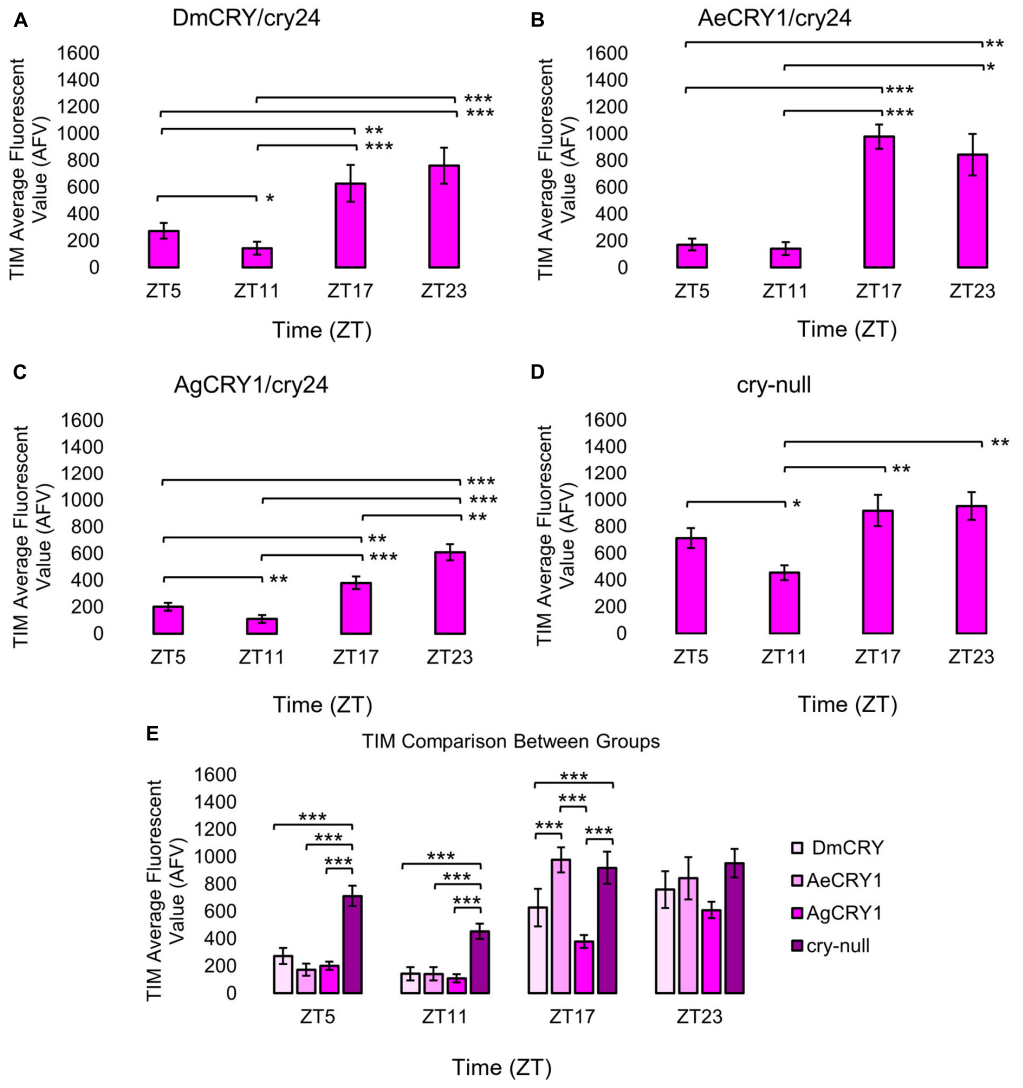

FIGURE 1
Transgenic mosquito CRY1 expression does not alter the overall pattern of cyclic TIM expression. Immunocytochemistry average fluorescent value of TIM expression over 12:12 h LD at ZT5, 11, 17, and 23 time points in LNvs (small + large) expressing **(A)** DmCRY (ZT5, n = 38; ZT11, n = 26; ZT17, n = 29; ZT23, n = 33), **(B)** AeCRY1 (ZT5, n = 15; ZT11, n = 10; ZT17, n = 26; ZT23, n = 26), **(C)** AgCRY1 (ZT5, n = 29; ZT11, n = 27; ZT17, n = 37; ZT23, n = 44), and **(D)** negative control *cry-null* (ZT5, n = 41; ZT11, n = 26; ZT17, n = 29; ZT23, n = 52). Fluorescent quantification of TIM signal was obtained by marking regions-of-interest on LNv soma identified by morphology and anatomical positioning within each brain sample. Fluorescent values for the total number of neurons in a brain are normalized to the background brain fluorescence, then measurements of all neurons from all brain samples are averaged together. **(E)** Comparison summary between genotypes for each time point measurement of average TIM fluorescence. Mann-Whitney *U*-tests with FDR adjustment were performed for statistical comparison. Data are represented as mean ± SEM for. *$p \leq 0.1$, **$p \leq 0.05$, ***$p \leq 0.01$.

(Baik et al., 2017; Au et al., 2022). The locomotor activity of individual flies was measured using the TriKinetics Locomotor Activity Monitoring System via dual infrared beam-crossing, recording total crosses in 1-min bins. Individual flies housed on glass tubes have a choice of exposure to a lighted side or in a dark side blocked by aluminum foil of the two infrared sensor tube. Percentage activity and statistics were measured using Microsoft Excel. Custom LED fixtures were built using Waveform Lighting blue and red LEDs with a narrow peak wavelength of 450 and 405 nm, respectively, and intensity-tuned to 10 and 400 μW/cm^2 for low and high intensity light exposures, respectively.

Quantification and statistical analysis

All reported values are represented as mean ± SEM. Values of n refer to the total number of experimental flies tested over all replicates of an experiment (minimum

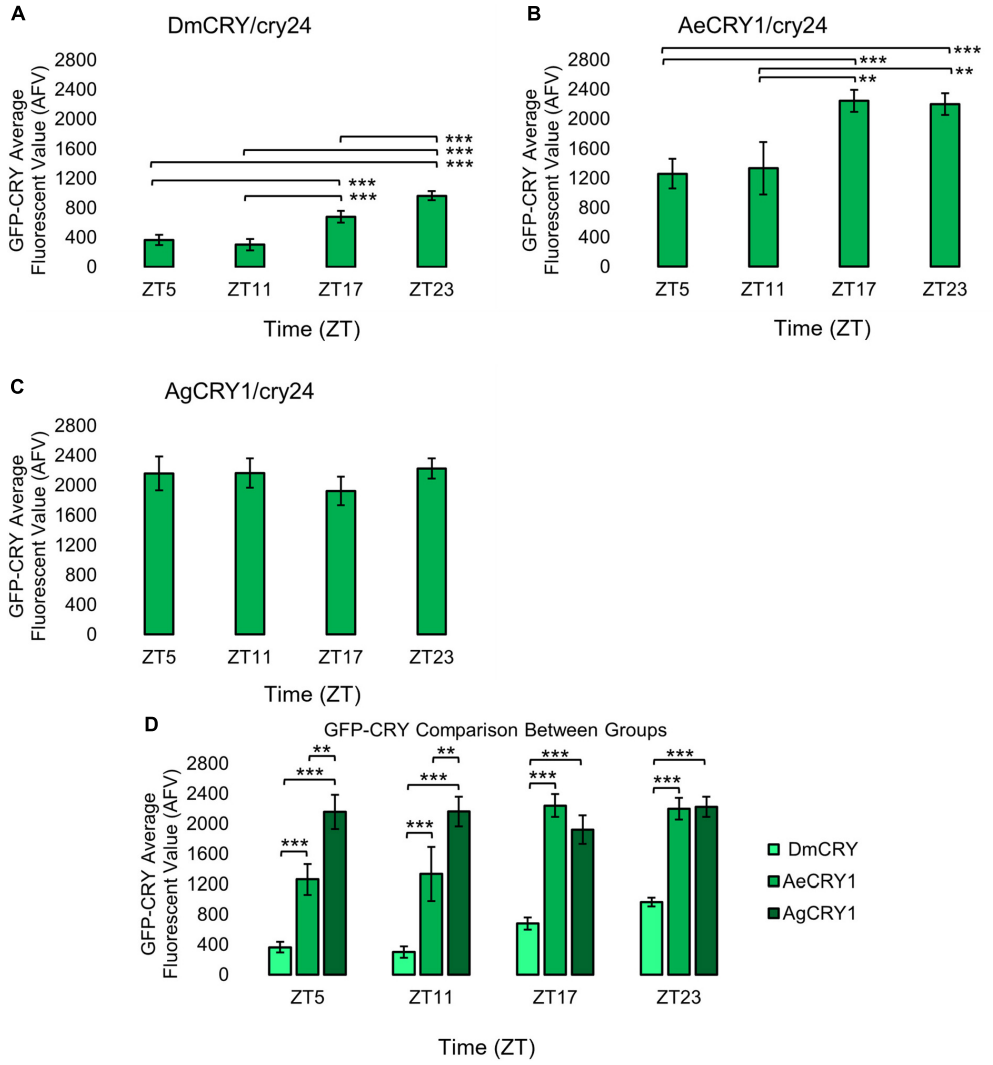

FIGURE 2
AeCRY1 and DmCRY shows lower protein levels during day and higher GFP-CRY during night, while AgCRY1 expression remains high throughout all time points. Immunocytochemistry average fluorescent value of GFP-CRY expression over 12:12 h LD at ZT5, 11, 17, and 23 time points in LNvs (small + large) expressing **(A)** DmCRY (ZT5, n = 38; ZT11, n = 26; ZT17, n = 29; ZT23, n = 33), **(B)** AeCRY1 (ZT5, n = 15; ZT11, n = 10; ZT17, n = 26; ZT23, n = 26), and **(C)** AgCRY1 (ZT5, n = 29; ZT11, n = 27; ZT17, n = 37; ZT23, n = 44). Fluorescent quantification of GFP-CRY signal was obtained by marking regions-of-interest on LNv soma identified by morphology and anatomical positioning within each brain sample. Fluorescent values for the total number of neurons in a brain are normalized to the background brain fluorescence, then measurements of all neurons from all brain samples are averaged together. **(D)** Comparison summary between genotypes for each time point measurement of average GFP-CRY fluorescence. Mann-Whitney U-tests with FDR adjustment were performed for statistical comparison. Data are represented as mean ± SEM. *$p \leq 0.1$, **$p \leq 0.05$, ***$p \leq 0.01$.

of three replicates). Firing frequency values are calculated as a ratio of spikes during the 5 s of lights on/average baseline firing rate binned in 10 s increments. Statistical tests were performed using Minitab, Matlab, and Microsoft Excel software. Statistical analysis began with performing an Anderson-Darling normality tests to determine normality of data. Variance was determined using F-tests for normally distributed data, then significance was determined using two-sample, one-tailed T-tests with alpha values of 0.5 before pairwise correction. Significance for non-normal data was determined by Mann-Whitney U-tests. Spike firing and membrane potential quantifications were performed using custom Matlab scripts and Clampfit software. Multi-comparison tests leading to Type I error/false positives were mitigated by a more stringent test of p-value adjustment based on false discovery rate (FDR, Benjamini and Hochberg, 1995, see also Au et al., 2022). A standard FDR threshold of 0.1 was then implemented in order to indicate significance as an expected proportion of false positives that is no greater than 10%.

Results

Anopheles gambiae and *Aedes aegypti* expression is not sufficient to alter diurnal/nocturnal behavior or stop circadian rhythmicity

Diurnal *Aedes aegypti* (*Ae. aegypti*) and nocturnal *Anopheles gambiae* (*An. gambiae*) mosquitoes are anthropophilic mosquitoes that occupy opposite day/night temporal niches. To determine whether heterologous CRY1 expression might disrupt the circadian clock, we compared circadian behavior in constant darkness (DD) in UAS-flies on a *cry-null* background expressing either *Drosophila* CRY (DmCRY), AeCRY1, AgCRY1 under the *crypGAL4-24* (drives expression in all cells that ordinarily express CRY, Zhao et al., 2003) vs. negative control *cry-null* flies using two white light intensities of 1 and 400 lux. The expression of AgCRY1 is not sufficient to confer nocturnal activity at either 1 or 400 lux white light (**Figures 3**, **4**) in *Drosophila*, in contrast to the robust nocturnal behavior seen in Anopheles mosquitoes (Baik et al., 2020). For low-intensity 1 lux LD entrainment, there are no significant differences in % rhythmicity between DmCRY, AeCRY1, and AgCRY1 expressing flies (**Figure 3**). In contrast, *cry-null* flies show significantly less % rhythmicity relative to DmCRY,

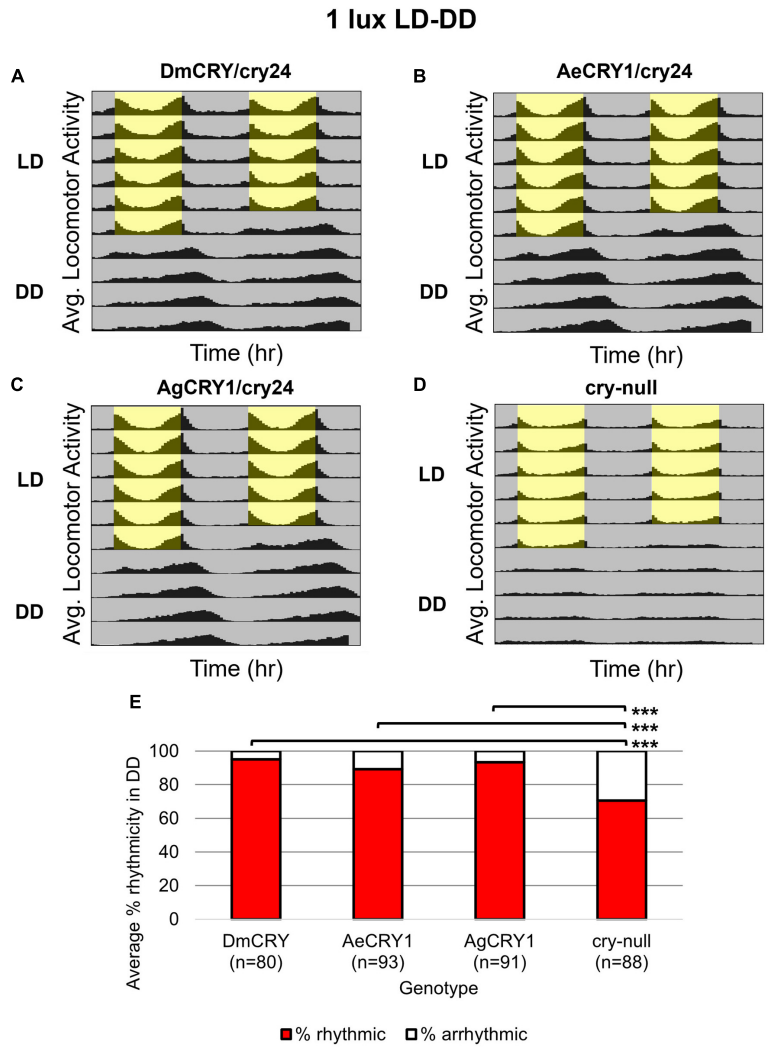

FIGURE 3
AgCRY1, AeCRY1 expressing flies and control groups maintain high rhythmicity in constant dark conditions after entrainment in low 1 lux LD white light. **(A–D)** Actogram plots containing 5 days of 12:12 h LD entrainment in 1 lux white light conditions followed by 5 days of constant dark (DD) conditions for flies expressing: **(A)** DmCRY (n = 80; $\tau_{avg,DD} \approx 24.7$, $power_{avg,DD} \approx 125.3$, $width_{avg,DD} \approx 4.5$), **(B)** AeCRY1 ($n$ = 93; $\tau_{avg,DD} \approx 24.8$, $power_{avg,DD} \approx 150.6$, $width_{avg,DD} \approx 5.0$), **(C)** AgCRY1 ($n$ = 91; $\tau_{avg,DD} \approx 25.1$, $power_{avg,DD} \approx 137.8$, $width_{avg,DD} \approx 5.1$), **(D)** *cry-null* ($n$ = 88; $\tau_{avg,DD} \approx 23.8$, $power_{avg,DD} \approx 90.5$, $width_{avg,DD} \approx 3.9$). **(E)** Quantification of fly rhythmicity (red) to arrhythmicity (white) in DD. Pairwise t-tests were used to determine significance: $*p \leq 0.1$, $**p \leq 0.05$, $***p \leq 0.01$.

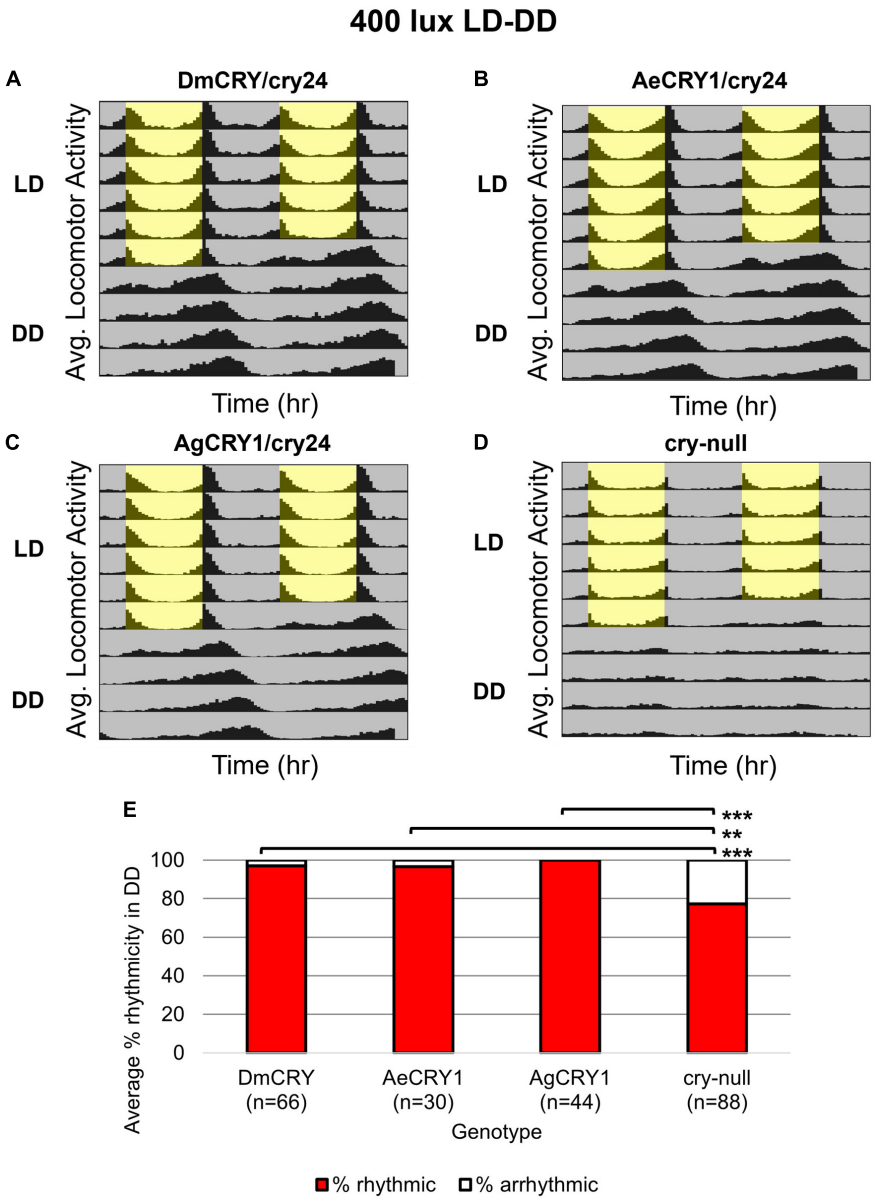

FIGURE 4
AgCRY1, AeCRY1 expressing flies and control groups maintain high rhythmicity in constant dark conditions after entrainment in moderately high 400 lux LD white light. **(A–D)** Actogram plots containing 5 days of 12:12 h LD entrainment in 400 lux white light conditions followed by 5 days of constant dark (DD) conditions for flies expressing: **(A)** DmCRY (n = 66; $\tau_{avg,DD}\approx$24.7, $power_{avg,DD}\approx$153.2, $width_{avg,DD}\approx$4.9), **(B)** AeCRY1 (n = 30; $\tau_{avg,DD}\approx$24.6, $power_{avg,DD}\approx$160.3, $width_{avg,DD}\approx$5.0), **(C)** AgCRY1 (n = 44; $\tau_{avg,DD}\approx$25.4, $power_{avg,DD}\approx$137.0, $width_{avg,DD}\approx$4.9), **(D)** *cry-null* (n = 88; $\tau_{avg,DD}\approx$23.6, $power_{avg,DD}\approx$84.5, $width_{avg,DD}\approx$3.3). **(E)** Quantification of fly rhythmicity (red) to arrhythmicity (white) in DD. Pairwise t-tests were used to determine significance: *$p \leq 0.1$, **$p \leq 0.05$, ***$p \leq 0.01$.

AeCRY1, and AgCRY1 expressing flies (Figure 3). Similarly, at the higher-intensity 400 lux LD entrainment, there are no significant differences in % rhythmicity between DmCRY, AeCRY1, and AgCRY1 expressing flies, while again *cry-null* flies show significantly less % rhythmicity relative to DmCRY, AeCRY1, and AgCRY1 expressing flies (Figure 4). Thus, AgCRY1 nor AeCRY1 expression disrupts the circadian clock in *Drosophila*. Further analysis shows that AgCRY1 expressing flies show significantly longer period length (tau, τ) in constant darkness compared with DmCRY, AeCRY1, and *cry-null* following 1 and 400 lux light entrainment (Supplementary Figure 1) and that *cry-null* flies show significantly shorter period length than DmCRY, AeCRY1, and AgCRY1 expressing flies following 1 and 400 lux light entrainment (Supplementary Figure 1). Further, AgCRY1 expressing flies show significantly less morning anticipatory behavior and significantly greater

evening anticipatory behavior compared with DmCRY, AeCRY1, and *cry-null* during 1 and 400 lux light entrainment (**Supplementary Figure 2**). In an earlier paper, we also found that circadian clock function measured by free running behavior in constant darkness and morning anticipatory behavior are not well correlated (Sheeba et al., 2010). Previous work from the Helfrich-Forster group concluded that eye photoreceptor inputs are primarily responsible for modulating morning anticipation in the absence of a functional circadian clock (Schlichting et al., 2015). However, the present results suggest that Cryptochromes may also modulate morning and evening anticipation, and perhaps this is not surprising that Cryptochromes from opposing temporal niches for diurnal vs. nocturnal animals might drive differences in anticipatory behavior.

Upon photoactivation, DmCRY resets the circadian molecular clock by binding with the clock protein TIMELESS (TIM) and setting it for degradation (Emery et al., 1998; Stanewsky et al., 1998; Koh et al., 2006). The circadian clock cycles in anti-phase fashion comparing diurnal *Aedes* mosquitoes (PER levels in the s-LNv peak at ZT23) vs. nocturnal *Anopheles* mosquitoes (PER levels in the s-LNv peak at ZT11, Baik et al., 2020). To determine if diurnal AeCRY1 or nocturnal AgCRY1 is sufficient to set the circadian clock to its peak timing of TIM protein expression, transgenic flies were entrained for at least 3 days of 12:12 h Light: Dark (LD) and immunocytochemistry experiments were used to measure TIM levels at time points ZT5, ZT11, ZT17, and ZT23. Fluorescent TIM signals were quantified in the ventral lateral neuronal subgroup (LNvs) and showed peak signal at ZT23 and the lowest signals at ZT5 and ZT11 for control DmCRY, AeCRY1, and AgCRY1 expressing flies (**Figures 1A–C**). Negative control *cry-null* flies show a similar TIM expression pattern in the LNvs (**Figure 1D**). Fluorescent measurements of TIM signal during ZT17 are significantly different and are more than twofold greater in flies expressing AeCRY1 than AgCRY1, suggesting diurnal AeCRY1 is less light sensitive than nocturnal AgCRY1. However, TIM signal at ZT5, ZT11, and ZT23 does not differ between AeCRY1 and AgCRY1 flies (summary of TIM measurements, **Figure 1E**). Transgenic expression of mosquito CRY1 in flies also includes N-terminal fusion of eGFP for protein expression verification. DmCRY expression measured by eGFP signal shows low expression during ZT5 and ZT11 with peak expression during ZT23 (**Figure 2A**). AeCRY1 expression is markedly higher than DmCRY, but exhibits a similar cycling pattern with ZT5 and ZT11 showing the lowest protein levels, and ZT17 and ZT23 showing the highest protein levels (**Figure 2B**). AgCRY1 protein expression is consistently high during all time points (**Figure 2C**), but the levels are within an order of magnitude compared with DmCRY and AeCRY1 protein expression levels (summary of CRY-GFP measurements, **Figure 2D**). In summary, AeCRY1 and AgCRY1 expression in flies does not disrupt the circadian clock nor alter the timing of the TIM expression peak. Between genotype differences in absolute protein levels may be due to codon usage or differences in protein stability of different CRY proteins.

Anopheles gambiae and *Aedes aegypti* mediate blue-light-evoked increases in electrophysiological action potential firing frequency

Drosophila ventral lateral neurons are circadian/arousal neurons that drive CRY-dependent acute electrophysiological light responses (Holmes et al., 2007; Sheeba et al., 2008b; Fogle et al., 2011, 2015; Giachello et al., 2016; Baik et al., 2017, 2019a; Hong et al., 2018; Au et al., 2022). We expressed AeCRY1, AgCRY1, and control DmCRY in *cry-null* genetic background flies with the UAS/GAL4 expression system, then measured the light on/light off ratio of action potential firing frequency in response to 200 $\mu W/cm^2$ 450 nm blue-light from whole-cell patch-clamp recordings of l-LNvs in transgenic flies. For these experiments, we used the *crypGAL4-24* driver line that drives expression in all CRY neurons (Zhao et al., 2003).

Positive control DmCRY expression driven by the *crypGAL4-24* line mediates robust and significant increases in action potential firing frequency (FF) in the l-LNvs in response to 200 $\mu W/cm^2$ blue-light (450 nm) relative to *cry-null* negative controls (**Figure 5A**, blue column vs. gray column) and mediates significant sustained increases in firing frequency in response to blue-light (**Figure 5A**). AeCRY1 driven by the *crypGAL4-24* line also shows significant increases in FF in the l-LNvs in response to 200 $\mu W/cm^2$ blue-light relative to *cry-null* negative controls (**Figure 5A**, orange column vs. gray column). However, after adjusting for false discovery rate (FDR), there is no significance difference observed between these two groups. This is unlike AgCRY1 driven by the *crypGAL4-24* line, which shows robust and significant increases in FF in the l-LNvs in response to 200 $\mu W/cm^2$ blue-light relative to *cry-null* negative controls (**Figure 5**, purple column vs. gray column) even after adjusting for FDR, suggesting a greater blue light response for AgCRY1 compared to AeCRY1. Further, the AgCRY1 blue-light FF response does not significantly differ from the DmCRY blue-light FF response (purple column vs. blue column, **Figure 5A**). Comparing the 200 $\mu W/cm^2$ blue-light-evoked FF ratio during stimulus and subsequent 10 s bins post-stimulus up to 40 s, AgCRY1 FF is significantly greater than AeCRY1 FF 30 s post-stimulus (**Figure 5E**), but again, does not show significance after FDR adjustment. The positive control DmCRY FF is significantly greater than the *cry-null* negative control FF during stimulus and at the 10 and 30 s bins (**Figure 5B**).

Previous work shows that light activated CRY mediates changes in membrane potential through the voltage gated

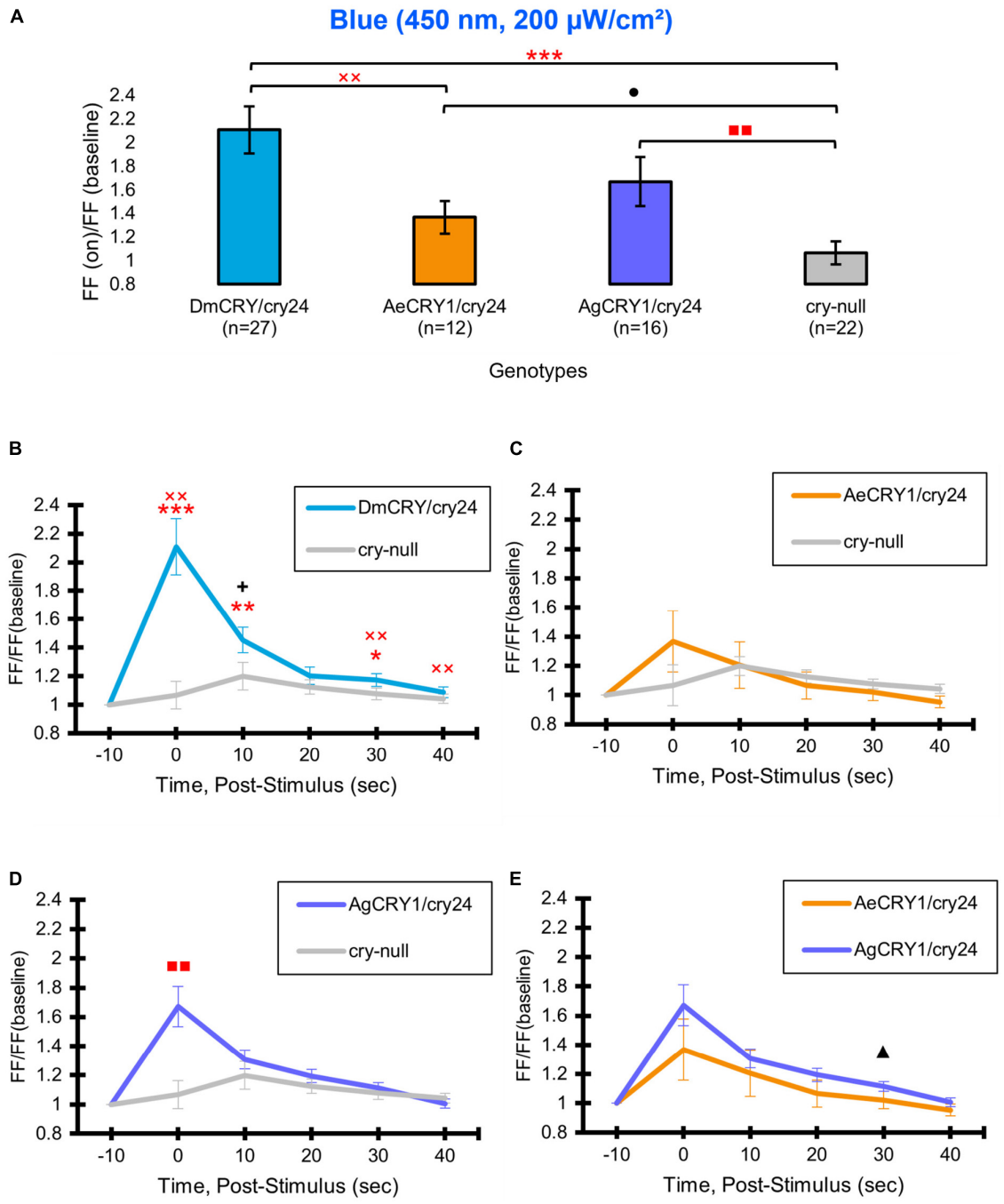

FIGURE 5
AeCRY1 and AgCRY1 mediate electrophysiological responses to blue-light. Light-evoked **(A)** FF ratio comparison of blue-light (450 nm, 200 µW/cm^2) excited l-LNvs expressing: DmCRY (blue, n = 27) and negative control cry-null (gray, n = 22), AeCRY1 (orange, n = 12), and AgCRY1 (purple, n = 16). Light-evoked **(B–E)** post-stimulus FF comparison of blue-light (450 nm, 200 µW/cm^2) excited l-LNvs expressing: DmCRY (blue, n = 27) and negative control cry-null (gray, n = 22), AeCRY1 (orange, n = 12), and AgCRY1 (purple, n = 16). Traces represent the average last 60 s of each recording for **(B)** DmCRY vs. cry-null, **(C)** AeCRY1 vs. cry-null, **(D)** AgCRY1 vs. cry-null, and **(E)** AeCRY1 vs. AgCRY1. Black + indicates two-sample t-test $p \leq 0.05$ between AgCRY1/cry24 and DmCRY/cry24. Black ▲ indicates two-sample t-test $p \leq 0.05$ between AgCRY1/cry24 and AeCRY1/cry24. Black • indicates two-sample t-test $p \leq 0.05$ between AeCRY1/cry24 and cry-null. Red * indicates FDR adjusted $p \leq 0.1$ between DmCRY/cry24 and cry-null. Red x indicates $p \leq 0.1$ between AeCRY1/cry24 and DmCRY/cry24. Red ■ indicates FDR adjusted $p \leq 0.1$ between AgCRY1/cry24 and cry-null. Data are represented as mean ± SEM. For black significance symbols: One symbol; $p \leq 0.05$, two symbols; $p \leq 0.005$, three symbols; $p \leq 0.001$. For red significance symbols: One symbol; $p \leq 0.1$, two symbols; $p \leq 0.05$, three symbols; $p \leq 0.01$.

potassium channel beta subunit and modulation of potassium channels (Fogle et al., 2011, 2015; Giachello et al., 2016; Baik et al., 2017, 2018, 2019a; Hong et al., 2018; Tabuchi et al., 2021). To determine whether mosquito CRY expression alters LNv basal electrophysiological processes, we plotted basal l-LNv firing rates, basal resting membrane potential values and firing mode (tonic vs. burst firing) across the time of day of the recordings (**Figure 6**). The range of l-LNv firing rates and the average resting membrane potentials from the present set of whole-cell patch-clamp recordings for DmCRY expressing neurons are similar to previously reported values around −40 mV (the mean is −37 mV, **Figures 6B,D,F**). Basal firing rates and resting membrane potentials for DmCRY expressing flies are significantly lower than *cry-null*, AeCRY1 and AgCRY1 expressing flies (**Figures 6E,F**). The majority of the l-LNv recordings are from neurons during the day between ZT6-ZT12 and include a few recordings for the first few hours of night up until ZT16. None of the genotypes shows clear time of day differences in basal firing rate or membrane resting potential. However, these experiments were not designed to test time of day distributions as the present data cluster during midday. There are relatively few nighttime recordings and recordings from early morning and late night are not represented. Previous publications designed to test this question, including several of our own, show firing rates trending high at the beginning of day that tend to decrease at night (Cao and Nitabach, 2008; Sheeba et al., 2008b, 2010; Flourakis et al., 2015; Smith et al., 2019). Consistent with most earlier publications, we observe predominantly tonic action potential firing in l-LNv recordings (Holmes et al., 2007; Cao and Nitabach, 2008; Sheeba et al., 2008b, 2010; McCarthy et al., 2011; Seluzicki et al., 2014; Flourakis and Allada, 2015; Flourakis et al., 2015; Fogle et al., 2015; Buhl et al., 2016, 2019; Baik et al., 2017, 2019a; Li et al., 2018; Smith et al., 2019; Au et al., 2022). Burst firing as the predominant firing mode in l-LNv has been reported by another group (Muraro and Ceriani, 2015; Fernandez-Chiappe et al., 2021), however, they do not systematically address firing mode as a function of time of day.

Light-evoked averaged potentials are more kinetically reliable than light onset and CRY mediated action potential firing (Fogle et al., 2011; Baik et al., 2019a; Au et al., 2022). The blue-light-evoked response of DmCRY relative to the *cry-null* negative control shows strong depolarization then a slowly tapering sustained response over the 10 s following light stimulus offset (**Figure 7A**) with a qualitatively similar response recorded from neurons expressing AeCRY1 relative to the *cry-null* negative control (**Figure 7B**). In contrast, the blue-light-evoked response of neurons expressing AgCRY1 relative to the *cry-null* negative control show sustained significant depolarization during lights on, followed by a very long sustained depolarization response that lasts tens of seconds (**Figure 7C**). The blue-light response of AgCRY1 relative to AeCRY1 exhibits a significantly longer and more sustained membrane depolarization event lasting for tens of seconds evoked by a 5 s pulse of 200 $\mu W/cm^2$ blue-light relative to the shorter-lasting AeCRY1 evoked blue-light potential (**Figure 7D**). The significantly higher AgCRY1 blue-light-evoked depolarization for most of the duration of the evoked potential occurs after approximately 15 s post-stimulus relative to AeCRY1 (**Figure 7D**). These results, particularly the similar duration of the evoked potential blue-light response between AeCRY1 and DmCRY, suggest no direct relationship between CRY expression levels (**Figure 3**) and the magnitude of the physiological light response (**Figures 2**, **5**, **6**), confirming earlier findings concerning this (Baik et al., 2017, 2019a,b; Au et al., 2022). The AgCRY1 blue-light-evoked potential is significantly greater than that for the *cry-null* negative control for almost the entire duration up to 40 s from the stimulus onset (**Figure 7C**), while the much weaker AeCRY1 evoked potential is only significantly higher than the *cry-null* negative control for the first few seconds following stimulus onset (**Figure 7B**), but after FDR adjustment, it does not show significant differences. AgCRY1 confers a more sustained light response than DmCRY (**Figures 7A,C**). Representative voltage traces showing light-evoked depolarization and increased action potential firing frequency in patch-clamp recordings of l-LNvs during the 5 s of blue-light stimuli and 60 s post-light stimulus for positive control DmCRY/cry24, AeCRY1/cry24, AgCRY1/cry24, and negative control *cry-null* flies are shown in **Figure 8**, where the blue bar indicates 5 s of 200 $\mu W/cm^2$ 450 nm blue-light stimulus.

As expected, there are no significant differences in light-evoked FF between all four CRY genotypes in response to 200 $\mu W/cm^2$ violet-light (405 nm) (**Figure 9A**), as there is a trough of the CRY action spectra around 405 nm and Rh7 and other opsin photoreceptors are activated in this range of the color spectra (Ni et al., 2017; Sakai et al., 2017; Baik et al., 2019b). The depolarization magnitude and duration of DmCRY, AeCRY1, AgCRY1, and negative control *cry-null* responses to violet-light are similar and indistinguishable from *cry-null* and are at a lower magnitude of FF ratio and depolarization magnitude and duration relative to intensity matched blue-light stimuli (compare **Figure 9** vs. **Figure 5**). The violet-light-evoked increases in l-LNv firing frequency (**Figures 9B–E**) and light-evoked depolarization (**Figure 10**) during and after the violet-light stimulus are weak and do not differ systematically between the different CRY genotypes. These results are consistent with earlier findings that CRY is not activated by violet-light and is consistent with earlier findings that Rh7 is the primary non-image forming visual violet-light photoreceptor in LNvs (Ni et al., 2017; Sakai et al., 2017;

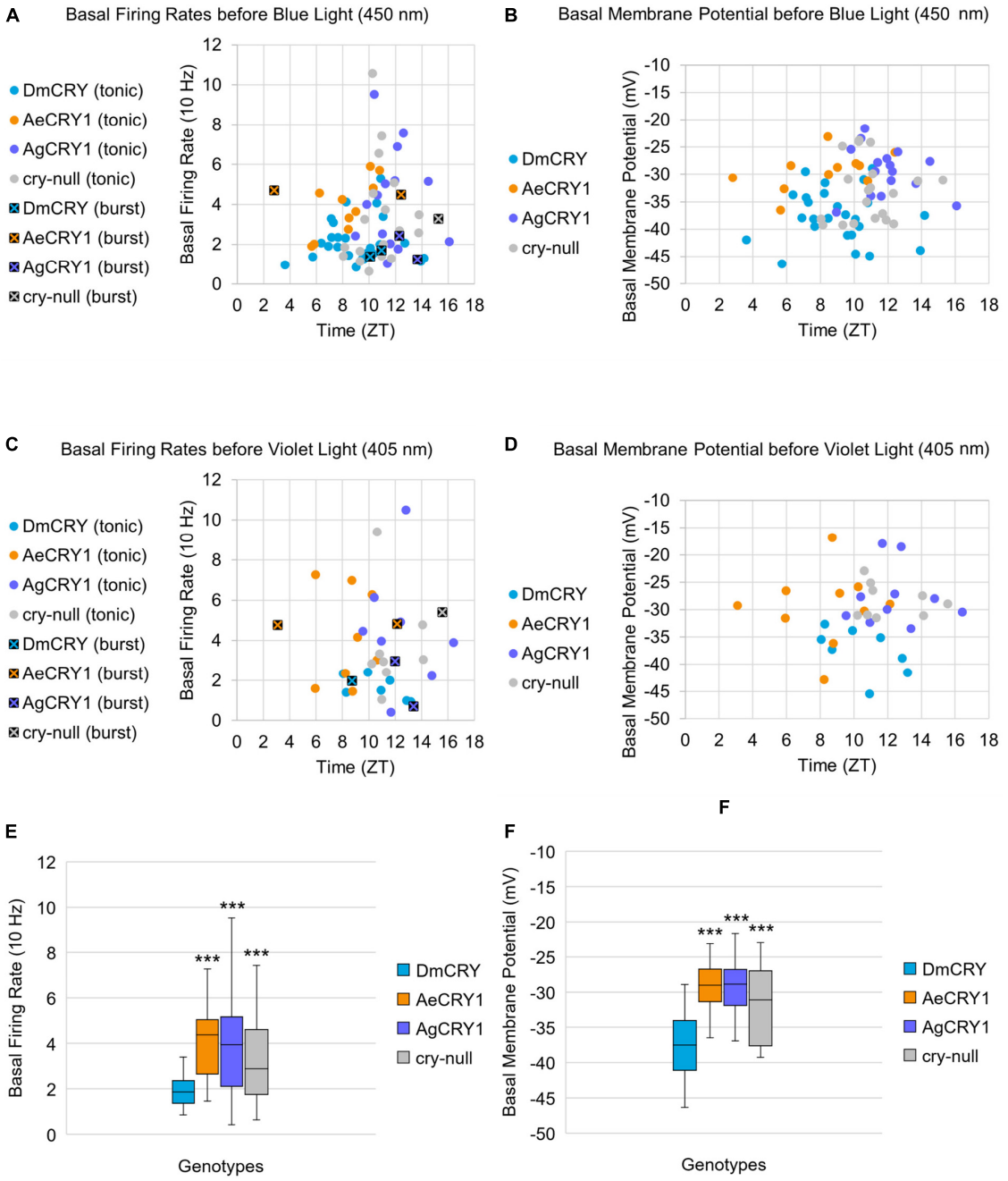

FIGURE 6
Basal firing rate and membrane potential are higher in all groups compared to the control DmCRY group and neither parameter exhibit time-of-day dependent effects. **(A)** Average basal firing rates and **(B)** average basal membrane potential before blue light stimulus plotted against the relative time-of-day of the recording for DmCRY (blue, n = 27), AeCRY1 (orange, n = 12), AgCRY1 (purple, n = 16), and *cry-null* (gray, n = 21). **(C)** Average basal firing rates and **(D)** average basal membrane potential before violet light stimulus plotted against the relative time-of-day of the recording for DmCRY (n = 8), AeCRY1 (n = 10), AgCRY1 (n = 10), and cry-null (n = 9). **(A,C)** Recordings that exhibit burst firing are denoted by a black square and cross for each respective genotype's color. **(E,F)** Box-and-whisker plot summary of the average **(E)** basal firing rate and **(F)** basal membrane potential for DmCRY [(n = 35) total, n (ZT0–12) = 30; n (ZT12–16) = 5], AeCRY1 [(n = 22) total, n (ZT0–12) = 20; n (ZT12–16) = 2], AgCRY1 [(n = 26) total, n (ZT0–12) = 14; n (ZT12–16) = 12], and *cry-null* [(n = 30) total, n (ZT0–12) = 22; n (ZT12–16) = 8]. Median values are denoted by a solid black line within each box of the plot. Black * indicates FDR adjusted two-sample t-test $p \leq 0.01$ vs. DmCRY/cry24. Data are represented as a range of means in a sample set ± maximum and minimum values within the set. One significance symbol; $p \leq 0.1$, two significance symbols; $p \leq 0.05$, three significance symbols; $p \leq 0.01$.

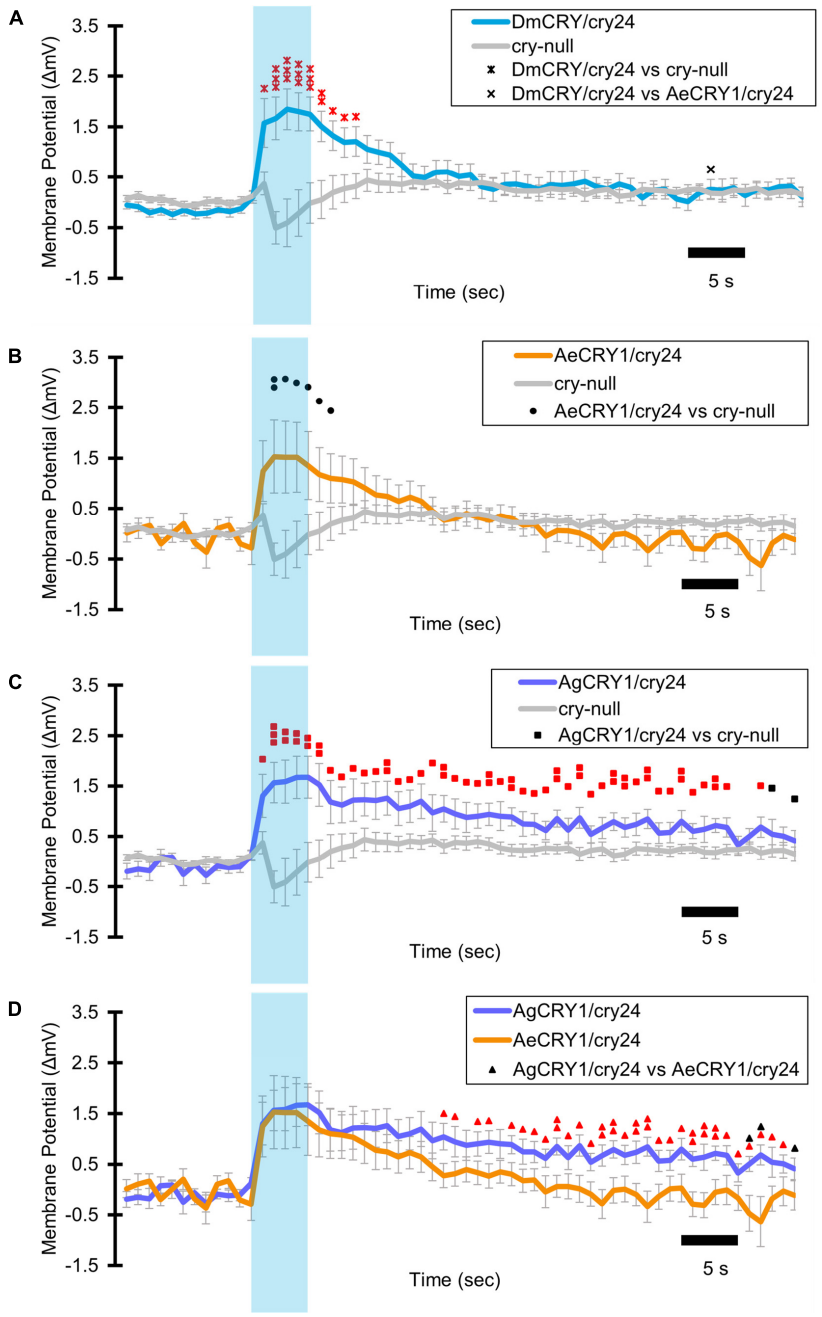

FIGURE 7
AgCRY1 mediate significantly greater and sustained membrane depolarization in responses to blue-light compared to AeCRY1. Light-evoked **(A–D)** membrane potential comparison of blue-light (450 nm, 200 μW/cm^2) excited l-LNvs expressing: DmCRY (blue, n = 27) and negative control *cry-null* (gray, n = 22), AeCRY1 (orange, n = 12), and AgCRY1 (purple, n = 16). Blue bar on membrane potential plots indicates the timing of the 5 s of blue-light stimuli and black scale-bar indicates 5 s. Traces represent the average last 60 s of each recording for **(A)** DmCRY vs. *cry-null*, **(B)** AeCRY1 vs. *cry-null*, **(C)** AgCRY1 vs. *cry-null*, and **(D)** AeCRY1 vs. AgCRY1. Black • indicates two-sample t-test $p \leq 0.05$ between AeCRY1/cry24 and *cry-null*. Black ▲ indicates two-sample t-test $p \leq 0.05$ between AgCRY1/cry24 and AeCRY1/cry24. Black **x** indicates two-sample t-test $p \leq 0.05$ between DmCRY/cry24 and AeCRY1/cry24. Black ■ indicates two-sample t-test $p \leq 0.05$ between AgCRY1/cry24 and *cry-null*. Black ▲ indicates two-sample t-test $p \leq 0.05$ between AgCRY1/cry24 and AeCRY1/cry24. Red * indicates FDR adjusted $p \leq 0.1$ between DmCRY/cry24 and *cry-null*. Red **x** indicates $p \leq 0.1$ between AeCRY1/cry24 and DmCRY/cry24. Red ■ indicates FDR adjusted $p \leq 0.1$ between AgCRY1/cry24 and *cry-null*. Red ▲ indicates FDR adjusted $p \leq 0.1$ between AgCRY1/cry24 and AeCRY1/cry24. Data are represented as mean ± SEM. For black significance symbols: One symbol; $p \leq 0.05$, two symbols; $p \leq 0.005$, three symbols; $p \leq 0.001$. For colored significance symbols: One symbol; $p \leq 0.1$, two symbols; $p \leq 0.05$, three symbols; $p \leq 0.01$.

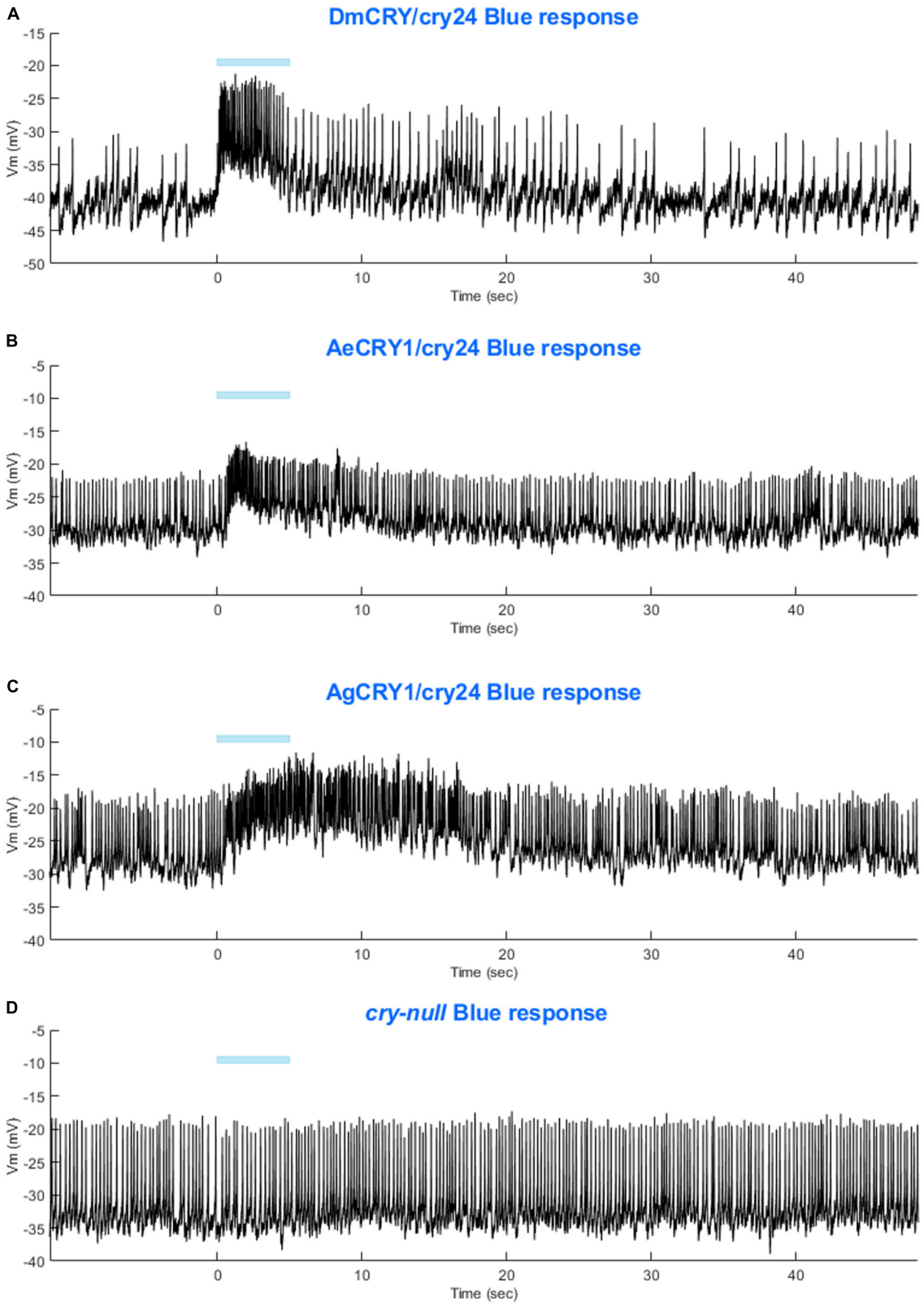

FIGURE 8
Representative voltage traces of l-LNvs electrophysiological responses to blue-light stimuli for all genotypes. Representative voltage traces of the last 60 s of a patch-clamp recording of l-LNvs subjected to 5 s of blue-light stimuli for **(A)** DmCRY/cry24, **(B)** AeCRY1/cry24, **(C)** AgCRY1/cry24, and **(D)** *cry-null* flies. Blue bar indicates 5 s of 200 $\mu W/cm^2$ blue-light stimulus.

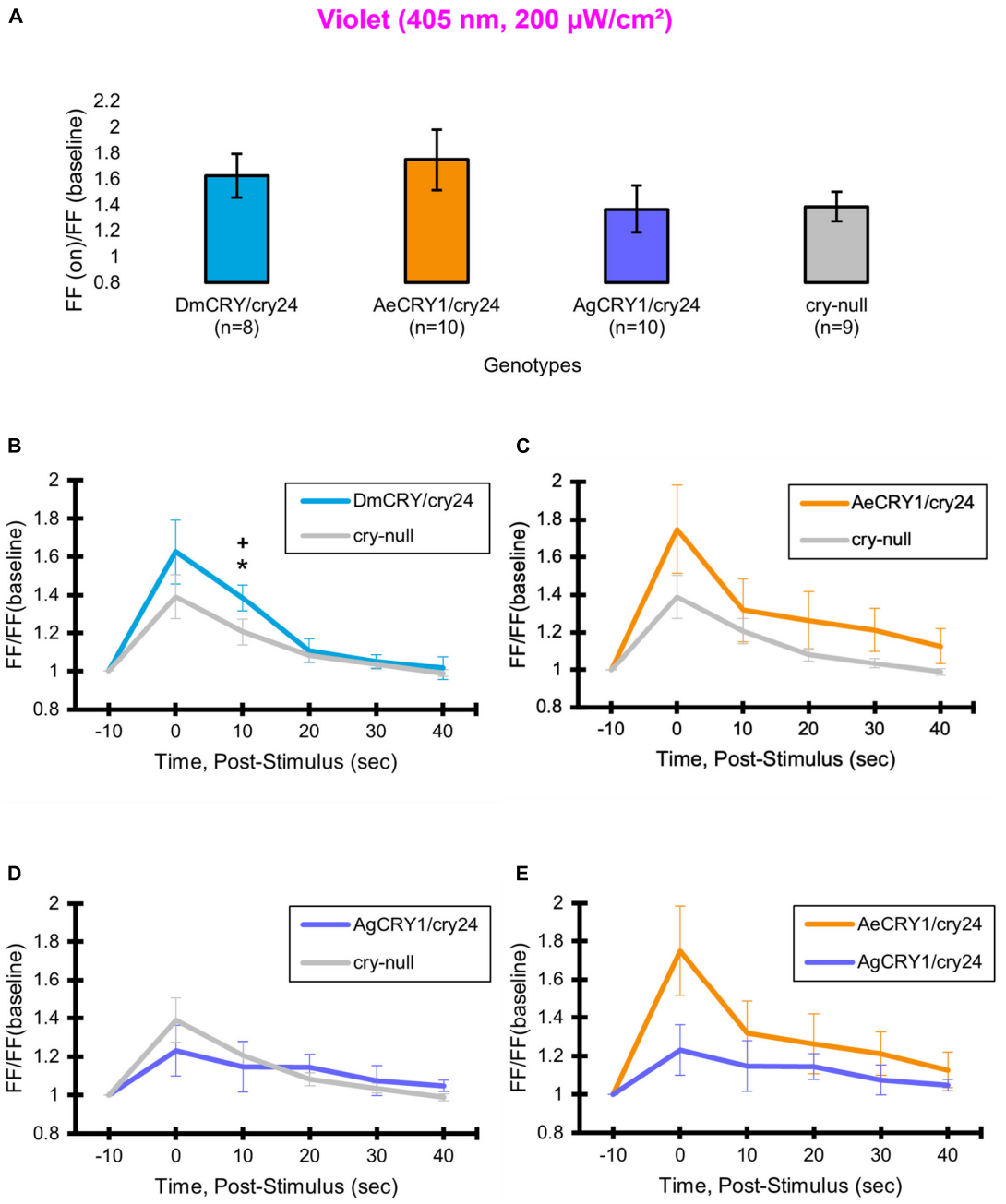

FIGURE 9
AeCRY1 and AgCRY1 FF ratios shows weak responses to violet-light. Light-evoked **(A)** FF ratio comparison of violet-light (405 nm, 200 μW/cm^2) excited l-LNvs expressing: DmCRY (blue, n = 8) and negative control cry-null (gray, n = 9), AeCRY1 (orange, n = 10), and AgCRY1 (purple, n = 10). Light-evoked **(B–E)** post-stimulus FF comparison of violet-light (405 nm, 200 μW/cm^2) excited l-LNvs expressing: DmCRY (blue, n = 8) and negative control cry-null (gray, n = 9), AeCRY1 (orange, n = 10), and AgCRY1 (purple, n = 10). Traces represent the average last 60 s of each recording for **(B)** DmCRY vs. cry-null, **(C)** AeCRY1 vs. cry-null, **(D)** AgCRY1 vs. cry-null, and **(E)** AeCRY1 vs. AgCRY1. Black * indicates two-sample t-test $p \leq 0.05$ between DmCRY/cry24 and cry-null. Black + indicates two-sample t-test $p \leq 0.05$ between AgCRY1/cry24 and DmCRY/cry24. Data are represented as mean ± SEM. For black significance symbols: One symbol; $p \leq 0.05$, two symbols; $p \leq 0.005$, three symbols; $p \leq 0.001$.

Baik et al., 2019b). Representative voltage traces showing light-evoked depolarization and increased action potential firing frequency in patch-clamp recordings of l-LNvs during the 5 s of violet-light stimuli and 60 s post-light stimulus for positive control DmCRY/cry24, AeCRY1/cry24, AgCRY1/cry24, and negative control *cry-null* flies are shown in **Figure 11**, where the violet bar indicates 5 s of 200 μW/cm^2 405 nm violet-light stimulus.

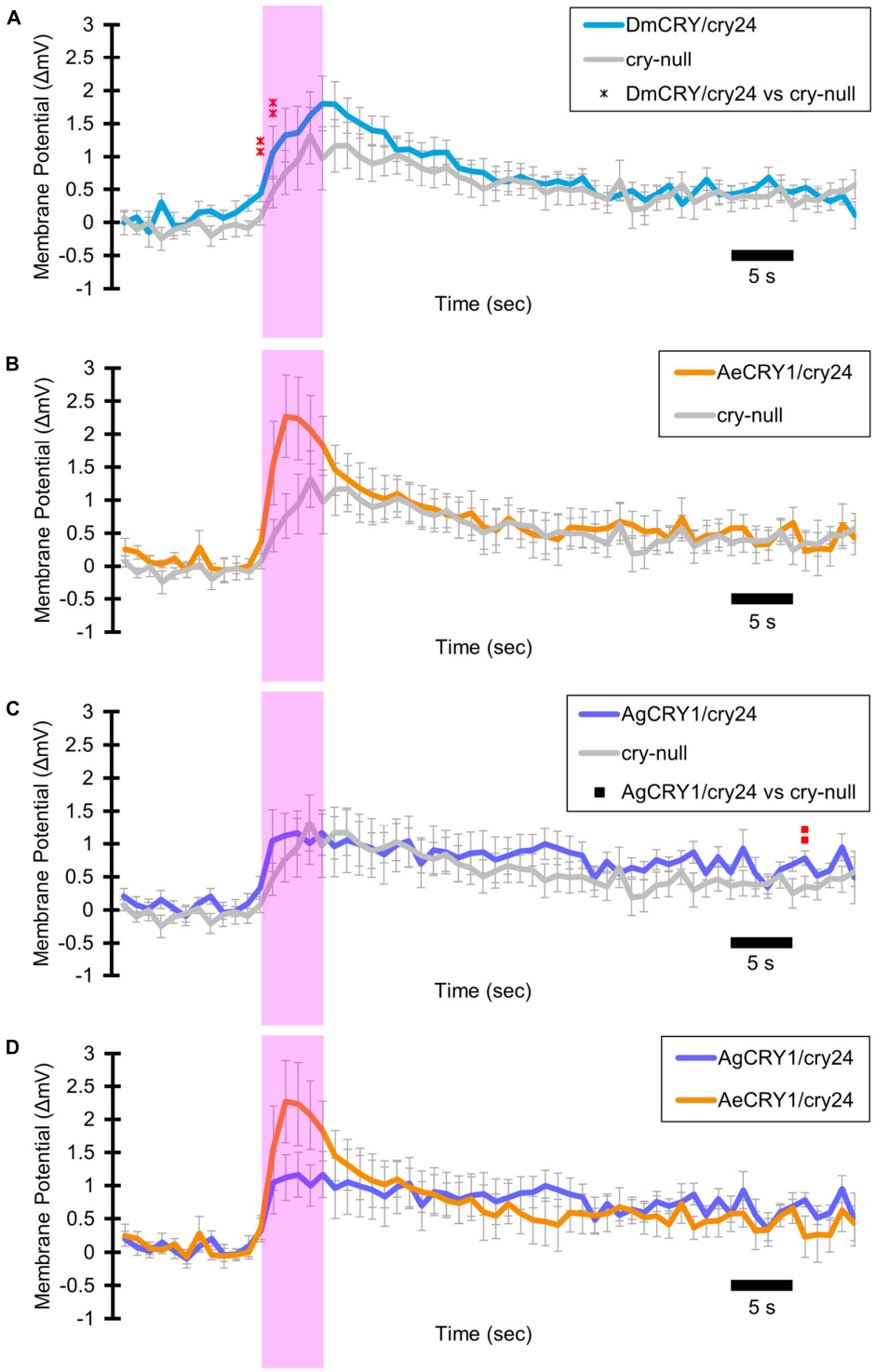

FIGURE 10
AeCRY1 and AgCRY1 RMP mediate weak membrane-evoked responses to violet-light. Light-evoked **(A–D)** membrane potential comparison of violet-light (405 nm, 200 μW/cm^2) excited l-LNvs expressing: DmCRY (blue, n = 8) and negative control cry-null (gray, n = 9), AeCRY1 (orange, n = 10), and AgCRY1 (purple, n = 10). Violet bar on membrane potential plots indicates the timing of the 5 s of violet-light stimuli and black scale-bar indicates 5 s. Traces represent the average last 60 s of each recording for **(A)** DmCRY vs. cry-null, **(B)** AeCRY1 vs. cry-null, **(C)** AgCRY1 vs. cry-null, and **(D)** AeCRY1 vs. AgCRY1. Red * indicates FDR adjusted $p \leq 0.1$ between DmCRY/cry24 and cry-null. Red ■ indicates FDR adjusted $p \leq 0.1$ between AgCRY1/cry24 and cry-null. Data are represented as mean ± SEM. For red significance symbols: One symbol; $p \leq 0.1$, two symbols; $p \leq 0.05$, three symbols; $p \leq 0.01$.

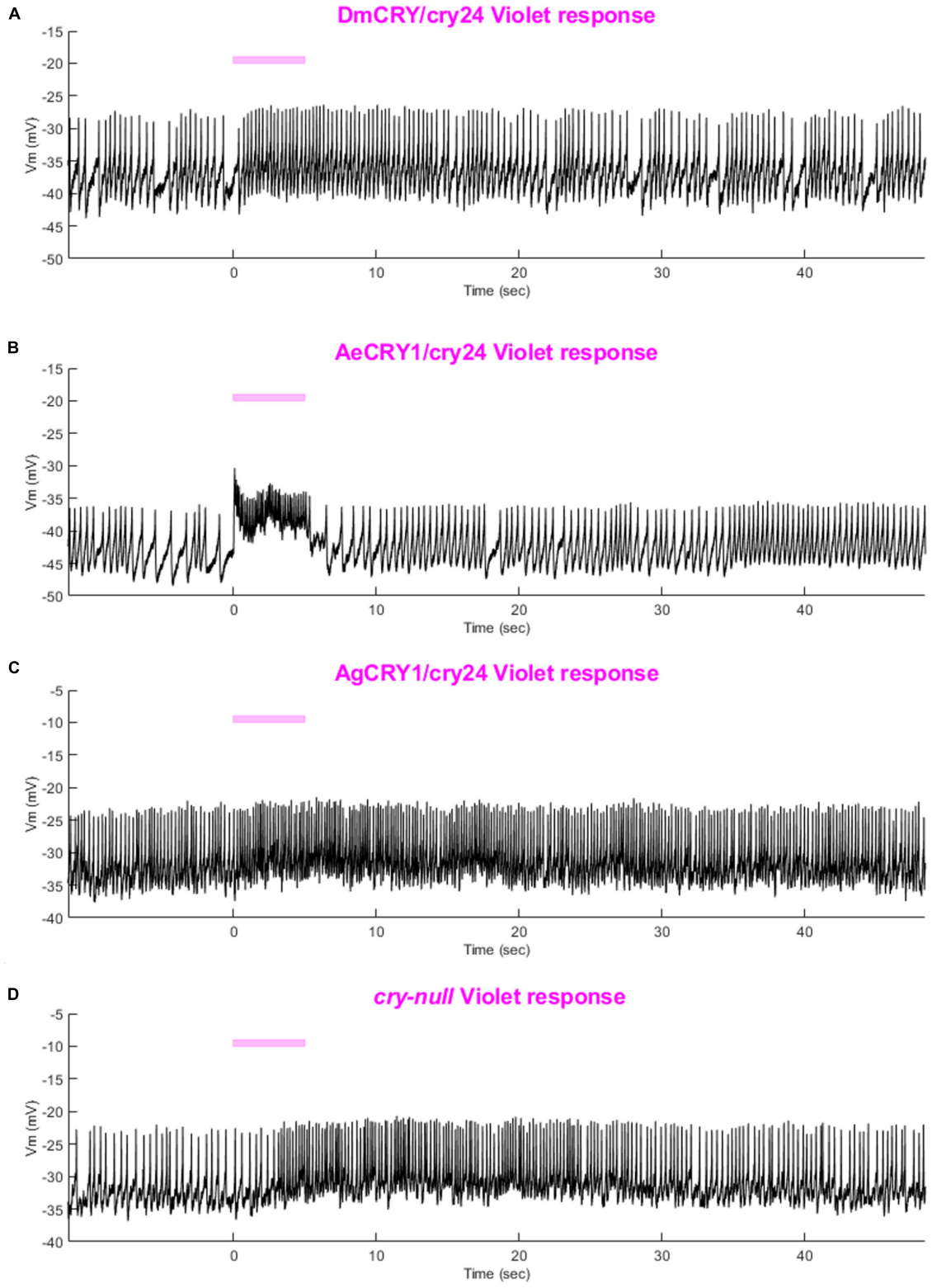

FIGURE 11
Representative voltage traces of l-LNvs electrophysiological response to violet light stimuli for all genotypes. Representative voltage traces of the last 60 s of a patch-clamp recording of l-LNvs subjected to 5 s of violet-light stimuli for **(A)** DmCRY/cry24, **(B)** AeCRY1/cry24, **(C)** AgCRY1/cry24, and **(D)** *cry-null* flies. Violet bar indicates 5 s of 200 $\mu W/cm^2$ violet-light stimulus.

Diurnal/nocturnal mosquito CRY1s confer species-specific and intensity-dependent behavioral attraction/avoidance responses to blue and violet-light

Diurnal mosquitoes are behaviorally attracted to short-wavelength light (UV, blue), while nocturnal mosquitoes behaviorally avoid short wavelength light (Baik et al., 2020). CRY1 is a strong photoreceptor candidate to drive these species-specific attraction/avoidance behavioral light responses. In our recent study Au et al. (2022) testing transgenic *Drosophila* that express diurnal AeCRY1 or nocturnal AgCRY1 in a *cry-null* genetic background, we find that AeCRY1 expressing flies show strong photo-attraction behavioral responses to a wide intensity range (1–400 $\mu W/cm^2$) of UV (365 nm) light. In contrast, nocturnal AgCRY1 expressing flies show discernable photo-attraction behavioral responses to UV light at very low intensities (1 $\mu W/cm^2$) but show significant photo-avoidance behavioral responses to higher UV light intensities (at 10 and 400 $\mu W/cm^2$ of UV light). Here, we examine the role for CRY1s for conferring day- vs. night-active mosquito species-specific light choice behaviors to other wavelengths by performing blue (450 nm) and violet (405 nm) light choice behavioral assays with flies expressing DmCRY, AgCRY1, AeCRY1 under the *crypGAL4-24* promoter at low (10 $\mu W/cm^2$) and high (400 $\mu W/cm^2$) light intensities using an environmental light choice preference test. At low intensity (10 $\mu W/cm^2$) 450 nm blue-light, *cry-null* flies show significantly greater attraction to blue-light relative to all CRY expressing fly groups (**Figures 12A–C**). Flies expressing DmCRY, AgCRY1, or AeCRY1 show weak or no behavioral attraction to low intensity blue-light (**Figures 12A–D**). The average% activity of flies in the blue lit environment over the first 30 min shows no significant differences between flies expressing DmCRY, AeCRY1, or AgCRY1 (**Figure 12E**).

In contrast, at higher intensity 400 $\mu W/cm^2$ 450 nm blue-light, the genotypes behavioral light responses diverge: DmCRY expressing flies exhibit relatively neutral responses to the blue lit environment, showing moderate photo-attraction for 15 min of blue-light exposure, then moderate photo-avoidance to 400 $\mu W/cm^2$ 450 nm blue-light for the next 15 min (**Figure 13A**). AeCRY1 expressing flies show significantly greater behavioral attraction to high intensity blue-light relative to *cry-null* and AgCRY1 expressing flies at many time points (**Figures 13B,D**). AgCRY1 expressing flies exhibit the greatest significant light avoidance to the high-intensity blue-light exposed environment relative to other genotypes (**Figures 13A–E**). This is confirmed by average% activity plots for each CRY expressing genotype showing that AeCRY1 expressing flies have significantly greater activity in higher intensity blue-light than either AgCRY1 or DmCRY, and that AgCRY1 have significantly the least amount of activity in high intensity blue-light relative to AeCRY1 or DmCRY (**Figure 13E**).

At low intensity 405 nm violet-light (10 $\mu W/cm^2$), DmCRY and AgCRY1 expressing flies both show behavioral photo-attraction to the low intensity violet lit environment (**Figures 14A,C,D**), while *cry-null* and AeCRY1 expressing flies show less behavioral photo-attraction to the violet lit environment (**Figures 14B,D**). The average% activity plots for each CRY expressing genotype shows AeCRY1 expressing flies show significantly the least behavioral activity in low intensity violet-light while DmCRY expressing flies show significantly the most behavioral activity in low intensity violet-light (**Figure 14E**). Control *cry-null* and DmCRY expressing flies both behaviorally avoid high intensity violet-light (400 $\mu W/cm^2$, **Figure 15A**), except during the first 10 min of violet-light exposure for DmCRY expressing flies. The behavioral responses to high intensity violet-light are divergent between AgCRY1 and AeCRY1 expressing flies: AgCRY1 expressing flies behaviorally avoid high intensity violet-light while AeCRY1 expressing flies are behaviorally attracted to high intensity violet-light, consistent with the previously reported general attraction of *Ae. aegypti* mosquitoes to all visible light wavelengths (**Figures 15A–E**, see also Baik et al., 2020). The average% activity plots for each CRY expressing genotype shows that AeCRY1 expressing flies show significantly the greatest behavioral activity in high intensity violet-light while AgCRY1 expressing flies show significantly the least behavioral activity in high intensity violet-light (**Figure 15E**). Taken together for responses to varying intensities of violet-light, these complex behavioral effects may be due either to direct effects through mosquito CRY proteins or possibly due to unknown CRY interactions with the major violet-light sensor Rh7 that co-expresses in the LNv subgroups to mediate multi-photoreceptor inputs for light attraction/avoidance behavioral responses (Ni et al., 2017; Baik et al., 2018, 2019b), or image forming photoreception in the eyes Altogether, these results indicate the blue and violet-light intensity-dependent light attraction/avoidance behaviors significantly diverge between AeCRY1 and AgCRY1 expressing flies and that these behavioral results are consistent with the distinct diurnal and nocturnal mosquito attraction/avoidance responses to short-wavelength light. Taken together, the data provides further support to our conclusions that CRY photoreceptors mediate species-specific physiological and behavioral light responses (Baik et al., 2020; Au et al., 2022).

Discussion

This work was motivated by our recent findings that diurnal *Ae. aegypti* mosquitoes and nocturnal *An. coluzzii* (gambiae sub-family) mosquitoes exhibit very different attraction/avoidance

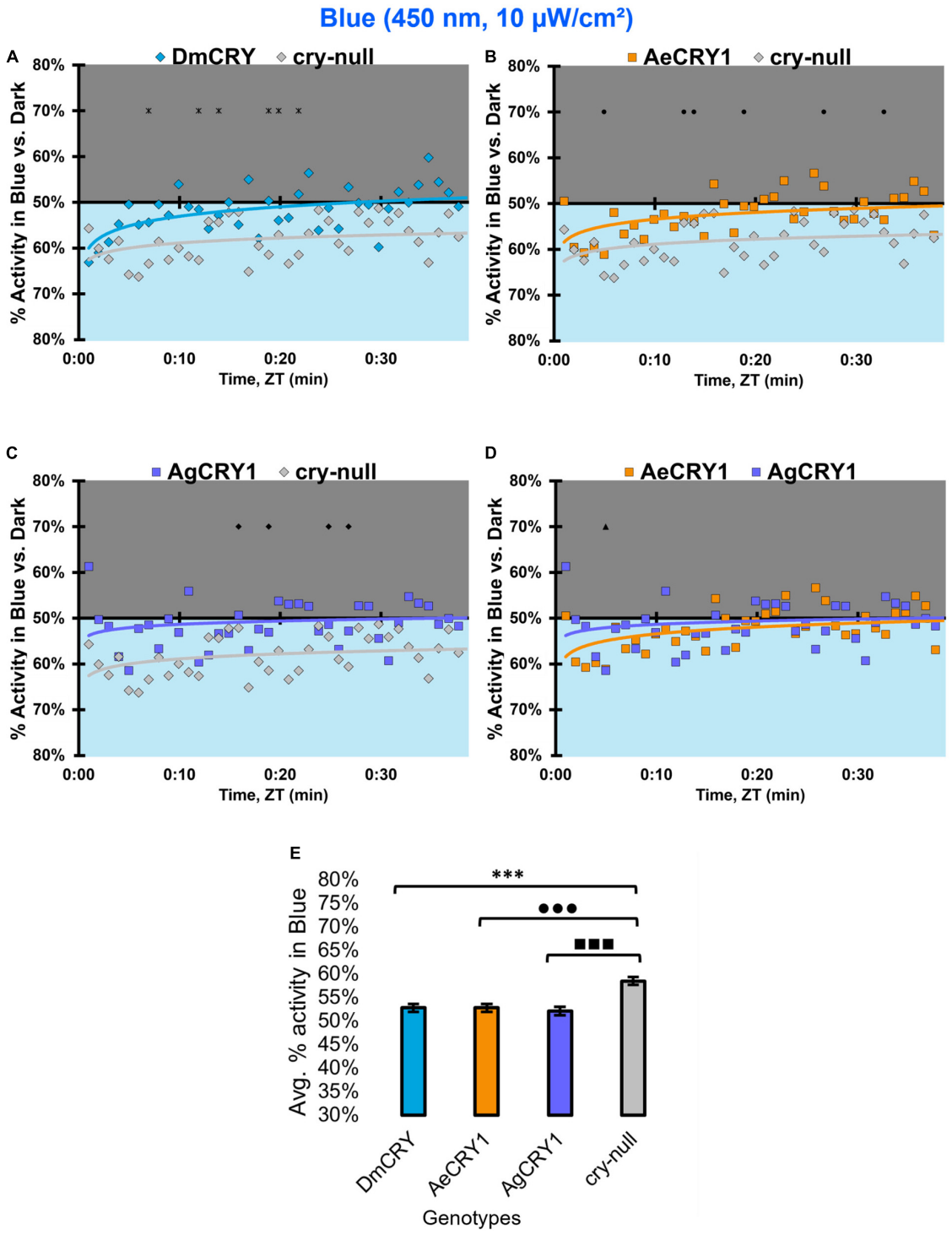

FIGURE 12
All transgenic groups exhibit little or no behavioral attraction to low-intensity blue-light. **(A–D)** Blue attraction/avoidance behavior is measured by % activity in a dark shaded environment vs. a low-intensity (10 μW/cm^2) blue-light-exposed environments (450 nm) during the light phase of a standard 12:12 h LD cycle. Preference is calculated by percentage of activity in each environment over total activity for each time bin for **(A)** DmCRY (blue, n = 53) vs. *cry-null* (red, n = 53), **(B)** diurnal AeCRY1 (orange, n = 46) vs. *cry-null*, **(C)** nocturnal AgCRY1 (purple, n = 47) vs. *cry-null*, and **(D)** AeCRY1 vs. AgCRY1. All plots are shown from ZT0 to 30 min in 1-min bins. **(E)** Quantified mean % activity of flies in blue environment across the first 30 min for low-intensity blue-light environments. Black * indicates two-sample t-test $p \leq 0.05$ between DmCRY/cry24 and *cry-null*. Black • indicates two-sample t-test $p \leq 0.05$ between AeCRY1/cry24 and *cry-null*. Black ■ indicates two-sample t-test $p \leq 0.05$ between AgCRY1/cry24 and *cry-null*. Black ▲ indicates two-sample t-test $p \leq 0.05$ between AgCRY1/cry24 and AeCRY1/cry24. Data are represented as mean ± SEM. One significance symbol; $p \leq 0.05$, two significance symbols; $p \leq 0.005$, three significance symbols; $p \leq 0.001$.

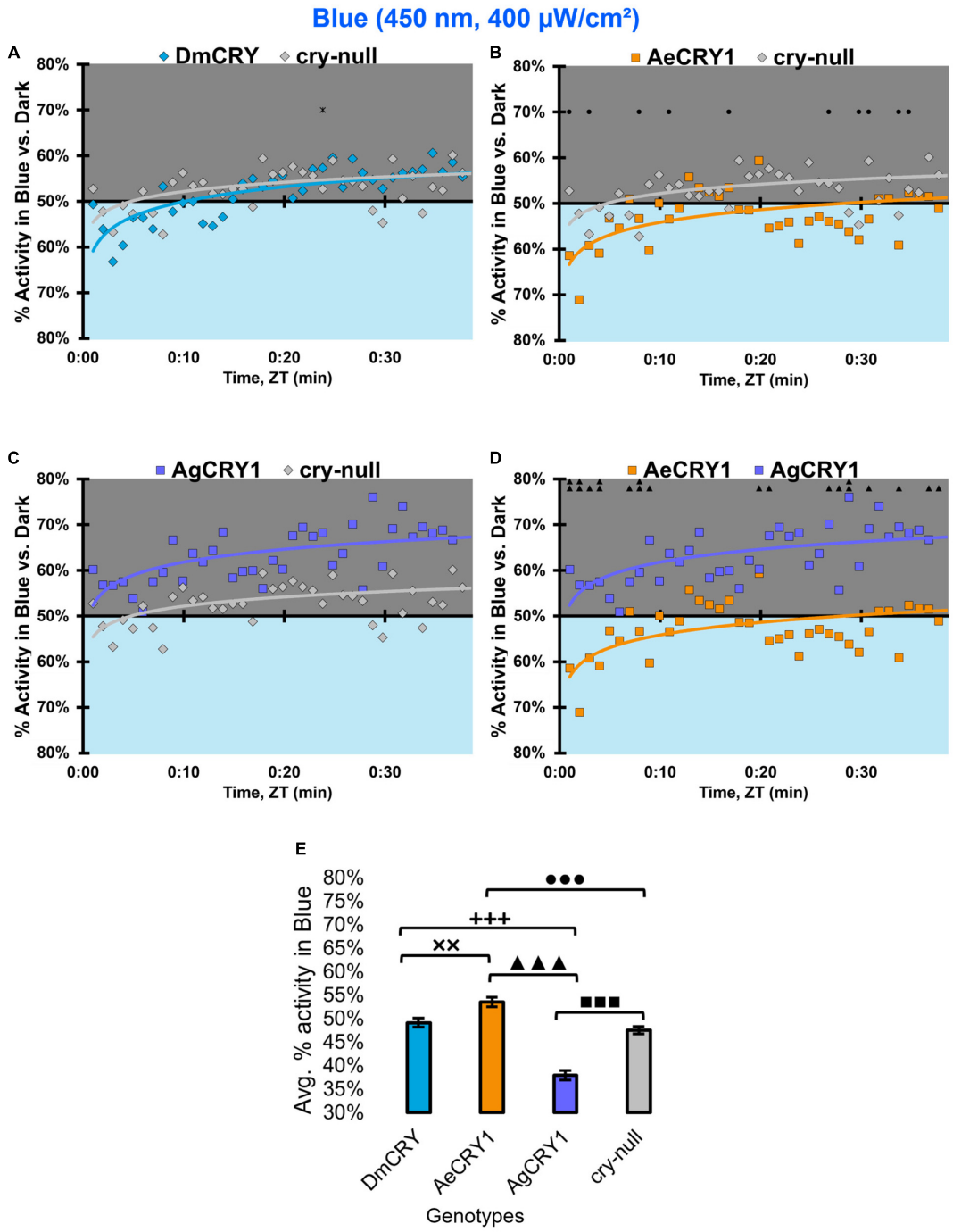

FIGURE 13
AgCRY1 flies behaviorally avoid high intensity blue-light. **(A–D)** Blue attraction/avoidance behavior is measured by % activity in a dark shaded environment vs. a high-intensity (400 µW/cm^2) blue-light-exposed environments (450 nm) during the light phase of a standard 12:12 h LD cycle. Preference is calculated by percentage of activity in each environment over total activity for each time bin for **(A)** DmCRY (blue, n = 52) vs. *cry-null* (red, n = 51), **(B)** diurnal AeCRY1 (orange, n = 39) vs. *cry-null*, **(C)** nocturnal AgCRY1 (purple, n = 46) vs. *cry-null*, and **(D)** AeCRY1 vs. AgCRY1. All plots are shown from ZT0 to 30 min in 1-min bins. **(E)** Quantified mean % activity of flies in blue environment across the first 30 min for high-intensity blue-light environments. Black * indicates two-sample t-test $p \leq 0.05$ between DmCRY/cry24 and *cry-null*. Black ■ indicates two-sample t-test $p \leq 0.05$ between AgCRY1/cry24 and *cry-null*. Black ● indicates two-sample t-test $p \leq 0.05$ between AeCRY1/cry24 and *cry-null*. Black ▲ indicates two-sample t-test $p \leq 0.05$ between AgCRY1/cry24 and AeCRY1/cry24. Black **+** indicates two-sample t-test $p \leq 0.05$ between AgCRY1/cry24 and DmCRY/cry24. Black **x** indicates two-sample t-test $p \leq 0.05$ between AeCRY1/cry24 and DmCRY/cry24. Data are represented as mean ± SEM. One significance symbol; $p \leq 0.05$, two significance symbols; $p \leq 0.005$, three significance symbols; $p \leq 0.001$.

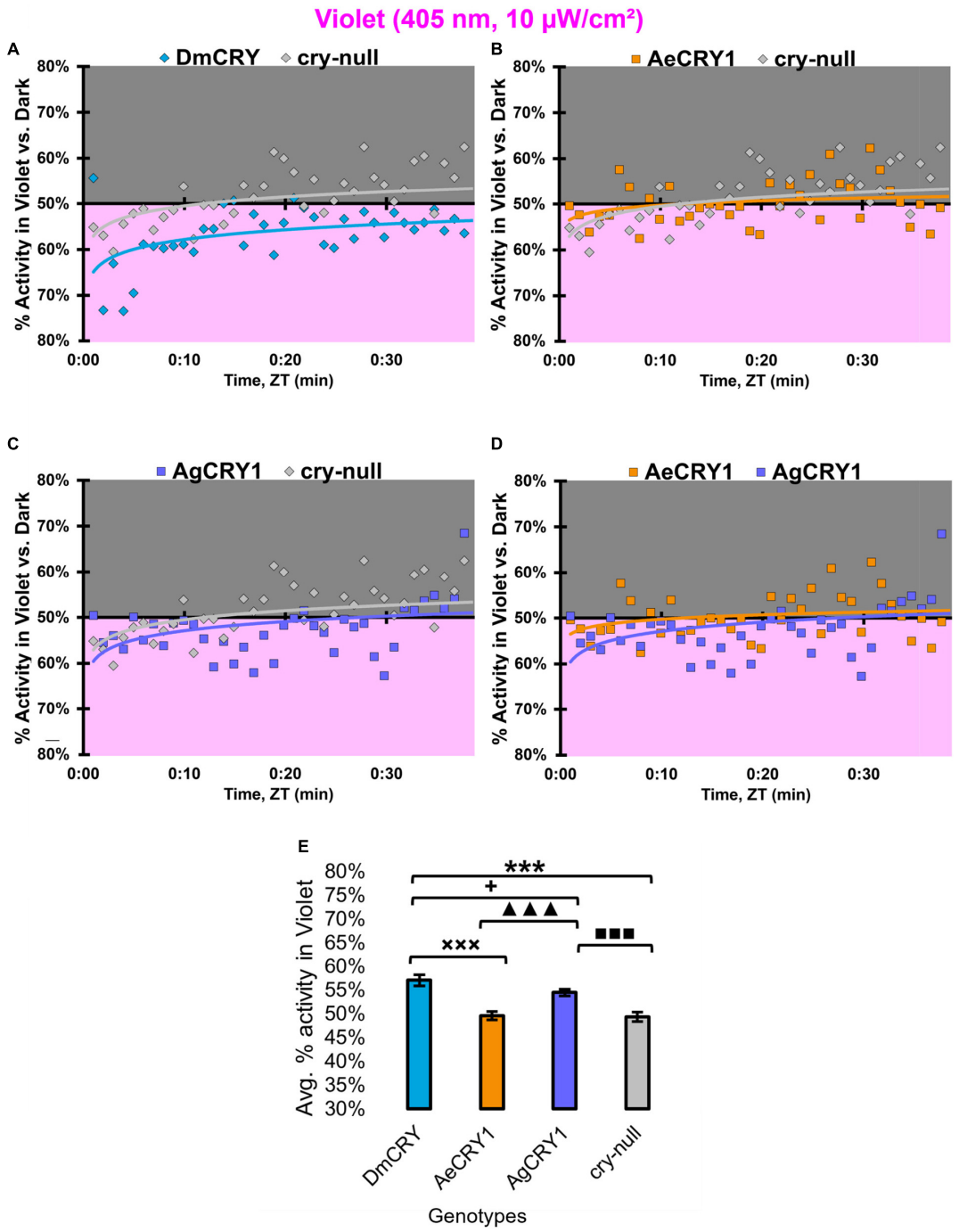

FIGURE 14
All transgenic groups exhibit weak-moderate behavioral attraction to low-intensity violet-light. **(A–D)** Violet attraction/avoidance behavior is measured by % activity in a dark shaded environment vs. a moderately low-intensity (10 μW/cm^2) violet-light-exposed environments (405 nm) during the light phase of a standard 12:12 h LD cycle. Preference is calculated by percentage of activity in each environment over total activity for each time bin for **(A)** DmCRY (blue, n = 43) vs. *cry-null* (red, n = 42), **(B)** diurnal AeCRY1 (orange, n = 35) vs. *cry-null*, **(C)** nocturnal AgCRY1 (purple, n = 36) vs. *cry-null*, and **(D)** AeCRY1 vs. AgCRY1. All plots are shown from ZT0 to 30 min in 1-min bins. **(E)** Quantified mean % activity of flies in violet environment across the first 30 min for moderately low-intensity violet-light environments. Black * indicates two-sample t-test $p \leq 0.05$ between DmCRY/cry24 and *cry-null*. Black ■ indicates two-sample t-test $p \leq 0.05$ between AgCRY1/cry24 and *cry-null*. Black **+** indicates two-sample t-test $p \leq 0.05$ between AgCRY1/cry24 and DmCRY/cry24. Black **x** indicates two-sample t-test $p \leq 0.05$ between AeCRY1/cry24 and DmCRY/cry24. Black ▲ indicates two-sample t-test $p \leq 0.05$ between AgCRY1/cry24 and AeCRY1/cry24. Data are represented as mean ± SEM. One significance symbol; $p \leq 0.05$, two significance symbols; $p \leq 0.005$, three significance symbols; $p \leq 0.001$.

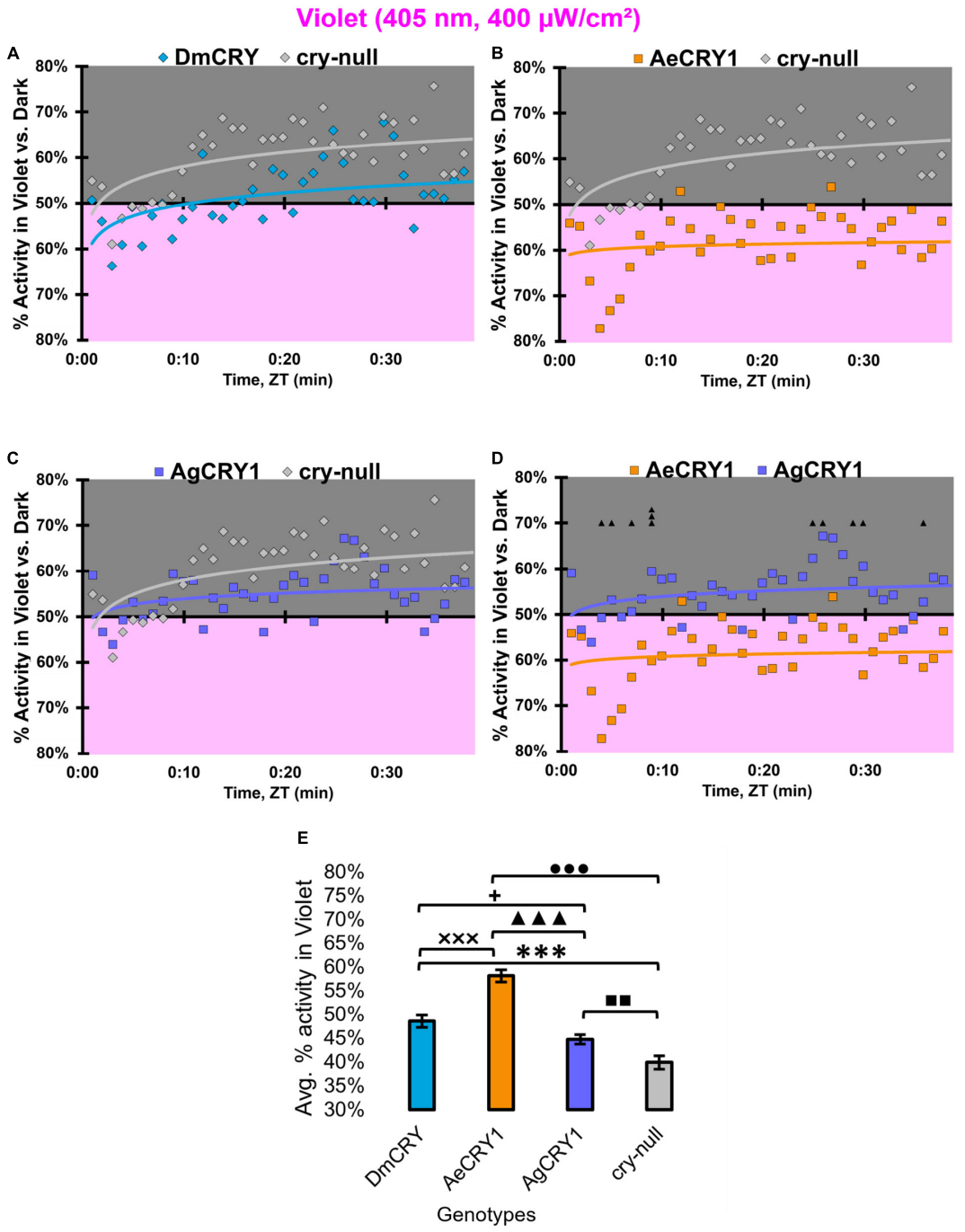

FIGURE 15
AeCRY1 flies exhibit behavioral attraction to high intensity violet-light. **(A–D)** Violet attraction/avoidance behavior is measured by % activity in a dark shaded environment vs. a high-intensity (400 μW/cm^2) violet-light-exposed environments (405 nm) during the light phase of a standard 12:12 h LD cycle. Preference is calculated by percentage of activity in each environment over total activity for each time bin for **(A)** DmCRY (blue, n = 35) vs. *cry-null* (red, n = 40), **(B)** diurnal AeCRY1 (orange, n = 34) vs. *cry-null*, **(C)** nocturnal AgCRY1 (purple, n = 40) vs. *cry-null*, and **(D)** AeCRY1 vs. AgCRY1. All plots are shown from ZT0 to 30 min in 1-min bins. **(E)** Quantified mean % activity of flies in violet environment across the first 30 min for high-intensity violet-light environments. Black ▲ indicates two-sample t-test $p \leq 0.05$ between AgCRY1/cry24 and AeCRY1/cry24. Black * indicates two-sample t-test $p \leq 0.05$ between DmCRY/cry24 and *cry-null*. Black ■ indicates two-sample t-test $p \leq 0.05$ between AgCRY1/cry24 and *cry-null*. Black ● indicates two-sample t-test $p \leq 0.05$ between AeCRY1/cry24 and cry-null. Black + indicates two-sample t-test $p \leq 0.05$ between AgCRY1/cry24 and DmCRY/cry24. Black x indicates two-sample t-test $p \leq 0.05$ between AeCRY1/cry24 and DmCRY/cry24. Data are represented as mean ± SEM. One significance symbol; $p \leq 0.05$, two significance symbols; $p \leq 0.005$, three significance symbols; $p \leq 0.001$.

behavioral responses to different light spectra that vary by time of day; and that these light driven behaviors are modulated by CRY in mosquitoes (Baik et al., 2020). We considered multiple hypotheses that might account for the distinct physiological light responses of diurnal and nocturnal mosquitoes and tested the simplest and most tractable hypothesis: informed by earlier work showing that *Drosophila* CRY codes for light avoidance responses to high intensity short wavelength light (Baik et al., 2017, 2018, 2019b), we tested the hypothesis that there are species-specific differences in the CRY light responses between *Ae. aegypti* and *An. gambiae* -family mosquitoes, predicting that nocturnal *An. gambiae* CRY1 exhibits stronger electrophysiological and behavioral responses to blue-light than *Ae. aegypti* CRY1. For the present work, the comparison between blue and violet-light responses is logically dictated by the relative spectral absorbance profiles of two non-imaging forming photoreceptors, CRY and Rh7 (Ni et al., 2017, p. 7; Sakai et al., 2017). Rh7 exhibits a broad absorption spectrum that peaks in the violet range while the base state of CRY shows a trough in the violet range of the spectra.

We recently published a related study comparing the effects of expressing the light sensitive CRYs from *Ae. aegypti* (AeCRY1), *An. gambiae* (AgCRY1), and *Drosophila melanogaster* (DmCRY, a positive control in a *cry-null Drosophila melanogaster* genetic background) in Au et al. (2022). While DmCRY is included as a positive control for the physiological assays, we acknowledge that DmCRY is a native protein in flies while mosquito CRYs are heterologously expressed. AeCRY1 is much less light sensitive than either AgCRY1 or DmCRY as shown by numerous physiological assays including partial behavioral rhythmicity seen in AeCRY1 expressing flies following constant light exposure (Au et al., 2022) and herein. Remarkably, expression of nocturnal AgCRY1 confers low survival to constant white light exposure as does expression of AeCRY1 to a much lesser extent, which may contribute to enforcing species-specific time-of-day behavioral activity. In that study, we show that AgCRY1 mediates significantly stronger electrophysiological cell autonomous responses to 365 nm ultraviolet (UV) light relative to AeCRY1 (Au et al., 2022). Further, AgCRY1 expression mediates electrophysiological and behavioral sensitivity to 635 nm red-light while AeCRY1 does not, consistent with species-specific mosquito red-light responses (Baik et al., 2020; Au et al., 2022). AgCRY1 and DmCRY mediate intensity-dependent avoidance behavior to UV light at different light intensity thresholds, while AeCRY1 does not, thus mimicking mosquito and fly behaviors (Au et al., 2022). These findings along with the present findings showing physiological responses to blue and violet-light collectively highlight CRY as a key non-image forming visual photoreceptor that mediates physiological and behavioral light-responses in a species-specific fashion.

Several mechanisms mediate inter-protein signaling following CRY light activation. For CRY mediated clock resetting in *Drosophila*, there is clear evidence that light activation leads to conformational changes in the CRY c-terminal tail that signal to downstream proteins (Busza et al., 2004; Dissel et al., 2004; Ozturk et al., 2011). However, CRY mediated light-evoked increases in action potential firing rate is still observed in flies that express a C-terminal truncated form of CRY (Fogle et al., 2011). This response remains relatively poorly resolved as it has not yet been examined using evoked potential analysis of membrane depolarization, a method that shows greater kinetic details of light evoked electrophysiological responses (Baik et al., 2019a; Au et al., 2022). The other CRY signaling mechanism involves inter-protein redox transfer for which the voltage-gated potassium beta subunit acts as a redox sensor and couple light activated CRY to changes in potassium channel activity (Fogle et al., 2015; Baik et al., 2017, 2018, 2019b; Hong et al., 2018). CRY phototransduction is mediated by light-evoked changes in the FAD redox state from an oxidized base state that absorbs UV (365 nm peak) and blue-light (450 nm) peak to its FAD•- anionic semiquinone semi-reduced state that also absorbs UV (Berndt et al., 2007; Bouly et al., 2007; Hoang et al., 2008; Öztürk et al., 2008; Lin et al., 2018). Photoactivation of the CRY FAD•- anionic semiquinone semi-reduced state yields the FADH• neutral radical state (Liu et al., 2010) which absorbs a broad peak between 580–640 nm (yellow to red) and a sharper peak at 325 nm (UV). We have yet to explore CRY physiological light responses to 325 nm UV light. Red-light photoactivation of the CRY FADH• neutral radical state is best characterized in plant CRYs, but more recent work shows that insect CRYs are also physiologically activated by red-light. This indicates that the CRY FADH• neutral radical state occurs *in vivo* (Öztürk et al., 2008; Baik et al., 2019a; Au et al., 2022). Most of the biophysical work done on the spectral absorbance properties of insect CRY proteins uses purified protein preparations. It appears that purified insect wild type CRYs do not absorb red-light when not in native cellular conditions (Berndt et al., 2007; Ozturk et al., 2011, 2014; Vaidya et al., 2013; Lin et al., 2018). It remains to be determined whether downstream signaling proteins like voltage-gated potassium subunits contribute further to species-specific differences in mosquito physiological light responses.

An alternative hypothesis for species-specific physiological light responses is based on comparative neuroanatomical analysis of diurnal *Ae. aegypti* mosquitoes and nocturnal *An. coluzzii* mosquitoes, differences in species-specific neural circuits, including PDF and PER expressing neurons may

dictate attraction/avoidance behavioral light responses. Using antibodies against the well conserved PDF and PER proteins, which cross-react across a wide range of insect species, there are both similar and species-distinct features of PDF and PER expressing neural circuits of *Ae. aegypti* and *An. coluzzii* mosquitoes. PDF and PER proteins are co-expressed in the ventral lateral area in both *Ae. aegypti* and *An. coluzzii* mosquito female adult brains that can be identified as large- (l-LNvs) and small-ventral lateral neurons (s-LNvs) based on their morphological projections common to the very well characterized brains of *Drosophila melanogaster* and other insect species (Baik et al., 2020). These include the large PDF + neuronal arbors in the optic lobes that likely project from the l-LNvs and PDF + dorsal projections to the putative dorsal neurons (DNs) that likely project from the s-LNvs for both mosquito species (Renn et al., 1999; Baik et al., 2020). There are noteworthy differences between *Ae. aegypti* and *An. coluzzii* mosquito female adult brains for their PDF and PER neural circuits, notably that for *An. coluzzii*, PDF + putative s-LNv dorsal projections continue medially to the pars intercerebralis (PI) region, a major neuroendocrine center in insect brains (de Velasco et al., 2007). The PI region integrates feeding and circadian information in insulin-like peptide expressing PI neurons (Barber et al., 2016). In contrast, this distinct s-LNv to PI neural projection is absent in *Ae. aegypti* mosquito female adult brains (Baik et al., 2020). Another species-specific difference between *Ae. aegypti* and *An. coluzzii* mosquitoes is a midline crossing contralateral projection of PDF + putative l-LNvs that is detected in *An. coluzzii* mosquito female adult brains, but is not detected in *Ae. aegypti* adult female brains (Baik et al., 2020). There are entire neuronal groups that can be found in one mosquito species but not the other, notably ∼5 PER + /PDF- neurons that are detected in the medial-anterior region of *Ae. aegypti* female brains but are not seen in *An. coluzzii* mosquito female adult brains (Baik et al., 2020). Reciprocally, there are ∼7 PER + /PDF- neurons in the PI region in *An. coluzzii* that are not detected in *Ae. aegypti* (Baik et al., 2020). These similarities and differences in diurnal vs. nocturnal mosquito PDF and PER expressing neural circuits are intriguing and while we cannot yet determine at present how much they may contribute to attraction/avoidance behavioral light responses; the results herein indicate that CRY1s themselves are sufficient to confer similar species-specific light responses observed in behaving mosquitoes. It would be interesting to express diurnal *Aedes* mosquito CRY1 in a nocturnal *Anopheles* mosquito and see how this transgenic mosquito behaves in response to different light wavelengths using the light attraction/avoidance assay, along with the reciprocal experiment of expressing nocturnal *Anopheles* CRY1 in diurnal *Aedes* mosquitoes.

These findings have interesting implications for evolutionary aspects of behavior and speciation. Many insects express two forms of CRY: light sensitive CRY1s and light insensitive CRY2s which act as transcriptional repressors (Yuan et al., 2007). The evolutionary divergence between CRY1s and CRY2s appear to have occurred prior to the Cambrian radiation as multiple *cry* genes are found in sponges, an early metazoan that precedes the evolution of animal opsins (Rivera et al., 2010). Different mosquito species have evolved distinct circadian timing of behaviors according to their temporal/ecological niches, including diurnal (*Ae. aegypti*) and nocturnal (*An. coluzzii*). Numerous mosquito species-specific behaviors change with time-of-day, including flight activity, mating, oviposition, and biting (Bidlingmayer, 1994; Ditzen et al., 2008). Such behaviors enforce speciation (Wilson, 1975). Due to their large impact on health and ecology, more work on the basis of diurnality/nocturnality, behavioral timing and how species-specific niches are enforced in mosquitoes is merited.

Data availability statement

The raw data supporting the conclusions of this article will be made available by the authors, without undue reservation.

Author contributions

DA and TH designed research, wrote, reviewed, and edited the manuscript. DA, JL, TN AF, and SP performed research. DA, JL, AF, SP, MD, and ZY analyzed data. All authors contributed to the article and approved the submitted version.

Funding

This study was funded by the NIH National Institute of General Medical Sciences (grant R35 GM127102) (TH) and (grant F31 GM140592) (DA).

Acknowledgments

We thank Francesco Tombola, Kevin Beier, and Brian Zoltowski for helpful discussions; Lisa Baik and Olga Jaime for research support; Jerry Houl for help generating transgenic lines; Mai Doan for analytical and statistical support; Parrish Powell for lab managerial support; and Janita Parpana, Lillian Li, Duke Park, and Terri Warren for administrative support.

Conflict of interest

The authors declare that the research was conducted in the absence of any commercial or financial relationships that could be construed as a potential conflict of interest.

Publisher's note

All claims expressed in this article are solely those of the authors and do not necessarily represent those of their affiliated organizations, or those of the publisher, the editors and the reviewers. Any product that may be evaluated in this article, or claim that may be made by its manufacturer, is not guaranteed or endorsed by the publisher.

Supplementary material

The Supplementary Material for this article can be found online at: https://www.frontiersin.org/articles/10.3389/fnins.2022.1042508/full#supplementary-material

References

Alonso San Alberto, D., Rusch, C., Zhan, Y., Straw, A. D., Montell, C., and Riffell, J. A. (2022). The olfactory gating of visual preferences to human skin and visible spectra in mosquitoes. *Nat. Commun.* 13:555. doi: 10.1038/s41467-022-28195-x

Au, D. D., Foden, A. J., Park, S. J., Nguyen, T. H., Liu, J. C., Tran, M. D., et al. (2022). Mosquito cryptochromes expressed in *Drosophila* confer species-specific behavioral light responses. *Curr. Biol.* 32, 3731–3744.e4. doi: 10.1016/j.cub.2022.07.021

Baik, L. S., Recinos, Y., Chevez, J. A., Au, D. D., and Holmes, T. C. (2019b). Multiple phototransduction inputs integrate to mediate UV light–evoked avoidance/attraction behavior in *Drosophila*. *J. Biol. Rhythms* 34, 391–400. doi: 10.1177/0748730419847339

Baik, L. S., Au, D. D., Nave, C., Foden, A. J., Enrriquez-Villalva, W. K., and Holmes, T. C. (2019a). Distinct mechanisms of *Drosophila* CRYPTOCHROME-mediated light-evoked membrane depolarization and in vivo clock resetting. *Proc. Natl. Acad. Sci. U.S.A.* 116, 23339–23344. doi: 10.1073/pnas.1905023116

Baik, L. S., Fogle, K. J., Roberts, L., Galschiodt, A. M., Chevez, J. A., Recinos, Y., et al. (2017). CRYPTOCHROME mediates behavioral executive choice in response to UV light. *Proc. Natl. Acad. Sci. U.S.A.* 114, 776–781. doi: 10.1073/pnas.1607989114

Baik, L. S., Nave, C., Au, D. D., Guda, T., Chevez, J. A., Ray, A., et al. (2020). Circadian regulation of light-evoked attraction and avoidance behaviors in daytime- versus nighttime-biting mosquitoes. *Curr. Biol.* 30, 3252–3259.e3. doi: 10.1016/j.cub.2020.06.010

Baik, L. S., Recinos, Y., Chevez, J. A., and Holmes, T. C. (2018). Circadian modulation of light-evoked avoidance/attraction behavior in *Drosophila*. *PLoS One* 13:e0201927. doi: 10.1371/journal.pone.0201927

Barber, A. F., Erion, R., Holmes, T. C., and Sehgal, A. (2016). Circadian and feeding cues integrate to drive rhythms of physiology in *Drosophila* insulin-producing cells. *Genes Dev.* 30, 2596–2606. doi: 10.1101/gad.288258.116

Benito, J., Houl, J. H., Roman, G. W., and Hardin, P. E. (2008). The blue-light photoreceptor CRYPTOCHROME is expressed in a subset of circadian oscillator neurons in the *Drosophila* CNS. *J. Biol. Rhythms* 23, 296–307. doi: 10.1177/0748730408318588

Benjamini, Y., and Hochberg, Y. (1995). Controlling the false discovery rate: A practical and powerful approach to multiple testing. *J. R. Stat. Soc. Ser. B Methodol.* 57, 289–300. doi: 10.1111/j.2517-6161.1995.tb02031.x

Berndt, A., Kottke, T., Breitkreuz, H., Dvorsky, R., Hennig, S., Alexander, M., et al. (2007). A novel photoreaction mechanism for the circadian blue light photoreceptor *Drosophila* cryptochrome. *J. Biol. Chem.* 282, 13011–13021. doi: 10.1074/jbc.M608872200

Bidlingmayer, W. L. (1994). How mosquitoes see traps: Role of visual responses. *J. Am. Mosq. Control Assoc.* 10, 272–279.

Bouly, J.-P., Schleicher, E., Dionisio-Sese, M., Vandenbussche, F., Van Der Straeten, D., Bakrim, N., et al. (2007). Cryptochrome blue light photoreceptors are activated through interconversion of flavin redox states. *J. Biol. Chem.* 282, 9383–9391. doi: 10.1074/jbc.M609842200

Buhl, E., Bradlaugh, A., Ogueta, M., Chen, K.-F., Stanewsky, R., and Hodge, J. J. L. (2016). Quasimodo mediates daily and acute light effects on *Drosophila* clock neuron excitability. *Proc. Natl. Acad. Sci. U.S.A.* 113, 13486–13491. doi: 10.1073/pnas.1606547113

Buhl, E., Higham, J. P., and Hodge, J. J. L. (2019). Alzheimer's disease-associated tau alters *Drosophila* circadian activity, sleep and clock neuron electrophysiology. *Neurobiol. Dis.* 130:104507. doi: 10.1016/j.nbd.2019.104507

Busza, A., Emery-Le, M., Rosbash, M., and Emery, P. (2004). Roles of the two *Drosophila* CRYPTOCHROME structural domains in circadian photoreception. *Science* 304, 1503–1506. doi: 10.1126/science.1096973

Cao, G., and Nitabach, M. N. (2008). Circadian control of membrane excitability in *Drosophila melanogaster* lateral ventral clock neurons. *J. Neurosci.* 28, 6493–6501. doi: 10.1523/JNEUROSCI.1503-08.2008

Chandrasekaran, S., Schneps, C. M., Dunleavy, R., Lin, C., DeOliveira, C. C., Ganguly, A., et al. (2021). Tuning flavin environment to detect and control light-induced conformational switching in *Drosophila* cryptochrome. *Commun. Biol.* 4:249. doi: 10.1038/s42003-021-01766-2

Chaturvedi, R., Stork, T., Yuan, C., Freeman, M. R., and Emery, P. (2022). Astrocytic GABA transporter controls sleep by modulating GABAergic signaling in *Drosophila* circadian neurons. *Curr. Biol.* 32, 1895–1908.e5. doi: 10.1016/j.cub.2022.02.066

Chiu, J. C., Low, K. H., Pike, D. H., Yildirim, E., and Edery, I. (2010). Assaying locomotor activity to study circadian rhythms and sleep parameters in *Drosophila*. *J. Vis. Exp.* 43:2157. doi: 10.3791/2157

Coombe, P. E. (1982). Visual behaviour of the greenhouse whitefly, *Trialeurodes vaporariorum*. *Physiol. Entomol.* 7, 243–251. doi: 10.1111/j.1365-3032.1982.tb00297.x

Damulewicz, M., and Mazzotta, G. M. (2020). One actor, multiple roles: The performances of cryptochrome in *Drosophila*. *Front. Physiol.* 11:99. doi: 10.3389/fphys.2020.00099

Das, S., and Dimopoulos, G. (2008). Molecular analysis of photic inhibition of blood-feeding in *Anopheles gambiae*. *BMC Physiol.* 8:23. doi: 10.1186/1472-6793-8-23

de Velasco, B., Erclik, T., Shy, D., Sclafani, J., Lipshitz, H., McInnes, R., et al. (2007). Specification and development of the pars intercerebralis and pars lateralis, neuroendocrine command centers in the *Drosophila* brain. *Dev. Biol.* 302, 309–323. doi: 10.1016/j.ydbio.2006.09.035

Dissel, S., Codd, V., Fedic, R., Garner, K. J., Costa, R., Kyriacou, C. P., et al. (2004). A constitutively active cryptochrome in *Drosophila melanogaster*. *Nat. Neurosci.* 7, 834–840. doi: 10.1038/nn1285

Ditzen, M., Pellegrino, M., and Vosshall, L. B. (2008). Insect odorant receptors are molecular targets of the insect repellent DEET. *Science* 319, 1838–1842. doi: 10.1126/science.1153121

Emery, P., So, W. V., Kaneko, M., Hall, J. C., and Rosbash, M. (1998). CRY, a *Drosophila* clock and light-regulated cryptochrome, is a major contributor to circadian rhythm resetting and photosensitivity. *Cell* 95, 669–679. doi: 10.1016/S0092-8674(00)81637-2

Emery, P., Stanewsky, R., Helfrich-Förster, C., Emery-Le, M., Hall, J. C., and Rosbash, M. (2000). *Drosophila* CRY Is a deep brain circadian photoreceptor. *Neuron* 26, 493–504. doi: 10.1016/S0896-6273(00)81181-2

Farnesi, L. C., Barbosa, C. S., Araripe, L. O., and Bruno, R. V. (2018). The influence of a light and dark cycle on the egg laying activity of *Aedes aegypti* (Linnaeus, 1762) (Diptera: Culicidae). *Mem. Inst. Oswaldo Cruz* 113:e170362. doi: 10.1590/0074-02760170362

Fernandez-Chiappe, F., Frenkel, L., Colque, C. C., Ricciuti, A., Hahm, B., Cerredo, K., et al. (2021). High-frequency neuronal bursting is essential for circadian and sleep behaviors in *Drosophila*. *J. Neurosci.* 41, 689–710. doi: 10.1523/JNEUROSCI.2322-20.2020

Flourakis, M., and Allada, R. (2015). "Patch-clamp electrophysiology in *Drosophila* circadian pacemaker neurons," in *Methods in enzymology*, (Amsterdam: Elsevier), 23–44. doi: 10.1016/bs.mie.2014.10.005

Flourakis, M., Kula-Eversole, E., Hutchison, A. L., Han, T. H., Aranda, K., Moose, D. L., et al. (2015). A conserved bicycle model for circadian clock control of membrane excitability. *Cell* 162, 836–848. doi: 10.1016/j.cell.2015.07.036

Fogle, K. J., Baik, L. S., Houl, J. H., Tran, T. T., Roberts, L., Dahm, N. A., et al. (2015). CRYPTOCHROME-mediated phototransduction by modulation of the potassium ion channel β-subunit redox sensor. *Proc. Natl. Acad. Sci. U.S.A.* 112, 2245–2250. doi: 10.1073/pnas.1416586112

Fogle, K. J., Parson, K. G., Dahm, N. A., and Holmes, T. C. (2011). CRYPTOCHROME is a blue-light sensor that regulates neuronal firing rate. *Science* 331, 1409–1413. doi: 10.1126/science.1199702

Gegear, R. J., Foley, L. E., Casselman, A., and Reppert, S. M. (2010). Animal cryptochromes mediate magnetoreception by an unconventional photochemical mechanism. *Nature* 463, 804–807. doi: 10.1038/nature08719

Giachello, C. N. G., Scrutton, N. S., Jones, A. R., and Baines, R. A. (2016). Magnetic fields modulate blue-light-dependent regulation of neuronal firing by cryptochrome. *J. Neurosci.* 36, 10742–10749. doi: 10.1523/JNEUROSCI.2140-16.2016

Green, C. H., and Cosens, D. (1983). Spectral responses of the tsetse fly, *Glossina morsitans morsitans*. *J. Insect Physiol.* 29, 795–800. doi: 10.1016/0022-1910(83)90009-4

Harrisingh, M. C., Wu, Y., Lnenicka, G. A., and Nitabach, M. N. (2007). Intracellular Ca2+ regulates free-running circadian clock oscillation in vivo. *J. Neurosci.* 27, 12489–12499. doi: 10.1523/JNEUROSCI.3680-07.2007

Hoang, N., Schleicher, E., Kacprzak, S., Bouly, J.-P., Picot, M., Wu, W., et al. (2008). Human and *Drosophila* cryptochromes are light activated by flavin photoreduction in living cells. *PLoS Biol.* 6:e160. doi: 10.1371/journal.pbio.0060160

Holmes, T. C., Sheeba, V., Mizrak, D., Rubovszky, B., and Dahdal, D. (2007). "Circuit-breaking and behavioral analysis by molecular genetic manipulation of neural activity in *Drosophila*," in *Invertebrate neurobiology*, eds G. North and R. Greenspan (Cold Spring Harbor, NY: Cold Spring Harbor Press), 19–52.

Hong, G., Pachter, R., and Ritz, T. (2018). Coupling *Drosophila melanogaster* cryptochrome light activation and oxidation of the Kvβ subunit hyperkinetic NADPH cofactor. *J. Phys. Chem. B* 122, 6503–6510. doi: 10.1021/acs.jpcb.8b03493

Jones, M. D. R., Hill, M., and Hope, A. M. (1967). The circadian flight activity of the mosquito, *Anopheles gambiae*?: Phase setting by the light regime. *J. Exp. Biol.* 47, 503–511. doi: 10.1242/jeb.47.3.503

Kistenpfennig, C., Nakayama, M., Nihara, R., Tomioka, K., Helfrich-Förster, C., and Yoshii, T. (2018). A tug-of-war between cryptochrome and the visual system allows the adaptation of evening activity to long photoperiods in *Drosophila melanogaster*. *J. Biol. Rhythms* 33, 24–34. doi: 10.1177/0748730417738612

Klarsfeld, A., Malpel, S., Michard-Vanhée, C., Picot, M., Chélot, E., and Rouyer, F. (2004). Novel features of cryptochrome-mediated photoreception in the brain circadian clock of *Drosophila*. *J. Neurosci.* 24, 1468–1477. doi: 10.1523/JNEUROSCI.3661-03.2004

Knop, E., Zoller, L., Ryser, R., Gerpe, C., Hörler, M., and Fontaine, C. (2017). Artificial light at night as a new threat to pollination. *Nature* 548, 206–209. doi: 10.1038/nature23288

Koh, K., Zheng, X., and Sehgal, A. (2006). JETLAG resets the *Drosophila* circadian clock by promoting light-induced degradation of TIMELESS. *Science* 312, 1809–1812. doi: 10.1126/science.1124951

Lazopulo, S., Lazopulo, A., Baker, J. D., and Syed, S. (2019). Daytime colour preference in *Drosophila* depends on the circadian clock and TRP channels. *Nature* 574, 108–111. doi: 10.1038/s41586-019-1571-y

Li, M.-T., Cao, L.-H., Xiao, N., Tang, M., Deng, B., Yang, T., et al. (2018). Hub-organized parallel circuits of central circadian pacemaker neurons for visual photoentrainment in *Drosophila*. *Nat. Commun.* 9:4247. doi: 10.1038/s41467-018-06506-5

Lin, C., Schneps, C. M., Chandrasekaran, S., Ganguly, A., and Crane, B. R. (2022). Mechanistic insight into light-dependent recognition of timeless by *Drosophila* cryptochrome. *Struct. Lond. Engl* 30, 851–861.e5. doi: 10.1016/j.str.2022.03.010

Lin, C., Top, D., Manahan, C. C., Young, M. W., and Crane, B. R. (2018). Circadian clock activity of cryptochrome relies on tryptophan-mediated photoreduction. *Proc. Natl. Acad. Sci. U.S.A.* 115, 3822–3827. doi: 10.1073/pnas.1719376115

Liu, B., Liu, H., Zhong, D., and Lin, C. (2010). Searching for a photocycle of the cryptochrome photoreceptors. *Curr. Opin. Plant Biol.* 13, 578–586. doi: 10.1016/j.pbi.2010.09.005

Liu, S., Lamaze, A., Liu, Q., Tabuchi, M., Yang, Y., Fowler, M., et al. (2014). WIDE AWAKE mediates the circadian timing of sleep onset. *Neuron* 82, 151–166. doi: 10.1016/j.neuron.2014.01.040

McCarthy, E. V., Wu, Y., Decarvalho, T., Brandt, C., Cao, G., and Nitabach, M. N. (2011). Synchronized bilateral synaptic inputs to *Drosophila melanogaster* neuropeptidergic rest/arousal neurons. *J. Neurosci.* 31, 8181–8193. doi: 10.1523/JNEUROSCI.2017-10.2011

Muraro, N. I., and Ceriani, M. F. (2015). Acetylcholine from visual circuits modulates the activity of arousal neurons in *Drosophila*. *J. Neurosci.* 35, 16315–16327. doi: 10.1523/JNEUROSCI.1571-15.2015

Nave, C., Roberts, L., Hwu, P., Estrella, J. D., Vo, T. C., Nguyen, T. H., et al. (2021). Weekend light shifts evoke persistent *Drosophila* circadian neural network desynchrony. *J. Neurosci.* 41, 5173–5189. doi: 10.1523/JNEUROSCI.3074-19.2021

Ni, J. D., Baik, L. S., Holmes, T. C., and Montell, C. (2017). A rhodopsin in the brain functions in circadian photoentrainment in *Drosophila*. *Nature* 545, 340–344. doi: 10.1038/nature22325

Nitabach, M. N., Blau, J., and Holmes, T. C. (2002). Electrical silencing of *Drosophila* pacemaker neurons stops the free-running circadian clock. *Cell* 109, 485–495. doi: 10.1016/S0092-8674(02)00737-7

Ozturk, N., Selby, C. P., Annayev, Y., Zhong, D., and Sancar, A. (2011). Reaction mechanism of *Drosophila* cryptochrome. *Proc. Natl. Acad. Sci. U.S.A.* 108, 516–521. doi: 10.1073/pnas.1017093108

Ozturk, N., Selby, C. P., Zhong, D., and Sancar, A. (2014). Mechanism of photosignaling by *Drosophila* cryptochrome. *J. Biol. Chem.* 289, 4634–4642. doi: 10.1074/jbc.M113.542498

Öztürk, N., Song, S.-H., Selby, C. P., and Sancar, A. (2008). Animal type 1 cryptochromes. *J. Biol. Chem.* 283, 3256–3263. doi: 10.1074/jbc.M708612200

Padilha, K. P., Resck, M. E. B., Cunha, O. A. T. da, Teles-de-Freitas, R., Campos, S. S., Sorgine, M. H. F., et al. (2018). Zika infection decreases *Aedes aegypti* locomotor activity but does not influence egg production or viability. *Mem. Inst. Oswaldo Cruz* 113:e180290. doi: 10.1590/0074-02760180290

Parisky, K. M., Agosto, J., Pulver, S. R., Shang, Y., Kuklin, E., Hodge, J. J. L., et al. (2008). PDF cells are a GABA-responsive wake-promoting component of the *Drosophila* sleep circuit. *Neuron* 60, 672–682. doi: 10.1016/j.neuron.2008.10.042

Peschel, N., Chen, K. F., Szabo, G., and Stanewsky, R. (2009). Light-dependent interactions between the *Drosophila* circadian clock factors cryptochrome, jetlag, and timeless. *Curr. Biol.* 19, 241–247. doi: 10.1016/j.cub.2008.12.042

Potdar, S., and Sheeba, V. (2018). Wakefulness is promoted during day time by PDFR signalling to dopaminergic neurons in *Drosophila melanogaster*. *eNeuro* 5:ENEURO.0129-18.2018. doi: 10.1523/ENEURO.0129-18.2018

Renn, S. C. P., Park, J. H., Rosbash, M., Hall, J. C., and Taghert, P. H. (1999). A pdf neuropeptide gene mutation and ablation of PDF neurons each cause severe abnormalities of behavioral circadian rhythms in *Drosophila*. *Cell* 99, 791–802. doi: 10.1016/S0092-8674(00)81676-1

Rivera, A. S., Pankey, M. S., Plachetzki, D. C., Villacorta, C., Syme, A. E., Serb, J. M., et al. (2010). Gene duplication and the origins of morphological complexity in pancrustacean eyes, a genomic approach. *BMC Evol. Biol.* 10:123. doi: 10.1186/1471-2148-10-123

Rund, S. S. C., Lee, S. J., Bush, B. R., and Duffield, G. E. (2012). Strain- and sex-specific differences in daily flight activity and the circadian clock of *Anopheles gambiae* mosquitoes. *J. Insect Physiol.* 58, 1609–1619. doi: 10.1016/j.jinsphys.2012.09.016

Sakai, K., Tsutsui, K., Yamashita, T., Iwabe, N., Takahashi, K., Wada, A., et al. (2017). *Drosophila melanogaster* rhodopsin Rh7 is a UV-to-visible light sensor with an extraordinarily broad absorption spectrum. *Sci. Rep.* 7:7349. doi: 10.1038/s41598-017-07461-9

Sawadogo, S. P., Costantini, C., Pennetier, C., Diabaté, A., Gibson, G., and Dabiré, R. K. (2013). Differences in timing of mating swarms in sympatric populations of *Anopheles coluzzii* and *Anopheles gambiae* s.s. (formerly *An. gambiae* M and S molecular forms) in Burkina Faso. *West Africa. Parasit. Vectors* 6:275. doi: 10.1186/1756-3305-6-275

Schlichting, M., Menegazzi, P., and Helfrich-Förster, C. (2015). Normal vision can compensate for the loss of the circadian clock. *Proc. R. Soc. B Biol. Sci. U.S.A.* 282:20151846. doi: 10.1098/rspb.2015.1846

Seluzicki, A., Flourakis, M., Kula-Eversole, E., Zhang, L., Kilman, V., and Allada, R. (2014). Dual PDF signaling pathways reset clocks via TIMELESS and acutely excite target neurons to control circadian behavior. *PLoS Biol.* 12:e1001810. doi: 10.1371/journal.pbio.1001810

Shang, Y., Griffith, L. C., and Rosbash, M. (2008). Light-arousal and circadian photoreception circuits intersect at the large PDF cells of the *Drosophila* brain. *Proc. Natl. Acad. Sci. U.S.A.* 105, 19587–19594. doi: 10.1073/pnas.0809577105

Sheeba, V., Fogle, K. J., and Holmes, T. C. (2010). Persistence of morning anticipation behavior and high amplitude morning startle response following functional loss of small ventral lateral neurons in *Drosophila*. *PLoS One* 5:e11628. doi: 10.1371/journal.pone.0011628

Sheeba, V., Sharma, V. K., Gu, H., Chou, Y.-T., O'Dowd, D. K., and Holmes, T. C. (2008c). Pigment dispersing factor-dependent and -independent circadian locomotor behavioral rhythms. *J. Neurosci.* 28, 217–227. doi: 10.1523/JNEUROSCI.4087-07.2008

Sheeba, V., Gu, H., Sharma, V. K., O'Dowd, D. K., and Holmes, T. C. (2008b). Circadian- and light-dependent regulation of resting membrane potential and spontaneous action potential firing of *Drosophila* circadian pacemaker neurons. *J. Neurophysiol.* 99, 976–988. doi: 10.1152/jn.00930.2007

Sheeba, V., Fogle, K. J., Kaneko, M., Rashid, S., Chou, Y.-T., Sharma, V. K., et al. (2008a). Large ventral lateral neurons modulate arousal and sleep in *Drosophila*. *Curr. Biol.* 18, 1537–1545. doi: 10.1016/j.cub.2008.08.033

Sheppard, A. D., Rund, S. S. C., George, G. F., Clark, E., Acri, D. J., and Duffield, G. E. (2017). Light manipulation of mosquito behaviour: Acute and sustained photic suppression of biting activity in the *Anopheles gambiae* malaria mosquito. *Parasit. Vectors* 10:255. doi: 10.1186/s13071-017-2196-3

Smith, P., Buhl, E., Tsaneva-Atanasova, K., and Hodge, J. J. L. (2019). Shaw and Shal voltage-gated potassium channels mediate circadian changes in *Drosophila* clock neuron excitability. *J. Physiol.* 597, 5707–5722. doi: 10.1113/JP278826

Stanewsky, R., Kaneko, M., Emery, P., Beretta, B., Wager-Smith, K., Kay, S. A., et al. (1998). The cryb mutation identifies cryptochrome as a circadian photoreceptor in *Drosophila*. *Cell* 95, 681–692. doi: 10.1016/S0092-8674(00)81638-4

Sumba, L. A., Okoth, K., Deng, A. L., Githure, J., Knols, B. G. J., Beier, J. C., et al. (2004). Daily oviposition patterns of the African malaria mosquito *Anopheles gambiae* Giles (Diptera: Culicidae) on different types of aqueous substrates. *J. Circadian Rhythms* 2:6. doi: 10.1186/1740-3391-2-6

Tabuchi, M., Coates, K. E., Bautista, O. B., and Zukowski, L. H. (2021). Light/clock influences membrane potential dynamics to regulate sleep states. *Front. Neurol.* 12:625369. doi: 10.3389/fneur.2021.625369

Taylor, B., and Jones, M. D. R. (1969). The circadian rhythm of flight activity in the mosquito *Aedes aegypti* (L.): The phase-setting effects of light-on and light-off. *J. Exp. Biol.* 51, 59–70. doi: 10.1242/jeb.51.1.59

Tokushima, Y., Uehara, T., Yamaguchi, T., Arikawa, K., Kainoh, Y., and Shimoda, M. (2016). Broadband photoreceptors are involved in violet light preference in the parasitoid fly *Exorista japonica*. *PLoS One* 11:e0160441. doi: 10.1371/journal.pone.0160441

Vaidya, A. T., Top, D., Manahan, C. C., Tokuda, J. M., Zhang, S., Pollack, L., et al. (2013). Flavin reduction activates *Drosophila* cryptochrome. *Proc. Natl. Acad. Sci. U.S.A.* 110, 20455–20460. doi: 10.1073/pnas.1313336110

Wilson, E. O. (1975). *Sociobiology: The new synthesis*. Cambridge, MA: Harvard University Press.

Yamaguchi, S., Desplan, C., and Heisenberg, M. (2010). Contribution of photoreceptor subtypes to spectral wavelength preference in *Drosophila*. *Proc. Natl. Acad. Sci. U.S.A.* 107, 5634–5639. doi: 10.1073/pnas.0809398107

Yoshii, T., Todo, T., Wülbeck, C., Stanewsky, R., and Helfrich-Förster, C. (2008). Cryptochrome is present in the compound eyes and a subset of *Drosophila*'s clock neurons. *J. Comp. Neurol.* 508, 952–966. doi: 10.1002/cne.21702

Yuan, Q., Metterville, D., Briscoe, A. D., and Reppert, S. M. (2007). Insect cryptochromes: Gene duplication and loss define diverse ways to construct insect circadian clocks. *Mol. Biol. Evol.* 24, 948–955. doi: 10.1093/molbev/msm011

Zhao, J., Kilman, V. L., Keegan, K. P., Peng, Y., Emery, P., Rosbash, M., et al. (2003). *Drosophila* clock can generate ectopic circadian clocks. *Cell* 113, 755–766. doi: 10.1016/S0092-8674(03)00400-8

frontiers | Frontiers in Neuroscience

TYPE Erratum
PUBLISHED 09 January 2023
DOI 10.3389/fnins.2022.1129968

OPEN ACCESS

APPROVED BY
Frontiers Editorial Office,
Frontiers Media SA, Switzerland

*CORRESPONDENCE
Frontiers Production Office
✉ production.office@frontiersin.org

SPECIALTY SECTION
This article was submitted to Neural Technology, a section of the journal Frontiers in Neuroscience

RECEIVED 22 December 2022
ACCEPTED 22 December 2022
PUBLISHED 09 January 2023

CITATION
Frontiers Production Office (2023) Erratum: Nocturnal mosquito Cryptochrome 1 mediates greater electrophysiological and behavioral responses to blue light relative to diurnal mosquito Cryptochrome 1. *Front. Neurosci.* 16:1129968. doi: 10.3389/fnins.2022.1129968

Erratum: Nocturnal mosquito Cryptochrome 1 mediates greater electrophysiological and behavioral responses to blue light relative to diurnal mosquito Cryptochrome 1

Frontiers Production Office*

Frontiers Media SA, Lausanne, Switzerland

KEYWORDS

cryptochrome, non-image forming vision, electrophysiology, light-evoked behavior, mosquito sensory biology, *Drosophila melanogaster*, *Anopheles gambiae*, *Aedes aegypti*

An Erratum on

Nocturnal mosquito Cryptochrome 1 mediates greater electrophysiological and behavioral responses to blue light relative to diurnal mosquito Cryptochrome 1

by Au, D. D., Liu, J. C., Nguyen, T. H., Foden, A. J., Park, S. J., Dimalanta, M., Yu, Z., and Holmes, T. C. (2022). *Front. Neurosci.* 16:1042508. doi: 10.3389/fnins.2022.1042508

Due to a production error, the contribution of junior reviewer Florencia Fernandez-Chiappe was omitted. It should appear as follows: Florencia Fernandez-Chiappe CONICET Instituto de Investigación en Biomedicina de Buenos Aires (IBioBA), Argentina, in collaboration with reviewer NM.

The publisher apologizes for this mistake. The original version of this article has been updated.

frontiers | Frontiers in Neuroscience

TYPE Original Research
PUBLISHED 21 December 2022
DOI 10.3389/fnins.2022.1087050

OPEN ACCESS

EDITED BY
Edgar Buhl,
University of Bristol, United Kingdom

REVIEWED BY
Berthold Gerhard Hedwig,
University of Cambridge,
United Kingdom
Fernando Montealegre-Z,
University of Lincoln, United Kingdom
Thorin Jonsson,
University of Graz, Austria

*CORRESPONDENCE
Ali Cillov
✉ ali.cillov@uni-goettingen.de

SPECIALTY SECTION
This article was submitted to Neural Technology, a section of the journal Frontiers in Neuroscience

RECEIVED 01 November 2022
ACCEPTED 02 December 2022
PUBLISHED 21 December 2022

CITATION
Cillov A and Stumpner A (2022) Local prothoracic auditory neurons in Ensifera.
Front. Neurosci. 16:1087050.
doi: 10.3389/fnins.2022.1087050

Local prothoracic auditory neurons in Ensifera

Ali Cillov* and Andreas Stumpner

Department of Cellular Neurobiology, Johann-Friedrich-Blumenbach-Institute of Zoology & Anthropology, University of Göttingen, Göttingen, Germany

A new method for individually staining insect neurons with metal ions was described in the late 60s, closely followed by the introduction of the first bright fluorescent dye, Lucifer Yellow, for the same purpose. These milestones enabled an unprecedented level of detail regarding the neuronal basis of sensory processes such as hearing. Due to their conspicuous auditory behavior, orthopterans rapidly established themselves as a popular model for studies on hearing (first identified auditory neuron: 1974; first local auditory interneuron: 1977). Although crickets (Ensifera, Gryllidae) surpassed grasshoppers (Caelifera) as the main model taxon, surprisingly few neuronal elements have been described in crickets. More auditory neurons are described for bush crickets (Ensifera, Tettigoniidae), but due to their great biodiversity, the described auditory neurons in bush crickets are scattered over distantly related groups, hence being confounded by potential differences in the neuronal pathways themselves. Our review will outline all local auditory elements described in ensiferans so far. We will focus on one bush cricket species, *Ancistrura nigrovittata* (Phaneropterinae), which has the so-far highest diversity of identified auditory interneurons within Ensifera. We will present one novel and three previously described local prothoracic auditory neuron classes, comparing their morphology and aspects of sensory processing. Finally, we will hypothesize about their functions and evolutionary connections between ensiferan insects.

KEYWORDS

orthoptera, bush cricket, neuronal processing, acoustic communication, local neurons

Introduction

Orthopterans (crickets, bush crickets/katydids, grasshoppers, and allies) exhibit an enormous variation of lifestyles. They can live in habitats as different as burrows and caves or the forest canopy, can be nocturnal or diurnal, flying or flightless. Yet, the majority uses acoustic signals for intraspecific communication and/or predator detection (e.g., Desutter-Grandcolas, 2003; Song et al., 2020). Their conspicuous behavior has intrigued researchers early on and some of the pioneering studies on insect hearing were done with orthopterans (Regen, 1913, 1914; Autrum, 1940; also see Gogala, 2014 for a summary of the early research history). After Roeder's studies on hearing

in moths (e.g., Roeder, 1966) demonstrated the potential for inferring behavior from neuronal activity, researchers started to study the neuronal basis of orthopteran hearing as well. Repeated recordings of the same physiological responses in different individuals brought about the need to identify these units morphologically. Staining cells with cobalt salts during extracellular recordings was the preferred technique (e.g., Rehbein et al., 1974). However, this method does not allow unambiguous matching of the recorded and the stained cell and was replaced by staining with Lucifer Yellow. Developed by Stewart (1978), Lucifer Yellow was the first commercially successful fluorescent dye. It was easy to apply by hyperpolarizing current and about 100 times more effective than its predecessor (Procion Yellow; Stretton and Kravitz, 1968), enabling very detailed morphological observations. The first publication showing auditory neurons stained with Lucifer Yellow came from Wohlers and Huber (1982) on six cricket interneurons, followed by studies on the neuronal basis of insect acoustic communication (for an outline, see Hoy et al., 1998; Hedwig, 2014), with a special focus on ensiferans (bush crickets: Bailey and Rentz, 1990; crickets: Huber et al., 1989). The increasing availability of confocal microscopes in the 1990s, coupled with a plethora of new fluorescent dyes, made multiple cell stains possible (e.g., Imaizumi and Pollack, 1999; Molina and Stumpner, 2005; Lefebvre et al., 2018). Thus, the "identified neuron concept" (Hoyle, 1983), characterizing cells so that they are recognizable by their anatomical and physiological characteristics in different individuals, became the dominant approach in insect neuroscience.

Ensiferan ears are located in the forelegs. Each foreleg tibia bears two tympanic membranes (an anterior and a posterior one) that are either open to the surrounding environment or covered with cuticular flaps. The tympana are mostly similar in size in bush crickets while one tympanum is often reduced in size and non-functional in many cricket species (Larsen et al., 1989; Mhatre et al., 2009). The tympana are coupled to the underlying branches of the acoustic trachea, which runs through the leg into the thorax, where it terminates at the (often greatly enlarged) acoustic spiracle in the mesothorax, thereby constituting another input for sound waves into the acoustic system (Hill and Boyan, 1976; Larsen and Michelsen, 1978). The auditory tracheae on the left and right are always connected in the thorax in crickets (Schmidt and Römer, 2016) and may be functionally coupled in bush crickets (Bailey, 1990). The sensory organ (called crista acustica in bush crickets) contains tonotopically organized scolopidia with sensory axons projecting exclusively into the prothoracic "auditory neuropile" (= anterior ring tract, Lakes and Schikorski, 1990). There, the sensory terminals connect to local, descending, ascending and T-fibers. Much of the final sound processing (e.g., song recognition, predator detection) likely happens in the brain (Huber and Thorson, 1985; Stumpner and Nowotny, 2014; Pollack and Hedwig, 2017).

Over decades, certain topics and phenomena (e.g., frequency and pattern coding, directionality, neuronal activity during behavior) established themselves as focal points for research on the ensiferan auditory system. One example, on the peripheral level, is the biophysical dynamics in the hearing organ and the tonotopy of sensory neurons (Oldfield, 1988; Michelsen et al., 1994; Imaizumi and Pollack, 1999; Schul and Patterson, 2003; Montealegre-Z et al., 2012; Vavakou et al., 2021). Another example and the biggest focus in terms of research interest is interneurons, especially the omega neuron 1 (in crickets *Acheta*: Atkins et al., 1984; Stumpner et al., 1995; *Gryllus*: Popov et al., 1978; Wohlers and Huber, 1982; Schildberger and Hörner, 1988; Hardt and Watson, 1994; *Teleogryllus*: Hennig, 1988; Faulkes and Pollack, 2001; in mole crickets *Scapteriscus*: Mason et al., 1998; in grigs *Cyphoderris*: Mason and Schildberger, 1993; in bush crickets *Ancistrura*: Molina and Stumpner, 2005; Stumpner and Molina, 2006; *Mecopoda*: Römer et al., 2002; Kostarakos and Römer, 2015; *Mygalopsis*: Römer and Bailey, 1986; Römer, 1987; *Neoconocephalus*: Triblehorn and Schul, 2009; Prešern et al., 2015; *Tettigonia*: Schul, 1997; Römer and Krusch, 2000). Together with the interneurons ascending to the brain, the song recognition network in the cricket brain has also attracted significant attention. Early work by Schildberger (1984) became the textbook example for a neuronal band-pass filter for temporal pattern extraction, but it was recently replaced by another concept and set of brain neurons as the most likely candidate for song recognition (Schöneich et al., 2015). Though technically demanding, even integrative aspects of the ensiferan nervous system have been investigated, such as initiating behavior by activation of single neurons (Nolen and Hoy, 1984) and corollary discharge dynamics during singing (Poulet and Hedwig, 2002, 2006).

While studies on ensiferan hearing became increasingly complex – from counting spikes to extracting information rates—there are still gaps in our knowledge regarding some basic points (e.g., transmitters of the described neurons, sources of inhibition). Although described first, the neurotransmitter of the omega neuron is still unclear. Moreover, very little is known as to how local circuits in thoracic ganglia shape the information relayed to the brain. Perhaps more fundamentally, properties of known neurons suggest that not all auditory units in these ganglia have been discovered yet (e.g., Stumpner, 1999; Faulkes and Pollack, 2001). Below, we will present a complete overview of the local prothoracic auditory neurons described in various ensiferan species and introduce two new elements in bush crickets.

Local prothoracic neurons in Ensifera—An overview

In Ensifera, sensory cells of the ear in the foreleg tibia project exclusively into the prothoracic ganglion (TG1)

(Rehbein, 1973). Thus, auditory information is first processed in TG1 and the local circuitry has to be considered when studying the neuronal basis of auditory behavior. Consequently, TG1 houses the highest diversity of identified auditory neurons in the central nervous system of ensiferans (see **Table 1**). The first such interneuron was the omega neuron 1 (ON1, see **Figure 1A**), initially named "large segmental auditory neuron". ON1 was first described in *Gryllus bimaculatus* by Andjan in 1976, and published in Popov et al. (1978). The discovery of the "homologous" neuron in *Teleogryllus oceanicus* happened simultaneously (Casaday and Hoy, 1977). A possible role of ON1 in directional hearing was suggested and finally demonstrated in 1985 (Selverston et al., 1985; Wiese and Eilts, 1985). The first report describing ON1 in a bush cricket (**Figure 1B**) came in 1983 (*Tettigonia cantans*, Zhantiev and Korsunovskaya, 1983) and its existence was demonstrated in further taxa in the following decade (grigs: Mason and Schildberger, 1993; mole crickets: Zhantiev and Korsunovskaya, 1990a, **Figure 2B**). ON1 described in different species have never been directly shown to be homologous, which would require its demonstration in a common ancestor or proof of a common developmental origin. Yet, their presence in a great number of orthopterans and the undeniable similarities in physiology and morphology make a compelling case for homology.

Another interneuron roughly similar to, but consistently different from ON1 in *Gryllus campestris* was named ON2 (Wohlers and Huber, 1982; **Figure 1A**). Yet, the physiological responses of ON2 reported in different studies proved to be controversial (see below for a detailed discussion). Based on a double staining, Mason and Schildberger (1993) proposed the presence of ON2 in the grig *Cyphoderris monstrosa*, but this finding leaves room for interpretation. Unlike ON1, ON2 was never described for any bush cricket species.

Gras et al. (1990) presented DUM neurons (dorsal unpaired median soma; Hoyle et al., 1974) in *G. bimaculatus* that responded to sound, but these neurons had high response thresholds and multimodal input. Morphologically, they all project into peripheral nerves or other segments. In contrast, a distinctly auditory population of DUM neurons occurs in the bush cricket *Ancistrura nigrovittata* (Lefebvre et al., 2018; **Figure 1B**). These were proposed to play a role in frequency processing through frequency-specific inhibition. Although frequency-specific inhibition is present in crickets as well, a similar neuron population has not been reported in any cricket species.

Two local neurons, named segmental neuron 1 and 2 (SN; **Figure 1B**) were described in bush crickets (SN2: *A. nigrovittata*: Stumpner, 1995; SN1: *Isophya rossica*, Zhantiev and Korsunovskaya, 1990b; both without very detailed characterization). SN1 has not been reported in any other ensiferan species, but a neuron described by Stiedl et al. (1997) in *Acheta domesticus* is broadly similar to SN2 (LN1, **Figure 1A**). Another neuron identified by Stiedl et al. (1997) has also never been reported in any other study in orthopterans (LN2. **Figure 1A**). This was also the last report of a new local auditory neuron in crickets to date.

The data on local auditory neurons come from different species, spread over several "subfamilies". Although research on hearing in ensiferans has a history spanning multiple decades, no single species became established as the preferred model. Unfortunately, there are no genetic tools available for any ensiferan species as for *Caenorhabditis elegans*, *Drosophila melanogaster*, or *Tribolium castaneum*. Consequently, insect hearing research shifted in focus from orthopterans to

TABLE 1 Types of local neurons and names as published for different taxa.

Neuron type	Name	Taxon	First reference
Omega	Omega neuron 1, ON1	Crickets	Wohlers and Huber, 1978
	Omega-neuron, ON	Bush crickets	Zhantiev and Korsunovskaya, 1983
	ON1	Mole crickets (*Gryllotalpa*)	Zhantiev and Korsunovskaya, 1990a
	LON (low-frequency tuned ON)	Mole crickets (*Scapteriscus*)	Mason et al., 1998
	HON (high-frequency tuned ON)	Mole crickets (*Scapteriscus*)	Mason et al., 1998
	Omega neuron 2, ON2	Crickets	Wohlers and Huber, 1982
Dorsal unpaired median	DUM	Bush crickets (*Ancistrura*)	Lefebvre et al., 2018
Segmental	LN1	Crickets (*Acheta*)	Stiedl et al., 1997
	LN2	Crickets (*Acheta*)	Stiedl et al., 1997
	SN1	Bush crickets (*Isophya*)	Zhantiev and Korsunovskaya, 1990b
	SN2	Bush crickets	Stumpner, 1995
Local descending	LDN	Bush crickets (*Ancistrura*)	This publication

If a neuron was only encountered in one species or genus, the genus name is given as well. The reference only cites the publication, in which this name was given for the first time.

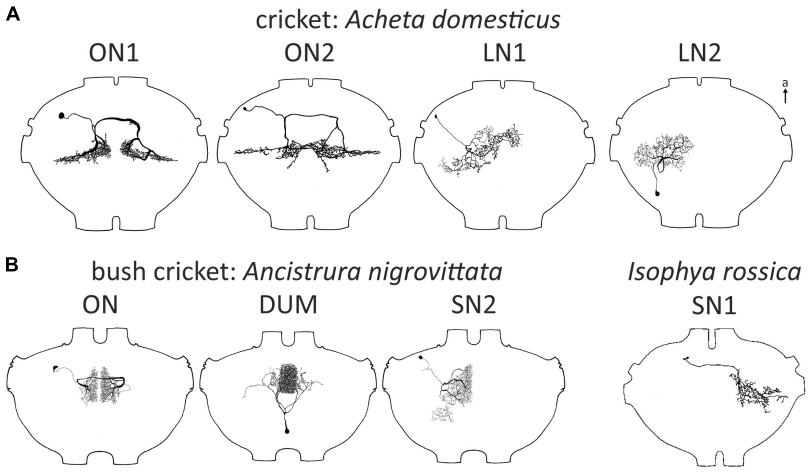

FIGURE 1
Local auditory neurons in crickets **(A)** and bushrickets **(B)**. All types also in the bush cricket *A. nigrovittata* except for SN1 described in *Isophya rossica*, which has not been described in any other Ensiferan. All ganglia of similar size but not exactly drawn to scale for better comparability. a, anterior; ax, axon. LN1, LN2 redrawn with permission after Stiedl et al. (1997), SN1 redrawn after Zhantiev and Korsunovskaya (1990b).

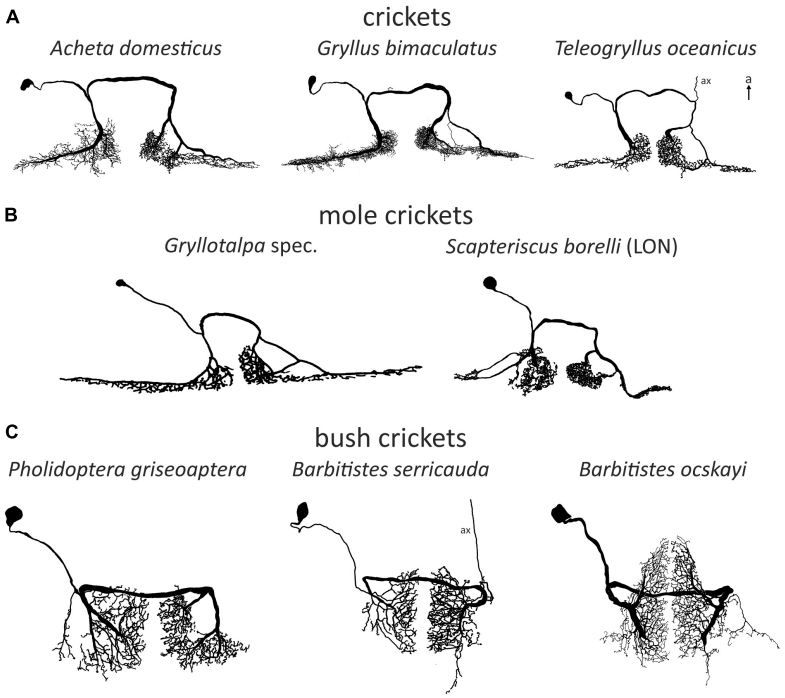

FIGURE 2
Examples of omega (1) neurons in Ensifera. Soma-ipsilateral branches have a fine dendritic structure, soma-contralateral branches have a more beaded appearance typical for axonic arborizations. **(A)** Field crickets. *T. oceanicus* modified with permission after Atkins and Pollack (1986). **(B)** Mole crickets. In *Scapteriscus* there are two ON1-like morphologies, one is interpreted as more ON1-like ("high-frequency-tuned omega neuron"). *Gryllotalpa* modified after Zhantiev and Korsunovskaya (1990a); *Scapteriscus* modified with permission after Mason et al. (1998). **(C)** Bush crickets. Neurons not drawn to scale for better comparability. a, anterior; ax, axon.

D. melanogaster (e.g., Caldwell and Eberl, 2002; Albert and Göpfert, 2015; Clemens et al., 2015). However, similar toolkits as for *Drosophila* are in development for *G. bimaculatus* (Kulkarni and Extavour, 2019). Furthermore, the proliferation of tools such as CRISPR-Cas (Pickar-Oliver and Gersbach, 2019), which can be applied to non-model insects, enables novel approaches to existing questions. These methodological developments may bring new momentum into orthopteran

auditory research, furthering our understanding as to how these "simple" insects perceive the sensory world around them and what evolutionary mechanisms underlie this process.

In the following, we will review existing data on all three identified local auditory neurons (i.e., any neuron without branches projecting into other ganglia or into the periphery) in Ensifera, focusing on species differences and potential functions. Additionally, we will present a new local neuron. We hope to convince the reader that even after half a century of research, we are far from understanding the full scope of neuronal processes, even outside the brain and how these drive acoustic perception and communication.

Omega neurons

Omega neurons, which occur as mirror images on both sides of TG1, are named after their outward similarity to the Greek capital letter Ω. Though this is informative about the morphology, the initial name used by (Popov et al., 1978), large segmental auditory neuron, is a better indicator as to why ON1 is the most intensively studied ensiferan neuron: it has unusually large main branches on both sides of the prothoracic ganglion and a thick crossing segment close to the tissue surface, which makes recordings technically simple. Recordings in soma-ipsilateral branches show strong graded potentials with action potentials, recordings on the soma-contralateral side show mainly action potentials (Wohlers and Huber, 1978), but may show IPSPs as well (Schul, 1997). Early studies found morphologically very similar neurons in different cricket species (*Acheta*: Atkins et al., 1984; *Gryllus*: Popov et al., 1978; *Teleogryllus*: Casaday and Hoy, 1977; see **Figure 2A**). In bush crickets, all studied species had a similar neuron as well, albeit with ca. 90° rotated arborizations (Zhantiev and Korsunovskaya, 1983; Boyan, 1984; Römer, 1985; compare **Figures 2A, C**). However, different bush cricket subfamilies vary slightly in the morphology of their ON1. Whereas Tettigoniinae (e.g., *Tettigonia*, *Pholidoptera*, *Metrioptera*) have a more rectangular dendritic tree and a crossing segment lying more anteriorly than the branching area, Phaneropterinae (e.g., *Ancistrura*, *Barbitistes*, *Leptophyes*) and Mecopodinae (*Mecopoda*) have a triangular arborization and the crossing segment appears to be "within" the dendrites (while actually being more ventral, **Figure 2C**). A neuron similar to ON1 was later also found in further ensiferan taxa, such as mole crickets (*Gryllotalpa*: Zhantiev and Korsunovskaya, 1990a; *Scapteriscus*: Mason et al., 1998) and grigs (*Cyphoderris*: Mason and Schildberger, 1993). The close similarities between omega neurons in various ensiferan groups are surprising, especially considering their significant evolutionary separation (mole crickets vs. true crickets 180–230 mya, bush crickets vs. true crickets 270–300 mya, Song et al., 2015, 2020).

Flying female crickets show two highly directional behaviors: positive phonotaxis toward a singing male and negative phonotaxis away from high-frequency bat echolocation calls (e.g., Pollack et al., 1984; Wyttenbach et al., 1996). The potential role of ON1 in sharpening directional decisions in behavior was alluded to in early studies. This was directly demonstrated for positive phonotaxis by suppressing its activity, though the effects were not fully congruent: besides the high interindividual variability, the effect was also dependent on the stimulus parameters (*Acheta*: Atkins et al., 1984; *Gryllus*: Schildberger and Hörner, 1988). Moreover, inactivating ON1 on both hemiganglia had no effect on positive phonotaxis, though the used measurement methods were not very sensitive in general (Atkins et al., 1984). The neuronal mechanisms underlying ON1's influence on directional behavior have also been elucidated. Photoinactivation and cell killing experiments show that the mirror image ON1 have strong contralateral mutual inhibition (Selverston et al., 1985; Wiese and Eilts, 1985). In *Teleogryllus*, ascending neuron 2 (AN2, also called Interneuron-1) plays a central role in negative phonotaxis in flight, and is both necessary and sufficient for this behavior (Nolen and Hoy, 1984). Similar to ON1, AN2 is also directionally inhibited (Moiseff and Hoy, 1983; Faulkes and Pollack, 2000). Although Harrison et al. (1988) did not find any connection between ON1 and AN2, Faulkes and Pollack (2000) demonstrated the loss of directional inhibition in AN2 in the same species (*T. oceanicus*) upon inactivation of ON1. Selverston et al. (1985) further demonstrated that AN2 is inhibited by the ON1 that receives excitation from the opposite ear. This inhibition can also affect positive phonotaxis (Schildberger and Hörner, 1988). Recordings of ON1 in bush crickets do not differ significantly from those in crickets and contralateral inhibition is also present as a prominent feature (Römer et al., 1988; Schul, 1997; Römer and Krusch, 2000). However, a combination of photoinactivation, pharmacological blocking, and mechanical ear destruction experiments indicate that there is contralateral inhibition in ON1 in addition to that of the mirror image in *A. nigrovittata* (Molina and Stumpner, 2005).

Electron microscopy studies in *Gryllus* have shown that ON1 receives monosynaptic input from auditory sensory cells (Watson and Hardt, 1996; Hirtz and Wiese, 1997). Data from *Teleogryllus*, however, strongly suggest that only input from high-frequency (HF) receptors is direct, whereas input from low-frequency (LF) receptors is polysynaptic (Faulkes and Pollack, 2001). This leads to a distinctly longer latency at LF, which may be relevant for temporal processing (see below). Furthermore, the distribution of synapses of ON1 is rather complex. Surprisingly, there are significant proportions of both input and output synapses on both sides of the ganglion, which are connected with neurons other than the auditory receptors and the mirror image ON1 (Watson and Hardt, 1996). Many of the inputs into ON1 are immunoreactive for γ-aminobutyric

acid (GABA) (e.g., potentially from the observed vibratory inhibition, see Wiese, 1981). Yet, ON1 itself does not use GABA as neurotransmitter, as shown by several studies in both crickets and bush crickets (e.g., Watson and Hardt, 1996; Stumpner et al., 2020). While there is strong functional evidence for histamine as the neurotransmitter of cricket ON1 (Skiebe et al., 1990), immunohistochemical studies failed to confirm this finding (Hörner, 1999). Similar approaches have revealed a morphologically similar, serotonergic neuron instead, although not in all individuals, indicating that ON1 may possess considerable concentrations of serotonin under unclear circumstances (Hörner et al., 1995). Indeed, there is still no conclusive evidence on the neurotransmitter used by ON1.

The temporal dynamics of ON1 activity might play a crucial role in its function. Wiese and Eilts (1985) suggested that the mutual inhibition of mirror image ON1 is most effective at pulse rates corresponding to that of the species-specific calling song in *G. bimaculatus*. Similarly, Nabatiyan et al. (2003) showed a peak in spike rates at the same temporal pattern. Studies using amplitude modulated sound in different cricket species further support this tuning to the song pattern, suggesting an evolutionary adaptation of the temporal filter properties of ON1 to each species' own calling song pattern (information coding: Farris et al., 2004; firing rate resonances and computational modeling: Tunstall and Pollack, 2005; Rau et al., 2015). ON1 has also been shown to inhibit the soma-ipsilateral AN1, which is the main relay for conspecific acoustic information to the brain (*Ancistrura*: Molina and Stumpner, 2005; *Acheta*: Stumpner et al., 1995; *Gryllus*: Horseman and Huber, 1994; *Teleogryllus*: Faulkes and Pollack, 2000). Reeve and Webb (2003) hypothesized the inhibition from ON1 might, from a circuit design standpoint, increase the dynamic range of AN1, as well as improve the encoding of the sound onset, therefore decreasing the overall noise in AN1. Nevertheless, it is still not fully clear whether the filter properties of ON1 affect the pattern recognition network in the cricket brain (Schöneich et al., 2015). Interestingly, ON1 with an ascending axon can occasionally occur in various bush cricket and cricket species, and could provide input to the brain alongside AN1 (Atkins and Pollack, 1986; Schul, 1997; Stiedl et al., 1997). However, these data come mostly from nymphs and young adults and are therefore interpreted as an incomplete reduction during development. The overwhelming majority of stained omega neurons in adults do not have an ascending axon and the terminal structures of the observed axons have never been reported.

AN1 and AN2, both receiving directional inhibition from ON1, are involved in opposite phonotactic behaviors in response to LF and HF sound respectively. Therefore, multiple studies looked into the frequency-specific processing of ON1. There are two peaks in the frequency tuning of cricket ON1 (with the exception of "high-frequency crickets" Eneopterinae, ter Hofstede et al., 2015): main peak at the calling song frequency and a secondary peak at HF (Popov et al., 1978; Wohlers and Huber, 1978; Atkins and Pollack, 1986; Stumpner et al., 1995; **Figure 3A**). On top of the fundamental differences in HF vs. LF receptor input into ON1 (Faulkes and Pollack, 2001), information transfer approaches show that high pulse rates are coded much better at HF—as can be found in bat calls—than in LF (Marsat and Pollack, 2004). Such differences may be correlated with the behavior of the animal: *T. oceanicus* is a more active flyer than *G. bimaculatus* and is therefore under stronger predation pressure from bats. A computational model suggested diverse causes that could underlie the frequency-specific responses of ON1, such as cell-intrinsic properties, spike triggered adaptation, interplay between excitation and inhibition, and network-based resonances (Rau et al., 2015). In stark contrast, ON1 in bush crickets does not have conspicuous frequency-dependent differences in input, and its frequency tuning corresponds to that of the whole hearing range except for very low frequencies (e.g., Römer, 1985; Römer et al., 1989; Stumpner, 2002; **Figure 3B**). This broad tuning is distinct from several other prothoracic interneurons, which are tuned to specific frequencies (e.g., Stumpner, 2002; Triblehorn and Schul, 2009).

Its large and horizontally spread-out branches in crickets make ON1 well suited to study Ca^{2+} dynamics. Ca^{2+} measurements were first used to examine the "cocktail party effect" in *A. domesticus*, demonstrating that forward masking limits the response of ON1 to louder stimuli (Sobel and Tank, 1994). This selective attention phenomenon was reported earlier in *T. oceanicus* (Pollack, 1988). A very similar forward masking/gain control effect was also found in the bush cricket *Tettigonia viridissima* (Römer, 1993; Römer and Krusch, 2000). Both Sobel and Tank (1994) and Römer and Krusch (2000) suggested that Ca^{2+}-dependent K^{+} channels inhibit ON1 following activation due to increased Ca^{2+} concentration, which can last for multiple seconds. Finally, a computational analysis corroborated this hypothesis, showing Ca^{2+}-dependent spike frequency adaptation and post-synaptic potential depression are sufficient for forward masking (Ponnath and Farris, 2010).

ON1 was the central element in a brilliant experimental setup that enabled electrophysiological recordings in the field (Rheinlaender and Römer, 1986; Römer and Bailey, 1986). This so-called "biological microphone" was used, among others, to record neuronal responses to conspecific calls under natural conditions. Such a setup only works well with rather large neurons, which can be extracellularly recorded in sufficient quality over a longer time even when freely moving the whole setup. Changes in directional responses and neuronal noise depending on the acoustic environment, as well as their behavioral correlates, such as the spacing in the habitat, have been vividly demonstrated with this approach (Römer and Bailey, 1998; Kostarakos and Römer, 2010; Schmidt and Römer, 2011; also see Römer, 2021).

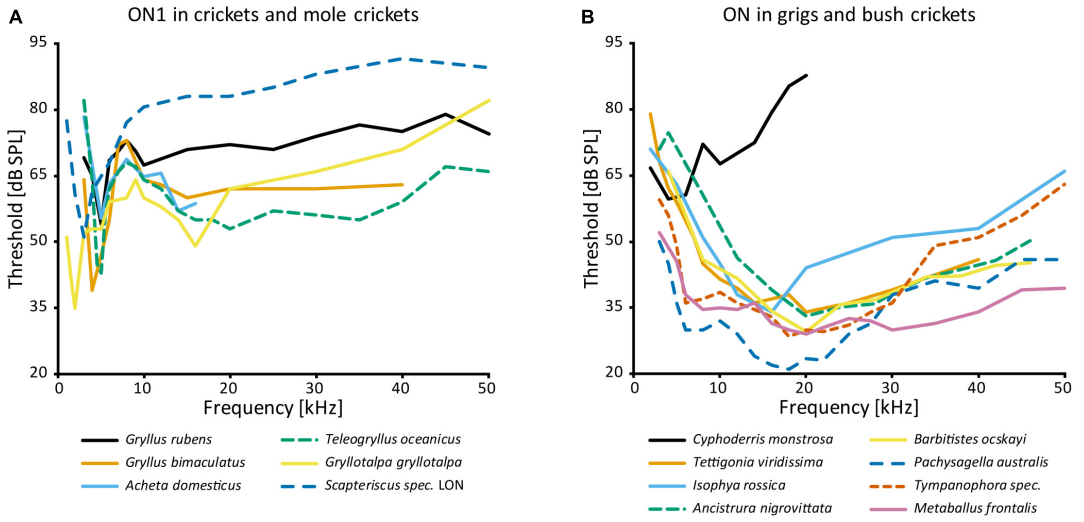

FIGURE 3
Frequency tuning of ON(1): **(A)** threshold curves of ON1 in crickets and mole crickets. Source of data: *G. rubens*: Farris et al., 2004, *G. bimaculatus*: Watson and Hardt, 1996; *A. domesticus*: Stumpner et al., 1995; *T. oceanicus*: Atkins and Pollack, 1986; *G. gryllotalpa*: Zhantiev and Korsunovskaya, 1990a; *Scapteriscus* spec.: Mason et al., 1998. **(B)** Threshold curves of the omega neuron in grigs and bush crickets. Source of data: *A. nigrovittata* and *B. ocskayi*: Stumpner, 2002; *C. monstrosa*: Mason and Schildberger, 1993; *I. rossica*: Korsunovskaya and Zhantiev, 1992; *Pachysagella australis*, *Metaballus frontalis,* and *Tympanophora* spec.: Römer et al., 1989; *Tettigonia viridissima*: Römer, 1985.

ON1 has also been used to analyze how acoustically active animals solve a common problem, that is strong adaptation of the peripheral nervous system to the animal's own song. A corollary discharge mechanism leads to primary afferent depolarization and strongly inhibits ON1 activity during singing, thus preserving sensitivity to subsequent external stimuli (Poulet and Hedwig, 2002, 2006). Even when the forewings were removed and the singing was merely fictive, presynaptic inhibition of auditory afferents was in place. Later, the responsible corollary discharge interneuron was also identified and shown to be part of a simple neural network (Poulet and Hedwig, 2007).

Finally, neuronal regeneration following ear lesion was investigated in various cricket neurons, including ON1. When disconnected from auditory receptors, soma-ipsilateral dendrites cross the midline and make new connections on the soma-contralateral neuropile. This process is more extensive in nymphs than in adults, but functionally restores synaptic connections in both cases (Schildberger et al., 1986; Schmitz, 1989). Such plasticity seems to be restricted to first-order interneurons (Lakes, 1990; Lakes et al., 1990). Therefore, the changes can be seen as evidence that ON1 receives monosynaptic input from the auditory receptors. Interestingly, some plasticity can also occur after soma-contralateral lesions. Since post-lesion changes are only seen in branches with direct input from afferents, ON1 has direct input from both ears, supporting electron microscopy data showing synapses with profiles matching those of sensory neurons on both sides of TG1 (Watson and Hardt, 1996). Weak excitation from the "inhibited" side following acute lesions has been reported in other directional orthopteran interneurons as well (Lakes et al., 1990).

A post-lesion regenerated ON1 is morphologically strikingly similar to ON2, which has another crossing segment within the auditory neuropile. ON2 occurs in multiple cricket species (*A. domesticus*: Atkins et al., 1984; *G. bimaculatus*: Schmitz, 1989; *G. campestris*: Wohlers and Huber, 1982; *Gryllus rubens*: Farris et al., 2004; *T. oceanicus*: Lewis, 1992). As for ON1, occasional thin ascending axons occur in ON2, but no terminals were stained (*A. domesticus*: Stiedl et al., 1997; *G. bimaculatus*: Schmitz, 1989). One staining in the grig *C. monstrosa* includes two omega neurons within the same hemiganglion, where one cell has a thin neurite crossing the midline, indicating this is ON2 (Mason and Schildberger, 1993). However, ON2 does not occur in any bush cricket species, even though Tettigoniidae (bush crickets) and Prophalangopsidae (which grigs belong to) share around 100 million years of common evolution after splitting off from the gryllid line (Song et al., 2015, 2020). A parsimonious explanation then would be that bush crickets lost ON2 secondarily. However, since the common ancestor of grigs and bush crickets had hearing, this loss must have happened in an active, established auditory processing network.

While the physiology of ON1 is consistent across different taxa, that of ON2 varies considerably, even within the same genus (**Figure 4**). The auditory response was shown to have lower thresholds for LF than HF in *G. campestris* and *G. rubens* (Wohlers and Huber, 1982; Farris et al., 2004, respectively). Yet, in regeneration experiments in *G. bimaculatus* it had similar

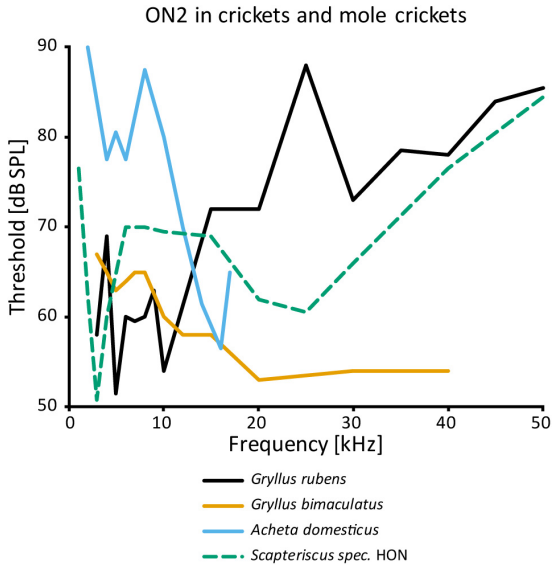

FIGURE 4
Frequency tuning of ON2 in female crickets and "high-frequency-tuned omega neuron" in a mole cricket. Source of data: *G. rubens*: Farris et al., 2004, *G. bimaculatus*: Watson and Hardt, 1996; *A. domesticus*: Stiedl et al., 1997; *Scapteriscus* spec.: Mason et al., 1998.

thresholds for both frequency ranges (Schmitz, 1989), while Watson and Hardt (1996) reported distinctly higher sensitivity to HF in the same species. The latter is congruent with data from other cricket species (*A. domesticus*: Stiedl et al., 1997; *T. oceanicus*: Lewis, 1992). However, all studies agree that ON2 receives excitatory input from both ears and has little directionality. With an elegant experimental approach using selective cold-inactivation of ears, Zhang and Hedwig (2019) could directly demonstrate bilateral excitatory input to ON2 in *G. bimaculatus*, consistent with earlier electron microscopy data (Watson and Hardt, 1996). Several studies reported that ON2 does not copy the temporal pattern of the conspecific song very well (e.g., Wohlers and Huber, 1982). Mason et al. (1998) identified two omega neurons in the mole cricket genus *Scapteriscus*. Although morphologically indistinguishable, these neurons differ in their frequency responses: one is tuned to LF, the other is additionally sensitive to HF. Therefore, the authors name them low and high-frequency-tuned omega neurons, and compare them to ON1 and ON2, respectively. No such differences were reported for any species in the only other extant mole cricket subfamily Gryllotalpinae.

Since ON1 provides inhibitory input in the prothoracic auditory network, ON2 could play a similar role. However, electron microscopy data show clear differences in the synaptic vesicles between ON1 and ON2, suggesting different neurotransmitters (Watson and Hardt, 1996). Like ON1, ON2 is not GABAergic. Inhibition by HF sound has been shown in ascending neurons in *G. campestris* (Boyd et al., 1984) and *A. domesticus* (Stumpner et al., 1995), with ON2 as a possible source. In the latter species, the inhibition remained after eliminating all soma-contralateral input, pointing to an ipsilateral source.

Dorsal unpaired median neurons

Unpaired median neurons constitute a class defined by the medial position of their cell bodies, forming a cluster at the posterior end of thoracic and abdominal ganglia (e.g., Hoyle, 1978; Lange and Orchard, 1984; Janiszewski and Otto, 1988; see **Figure 5A**). Unpaired median neurons occur across the dorsoventral axis and the distinction between the dorsal and ventral cells is usually artificial (Bräunig and Pflüger, 2001). Therefore, we will not differentiate unpaired neurons on this basis and will use the term "DUM neuron" for all such cells.

Although all DUM neurons within the same ganglion originate from the same neuroblast (Goodman and Spitzer, 1979), they are heterogeneous both in terms of morphology (e.g., cell body size, projection area) and function (e.g., neurotransmitter, sensory modality, role in behavior). DUM neurons occur in a variety of taxa, but were only investigated in detail in cockroaches (Tanaka and Washio, 1988; Washio, 2002) and orthopterans, especially grasshoppers. Within orthopterans, there are two distinct DUM neuron populations. The first group consists of neurons that have large cell bodies, project into the peripheral nerves or to other segments, are octopaminergic, and are commonly associated with neuromodulatory or motor control functions (Hoyle, 1975, 1978; Gras et al., 1990; Thompson and Siegler, 1991). The second and more numerous group has neurons that have smaller cell bodies, project mostly within the ganglion and rarely into connectives, and are immunoreactive for antibodies against GABA (Thompson and Siegler, 1993; Stumpner et al., 2020). Though DUM neurons have been extensively investigated regarding their neuromodulatory function or electrical properties (e.g., Grolleau and Lapied, 2000; Bräunig and Pflüger, 2001), there is limited data on their role in sensory processing. Diverse and evolutionarily far groups within Orthoptera have DUM neurons responsive to sound and/or vibration (grasshoppers: Marquart, 1985; Stumpner and Ronacher, 1991; Thompson and Siegler, 1991; crickets: Gras et al., 1990; cave crickets: Stritih and Stumpner, 2009; bush crickets: Lefebvre et al., 2018). Yet, the only detailed studies on auditory DUM neurons have been in the prothoracic ganglion of *A. nigrovittata* (Lefebvre et al., 2018; Stumpner et al., 2019, 2020).

Auditory DUM neurons in *A. nigrovittata* constitute a heterogenous group with multiple morphological types, which correspond to their physiological response properties only to a limited extent (Lefebvre et al., 2018; also **Figure 5A**). Some

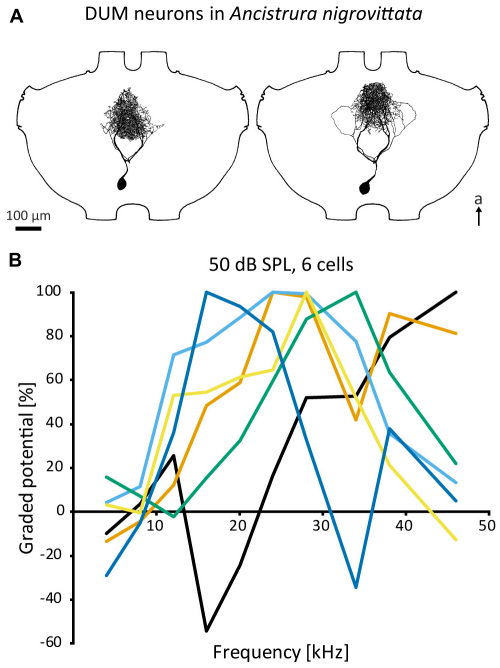

FIGURE 5
DUM neurons in *A. nigrovittata*. **(A)** Two DUM neurons in males, the left one is morphologically classified as "narrow" and high frequency tuned, the right one is classified as "loops" and mid frequency tuned. **(B)** Iso-intensity responses of 6 out of 11 DUM-neurons recorded in one female with the relative graded responses (sum of excitation and leading inhibition normalized to the maximum response in each curve). Each cell has a different frequency tuning. a, anterior.

types have extensive arborizations within the auditory neuropile and are sensitive to airborne sound, while other DUM types project also or exclusively to ganglion regions outside the auditory neuropile and can be sensitive to vibration. Auditory DUM neurons differ significantly in their frequency tuning (**Figure 5B**). Different cells have different best frequencies and this tuning is sharpened by the extensive frequency-dependent inhibition (Lefebvre et al., 2018). The population includes 15 or more cells, covers a wide frequency range, and is thought to constitute a filter bank. This proposed function extends to temporal processing as well (Stumpner et al., 2019). Their diverse filtering properties and inhibitory output make DUM neurons the main candidates for inhibitory effects—especially frequency dependent inhibition—in auditory interneurons within the prothoracic network. Therefore, they could represent a major part of the early sensory processing.

Segmental neurons

The term "segmental neuron" (SN) denotes some local interneurons that are branching mostly within one hemiganglion of the central nervous system. The first auditory SN were described in *Locusta migratoria* (SN1 and SN2, Römer and Marquart, 1984). Like DUM neurons, SN are only defined by their morphological features. They vary considerably in their morphology, such as projection areas, as well as physiological properties, and do not constitute a functional class.

In total, four auditory SN have been reported in three ensiferan species: two cells in *A. domesticus* (local neuron (LN) 1 and 2, Stiedl et al., 1997; **Figure 1A**), and one each in the bush crickets *I. rossica* (SN1, Zhantiev and Korsunovskaya, 1990b) and *A. nigrovittata* (SN2, Stumpner, 1995) (**Figure 1B**). SN2 also occurs in several *Barbitistes* species (A. Stumpner, unpublished data). In contrast to the SN described in the grasshopper *L. migratoria*, which spread over both sides of the ganglion, segmental neurons in ensiferans have the majority of their arborizations within a single hemiganglion. LN1 and LN2 in *A. domesticus* are both non-spiking and tuned to low frequencies around the carrier frequency of the species calling song (~5 kHz) (Stiedl et al., 1997). LN1 is inhibited by high-frequency sound, whereas LN2 is inhibited by vibration, but activated by wind. SN1 in *I. rossica* responds to 12–16 kHz sounds very sensitively (<30 dB SPL) with tonic spike trains (Zhantiev and Korsunovskaya, 1990b; Korsunovskaya and Zhantiev, 1992). Intriguingly, the projection area of SN1 lies completely outside the auditory neuropile, since there is no overlap with the branches of ON1 from the same species (Zhantiev and Korsunovskaya, 1990b; Korsunovskaya and Zhantiev, 1992). This suggests an auditory input coming exclusively from other interneurons, which is unusual for local neurons. Information on SN2 up to now has only been cursorily reported (Stumpner, 1995; Stumpner and Nowotny, 2014).

Detailed morphological and physiological data on SN2 exist only in *A. nigrovittata*. SN2 is a local auditory interneuron with a lateral cell body and extensive arborization within the auditory neuropile, as well as a secondary, more posterior projection area (**Figure 6A**). This area is situated posterior to the ventral median tract (VMC) and lies in the approximate position of the supra median commissure (SMC, Wohlers and Huber, 1985; Lakes and Schikorski, 1990). SN2 can differ significantly in the details of their posterior branches (**Figure 6B**). Yet, they all have the auditory neuropile as their primary projection area. This projection completely covers the neuropile (**Figure 6C**).

Despite the notable variation, there are no distinct morphological subtypes of SN2. Yet, physiological data can be categorized in two groups. "Broad" SN2 have a broadband frequency tuning with the lowest thresholds around 20 kHz. "HF-tuned" SN2 share the > 35 kHz section of their tuning with the "broad" type, but are on average much less sensitive to low-frequency sound and show larger interindividual variation than "broad" SN2 (**Figure 7A**). Basic response patterns of SN2 can vary greatly. Though all SN2 share an underlying phasic-tonic motif, the ratio between the phasic and tonic portions changes significantly between cells (**Figure 7B**). Even the presence or absence of spikes can differ between recordings (all recordings

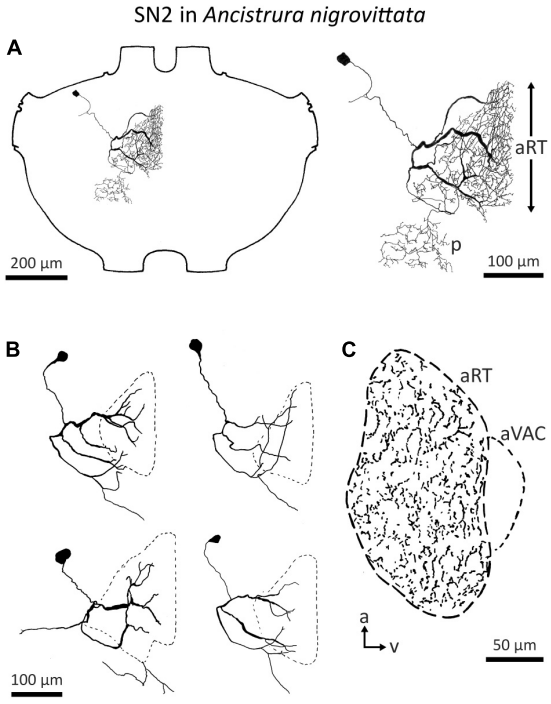

FIGURE 6
Morphology of SN2 in *A. nigrovittata*. **(A)** Wholemount and detailed view of SN2 in a female. The extent of the anterior ring tract (aRT) is indicated by the arrows; the secondary branching area marked with p lies posterior and more laterally to the aRT. **(B)** Four examples of the main branches in two females (upper) and two males (lower). The extensions of the dendritic trees are indicated by a dashed line. **(C)** Parasagittal section (16 µm) close to the midline showing the arborizations of SN2 in a female. The dashed line delimits the auditory neuropile, corresponding to aRT, the smaller dashed line on the ventral side indicates the anterior ventral association center (aVAC; e.g., Lakes and Schikorski, 1990).

were done in or close to the auditory neuropile). Nevertheless, SN2 can reliably represent the species-specific calling song, although the relative response strength to male and female calls varies (**Figure 7C**). "Broad" SN2 have similar intensity response curves for frequencies between 16 and 28 kHz and a wide dynamic range spanning the entirety of the tested stimulus space (30–90 dB SPL) (**Figure 7D**). In contrast, "HF-tuned" SN2 show higher activity for 28 kHz than 16 kHz (**Figure 7E**). The dynamic range of the "HF-tuned" SN2 could not be revealed, as– likely due to the high thresholds—the maximum stimulus intensity did not saturate the neuron. "Broad" SN2 are much more directional than the "HF-tuned" at 16 and 28 kHz, with maximum response difference between ipsi- and contralateral side reaching >40 dB (median: 16 kHz: 17.3 vs. 11.9 dB; 28 kHz: 23.0 vs. 12.1 dB, respectively; **Figure 8A**). Data present a complicated picture for SN2: there seem to be two physiological subtypes without consistent morphological delimitation. In one individual, two SN2 with adjacent cell bodies on the same hemiganglion and similar frequency tuning (both "broad") were stained, suggesting the existence of more than one cell on each side. The broad variety has been recorded twice as often as the HF-tuned within the dataset (23 cells in total, 18 with complete physiology, compare **Figure 7A**). This could be interpreted as there being three SN2 on each side of the prothoracic ganglion: two broad and one HF-tuned SN2. So far, only two SN2 have been stained in the same hemiganglion.

"Local descending neuron"

An auditory interneuron has been characterized in *A. nigrovittata* and coined "local descending neuron" (LDN). Though a contradictory name, we believe it represents the morphological properties of this cell type rather accurately. LDN is similar to a descending neuron in *A. nigrovittata* ("DN4," Stumpner and Nowotny, 2014) and two descending neurons from *Decticus albifrons* (Sickmann, 1997). One LDN occurs on each side of the prothoracic ganglion, with the cell body in an anteromedian cluster of somata, adjacent to those of other descending neurons (Stumpner and Nowotny, 2014; A. Cillov, unpublished data; also **Figure 9A**). LDN has dense and extensive arbors in the auditory neuropile (**Figures 9B–E**). Unlike other DN, the primary neurite of LDN splits into fine branches upon entering the auditory neuropile without a crossing segment or axon running through the arborizations. In 12 out of 21 stains, a fine projection originates from the contralateral branches and terminates before reaching the connective. Only in one case the projection reached the connective, but it ended before reaching the mesothoracic ganglion. We interpret this projection as a rudimentary axon. This could be a case of deterioration in the course of development, though two subadult animals had similarly thin and prematurely terminating axons. LDN has some interindividual morphological variety in the projection of its lateral branches (**Figure 9C**). The branching pattern is always on both sides of the ganglion with no clear difference in the size or shape of the dendrites (**Figure 9D**). Like SN2, LDN projects to the entire auditory neuropile and the dense branches are mostly restricted to the neuropile (**Figure 9E**).

In the frequency domain, LDN is broadly tuned, though overall less sensitive than SN2 and has its peak around 20 kHz (**Figure 10A**). The responses of different LDN are much more consistent than those of SN2. LDN is non-spiking and responds to vibration little if at all, and with acoustic stimuli, it is a phasic-tonic neuron (**Figure 10B**). In most cases, a phasic fall of the cell potential occurs shortly after the onset of excitation, the extent of which varies between cells (**Figure 10B**). LDN faithfully copies the species' duet between the male and female (**Figure 10C**).

A non-linearity occurs in the intensity response curves of different frequencies. Frequencies <20 kHz (**Figure 10D**) have a steeper slope and a narrowed dynamic range compared to frequencies >20 kHz (**Figure 10E**). Unfortunately, it

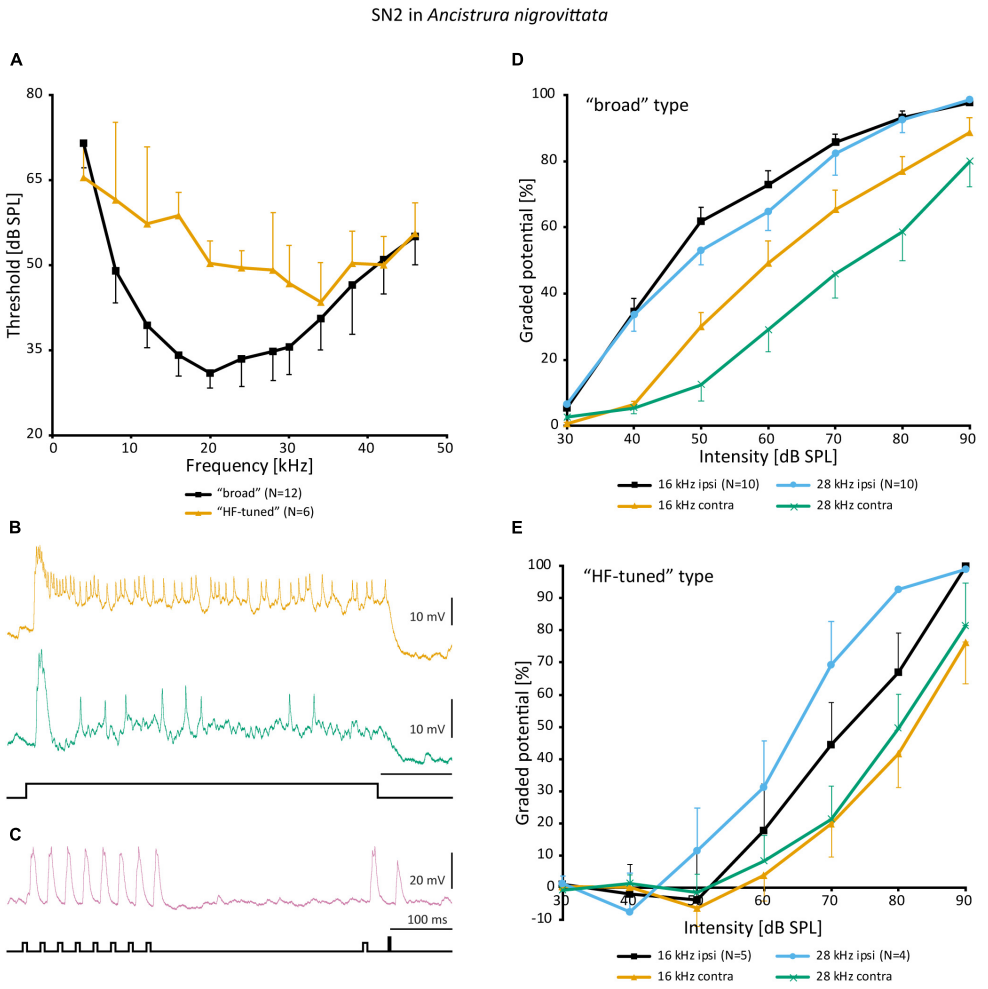

FIGURE 7
Physiology of SN2 in *A. nigrovittata*. **(A)** Frequency tuning (mean ± SD) of "broad" (black; 8 females, 4 males) and "HF-tuned" SN2 (orange; 3 f, 3 m). **(B)** Response patterns of two SN2 in males to a 500 ms white noise stimulus of 70 dB SPL. Upper trace from a "broad", lower from an "HF-tuned" neuron. **(C)** Response of a "broad" SN2 to an artificial duet between a male (smaller pulses, 16 kHz) and a female (larger single pulse, 28 kHz) at 60 dB SPL. **(D,E)** Intensity response curves for soma-ipsilateral (ipsi) and soma-contralateral (contra) 100 ms stimuli at 16 and 28 kHz (mean ± SEM). **(D)** "Broad" neurons (6 f, 4 m). **(E)** "HF-tuned" neurons (16 kHz: 3f, 2m; 28 kHZ: 3f, 1 m).

is not possible to directly calculate and compare dynamic ranges, as responses on both ends of the spectrum have not reached saturation within the tested intensity range. This could imply that different inputs into LDN are weighted differently depending on the frequency or that there is additional polysynaptic input at HF, which, however, is not indicated by the latencies. Such a finding would also suggest that a wider dynamic range is of particular importance to the unidentified postsynaptic targets.

Auditory interneurons in *A. nigrovittata* are clearly directional (e.g., ON1, AN1, TN1; Stumpner and Molina, 2006). LDN, however, has remarkably small response differences between stimuli from opposite directions. The maximum dB difference in response to left and right stimulation for LDN is ∼8 dB for 16 and 28 kHz, the frequencies of male and female song in *A. nigrovittata*. This is noticeably lower than for both SN2 subtypes (**Figure 8A**).

Leg cut experiments with "broad" SN2 have diverse results: only input from the ipsilateral ear, inhibition from the contralateral ear, or clear excitation from both ears. The dB difference in LDN is also lower than that in sensory neurons (13–17 dB; Lefebvre et al., 2018), and similar to that of DUM neurons, which are excited by both ears (Lefebvre et al., 2018).

Discussion

Local auditory interneurons in the prothoracic ganglion represent a major part of the first level of information processing in ensiferan insects and still harbor unexplored complexity. Data

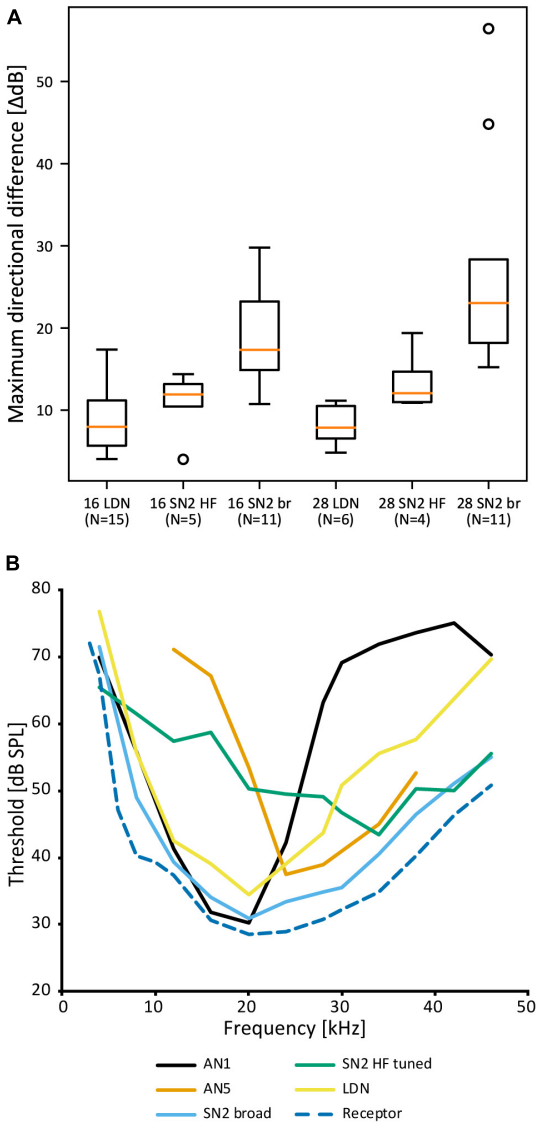

FIGURE 8
Comparison of SN2 and LDN to other neurons in *A. nigrovittata*. **(A)** Box plot (median in orange, lower and upper quartile; whiskers represent the minimum/maximum value within 1.5 times the interquartile range; outliers shown as circles) of the maximum difference in dB between the responses to ipsilateral and contralateral stimulation measured within the dynamic range of intensity scans as shown in **Figures 7D,E**. 16 and 28 represent the tested carrier frequencies in kHz; SN2 are divided as "broad" (br) and "HF-tuned" (HF). **(B)** Frequency thresholds of LDN and SN2 in comparison to the overall hearing threshold (minimal values from auditory receptor neurons; see Ostrowski and Stumpner, 2010) and that of the spikes of the ascending neurons tuned best to the male song (AN1, mean of 21–23 (30 kHz: 10) males and females) or tuned best to the female song (AN5-AG7, mean of 4–8 males; see Stumpner and Molina, 2006).

across the breadth of ensiferan taxa show that bush crickets have by far the highest diversity of local auditory neurons. This could be confounded by the focus on a subset of bush crickets, namely Phaneropterinae, as other bush cricket subfamilies (e.g., Tettigoniinae) do not seem to exhibit the same variety of local auditory cells.

ON(1) is the only local neuron found across all investigated ensiferan taxa and thus is a good starting point for comparisons between groups. ON(1) seems to be both morphologically and physiologically, conserved throughout Ensifera, as all records share certain hallmarks. ON(1) is always highly directional due to mutual contralateral inhibition. In addition, it is involved in sound localization by inhibiting the ascending neuron(s) that receive their main excitatory input from the soma-contralateral ear. Other proposed functions are gain control and coding sound onset more precisely, though none have been shown directly. Temporal tuning of ON(1) demonstrates evolutionary adaptation to each species' own calling song (Farris et al., 2004; Tunstall and Pollack, 2005; Rau et al., 2015), though it is also involved in general sound source localization, including that of predators (Selverston et al., 1985; Schildberger and Hörner, 1988).

At least two other local neurons are likely to be inhibitory. ON2 could be involved in inhibition more pronounced at high frequencies. In crickets, this could help with the separation of conspecific (LF) vs. predator (HF) auditory channels. In contrast, GABAergic DUM neurons in (certain) bush crickets provide a much more granular filter bank for frequency-specific inhibition. This fine separation could help code the difference between the auditory channels of the male and female signals, which can be at different frequencies as part of duets, as in *A. nigrovittata*. Fine separation might also allow sexual selection by fitness or size correlated song parameters, although such effects are hard to demonstrate in Orthoptera (e.g., Shaw and Herlihy, 2000; Verburgt and Ferguson, 2010). A broad filter bank for frequency specific inhibition could facilitate rapid speciation through changes in the calling song frequency. Such cladogenesis events are known to have occurred in the bush cricket evolutionary line, though presumably due to geographical separation (e.g., Heller et al., 2011). Immunohistochemical data show that crickets also have a GABAergic DUM cluster at the same position as bush crickets, but these likely have a non-auditory, possibly vibratory function (Cillov, 2020).

Data on segmental neurons is exceedingly patchy. LN1/LN2 and SN1 are only known from single species (*A. domesticus* and *I. rossica*, respectively); SN2 from two closely related genera (*Ancistrura* and *Barbitistes*). SN1 is intriguing due to its morphology and is unlike any other known local auditory neuron in Ensifera. Both LN1 and LN2 are tuned to low frequencies and are sensitive enough to be involved in intraspecific communication. If LN exist in other cricket groups and are excitatory, they could be the source of the LF polysynaptic input to ON1 (Faulkes and Pollack, 2001), for which there are no other candidates among local auditory neurons. If they are inhibitory, they could be the LF counterparts

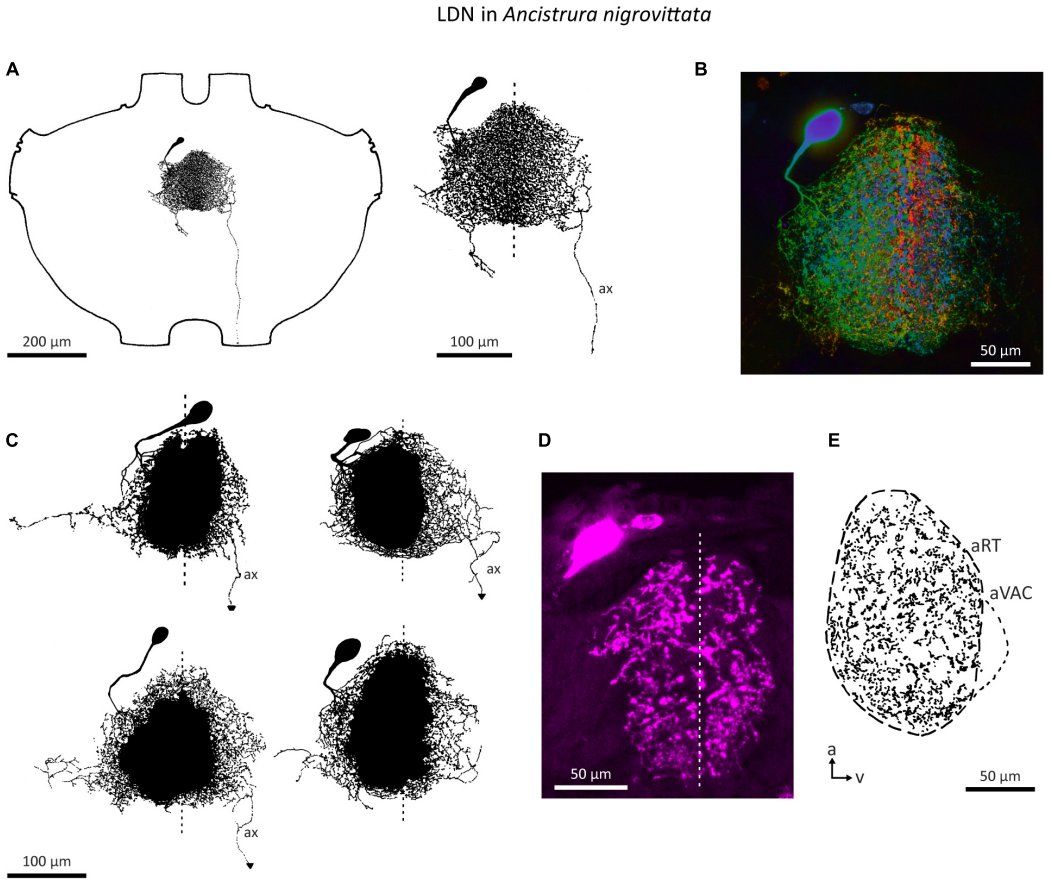

FIGURE 9
Morphology of the local neuron LDN in *A. nigrovittata*. **(A)** Wholemount and detailed view of LDN in a male. **(B)** Color coded (warm = dorsal, cold = ventral) maximum projection of a confocal stack of LDN filled with neurobiotin and developed with streptavidin-Cy3 in a female. **(C)** Four examples of the main branches in two males (upper) and two females (lower). A dashed line indicates the ganglion midline. **(D,E)** Sections (10 µm) of LDN in a female **(D)** and a male **(E)**. **(D)** Confocal image of a transversal section showing the similarity of branches in both hemiganglia. **(E)** Drawing of a parasagittal section showing the arborizations in the auditory neuropile. a, anterior; aRT, anterior ring tract; aVAC, anterior ventral associations center; ax, axon-like branch; v, ventral.

to ON2 and provide LF inhibition to ON2 and AN2. Any inhibition in the frequency or temporal domain in bush crickets is likely to be fulfilled by DUM neurons, which cover a wide frequency range when taken as a whole.

Local descending neuron is known from a phaneropterid species (*A. nigrovittata*), though similar neurons of prothoracic origin with projections in posterior ganglia are known from several bush cricket species (Sickmann, 1997; Kostarakos and Römer, 2015). SN2 and LDN are both unlikely to contribute to song recognition, as neither provides any conspicuous filtering in the frequency or temporal domain. Only two SN2 members had signs of inhibition in high frequencies. As ON(1) already is a source of broadband inhibition, one might except SN2 and LDN to be excitatory, but there are no conclusive results from immunohistochemical experiments.

LDN and SN2—especially the "broad" subtype—could function as reference neurons. They would represent the whole auditory spectrum without any obvious filtering and represent the presence of sound. "Broad" SN2 have a frequency tuning like the most sensitive auditory receptor cells, just with few dB higher thresholds (**Figure 8B**). LDN is even less sensitive with more pronounced interindividual differences in the ultrasound. "Broad" SN2's tuning encompasses those of the most specific intersegmental neurons for male and female song in *A. nigrovittata* (AN1 and AN5-AG7, respectively; **Figure 8B** and Molina and Stumpner, 2005). LDN and SN2 HF complement each other by being more responsive to lower and higher frequencies, respectively. Neurons with similar broad tuning as SN2 are found among ascending neurons in several Orthoptera, though their roles in the greater network are unknown (AN3 in bush crickets: Stumpner and Molina, 2006; AN6 in Caelifera: Römer and Marquart, 1984; Stumpner and Ronacher, 1991). A role of such neurons could be in multimodal integration between acoustics and wind or vibration. A problem with the reference neuron hypothesis is the rarity of such neurons. One example is in the primate auditory cortex (Brasselet et al.,

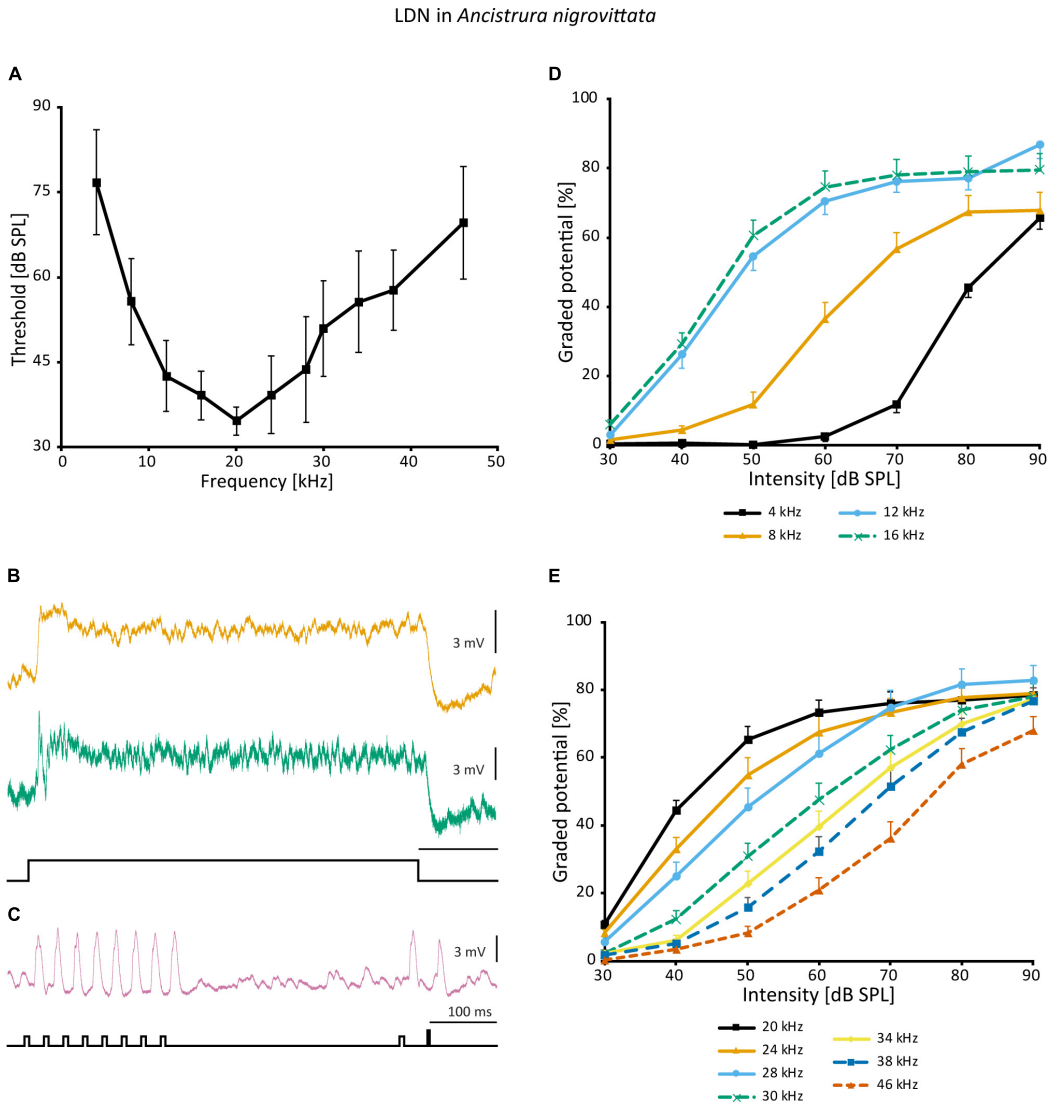

FIGURE 10
Auditory responses of LDN in *A. nigrovittata*. **(A)** Frequency tuning (mean ± SD) of LDN from 9 to 10 females and 7 to 8 males. **(B)** Response patterns of two LDN in a female (upper) and a male (lower) to a 500 ms white noise stimulus of 70 dB SPL. **(C)** Response of an LDN in a female to an artificial duet between a male and a female at 60 dB SPL. **(D,E)** Intensity response curves for the indicated frequencies with 50 ms stimuli (mean ± SEM; 10 females and 8 males, except for 8 kHz (9f, 7 m) and 38 kHz (10 f, 7 m). Response curves up to 16 kHz **(D)** have a steeper rise and a narrower dynamic range than those in the ultrasound **(E)**.

2012), but in this framework, reference neurons are marked for their low and precise latencies, which is not indicated for SN2 and LDN.

With a soma diameter of 30 µm or more, LDN is reminiscent of neuromodulatory cells, such as octopaminergic DUM neurons, which have big cell bodies. Combined with its dense arborization throughout the auditory neuropile, LDN could be a candidate for modulating auditory processing. However, previous work did not find any hints for anterior cell bodies with biogenic amines like serotonin or octopamine in bush crickets (A. Stumpner, unpublished data) nor in crickets (Hörner et al., 1995). Octopamine, however, like histamine, influences the responses of ON1 in crickets (Skiebe et al., 1990; Lühr et al., 1994). The low interindividual variability of most prothoracic auditory neurons does not support a strong neuromodulatory influence.

To conclude, though the insect central nervous system is simpler than that of vertebrates, we are unable to even reveal the early "subcortical" networks in a taxon that has been continuously studied for over 50 years. Though in Ensifera, the data also suffer from fragmentation over several groups. Yet, even in *G. bimaculatus*, which is the most intensively studied species, neither the neurotransmitters of auditory neurons nor

their connectivity to each other is known, except for a handful of cases. It is even likely there to be undiscovered auditory neurons relevant for behavior. We severely need data on components of the local auditory processing network other than ON. With the tools available right now, these are mostly limited to electrophysiological data. Yet, they may enable us to understand the exact neuronal mechanisms underlying auditory perception, as well as to elucidate the evolutionary pressures and processes shaping the nervous system and speciation in this group with sophisticated acoustic communication. Though one thing is certain: even the fragments we have hint at a system much more complex than we are aware of at the moment.

Materials and methods

Figures 1–5 present in parts so far unpublished data, **Figures 6–10** new data. The methods are described in short, but are in detail in Lefebvre et al. (2018).

Animals: *Ancistrura nigrovittata* (Brunner von Wattenwyl, 1878) were caught in Northern Greece and reared in the laboratory for up to 9 generations. *Barbitistes serricauda* (Fabricius, 1798) were F1-generations originating from Lower Saxony, Germany. *Barbitistes ocskayi* (Brunner von Wattenwyl, 1878) were F1-generations from southwestern Slovenia. *Gryllus bimaculatus* (De Geer, 1773) came from a laboratory culture that existed for many years in the Zoological Institute of the University of Göttingen. *Pholidoptera griseoaptera* (De Geer, 1773) were caught in Göttingen, Germany.

Neuron morphologies were revealed by intracellular stainings with Lucifer Yellow CH, Alexa 555 Hydrazide or neurobiotin, which was coupled to streptavidin-Cy3. Neurons were either drawn from an epifluorescent microscope with a drawing tube or from confocal images (Leica SP8 AOBS, maximum projections of z-stacks and single images). All neuronal morphologies were transferred into standard ganglia for crickets or bush crickets for better comparability. For comparative figures unpublished stainings are shown whenever available. In the remaining cases, neurons were redrawn from publications (photos, drawings) for a homogeneous design. For histological analysis, ganglia were embedded in Agar 100 and sectioned (10–16 μm). Neuronal projections were drawn from microscope and confocal images.

Physiological data for DUM neurons, SN2, and LDN were recorded with a standard intracellular bridge-amplifier (NPI, Germany), stored on DAT-tape (SONY, Japan) or directly digitized using a commercial AD-converter and the software Spike2 (CED, UK). Data were analyzed with custom-written scripts in Spike 2. Graded potentials are given as area (positive or negative; mV * ms) between resting potential and actual membrane potential (spikes clipped) during the response to a stimulus and normalized to the maximum response. Stimuli were presented using a custom-made setup. Stimulus envelopes (1.5–2 ms rise and fall times) were filled with sine waves or white noise (ca. 2–50 kHz) and repeated 5 times (except for the long white noise stimuli from **Figures 7A, 10A**). Data points in the frequency threshold curves show individual means of several animals and standard deviation (SD), individual values were calculated once from frequency-intensity scans. In all other cases, the means and standard errors (SEM) are shown, each data point is the mean of the averaged measurements from different individuals.

Data availability statement

The raw data supporting the conclusions of this article will be made available by the authors, without undue reservation.

Author contributions

AS made the neuron drawings, replotted data from previous studies, gathered the literature, generated the SN2 data, and provided the cookies. AC made the figures and generated the LDN data. Both authors wrote the manuscript.

Funding

Part of the studies presented here were supported by grants from the German Research Association (DFG) to Andreas Stumpner (DFG STU 189/1-1,2,3,4, STU 189/9-1 and STU 189/10-1).

Acknowledgments

We acknowledge support by the Open Access Publication Funds of the Göttingen University. We thank Silvia Gubert for animal care, embedding ganglia and making the histological sections. Martin Göpfert supported us throughout the studies. George Theophilidis, Aristotle University of Thessaloniki, Greece, helped importantly in receiving the permit to catch and export the insects. We are grateful to three reviewers for their valuable comments, which greatly improved the quality of the manuscript.

Conflict of interest

The authors declare that the research was conducted in the absence of any commercial or financial relationships that could be construed as a potential conflict of interest.

Publisher's note

References

Albert, J. T., and Göpfert, M. C. (2015). Hearing in *Drosophila*. *Curr. Opin. Neurobiol.* 34, 79–85. doi: 10.1016/j.conb.2015.02.001

Atkins, G., Ligman, S., Burghardt, F., and Stout, J. F. A. (1984). Changes in phonotaxis by the female cricket *Acheta domesticus* L. after killing identified acoustic interneurons. *J. Comp. Physiol. A* 154, 795–804. doi: 10.1007/BF00610680

Atkins, G., and Pollack, G. S. (1986). Age-dependent occurrence of an ascending axon on the omega neuron of the cricket, *Teleogryllus oceanicus*. *J. Comp. Neurol.* 243, 527–534. doi: 10.1002/cne.902430407

Autrum, H. (1940). Über Lautäusserungen und Schallwahrnehmung bei Arthropoden II: Das Richtungshören von *Locusta* und Versuch einer Hörtheorie für Tympanalorgane vom Locustidentyp. *Z. Für Vgl. Physiol.* 28, 326–352. doi: 10.1007/BF00342439

Bailey, W. J. (1990). "The ear of the bushcricket," in *The tettigoniidae: Biology, systematics and evolution*, eds W. J. Bailey and D. C. F. Rentz (Berlin: Springer Verlag), 217–247.

Bailey, W. J., and Rentz, D. C. F. (eds) (1990). *The tettigoniidae: Biology, systematics and evolution*. Berlin: Springer Verlag.

Boyan, G. S. (1984). Neural mechanisms of auditory information processing by identified interneurones in *Orthoptera*. *J. Insect Physiol.* 30, 27–41. doi: 10.1016/0022-1910(84)90106-9

Boyd, P., Kühne, R., Silver, S., and Lewis, B. (1984). Two-tone suppression and song coding by ascending neurones in the cricket *Gryllus campestris* L. *J. Comp. Physiol. A* 154, 423–430. doi: 10.1007/BF00605241

Brasselet, R., Panzeri, S., Logothetis, N. K., and Kayser, C. (2012). Neurons with stereotyped and rapid responses provide a reference frame for relative temporal coding in primate auditory cortex. *J. Neurosci.* 32, 2998–3008. doi: 10.1523/JNEUROSCI.5435-11.2012

Bräunig, P., and Pflüger, H.-J. (2001). The unpaired median neurons of insects. *Adv. Insect Physiol.* 28, 185–266. doi: 10.1016/S0065-2806(01)28011-4

Caldwell, J. C., and Eberl, D. F. (2002). Towards a molecular understanding of *Drosophila* hearing. *J. Neurobiol.* 53, 172–189. doi: 10.1002/neu.10126

Casaday, G. B., and Hoy, R. R. (1977). Auditory interneurons in the cricket *Teleogryllus oceanicus*: Physiological and anatomical properties. *J. Comp. Physiol. A* 121, 1–13. doi: 10.1007/BF00614177

Cillov, A. (2020). *On the trail of auditory DUM neurons in crickets*. Master thesis. Göttingen: Georg-August-Universität Göttingen.

Clemens, J., Girardin, C. C., Coen, P., Guan, X.-J., Dickson, B. J., and Murthy, M. (2015). Connecting neural codes with behavior in the auditory system of *Drosophila*. *Neuron* 87, 1332–1343. doi: 10.1016/j.neuron.2015.08.014

Desutter-Grandcolas, L. (2003). Phylogeny and the evolution of acoustic communication in extant Ensifera (*Insecta*, *Orthoptera*). *Zool. Scr.* 32, 525–561. doi: 10.1046/j.1463-6409.2003.00142.x

Farris, H. E., Mason, A. C., and Hoy, R. R. (2004). Identified auditory neurons in the cricket *Gryllus rubens*: Temporal processing in calling song sensitive units. *Hear. Res.* 193, 121–133. doi: 10.1016/j.heares.2004.02.008

Faulkes, Z., and Pollack, G. S. (2000). Effects of inhibitory timing on contrast enhancement in auditory circuits in crickets (*Teleogryllus oceanicus*). *J. Neurophysiol.* 84, 1247–1255. doi: 10.1152/jn.2000.84.3.1247

Faulkes, Z., and Pollack, G. S. (2001). Mechanisms of frequency-specific responses of ω neuron 1 in crickets (*Teleogryllus oceanicus*): A polysynaptic pathway for song? *J. Exp. Biol.* 204, 1295–1305. doi: 10.1242/jeb.204.7.1295

Gogala, M. (2014). "Sound or Vibration, an Old Question of Insect Communication," in *Studying vibrational communication, animal signals and communication*, eds R. B. Cocroft, M. Gogala, P. S. M. Hill, and A. Wessel (Berlin: Springer Verlag), 31–46. doi: 10.1007/978-3-662-43607-3_3

Goodman, C. S., and Spitzer, N. C. (1979). Embryonic development of identified neurones: Differentiation from neuroblast to neurone. *Nature* 280, 208–214. doi: 10.1038/280208a0

Gras, H., Hörner, M., Runge, L., and Schürmann, F.-W. (1990). Prothoracic DUM neurons of the cricket *Gryllus bimaculatus* - responses to natural stimuli and activity in walking behavior. *J. Comp. Physiol. A* 166, 901–914. doi: 10.1007/BF00187337

Grolleau, F., and Lapied, B. (2000). Dorsal unpaired median neurones in the insect central nervous system: Towards a better understanding of the ionic mechanisms underlying spontaneous electrical activity. *J. Exp. Biol.* 203, 1633–1648. doi: 10.1242/jeb.203.11.1633

Hardt, M., and Watson, A. H. D. (1994). Distribution of synapses on two ascending interneurones carrying frequency-specific information in the auditory system of the cricket: Evidence for gabaergic inputs. *J. Comp. Neurol.* 345, 481–495. doi: 10.1002/cne.903450402

Harrison, L., Horseman, G., and Lewis, B. (1988). The coding of the courtship song by an identified auditory neurone in the cricket *Teleogryllus oceanicus* (Le Guillou). *J. Comp. Physiol. A* 163, 215–225. doi: 10.1007/BF00612430

Hedwig, B. (ed.) (2014). *Insect hearing and acoustic communication, 1st ed. 2014. ed, animal signals and communication*. Berlin: Springer Verlag, doi: 10.1007/978-3-642-40462-7

Heller, K.-G., Willemse, L., Odé, B., Volleth, M., Feist, R., and Reinhold, K. (2011). Bioacoustics and systematics of the *Poecilimon hamatus* group (*Tettigonioidea*: *Phaneropteridae*: *Poecilimon:* Hamatopoecilimon n. subg.). *J. Orthoptera Res.* 20, 81–95. doi: 10.1665/034.020.0108

Hennig, R. M. (1988). Ascending auditory interneurons in the cricket *Teleogryllus commodus* (Walker): Comparative physiology and direct connections with afferents. *J. Comp. Physiol. A* 163, 135–143. doi: 10.1007/BF00612003

Hill, K. G., and Boyan, G. S. (1976). Directional hearing in crickets. *Nature* 262, 390–391. doi: 10.1038/262390a0

Hirtz, R., and Wiese, K. (1997). Ultrastructure of synaptic contacts between identified neurons of the auditory pathway in *Gryllus bimaculatus* DeGeer. *J. Comp. Neurol.* 386, 347–357. doi: 10.1002/(SICI)1096-9861(19970929)386:3<347::AID-CNE2<3.0.CO;2-1

Hörner, M. (1999). Cytoarchitecture of histamine-, dopamine-, serotonin- and octopamine-containing neurons in the cricket ventral nerve cord. *Microsc. Res. Tech.* 44, 137–165. doi: 10.1002/(SICI)1097-0029(19990115/01)44:2/3<137::AID-JEMT7<3.0.CO;2-3

Hörner, M., Spörhase-Eichmann, U., Helle, J., Venus, B., and Schürmann, F.-W. (1995). The distribution of neurones immunoreactive for β-tyrosine hydroxylase, dopamine and serotonin in the ventral nerve cord of the cricket, *Gryllus bimaculatus*. *Cell Tissue Res.* 280, 583–604. doi: 10.1007/BF00318362

Horseman, G., and Huber, F. (1994). Sound localisation in crickets I. Contralateral inhibition of an ascending auditory interneuron (AN1) in the cricket *Gryllus bimaculatus*. *J. Comp. Physiol. A* 175, 389–398. doi: 10.1007/BF00199247

Hoy, R. R., Popper, A. N., and Fay, R. R. (eds) (1998). *Comparative hearing: Insects, springer handbook of auditory research*. New York, NY: Springer Verlag, doi: 10.1007/978-1-4612-0585-2

Hoyle, G. (1975). Evidence that insect dorsal unpaired medican (DUM) neurons are octopaminergic. *J. Exp. Zool.* 193, 425–431. doi: 10.1002/jez.1401930321

Hoyle, G. (1978). The dorsal, unpaired, median neurons of the locust metathoracic ganglion. *J. Neurobiol.* 9, 43–57. doi: 10.1002/neu.480090105

Hoyle, G. (1983). "On the way to neuroethology: The identified neuron approach," in *Neuroethology and behavioral physiology*, eds F. Huber and H. Markl (Berlin: Springer Verlag), 9–25. doi: 10.1007/978-3-642-69271-0_2

Hoyle, G., Dagan, D., Moberly, B., and Colquhoun, W. (1974). Dorsal unpaired median insect neurons make neurosecretory endings on skeletal muscle. *J. Exp. Zool.* 187, 159–165. doi: 10.1002/jez.1401870119

Huber, F., Loher, W., and Moore, T. E. (eds) (1989). *Cricket behavior and neurobiology*. Ithaca: Cornell University Press.

Huber, F., and Thorson, J. (1985). Cricket auditory communication. *Sci. Am.* 253, 60–68. doi: 10.1038/scientificamerican1285-60

Imaizumi, K., and Pollack, G. S. (1999). Neural coding of sound frequency by cricket auditory receptors. *J. Neurosci.* 19, 1508–1516. doi: 10.1523/JNEUROSCI.19-04-01508.1999

Janiszewski, J., and Otto, D. (1988). Modulation of activity of identified suboesophageal neurons in the cricket *Gryllus bimaculatus* by local changes in body temperature. *J. Comp. Physiol. A* 162, 739–746. doi: 10.1007/BF00610963

Korsunovskaya, O. S., and Zhantiev, R. D. (1992). Auditory interneurons in the phaneropterid bush-crickets (*Orthoptera*, *Phaneropteridae*). *Entomol. Obozr.* Энтомологическое Обозрение 4, 721–730.

Kostarakos, K., and Römer, H. (2010). Sound transmission and directional hearing in field crickets: Neurophysiological studies outdoors. *J. Comp. Physiol. A* 196, 669–681. doi: 10.1007/s00359-010-0557-x

Kostarakos, K., and Römer, H. (2015). Neural mechanisms for acoustic signal detection under strong masking in an insect. *J. Neurosci.* 35, 10562–10571. doi: 10.1523/JNEUROSCI.0913-15.2015

Kulkarni, A., and Extavour, C. G. (2019). "The cricket *Gryllus bimaculatus*: Techniques for quantitative and functional genetic analyses of cricket biology," in *Evo-devo: Non-model species in cell and developmental biology, results and problems in cell differentiation*, eds W. Tworzydlo and S. M. Bilinski (Berlin: Springer International Publishing), 183–216. doi: 10.1007/978-3-030-23459-1_8

Lakes, R. (1990). "Plasticity of the nervous system of *orthopterans*," in *Sensory systems and communication in arthropods*, eds F. G. Gribakin, K. Wiese, and A. V. Popov (Basel: Birkhäuser Verlag), 280–284.

Lakes, R., Kalmring, K., and Engelhard, K.-H. (1990). Changes in the auditory system of locusts (*Locusta migratoria* and *Schistocerca gregaria*) after deafferentation. *J. Comp. Physiol. A* 166, 553–563. doi: 10.1007/BF00192026

Lakes, R., and Schikorski, T. (1990). "Neuroanatomy of tettigoniids," in *The tettigoniidae: Biology, systematics and evolution*, eds W. J. Bailey and D. C. F. Rentz (Berlin: Springer Verlag), 166–190.

Lange, A. B., and Orchard, I. (1984). Dorsal unpaired median neurons, and ventral bilaterally paired neurons, project to a visceral muscle in an insect. *J. Neurobiol.* 15, 441–453. doi: 10.1002/neu.480150605

Larsen, O. N., Kleindienst, H. U., and Michelsen, A. (1989). "Biophysical aspects of sound reception," in *Cricket behavior and neurobiology*, eds F. Huber, W. Loher, and T. E. Moore (Ithaca: Cornell University Press), 364–390.

Larsen, O. N., and Michelsen, A. (1978). Biophysics of the ensiferan ear. III. The cricket ear as a four-input system. *J. Comp. Physiol. A* 123, 217–227. doi: 10.1007/BF00656874

Lefebvre, P. C., Seifert, M., and Stumpner, A. (2018). Auditory DUM neurons in a bush-cricket: A filter bank for carrier frequency. *J. Comp. Neurol.* 526, 1166–1182. doi: 10.1002/cne.24399

Lewis, B. (1992). "The processing of auditory signals in the CNS of *Orthoptera*," in *The evolutionary biology of hearing*, eds D. B. Webster, A. N. Popper, and R. R. Fay (New York, NY: Springer Verlag), 95–114. doi: 10.1007/978-1-4612-2784-7_7

Lühr, B., Hirtz, R., and Wiese, K. (1994). Octopaminergic modulation of cellular parameters and performance of the ON1-circuit in the CNS of an arthropod. *Verh. Dtsch. Zool. Ges.* 87:13.

Marquart, V. (1985). *Auditorische Interneurone im thorakalen Nervensystem von Heuschrecken: Morphologie, Physiologie und synaptische Verbindungen*. Ph.D thesis. Bochum: Ruhr-Universität Bochum.

Marsat, G., and Pollack, G. S. (2004). Differential temporal coding of rhythmically diverse acoustic signals by a single interneuron. *J. Neurophysiol.* 92, 939–948. doi: 10.1152/jn.00111.2004

Mason, A. C., Forrest, T. G., and Hoy, R. R. (1998). Hearing in mole crickets (*Orthoptera*: *Gryllotalpidae*) at sonic and ultrasonic frequencies. *J. Exp. Biol.* 201, 1967–1979. doi: 10.1242/jeb.201.12.1967

Mason, A. C., and Schildberger, K. (1993). Auditory interneurons in *Cyphoderris monstrosa* (*Orthoptera*: *Haglidae*). *J. Comp. Physiol. A* 171, 749–757. doi: 10.1007/BF00213071

Mhatre, N., Montealegre-Z, F., Balakrishnan, R., and Robert, D. (2009). Mechanical response of the tympanal membranes of the tree cricket *Oecanthus henryi*. *J. Comp. Physiol. A* 195, 453–462. doi: 10.1007/s00359-009-0423-x

Michelsen, A., Popov, A. V., and Lewis, B. (1994). Physics of directional hearing in the cricket *Gryllus bimaculatus*. *J. Comp. Physiol. A* 175, 153–164. doi: 10.1007/BF00215111

Moiseff, A., and Hoy, R. R. (1983). Sensitivity to ultrasound in an identified auditory interneuron in the cricket: A possible neural link to phonotactic behavior. *J. Comp. Physiol. A* 152, 155–167. doi: 10.1007/BF00611181

Molina, J., and Stumpner, A. (2005). Effects of pharmacological treatment and photoinactivation on the directional responses of an insect neuron. *J. Exp. Zool. Part A* 303A, 1085–1103. doi: 10.1002/jez.a.228

Montealegre-Z, F., Jonsson, T., Robson-Brown, K. A., Postles, M., and Robert, D. (2012). Convergent evolution between insectand mammalian audition. *Science* 338, 968–971. doi: 10.1126/science.1225271

Nabatiyan, A., Poulet, J. F. A., de Polavieja, G. G., and Hedwig, B. (2003). Temporal pattern recognition based on instantaneous spike rate coding in a simple auditory system. *J. Neurophysiol.* 90, 2484–2493. doi: 10.1152/jn.00259.2003

Nolen, T. G., and Hoy, R. R. (1984). Initiation of behavior by single neurons: The role of behavioral context. *Science* 226, 992–994. doi: 10.1126/science.6505681

Oldfield, B. P. (1988). Tonotopic organization of the insect auditory pathway. *Trends Neurosci.* 11, 267–270. doi: 10.1016/0166-2236(88)90108-7

Ostrowski, T. D., and Stumpner, A. (2010). Frequency processing at consecutive levels in the auditory system of bush crickets (tettigoniidae). *J. Comp. Neurol.* 518, 3101–3116. doi: 10.1002/cne.22385

Pickar-Oliver, A., and Gersbach, C. A. (2019). The next generation of CRISPR–Cas technologies and applications. *Nat. Rev. Mol. Cell Biol.* 20, 490–507. doi: 10.1038/s41580-019-0131-5

Pollack, G. S. (1988). Selective attention in an insect auditory neuron. *J. Neurosci.* 8, 2635–2639. doi: 10.1523/JNEUROSCI.08-07-02635.1988

Pollack, G. S., and Hedwig, B. (2017). "The cricket auditory pathway: Neural processing of acoustic signals," in *The cricket as a model organism*, eds H. W. Horch, T. Mito, A. Popadić, H. Ohuchi, and S. Noji (Tokyo: Springer Verlag), 155–167. doi: 10.1007/978-4-431-56478-2_11

Pollack, G. S., Huber, F., and Weber, T. (1984). Frequency and temporal pattern-dependent phonotaxis of crickets (*Teleogryllus oceanicus*) during tethered flight and compensated walking. *J. Comp. Physiol. A* 154, 13–26. doi: 10.1007/BF00605385

Ponnath, A., and Farris, H. E. (2010). Calcium-dependent control of temporal processing in an auditory interneuron: A computational analysis. *J. Comp. Physiol. A* 196, 613–628. doi: 10.1007/s00359-010-0547-z

Popov, A. V., Markovich, A. M., and Andjan, A. S. (1978). Auditory interneurons in the prothoracic ganglion of the cricket, *Gryllus bimaculatus* deGeer: I. The large segmental auditory neuron (LSAN). *J. Comp. Physiol. A* 126, 183–192. doi: 10.1007/BF00666372

Poulet, J. F. A., and Hedwig, B. (2002). A corollary discharge maintains auditory sensitivity during sound production. *Nature* 418, 872–876. doi: 10.1038/nature00919

Poulet, J. F. A., and Hedwig, B. (2006). The cellular basis of a corollary discharge. *Science* 311, 518–522. doi: 10.1126/science.1120847

Poulet, J. F. A., and Hedwig, B. (2007). New insights into corollary discharges mediated by identified neural pathways. *Trends Neurosci.* 30, 14–21. doi: 10.1016/j.tins.2006.11.005

Prešern, J., Triblehorn, J. D., and Schul, J. (2015). Dynamic dendritic compartmentalization underlies stimulus-specific adaptation in an insect neuron. *J. Neurophysiol.* 113, 3787–3797. doi: 10.1152/jn.00945.2014

Rau, F., Clemens, J., Naumov, V., Hennig, R. M., and Schreiber, S. (2015). Firing-rate resonances in the peripheral auditory system of the cricket, *Gryllus bimaculatus*. *J. Comp. Physiol. A* 201, 1075–1090. doi: 10.1007/s00359-015-1036-1

Reeve, R. E., and Webb, B. H. (2003). New neural circuits for robot phonotaxis. *Philos. Trans. R. Soc. Lond. Ser. Math. Phys. Eng. Sci.* 361, 2245–2266. doi: 10.1098/rsta.2003.1274

Regen, J. (1913). Über die Anlockung des Weibchens von *Gryllus campestris* L. durch telephonisch übertragene Stridulationslaute des Männchens: Ein Beitrag zur Frage der Orientierung bei den *Insekten. Pflüg. Arch. Für Gesamte Physiol. Menschen Tiere* 155, 193–200. doi: 10.1007/BF01680887

Regen, J. (1914). Untersuchungen über die Stridulation und das Gehör von *Thamnotrizon apterus* Fab. *Sitzungsber. Kais. Akad. Wiss. Wien Math. Naturwiss. Kl* 123, 853–892.

Rehbein, H. (1973). Experimentell-anatomische Untersuchungen über den Verlauf der Tympanalnervenfasern im Bauchmark von Feldheuschrecken, Laubheuschrecken und Grillen. *Verh. Dtsch. Zool. Ges.* 66, 184–189.

Rehbein, H., Kalmring, K., and Römer, H. (1974). Structure and function of acoustic neurons in the thoracic ventral nerve cord of *Locusta migratoria* (*Acrididae*). *J. Comp. Physiol. A* 95, 263–280. doi: 10.1007/BF00625448

Rheinlaender, J., and Römer, H. (1986). Insect hearing in the field: I. The use of identified nerve cells as "biological microphones.". *J. Comp. Physiol. A* 158, 647–651. doi: 10.1007/BF00603821

Roeder, K. D. (1966). Auditory system of noctuid moths: Complex nerve mechanisms enable moths to detect the ultrasonic cries of insect-eating bats. *Science* 154, 1515–1521. doi: 10.1126/science.154.3756.1515

Römer, H. (1985). "Anatomical representation of frequency and intensity in the audiory system of *Orthoptera*," in *Proceedings of the Acoustic and vibrational communication in insects: Proceedings from the XVII. International congress of entomology held at the university of hamburg, august 1984. presented at the 17th international congress of entomology* (Berlin: Verlag Paul Parey).

Römer, H. (1987). Representation of auditory distance within a central neuropil of the bushcricket *Mygalopsis marki*. *J. Comp. Physiol. A* 161, 33–42. doi: 10.1007/BF00609453

Römer, H. (1993). Environmental and biological constraints for the evolution of long-range signalling and hearing in acoustic insects. *Philos. Trans. R. Soc. Lond. B Biol. Sci.* 340, 179–185. doi: 10.1098/rstb.1993.0056

Römer, H. (2021). Neurophysiology goes wild: From exploring sensory coding in sound proof rooms to natural environments. *J. Comp. Physiol. A* 207, 303–319. doi: 10.1007/s00359-021-01482-6

Römer, H., and Bailey, W. (1998). Strategies for hearing in noise: Peripheral control over auditory sensitivity in the bushcricket *Sciarasaga quadrata* (*Austrosaginae*: *Tettigoniidae*). *J. Exp. Biol.* 201, 1023–1033. doi: 10.1242/jeb.201.7.1023

Römer, H., Bailey, W., and Dadour, I. (1989). Insect hearing in the field: III. Masking by noise. *J. Comp. Physiol. A* 164, 609–620. doi: 10.1007/BF00614503

Römer, H., and Bailey, W. J. (1986). Insect hearing in the field: II. Male spacing behaviour and correlated acoustic cues in the bushcricket *Mygalopsis marki*. *J. Comp. Physiol. A* 159, 627–638. doi: 10.1007/BF00612036

Römer, H., Hedwig, B., and Ott, S. R. (2002). Contralateral inhibition as a sensory bias: The neural basis for a female preference in a synchronously calling bushcricket, *Mecopoda elongata*: Sensory bias and female preferences in acoustic insects. *Eur. J. Neurosci.* 15, 1655–1662. doi: 10.1046/j.1460-9568.2002.02003.x

Römer, H., and Krusch, M. (2000). A gain-control mechanism for processing of chorus sounds in the afferent auditory pathway of the bushcricket *Tettigonia viridissima* (*Orthoptera*; *Tettigoniidae*). *J. Comp. Physiol. A* 186, 181–191. doi: 10.1007/s003590050018

Römer, H., and Marquart, V. (1984). Morphology and physiology of auditory interneurons in the metathoracic ganglion of the locust. *J. Comp. Physiol. A* 155, 249–262. doi: 10.1007/BF00612642

Römer, H., Marquart, V., and Hardt, M. (1988). Organization of a sensory neuropile in the auditory pathway of two groups of *Orthoptera*. *J. Comp. Neurol.* 275, 201–215. doi: 10.1002/cne.902750204

Schildberger, K. (1984). Temporal selectivity of identified auditory neurons in the cricket brain. *J. Comp. Physiol. A* 155, 171–185. doi: 10.1007/BF00612635

Schildberger, K., and Hörner, M. (1988). The function of auditory neurons in cricket phonotaxis: I. Influence of hyperpolarization of identified neurons on sound localization. *J. Comp. Physiol. A* 163, 621–631. doi: 10.1007/BF00603846

Schildberger, K., Wohlers, D. W., Schmitz, B., Kleindienst, H.-U., and Huber, F. (1986). Morphological and physiological changes in central auditory neurons following unilateral foreleg amputation in larval crickets. *J. Comp. Physiol. A* 158, 291–300. doi: 10.1007/BF00603613

Schmidt, A. K. D., and Römer, H. (2011). Solutions to the cocktail party problem in insects: Selective filters, spatial release from masking and gain control in tropical crickets. *PLoS One* 6:e28593. doi: 10.1371/journal.pone.0028593

Schmidt, A. K. D., and Römer, H. (2016). Functional relevance of acoustic tracheal design in directional hearing in crickets. *J. Exp. Biol.* 219, 3294–3300. doi: 10.1242/jeb.145524

Schmitz, B. (1989). Neuroplasticity and phonotaxis in monaural adult female crickets (*Gryllus bimaculatus* de Geer). *J. Comp. Physiol. A* 164, 343–358. doi: 10.1007/BF00612994

Schöneich, S., Kostarakos, K., and Hedwig, B. (2015). An auditory feature detection circuit for sound pattern recognition. *Sci. Adv.* 1:e1500325. doi: 10.1126/sciadv.1500325

Schul, J. (1997). Neuronal basis of phonotactic behaviour in *Tettigonia viridissima*: Processing of behaviourally relevant signals by auditory afferents and thoracic interneurons. *J. Comp. Physiol. A* 180, 573–583. doi: 10.1007/s003590050074

Schul, J., and Patterson, A. C. (2003). What determines the tuning of hearing organs and the frequency of calls? A comparative study in the katydid genus *Neoconocephalus* (*Orthoptera*, *Tettigoniidae*). *J. Exp. Biol.* 206, 141–152. doi: 10.1242/jeb.00070

Selverston, A. I., Kleindienst, H. U., and Huber, F. (1985). Synaptic connectivity between cricket auditory interneurons as studied by selective photoinactivation. *J. Neurosci.* 5, 1283–1292. doi: 10.1523/JNEUROSCI.05-05-01283.1985

Shaw, K. L., and Herlihy, D. P. (2000). Acoustic preference functions and song variability in the Hawaiian cricket *Laupala cerasina*. *Proc. R. Soc. Lond. B Biol. Sci.* 267, 577–584. doi: 10.1098/rspb.2000.1040

Sickmann, T. (1997). *Vergleichende funktionelle und anatomische Untersuchung zum Aufbau der Hör- und Vibrationsbahn im thorakalen Bauchmark von Laubheuschrecken*. Ph.D thesis. Marburg: Philipps-Universität Marburg.

Skiebe, P., Corrette, B. J., and Wiese, K. (1990). Evidence that histamine is the inhibitory transmitter of the auditory interneuron ON1 of crickets. *Neurosci. Lett.* 116, 361–366. doi: 10.1016/0304-3940(90)90102-F

Sobel, E. C., and Tank, D. W. (1994). *In vivo* Ca $^{2+}$ dynamics in a cricket auditory neuron: An example of chemical computation. *Science* 263, 823–826. doi: 10.1126/science.263.5148.823

Song, H., Amédégnato, C., Cigliano, M. M., Desutter-Grandcolas, L., Heads, S. W., Huang, Y., et al. (2015). 300 million years of diversification: Elucidating the patterns of orthopteran evolution based on comprehensive taxon and gene sampling. *Cladistics* 31, 621–651. doi: 10.1111/cla.12116

Song, H., Béthoux, O., Shin, S., Donath, A., Letsch, H., Liu, S., et al. (2020). Phylogenomic analysis sheds light on the evolutionary pathways towards acoustic communication in *Orthoptera*. *Nat. Commun.* 11:4939. doi: 10.1038/s41467-020-18739-4

Stewart, W. W. (1978). Functional connections between cells as revealed by dye-coupling with a highly fluorescent naphthalimide tracer. *Cell* 14, 741–759. doi: 10.1016/0092-8674(78)90256-8

Stiedl, O., Stumpner, A., Mbungu, D. N., Atkins, G., and Stout, J. F. (1997). Morphology and physiology of local auditory interneurons in the prothoracic ganglion of the cricket *Acheta domesticus*. *J. Exp. Zool.* 279, 43–53. doi: 10.1002/(SICI)1097-010X(19970901)279:1<43::AID-JEZ4<3.0.CO;2-1

Stretton, A. O. W., and Kravitz, E. A. (1968). Neuronal geometry: Determination with a technique of intracellular dye injection. *Science* 162, 132–134. doi: 10.1126/science.162.3849.132

Stritih, N., and Stumpner, A. (2009). Vibratory interneurons in the non-hearing cave cricket indicate evolutionary origin of sound processing elements in *Ensifera*. *Zoology* 112, 48–68. doi: 10.1016/j.zool.2008.04.005

Stumpner, A. (1995). "Some new local and descending auditory neurons in the prothoracic ganglion of crickets and bushcrickets," in *Proceedings of the 23rd Göttingen neurobiology conference. presented at the 23rd Göttingen neurobiology conference*, eds N. Elsner and R. Menzel (Stuttgart: Thieme Verlag).

Stumpner, A. (1999). An interneurone of unusual morphology is tuned to the female song frequency in the bushcricket *Ancistrura nigrovittata* (*Orthoptera*, *Phaneropteridae*). *J. Exp. Biol.* 202, 2071–2081. doi: 10.1242/jeb.202.15.2071

Stumpner, A. (2002). A species-specific frequency filter through specific inhibition, not specific excitation. *J. Comp. Physiol. A* 188, 239–248. doi: 10.1007/s00359-002-0299-5

Stumpner, A., Atkins, G., and Stout, J. F. (1995). Processing of unilateral and bilateral auditory inputs by the ON1 and L1 interneurons of the cricket *Acheta domesticus* and comparison to other cricket species. *J. Comp. Physiol. A* 177, 379–388. doi: 10.1007/BF00192427

Stumpner, A., Gubert, S., Knorr, D. Y., and Göpfert, M. C. (2020). Auditory DUM neurons in a bush-cricket: Inhibited inhibitors. *J. Comp. Physiol. A* 206, 793–807. doi: 10.1007/s00359-020-01438-2

Stumpner, A., Lefebvre, P. C., Seifert, M., and Ostrowski, T. D. (2019). Temporal processing properties of auditory DUM neurons in a bush-cricket. *J. Comp. Physiol. A* 205, 717–733. doi: 10.1007/s00359-019-01359-9

Stumpner, A., and Molina, J. (2006). Diversity of intersegmental auditory neurons in a bush cricket. *J. Comp. Physiol. A* 192, 1359–1376. doi: 10.1007/s00359-006-0164-z

Stumpner, A., and Nowotny, M. (2014). "Neural processing in the bush-cricket auditory pathway," in *Insect hearing and acoustic communication, animal signals and communication*, ed. B. Hedwig (Berlin: Springer Verlag), 143–166. doi: 10.1007/978-3-642-40462-7_9

Stumpner, A., and Ronacher, B. (1991). Auditory interneurones in the metathoracic ganglion of the grasshopper *Chorthippus biguttulus* : I. Morphological and physiological characterization. *J. Exp. Biol.* 158, 391–410. doi: 10.1242/jeb.158.1.391

Tanaka, Y., and Washio, H. (1988). Morphological and physiological properties of the dorsal unpaired median neurons of the cockroach metathoracic ganglion. *Comp. Biochem. Physiol. A Physiol.* 91, 37–41. doi: 10.1016/0300-9629(88)91589-7

ter Hofstede, H. M., Schöneich, S., Robillard, T., and Hedwig, B. (2015). Evolution of a communication system by sensory exploitation of startle behavior. *Curr. Biol.* 25, 3245–3252. doi: 10.1016/j.cub.2015.10.064

Thompson, K. J., and Siegler, M. V. S. (1991). Anatomy and physiology of spiking local and intersegmental interneurons in the median neuroblast lineage of the grasshopper. *J. Comp. Neurol.* 305, 659–675. doi: 10.1002/cne.903050409

Thompson, K. J., and Siegler, M. V. S. (1993). Development of segment specificity in identified lineages of the grasshopper CNS. *J. Neurosci.* 13, 3309–3318. doi: 10.1523/JNEUROSCI.13-08-03309.1993

Triblehorn, J. D., and Schul, J. (2009). Sensory-encoding differences contribute to species-specific call recognition mechanisms. *J. Neurophysiol.* 102, 1348–1357. doi: 10.1152/jn.91276.2008

Tunstall, D. N., and Pollack, G. S. (2005). Temporal and directional processing by an identified interneuron, ON1, compared in cricket species that sing with different tempos. *J. Comp. Physiol. A* 191, 363–372. doi: 10.1007/s00359-004-0591-7

Vavakou, A., Scherberich, J., Nowotny, M., and van der Heijden, M. (2021). Tuned vibration modes in a miniature hearing organ: Insights from the bushcricket. *Proc. Natl. Acad. Sci.U.S.A.* 118:e2105234118. doi: 10.1073/pnas.2105234118

Verburgt, L., and Ferguson, J. W. H. (2010). Mate choice in field crickets: Can females acoustically detect male body size? *J. Ethol.* 28, 141–151. doi: 10.1007/s10164-009-0166-8

Washio, H. (2002). Glutamate receptors on the somata of dorsal unpaired median neurons in cockroach, *Periplaneta americana,* thoracic ganglia. *Zool. Sci.* 19, 153–162. doi: 10.2108/zsj.19.153

Watson, A. H. D., and Hardt, M. (1996). Distribution of synapses on two local auditory interneurones, ON1 and ON2, in the prothoracic ganglion of the cricket: Relationships with GABA-immunoreactive neurones. *Cell Tissue Res.* 283, 231–246. doi: 10.1007/s004410050534

Wiese, K. (1981). Influence of vibration on cricket hearing: Interaction of low frequency vibration and acoustic stimuli in the omega neuron. *J. Comp. Physiol. A* 143, 135–142. doi: 10.1007/BF00606077

Wiese, K., and Eilts, K. (1985). Evidence for matched frequency dependence of bilateral inhibition in the auditory pathway of *Gryllus bimaculatus*. *Zool. JB. Physiol.* 89, 181–201.

Wohlers, D. W., and Huber, F. (1978). Intracellular recording and staining of cricket auditory interneurons (*Gryllus campestris* L., *Gryllus bimaculatus* DeGeer). *J. Comp. Physiol. A* 127, 11–28. doi: 10.1007/BF00611922

Wohlers, D. W., and Huber, F. (1982). Processing of sound signals by six types of neurons in the prothoracic ganglion of the cricket, *Gryllus campestris* L. *J. Comp. Physiol. A* 146, 161–173. doi: 10.1007/BF00610234

Wohlers, D. W., and Huber, F. (1985). Topographical organization of the auditory pathway within the prothoracic ganglion of the cricket *Gryllus campestris* L. *Cell Tissue Res.* 239, 555–565. doi: 10.1007/BF00219234

Wyttenbach, R. A., May, M. L., and Hoy, R. R. (1996). Categorical perception of sound frequency by crickets. *Science* 273, 1542–1544.

Zhang, X., and Hedwig, B. (2019). Bilateral auditory processing studied by selective cold-deactivation of cricket hearing organs. *J. Exp. Biol.* 222:jeb210799. doi: 10.1242/jeb.210799

Zhantiev, R. D., and Korsunovskaya, O. S. (1983). Structure and functions of two auditory neurons in the bush cricket *Tettigonia cantans* Fuess. (*Orthoptera*, *Tettigoniidae*). *Entomol. Obozr.* Энтомологическое Обозрение 3, 462–469.

Zhantiev, R. D., and Korsunovskaya, O. S. (1990a). "Auditory interneurons in mole crickets (*Orthoptera*: *Gryllotalpidae*)," in *Sensory systems and communication in arthropods*, eds F. G. Gribakin, K. Wiese, and A. V. Popov (Basel: Birkhäuser Verlag), 407–416. doi: 10.1007/978-3-0348-6410-7_70

Zhantiev, R. D., and Korsunovskaya, O. S. (1990b). "Sound communication of *Phaneropteridae* (*Orthoptera*)," in *Sensory systems and communication in arthropods*, eds F. G. Gribakin, K. Wiese, and A. V. Popov (Basel: Birkhäuser Verlag), 402–406. doi: 10.1007/978-3-0348-6410-7_69

frontiers | Frontiers in Neuroscience

TYPE Review
PUBLISHED 22 December 2022
DOI 10.3389/fnins.2022.1072974

OPEN ACCESS

EDITED BY
James Newcomb,
New England College, United States

REVIEWED BY
Leonid L. Moroz,
University of Florida, United States
Brett Szymik,
Augusta University/University of Georgia Medical Partnership, Georgia

*CORRESPONDENCE
Thomas J. Pirtle
✉ tpirtle@collegeofidaho.edu

SPECIALTY SECTION
This article was submitted to Neural Technology, a section of the journal Frontiers in Neuroscience

RECEIVED 18 October 2022
ACCEPTED 05 December 2022
PUBLISHED 22 December 2022

CITATION
Pirtle TJ (2022) A review of the circuit-level and cellular mechanisms contributing to locomotor acceleration in the marine mollusk *Clione limacina*. *Front. Neurosci.* 16:1072974. doi: 10.3389/fnins.2022.1072974

A review of the circuit-level and cellular mechanisms contributing to locomotor acceleration in the marine mollusk *Clione limacina*

Thomas J. Pirtle*

Department of Biology, The College of Idaho, Caldwell, ID, United States

The pteropod mollusk, *Clione limacina*, is a useful model system for understanding the neural basis of behavior. Of particular interest are the unique swimming behavior and neural circuitry that underlies this swimming behavior. The swimming system of *Clione* has been studied by two primary groups—one in Russia and one in the United States of America—for more than four decades. The neural circuitry, the cellular properties, and ion channels that create and change the swimming locomotor rhythm of *Clione*—particularly mechanisms that contribute to swimming acceleration—are presented in this review.

KEYWORDS

***Clione*, CPG, locomotion, modulation, HCN, statocyst function, feeding behavior, neural circuit**

Introduction

Many animals, by virtue of neural circuits called central pattern generators (CPGs) in their central nervous system, can create and control rhythmic movements (Delcomyn, 1980; Guertin, 2013; Bucher et al., 2015). These movements may be visceral in nature, controlling for example, heartbeat and digestive movement (Selverston et al., 1976; Arbas and Calabrese, 1984), or somatic, controlling body movements related to locomotion (Getting, 1981; Grillner and Wallén, 1985; Pearson and Wolf, 1987; Brodfuehrer et al., 1995; Arshavsky et al., 1998; Jing and Gillette, 1999; Thompson and Watson, 2005; Guertin, 2009; Fetcho and McLean, 2010; Zhong et al., 2012; Stein, 2018). This review summarizes the circuit-level and cellular properties of CPG interneurons of the marine pteropod mollusk, *Clione limacina*, that create and control the rhythmic movement of the animal's wing-like parapodia. An added emphasis is on the mechanisms contributing to an increase in *Clione* locomotor speed.

Clione, its major internal organs, and its central nervous system along with some peripheral nerves is shown in **Figure 1**. The *Clione* depicted in **Figure 1A**. is representative of the animal in its slow swimming mode in which the long axis of the

body is oriented vertically in the water column with the head (containing the buccal cones, BC, and buccal mass, BM) pointing upward toward the water's surface and tail (T) pointing directly downward toward the ocean bottom. Within the head are the prey capturing BC and feeding structures of the BM. There are three laterally placed BC on each side of *Clione*'s head that rapidly inflate to capture its prey, the shelled thecosome pteropod mollusk, *Limacina helicina*. The BM contains a feeding apparatus that includes chitinous hooks and radula, along with associated musculature. The hooks and radula grasp the *Limacina* and pull it from the shell to be swallowed. Other organs depicted in **Figure 1** include organs of the reproductive system, the ovotestis (OT), organs of the digestive system, the esophagus (E) and digestive gland (DG), and the circulatory system, the heart (H; Wagner, 1885; Lalli and Gilmer, 1989). Because protraction of the prey capturing BC, and an increase in heartbeat occur with swimming acceleration, these structures are relevant to the discussion of the control of *Clione* swimming speed and are addressed in this review (Arshavsky et al., 1990; Norekian and Satterlie, 1995).

The central nervous system of *Clione*, shown in **Figure 1B**, like that of other gastropod mollusks, consists of pairs of connected ganglia that encircle the esophagus (E in **Figure 1A**) as a circumesophageal ring. From anterior to posterior, the ganglion of *Clione* includes paired buccal ganglia (B), cerebral ganglia (C), pleural ganglia (Pl), pedal ganglia (Pd), and intestinal ganglia (I). The right and left paired ganglia are connected by commissures, such as the right and left pedal ganglia that are connected *via* a pedal commissure (PC), or are fused together, such as the intestinal ganglia. There is no connecting commissure between the right and left pleural ganglia. Also shown in **Figure 1B** are the statocysts (St) that make up the vestibular or statomotor system of *Clione*, which contribute to the ability of *Clione* to orient its body within the water column and, during slow swimming, maintain the vertical body orientation as depicted in **Figure 1B** (Satterlie et al., 1985; Satterlie and Spencer, 1985; Panchin et al., 1995a). The wing nerve (WN) carries axons that innervate the parapodia and branches into two main branches, the anterior and posterior branches (NWA and NWP, respectively; Zelenin and Panchin, 2000).

Swimming locomotion in *Clione* is produced by the dorsal-ventral movement of its parapodia (P in **Figure 1A**; also referred to as wings). Parapodial movement is controlled by swimming musculature that is in turn controlled by motoneurons whose rhythmic activity is produced and controlled by a circuit of swim interneurons making up the animal's swim CPG (Arshavsky et al., 1985a,b,c; Satterlie, 1985; Satterlie and Spencer, 1985). A simple schematic diagram of the *Clione* swim CPG is illustrated in **Figure 2**. This diagram is a classic example of the half-center model first proposed by Brown (1911) and shows that the *Clione* swim CPG consists of two groups of swim interneurons. One group of swim interneurons controls

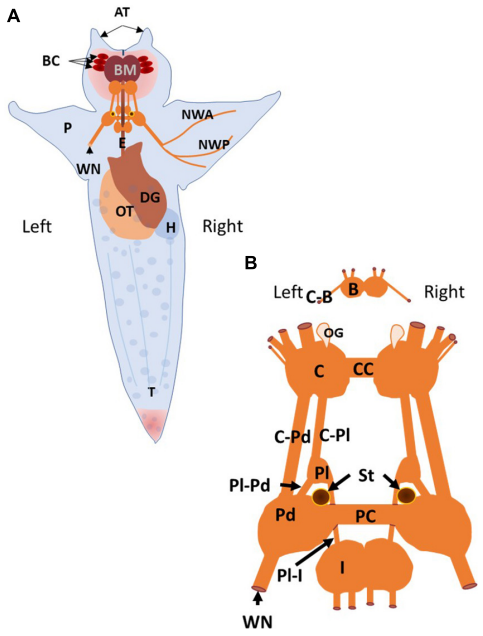

FIGURE 1
The anatomy of *Clione* and the organization of its central nervous system and related structures are illustrated. **(A)** The dorsal surface of *Clione* is depicted. *Clione* is typically engaged in slow, hovering swimming in which the long axis of the body is oriented perpendicularly to the ocean surface and ocean bottom with the head pointing upward and the tail pointing downward as depicted. The structures that are identified include retracted buccal cones (BC) and buccal mass (BM) found in the head and are important in prey capture and feeding. The buccal cones participate in prey capture and the buccal mass includes the radula and as set of chitinous hooks with associated musculature for extracting the prey, *Limacina helicina*, from its shell. Additionally, there are two laterally placed cephalic appendages, the anterior tentacles (AT) connected with the head of *Clione*. Between the anterior tentacles is slit-like mouth flanked by lips. *Limacina* is swallowed whole and passes down the esophagus (E) that is encircled by the central nervous system (CNS) composed of interconnected ganglia. Other organs identified include reproductive organs, the ovotestis (OT), digestive organs, the digestive gland (DG), and cardiovascular organs, the heart (H). Additionally, the major nerve innervating the wing-like parapodia (P), the wing nerve (WN) and its two primary branches (NWA and NWP) are identified. **(B)** The *Clione* CNS consists of paired ganglia that include the buccal ganglia (B), the cerebral ganglia (C), the pleural ganglia (Pl), the pedal ganglia (Pd), and intestinal ganglia (I). The buccal ganglia are connected to the cerebral ganglia *via* cerebro-buccal connectives (C-B; cut), the left and right cerebral ganglia are connected to each other by a commissure (CC) and connected to the ipsilateral pleural ganglia and ipsilateral pedal ganglia *via* the cerebro-pleural connective (C-Pl) and the cerebro-pedal connective (C-Pd), respectively. The pleural ganglia are connected to the ipsilateral pedal and intestinal ganglia *via* the pleuro-pedal and pleuro-intestinal connectives, respectively. The left and right pedal ganglia are connected to each other by the pedal commissure. The wing nerve is also connected to the pedal ganglia and carries afferent and efferent information related to the wing-like parapodia (P). Other structures identified include the sensory structures labeled OG, the olfactory organ, and ST, the statocysts (Wagner, 1885; Arshavsky et al., 1985a,b,c, 1990; Lalli and Gilmer, 1989; Hermans and Satterlie, 1992; Satterlie et al., 1995; Moroz et al., 2000; Zelenin and Panchin, 2000).

the dorsal (or upstroke) movement of the parapodia, and the other group of swim interneurons controls the ventral (or downstroke) movement of the parapodia. Dorsal and ventral swim interneurons reciprocally inhibit each other so that when one group is active it simultaneously causes an inhibitory postsynaptic potential (IPSP) in the other group, thus inhibiting the other group. This reciprocal inhibition creates the alternating dorsal-ventral movement of the parapodia, and the duration of the IPSP is a principal variable that controls *Clione* swimming frequency (Arshavsky et al., 1993a; Satterlie et al., 2000). Furthermore, each swim interneuron produces a single broad action potential that conveys information to control synergistic motoneurons whose activity then controls the corresponding parapodial muscle contractions. Thus, there is a one-to-one correspondence between the activity of the interneuron, its synergistic motoneurons, and the parapodial muscle contraction produced by motoneuron innervation (Arshavsky et al., 1985b; Satterlie and Spencer, 1985).

The interneurons that compose the *Clione* swim CPG, the motoneurons that the CPG controls, and the neurons that contribute to the variability of locomotor activity and other related behaviors such as feeding and heartbeat regulation are illustrated in **Figures 3A–E**.

The buccal ganglia are shown in **Figure 3A**. The three neuronal somas (colored red) in the buccal ganglia shown in **Figure 3A** are GABAergic (see also **Figure 4D**) and control aspects of feeding behavior. The GABAergic neuron indicated by the white arrowhead and outlined with a dashed line is located on the ventral surface of the buccal ganglion. Within the cerebral ganglia shown in **Figure 3B**, are serotonergic neurons (orange) that are important mediators of swim acceleration. One of these serotonergic neurons is found on the ventral surface of the cerebral ganglion (gray arrowhead and outlined with a dashed line). Additionally, shown in red and located laterally and caudally near the cerebro-pedal connective are four GABAergic neurons (see also **Figure 4D**) that participate in feeding behavior (Norekian, 1999). Within the pleural ganglia (**Figure 3C**) are neurons that include swim interneuron 12 that is recruited into the CPG circuit during swim acceleration (Arshavsky et al., 1985d, 1989; Pirtle and Satterlie, 2006). Additionally, the neurons controlling whole body withdrawal and inhibition of swimming are in the pleural ganglia and include Pl-W neurons labeled 1–4 (Norekyan, 1989; Norekian and Satterlie, 1996a). The large asymmetrical white cell (blue arrowhead in **Figure 3C**) found in the right pleural ganglia mediates egg laying (Norekian and Satterlie, 2001). The neurons of the pedal ganglia include the swim interneurons composing the *Clione* swim CPG and the swim motoneurons controlled by the CPG circuit. Swim interneurons and the synergistic swim motoneurons that control the dorsal flexion of the parapodia are designated by odd numbers while the swim interneurons and the synergistic swim motoneurons that control the ventral flexion of the parapodia are designated by even numbers. Swim interneurons include the dorsal swim interneurons, 7, and ventral swim interneurons, 8 (see also **Figure 2**). There are swim motoneurons with relatively small soma called small motoneurons labeled 1, 2, 3, and 4. These small motoneurons have restricted innervation fields and control only the slow-twitch swim muscle of the parapodia. Two neurons labeled 1A and 2A are large motoneurons (referred to as general

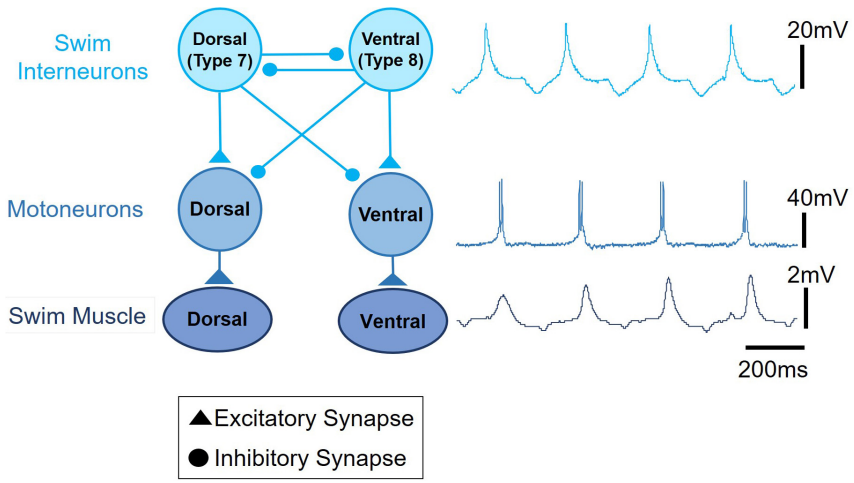

FIGURE 2
A schematic circuit representation of the *Clione* swim central pattern generator (swim CPG) network. The single broad action potential recorded from a dorsal swim interneuron, the burst of action potentials recorded from a synergistic dorsal small motoneuron, and the uncalibrated movement of the parapodia are displayed on the right next to the circuit diagram. Excitatory synaptic communication is shown by filled triangles and inhibitory synaptic communication is shown by closed circles. An important network feature of the *Clione* swim CPG is the reciprocal inhibitory synaptic communication between antagonistic groups of swim interneurons.

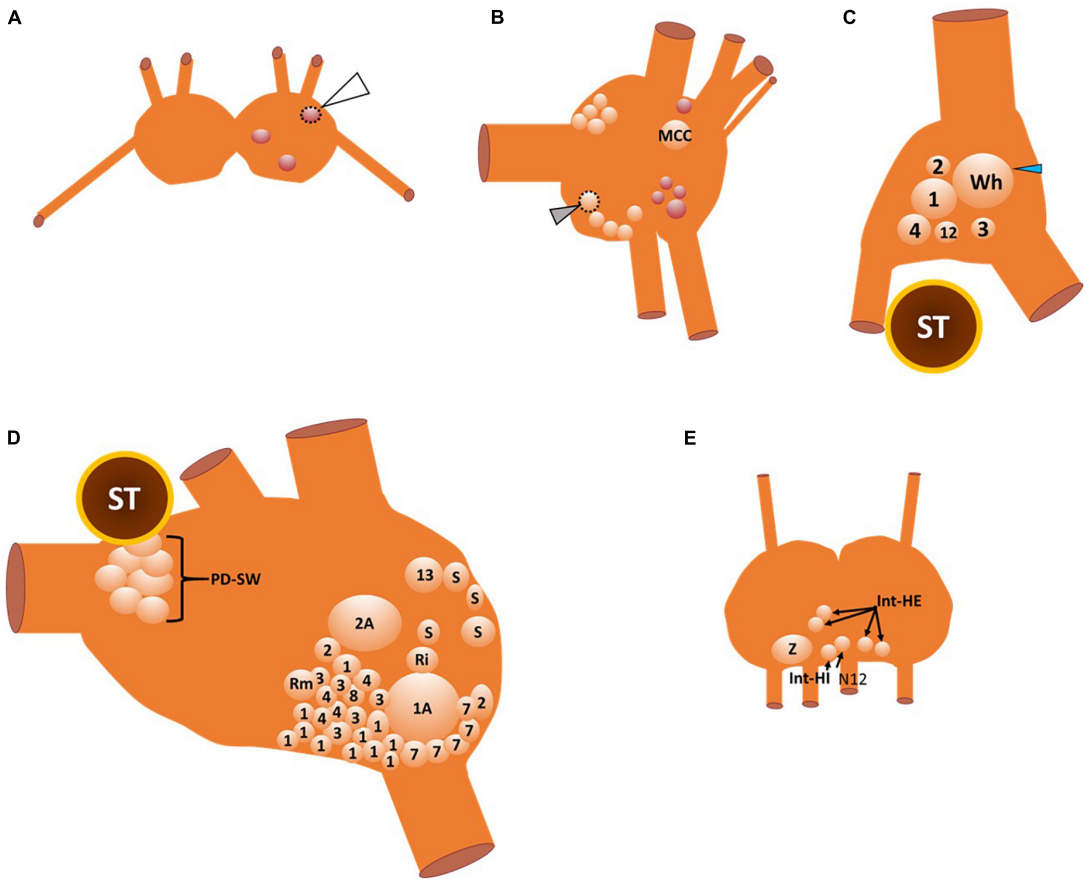

FIGURE 3
A map of the neuronal somas of the buccal ganglia **(A)**, right cerebral ganglion **(B)**, right pleural ganglion **(C)**, right pedal ganglion **(D)**, and intestinal ganglia **(E)**. Cells that are outlined by a dashed line are located on the ventral surface, otherwise all other somas are located on the dorsal surface. There are three neurons in the buccal ganglia **(A)** that are all GABAergic (see also **Figure 4D**). The one buccal ganglia soma that is outlined by the dotted line and indicated by the white arrowhead is located on the ventral surface of the buccal ganglia. The neurons of the cerebral ganglia **(B)** include the large serotonergic metacerebral cell that participates in feeding behaviors. The cluster of neuronal somas that occur posteromedial (including the ventral cell that is outlined with a dotted line and indicated by the gray arrowhead) and anteromedial near the cerebral commissure (cut) are serotonergic cells that evoke locomotor speed acceleration when stimulated. GABAergic neurons that are shown in red are important elements of the control of feeding behavior. In the right pleural ganglia **(C)** there are six neuronal somas (all located on the dorsal surface) identified that participate in swimming, whole-body withdrawal, and reproduction. The neuronal soma labeled 12 is the type 12 interneuron that is recruited into the *Clione* swim CPG during swim acceleration. Neuronal somas 1–4 participate in the whole-body withdrawal response that promotes wing and buccal cone retraction and inhibit swimming. The large soma labeled Wh and indicated by the blue arrowhead is the asymmetric pleural white cell that is only located in the right pleural ganglia. Wh participates in reproduction and egg laying. The neuronal somas of the right pedal ganglia **(D)** include interneurons that compose the *Clione* swim CPG, motoneurons, neurons that control the strength of parapodial movement, and neurons related to the parapodial (wing) withdrawal reflex. Odd numbers designate neurons that control the dorsal flexion of the parapodia while even numbers designate neurons that control the ventral flexion of the parapodia during swimming. The neurons labeled 7 and 8 are swim interneurons that compose the *Clione* swim CPG. The neurons labeled 1, 2, 3, and 4 are small motoneurons whose activity controls the slow-twitch swim muscle fibers within restricted innervation fields of the ipsilateral parapodia. Neurons 1A and 2A are large motoneurons that are also referred to as general excitor motoneurons (GEMN or GE) that innervate the entire expanse of the parapodia and communicate to both slow-twitch and fast-twitch swim muscle fibers in the parapodia. Neuron 13 is dopaminergic and controls swim inhibition. Neurons designated S, Ri, and Rm are sensory, interneuron, and motoneurons, respectively, that control the wing retraction reflex. Neuronal somas identified in the intestinal ganglia **(E)** control the heartbeat (all on the dorsal surface of the ganglia). These neurons include the intestinal heart excitor cells (Int-HE), Z cell (Z), and intestinal heart inhibitory cells (Int-HI). Axons of these neurons exit the median nerve, N12 (Arshavsky et al., 1985a,b,c, 1989, 1990; Satterlie, 1985, 1995a; Satterlie and Spencer, 1985; Norekyan, 1989; Huang and Satterlie, 1990; Norekian and Satterlie, 1996a; Malyshev et al., 2008).

excitor motoneurons; GEMN or GE) that have an expansive innervation field covering the entire parapodia and control the contraction of both slow-twitch and fast-twitch swim muscle fibers (Arshavsky et al., 1985b; Satterlie and Spencer, 1985; Satterlie, 1993). Located in the medial part of the pedal ganglia near the pedal commissure are a cluster of serotonergic neurons called Pd-SW neurons that control the contractile force of parapodial slow-twitch muscle fibers (Satterlie, 1995b; Plyler and Satterlie, 2020). A single asymmetric serotonergic neuron in the left pedal ganglia is the heart excitor neuron (HE)

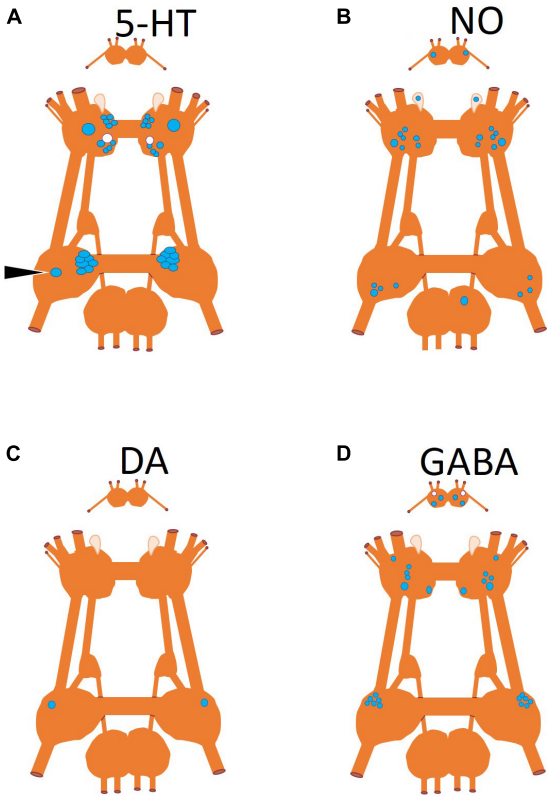

FIGURE 4
Neuronal somas mapped according to neurotransmitter produced by the neuron. **(A)** Serotonin (5-HT) identified by immunohistochemistry (Satterlie et al., 1995), **(B)** nitric oxide (NO) identified by nicotinamide adenine dinucleotide phosphate diaphorase (NADPH-d) histochemistry (Moroz et al., 2000), **(C)** dopamine identified through pharmacological antagonist blocking its physiological effect (Norekyan, 1989), and **(D)** gamma-aminobutyric acid (GABA) identified by immunohistochemistry (Norekian, 1999; Norekian and Malyshev, 2006). Somas that are blue are located on the dorsal surface of the ganglion and somas in white are located on the ventral surface of the ganglion.

that controls the heartbeat (**Figure 4A**; Arshavsky et al., 1990; Satterlie et al., 1995; Malyshev et al., 2008). The remaining neurons labeled in the pedal ganglion are the neurons that control the wing withdrawal reflex when the parapodia (wings) receive tactile stimulation. These neurons include sensory neurons (S), wing-retraction interneurons (Ri), and wing-retraction motoneurons (Rm; Huang and Satterlie, 1990). Interneuron 13 is dopaminergic and mediates swim inhibition (Norekyan, 1989). The neuronal somas in the intestinal ganglia shown in **Figure 3E** control the heart rate and include heart excitors that increase the heart rate, Int-HE and Z cell, and heart inhibitors, Int-HI, that decrease heart rate (Arshavsky et al., 1990; Malyshev et al., 2008).

In addition to the anatomical locations of neurons that control the behaviors of *Clione*, **Figure 4** shows the neurotransmitters characteristic of these neurons (**Figures 4A–D**). The neurotransmitters, serotonin and GABA, were localized by immunohistochemistry (Norekian, 1999). Nitric oxide (NO) was localized using nicotinamide adenine dinucleotide phosphate diaphorase (NADPH-d) histochemistry (Moroz et al., 2000). The single pedal, neuron 13 (**Figure 4**) was identified as dopaminergic through pharmacological methods (Norekyan, 1989).

The neurons contained within the ganglia as described above were characterized by two different research groups—one in the United States of America (Satterlie and Norekian) and one in Russia (Arshavsky). Hence, the names of the same neurons are often different. **Table 1** summarizes the names and other aspects of neurons to aid the reader in identifying the various names of neurons characterized by both Satterlie and Arshavsky research groups.

Two cellular properties of *Clione* swim interneurons that contribute to locomotor pattern generation are the sag potential and postinhibitory rebound (Pirtle and Satterlie, 2007, 2021; Pirtle et al., 2010). The sag potential, which relates to the current called I_h mediated by hyperpolarization-cyclic nucleotide-gated ion channels (HCN channels) will be addressed later in this review. Postinhibitory rebound is a depolarization that occurs following inhibition of swim interneurons. Thus, postinhibitory rebound plays a crucial role in locomotor pattern generation by allowing inhibited swim interneurons to quickly rebound to reach the threshold and produce an action potential (Satterlie, 1985; Arshavsky et al., 1993a; Satterlie et al., 2000; Pirtle and Satterlie, 2004, 2007). **Figure 5** shows how postinhibitory rebound produced in a ventral swim interneuron by applying a−1 nA current injection can quickly bring about swimming in *Clione* during a state of swimming cessation. Following the −1 nA current injection, the ventral swim interneuron produces an action potential that in turn inhibits the dorsal interneurons. A simultaneous recording of membrane potential from the dorsal swim interneuron shows that it also generates a postinhibitory rebound-induced action potential that inhibits the ventral swim interneuron. This alternating pattern of activity continues as a brief bout of fictive swimming that lasts approximately 4 s.

Several molluscan species have contributed to our understanding of locomotor CPGs and their modulation. Among these are *Tritonia diomedea* (Getting, 1981), *Pleurobranchaea californica* (Jing and Gillette, 1999), *Aplysia brasiliana* (Gamkrelidze et al., 1995), *Melibe leonina* (Thompson and Watson, 2005), and *C. limacina* (Arshavsky et al., 1985a,b,c; Satterlie, 1985; Satterlie and Spencer, 1985). All these molluscan species are useful model systems for elucidating mechanisms of locomotor control because, compared to the more complex vertebrate animals, they all have simple neural circuits and large re-identifiable (i.e., neurons that can be identified in the same ganglion location between individual animals) neurons whose electrical properties can be studied in reduced semi-intact

TABLE 1 Summary of neurons in this review: their alternative names and description.

	Satterlie and Norekian	Arshavsky	Description
Buccal	Bc-PIN	Bc-PIN	Arshavsky et al. (1993b); two paired symmetrical neurons
Cerebral	Metacerebral cell (MCC)	Metacerebral cell (MCC)	Arshavsky et al. (1993b) and Satterlie et al. (1995); two paired symmetrical neurons with somas of 90 μm; serotonergic
	Cr-SA	CPA1	Panchin et al. (1995b) and Satterlie et al. (1995); serotonergic with somas of 15–20 μm; located anteriorly near cerebral commissure; stimulation results in swim acceleration
	Cr-SP	CPB1	Panchin et al. (1995b) and Satterlie et al. (1995); serotonergic with somas of 15–30 μm; located posteriorly near cerebral commissure; stimulation results in swim acceleration
	Cr-SV		Norekian and Satterlie (1996a, 2001); serotonergic; soma located on ventral surface of cerebral ganglia. Left Cr-SV soma is 50 μm and right Cr-SV soma is 30 μm; inhibit pleural withdrawal (Pl-W) neurons.
	Cr-T		Norekian (1995); exist as a bilateral pair (Cr-T1 and Cr-T2) on the ventral surface of the cerebral ganglia; somas are 80 μm for Cr-T1 and 60 μm for Cr-T2
	Cr-A	TenMN	Norekian and Satterlie (1993) and Arshavsky et al. (1993b); 50–100 μm depending on specific member of the Cr-A group; somas located on both dorsal and ventral surfaces of cerebral ganglia; motoneuron that triggers buccal cone eversion (protraction)
	Cr-B		Norekian and Satterlie (1993); soma diameters of 40–60 μm depending on the specific member of the Cr-B group; somas located on both dorsal and ventral surfaces of cerebral ganglia; motoneuron that triggers buccal cone withdrawal (retraction)
	Cr-Pc		Norekian and Satterlie (1995); somas 35 μm; symmetrical left-right pairs located in anterior cerebral ganglia
	Cr-BM		Norekian and Malyshev (2005); somas 25–30 μm; GABAergic
Pleural	Type 12 interneuron	Type 12 interneuron	Arshavsky et al. (1989); single neuronal soma in each of the pleural ganglia with somas of 30–40 μm
	Pl-W	Pl-W	Norekian and Satterlie (1996a); several neurons in the pleural ganglia compose the group with the majority being small (45–55 μm diameter somas) and one large with 150 μm diameter soma
	White cell	Pl-Wh	Norekian and Satterlie (2001); single asymmetric neuronal soma in the right pleural ganglion; becomes opaque with sexual maturation, involved in egg laying
Pedal	Up or dorsal swim interneuron	7	Arshavsky et al. (1985b), Satterlie (1985), and Panchin and Sadreyev (1997); compose the *Clione* swim CPG controlling the dorsal flexion of parapodia; 20–40 μm diameter soma; cholinergic
	Down or ventral swim interneuron	8	Arshavsky et al. (1985b), Satterlie (1985), and Panchin and Sadreyev (1997); compose the *Clione* swim CPG controlling the ventral flexion of parapodia; 20–40 μm diameter soma; glutaminergic
	Up/dorsal or down/ventral small motoneurons	1, 2, 3, and 4	Arshavsky et al. (1985b), Satterlie (1995a), and Satterlie and Courtney (2008); innervate limited areas of the parapodial slow-twitch swim musculature; somas with diameters of 20–40 μm; odd numbers control dorsal flexion of parapodia and even numbers control ventral flexion of parapodia; cholinergic
	Up/dorsal or down/ventral general excitor motoneurons	1A and 2A	Arshavsky et al. (1985b) and Satterlie (1995a); innervate the entire expanse of the parapodia and innervate both slow-twitch and fast-twitch swim muscle fibers; somas are 80 μm; odd numbers control dorsal flexion of parapodia and even numbers control ventral flexion of parapodia
	Pd-SW	Pd-SW	Plyler and Satterlie (2020); 5–9 somas with 20–80 μm diameter near the pedal commissure; serotonergic; innervates slow-twitch muscle fibers to increase the contractility of these muscle fibers
	HE	HE	Arshavsky et al. (1990) and Satterlie et al. (1995); asymmetric serotonergic neuron of left pedal ganglia; 30–40 μm diameter soma; excites ventricle
	S		Huang and Satterlie (1990); 30–40 μm diameter somas; sensory neuron mediating wing retraction reflex
	Ri		Huang and Satterlie (1990); 15–20 μm diameter somas; interneuron mediating wing retraction reflex
	Rm		Huang and Satterlie (1990); 30–40 μm diameter somas; motoneuron mediating wing retraction reflex
Intestinal	Int-HE	Int-HE	Malyshev et al. (1999); 50 μm diameter somas; excites both auricle and ventricle
	Int-HI		Arshavsky et al. (1990); 20–30 μm diameter somas; inhibits both auricle and ventricle
	Z cell		Malyshev et al. (2008); asymmetric neuron in left intestinal ganglia with soma (largest in left intestinal ganglia) of 150 μm diameter somas; excites auricle

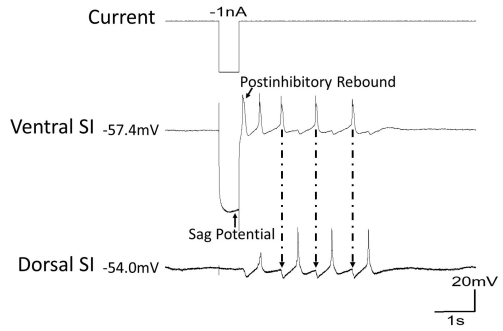

FIGURE 5
During a time of swim cessation, a hyperpolarizing current of −1 nA injected into the ventral swim interneuron of *Clione* evokes a sag potential during the hyperpolarization followed by a rebound in action potential activity creating a short bout of swimming. Arrows with dashed lines show the inhibitory postsynaptic potentials (IPSPs) in the dorsal swim interneuron produced by the action potentials of the ventral swim interneuron.

preparations. Additionally, mollusks show complex behaviors related to locomotion within an environmental context.

Advantages among the molluscan species used as a model for studying locomotor CPGs stem from their differences in ecological niche and related behaviors. *Clione* is unique among the related mollusks used in the study of locomotor CPGs for two major reasons. First, *Clione* occupies the midwater realm of the ocean where it keeps its position within the water column by virtually constantly swimming (Mackie and Mills, 1983; Arshavsky et al., 1985a; Mackie, 1985; Satterlie et al., 1985). *Clione* begins to sink if it ceases to swim, and it is hypothesized that *Clione* migrates up and down in the water column (Mackie, 1985) through the modulation of swimming behavior—*Clione* moves upward towards the surface of the water column by swimming and moves down the water column by inhibiting its swimming behavior (Arshavsky et al., 1992; Satterlie et al., 1985). Because *Clione* typically keeps its position within the water column by hovering locomotion, it is virtually in a constant state of motion. Thus, one advantage of *Clione* is that there is little need to activate the swim CPG interneurons to produce fictive swimming behavior by virtue of the animal being in a state of near-continuous swimming (Satterlie et al., 1985). Second, *Clione* can change its locomotor speed in response to feeding and predator avoidance (Arshavsky et al., 1985a). Thus, *Clione* is an invaluable model system for assessing the mechanisms that underlie locomotor speed change. Much of the research done on the *Clione* swim CPG has focused on mechanisms contributing to swim acceleration at both the circuit-level and cellular level within the swim CPG (Arshavsky et al., 1989; Kabotyanskii and Sakharov, 1991; Satterlie, 1991; Norekian and Satterlie, 1996a; Panchin et al., 1996; Satterlie and Norekian, 1996; Satterlie et al., 2000; Pirtle and Satterlie, 2021).

Clione is holoplanktonic and, as previously said, lives in the midwater where it keeps its position in the water column by engaging in active swimming (Lalli, 1967; Mackie and Mills, 1983; Mackie, 1985; Lalli and Gilmer, 1989). However, *Clione* can stop and restart locomotion depending on behavioral contexts. For example, *Clione* will accelerate swimming when hunting and when escaping potential predators (Arshavsky et al., 1985a, 1992; Satterlie and Spencer, 1985). Similarly, tactile stimuli to the animal's anterior region or parapodia elicit a behavioral response that consists of retraction of the head, the parapodia, and the tail leading to inhibition of swimming—a "whole-body withdrawal" response (Norekian and Satterlie, 1996a). Therefore, neural circuitry that controls *Clione* swimming behavior must be malleable to alter the locomotor speed.

Animals, including *Clione*, can accelerate locomotor speed by increasing the rate of locomotor appendage displacement, increasing the applied force of the locomotor appendage, or a combination of both increasing the rate of locomotor appendage displacement and increasing the applied force of the locomotor appendage (Satterlie, 1995a,b). Additionally, *Clione* can alter their locomotor speed through mechanical changes in their parapodia that include changing the stiffness of the parapodia and changing the angle of attack of the parapodia (Szymik and Satterlie, 2011, 2017). Stimulation of cerebral serotonergic neurons in *Clione* accelerates swimming locomotion at the circuit level through reconfiguration of the animal's CPG and recruitment of more neurons.

Stimulation of serotonergic neurons found in the anterior and posterior portions of the cerebral ganglia (Cr-SA and Cr-SP neurons, respectively) and a serotonergic neuron on the ventral surface of the cerebral ganglia (Cr-SV) in *Clione* modulates swimming behavior by increasing locomotor speed through circuit level and cellular level mechanisms (Panchin et al., 1995b, 1996; Satterlie, 1995b; Satterlie et al., 1995; Satterlie and Norekian, 1995, 1996). From a non-modulated state of slow swimming, serotonergic modulation can initiate swim acceleration in *Clione* by one of three general mechanisms: (1) by increasing parapodial contractility without a change in the frequency of parapodial movement (peripheral modulation only), (2) by increasing the frequency of parapodial movement without a change in parapodial contractility (central modulation only), or (3) by increasing both the parapodial contractility and by increasing the frequency of parapodial movement (both peripheral and central modulation; Satterlie and Norekian, 1996).

Central and peripheral serotonergic modulation of *Clione* locomotor activity involves changes at the circuit and cellular levels. At the circuit level, serotonin reconfigures the CPG circuit by recruiting several neurons that include 1A and 2A motoneurons, also called general excitor motoneurons (GEMN), in the pedal ganglia, pedal serotonergic neurons (Pd-SW) in the pedal ganglia, type 12 interneurons in the pleural

ganglia, and type 8e interneurons of the pedal ganglion (Satterlie and Norekian, 1996; Arshavsky et al., 1998). These circuit-level changes that recruit neurons are shown in **Figures 6–10**.

Circuit-level reconfiguration of the *Clione* swim system: Type 1A and 2A motoneurons (general excitor motoneurons), pedal serotonergic neurons, and type 12 interneurons

Stimulation of cerebral serotonergic neurons, Cr-SA and Cr-SP neurons (**Figure 6A**) reconfigures the *Clione* swim system by recruiting large motoneurons 1A and 2A (GEMN) motoneurons in the pedal ganglia (Arshavsky et al., 1985b; Satterlie, 1993; Norekian and Satterlie, 1996b, 2001). These large motoneurons (80 μm diameter somas) innervate the entire parapodial muscular system—both slow-twitch fatigue resistant and fast-twitch fatigable muscle fibers—*via* the wing nerve. These large GEMNs contrast with the small motoneurons that innervate limited areas of the parapodial muscular system and only innervate the slow-twitch muscle fibers of the parapodia. Thus, when active, GEMNs increase the frequency and contractility of both the slow-twitch muscle and fast-twitch muscle fibers throughout the entire parapodia to increase the locomotor speed of *Clione* (Satterlie, 1993, 1995a).

Anterior and posterior portions of the cerebral ganglia excite the Pd-SW serotonergic neurons in the pedal ganglia and the asymmetric HE neuron in the left pedal ganglia. Additionally, Cr-V neurons weakly stimulate Pd-SW and HE neurons while inhibiting Pl-W neurons that will be described later (**Figure 6A**; Norekian and Satterlie, 1996b, 2001). Both the right and the left pedal ganglia have in their antero-medial regions an agglomeration of serotonergic neurons called Pd-SW neurons (Satterlie, 1995b). Plyler and Satterlie (2020) describe each group of Pd-SW neurons as consisting of 5–9 somas that range from 20 to 80 μm with no difference in number of somas in the right and the left pedal ganglia. Furthermore, Plyler and Satterlie (2020) describe two types of Pd-SW neurons that show different innervation patterns and electrophysiological properties. These findings suggest that one group of Pd-SW neurons innervates the slow-twitch muscles fibers of the parapodia *via* the wing-nerve and plays a role in increasing locomotor speed by increasing the force of parapodial contractions during either slow swimming or fast swimming modes.

Stimulation of Cr-SA and Cr-SP evokes plateau potentials in type 12 interneurons that are in the pleural ganglia. A simultaneous recording of swim interneuron and type 12 interneuron during slow fictive swimming is shown in **Figure 3**. There is one type 12 interneuron soma in each of the two pleural ganglia whose axons exit each pleural ganglia *via* the pleural-pedal connective entering the ipsilateral pedal ganglia and traversing to the contralateral pedal ganglia *via* the pedal commissure. Type 12 interneurons are functionally incorporated into the *Clione* swim CPG when stimulated to activity by cerebral serotonergic neurons. Thus, the inclusion of type 12 interneurons into the CPG is one of the types of circuit-level reconfiguration that occurs to change the swimming locomotor speed in *Clione* (**Figure 6A**; Arshavsky et al., 1985d, 1989; Satterlie and Norekian, 1995, 1996; Pirtle and Satterlie, 2006).

The morphology of the type 12 interneuron in relationship to the anatomy of the ganglia has permitted Pirtle and Satterlie (2006) to show the relative contribution of the type 12 interneuron to the acceleration of *Clione* swimming. In these experiments, the pleural-pedal connective was cut and the dissected preparation of *Clione* (consisting of the isolated ganglia and parapodia) was subjected to a 48-hour refrigerated (4–6°C) incubation period. Thus, these experiments effectively prevent the contribution of the type 12 interneurons from influencing the locomotor CPG and therefore swim acceleration through feedback inhibition. Pirtle and Satterlie (2006) show that the type 12 interneurons cannot, by themselves, produce the swim acceleration of *Clione*, but work simultaneously with cellular changes to swim interneurons and swim motoneurons that are produced by serotonin.

Experiments by Pirtle and Satterlie (2006) suggest that type 12 interneurons may contribute to locomotor speed in several ways. First, type 12 interneurons may help produce swimming stability by enhancing synaptic communication among the CPG interneurons. Several cellular changes occur to swim CPG interneurons. One of these cellular changes is a decrease in the duration of swim CPG interneurons, also referred to as spike narrowing (Satterlie et al., 2000). This spike narrowing is hypothesized to reduce the synaptic efficacy among the swim CPG swim interneurons. Thus, one of the possible roles of type 12 interneurons is to supply enhanced synaptic efficacy to counter the loss of such synaptic efficacy because of spike narrowing of the component swim interneurons of the *Clione* swim CPG.

Second, the feedback provided by type 12 interneurons may be a source of parapodial synchronization during fast swimming in *Clione*. As previously shown, the type 12 interneurons extend their axon through the pleural-pedal connective to the ipsilateral pedal ganglia. However, an extension of the type 12 interneuron axon also crosses to the opposite side *via* the pedal commissure to the contralateral pedal ganglia. Thus, a type 12 interneuron on one side will synaptically communicate with CPG swim interneurons found in both the right and left pedal ganglia. Therefore, the type 12 interneurons may influence the timing of swim interneuron activity by causing the right and left swim interneuron activity to better coincide in time. Furthermore, active plateau potentials of type 12 interneurons only reduce the cycle period of *Clione* CPG interneuron firing between the second to the third and between the third to the fourth cycle of

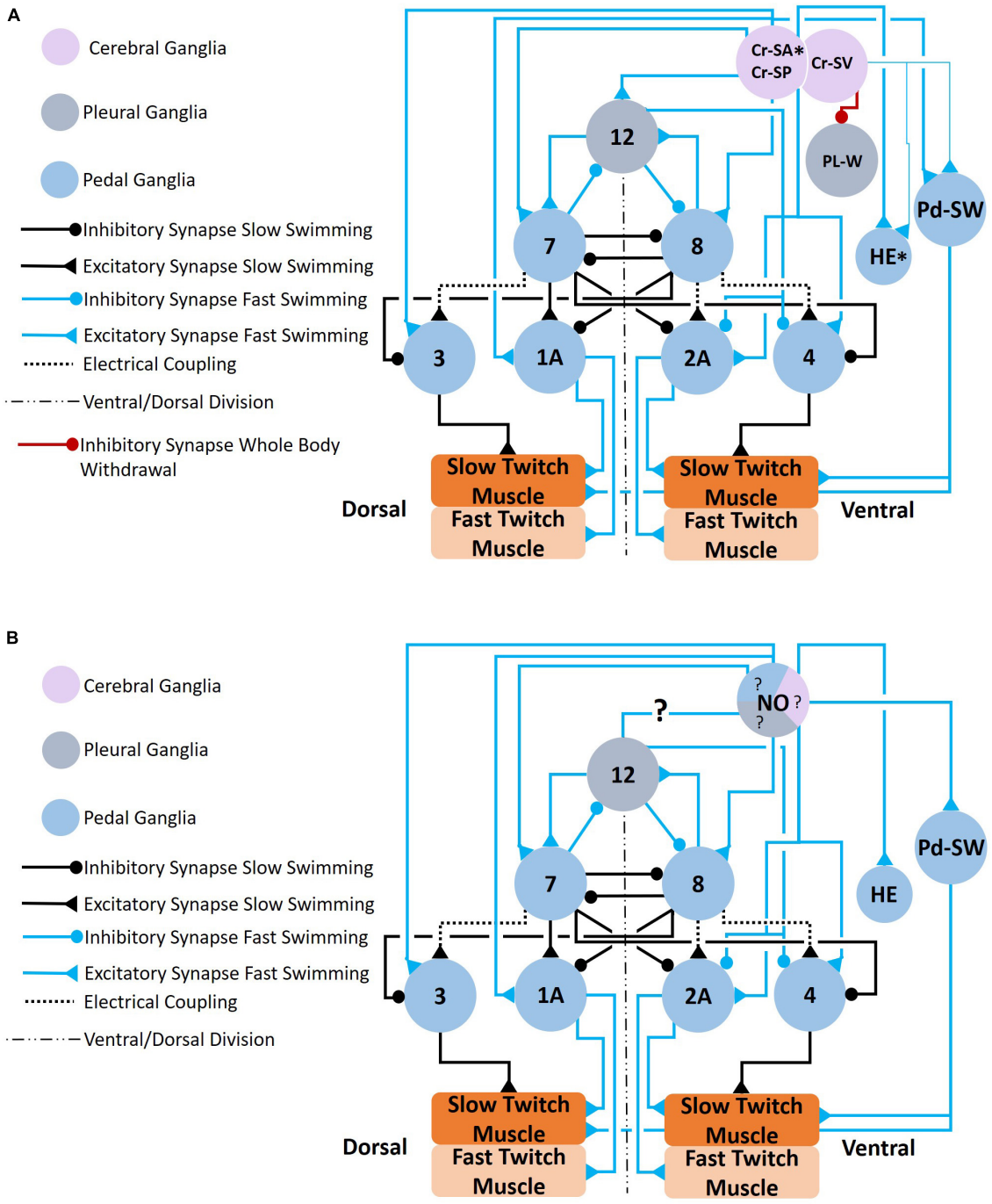

FIGURE 6
(A) Circuit mediating locomotor acceleration through the recruitment of neurons (blue connections). Three groups of cerebral serotonergic neurons, Cr-SA, Cr-SP, and Cr-SV, control recruitment of both interneurons and motoneurons in the swim system during swim acceleration. The Cr-SA and Cr-SP neurons (all on the dorsal surface of the cerebral ganglia) have overlapping functions—they recruit the type 12 interneuron into the *Clione* swim CPG, recruit large 1A and 2A (GEMNs), and recruit serotonergic neurons, Pd-SW neurons (that control force of contraction of slow-twitch swim muscle). The Cr-SA neurons are the only member of the Cr-SA/Cr-SP group to stimulate the asymmetric heart excitor (HE) neuron of the left pedal ganglia, which is indicated by the asterisk. The Cr-SV neuron is found on the ventral surface of the cerebral ganglia and weakly excite the HE and Pd-SW neurons as indicated by the thinner blue lines. The Cr-SV neuron also simultaneously inhibits the pleural withdrawal neurons, Pl-W, that participate in the competing whole-body withdrawal response. **(B)** Circuit mediating swim acceleration by NO. Nitrergic neurons are found in the cerebral (purple), pleural (gray), and pedal (blue) ganglia. However, it is not known which specific nitrergic neurons participate in swim acceleration. The responses of the elements of the swim system to NO were determined experimentally by bath application of NO-donors. The effect that NO has on the type 12 interneuron of the pleural ganglia has not been established (Norekian and Satterlie, 1996b, 2001; Satterlie and Norekian, 1996; Moroz et al., 2000; Pirtle and Satterlie, 2021).

the swim rhythm. Thus, the role of the type 12 interneurons may be to boost locomotor acceleration prior to the contribution of serotonergic alteration of endogenous cellular properties of the swim interneurons (Pirtle and Satterlie, 2006).

The effect of the nitrergic system on swimming locomotor regulation is shown in **Figure 6B**. NO has been shown (through bath application of NO donors) to activate many of the same neural elements of the swim system including swim interneurons, swim motoneurons, and Pd-SW neurons (Moroz et al., 2000; Pirtle and Satterlie, 2021). However, the effect of NO on type 12 neurons and their recruitment into the swim CPG has not been demonstrated—hence the ?s in **Figure 6B**. There are several locations for nitrergic neurons in the ganglia of *Clione* illustrated in **Figure 4B**. However, the exact nitrergic neurons that stimulate Pd-SW neurons remains unknown.

The serotonergic and nitrergic neurons accelerate *Clione* swimming locomotion. On the other hand, the Pl-W neurons (Norekian and Satterlie, 1996a), pedal swim inhibitory neuron 13 (Norekyan, 1989), and the wing retraction reflex (Huang and Satterlie, 1990), inhibit swimming locomotion (**Figures 7A, B**). Also shown in **Figure 7A** are the Cr-A neurons that promote buccal cone eversion during prey capture by inhibiting Pl-W neurons. The Pl-W neuron prevents the extrusion of the BC—appendages that engage in prey capture during fast swimming—and promote their withdrawal by stimulating Cr-B neurons (**Figure 7A**). Dopamine has been shown to inhibit swimming locomotion in *Clione* (Kabotyanski and Sakharov, 1988), but the only confirmed dopaminergic neuron mediating withdrawal and hence swim inhibition is cell 13 in the pedal ganglion (**Figures 3D**, **4C; Norekyan, 1989**). Additionally, Huang and Satterlie (1990), describe a wing retraction reflex in which tactile stimuli to the parapodia evoke a parapodial (wing) retraction and inhibit swimming (**Figures 3D**, **7B**).

Swim acceleration and whole-body withdrawal/wing retraction are competing behaviors—when one behavior is active the other behavior is suppressed. Thus, swim acceleration and whole-body withdrawal/wing retraction are said to be "mutually exclusive" (Norekian and Satterlie, 1996a). Additionally, Norekian and Satterlie (1996a) describe the *Clione* swim and passive defensive withdrawal behaviors in terms of a hierarchy in which one behavior takes precedence over the other. In their analysis, slow swimming represents the base behavior and whole-body withdrawal supersedes slow swimming. On the other hand, swim acceleration as occurs during hunting and feeding, supersedes the whole-body withdrawal behavior. Thus, the whole-body withdrawal circuit inhibits the swimming circuit during slow swimming. Contrastingly, hunting and feeding behavior excites the swim circuit while simultaneously inhibiting the whole-body withdrawal circuit. **Figure 6A** shows the serotonergic Cr-SV neurons inhibit the Pl-W neurons during swim acceleration (Norekian and Satterlie, 1996a,b; Satterlie and Norekian, 2001).

Reconfiguration of the swim CPG and recruitment of neurons during the swim acceleration also activates circuits regulating the heartbeat, feeding apparatus, and tail and statomotor system

The heartbeat of *Clione* increases when tactile stimuli are applied to the tail and is directly influenced by neurons of the pedal and intestinal ganglia (Arshavsky et al., 1990; Malyshev et al., 2008). When engaged in fast swimming, a circuit of neurons favors an increase in the heart rate (**Figure 8**). The Cr-SA serotonergic neurons contribute to an increase in heart rate by exciting the asymmetric heart excitor (HE) neuron found in the dorsal surface of the left pedal ganglion. HE in turn stimulates contraction of the ventricle (Satterlie and Norekian, 1995; Malyshev et al., 2008). The HE neuron also stimulates the Z cell found in the left intestinal ganglia, and the Z cell subsequently stimulates auricle contraction. Another finding by Malyshev et al. (2008) is that tail stimulation excites intestinal heart excitor neurons (Int-HE neurons) and these neurons stimulate the contraction of both the ventricle and the auricle. While NO stimulates the HE neuron (Moroz et al., 2000) it is unknown which nitrergic neurons participate in this response (**Figures 4B**, **6B**).

Decreased heart rate is favored when the Pl-W neurons of the pleural ganglion's whole-body withdrawal system excites Int-HI neurons. The Int-HI neurons subsequently inhibit both ventricular and auricle contraction (Malyshev et al., 2008). A somewhat contradictory finding by Malyshev et al. (2008) is that the Pl-W neurons weakly stimulate Int-HE cells and Z cells. Malyshev et al. (2008) Suggest that this action of Pl-W neurons is to help prime the heart (i.e., "fill the ventricle") so that upon resumed swimming the heart is poised to efficiently "re-inflate" the flaccid *Clione* body.

Clione has an open circulatory system and a hydrostatic skeleton. The increased heart rate that occurs during tail stimulation or during feeding may contribute to swim acceleration and facilitate hydraulic inflation of the BC (Arshavsky et al., 1990). Szymik and Satterlie (2017) have shown that fluid in *Clione*'s hemocoel is distributed to the parapodia and head and that constriction of the neck of *Clione* occurs during buccal cone eversion. Additionally, the distribution of hemocoelic fluid to the wings may control wing stiffness to contribute to swimming speed (Szymik and Satterlie, 2011).

The coordination of locomotor acceleration and feeding is accomplished in part by a cerebral neuron referred to as a cerebral prey capture neuron (Cr-Pc; Norekian and Satterlie, 1995) illustrated in **Figures 9A, B**. Cr-Pc neurons excite the swim system, heart, and neurons that control buccal cone eversion. Thus, Cr-Pc neurons coordinate locomotor and feeding circuits when *Clione* is engaged in feeding on its prey,

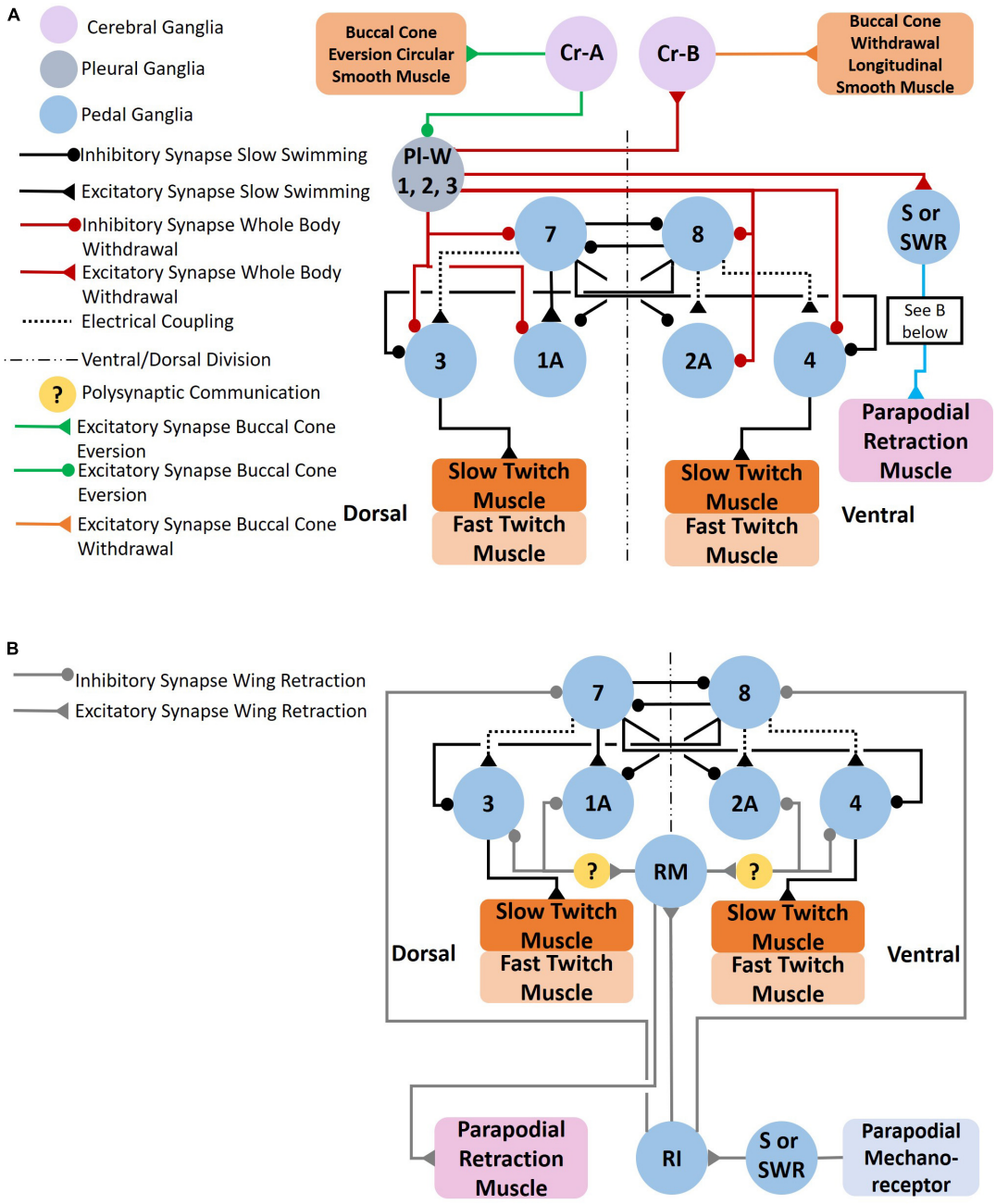

FIGURE 7
(A) Circuit mediating the *Clione* whole-body withdrawal response and buccal cone eversion and withdrawal. Stimulus to the head of *Clione* elicits the passive defensive withdrawal behavior through the activation of Pl-W neurons. Pl-W neurons in the pleural ganglia promote a passive defensive withdrawal behavior by inhibiting the swim system and promoting the withdrawal of buccal cones through the activation of Cr-B neurons that control the longitudinal smooth muscle of the buccal cones consequently leading to buccal cone withdrawal. The Pl-W neurons not only inhibit the swim CPG interneurons and swim motoneurons, but also work in concert with pedal neurons mediating the wing retraction reflex **(B)** by stimulating the wing mechanosensory neurons in the pedal ganglia (labeled S in **Figure 3D**) that mediate the wing retraction reflex. Furthermore, Pl-W neurons stimulate intestinal heart inhibitory neurons (Int-HI; see **Figure 8**) to inhibit the heartbeat. Feeding behavior overrides the withdrawal reflex. When feeding, Cr-A neurons simultaneously promote buccal cone eversion (see also **Figures 9A, B**) and inhibit Pl-W neurons (Norekyan, 1989; Huang and Satterlie, 1990; Norekian and Satterlie, 1996a; Malyshev et al., 2008).

L. helicina. As already mentioned, coordination of locomotion and heartbeat are important aspects of feeding behavior. In addition to activating elements of *Clione*'s swim system and the HE neuron, Cr-Pc neurons are responsible for controlling the circular smooth muscle in the BC that promote buccal cone eversion while simultaneously inhibiting neurons Cr-B

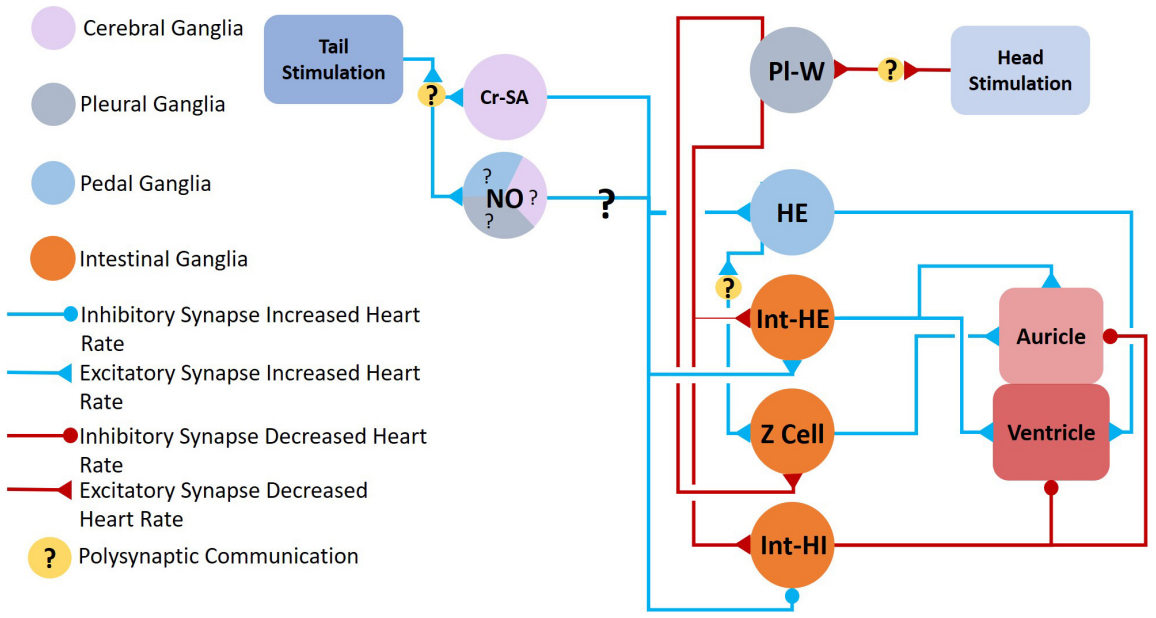

FIGURE 8
Neural circuit mediating changes in heartbeat. *Clione* heart rate increases during swim acceleration and is controlled by serotonergic Cr-SA neurons and NO, both of which also mediate swim acceleration. The exact nitrergic neurons involved is unknown (hence, the question marks—?—for NO). Tail stimulation accelerates swimming locomotion and increases heart rate through the excitation of serotonergic heart excitor (HE) neurons and neurons of the intestinal ganglia, Int-HE and Z cell. Head stimulation produces the opposite response—a decrease in heart rate—through stimulation of heart inhibitory neurons in the intestinal ganglia, Int-HI. Polysynaptic communication is indicated (Arshavsky et al., 1990; Satterlie and Norekian, 1995; Malyshev et al., 2008).

and Cr-L that control buccal cone withdrawal (**Figure 9A**; Norekian and Satterlie, 1995). The antagonistic neurons, Cr-A and Cr-B, that produce opposite effects on the BC are also coordinated during feeding such that both neurons are activated simultaneously during the late phase of feeding behavior. This coordination is achieved by the recruitment of the GABAergic Cr-Aint neurons as illustrated in **Figure 9B** (Norekian and Satterlie, 1993; Norekian and Malyshev, 2006).

In the circuit illustrated in **Figure 9B**, GABAergic Cr-BM neurons mediate the co-activation of both Cr-A and Cr-B neurons through a buccal ganglion interneuron, Bc-PIN. The GABAergic Cr-BM neurons excite Bc-PIN interneurons that then communicate with three neurons in the cerebral ganglion that control buccal cone eversion and withdrawal—the Cr-Aint, Cr-A and Cr-B neurons. The Bc-PIN interneurons are the linkage that co-activates both Cr-A and Cr-B neurons during feeding behavior. Functionally, the recruitment of Cr-BM neurons may allow differential movement of the BC during different phases of feeding behavior (Norekian and Malyshev, 2006; Norekian et al., 2019).

During slow swimming, *Clione* maintains a relatively stable vertical position in the water column. However, during feeding *Clione* may make circular and spiraling movements as it hunts and captures its prey. Therefore, reconfiguration of the *Clione* swim system also coordinates the swim system to tail movements that control the posture of *Clione*. Control of tail movements has been described by Norekian (1995) and Panchin et al. (1995a). The circuits controlling the tail movements of *Clione* are illustrated in **Figures 10A, B**.

A key component of postural control in *Clione* are the paired statocysts that reside on the dorsal surface of the pedal ganglia. The statocysts have been described by Tsirulis (1974) and consist of 9–11 receptor cells (statocyst receptor cells, SRCs) forming a spherical structure with a cavity in which resides a statolith. The SRCs respond to gravity and receive differential input from CPC1 neurons located in the cerebral ganglia. Some SRCs receive excitatory input from CPC1 neurons while others receive inhibitory input from CPC1 neurons (**Figure 10A**). Panchin et al., 1995a,b propose that the differential inputs to SRCs from CPC1 neurons modify the output of SRCs during behavioral responses. The SRCs excite several cerebral neurons that control swimming and movement of the tail—these include the CPA1/CPB1, CPB2, and CPB3 neurons.

CPA1/CPB1 neurons are likely serotonergic (Panchin et al., 1995b) and correspond to Cr-SA and Cr-SP neurons respectively as described by Satterlie and Norekian (1995). The CPA1/CPB1 neurons excite both swim interneurons composing the swim CPG and swim motoneurons. Thus, SRCs can alter the locomotor speed of *Clione* through this part of the statocyst circuit. CPB2 neurons are excited by the SRCs and in turn excite swim motoneurons. The CPB3 neurons are excited by the

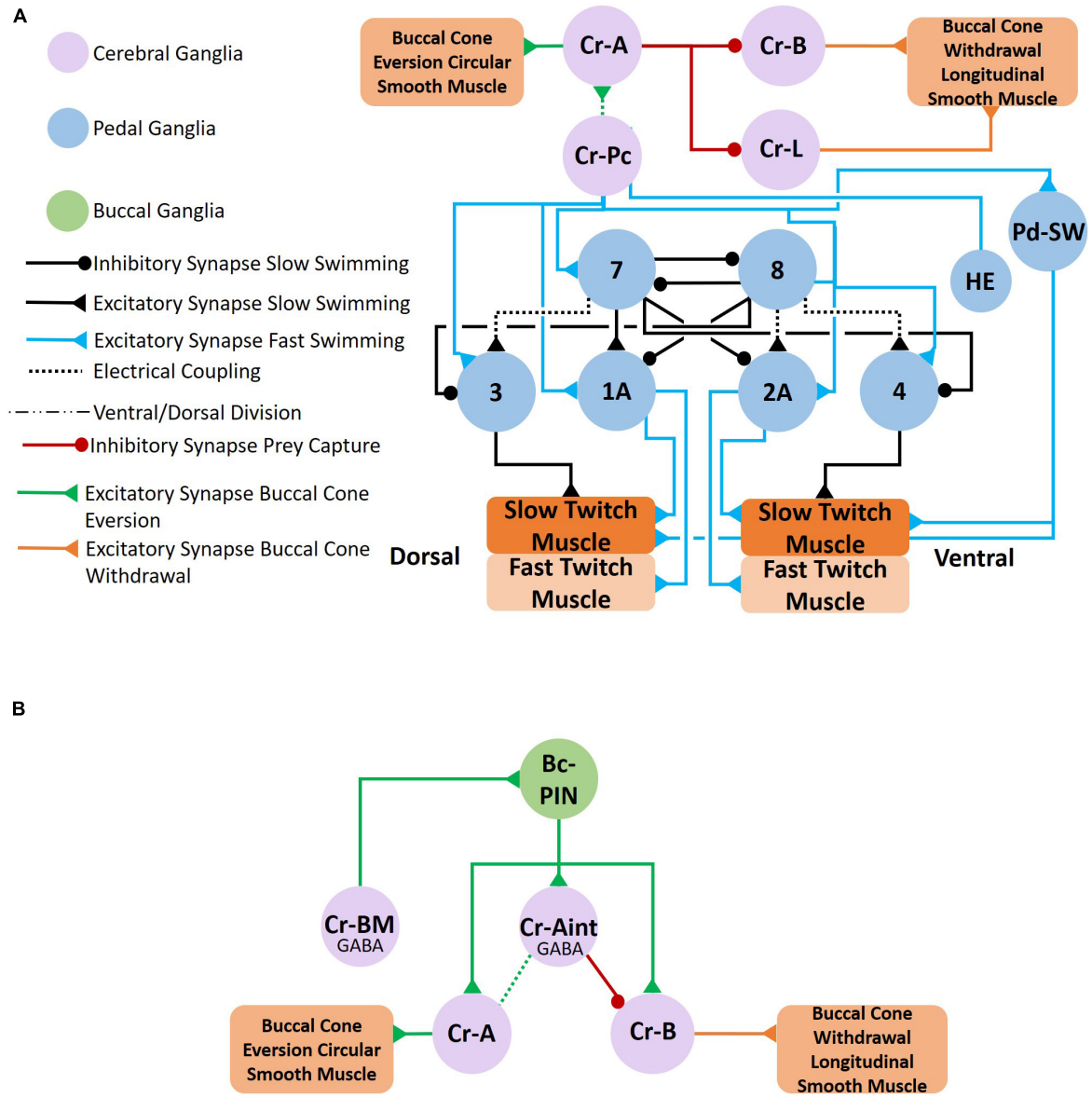

FIGURE 9
Feeding behavior is evoked when *Clione* encounters its prey, *Limacina helicina*. Feeding behavior involves the eversion of prey capture appendages—the buccal cones—and results in swim acceleration. **(A)** Cr-Pc (prey capture neurons) in the cerebral ganglia coordinate both feeding behavior and locomotor acceleration. First, Cr-Pc neurons activate Cr-A neurons through chemical synaptic communication and electrical coupling. The Cr-A neurons in turn activate circular smooth muscle in the buccal cones to facilitate buccal cone eversion during prey capture. Cr-Pc neurons also stimulate swim interneurons of the *Clione* swim CPG, stimulate motoneurons (including 1A and 2A motoneurons), Pd-SW neurons and the HE neuron. Thus, Cr-Pc neurons promote swim acceleration and increased heart rate, the later contributing to hydraulic inflation of the buccal cones during prey capture. In addition to promoting buccal cone eversion, Cr-A neurons simultaneously inhibit the competing buccal cone withdrawal by inhibiting Cr-B and Cr-L neurons that stimulate the buccal cone's longitudinal smooth muscle fibers. **(B)** The cerebral GABAergic neurons, Cr-BM and Cr-Aint, mediate co-activation of motoneurons that control both buccal cone eversion and buccal cone withdrawal. Cr-BM excites the Bc-PIN interneuron of the buccal ganglia. The Bc-PIN in turn excites the Cr-Aint and simultaneously excites competing motoneurons, Cr-A motoneurons that control the buccal cone circular smooth muscle and promote buccal cone eversion and Cr-B motoneurons the control the buccal cone longitudinal smooth muscle and promote buccal cone withdrawal. Co-activation of Cr-A and Cr-B motoneurons occur during removal of the prey, *L. helicina*, from its shell (Arshavsky et al., 1993a,b; Norekian and Satterlie, 1993, 1995; Norekian, 1995; Norekian and Malyshev, 2005, 2006).

SRCs and control tail movement through the excitation of tail motoneurons in the pedal ganglion (**Figure 10A**; Panchin et al., 1995a).

In addition to the neurons described above by Panchin et al. (1995a), there are neurons identified by Norekian (1995) that control *Clione* tail movements. These neurons are designated

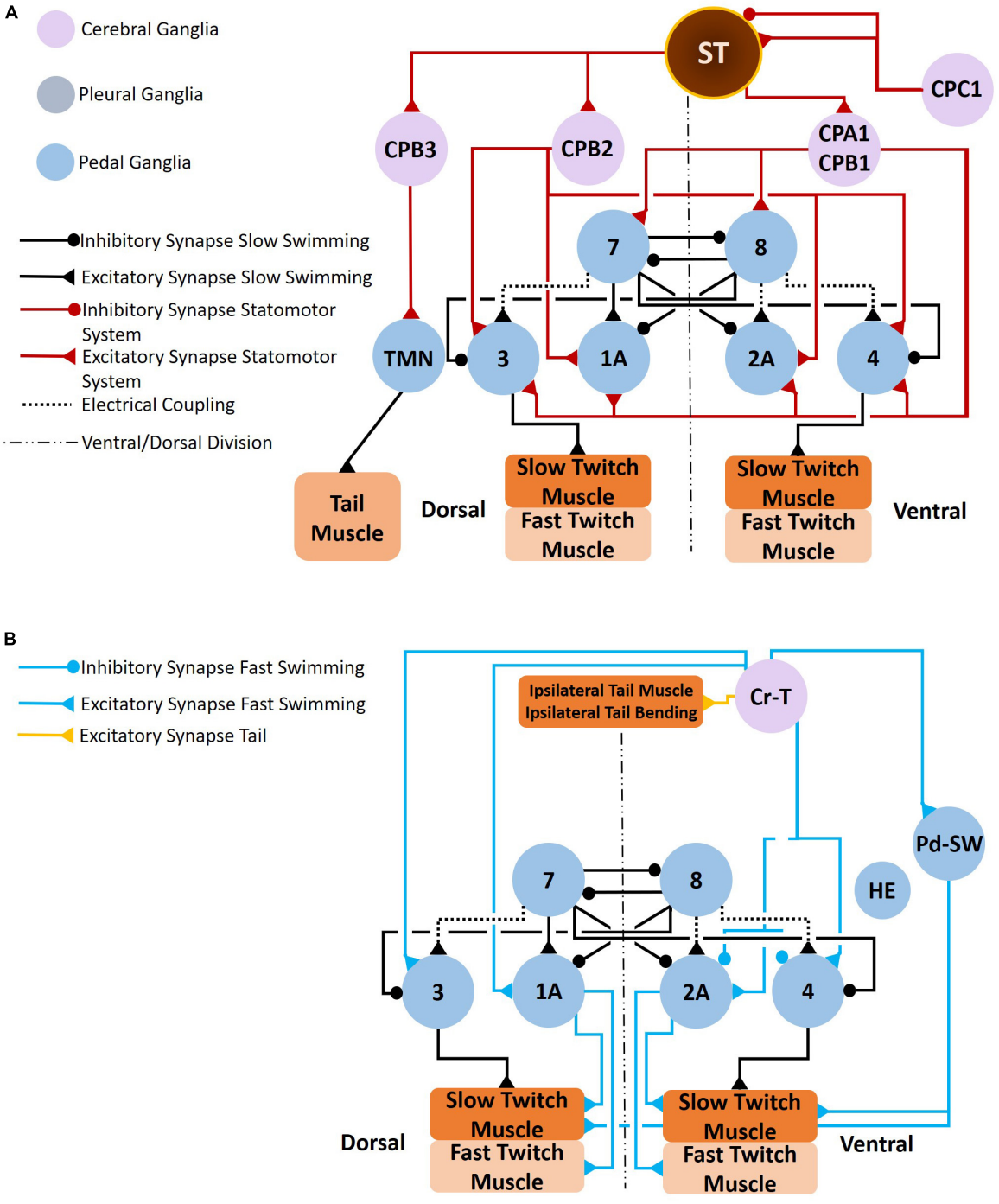

FIGURE 10
Clione postural responses, which involve tail movements, change in response to swim acceleration and feeding behavior. The circuit that coordinate tail movements to swim acceleration are illustrated in **A,B**. As shown in **A**, the statocyst receives input from both gravity and CPC1 neurons. CPC1 neurons have differential affects on the statocyst receptor cells (SRCs) depending on SRCs innervated. The SRCs of the statocysts send excitatory signals to CPA1/CPA2 neurons, CPB2 neurons, and CPB3 neurons. The CPA1/CPB1 neurons stimulate interneurons of the *Clione* locomotor CPG and stimulate swim motoneurons (including the large 1A and 2A motoneurons). The CPB2 neurons stimulate only motoneurons (including the large 1A and 2A motoneurons). Thus, the SRCs promote swim acceleration. Furthermore, SRCs stimulate CPB3 neurons that control tail motoneurons (TMN) that in turn control the bending of the *Clione* tail (T in Figure 1A). Tail bending acts like a rudder to steer *Clione* in circular and spiraling movements that are characteristic of feeding behavior. Coordinated tail bending is also achieved through the activation of Cr-T neurons **(B)**. Cr-T neurons stimulate Pd-SW neurons to enhance the force of parapodial contraction, stimulate motoneurons (including the large 1A and 2A motoneurons), and stimulate the tail musculature to bend the tail in a coordinated fashion (Norekian, 1995; Panchin et al., 1995a,b,c).

cerebral T neurons (Cr-T in **Figure 10B**). Cr-T neurons occur in pairs on the ventral side in each of the cerebral ganglia (both right and left cerebral ganglia). One member of the Cr-T pair, Cr-T1, has a soma of 80 μm and is positioned near the emergence of the cerebral commissure while the other member of the Cr-T pair, Cr-T2, has a soma of 60 μm and is positioned immediately anterior to Cr-T1. The axons of Cr-T1 and Cr-T2 neurons ultimately exit the ipsilateral pedal ganglion to innervate the ipsilateral dorsolateral tail muscles in the body wall.

Stimulation of Cr-T1 and Cr-T2 neurons produce tail bending in a coordinated fashion. When a single Cr-T1 neuron is stimulated it will produce ipsilateral bending of the tail such that the tail bends to the ipsilateral direction. However, when a left and right Cr-T1 neurons are stimulated together, the tail bends in a dorsal direction without deviating from the midline of the long body axis. There are no synaptic connections between Cr-T neurons and the neurons previously described that control buccal cone eversion (i.e., Cr-A neurons). Currently, there is also no evidence that the Cr-T neurons interact with SRCs or the other neurons described in **Figure 10A**. However, Cr-T neurons do monosynaptically excite swim motoneurons (both small motoneuron and large 1A/2A, general excitor motoneurons; Norekian, 1995).

Nitric oxide participates in locomotor and feeding circuits and excites the HE neuron to affect heart rate (Moroz et al., 2000). Additionally, NO may participate in the statomotor system (Panchin et al., 1995c; Moroz et al., 2000). However, the exact role that the specific nitrergic neurons play in modulation of locomotor behavior, feeding behavior, heartbeat regulation, and body orientation in *Clione* remains unclear—hence the question marks in **Figure 6B** that indicates that it is currently unknown what nitrergic neurons are involved. Nitrergic modulation at the circuit level may be a redundant system to that of serotonin because serotonergic neurons participate (e.g., Cr-SA and CPA1/CPB1 neurons). On the other hand, nitrergic modulation may work in separately or more subtly in combination with the serotonergic system in controlling locomotor speed, heartbeat, feeding, and body orientation at the circuit level. Further research of the circuit level role of NO is required to confirm these hypotheses.

Cellular mechanisms and ion channels modulating *Clione* locomotor speed

Neuromodulation involves the release of substances (i.e., neuromodulators) that change ongoing activity in neural circuits such that the output of the neural circuit is changed. Neuromodulation may affect synaptic communication among neurons forming a CPG, may affect the electrical characteristics of neurons forming a CPG, or may affect both synaptic communication and electrical characteristics of neurons forming a CPG. The change in neural circuit output commonly results when the neuromodulator binds to a receptor of one or more neurons in the circuit to start a signal transduction cascade in these target neurons that ultimately change their synaptic communication, electrical properties, or both synaptic communication and electrical properties. Neuromodulation may involve enhancement or depression of the neural circuit output to adjust behavior to suit changing environmental conditions (Kaczmarek and Levitan, 1987; Marder and Thirumalai, 2002; Dickinson, 2006; Harris-Warrick, 2011; Bucher and Marder, 2013; Nadim and Bucher, 2014; Golowasch, 2019). Moreover, the complexity and diversity of neuromodulatory effects may involve interconnected elements that are extrinsic to the CPG circuitry or that are an intrinsic part of the CPG circuitry (Katz, 1998).

In *Clione*, serotonin and NO are two neuromodulator substances that enhance swim CPG output and thus contribute to locomotor acceleration. Both serotonin and NO are extrinsic to the *Clione* swim CPG. Furthermore, both serotonin and NO modulate *Clione* swimming locomotion by eliciting changes in swim interneurons comprising the *Clione* swim CPG circuit (Satterlie and Norekian, 1995; Moroz et al., 2000; Satterlie et al., 2000). Nitric oxide's ability to alter *Clione* swimming locomotion is mediated by soluble guanylyl cyclase (sGC), the production of cyclic guanosine monophosphate (cGMP) by sGC, and the activation of cGMP-dependent protein kinase activity (Pirtle and Satterlie, 2021). Less is known about the signal transduction mechanisms that mediate the similar acceleration of swimming locomotion by serotonin. However, Pirtle and Satterlie (2021) have shown that the ability of serotonin to increase *Clione* locomotor speed is not dependent on cGMP while the effect of NO on increasing locomotor speed is dependent on cGMP.

Both serotonin and NO-cGMP signaling cause the acceleration of *Clione* swimming through a common set of cellular mechanisms that involve modification of the electrical properties of swim interneurons. These cellular mechanisms include (1) spike-narrowing, (2) baseline depolarization, (3) an enhanced sag potential, and (4) enhanced postinhibitory rebound (Satterlie and Norekian, 1995, 2001; Satterlie et al., 2000; Pirtle and Satterlie, 2021). These cellular mechanisms are dependent on the involvement of ion channels and their corresponding ion conductance. Knowledge of ion channel operation within CPG circuits is essential for understanding how CPGs create rhythmic output and how this rhythmic output is modulated (Grillner, 1999; Brocard, 2019). The ion channels that are involved in the *Clione* swim CPG have been described with some difficulty.

The ionic currents characteristic of *Clione* swim CPG interneurons is challenging to study for several reasons. First, these swim interneurons must be found electrophysiologically by impaling them with microelectrodes. A second problem arises because the electrical coupling between other synergistic

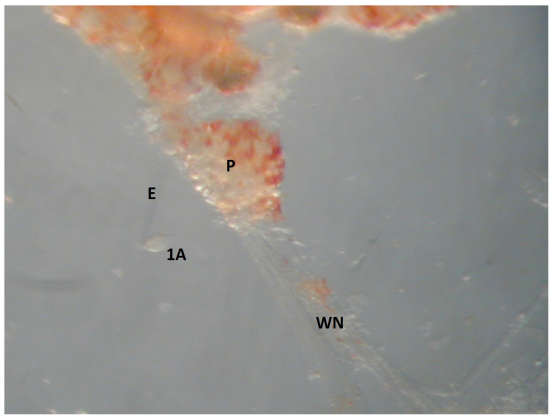

FIGURE 11
An image of the cell isolation method used in single electrode voltage clamp experiments. The soma of a large motoneuron, 1A, is isolated by the recording electrode E. The width of the 1A motoneuron is 30 μm and the width of the pedal ganglia, P, is 350 μm.

swim interneurons and between synergistic motoneurons creates space clamp issues when recording membrane currents of swim interneurons in single electrode voltage clamp experiments. To overcome the space clamp problem, an electrically identified swim interneuron must be physically isolated by using the recording electrode to pull the identified swim CPG interneuron out of the pedal ganglia. This isolation process is done by slowly moving the microelectrode impaling the swim CPG interneuron *via* a micromanipulator to gradually wrench the interneuron soma away from surrounding cells within the ganglia without rupturing its plasma membrane (**Figure 11**).

Ionic currents have been characterized in *Clione* swim interneurons using this method of physically isolating the swim interneuron in single-electrode voltage clamp experiments (Pirtle and Satterlie, 2004). **Figure 12A** shows the intracellular recording of a type 7 swim interneuron before isolation. One current of particular interest is the hyperpolarization-activated cyclic nucleotide-gated cation current, I_h, mediated by HCN ion channels). I_h is evoked in single electrode voltage clamp experiments with hyperpolarizing voltage steps that are applied from a holding potential of −40 mV. I_h is characterized by a slowly developing inward current that is mediated by an increase in both Na^+ and K^+ conductance (Pape, 1996; Lüthi and McCormick, 1998). In intracellular—or current clamp—recordings, the I_h current manifests as a slow depolarizing drift in the membrane potential during the application of hyperpolarizing current injection. This slow depolarizing drift in membrane potential is called a sag potential. Much of the information about I_h in *Clione* swim interneurons is inferred from changes in the sag potential produced by applying hyperpolarizing current to these cells during the intracellular recording of membrane potential in these cells (**Figures 12B, C**; Pirtle et al., 2010; Pirtle and Satterlie, 2021).

Intracellular recording of the sag potential requires isolating cells, not because of space clamp issues as associated with single electrode voltage clamp, but because these cells receive synaptic input that interferes with the recording of individual cellular properties of swim interneurons. Synaptic blockade using the muscarinic acetylcholine receptor antagonists, atropine, the glutamate receptor antagonist, 6-cyano-7-nitroquinoxaline-2,3-dione disodium (CNQX), and the sodium ion channel blocker, tetrodotoxin is used to thus chemically isolate *Clione* swim interneurons for intracellular recordings (Pirtle and Satterlie, 2004). The sag potential of swim interneurons can change with the application of the neuromodulator serotonin and the second messenger, cGMP. The addition of serotonin or cGMP increases fictive swim frequency as recorded intracellular from *Clione* swim CPG interneurons. Furthermore, serotonin and cGMP enhance the sag potential of *Clione* swim CPG interneurons by making the trajectory of the sag potential reach a more depolarized level faster. Thus, the enhancement of the sag contributes to increased frequency of swim interneuron action potentials and therefore an increase of the locomotor speed of *Clione* (Pirtle et al., 2010; Pirtle and Satterlie, 2021).

Because both serotonin and NO contribute to the enhancement of the sag potential, both serotonergic and nitrergic modulatory inputs converge to affect the activity of a common ion channel—the HCN ion channel that produces I_h and corresponding sag potential—in the same swim interneurons comprising the *Clione* swim CPG. In this respect, the *Clione* swim CPG is like the noradrenergic and serotonergic modulation of I_h in thalamic relay neurons where both noradrenalin and serotonin enhance I_h (McCormick and Pape, 1990). Kintos et al. (2016) indicate that the "functional consequences" of the convergence are "less clear." Kintos et al. (2016) use a model of the crab gastric mill to demonstrate that the convergence of two neuromodulators onto a single ion channel is not merely redundant but may produce "distinct effects." It is possible that the serotonergic and nitrergic modulation of the *Clione* swim CPG are not just redundant systems that affect the locomotor speed in the same way—or additive way. Rather, it may be that serotonergic and nitrergic effects are subtly different in their effects.

It is known with certainty that NO produces swim acceleration in *Clione* through cGMP-mediated changes in the cellular properties of neurons forming the *Clione* swim locomotor CPG (Moroz et al., 2000; Pirtle and Satterlie, 2021). However, it is not known what signal transduction mechanism mediates the serotonergic modulation of *Clione* swimming speed. One possible candidate is that serotonin binds to a G-protein coupled receptor that starts a cAMP signal transduction cascade. This is a likely candidate because both cAMP (through binding of epinephrine to beta-1 adrenergic receptors and subsequent activation of adenylyl cyclase) and

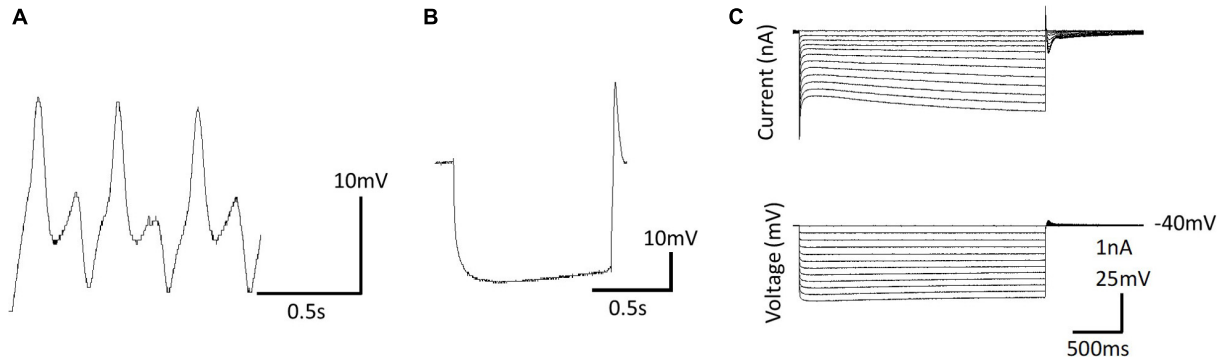

FIGURE 12
(A) Intracellular recording of a dorsal swim interneuron (type 7 swim interneuron) before physically isolating the cell. **(B)** Postinhibitory rebound and sag potential evoked by injecting a −1 nA, 1 s duration current pulse into the isolated cell identified in **A**. **(C)** Single electrode voltage clamp of the isolated cell **(A)** showing the development of slow inward current evoked by hyperpolarizing voltage steps from a holding potential of −40 mV—the hyperpolarization-activated cyclic nucleotide-gated inward current, I_h.

cGMP (through NO stimulation of sGC) modulate I_f—I_h associated with the vertebrate sinoatrial node pacemaker cells (Musialek et al., 1997; Accili et al., 2002; Biel et al., 2009; Hennis et al., 2022) by binding to the intracellular C-terminal cyclic nucleotide binding domain (CNBD) of the HCN channels to promote their opening (Biel et al., 2002; Hennis et al., 2022). While the binding of cAMP to the CNBD is greater than cGMP in mammalian HCN channels, the effect of both cAMP and cGMP is to increase heart rate (Accili et al., 2002; Craven and Zagotta, 2006). Additionally, the crayfish swimmeret motoneurons respond to both cAMP and cGMP in cooperative way to increase the frequency of rhythmic bursting in these motoneurons. In the crayfish swimmeret system, cAMP increases locomotor frequency while cGMP (mediated by NO) is facilitatory (Mita et al., 2014). Similar signal transduction mechanisms involving cAMP and cGMP may function in *Clione* swim interneurons to modulate swimming locomotor speed through an increase in CPG interneuron excitability.

There are several metabotropic 5-HT receptor subtypes in invertebrates, including mollusks (Tierney, 2001) and some of these molluscan 5-HT receptors are linked to cAMP production *via* activation of adenylyl cyclase (Cohen et al., 2003). However, preliminary experimental results indicate that cAMP inhibits swimming locomotion in *Clione*. When the membrane permeable cAMP analog, 8-bromo-cAMP is administered, a decrease in fictive locomotor activity is recorded from *Clione* swim interneurons (Pirtle, unpublished data). Thus, cAMP does not contribute to swimming acceleration in *Clione*, but rather inhibits swimming. These unpublished data are consistent with the findings that the HCN ion channel cloned from the closely related marine mollusk, *Aplysia californica,* is more sensitive to cGMP than to cAMP (Yang et al., 2015) and that in *Clione*, the CNBD of HCN channels may preferentially bind cGMP. Cyclic AMP also disrupts swimming locomotion in the escape swim CPG of *Tritonia* (Clemens et al., 2007). Clemens et al. (2007) hypothesize that fluctuating concentrations of cAMP and intracellular Ca^{2+} may be involved in controlling the timing of the swimming activity in *Tritonia*—especially the termination of swimming. Levels of cGMP and cAMP in *Clione* swim interneurons may work similarly. In *Clione*, cGMP works as an accelerator (Pirtle and Satterlie, 2021) and cAMP (unpublished data) works as a brake. The balance of cGMP and cAMP may be critical for determining the frequency of action potentials generated in *Clione* swim interneurons and thus influence locomotor speed.

Discussion

Modulation of swimming behavior in *Clione* involves both circuit-level and cellular changes. At the circuit level, recruitment of interneurons (i.e., type 12 interneurons) to reconfigure the swim CPG and recruitment of motoneurons (i.e., general excitor motoneurons—or 1A and 2A motoneurons and Pd-SW neurons) are essential components to *Clione* swim acceleration. Swimming in *Clione* involves a two-geared system and modulation of swimming speed can occur by a change of gears or a change within gears—the former requiring a change in the frequency output of the *Clione* swim CPG and the later requiring changes in muscle contractility (Satterlie et al., 1990; Satterlie, 1991, 1993; Plyler and Satterlie, 2020). Cellular changes that occur during swim acceleration addressed in this review focus on how the hyperpolarization-activated cyclic nucleotide channel current, I_h, contributes to swim acceleration in *Clione*.

Experiments by Pirtle and Satterlie (2006) suggest that the role of type 12 interneuron may involve more than providing feedback inhibition as originally suggested (Arshavsky et al., 1985d, 1993a). The involvement of type 12 interneurons to synaptic efficacy and synchronization of the locomotor

appendages, the parapodia, represent critical gaps in the current understanding of how an interneuron's recruitment into a CPG contributes to reconfiguration locomotor output (Pirtle and Satterlie, 2006). Additionally, while it is known that serotonin recruits *Clione* type 12 interneurons it is not known how NO affects these cells. Additional, experiments to identify how NO may contribute to type 12 interneuron recruitment are necessary.

There are several unanswered questions regarding motoneuron recruitment in *Clione*—particularly the recruitment of Pd-SW cells. It is clear that one group of Pd-SW cells is responsible for increasing the strength of parapodial movement through the modulation of slow-twitch muscle fibers (Satterlie, 1995b; Plyler and Satterlie, 2020). However, the role of Pd-SW neurons in modulating *Clione* swimming speed within the slow swimming gear is unclear. Furthermore, the contribution of one group of Pd-SW cells that are hypothesized to control the body wall musculature during fast swimming remains unresolved primarily due to the lack of morphological data on the distribution of these neurons to the body wall. The Pd-SW neurons to the body wall may work in concert with serotonergic modulation of heartbeat to distribute hemolymph to the wings resulting in enhanced wing stiffness as a mechanism to increase locomotor speed (Arshavsky et al., 1990; Szymik and Satterlie, 2017; Plyler and Satterlie, 2020). Because NO also modulates both locomotor behavior and heartbeat in *Clione* (Moroz et al., 2000; Pirtle and Satterlie, 2021), the coordination and relative contribution of serotonergic and nitrergic systems in controlling this possible mechanism requires attention.

At the cellular level, the HCN ion channels contribute to modulation of swimming in *Clione*. HCN ion channels produce the I_h current and corresponding sag potential. Blocking I_h with ZD7288 slows but does not completely abolish swimming in *Clione*. However, blocking I_h with ZD7288 does prevent serotonin-induced swim acceleration in *Clione* (Pirtle et al., 2010). Therefore, I_h is a modulatory target for serotonin but is not essential for rhythm generation. I_h is also a target for NO-cGMP modulation of *Clione* swimming (Pirtle and Satterlie, 2021). Other possible roles for I_h may include modulation of synaptic communication. I_h has been shown by Yang et al. (2015) to be found in siphon motoneurons of *Aplysia*, and in this regard, I_h contributes to classical conditioning of the siphon withdrawal reflex through a NO signaling pathway and synaptic facilitation. Additionally, I_h has been shown to modulate synaptic transmission and synaptic strength through serotonin-induced cAMP production in the neuromuscular junction of crayfish (Beaumont and Zucker, 2000). Therefore, there may be a similar role of I_h in *Clione*. I_h in *Clione* swim interneurons may respond to a NO-cGMP signal to enhance transmitter release during fast swimming speed. This possible mechanism may work in concert with type 12 interneuron recruitment to help strengthen synaptic communication to oppose the decreased synaptic efficacy associated with swim interneuron spike narrowing during swim acceleration (Satterlie et al., 2000; Pirtle and Satterlie, 2007).

Finally, the effect of both serotonin and NO on swim acceleration are similar—both serotonergic and nitrergic modulatory systems accelerate *Clione* swimming through common mechanisms that involve I_h (Satterlie and Norekian, 1996; Satterlie et al., 2000; Pirtle et al., 2010; Pirtle and Satterlie, 2021). Currently, the signal transduction mechanism and second messengers that mediate the serotonergic response in *Clione* swim interneurons is unknown. Serotonin and NO may be redundant neuromodulators that work separately or together. Additionally, there may be cross communication between serotonergic and nitrergic neuromodulatory systems, however, there may also be subtle differences in the modulatory effects of serotonergic and nitrergic modulation in the *Clione* swim system. Identification of the second messengers that mediate serotonergic modulation of *Clione* will be essential to elucidate these possibilities.

The modulation of the *Clione* swim CPG shares many common features with that of other locomotor systems. Two modulatory paradigms that function in the *Clione* swim CPG are (1) motoneuron and interneuron recruitment and (2) modification of cellular properties and ion channels. Further research of the *Clione* swim system may reveal more fundamental similarities and differences with other invertebrate and vertebrate locomotor CPGs. An important part of the locomotor control mechanism in *Clione* that needs further clarification is the role of second messengers. Signal transduction involving second messengers is critical for determining how locomotor CPG circuits are modulated (Clemens and Katz, 2001; Clemens et al., 2007). A complete analysis of the role of cyclic nucleotides in changing locomotor speed in *Clione* promises to yield significant information regarding how locomotor CPGs are modulated.

The evolution of locomotor activity in *Clione* in relationship to other marine gastropod mollusks should be addressed. Several other molluscan species exhibit locomotor activity that has evolved repeatedly and involves the gastropod foot. In *Clione*, the parapodia are derived from the foot and it is the dorsal-ventral flexion of the parapodia that propel *Clione* in swimming locomotion. In other marine gastropods, the dorsal-ventral bending of the body wall (e.g., *Tritonia* and *Pleurobranchaea*) and lateral bending of the body wall (e.g., *Melibe*) produces swimming locomotor activity and, in both instances, is associated with muscles of the foot. The differences in locomotor abilities among the various marine gastropods likely reflects adaptive radiation as the different species occupy different ecological niches. For example, *Clione* is holoplanktonic and is typically in a state of continuous swimming to maintain its position in the water column. This contrast with, for example, the benthic *Tritonia* that crawls on the ocean bottom and only swims as a means of predatory

avoidance (Katz et al., 2001; Willows, 2001). Despite the different modes of swimming among the different marine gastropods, the neural circuitry in each share a common ancestry. For example, the cerebral serotonergic neurons, the *Clione* Cr-SP group, are homologs of the *Tritonia* serotonergic dorsal swim interneurons (DSIs). One of the unique differences in evolution that has occurred is the different roles that these homologous neurons take in terms of swimming behavior. In *Tritonia*, the serotonergic DSIs are both part of the *Tritonia* CPG and modulate swimming behavior. The DSIs are therefore considered to participate in intrinsic neuromodulation of *Tritonia* swim behavior. In *Clione*, these homologs, the Cr-SP neurons, are extrinsic neuromodulators (Katz et al., 2001). These evolutionary differences, as previously stated, are principally because *Tritonia* and *Clione* locomotor behavior are specific for the ecological niche that these two species occupy.

Additionally, the closely related *Clione antarctica* of the southern hemisphere shows significant differences in its locomotor system when compared to the northern hemisphere congener, *C. limacina* (Rosenthal et al., 2009; Dymowska et al., 2012). Foremost of the differences between *C. antarctica* and *C. limacina* is the absence of fast swimming in *C. antarctica* and associated loss of the neural circuitry (1A and 2A motoneurons) and fast-twitch musculature that produces fast swimming. Rosenthal et al. (2009) suggest that the loss of fast swimming in *C. antarctica* is an evolutionary adaptive tradeoff in which the species lost locomotor acceleration in favor of increased aerobic metabolism in response to living in a much colder environment. The evolutionary differences of *C. limacina* and *C. antarctica* evoke important questions. For example, both *C. limacina* and *C. antarctica* are feeding specialist that prey on *L. helicina* (Dymowska et al., 2012). The neural circuitry underlying locomotion, feeding, and statomotor systems are linked in *C. limacina*. The connections, or lack thereof, between locomotor, feeding, and statomotor systems in *C. antarctica* remain unknown. Additionally, similarities and differences in the neuromodulatory serotonergic and nitrergic systems between *C. limacina* and *C. antarctica* need to elucidated.

Author contributions

The author confirms being the sole contributor of this work and has approved it for publication.

Funding

Funding for this publication was provided by the College of Idaho Jolley Fund. There is no associated grant number for this funding source as this funding source is an internal funding source provided by donations to The College of Idaho.

Acknowledgments

This work was not possible without the continued support of Friday Harbor Laboratories, Friday Harbor, Washington. The author thanks the College of Idaho Jolley Fund for covering the publishing costs for this review.

Conflict of interest

The author declares that the research was conducted in the absence of any commercial or financial relationships that could be construed as a potential conflict of interest.

Publisher's note

References

Accili, E. A., Proenza, C., Baruscotti, M., and DiFrancesco, D. (2002). From funny current to HCN channels: 20 years of excitation. *News Physiol. Sci.* 17, 32–37. doi: 10.1152/physiologyonline.2002.17.1.32

Arbas, E. A., and Calabrese, R. L. (1984). Rate modification in the heartbeat central pattern generator of the medicinal leech. *J. Comp. Physiol.* 155, 783–794. doi: 10.1007/BF00611595

Arshavsky, Y. I., Deliagina, T. G., Orlovsky, G. N., Panchin, Y. V., Popova, L. B., and Sadreyev, R. I. (1998). Analysis of the central pattern generator for swimming in the mollusk *Clione*. *Ann. NY Acad. Sci.* 16, 51–69. doi: 10.1111/j.1749-6632.1998.tb09038.x

Arshavsky, Y., Orlovsky, G., Panchin, Y., Roberts, A., and Soffe, S. (1993a). Neuronal control of swimming locomotion: Analysis of the pteropod mollusc *Clione* and embryos of the amphibian *Xenopus*. *Trends Neurosci.* 16, 227–233. doi: 10.1016/0166-2236(93)90161-e

Arshavsky, Y. I., Deliagina, T. G., Gamkrelidze, G. N., Orlovsky, G. N., Panchin, Y. V., and Popova, L. B. (1993b). Pharmacologically induced elements of the hunting and feeding behavior in the pteropod mollusk *Clione limacina*. II. Effects of physostigmine. *J. Neurophyiol.* 69, 522–532. doi: 10.1152/jn.1993.69.2.522

Arshavsky, Y. I., Beloozerova, I. N., Orlovsky, G. N., Panchin, Y. V., and Pavlova, G. A. (1985a). Control of locomotion in marine mollusc *Clione limacina* I. Efferent activity during actual and fictitious swimming. *Exp. Brain Res.* 58, 255–262. doi: 10.1007/BF00235307

Arshavsky, Y. I., Beloozerova, I. N., Orlovsky, G. N., Panchin, Y. V., and Pavlova, G. A. (1985b). Control of locomotion in marine mollusc *Clione limacina* II.

Rhythmic neurons of pedal ganglion. *Exp. Brain Res.* 58, 263–272. doi: 10.1007/BF00235308

Arshavsky, Y. I., Beloozerova, I. N., Orlovsky, G. N., Panchin, Y. V., and Pavlova, G. A. (1985c). Control of locomotion in marine mollusc *Clione limacina* III. On the origin of locomotory rhythm. *Exp. Brain Res.* 58, 273–284. doi: 10.1007/BF00235309

Arshavsky, Y. I., Beloozerova, I. N., Orlovsky, G. N., Panchin, Y. V., and Pavlova, G. A. (1985d). Control of locomotion in marine mollusc *Clione limacina* IV. Role of type 12 interneurons. *Exp. Brain Res.* 58, 285–293. doi: 10.1007/BF00235310

Arshavsky, Y. I., Deliagina, T. G., Gelfand, I. M., Orlovsky, G. N., Panchin, Y. V., Pavlova, G. A., et al. (1990). Neural control of heart beat in the pteropod mollusc *Clione limacina*: Coordination of circulatory and locomotory systems. *J. Exp. Biol.* 148, 461–475. doi: 10.1242/jeb.148.1.461

Arshavsky, Y. I., Deliagina, T. G., Orlovsky, G. N., Panchin, Y. V., and Papova, L. B. (1992). Interneurones mediating the escape reaction of the marine mollusc *Clione limacina*. *J. Exp. Biol.* 164, 307–314. doi: 10.1242/jeb.164.1.307

Arshavsky, Y. I., Orlavsky, G. N., Panchin, Y. V., and Pavlova, G. A. (1989). Control of locomotion in marine mollusc *Clione limacina*. VII reexamination of type 12 interneurons. *Exp. Brain Res.* 78, 398–406. doi: 10.1007/BF00228912

Beaumont, V., and Zucker, R. S. (2000). Enhancement of synaptic transmission by cyclic AMP modulation of presynaptic I_h channels. *Nat. Neurosci.* 3, 133–141. doi: 10.1038/72072

Biel, M., Schneider, A., and Wahl, C. (2002). Cardiac HCN channels: Structure, function, and modulation. *Trends Cardiovasc. Med.* 12, 206–213. doi: 10.1016/S1050-1738(02)00162-7

Biel, M., Wahl-Schott, C., Michalakis, S., and Zong, X. (2009). Hyperpolarization-activated cation channels: From genes to function. *Physiol. Rev.* 89, 847–885. doi: 10.1152/physrev.00029.2008

Brocard, F. (2019). New channel lineup in spinal circuits governing locomotion. *Curr. Opin. Physiol.* 8, 14–22. doi: 10.1016/j.cophys.2018.11.009

Brodfuehrer, P. D., Debski, E. A., O'Gara, B. A., and Friesen, W. O. (1995). Neural control of leech swimming. *J. Neurobiol.* 27, 403–428. doi: 10.1002/neu.480270312

Brown, T. G. (1911). The intrinsic factors in the act of progression in the mammal. *Proc. R. Soc. Lond.* 84, 308–319. doi: 10.1098/rspb.1911.0077

Bucher, D., Haspel, G., Golowasch, J., and Nadim, F. (2015). "Central pattern generators," in *eLS* (Chichester: John Wiley & Sons, Ltd.), 1–12. doi: 10.1002/9780470015902.a0000032.pub2

Bucher, D., and Marder, E. (2013). SnapShot: Neuromodulation. *Cell* 155, 482–482.e1.

Clemens, S., Calin-Jageman, R., Sakurai, A., and Katz, P. S. (2007). Altering cAMP levels within a central pattern generator modifies or disrupts rhythmic motor output. *J. Comp. Physiol. A Neuroethol. Sens. Neural Behav. Physiol.* 193, 1265–1271. doi: 10.1007/s00359-007-0280-4

Clemens, S., and Katz, P. S. (2001). G protein signaling in a neuronal network is necessary for rhythmic motor pattern production. *J. Neurophysiol.* 89, 762–772. doi: 10.1152/jn.00765.2002

Cohen, J. E., Onyike, C. U., McElroy, E., Lin, A. H., and Abrams, T. W. (2003). Pharmacological characterization of an adenylyl cyclase-coupled 5-HT receptor in *Aplysia*: Comparison with mammalian 5-HT receptors. *J. Neurophysiol.* 89, 1440–1455. doi: 10.1152/jn.01004.2002

Craven, K. B., and Zagotta, W. N. (2006). CNG and HCN channels: Two peas, one pod. *Annu. Rev. Physiol.* 68, 375–401. doi: 10.1146/annurev.physiol.68.040104.134728

Delcomyn, F. (1980). Neural basis of rhythmic behavior in animals. *Science* 210, 492–498. doi: 10.1126/science.7423199

Dickinson, P. S. (2006). Neuromodulation of central pattern generators in invertebrates and vertebrates. *Curr. Opin. Neurobiol.* 16, 604–614. doi: 10.1016/j.conb.2006.10.007

Dymowska, A. K., Manfredi, T., Rosenthal, J. J. C., and Seibel, B. A. (2012). Temperature compensation of aerobic capacity and performance in the Antarctic pteropod, *Clione antarctica*, compared with its northern congener, *C. limacina*. *J. Exp. Biol.* 215, 3370–3378. doi: 10.1242/jeb.07060

Fetcho, J. R., and McLean, D. L. (2010). Some principles of organization of spinal neurons underlying locomotion in zebrafish and their implications. *Ann. N. Y. Acad. Sci.* 1198, 94–104. doi: 10.1111/j.1749-6632.2010.05539.x

Gamkrelidze, G. N., Laurienti, P. J., and Blankenship, J. E. (1995). Identification and characterization of cerebral ganglion neurons that induce swimming and modulate swim-related pedal ganglion neurons in *Aplysia brasiliana*. *J. Neurophysiol.* 74, 1444–1462. doi: 10.1152/jn.1995.74.4.1444

Getting, P. A. (1981). Mechanisms of pattern generation underlying swimming in *Tritonia*. I. neural network formed by monosynaptic connections. *J. Neurophysiol.* 46, 65–79. doi: 10.1152/jn.1981.46.1.65

Golowasch, J. (2019). Neuromodulation of central pattern generators and its role in the functional recovery of pattern generator activity. *J. Neurophysiol.* 122, 300–315.

Grillner, S. (1999). Bridging the gap—from ion channels to networks and behavior. *Curr. Opin. Neurobiol.* 9, 663–669. doi: 10.1016/S0959-4388(99)00036-7

Grillner, S., and Wallén, P. (1985). Central pattern generators for locomotion, with special reference to vertebrates. *Ann. Rev. Neurosci.* 8, 233–261. doi: 10.1146/annurev.ne.08.030185.001313

Guertin, P. A. (2009). The mammalian central pattern generator. *Brain Res. Rev.* 62, 45–56. doi: 10.1016/j.brainresrev.2009.08.002

Guertin, P. A. (2013).). Central pattern generators for locomotion: Anatomical, physiological, and pathological considerations. *Front. Neurol.* 3:183. doi: 10.3389/fneur.2012.00183

Harris-Warrick, R. M. (2011). Neuromodulation and flexibility in central pattern generator networks. *Curr. Opin. Neurobiol.* 21, 685–692. doi: 10.1016/j.conb.2011.05.011

Hennis, K., Biel, M., Fenske, S., and Wahl-Schott, C. (2022). Paradigm shift: New concepts for HCN4 function in cardiac pacemaking. *Pflugers Arch.* 474, 649–663. doi: 10.1007/s00424-022-02698-4

Hermans, C. O., and Satterlie, R. A. (1992). Fast-strike feeding behavior in a pteropod mollusk, *Clione limacina* phipps. *Biol. Bull.* 182, 1–7. doi: 10.2307/1542175

Huang, Z., and Satterlie, R. A. (1990). Neuronal mechanisms underlying behavioral switching in a pteropod mollusc. *J. Comp. Physiol. A Neuroethol. Sens. Neural. Behav. Physiol.* 166, 875–887. doi: 10.1007/BF00187335

Jing, J., and Gillette, R. (1999). Central pattern generator for escape swimming in the notapsid sea slug *Pleurobranchaea californica*. *J. Neurophysiol.* 81, 654–667. doi: 10.1152/jn.1999.81.2.654

Kabotyanski, E. A., and Sakharov, D. A. (1988). Monoamine-dependent behavioral states in the pteropod mollusc *Clione limacina*. *Symp. Biol. Hung.* 36, 463–477.

Kabotyanskii, E. A., and Sakharov, D. A. (1991). Neuronal correlates of the serotonin-dependent behavior of the pteropod mollusc *Clione limacina*. *Neurosci. Behav. Physiol.* 21, 422–435. doi: 10.1007/BF01200277

Kaczmarek, L. K., and Levitan, I. B. (1987). *What is neuromodulation? Neuromodulation the biochemical control of neuronal excitability*, Chap. New York, NY. Oxford University Press, 3–17.

Katz, P. S. (1998). Comparison of extrinsic and intrinsic neuromodulation in two central pattern generator circuits in invertebrates. *Exp. Physiol.* 83, 281–292. doi: 10.1113/expphysiol.1998.sp004113

Katz, P. S., Fickbohm, D. J., and Lynn-Bullock, C. P. (2001). Evidence that the central pattern generator for swimming in *Tritonia* arose from a non-rhythmic neuromodulatory arousal system: Implication for the evolution of specialized behavior. *Am. Zool.* 41, 962–975. doi: 10.1093/icb/41.4.962

Kintos, N., Nusbaum, M. P., and Nadim, F. (2016). Convergent neuromodulation onto a network neuron can have divergent effects at the network level. *J. Comput. Neurosci.* 40, 113–135. doi: 10.1007/s10827-015-0587-z

Lalli, C. M. (1967). *Studies on the structure and biology of two gymnostomatous pteropods, Clione limacina Agersborg and Curcibranchaea machrochira (Meisenheimer)*. Ph.D. thesis. Seattle, WA: University of Washington.

Lalli, C. M., and Gilmer, R. W. (1989). *Pelagic snails: The biology of holoplanktonic gastropod mollusks*. Stanford: Standford University Press.

Lüthi, A., and McCormick, D. A. (1998). H-current: Properties of a neuronal and network pacemaker. *Neuron* 21, 9–12.

Mackie, G. O. (1985). Midwater macroplankton of British Columbia studied by submersible *PISCES IV*. *J. Plankton Res.* 7, 753–777.

Mackie, G. O., and Mills, C. E. (1983). Use of the *Pisces IV* submersible for zooplankton studies in coastal waters of British Columbia. *Can. J. Fish Aquat. Sci.* 40, 763–776.

Malyshev, A. Y., Norekian, T. P., and Balaban, P. M. (2008). Neural control of heartbeat during two antagonistic behaviors: Whole body withdrawal and escape swimming in the mollusk *Clione limacina*. *J. Comp. Physiol. A Neuroethol. Sens. Neural Behav. Physiol.* 194, 899–906. doi: 10.1007/s00359-008-0362-y

Malyshev, A. Y., Norekian, T. P., and Willows, A. O. D. (1999). Differential effects of serotonergic and peptidergic cardioexcitatory neurons on the heart activity in the pteropod mollusc, *Clione limacina*. *J. Comp. Physiol. A* 185, 551–560. doi: 10.1007/s003590050415

Marder, E., and Thirumalai, V. (2002). Cellular, synaptic and network effects of neuromodulation. *Neural Netw.* 15, 479–493. doi: 10.1016/s0893-6080(02)00043-6

McCormick, D. A., and Pape, H. C. (1990). Noradrenergic and serotonergic modulation of a hyperpolarization-activated cation current in thalamic relay neurons. *J. Physiol.* 431, 319–342. doi: 10.1113/jphysiol.1990.sp018332

Mita, A., Yoshida, M., and Nagayama, T. (2014). Nitric oxide modulates a swimmeret beating rhythm in the crayfish. *J. Exp. Biol.* 217(Pt. 24), 4423–4431. doi: 10.1242/jeb.110551

Moroz, L. L., Norekian, T. P., Pirtle, T. J., Robertson, K. J., and Satterlie, R. A. (2000). Distribution of NADPH-diaphorase reactivity and effects of nitric oxide on feeding and locomotory circuitry in the pteropod mollusc, *Clione limacina*. *J. Comp. Neurol.* 427, 247–284. doi: 10.1002/1096-9861(20001113)427:2<274::AID-CNE8<3.0.CO;2-\#

Musialek, P., Lei, M., Brown, H. F., Paterson, D. J., and Casadei, B. (1997). Nitric oxide can increase heart rate by stimulating the hyperpolarization-activated inward current, I(f). *Circ. Res.* 81, 60–68. doi: 10.1161/01.RES.81.1.60

Nadim, F., and Bucher, D. (2014). Neuromodulation of neurons and synapses. *Curr. Opin. Neurobiol.* 29, 48–56.

Norekian, T. P. (1995). Prey capture phase of feeding behavior in the pteropod mollusc, *Clione limacina*: Neural mechanisms. *J. Comp. Physiol. A* 177, 41–53. doi: 10.1007/BF00243397

Norekian, T. P. (1999). GABAergic excitatory synapses and electrical coupling sustain prolonged discharges in the prey capture neural network of *Clione* limacina. *J. Neurosci.* 19, 1863–1875. doi: 10.1523/JNEUROSCI.19-05-01863.1999

Norekian, T. P., Hermans, C. O., and Satterlie, R. A. (2019). Organization of buccal cone musculature in the pteropod mollusc *Clione limacina*. *Biol. Bull.* 273, 36–47. doi: 10.1086/704737

Norekian, T. P., and Malyshev, A. Y. (2005). Coordinated excitatory effect of GABAergic interneurons on three feeding motor programs in the mollusk *Clione* limacina. *J. Neurophysiol.* 93, 305–315. doi: 10.1152/jn.00722.2004

Norekian, T. P., and Malyshev, A. Y. (2006). Neural mechanisms underlying co-activation of functionally antagonistic motoneurons during a *Clione* feeding behavior. *J. Neurophysiol.* 95, 2560–2569. doi: 10.1152/jn.01174.2005

Norekian, T. P., and Satterlie, R. A. (1993). Cerebral neurons underlying prey capture movements in the pteropod mollusc, *Clione limacina* I. Physiology, morphology. *J. Comp. Physiol. A* 172, 153–169. doi: 10.1007/BF00189393

Norekian, T. P., and Satterlie, R. A. (1995). An identified cerebral interneuron initiates different elements of prey capture behavior in the pteropod mollusc, *Clione limacina*. *Invertebr. Neurosci.* 1, 235–248. doi: 10.1007/BF02211025

Norekian, T. P., and Satterlie, R. A. (1996a). Whole body withdrawal circuit and its involvement in the behavioral hierarchy of the mollusk *Clione limacina*. *J. Neurophysiol.* 75, 529–537. doi: 10.1152/jn.1996.75.2.529

Norekian, T. P., and Satterlie, R. A. (1996b). Cerebral serotonergic neurons reciprocally modulate swim and withdrawal neural networks in the mollusk *Clione* limacina. *J. Neurophysiol.* 75, 538–546. doi: 10.1152/jn.1996.75.2.538

Norekian, T. P., and Satterlie, R. A. (2001). Serotonergic neural system not only activates swimming but also inhibits competing neural centers in a pteropod mollusc. *Am. Zool.* 41, 993–1000. doi: 10.1093/icb/41.4.993

Norekyan, T. P. (1989). Neurons determining the passive defensive response in the pteropod mollusk *Clione limacina*. *Neurophysiology* 21, 495–502.

Panchin, Y. V., Arshavsky, Y. I., Deliagina, T. G., Orlovsky, G. N., Popova, L. B., and Selverston, A. I. (1996). Control of locomotion in the marine mollusc *Clione limacina*. XI. Effects of serotonin. *Exp. Brain Res.* 109, 361–365. doi: 10.1007/BF00231794

Panchin, Y. V., Arshavsky, Y. I., Deliagina, T. G., Popova, L. B., and Orlovsky, G. N. (1995a). Control of locomotion in marine mollusk *Clione limacina* IX. Neuronal mechanisms of spatial orientation. *J. Neurophysiol.* 73, 1924–1937. doi: 10.1152/jn.1995.73.5.1924

Panchin, Y. V., Popova, L. B., Deliagina, T. G., Orlovsky, G. N., and Arshavsky, Y. I. (1995b). Control of locomotion in marine mollusk *Clione limacina*. VIII. cerebropedal neurons. *J. Neurophysiol.* 73, 1912–1923. doi: 10.1152/jn.1995.73.5.1912

Panchin, Y. V., and Sadreyev, R. I. (1997). Effects of acetylcholine and glutamate on isolated neurons of locomotory network of *Clione*. *Neuroreporat* 8, 2897–2901. doi: 10.1097/00001756-199709080-00019

Panchin, Y. V., Sadreyev, R. I., and Arshavsky, Y. I. (1995c). Statomotor system in the marine mollusk *Clione limacina*. *J. Neurophysiol.* 73, 407–410. doi: 10.1152/jn.1995.73.1.407

Pape, H.-C. (1996). Queer current and pacemaker: The hyperpolarization-activated cation curren in neurones. *Ann. Rev. Physiol.* 58, 299–327. doi: 10.1146/annurev.ph.58.030196.001503

Pearson, K. C., and Wolf, H. (1987). Comparison of motor patterns in the intact and deafferented flight system of the locust I. electromyographic analysis. *J. Comp. Physiol. A* 160, 259–268. doi: 10.1007/BF00609731

Pirtle, T. J., and Satterlie, R. A. (2021). Cyclic guanosine monophosphate modulates locomotor acceleration induced by nitric oxide but not serotonin in *Clione limacina* central pattern generator swim interneurons. *Integr. Org. Biol.* 3:obaa045. doi: 10.1093/iob/obaa045

Pirtle, T. P., and Satterlie, R. A. (2004). Cellular mechanisms underlying swim acceleration in the pteropod mollusk *Clione limacina*. *Integr. Comp. Biol.* 44, 37–46. doi: 10.1093/icb/44.1.37

Pirtle, T. P., and Satterlie, R. A. (2006). The contribution of the pleural type 12 interneurons to swim acceleration in *Clione limacina*. *Invert. Neurosci.* 6, 161–168. doi: 10.1007/s10158-006-0029-8

Pirtle, T. P., and Satterlie, R. A. (2007). The role of postinhibitory rebound in the locomotor central-pattern generator of *Clione limacina*. *Integr. Comp. Biol.* 47, 451–456. doi: 10.1093/icb/icm085

Pirtle, T. P., Willingham, K., and Satterlie, R. A. (2010). A hyperpolarization-activated inward current alters swim frequency of the pteropod mollusk *Clione limacina*. *Comp. Biochem. Physiol. A Mol. Integr. Physiol.* 157, 319–327. doi: 10.1016/j.cbpa.2010.07.025

Plyler, J. B., and Satterlie, R. A. (2020). Pedal serotonergic neuron clusters of the pteropod mollusc, *Clione limacina*, contain two morphological subtypes with different innervation targets. *Invert. Neurosci.* 20:21. doi: 10.1007/s10158-020-00256-0

Rosenthal, J. J. C., Seibel, B. A., Dymowska, A., and Benzanilla, F. (2009). Trade-off between aerobic capacity and locomotor capability in an Antarctic pteropod. *Proc. Natl. Acad. Sci. U. S. A.* 106, 6192–6196. doi: 10.1073/pnas.0901321106

Satterlie, R. A. (1985). Reciprocal inhibition and postinhibitory rebound produce reverberation in a locomotor pattern generator. *Science* 229, 402–404. doi: 10.1126/science.229.4711.4

Satterlie, R. A. (1991). Neural control of speed changes in an opisthobranch locomotory system. *Biol. Bull.* 180, 228–233. doi: 10.2307/1542392

Satterlie, R. A. (1993). Neuromuscular organization in the pteropod mollusc *Clione limacina*. *J. Exp. Biol.* 181, 119–140. doi: 10.1242/jeb.181.1.119

Satterlie, R. A. (1995b). Serotonergic modulation of swimming speed in the pteropod mollusc *Clione limacina*. II. Peripheral modulatory neurons. *J. Exp. Biol.* 198, 905–916. doi: 10.1242/jeb.198.4.905

Satterlie, R. A. (1995a). Peripheral variability in the locomotory system of the pteropod mollusc *Clione limacina*. *Am. Zool.* 35, 542–547. doi: 10.1093/icb/35.6.542

Satterlie, R. A., and Courtney, C. (2008). Hexamethonium sensitivity of the swim musculature of the pteropod mollusc, *Clione limacina*. *Invert. Neurosci.* 8, 157–166. doi: 10.1007/s10158-008-0079-1

Satterlie, R. A., Goslow, G. E., and Reyes, A. (1990). Two types of striated muscle suggest two-geared swimming in the pteropod mollusc *Clione limacina*. *Exp. Biol.* 255, 131–140. doi: 10.1002/jez.1402550202

Satterlie, R. A., Labarbera, M., and Spencer, A. N. (1985). Swimming in the pteropod mollusc, *Clione limacina*: I. Behaviour and morphology. *J. Exp. Biol.* 116, 189–204. doi: 10.1242/jeb.116.1.189

Satterlie, R. A., and Norekian, T. P. (1995). Serotonergic modulation of swimming speed in the pteropod mollusc *Clione limacina*. III. Cerebral neurons. *J. Exp. Biol.* 198, 917–930. doi: 10.1242/jeb.198.4.917

Satterlie, R. A., and Norekian, T. P. (1996). Modulation of swimming in the pteropod mollusc, *Clione limacina*: Role of a compartmental serotonergic system. *Invert. Neurosci.* 2, 157–165. doi: 10.1007/BF02214171

Satterlie, R. A., and Norekian, T. P. (2001). Mechanisms of locomotory speed change: The pteropod solution. *Am. Zool.* 41, 1001–1008. doi: 10.1093/icb/41.4.1001

Satterlie, R. A., Norekian, T. P., Jordan, S., and Kazilek, C. J. (1995). Serotonergic modulation of swimming speed in the pteropod mollusc *Clione limacina*. I. Serotonin immunoreactivity in the central nervous system and wings. *J. Exp. Biol.* 98, 895–904. doi: 10.1242/jeb.198.4.895

Satterlie, R. A., Norekian, T. P., and Pirtle, T. J. (2000). Serotonin-induced spike narrowing in a locomotor pattern generator permits increases in cycle frequency during accelerations. *J. Nuerophysiol.* 83, 2163–2170. doi: 10.1152/jn.2000.83.4.2163

Satterlie, R. A., and Spencer, A. N. (1985). Swimming in the pteropod mollusc, *Clione limacina*: II. Physiology. *J. Exp. Biol.* 116, 205–222. doi: 10.1242/jeb.116.1.205

Selverston, A. I., Russell, D. F., Miller, J. P., and King, D. G. (1976). The stomatogastric nervous system: Structure and function of a small neural network. *Prog. Neurobiol.* 7, 215–290. doi: 10.1016/0301-0082(76)90008-3

Stein, P. S. (2018). Central pattern generators in the turtle spinal cord: Selection among the forms of motor behaviors. *J. Neurophysiol.* 119, 422–440. doi: 10.1152/jn.00602.2017

Szymik, B. G., and Satterlie, R. A. (2011). Changes in wingstroke kinematics associated with a change in swimming in a pteropod mollusk, *Clione limacina*. *J. Exp. Biol.* 214, 3935–3947. doi: 10.1242/jeb.058461

Szymik, B. G., and Satterlie, R. A. (2017). Circulation of hemocoelic fluid during slow and fast swimming in the pteropod mollusc *Clione limacina*. *Invert. Biol.* 136, 290–300. doi: 10.1111/IVB.12182

Thompson, S., and Watson, W. H. III. (2005). Central pattern generator for swimming in *Melibe*. *J. Exp. Biol.* 208, 1347–1361. doi: 10.1242/jeb.01500

Tierney, A. J. (2001). Structue and function of invertebrate 5-HT receptors: A review. *Comp. Biochem. Physiol. A Mol. Integr. Physiol.* 128, 791–804.

Tsirulis, T. P. (1974). The fine structure of the statocyst in the pteropod mollusc *Clione limacina*. *J. Evol. Biochem. Physiol.* 10, 181–189.

Wagner, N. (1885). *Die wirbellosen des weissen meeres: Zoologische forschungen an der kuste des solowetzkischen meerbusens in den sommermonaten der jahre 1877, 1878, 1879 und 1882*. Leipzig: Verlag von Wilhelm Engelmann.

Willows, A. O. D. (2001). Costs and benefits of opisthobranch swimming and neurobehavioral mechanisms. *Am. Zool.* 41, 943–951. doi: 10.1093/icb/41.4.943

Yang, Q., Kuzyk, P., Antonov, I., Bostwick, C. J., Kohn, A. B., Moroz, L. L., et al. (2015). Hyperpolarization-activated, cyclic nucleotide-gated cation channels in *Aplysia*: Contribution to classical conditioning. *Proc. Natl. Acad. Sci. U. S. A.* 112, 16030–16035. doi: 10.1073/pnas.1501731113

Zelenin, P. V., and Panchin, Y. V. (2000). Projection pattern and target selection of *Clione limacina* motoneurons sprouting within an intact environment. *J. Comp. Neurol.* 423, 220–226. doi: 10.1002/1096-9861(20000724)423:2<220::AID-CNE3<3.0.CO;2-M

Zhong, G., Shevtsova, N. A., Rybak, I. A., and Harris-Warrick, R. M. (2012). Neural activity in the isolated mouse spinal cord during spontaneous deletions in fictive locomotion: Insights into locomotor central pattern generator organization. *J. Physiol.* 590, 4735–4759. doi: 10.1113/jphysiol.2012.240895

frontiers | Frontiers in Neuroscience

TYPE Review
PUBLISHED 22 December 2022
DOI 10.3389/fnins.2022.1080027

OPEN ACCESS

EDITED BY
James Newcomb,
New England College, United States

REVIEWED BY
Konstantin Nikolic,
University of West London, United Kingdom
Geoffrey Luke,
Dartmouth College, United States

*CORRESPONDENCE
Junqi Zhuo
jxz624@case.edu
Hillel J. Chiel
hjc@case.edu
Michael W. Jenkins
mwj5@case.edu

SPECIALTY SECTION
This article was submitted to Neural Technology, a section of the journal Frontiers in Neuroscience

RECEIVED 25 October 2022
ACCEPTED 29 November 2022
PUBLISHED 22 December 2022

CITATION
Zhuo J, Gill JP, Jansen ED, Jenkins MW and Chiel HJ (2022) Use of an invertebrate animal model (*Aplysia californica*) to develop novel neural interfaces for neuromodulation. *Front. Neurosci.* 16:1080027. doi: 10.3389/fnins.2022.1080027

Use of an invertebrate animal model (*Aplysia californica*) to develop novel neural interfaces for neuromodulation

Junqi Zhuo[1]*, Jeffrey P. Gill[2], E. Duco Jansen[3,4,5], Michael W. Jenkins[1,6]* and Hillel J. Chiel[1,2,7]*

[1]Department of Biomedical Engineering, Case Western Reserve University, Cleveland, OH, United States, [2]Department of Biology, Case Western Reserve University, Cleveland, OH, United States, [3]Department of Biomedical Engineering, Vanderbilt University, Nashville, TN, United States, [4]Biophotonics Center, Vanderbilt University, Nashville, TN, United States, [5]Department of Neurological Surgery, Vanderbilt University, Nashville, TN, United States, [6]Department of Pediatrics, Case Western Reserve University, Cleveland, OH, United States, [7]Department of Neurosciences, Case Western Reserve University, Cleveland, OH, United States

New tools for monitoring and manipulating neural activity have been developed with steadily improving functionality, specificity, and reliability, which are critical both for mapping neural circuits and treating neurological diseases. This review focuses on the use of an invertebrate animal, the marine mollusk *Aplysia californica*, in the development of novel neurotechniques. We review the basic physiological properties of *Aplysia* neurons and discuss the specific aspects that make it advantageous for developing novel neural interfaces: First, *Aplysia* nerves consist only of unmyelinated axons with various diameters, providing a particularly useful model of the unmyelinated C fibers in vertebrates that are known to carry important sensory information, including those that signal pain. Second, *Aplysia's* neural tissues can last for a long period in an *ex vivo* experimental setup. This allows comprehensive tests such as the exploration of parameter space on the same nerve to avoid variability between animals and minimize animal use. Third, nerves in large *Aplysia* can be many centimeters in length, making it possible to easily discriminate axons with different diameters based on their conduction velocities. *Aplysia* nerves are a particularly good approximation of the unmyelinated C fibers, which are hard to stimulate, record, and differentiate from other nerve fibers in vertebrate animal models using epineural electrodes. Fourth, neurons in *Aplysia* are large, uniquely identifiable, and electrically compact. For decades, researchers have used *Aplysia* for the development of many novel neurotechnologies. Examples include high-frequency alternating current (HFAC), focused ultrasound (FUS), optical neural stimulation, recording, and inhibition, microelectrode arrays, diamond electrodes, carbon fiber microelectrodes, microscopic magnetic stimulation and magnetic resonance electrical impedance tomography (MREIT). We also review a specific example that illustrates the power of *Aplysia* for accelerating technology development: selective infrared neural inhibition of small-diameter unmyelinated axons, which may lead to a translationally useful treatment in the future. Generally, *Aplysia* is suitable for testing modalities

whose mechanism involves basic biophysics that is likely to be similar across species. As a tractable experimental system, *Aplysia californica* can help the rapid development of novel neuromodulation technologies.

KEYWORDS

***Aplysia*, thermal inhibition, infrared neural modulation, small-diameter axon block, infrared neural inhibition, infrared neural stimulation, neuromodulation**

Introduction

New tools for monitoring and manipulating neural activity will be critical for understanding the function of neural circuits and for treating nervous system diseases. In recent years, many new approaches have been developed whose functionality, specificity, and reliability have steadily improved. Here we review the use and utility of an invertebrate animal, the marine mollusk *Aplysia californica*, to develop novel neural interface technologies for recording and/or modulating neural activity. After briefly describing the advantages of *Aplysia's* physiology for developing novel neural interfaces, we will focus on a specific example that illustrates the power of *Aplysia* for accelerating technology development: using heat to selectively inhibit small-diameter unmyelinated axons.

In the 1960s, *Aplysia's* large, pigmented neurons attracted the attention of neuroscientists who wanted to better understand the biophysical properties of individual neurons. Early studies demonstrated that the neurons could be repeatedly and reliably identified by their location and anatomy, their electrophysiological properties, their synaptic inputs and followers, their biochemical properties, and their functional roles as sensory neurons, motor neurons, and interneurons (Frazier et al., 1967; Kandel, 1976). The neurons' somata (cell bodies) are very large (about 30 to 500 μm in diameter). A major advantage of *Aplysia's* neurons is that its soma is electrically compact just like vertebrate neurons (Shapiro et al., 1980; Connor et al., 1986), allowing the neurites to be electrically manipulated from a single control point. In contrast, arthropod neurons (e.g., crustacean and insect neurons) are often not electrically compact and their somata are not often excitable (Smarandache-Wellmann, 2016). Thus, in *Aplysia*, researchers can easily monitor the neuronal activity *via* the soma, which is the largest and most accessible part of the cell. Furthermore, because the *Aplysia* neuron's soma is electrically excitable, activating or inhibiting neurons at these locations can turn the rest of the neuron on or off, making it possible to test the ability of novel neural interfaces to monitor and manipulate individual identified neurons in a neural circuit. The neurons are arranged in groups (referred to as ganglia) that generally contain ∼2,000 neurons. The entire nervous system contains approximately 20,000 neurons. Studies of neural circuitry and behavior in *Aplysia* have clarified the neural, biophysical, and molecular basis of learning and memory (Mayford et al., 2012; Tam et al., 2020), sleep (Keene and Duboue, 2018; Thiede et al., 2021), and complex behaviors such as mating (Painter et al., 1991) and feeding (Kandel, 1979; Susswein and Chiel, 2012). Many novel technologies can take advantage of the deep understanding of neural circuitry controlling behavior in *Aplysia* to study the effects of manipulating single neurons or small numbers of neurons on behavior in both reduced preparations and in intact, behaving animals.

Advantages and examples of using *Aplysia* for developing novel neural interfaces

In addition to the advantages that led researchers to initially use the *Aplysia*'s nervous system in their work, there are several other reasons to use *Aplysia*. Here, we highlight the rationale for using *Aplysia* for the development of novel interface technologies that focus on monitoring or manipulating axons.

First, *Aplysia* does not produce myelin. Nerves connecting the different ganglia to one another and to the animal's body consist of populations of unmyelinated axons whose diameters range from less than 1 μm to over 10 μm. Thus, one can examine the effects of a variety of techniques for manipulating axonal activity in a pure population of unmyelinated axons that vary greatly in diameter. This makes the animal a particularly useful model of the unmyelinated C fibers in vertebrates that are known to carry important sensory information, including those that signal pain. For example, *Aplysia* nerves helped researchers explore the feasibility of selective neural inhibition using high-frequency alternating current (HFAC), which has been studied for decades for its capability to reversibly and repeatedly block neural conduction in frogs, rats, and cats (Kilgore and Bhadra, 2004; Bhadra and Kilgore, 2005; Bhadra et al., 2006). From computational simulations and experimental studies, it was hypothesized that the block threshold (i.e., minimum HFAC amplitude required) increases monotonically with frequency for all nerve fibers, and that small-diameter axons would have a higher block threshold than larger-diameter axons. These observations suggested that it would be impossible to selectively inhibit small-diameter axons with HFAC, as it would primarily block the large-diameter axon first. However, a more recent

experiment on unmyelinated *Aplysia* axons (Joseph and Butera, 2009) showed that, once the HFAC frequency was higher than 12 kHz, the block threshold of these unmyelinated small-diameter axons would begin to decrease, instead of constantly increasing as previously believed. Therefore, findings from this *Aplysia* experiment provided a theoretical basis for selective inhibition of different axon types with different frequencies. In other words, with high enough HFAC frequency, the block threshold for small-diameter axons could be decreased to be lower than the threshold for large-diameter axons, which would permit selective inhibition of small-diameter axons. This hypothesis for selective inhibition was successfully verified in frogs and rats (Joseph and Butera, 2011; Patel and Butera, 2015). Additionally, researchers used *Aplysia* to demonstrate the possibility of combining HFAC with infrared neural inhibition (INI) to block the onset response during HFAC application (Lothet et al., 2014).

Second, neural tissue harvested from *Aplysia* can be kept viable with active neural signaling for many hours. The reason is that *Aplysia* lives in the intertidal zone. Thus, unlike many marine animals that live in the ocean, *Aplysia* are regularly found in tide pools that are exposed to significant changes in temperature, salinity (e.g., high salinity as pools dry out and low salinity during rain), and tidal surge. Since the animals do not maintain a fixed body temperature, and their soft bodies readily change volume in response to osmotic changes, their nervous systems, which are exposed to the animal's open circulatory system, are very robust. Excised musculature and nervous systems from *Aplysia* can be maintained without anesthesia at room temperature. The excised tissue respires slowly, so it can be studied for many hours without significant changes in function. Although rarely mentioned in research articles, this advantage greatly extends the experimental time and increases the ability to collect longitudinal data from the same animal, and limits data noise due to inter-animal variance. These advantages are especially important for novel neuromodulation technologies, as researchers need to explore the parameter space to identify an effective configuration. As an example, it has been demonstrated that focused ultrasound (FUS) applied to the central nervous system can stimulate or inhibit neural activity in a wide range of vertebrate animal models, but the optimal paradigm for each type of effect is still yet to be determined due to the complexity of neural circuits in the brain (Baek et al., 2017; di Biase et al., 2019). In contrast, *Aplysia* ganglia consist of much smaller numbers of neurons and therefore provide a more tractable animal model for researchers to study. It has been reported that FUS can alter the excitation level of *Aplysia* neurons (Mori et al., 1987). In recent studies, an *ex vivo* FUS testing system used an isolated *Aplysia* ganglion and connected nerve, enabling the researchers to thoroughly explore the FUS parameter space on the same ganglion, and investigate the mechanisms of action (Jordan et al., 2022).

Third, in large *Aplysia*, the nerves between the ganglia may be many centimeters in length. The nerve length makes it possible to easily discriminate large-diameter axons from small-diameter axons based on the different conduction velocities. When stimulating a nerve, a compound action potential (CAP) can be evoked, which is the summation of action potentials conducted on all the different axons. Since axonal conduction velocity varies proportionally to the square root of axon diameter in unmyelinated axons, by the time the CAP reaches the other end of the long nerve, it naturally separates into different components. Researchers can explore the size selectivity of a given neuromodulation modality based on the response from different CAP components.

In addition, *Aplysia* neurons are large and can be repeatedly identified, which has been used to develop novel single-cell neural interfaces. *Aplysia* neurons have been used to develop multielectrode arrays (Regehr et al., 1989; Eggers et al., 1998), diamond electrodes (Halpern et al., 2006) and carbon fiber microelectrodes (Huan et al., 2021). In all of these studies, *Aplysia* was selected as the animal model because there are neural circuits that are thoroughly studied with standard electrophysiological methodologies that can be used as the gold standard for comparison. The surgical procedures are also simpler than in rats, mice, or other vertebrate animals, so that iterations of the novel neural interface design can be tested rapidly to quickly achieve the goal. **Table 1** provides a comprehensive overview of the published literature that used *Aplysia* as a model system for the development of neuromodulation and related technologies.

A detailed example: Exploring infrared neural inhibition for heat-based selective inhibition of small-diameter axons with *Aplysia*

A compelling example of how novel neural technologies can be effectively explored using *Aplysia* has been the recent exploration of modalities for selectively and reversibly inhibiting small-diameter axons using heat. The motivation for selective inhibition of small-diameter axons is the critical sensory role that small-diameter axons play in the mammalian nervous system. For example, nociceptive signals are carried by small-diameter unmyelinated C fibers (Besson and Chaouch, 1987), and the maintenance of homeostasis relies on controlling peripheral glands *via* small-diameter unmyelinated motor axons (Gabella, 1976). The dysfunction of small-diameter axons is related to neuropathic pain (Nickel et al., 2012), autonomic nervous system disorders (Phillips, 2005; Kishi, 2012), and other neural pathologies. Each of these small-fiber diseases adversely affects patients' quality of life and work productivity, eventually putting a toll on the whole of society. Hence, the capability to

TABLE 1 Summary of examples using *Aplysia* in the development of neurotechnologies.

Neurotechnology	Tissue type	Simplified summary	References
High-frequency alternating current (HFAC)	*Aplysia* pleural-abdominal connective	The threshold for inhibiting unmyelinated axons showed a unique decreasing trend when HFAC frequency was higher than 12 kHz	Joseph and Butera, 2009
HFAC combined with infrared neural inhibition (INI)	*Aplysia* pleural-abdominal connective nerve	HFAC combined with INI can produce onset-free neural inhibition	Lothet et al., 2014
Focused ultrasound (FUS)	*Aplysia* cerebral ganglia	FUS can alter the excitation level of *Aplysia* neurons	Mori et al., 1987
FUS	Isolated *Aplysia* abdominal ganglia and connected nerve	An *ex vivo* FUS testing system was built for exploring the FUS parameter space on isolated *Aplysia* ganglion and connected nerve	Jordan et al., 2022
Infrared neural inhibition (INI)	*Aplysia* buccal nerve and rat sciatic nerve	Parameters for spatially selective infrared neural inhibition were determined in *Aplysia* and were extended to rat sciatic nerve	Duke et al., 2013
INI	*Aplysia* buccal ganglia, pleural-abdominal connective and vagus nerve from musk shrew	Size-selective infrared neural inhibition protocols were developed in *Aplysia* and applied to musk shrew vagus nerve	Lothet et al., 2017
INI	*Aplysia* pleural-abdominal connective	Experiments confirmed that the theoretically predicted role of voltage-gated potassium ion channels was critical for INI	Ganguly et al., 2019a
INI	*Aplysia* pleural-abdominal connective	Experiments explored the optimal IR illumination length for minimizing the IR power threshold for INI	Ford et al., 2020, 2021
INI	*Aplysia* pleural-abdominal connective	Isotonic ion replacement can reduce the dose threshold of INI	Zhuo et al., 2021
Resistive heating and INI	*Aplysia* pleural-abdominal connective	Resistive heating can reproduce the selective infrared neural inhibition of small-diameter axons	Zhuo et al., 2022
Infrared neural stimulation (INS)	*Aplysia* buccal nerve and rat sciatic nerve	Demonstration of spatial and temporal selectivity of INS	Duke et al., 2012
Optical neural stimulation	*Aplysia* neuron and stained *Sepia* giant axon	Optical radiation with both visible (400–700 nm) and infrared (750–4,000 nm) light showed both excitatory and inhibitory effects	Arvanitaki and Chalazonitis, 1961
Optical neural stimulation	*Aplysia* abdominal ganglia	Laser radiation at 488 nm selectively stimulates neurons in the abdominal ganglion	Fork, 1971
Optical monitoring of neural activity	*Aplysia*-nerve trunks, abdominal ganglia, and eyes	Two membrane-associated dyes (WW375 and NK2367) were used to record neural activities by monitoring the change of their light absorption coefficient	Woolum and Strumwasser, 1978
Optical neural recording with fluorescent dyes	*Aplysia* buccal ganglia	Neuronal patterns of activity in the buccal ganglion of *Aplysia* were mapped by fluorescence imaging	Morton et al., 1991; Nakashima et al., 1992
Optical neural recording with fluorescent dyes	Cultured left upper quadrant neurons from the *Aplysia* abdominal ganglion	Experimental results demonstrated that prolonged asynchronous activity from synaptically interacting *Aplysia* neurons in culture can be recorded by fluorescence imaging	Parsons et al., 1989
Confocal fluorescence microscopy	*Aplysia* sensory neurons either in culture or in intact cell clusters	Experimental results demonstrated the value of fluorescence imaging of live cells for the spatial and temporal determination of the concentrations of second messengers.	Bacskai et al., 1993
Functional optical coherence tomography (fOCT)	*Aplysia* abdominal ganglia and nerves	The fOCT image provided significant scattering signal that correlates with neural activity	Lazebnik et al., 2003; Graf et al., 2009
Planar Microelectrode Array	*Aplysia* abdominal ganglia	A microelectrode array was built for extracellular recording from an *Aplysia* ganglion and spatial localization of identified cells in the ganglion	Novak and Wheeler, 1986
Multi-electrode array (MEA)	Cultured *Aplysia* neurons	A multi-electrode array was built to record and stimulate neural activity extracellularly	Regehr et al., 1989; Eggers et al., 1998
Gold-spine microelectrode array	Cultured left upper quadrant neurons from the *Aplysia* abdominal ganglion and cultured neurons from *Aplysia* buccal ganglion	A spine-shaped gold protrusion was developed to improve adhesion between electrode and neuron and achieve "intracellular-like" field potential recordings	Hai et al., 2009, 2010
Flexible microelectrode array	*Aplysia* buccal ganglia	A flexible microelectrode array was constructed to record action potentials and single- and multi-unit neural activities from the ganglionic surface	Sperry et al., 2018
Diamond electrode	*Aplysia* buccal ganglia and nerve	Diamond electrodes were developed for extracellular recording and stimulation	Halpern et al., 2006, 2010

(Continued)

TABLE 1 (Continued)

Neurotechnology	Tissue type	Simplified summary	References
Carbon fiber microelectrodes	*Aplysia* buccal ganglia and nerve	A carbon fiber microelectrode array demonstrated that the fibers could both provide stable multi-channel recording while stimulating and recording intracellularly	Huan et al., 2021
Implantable neural recording hardware	*Aplysia* buccal ganglia	A microcontroller-based wireless recording unit was developed for the recording of neural activity in seawater	Chestek et al., 2006
Pulse code modulation (PCM) microfluidic chips	*Aplysia* buccal and cerebral ganglia	Experiments demonstrated that PCM microfluidic chip could be used to apply chemical neural stimulation and induce rhythmic activity through the sheath of the ganglion	Azizi et al., 2010
Microscopic magnetic stimulation	*Aplysia* buccal ganglia and nerve	Microscopic magnetic stimulation demonstrated the capability to reversibly block action potentials in unmyelinated axons using a submillimeter magnetic coil. Modeling results showed that the microscopic magnetic stimulation caused a local depolarization that altered activation dynamics of the sodium channels and blocked neural conduction.	Skach et al., 2020
Magnetic resonance electrical impedance tomography (MREIT)	*Aplysia* abdominal ganglia	MREIT detected significant changes in ganglion images *in vitro* and could be used as a new modality to directly detect neural activity	Sadleir et al., 2019

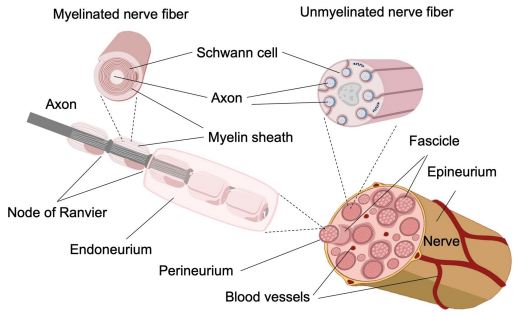

FIGURE 1
Schematic of the structure of a peripheral nerve (Guedan-Duran et al., 2020. The original work is published with permission under a Creative Commons Attribution 4.0 International License. To view a copy of this license, visit http://creativecommons.org/licenses/by/4.0/).

selectively inhibit small-diameter axons without compromising the function of large-diameter axons is a critical unmet medical need.

Selectively inhibiting small-diameter axons in vertebrate nerves is challenging because both small- and large-diameter axons are co-located in peripheral nerve fascicles, as shown in **Figure 1**. Consequently, inhibitory modalities that do not have size selectivity will block neural conduction of both small- and large-diameter axons. As the large-diameter axons are commonly associated with motor functions, a universal neural block could cause impairment of motor function and other unwanted side effects. Conventional pharmaceuticals for pain management not only lack selectivity for small-diameter axons, owing to their systemic distribution, but also lead to severe side effects, including addiction and overdosing that has led to the current opioid epidemic in the United States (Chou et al., 2015; Morrone et al., 2017; Vadivelu et al., 2018). Electrode-based neural modulation has been explored for selective inhibition of small-diameter axons. However, as the transmembrane potential evoked by extracellular electrodes is proportional to axon diameter (Rattay, 1986; Tai et al., 2009), it is an intrinsic property of electrode-based neuromodulation to affect the large-diameter axons first. Additional efforts such as multi-electrode arrays (Rozman et al., 1993; Lertmanorat and Durand, 2004) or changing the frequency of high-frequency alternating current (Joseph and Butera, 2011; Patel and Butera, 2015) are required for electrode-based neuromodulation to achieve selectivity on small-diameter axons, which increases the system's complexity and hinders development. Therefore, a novel neural inhibitory modality that can selectively inhibit small-diameter axons while maintaining the functionality of large-diameter axons is required.

In 2012, Duke et al. (2012) first reported the inhibitory effect of pulsed infrared light application in *Aplysia* nerves, which they discovered while exploring temporal factors affecting the threshold of hybrid electro-optical stimulation. The inhibitory effect was further explored in *Aplysia,* since the anatomy of a buccal nerve and its branches make it tractable for testing the spatial selectivity of infrared neural inhibition (INI), as shown in **Figure 2** (Duke et al., 2013). They demonstrated that infrared (IR) laser light could transiently and reversibly induce inhibition in *Aplysia* axons with precise spatial selectivity. As illustrated in **Figure 2**, electrical stimulation was applied to the proximal buccal nerve trunk and recording was done at all three distal branches. When the infrared laser was applied concurrently with electrical stimulation to one region of the proximal nerve trunk, neural conduction to the corresponding branch was blocked. Once the INI protocol was explored on *Aplysia* axons (**Figures 2A–D**), the investigators were able to use a nearly identical stimulation protocol to block action potential propagation on the tibial branch of the rat sciatic nerve (**Figures 2E–H**). The measured threshold temperature elevation

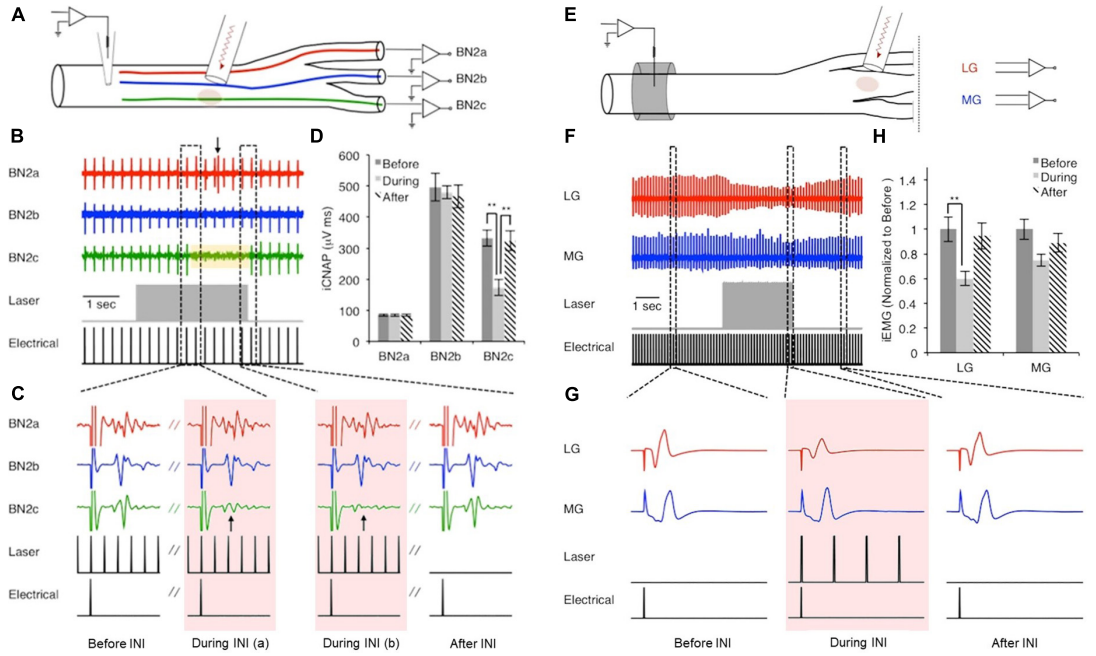

FIGURE 2
Nerve conduction block in buccal nerve 2 (BN2) of *Aplysia* **(A–D)** and in rat sciatic nerve **(E–H)**. Panels **(A–D)**: A train of low radiant exposure (0.50 ± 0.02 J/cm^2), high frequency (200 Hz) infrared pulses (λ = 1,450 nm, pulse width = 0.2 ms) produced a rise in local tissue temperature and blocked responses projecting to BN2c. Panel **(A)**: Experimental setup; panel **(B)**: Overall view of the recorded responses; panel **(C)**: Representative signals showing the response before, during (arrow indicates block of CAP), and after the presence of infrared neural inhibition effect; panel **(D)**: Calculated area under the curve showed the spatial selective inhibitory effect. Panels **(E–H)**: Similarly, applying infrared pulses (same temporal parameters, 75.7 ± 5.3 mJ/cm^2) to the tibial branch of the rat sciatic nerve, approximately 1 cm distal to the site of electrical stimulation, reduced evoked EMG amplitude of the lateral gastrocnemius (LG) but not the medial gastrocnemius (MG). Panel **(E)**: Experimental setup; panel **(F)**: Overall view of the recorded responses; panel **(G)**: Representative signals showing the response before, during, and after the infrared light application; panel **(H)**: Calculated area under the curve showed the spatial selective inhibitory effect. [Reproduced with permission from Duke et al. (2013). The original work is published under a Creative Commons Attribution-Non-commercial-NoDerivs 3.0 Unported License. To view a copy of this license, visit http://creativecommons.org/licenses/by-nc-nd/3.0/].

for the inhibitory effect on both overall nerve compound action potential and muscle contraction was ∼7.0°C on *Aplysia* buccal nerve and ∼5.2°C on the tibial branch of rat sciatic nerve. When the infrared laser was turned off, the temperature rapidly dropped, and the inhibitory effect ceased. According to the temporal response test by Lothet et al., the inhibitory effect of INI is caused by a baseline temperature elevation (Lothet et al., 2017) rather than a spatiotemporal temperature gradient, which is critical for infrared neural stimulation (Wells J. et al., 2005). The robustness of the *Aplysia* nerve preparation permitted Duke et al. to develop their sophisticated experimental design consisting of four electrodes and two optical fibers, which they used to establish their infrared inhibition protocol and demonstrate its capabilities. As the authors wrote in their paper (Duke et al., 2013), "hours of intermittent stimulation" was done and the response was stable without visibly identifiable damage or significant change in the physiological recordings. This provided an ideal testing platform for the researchers to explore novel neuromodulation modalities without preparation run-down.

In 2017, Lothet et al. presented a general theory for how the effects of any modality that primarily acted on the axonal surface to modulate neural conduction could scale with axon diameter and induce size selectivity (Lothet et al., 2017, see the supplemental material). When a neuromodulation modality (e.g., INI), primarily affects the ion channels in the axon membrane, it was shown that the minimum required exposure length is proportional to the square root of the axon diameter. The theory therefore suggested that small-diameter axons would be more susceptible to inhibition induced by baseline temperature elevation than large-diameter axons. Ganguly and colleagues modeled and then experimentally demonstrated that the thermal acceleration of voltage-gated potassium ion channels was the critical factor during INI (Ganguly et al., 2019a, b). The mechanism of infrared inhibition is distinct from that of infrared stimulation, which depends on the rapid generation of a spatial and temporal temperature gradient induced by infrared neural stimulation (INS) that can cause changes in the membrane capacitance and evoke action potentials (Shapiro et al., 1980; Wells J. D. et al., 2005; Duke et al., 2012; Plaksin et al., 2018).

To test the size selectivity of INI, Lothet et al. directly used individually identified neurons (B3 and B43) in *Aplysia* that had large and small diameter axons, respectively. As **Figure 3** shows, the B3 and B43 neurons were electrically stimulated intracellularly while extracellular electrodes recorded propagation of their action potentials through a nerve both before and after an infrared laser application. When infrared light was delivered, only the small diameter axon was inhibited. The experiment was enabled by three unique features of *Aplysia* neurons. First, the average neuron soma size is larger than commonly studied mammalian neurons, making it easier to conduct intracellular stimulation. Second, there are a variety of neuron sizes accessible in the same ganglion, enabling the comparison between large and small-diameter axons. Third, those specific neurons with different sizes (B3 and B43) are identified and can be found across different individuals, making it possible to repeat the experiment with minimal variance. These features enabled the researchers to directly demonstrate the size-selectivity on small-diameter axons by infrared neural inhibition without ambiguity.

Furthermore, after establishing size-selectivity during INI using single neuron stimulation, the size-selectivity of INI was verified at the whole nerve level using compound action potentials (CAPs). When stimulating the whole nerve, action potentials from all axons with different diameters can be evoked simultaneously and propagate along the axons throughout the length of the nerve. The summation of those action potentials recorded extracellularly forms the CAP. In unmyelinated axons, conduction velocity is proportional to the square root of the axon diameter (Jack et al., 1975). Therefore, as the CAP travels along the nerve, the latencies of different CAP components represent the response from different axon-size subpopulations. The long nerves of *Aplysia* combined with the relatively slow conduction velocity of unmyelinated axons permits researchers to easily differentiate the response from different axon-size subpopulations. Lothet et al. developed a size-selective infrared neural inhibition protocol for small-diameter axons in *Aplysia* that was successfully transferred to the vagus nerve in the musk shrew (*Suncus murinus*) (**Figure 4**). In contrast to *Aplysia*, individual nerve fibers had to be teased out of the vagus nerve to establish that they were unmyelinated C fibers (Lothet et al., 2017). It is also worth noting that owing to species difference, the baseline temperature elevation threshold for size-selective inhibition on small-diameter axons was reduced from ~9°C to ~3°C after transferring the INI protocol from *Aplysia* nerve to the vagus nerve of musk shrew (Lothet et al., 2017).

Ganguly et al. (2019a) used a NEURON simulation of a squid giant axon to demonstrate that a likely mechanism for thermal inhibition was the acceleration of the kinetics of the voltage-gated potassium ion channels, resulting in a rapid depolarization-activated hyperpolarization due to elevated temperature. They showed that this inhibitory effect would be greater in smaller-diameter axons (see **Figures 5A,B**).

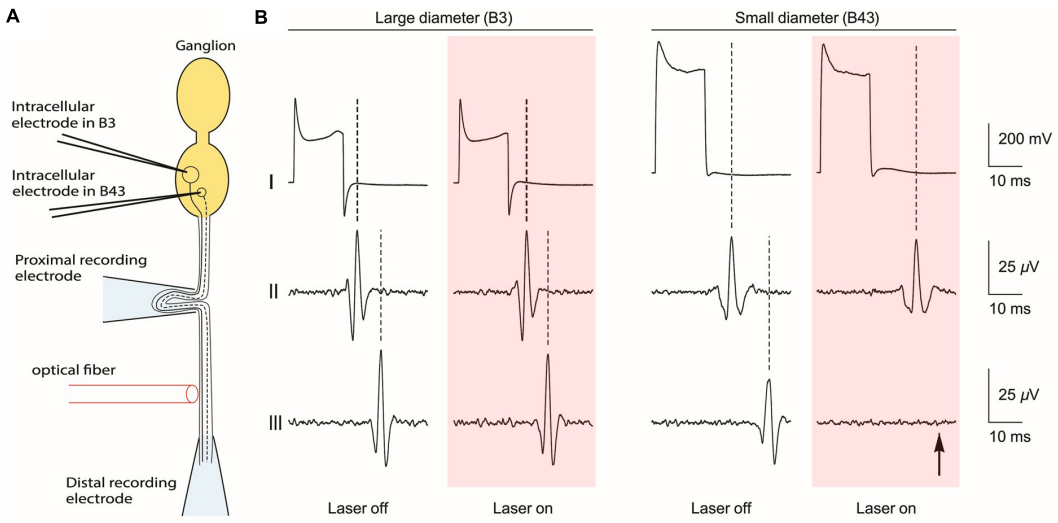

FIGURE 3
Direct demonstration of size-selective neural inhibition with B3 and B43 neurons in the *Aplysia* buccal ganglion. **(A)** Schematic of the experiment, which is aligned to the traces in part b of the figure. **(B)** Recordings from the soma (top), proximal recording electrode (middle) and the distal recording electrode (bottom). Pink boxes indicate the time of application of laser light. Intracellular electrical stimulation was applied to a large-diameter neuron (B3) and to a small-diameter neuron (B43), both of which have axons that project through a common nerve. When infrared laser light was applied *via* an optical fiber that was positioned between two extracellular recording electrodes on the nerve, only the neural conduction on the small-diameter axon was blocked (indicated by arrow). [Reproduced with permission from Lothet et al. (2017). The original work is published under a Creative Commons Attribution 4.0 International License. To view a copy of this license, visit http://creativecommons.org/licenses/by/4.0/].

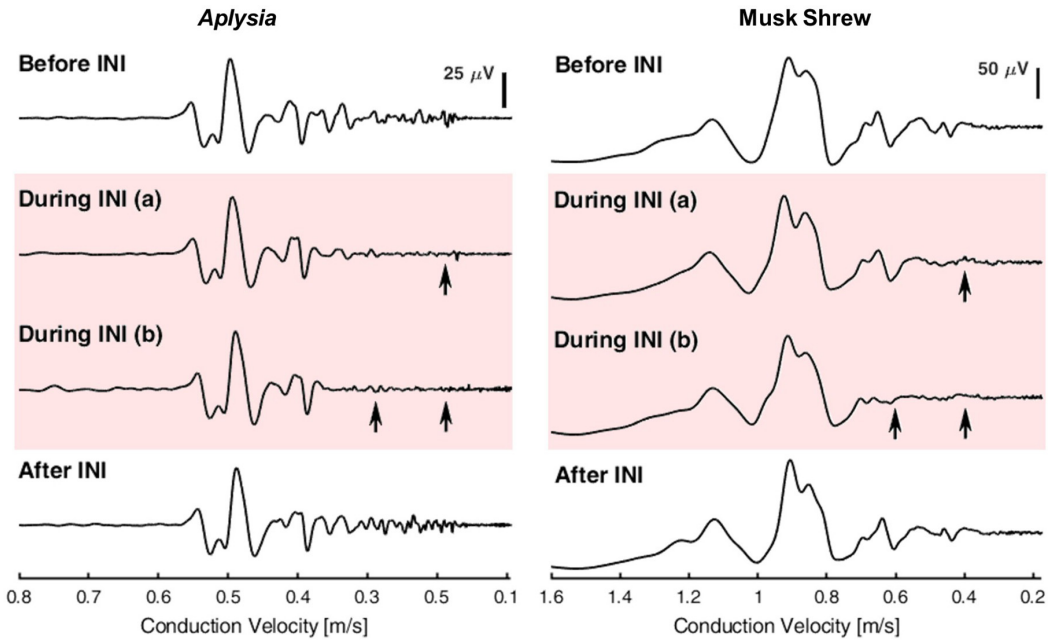

FIGURE 4
Demonstration of selective inhibition on small-diameter axons in *Aplysia* **(left)** and musk shrew **(right)**. Compound action potentials (CAPs) were evoked and recorded before, during, and after infrared neural inhibition (INI). Arrows indicate the selective inhibition effect on small-diameter axons that have a slower conduction velocity. The CAPs before and after INI remained similar, suggesting that the selective inhibition effect was reversible and the nerve's health was not compromised acutely. Reproduced with permission from Lothet et al. (2017). The original work is published under a Creative Commons Attribution 4.0 International License. To view a copy of this license, visit http://creativecommons.org/licenses/by/4.0/].

Ganguly et al. (2019b) then provided experimental evidence for the hypothesis using *Aplysia* nerves (see **Figures 5C, D**). As the *Aplysia* axon and squid giant axon are both unmyelinated axons with different diameters, the qualitative conclusions from the modeling work should apply directly to *Aplysia* axons. As **Figure 5D** shows, selectively blocking voltage-gated potassium ion channels (using TEA) eliminated the thermal inhibition, whereas blocking voltage-dependent sodium ion channels (using TTX) did not prevent thermal inhibition. Thus, experimental evidence from *Aplysia* confirmed the modeling work based on the squid giant axon and demonstrated that the infrared neural inhibition relies on the accelerated potassium-channel kinetics during baseline temperature elevation induced by the absorption of infrared light by the nerve. The success of the experiment relies on *Aplysia*'s unmyelinated axons of different diameters, providing an animal model in which the modeling conclusions from a Hodgkin-Huxley model and its variants can be directly tested in the laboratory.

These studies were extended by Ford et al. (2020, 2021) showing that one could reduce the IR dose required for thermal inhibition by illuminating a greater length of the nerve, and by Zhuo et al. (2021) showing that ion substitution could also reduce the dose of laser light needed for thermal inhibition. Both studies explored the parameter space to determine the change in IR threshold, which required a substantial number of repeated experiments on the same nerve to avoid variation between animals. The robustness of the *Aplysia* preparation enabled the two studies to be conducted in a reasonable amount of time and with a minimal number of animals. Most recently, Zhuo et al. (2022) have demonstrated that selective IR inhibition can be reproduced by resistive heating. The *ex vivo Aplysia* model provided a robust testing platform for the researchers to apply both heating modalities with different levels of power on the same nerve sequentially and compare the responses, which helped minimize the impact of variance between the animals and lowered the number of animals needed.

Differences between *Aplysia* and vertebrate neurons

Given all these advantages, *Aplysia* should be considered a useful model system for developing novel neuromodulation technologies. It is also important to consider the similarities and differences between *Aplysia*, other model animals, and humans. Two major differences are (1) *Aplysia* axons lack myelination and (2) *Aplysia's* nervous system consists of several separated ganglia rather than a single complex brain connected to a peripheral nervous system. It is worth noting, however, that the peripheral ganglia in vertebrates and humans have some similarities to those in *Aplysia*. The unmyelinated *Aplysia* axon can serve as a good model of the small-diameter unmyelinated

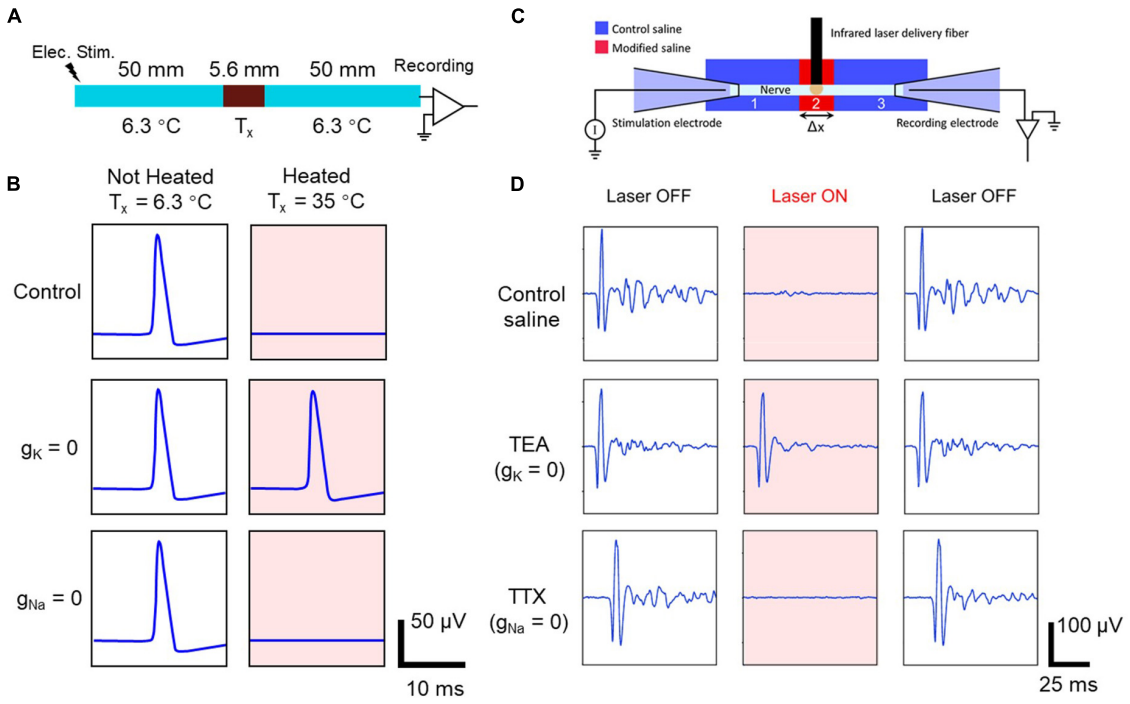

FIGURE 5
Computational modeling **(A,B)**, and experimental validation in an *Aplysia* nerve **(C,D)** of the effect of blocking different ion channels on the heat-induced neural block. Panel **(A)**: A schematic of a model axon with a central region where the temperature can be locally elevated (representing the thermal effect during IR application) and where the ion channel conductance can be set to zero (representing the local application of an ion channel blocker). Panel **(B)**: The modeled action potential recordings under different conditions. Only when voltage-gated potassium channels are blocked (g_K = 0) is the heat-induced block effect reversed, allowing the action potential to propagate through the heated area and be recorded at the distal end of the axon (right hand pink panels), suggesting that the heat-induced block requires voltage-gated potassium channels. Panel **(C)**: An experimental schematic of an *ex vivo* electrophysiology test using an *Aplysia* nerve. IR light was applied to the central region of the nerve, which was also exposed to modified saline with different ion channel blockers. Panel **(D)**: The recorded CAPs during different combinations of IR light application and ion channel blockers. In agreement with the modeling prediction, only when TEA was applied to block the voltage-gated potassium ion channels was the IR neural inhibition effect reversed, allowing the action potential to propagate through the heated area and be recorded at the distal end of the axon. Reproduced from Ganguly et al., 2019a, b with permission. The original works are licensed under the terms of the Creative Commons Attribution 3.0 License and Creative Commons Attribution 4.0 Unported License, respectively. See license detail at https://creativecommons.org/licenses/by/3.0/ and https://creativecommons.org/licenses/by/4.0/].

C fibers in vertebrates. The left and right pleural-abdominal connectives in *Aplysia* consist of 1,388 and 1,832 axons, respectively, with similar axon diameter distribution ranging from 0.1 to > 25 µm with the majority of axons less than 4 µm in diameter (Frazier et al., 1967; Bedini and Geppetti, 2000). The range of *Aplysia* axon diameters covers the entire diameter range of axons in vertebrates, while the majority of axon diameters are similar to the diameters of unmyelinated C fibers (Terzis et al., 1991), which range from 0.5 to 2 µm. Also, the lack of myelination limits the conduction velocity of *Aplysia* axons to about 0.1–0.7 m/s (Lothet et al., 2017), which is similar to the conduction velocities of unmyelinated C fibers in vertebrates (Terzis et al., 1991). Previous studies have demonstrated that infrared neural inhibition can be developed using *Aplysia* and then migrated to vertebrate animals (Duke et al., 2013; Lothet et al., 2017) to selectively inhibit the slow-conducting axons, which are primarily the unmyelinated C fibers. The threshold for inhibition of myelinated larger-diameter axons is higher due to the presence of myelin, which blocks the penetration of infrared light and limits the interaction between infrared light and voltage-gated ion channels to the nodes of Ranvier. Similarly, the myelination of axons contributes to the limited sensitivity of vertebrate nerves to infrared neural stimulation (Duke et al., 2012; Peterson and Tyler, 2013).

Aplysia has the basic complement of ion channels found in neurons throughout evolution (Franciolini and Petris, 1989; Moran et al., 2015). There is a common ancestral four-domain voltage-gated cation channel (FVCC) that evolved into all eukaryotic FVCC subfamilies (Pozdnyakov et al., 2018). Different voltage-gated channels (Nav1, Nav2, Cav1, Cav2, and Cav3) and leak channels (NALCN) all share a common 24 transmembrane pore segment (4 × 6 TM) template and the change of ion-selectivity only requires a single lysine residue change in the ion selectivity filter domain (Fux et al., 2018). Research on *Aplysia's* potassium channel also showed that potassium channels originated much earlier, before the split of

mollusks and arthropods (Zhao, 1993). Like other invertebrates, *Aplysia* possesses both Nav1 and Nav2 ion channel families, whereas vertebrates only possess the Nav1 family (Zakon, 2012). The Nav1 family has expanded significantly during vertebrate evolution and gained the capability to cluster at axon initial segments and the nodes of Ranvier of myelinated axons (Zakon, 2012; Fux et al., 2018). The similarity of ion channel proteins would allow neural manipulation of many *Aplysia* ion channels to be robustly translatable to vertebrates and even humans. Moreover, if there are differences, this could highlight the unique aspects of vertebrate and human biophysics, such as the unique diversity of the Nav1 family in vertebrates.

The similarity and differences between *Aplysia* and vertebrates also exist in other aspects of their molecular biology. A study of the *Aplysia* transcriptome showed that the evolutionary distance from humans to *Aplysia* is shorter than the distance from humans to *Drosophila* and *C. elegans* (Moroz et al., 2006). Another recent comparative transcriptome study showed that *Aplysia* possesses synaptic proteins very similar to those of *Octopus*, whereas several synaptic scaffold protein families in both mollusks are missing in vertebrate lineages (Orvis et al., 2022). The similarity in synaptic proteins and difference in neural network structure (separated ganglia vs. an elaborated central brain) between *Aplysia* and *Octopus* suggested that the difference in cognitive capacity is more related to the difference in neural network structure than to the lower-level differences of molecular biophysics (Orvis et al., 2022). Another recent study mapped the *Aplysia* proteome to humans and cross-referenced it with two databases of genes of interest in Alzheimer's disease research. The results identified 898 potential orthologs of interest in *Aplysia*, 59 of which showed concordant differential expression across species (Kron and Fieber, 2022). *Aplysia* provides an experimentally tractable animal platform for researchers to explore neuromodulation techniques that rely on basic physiological mechanisms. The differences in neural network structure and cognitive capability between *Aplysia* and vertebrates present both a challenge and a potential negative control for exploring the mechanism of diseases and neuromodulation techniques.

Thus, while *Aplysia* is a useful animal model that lends itself well to initial validation of neuromodulatory devices and optimization of parameters, in the translation of the findings from *Aplysia* studies, it is likely that investigators will have to adjust and modify the details of the approach and parameters in order to optimize these for the specific applications, anatomy, physiology, and geometry of their system of interest.

Summary

Overall, these results demonstrate that *Aplysia californica* as a tractable experimental system has several unique advantages: Neurons that can be repeatedly identified and excited; neural tissues that can last for a long period of time in an *ex vivo* experimental setup; nerves consisting of pure unmyelinated axons with different diameters; and neural circuits that are well-studied and that permit different levels of experimental design (from single neuron tests to whole behavioral tests). Generally, *Aplysia* is suitable for testing modalities in which the basic biophysics of that modality is likely to be similar across species (e.g., responses to temperature or changes in ionic concentration), and during initial tests of novel modalities in which the exploration of parameter spaces and the determination of fundamental mechanisms are likely to be broadly applicable across species. As discussed in this review, previous studies have demonstrated that novel technologies that interface with and manipulate the nervous system can be developed using *Aplysia* and then migrated to vertebrate animals (e.g., Duke et al., 2013; Lothet et al., 2017). Overall, the use of invertebrate animal models, such as *Aplysia californica*, should be considered an important tool for the development of novel neural interfaces for neuromodulation.

Author contributions

JZ and HJC wrote the review and prepared the figures. JG revised the review and figures. EJ, HJC, and MJ critically revised the manuscript. All authors contributed to the article and approved the submitted version.

Funding

This research was supported by the National Institutes of Health (NIH) under Grant Nos. 3OT2 OD025307-01S4, R01 HL126747, and R01 NS121372. JZ was supported by the China Scholarship Council. The content is solely the responsibility of the authors and does not necessarily represent the official views of the National Institutes of Health.

Conflict of interest

The authors declare that the research was conducted in the absence of any commercial or financial relationships that could be construed as a potential conflict of interest.

Publisher's note

References

Arvanitaki, A., and Chalazonitis, N. (1961). "Excitatory and inhibitory processes initiated by light and infra-red radiations in single identifiable nerve cells (giant ganglion cells of *Aplysia*)," in *Nervous inhibition: Proceedings / Edited by Ernst Florey*. International symposium on nervous inhibition, ed. E. Florey (Oxford: Pergamon Press).

Azizi, F., Lu, H., Chiel, H. J., and Mastrangelo, C. H. (2010). Chemical neurostimulation using pulse code modulation (PCM) microfluidic chips. *J. Neurosci. Methods* 192, 193–198. doi: 10.1016/j.jneumeth.2010.07.011

Bacskai, B. J., Hochner, B., Mahaut-Smith, M., Adams, S. R., Kaang, B.-K., Kandel, E. R., et al. (1993). Spatially resolved dynamics of cAMP and protein kinase A subunits in *Aplysia* sensory neurons. *Science* 260, 222–226. doi: 10.1126/science.7682336

Baek, H., Pahk, K. J., and Kim, H. (2017). A review of low-intensity focused ultrasound for neuromodulation. *Biomed. Eng. Lett.* 7, 135–142. doi: 10.1007/s13534-016-0007-y

Bedini, C., and Geppetti, L. (2000). A morphological study on the amount and origin of axons in the pleuroabdominal connectives of *Aplysia* fasciata. *Ital. J. Zool.* 67, 9–18. doi: 10.1080/11250000009356288

Besson, J. M., and Chaouch, A. (1987). Peripheral and spinal mechanisms of nociception. *Physiol. Rev.* 67:186. doi: 10.1152/physrev.1987.67.1.67

Bhadra, N., and Kilgore, K. L. (2005). High-frequency electrical conduction block of mammalian peripheral motor nerve. *Muscle Nerve* 32, 782–790. doi: 10.1002/mus.20428

Bhadra, N., Bhadra, N., Kilgore, K., and Gustafson, K. J. (2006). High frequency electrical conduction block of the pudendal nerve. *J. Neural Eng.* 3, 180–187. doi: 10.1088/1741-2560/3/2/012

Chestek, C. A., Samsukha, P., Tabib-Azar, M., Harrison, R. R., Chiel, H. J., and Garverick, S. L. (2006). Microcontroller-based wireless recording unit for neurodynamic studies in saltwater. *IEEE Sens. J.* 6, 1105–1114. doi: 10.1109/JSEN.2006.881348

Chou, R., Turner, J. A., Devine, E. B., Hansen, R. N., Sullivan, S. D., Blazina, I., et al. (2015). The effectiveness and risks of long-term opioid therapy for chronic pain: A systematic review for a national institutes of health pathways to prevention workshop. *Ann. Intern. Med.* 162, 276–286. doi: 10.7326/M14-2559

Connor, J. A., Kretz, R., and Shapiro, E. (1986). Calcium levels measured in a presynaptic neurone of *Aplysia* under conditions that modulate transmitter release. *J. Physiol.* 375, 625–642. doi: 10.1113/jphysiol.1986.sp016137

di Biase, L., Falato, E., and Di Lazzaro, V. (2019). Transcranial focused ultrasound (tFUS) and transcranial unfocused ultrasound (tUS) neuromodulation: From theoretical principles to stimulation practices. *Front. Neurol.* 10:549. doi: 10.3389/fneur.2019.00549

Duke, A. R., Jenkins, M. W., Lu, H., McManus, J. M., Chiel, H. J., and Jansen, E. D. (2013). Transient and selective suppression of neural activity with infrared light. *Sci. Rep.* 3:2600. doi: 10.1038/srep02600

Duke, A. R., Lu, H., Jenkins, M. W., Chiel, H. J., and Jansen, E. D. (2012). Spatial and temporal variability in response to hybrid electro-optical stimulation. *J. Neural Eng.* 9, 036003. doi: 10.1088/1741-2560/9/3/036003

Eggers, M. D., Astolfi, D. K., Liu, S., Zeuli, H. E., Doeleman, S. S., McKay, R., et al. (1998). Electronically wired petri dish: A microfabricated interface to the biological neuronal network. *J. Vac. Sci. Technol. B Microelectron. Process. Phenom.* 8:1392. doi: 10.1116/1.585084

Ford, J. B., Ganguly, M., Poorman, M. E., Grissom, W. A., Jenkins, M. W., Chiel, H. J., et al. (2020). Identifying the role of block length in neural heat block to reduce temperatures during infrared neural inhibition. *Lasers Surg. Med.* 52, 259–275. doi: 10.1002/lsm.23139

Ford, J. B., Ganguly, M., Zhuo, J., McPheeters, M. T., Jenkins, M. W., Chiel, H. J., et al. (2021). Optimizing thermal block length during infrared neural inhibition to minimize temperature thresholds. *J. Neural Eng.* 18:056016. doi: 10.1088/1741-2552/abf00d

Fork, R. L. (1971). Laser stimulation of nerve cells in *Aplysia*. *Science* 171, 907–908. doi: 10.1126/science.171.3974.907

Franciolini, F., and Petris, A. (1989). Evolution of ionic channels of biological membranes. *Mol. Biol. Evol.* 6, 503–513. doi: 10.1093/oxfordjournals.molbev.a040562

Frazier, W. T., Kandel, E. R., Kupfermann, I., Waziri, R., and Coggeshall, R. E. (1967). Morphological and functional properties of identified neurons in the abdominal ganglion of *Aplysia* californica. *J. Neurophysiol.* 30, 1288–1351. doi: 10.1152/jn.1967.30.6.1288

Fux, J. E., Mehta, A., Moffat, J., and Spafford, J. D. (2018). Eukaryotic voltage-gated sodium channels: On their origins, asymmetries, losses, diversification and adaptations. *Front. Physiol.* 9:1406. doi: 10.3389/fphys.2018.01406

Gabella, G. (1976). *Structure of the autonomic nervous system*. Dordrecht: Springer Netherlands, doi: 10.1007/978-94-009-5745-9

Ganguly, M., Ford, J. B., Zhuo, J., McPheeters, M. T., Jenkins, M. W., Chiel, H. J., et al. (2019a). Voltage-gated potassium channels are critical for infrared inhibition of action potentials: An experimental study. *Neurophotonics* 6:040501. doi: 10.1117/1.NPh.6.4.040501

Ganguly, M., Jenkins, M. W., Jansen, E. D., and Chiel, H. J. (2019b). Thermal block of action potentials is primarily due to voltage-dependent potassium currents: A modeling study. *J. Neural Eng.* 16:036020. doi: 10.1088/1741-2552/ab131b

Graf, B. W., Ralston, T. S., Ko, H.-J., and Boppart, S. A. (2009). Detecting intrinsic scattering changes correlated to neuron action potentials using optical coherence imaging. *Opt. Express* 17, 13447–13457. doi: 10.1364/OE.17.013447

Guedan-Duran, A., Jemni-Damer, N., Orueta-Zenarruzabeitia, I., Guinea, G. V., Perez-Rigueiro, J., Gonzalez-Nieto, D., et al. (2020). Biomimetic approaches for separated regeneration of sensory and motor fibers in amputee people: Necessary conditions for functional integration of sensory-motor prostheses with the peripheral nerves. *Front. Bioeng. Biotechnol.* 8:584823. doi: 10.3389/fbioe.2020.584823

Hai, A., Dormann, A., Shappir, J., Yitzchaik, S., Bartic, C., Borghs, G., et al. (2009). Spine-shaped gold protrusions improve the adherence and electrical coupling of neurons with the surface of micro-electronic devices. *J. R. Soc. Interface* 6, 1153–1165. doi: 10.1098/rsif.2009.0087

Hai, A., Shappir, J., and Spira, M. E. (2010). In-cell recordings by extracellular microelectrodes. *Nat. Methods* 7, 200–202. doi: 10.1038/nmeth.1420

Halpern, J. M., Cullins, M. J., Chiel, H. J., and Martin, H. B. (2010). Chronic in vivo nerve electrical recordings of *Aplysia* californica using a boron-doped polycrystalline diamond electrode. *Diam. Relat. Mater.* 19, 178–181. doi: 10.1016/j.diamond.2009.08.006

Halpern, J. M., Xie, S., Sutton, G. P., Higashikubo, B. T., Chestek, C. A., Lu, H., et al. (2006). Diamond electrodes for neurodynamic studies in *Aplysia* californica. *Diam. Relat. Mater.* 15, 183–187. doi: 10.1016/j.diamond.2005.06.039

Huan, Y., Gill, J. P., Fritzinger, J. B., Patel, P. R., Richie, J. M., Valle, E. D., et al. (2021). Carbon fiber electrodes for intracellular recording and stimulation. *J. Neural Eng.* 18:066033. doi: 10.1088/1741-2552/ac3dd7

Jack, J. J. B., Noble, D., and Tsien, R. W. (1975). *Electric current flow in excitable cells*. Oxford: Clarendon Press.

Jordan, T., Newcomb, J. M., Hoppa, M. B., and Luke, G. P. (2022). Focused ultrasound stimulation of an ex-vivo *Aplysia* abdominal ganglion preparation. *J. Neurosci. Methods* 372, 109536. doi: 10.1016/j.jneumeth.2022.109536

Joseph, L., and Butera, R. J. (2009). Unmyelinated *Aplysia* nerves exhibit a nonmonotonic blocking response to high-frequency stimulation. *IEEE Trans. Neural Syst. Rehabil. Eng.* 17, 537–544. doi: 10.1109/TNSRE.2009.2029490

Joseph, L., and Butera, R. J. (2011). High-frequency stimulation selectively blocks different types of fibers in frog sciatic nerve. *IEEE Trans. Neural Syst. Rehabil. Eng.* 19, 550–557. doi: 10.1109/TNSRE.2011.2163082

Kandel, E. R. (1976). *Cellular basis of behavior: An introduction to behavioral neurobiology*. San Francisco: W.H. Freeman.

Kandel, E. R. (1979). *Behavioral biology of aplysia: A contribution to the comparative study of opisthobranch molluscs*. San Francisco: W.H. Freeman.

Keene, A. C., and Duboue, E. R. (2018). The origins and evolution of sleep. *J. Exp. Biol.* 221:jeb159533. doi: 10.1242/jeb.159533

Kilgore, K. L., and Bhadra, N. (2004). Nerve conduction block utilising high-frequency alternating current. *Med. Biol. Eng. Comput.* 42, 394–406. doi: 10.1007/BF02344716

Kishi, T. (2012). Heart failure as an autonomic nervous system dysfunction. *J. Cardiol.* 59, 117–122. doi: 10.1016/j.jjcc.2011.12.006

Kron, N. S., and Fieber, L. A. (2022). *Aplysia* neurons as a model of Alzheimer's disease: Shared genes and differential expression. *J. Mol. Neurosci.* 72, 287–302. doi: 10.1007/s12031-021-01918-3

Lazebnik, M., Marks, D. L., Potgieter, K., Gillette, R., and Boppart, S. A. (2003). Functional optical coherence tomography for detecting neural activity through scattering changes. *Opt. Lett.* 28, 1218–1220. doi: 10.1364/OL.28.001218

Lertmanorat, Z., and Durand, D. M. (2004). A novel electrode array for diameter-dependent control of axonal excitability: A Simulation study. *IEEE Trans. Biomed. Eng.* 51, 1242–1250. doi: 10.1109/TBME.2004.827347

Lothet, E. H., Kilgore, K. L., Bhadra, N., Bhadra, N., Vrabec, T., Wang, Y. T., et al. (2014). Alternating current and infrared produce an onset-free reversible nerve block. *Neurophotonics* 1:011010. doi: 10.1117/1.NPh.1.1.011010

Lothet, E. H., Shaw, K. M., Lu, H., Zhuo, J., Wang, Y. T., Gu, S., et al. (2017). Selective inhibition of small-diameter axons using infrared light. *Sci. Rep.* 7:3275. doi: 10.1038/s41598-017-03374-9

Mayford, M., Siegelbaum, S. A., and Kandel, E. R. (2012). Synapses and Memory Storage. *Cold Spring Harb. Perspect. Biol.* 4:a005751. doi: 10.1101/cshperspect.a005751

Moran, Y., Barzilai, M. G., Liebeskind, B. J., and Zakon, H. H. (2015). Evolution of voltage-gated ion channels at the emergence of Metazoa. *J. Exp. Biol.* 218, 515–525. doi: 10.1242/jeb.110270

Mori, T., Sato, T., Shigematsu, Y., Yamada, M., and Nomura, H. (1987). Can't ultrasound activate the nervous system. *IEICE Trans* 1976-1990 E70-E, 183–184. **.

Moroz, L. L., Edwards, J. R., Puthanveettil, S. V., Kohn, A. B., Ha, T., Heyland, A., et al. (2006). Neuronal transcriptome of *Aplysia*: Neuronal compartments and circuitry. *Cell* 127, 1453–1467. doi: 10.1016/j.cell.2006.09.052

Morrone, L., Scuteri, D., Rombola, L., Mizoguchi, H., and Bagetta, G. (2017). Opioids resistance in chronic pain management. *Curr. Neuropharmacol.* 15, 444–456. doi: 10.2174/1570159X14666161101092822

Morton, D. W., Chiel, H. J., Cohen, L. B., and Wu, J. (1991). Optical methods can be utilized to map the location and activity of putative motor neurons and interneurons during rhythmic patterns of activity in the buccal ganglion of *Aplysia*. *Brain Res* 564, 45–55. doi: 10.1016/0006-8993(91)91350-A

Nakashima, M., Yamada, S., Shiono, S., Maeda, M., and Satoh, F. (1992). 448-Detector optical recording system: Development and application to *Aplysia* gill-withdrawal reflex. *IEEE Trans. Biomed. Eng.* 39, 26–36. doi: 10.1109/10.108124

Nickel, F. T., Seifert, F., Lanz, S., and Maihöfner, C. (2012). Mechanisms of neuropathic pain. *Eur. Neuropsychopharmacol.* 22, 81–91. doi: 10.1016/j.euroneuro.2011.05.005

Novak, J. L., and Wheeler, B. C. (1986). Recording from the *Aplysia* abdominal ganglion with a planar microelectrode array. *IEEE Trans. Biomed. Eng.* 33, 196–202. doi: 10.1109/TBME.1986.325891

Orvis, J., Albertin, C. B., Shrestha, P., Chen, S., Zheng, M., Rodriguez, C. J., et al. (2022). The evolution of synaptic and cognitive capacity: Insights from the nervous system transcriptome of *Aplysia*. *Proc. Natl. Acad. Sci. U.S.A.* 119:e2122301119. doi: 10.1073/pnas.2122301119

Painter, S. D., Chong, M. G., Wong, M. A., Gray, A., Cormier, J. G., and Nagle, G. T. (1991). Relative contributions of the egg layer and egg cordon to pheromonal attraction and the induction of mating and egg-laying behavior in *Aplysia*. *Biol. Bull.* 181, 81–94. doi: 10.2307/1542491

Parsons, T. D., Kleinfeld, D., Raccuia-Behling, F., and Salzberg, B. M. (1989). Optical recording of the electrical activity of synaptically interacting *Aplysia* neurons in culture using potentiometric probes. *Biophys. J.* 56, 213–221. doi: 10.1016/S0006-3495(89)82666-9

Patel, Y. A., and Butera, R. J. (2015). Differential fiber-specific block of nerve conduction in mammalian peripheral nerves using kilohertz electrical stimulation. *J. Neurophysiol.* 113, 3923–3929. doi: 10.1152/jn.00529.2014

Peterson, E. J., and Tyler, D. J. (2013). Motor neuron activation in peripheral nerves using infrared neural stimulation. *J. Neural Eng.* 11:016001. doi: 10.1088/1741-2560/11/1/016001

Phillips, J. K. (2005). Pathogenesis of hypertension in renal failure: Role of the sympathetic nervous system and renal afferents. *Clin. Exp. Pharmacol. Physiol.* 32, 415–418. doi: 10.1111/j.1440-1681.2005.04204.x

Plaksin, M., Shapira, E., Kimmel, E., and Shoham, S. (2018). Thermal transients excite neurons through universal intramembrane mechanoelectrical effects. *Phys. Rev. X* 8:011043.

Pozdnyakov, I., Matantseva, O., and Skarlato, S. (2018). Diversity and evolution of four-domain voltage-gated cation channels of eukaryotes and their ancestral functional determinants. *Sci. Rep.* 8:3539. doi: 10.1038/s41598-018-21897-7

Rattay, F. (1986). Analysis of models for external stimulation of axons. *IEEE Trans. Biomed. Eng.* 33, 974–977. doi: 10.1109/TBME.1986.325670

Regehr, W. G., Pine, J., Cohan, C. S., Mischke, M. D., and Tank, D. W. (1989). Sealing cultured invertebrate neurons to embedded dish electrodes facilitates long-term stimulation and recording. *J. Neurosci. Methods* 30, 91–106. doi: 10.1016/0165-0270(89)90055-1

Rozman, J., Sovinec, B., Trlep, M., and Zorko, B. (1993). Multielectrode spiral cuff for ordered and reversed activation of nerve fibres. *J. Biomed. Eng.* 15, 113–120. doi: 10.1016/0141-5425(93)90039-2

Sadleir, R. J., Fu, F., and Chauhan, M. (2019). Functional magnetic resonance electrical impedance tomography (fMREIT) sensitivity analysis using an active bidomain finite-element model of neural tissue. *Magn. Reson. Med.* 81, 602–614. doi: 10.1002/mrm.27351

Shapiro, E., Castellucci, V. F., and Kandel, E. R. (1980). Presynaptic membrane potential affects transmitter release in an identified neuron in *Aplysia* by modulating the Ca2+ and K+ currents. *Proc. Natl. Acad. Sci.* 77, 629–633. doi: 10.1073/pnas.77.1.629

Skach, J., Conway, C., Barrett, L., and Ye, H. (2020). Axonal blockage with microscopic magnetic stimulation. *Sci. Rep.* 10:18030. doi: 10.1038/s41598-020-74891-3

Smarandache-Wellmann, C. R. (2016). Arthropod neurons and nervous system. *Curr. Biol.* 26, R960–R965. doi: 10.1016/j.cub.2016.07.063

Sperry, Z. J., Na, K., Parizi, S. S., Chiel, H. J., Seymour, J., Yoon, E., et al. (2018). Flexible microelectrode array for interfacing with the surface of neural ganglia. *J. Neural Eng.* 15:036027. doi: 10.1088/1741-2552/aab55f

Susswein, A. J., and Chiel, H. J. (2012). Nitric oxide as a regulator of behavior: New ideas from *Aplysia* feeding. *Prog. Neurobiol.* 97, 304–317. doi: 10.1016/j.pneurobio.2012.03.004

Tai, C., Roppolo, J. R., and de Groat, W. C. (2009). Analysis of nerve conduction block induced by direct current. *J. Comput. Neurosci.* 27, 201–210. doi: 10.1007/s10827-009-0137-7

Tam, S., Hurwitz, I., Chiel, H. J., and Susswein, A. J. (2020). Multiple local synaptic modifications at specific sensorimotor connections after learning are associated with behavioral adaptations that are components of a global response change. *J. Neurosci.* 40, 4363–4371. doi: 10.1523/JNEUROSCI.2647-19.2020

Terzis, J. K., Smith, K. L., and Orgel, M. G. (1991). The peripheral nerve: Structure. Function, reconstruction. *Plast. Reconstr. Surg.* 87, 1138–1139.

Thiede, K. I., Born, J., and Vorster, A. P. A. (2021). Sleep and conditioning of the siphon withdrawal reflex in *Aplysia*. *J. Exp. Biol.* 224:jeb242431. doi: 10.1242/jeb.242431

Vadivelu, N., Kai, A. M., Kodumudi, V., Sramcik, J., and Kaye, A. D. (2018). The Opioid Crisis: A Comprehensive Overview. *Curr. Pain Headache Rep.* 22:16. doi: 10.1007/s11916-018-0670-z

Wells, J. D., Kao, C., Jansen, E. D., Konrad, P. E., and Mahadevan-Jansen, A. (2005). Application of infrared light for in vivo neural stimulation. *J. Biomed. Opt.* 10:064003.

Wells, J., Kao, C., Mariappan, K., Albea, J., Jansen, E. D., Konrad, P., et al. (2005). Optical stimulation of neural tissue in vivo. *Opt. Lett.* 30, 504–506. doi: 10.1364/ol.30.000504

Woolum, J. C., and Strumwasser, F. (1978). Membrane-potential-sensitive dyes for optical monitoring of activity in *Aplysia* neurons. *J. Neurobiol.* 9, 185–193. doi: 10.1002/neu.480090302

Zakon, H. H. (2012). Adaptive evolution of voltage-gated sodium channels: The first 800 million years. *Proc. Natl. Acad. Sci. U.S.A.* 109, 10619–10625. doi: 10.1073/pnas.1201884109

Zhao, B. (1993). *Molecular and functional studies of potassium ion channels in the nervous system of Aplysia*. Available Online at: https://www.proquest.com/docview/304051250/abstract/DFDC0BCFB5784544PQ/1 (accessed November 11, 2022).

Zhuo, J., Ou, Z., Zhang, Y., Jackson, E. M., Shankar, S. S., McPheeters, M. T., et al. (2021). Isotonic ion replacement can lower the threshold for selective infrared neural inhibition. *Neurophotonics* 8:015005. doi: 10.1117/1.NPh.8.1.015005

Zhuo, J., Weidrick, C. E., Liu, Y., Moffitt, M. A., Jansen, E. D., Chiel, H. J., et al. (2022). "Selective IR inhibition can be reproduced by resistance heating," in *Procedings of the optogenetics and optical manipulation 2022* (SPIE), (Bellingham, WC), C1194706. doi: 10.1117/12.2610130

frontiers | Frontiers in Neuroscience

TYPE Original Research
PUBLISHED 09 March 2023
DOI 10.3389/fnins.2023.1113843

OPEN ACCESS

EDITED BY
James Newcomb,
New England College, United States

REVIEWED BY
Dawn M. Blitz,
Miami University, United States
Carola Staedele,
Illinois State University, United States

*CORRESPONDENCE
Patsy S. Dickinson
✉ pdickins@bowdoin.edu

SPECIALTY SECTION
This article was submitted to Neural Technology, a section of the journal Frontiers in Neuroscience

RECEIVED 01 December 2022
ACCEPTED 23 February 2023
PUBLISHED 09 March 2023

CITATION
Powell DJ, Owens E, Bergsund MM, Cooper M, Newstein P, Berner E, Janmohamed R and Dickinson PS (2023) The role of feedback and modulation in determining temperature resiliency in the lobster cardiac nervous system. *Front. Neurosci.* 17:1113843. doi: 10.3389/fnins.2023.1113843

The role of feedback and modulation in determining temperature resiliency in the lobster cardiac nervous system

Daniel J. Powell[1,2], Elizabeth Owens[2], Marie M. Bergsund[2], Maren Cooper[2], Peter Newstein[2], Emily Berner[2], Rania Janmohamed[2] and Patsy S. Dickinson[1,2]*

[1]Department of Biology, Bowdoin College, Brunswick, ME, United States, [2]Program in Neuroscience, Bowdoin College, Brunswick, ME, United States

Changes in ambient temperature affect all biological processes. However, these effects are process specific and often vary non-linearly. It is thus a non-trivial problem for neuronal circuits to maintain coordinated, functional output across a range of temperatures. The cardiac nervous systems in two species of decapod crustaceans, *Homarus americanus* and *Cancer borealis*, can maintain function across a wide but physiologically relevant temperature range. However, the processes that underlie temperature resilience in neuronal circuits and muscle systems are not fully understood. Here, we demonstrate that the non-isolated cardiac nervous system (i.e., the whole heart: neurons, effector organs, intrinsic feedback systems) in the American lobster, *H. americanus*, is more sensitive to warm temperatures than the isolated cardiac ganglion (CG) that controls the heartbeat. This was surprising as modulatory processes known to stabilize the output from the CG are absent when the ganglion is isolated. One source of inhibitory feedback in the intact cardiac neuromuscular system is nitric oxide (NO), which is released in response to heart contractions. We hypothesized that the greater temperature tolerance observed in the isolated CG is due to the absence of NO feedback. Here, we demonstrate that applying an NO donor to the isolated CG reduces its temperature tolerance. Similarly, we show that the NO synthase inhibitor L-nitroarginine (LNA) increases the temperature tolerance of the non-isolated nervous system. This is sufficient to explain differences in temperature tolerance between the isolated CG and the whole heart. However, in an intact lobster, the heart and CG are modulated by an array of endogenous peptides and hormones, many of which are positive regulators of the heartbeat. Many studies have demonstrated that excitatory modulators increase temperature resilience. However, this neuromuscular system is regulated by both excitatory and inhibitory peptide modulators. Perfusing SGRNFLRFamide, a FLRFamide-like peptide, through the heart increases the non-isolated nervous system's tolerance to high temperatures. In contrast, perfusing myosuppressin, a peptide that negatively regulates the heartbeat frequency, decreases the temperature tolerance. Our data suggest that, in this nervous system,

positive regulators of neural output increase temperature tolerance of the neuromuscular system, while modulators that decrease neural output decrease temperature tolerance.

KEYWORDS

myosuppressin, FMRFamide-like neuropeptide, nitric oxide, cardiac ganglion, crash temperature, L-arginine, temperature dependencies

1. Introduction

The nervous systems of all animals are subject to changes in temperature. Some mammalian and avian central nervous systems are under homeostatic regulation and are maintained within a few degrees Celsius. However, there exist examples of both mammals and birds that can withstand drastic variations in their internal body temperature, such as those that hibernate, enter torpor, or enter periods of dormancy (Ruf and Geiser, 2015; Junkins et al., 2022). While it is common for many physiological functions to arrest during periods of stasis, both the cardiac and nervous systems maintain function, albeit at a reduced capacity (Junkins et al., 2022). Many poikilotherms, animals that do not regulate their internal temperature, can maintain cardiac and neural function across a wide range of temperatures, which allows them to inhabit environments that experience daily and seasonal temperature changes (Fry, 1958; Hazel and Prosser, 1974; Macdonald, 1981; Prosser and Nelson, 1981; Zhurov and Brezina, 2005; Manning and Pelletier, 2009; Beverly et al., 2011; Robertson and Money, 2012; Soofi et al., 2014; Kushinsky et al., 2019).

Neural compensation in response to temperature change is not trivial as temperature affects all aspects of cellular function. Temperature resilience of pacemaker circuits is particularly important, as they are necessary for maintaining given behavioral states (Carpenter, 1967; Montgomery and Macdonald, 1990; Xu and Robertson, 1994; Busza et al., 2007; Reig et al., 2010; Tang et al., 2010; Robertson and Money, 2012; Rinberg et al., 2013; Kushinsky et al., 2019; Versteven et al., 2020; Powell et al., 2021; Ratliff et al., 2021). The relationship between a single biological process's output and temperature often follows an exponential relationship (Mundim et al., 2020). For instance, changes in ion channel conductance can range from 2–20 fold in response to a 10°C temperature change (Zečević et al., 1985; Klöckner et al., 1990; Moran et al., 2004; Cao and Oertel, 2005; Fohlmeister et al., 2010; Kang et al., 2011; Robertson and Money, 2012; Tang et al., 2012; Yang and Zheng, 2014). Because each ion channel type can be differently affected by changes in temperature, predicting how temperature change will affect even a single neuron is not simple (Caplan et al., 2014; O'Leary and Marder, 2016; Alonso and Marder, 2020). These predictions are even more difficult to understand when extrapolating to neural circuits, as synaptic (Tang et al., 2010; Rinberg et al., 2013; Soofi et al., 2014; Städele et al., 2015; O'Leary and Marder, 2016; Alonso and Marder, 2020; Powell et al., 2021; Ratliff et al., 2021; Städele and Stein, 2022) and muscle physiology (Harri and Florey, 1977; Foldes et al., 1978; Rutkove, 2001; Racinais and Oksa, 2010; Thuma et al., 2013; Kushinsky et al., 2019; this paper) are also affected. Some processes of temperature compensation in the neural circuits of poikilotherms have been revealed (Harri and Florey, 1977; Foldes et al., 1978; Rutkove, 2001; Racinais and Oksa, 2010; Kushinsky et al., 2019). For example, within the stomatogastric ganglion (STG) of the Jonah crab, there are two coupled pattern generating circuits. While each circuit has different processes that enable temperature compensation, they are both able to maintain function across a similar range of temperature (~7–30°C) (Tang et al., 2010; Tang et al., 2012; Rinberg et al., 2013; Soofi et al., 2014; Städele et al., 2015; Haddad and Marder, 2018; Powell et al., 2021; Ratliff et al., 2021; Städele and Stein, 2022). For instance, one such compensatory process includes similar increases in maximal conductance and gating rates for Na^+ and K^+ mediated ion channel currents that contribute to bursting (I_h, I_A, and synaptic currents). Because these processes have opposing impacts on neuron membrane potential, they offset one another as temperature is increased (Tang et al., 2010). It has been shown that exogenous application of neuromodulators that are normally present in the intact animal can extend the functional temperature range of these circuits (Städele et al., 2015; Haddad and Marder, 2018; Städele and Stein, 2022; this paper). Many of these modulatory peptides operate an inward-current that is both modulator dependent and voltage gated (I_{MI}; Golowasch and Marder, 1992; Swensen and Marder, 2000). Activation of I_{MI} has been shown to allow neurons to maintain activity as temperature is increased by offsetting the temperature dependent increase in leak currents (Städele et al., 2015).

While the cardiac nervous system in decapod crustaceans has been shown to maintain function across an ecologically relevant temperature range (Camacho et al., 2006; Worden et al., 2006; Hamilton et al., 2007; Kushinsky et al., 2019), the processes that contribute to temperature resiliency in this nervous system are not fully known. Given that the neural circuit governing the heartbeat (the cardiac ganglion, nine neurons) has substantially fewer neurons than the STG (~30 neurons), and that the circuit is configured differently, it is unclear that the same principles will confer temperature compensation in this nervous system. To address this, we used the cardiac nervous system found in the American lobster (*H. americanus*). The lobster heartbeat is driven by a nine-neuron pacemaker circuit called the cardiac ganglion (CG). The four Small Cells (SCs) are pacemaker neurons that rhythmically, synchronously excite five Large Cells (LCs; motor neurons) that drive the cardiac muscle contractions (**Figure 1**). All nine neurons are electrically coupled with recurrent excitatory, chemical synaptic connections between the SCs and LCs. Consequently, the output of this circuit is a monophasic burst of action potentials that results in the synchronous muscle contractions that constitute the heartbeat (Cooke, 2002). Given that the heartbeat is responsible for circulating nutrients to all tissues in these animals as well as delivering the modulators that confer

temperature robustness to the STG, we would expect that the CG is capable of maintaining stable output across a physiological range of temperatures.

The neurons of the CG and the cardiac muscles are known to be regulated by a variety of processes, including two intrinsic feedback systems. Each heart contraction activates stretch receptors that positively feed back onto the CG neurons and result in an increase in heartbeat frequency (Dickinson et al., 2016). Nitric oxide (NO) synthase, located in the cardiac muscles, releases NO, which is a negative regulator of the heartbeat (Mahadevan et al., 2004). Application of NO donors mimics this negative feedback pathway, resulting in a decrease in beat frequency and stroke volume in the intact heart (Mahadevan et al., 2004). However, the effects of NO on the muscle contractile force appear to be indirect, as NO does not alter muscle contraction parameters (Mahadevan et al., 2004). Instead, NO decreases the frequency of the synchronous LC and SC bursts by increasing the interburst interval of the action potential bursts. However, it does not affect the burst duration of the CG motor neurons (Mahadevan et al., 2004).

The heart is also modulated by a plethora of neuropeptides and hormones, including a variety of FLRFamide-like peptides, that are volume released into circulation by the pericardial organs (Ma et al., 2008; Chen et al., 2010). To our knowledge, these modulatory peptides act on the cardiac nervous system in a feedforward manner. While some of these modulators act directly on the pacemaker and motor neurons, some of these peptides modulate the neuromuscular junctions and/or regulate the muscles directly (Stevens et al., 2009; Dickinson et al., 2016). Here we investigate how both feedback and feedforward processes contribute to temperature resiliency in the cardiac neuromuscular system. Many studies have focused on how modulatory input increases the temperature tolerance of nervous systems (Städele et al., 2015; Haddad and Marder, 2018; DeMaegd and Stein, 2021; Städele and Stein, 2022). There are also a few that indicate either directly (Srithiphaphirom et al., 2019) or indirectly (Alonso and Marder, 2020) that decreasing neural excitability decreases temperature tolerance. Here we demonstrate that in the cardiac neuromuscular system, at least one feedforward modulator that increases excitability (SGRNFLRFamide; SGRN) increased the operational temperature range of the system, and that two negative regulators of excitability (NO and myosuppressin) decreased the temperature tolerance of this neuromuscular system.

While the goal of this study was to examine processes that affect the temperature tolerance of the cardiac ganglion and intact heart, responses to high temperatures have not been previously characterized in either of these structures. Therefore, some of the data detailed here describe the physiological responses we observed when this neuromuscular organ was subjected to a wide range of temperatures.

2. Materials and methods

2.1. Animals

Male and female American lobsters, *Homarus americanus*, were purchased from seafood retailers in Brunswick, ME. Lobsters were fed weekly with chopped squid or shrimp, and were housed in recirculating natural seawater tanks between 10°C and 12°C. To minimize the effects of the temperature at which lobsters had been caught, particularly summer vs. winter lobsters, most lobsters were acclimated at 10–12°C for a minimum of two weeks. In a subset of experiments described below (Section "2.9. Neuropeptide applications"), animals were used after shorter acclimation periods due to availability. Because these studies involved only crustaceans, the Bowdoin College Institutional Care and Use Committee (IACUC) did not require ethics approval for this study.

2.2. Whole heart preparations

Lobster hearts were dissected, and the activity of the cardiac neuromuscular system was recorded using techniques described previously (Stevens et al., 2009; Dickinson et al., 2018). Lobsters were anaesthetized on ice for 30–60 min before dissection. The heart was removed, still attached to the overlaying section of the dorsal thoracic carapace. It was then pinned ventral-side-up in a Sylgard 170-coated dish (Dow Corning, Midland, MI, USA) filled with cold lobster physiological saline (composition in mM: 479.12 NaCl, 12.74 KCl, 13.67 $CaCl_2$, 20.00 $MgSO_4$, 3.91 Na_2SO_4, 11.45 Trizma base, and 4.82 maleic acid; pH 7.45 at 25°C). The heart remained attached to the carapace to maintain the natural stretch present in the intact animal.

The heart was cannulated with a short (<1 cm) piece of tubing through the posterior artery (arrow in **Figure 1A**) and continuously perfused with cold (8–10°C) physiological saline at a flow rate of 2.5 ml/min. Saline thus entered through the artery and exited through the ostia toward the anterior end of the heart. A second perfusion line, also at a flow rate of 2.5 ml/min, superfused cold saline across the top of the heart to maintain the temperature on the exterior of the heart. A temperature probe (TA-29, Warner Instruments, Hamden, CT, USA) was fitted alongside the bottom of the external perfusion tubing, which was identical to the perfusion tubing cannulating the heart, and lay directly on the exterior ventral wall of the heart. The temperature was continuously monitored and controlled using an in-line temperature control system (CL-100 bipolar temperature controller and SC-20 solution heater/cooler; Warner Instruments). Both perfusion tubes came from the same heater/cooler, and so the temperature of the saline at the point measured by the external temperature probe was identical to that of the saline entering the heart. Hearts were maintained at a baseline temperature of 8–10°C until temperature ramps were applied.

To record heart contractions, the anterior arteries were tied with 6/0 Suture Silk to a Grass FT03 force-displacement transducer (Astro-Med, West Warwick, RI, USA) at an angle of approximately 30–45° from the horizontal plane. The anterior arteries were stretched to produce a baseline tonus of 2 g, which mimics the stretch in the intact animal. The contraction output was amplified using an ETH-250 Bridge amplifier (CB Sciences, Dover, NH, USA) with a high pass filter (4 Hz), and further amplified using a Brownlee 410 amplifier (Brownlee Precision, San Jose, CA, USA).

2.3. Semi-intact heart preparations

For semi-intact heart recordings, preparations were identical to whole heart preparations, with one exception: a small hole was

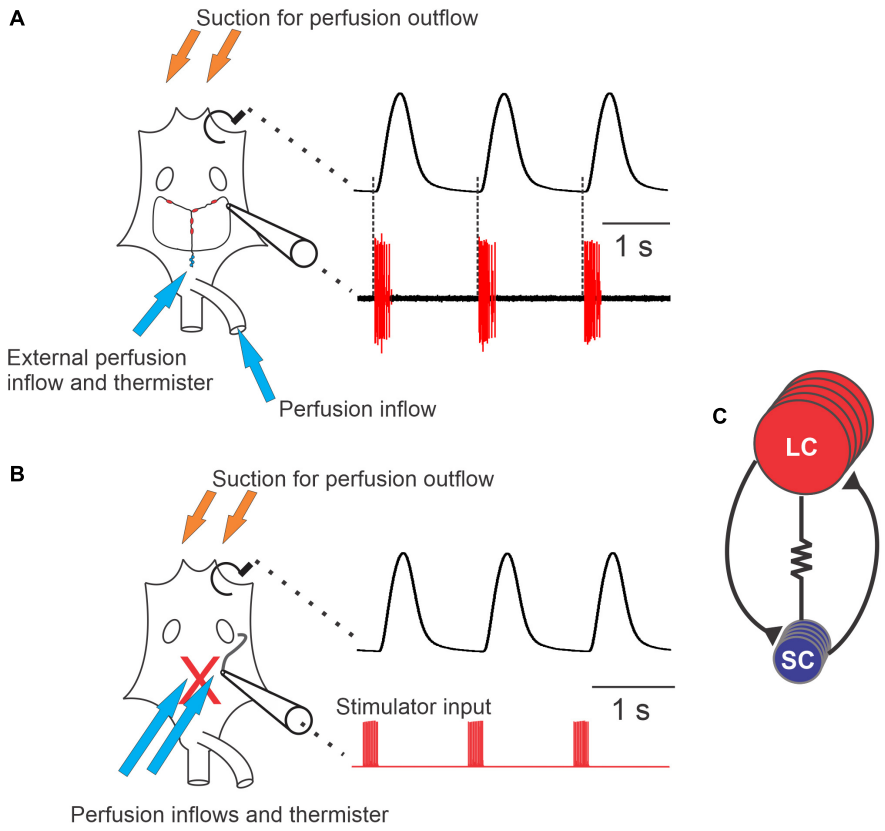

FIGURE 1
Diagram of the cardiac neuromuscular system. **(A)** A schematic of a semi-intact preparation that allowed for simultaneous recordings of the force produced from each heartbeat (upper trace) and the neuron activity of the ganglion (lower trace). The cartoon of the heart (left) shows the relative location of the cardiac ganglion, location of the small cells (SCs, small blue circles) and the locations of the large cells (LCs, red ovals). Synaptic and axonal processes are depicted as black lines connecting the neurons. Large unfilled ovals show the relative location of the ventral ostia. Note that when comparing the timing of neuron action potential bursts and the heartbeat, each burst of action potentials precedes and corresponds to a contraction of the heart (dashed lines). **(B)** Schematic of a preparation in which the neurons have been removed from heart (replaced by the red "X"), leaving only a section of nerve intact (black tortuous line connected to the cartoon electrode) that can be stimulated. The traces to the right of the schematic show that the axons left in the motor nerve can be stimulated (red, lower trace) in order to generate fictive cardiac muscle contractions (black, upper trace). **(C)** Wiring diagram of the neurons in the CG, which contains five large cells (LCs) (red) and four small cells (SCs) (blue). While all neurons are electrically coupled, this cartoon only depicts coupling between neuron types (resistor symbol). Both large and small cells excite one another *via* chemical synapses (black lines terminating in black triangles). Arrows in panels **(A,B)** show approximate locations of perfusion inflows (blue) and outflows (orange), as well as the location of the thermistors used to measure temperature.

cut into the ventral heart wall slightly posterior to the ostia. This exposed the cardiac ganglion without decreasing contraction force. A small portion of one of the anterolateral nerves was sucked into a suction electrode to record the extracellular electrical output of the ganglion while still connected to the heart muscle (Figure 1A). The electrode signal was recorded and amplified with a Model 1700 A-M Systems Differential AC Amplifier (Sequim, WA, USA) and a Model 410 Brownlee Precision Instrumentation Amplifier (Brownlee Precision, San Jose, CA, USA).

Both whole hearts and semi-intact hearts were allowed to equilibrate for one hour at control temperature (~8–10°C) before testing.

2.4. Isolated cardiac ganglion

For isolated CG experiments, the cardiac ganglion was isolated from hearts that had previously been recorded as either whole heart or semi-intact preparations, or from hearts freshly dissected from lobsters. The heart was separated from the dorsal carapace and pinned to a Sylgard 170-lined dish filled with cold physiological saline. The ventral wall of the heart was opened, and the cardiac ganglion was dissected from the dorsal heart wall. For CGs that were dissected from hearts previously used in semi-intact recordings, the ganglion was removed immediately after the completion of the semi-intact recordings, with the heart and CG maintained in cold saline throughout the remainder of the dissection. The ganglion was pinned to a Sylgard 184-lined dish and superfused with cold (8–10°C) physiological saline at a rate of approximately 5 ml/min throughout the experiment.

To provide maximal temperature control and accuracy of temperature measurements at the ganglion, we used two perfusion inflows, one directed at the SC area and one at the LC region. Inflows were placed close to the ganglion (within 1 cm), and the thermistor (TA-29) used to measure temperature was placed within ~1 mm of the ganglion, near one of the saline inflows. Outflows were placed on the far side of the ganglion, some distance (2–3 cm) away, so that the flow was directed across the ganglion. Because the

CG is a distributed ganglion, not all regions of the ganglion were equally close to the inflow, so some variation in temperature among different regions of the ganglion was inevitable.

Neural activity was recorded using either stainless steel pin electrodes or a suction electrode. For the former method, a petroleum jelly well was made around one of the anterolateral nerves of the ganglion. One pin electrode was put into the well to record the electrical activity of the motor neuron axons in the anterolateral nerve; the other was placed nearby in the bath. For suction electrode recordings, a glass suction electrode was attached to one of the anterolateral nerves with a watertight seal. Signals from the pin electrode or the suction electrode were amplified using the same instrumentation as for the semi-intact preparation.

2.5. Stimulated heart preparation

To examine the effects of temperature on the neuromuscular junction and the cardiac muscle itself, we used a stimulated heart preparation (Stevens et al., 2009) in hearts that had previously been tested in the semi-intact configuration. After the semi-intact temperature ramp was completed, the opening in the ventral wall of the heart was extended from the dorsal abdominal artery to the ostia, leaving the anterior half of the heart intact. The ganglion was removed, leaving one anterolateral nerve long enough to be visible and accessible for stimulation. The severed nerve ending was stimulated using a suction electrode (**Figure 1B**). Stimuli, 0.5 ms in duration, were delivered in bursts having a frequency of 60 Hz and a burst duration of 300 ms. These bursts were repeated with a period of 1.3 s in trains of 15 bursts each. After each train of bursts, the nerve was left unstimulated for 60 s, after which another train of 15 bursts was delivered. Previous studies have found that this pattern of stimulation helps to prevent the degradation of muscle activity that occurs with continual stimulation (Stevens et al., 2009). Electrical impulses were generated using a CED Micro 1401 data acquisition board (Cambridge Electronic Design, Cambridge, UK) and controlled by a custom Spike2 (CED) sequencer file. Current was delivered using a Model 1700 A-M Systems Differential AC Amplifier (Sequim, WA, USA). Both saline perfusion tubes were set to flow into the intact portion of the heart, over the muscle and nerve ending being stimulated. Muscle contractions and injected current were recorded using the same instrumentation and software as for the semi-intact heart preparation. Sequencer files can be made available upon request.

2.6. Physiological recordings

All recordings (muscle force, electrical activity, stimulation) were made using CED 1401 data acquisition boards and Spike2 software (v 6,7, or 9; CED, Cambridge, UK). Data were recorded onto a Dell PC (Austin, TX, USA).

2.7. Temperature manipulations

Baseline functioning was recorded for 10 min at 8–10°C. The temperature of the perfused physiological saline was then increased by steps, controlled by the CL-100 temperature controller (set on fast cycle frequency) using a sequencer script in the Spike2 program. Steps were set to change instantaneously, and then remain steady for the remainder of the 1-min step time. Because the temperature of the SC-20 cannot change instantly, the change was more gradual, asymptoting at the new temperature in approximately 20 s. Temperature was increased in steps of 0.75°C, 1°C, or 1.25°C until the heart crashed. A crash was characterized as the muscles failing to beat or the ganglion failing to burst more than twice in 30 s. After the heart crashed, the temperature was decreased back to baseline at a rate of 1–2°C/min in most experiments; in some experiments, temperature was returned to baseline at 5°C/min. The heart was then allowed to stabilize at 8–10°C for at least 20 min to ensure its functioning returned to baseline. Preparations in which any crash temperatures were over 45°C were excluded. If the heart, nervous system, or muscle failed to produce physiological output when returned to baseline temperature, the crash was considered lethal, and the lobster was excluded.

For the stimulated preparation, the temperature was increased by 1.5°C (stepwise) after each set of 15 stimulation trains, until the temperature reached the crash temperature of the semi-intact preparation from which it was derived. It was maintained at the new temperature for the 60 s before the next train of stimulations was delivered, as well as during those 15 stimulus trains (i.e., another 15 s). Preliminary experiments showed that if the stimulated muscle was allowed to reach a temperature at which muscle contractions stopped entirely, activity could not be recovered upon return of temperature to baseline values. Therefore, the maximum temperature for each stimulated preparation was based on the crash temperature of that heart recorded in the semi-intact configuration.

2.8. Nitric oxide experimental manipulations

To determine whether nitric oxide (NO) released from the cardiac muscle (Mahadevan et al., 2004) was at least partly responsible for differences in the responses of the whole or semi-intact heart vs. the isolated CG, we conducted two types of experiments. In the first, we examined the effects of NO on the whole heart preparation or on the isolated CG. For whole heart experiments, we used the NO donor PAPA NONOate (Cayman Chemical Company, Ann Arbor, MI, USA) at a concentration of 10^{-5}M (Cheng et al., 2011). This led to a clear decrease in contraction frequency and amplitude that lasted throughout the duration of the donor application. For experiments examining the effects of NO on the isolated CG, the nitric oxide donor SNAP (Cayman Chemical Company) was applied at a concentration of 10^{-5} M (Mahadevan et al., 2004) during temperature ramps. After control temperature ramps in saline, 10^{-5} M SNAP or PAPA NONOate was applied to isolated CG or whole heart preparations, respectively, through the perfusion system. After beginning the perfusion of NO donors, baseline functioning was recorded for 10 min at 8–10°C, then a temperature ramp was applied; the NO donor application was continued throughout the entirety of the temperature ramp.

In the second set of experiments, we blocked the production of NO in the whole heart using L-nitroarginine (LNA; Cayman

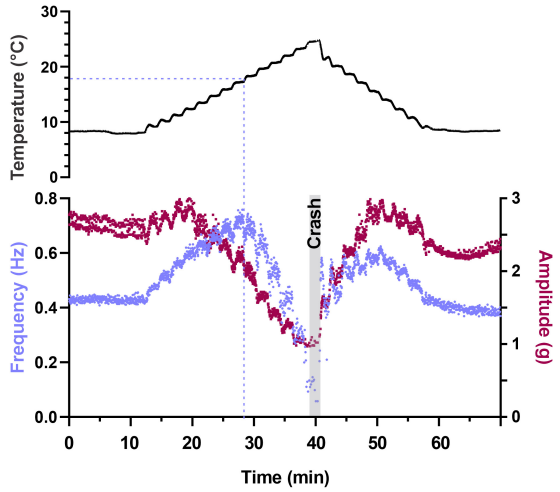

FIGURE 2
Depiction of changes in heartbeat parameters as temperature is increased to its crash temperature and then decreased to baseline. Plot of two parameters that characterize the heartbeat as temperature is increased to crash in a semi-intact preparation. Instantaneous contraction frequency is plotted on the left y-axis (purple) and contraction amplitude (force) on the right y-axis (maroon) as a function of time to crash. Each data point represents a single heartbeat. Temperature steps are indicated above the plot (1.25°C increments) and the gray bar labeled "Crash" denotes the time and temperature at which the preparation crashed (fewer than two beats in 30 s). Note that contraction amplitude decreased as temperature was increased above ~12°C and frequency initially increased with increased temperature. This is followed by a decrease in both parameters (amplitude decreases at temperatures greater than ~14°C and frequency decreases at temperatures greater than ~20°C). Also note that when temperature is stepped back to 8°C, we observe a mirrored response in both frequency and amplitude relative to the temperature ramp to crash.

Chemical Company), a competitive inhibitor of nitric oxide synthase (NOS). Using the whole heart preparation, the crash temperature of the heart was determined in control saline. The heart was then perfused with 3.30×10^{-4} M LNA at the baseline temperature for 20 min to block nitric oxide feedback before being subjected to a temperature ramp in LNA. To ensure that the NO precursor arginine did not alter the temperature resilience of the cardiac neuromuscular system, saline containing 1.1×10^{-4} M arginine was perfused through the heart. Crash temperature was not affected by arginine alone (data not shown).

2.9. Neuropeptide applications

To ask whether neuropeptides are able to stabilize the heart and increase its resiliency to temperature stress, as has been seen in other systems, we examined the effects of two native *Homarus* neuropeptides, SGRNFLRFamide (SGRN), and myosuppressin (pQDLDHVFLRFamide). Both peptides were custom synthesized by GenScript (Piscataway, NJ, USA). SGRN was dissolved in deionized water and stored as a 10^{-3} M stock solution at −20°C. Myosuppressin was initially dissolved in dimethyl sulfoxide (DMSO). The dissolved peptide was then diluted with deionized water to a solution containing 10^{-3} M myosuppressin and 10% DMSO. Previous experiments have shown that DMSO, when diluted to the concentrations used here, has no effect on the cardiac neuromuscular system (Stevens et al., 2009). This solution was stored as a stock solution at −20°C. Just before use, an aliquot was thawed and diluted to the working concentration in saline. After a temperature ramp in control saline was completed, peptide was perfused through the whole heart preparation for a 15 min acclimation period at baseline temperature before a temperature ramp was repeated in the presence of 10^{-8} M SGRN or 10^{-7} M myosuppressin. These experiments were conducted using the whole heart in summer lobsters that had been acclimated in our tanks for less than two weeks; the crash temperatures in control saline were noticeably higher than in other experiments.

2.10. Data analysis

Recordings of muscle contractions in whole heart, semi-intact heat, and stimulated preparations were analyzed for contraction amplitude and frequency. Recordings of ganglion bursting activity in semi-intact and isolated CG preparations were analyzed for burst frequency, burst duration, and duty cycle (defined as the burst duration over cycle period). Contraction parameters were determined using the built-in functions in Spike2. Bursting parameters were calculated using scripts for Spike2 written by Dr. Dirk Bucher (Rutgers University and New Jersey Institute of Technology).

To characterize the pattern of changes recorded as the temperature was increased toward crash temperature, we divided the entire temperature range into 1°C bins and averaged each parameter across all bursts within that temperature bin for each preparation. Values plotted at each temperature thus reflect the values for all cycles in a 1°C range around that value (e.g., the binned value at 12°C includes all cycles in which the temperature was 11.501°C through 12.500°C.) To enable us to pool data from multiple individual hearts or cardiac ganglia, each of which had different starting values for all parameters, we normalized all values for a given preparation to the value recorded at ~8°C, before the start of the temperature ramp, in that preparation. Pooled data for bursting and contraction parameters are thus shown as normalized averages from multiple preparations. Crash temperatures were not normalized.

All data sets were tested for normality to determine the statistical tests to be used. For all student's *t*-tests, we used a Shapiro–Wilk test to determine sample normality (particularly when sample sizes were small), and when appropriate, a Levene's test to assess equal variance between groups. When normality could either not be assessed or when distributions failed a Shapiro–Wilk test, we used a Wilcoxon Sign-Rank test for paired data and a Friedman test with Dunn's multiple comparisons for repeated measures data involving more than two sets of values. These tests were carried out in both MATLAB (Mathworks, Nantucket, MA, USA) and GraphPad Prism (Dotmatics, Boston, MA, USA).

When comparing the responses to LNA perfusion through the whole heart preparations (**Figure 9A**), we used a Wilcoxon Sign Rank test to determine if there was an increase in crash temperature for preparations whose contraction frequency was increased by LNA. We also used a Wilcoxon Sign Rank test to determine if there was a decrease in crash temperature for preparations

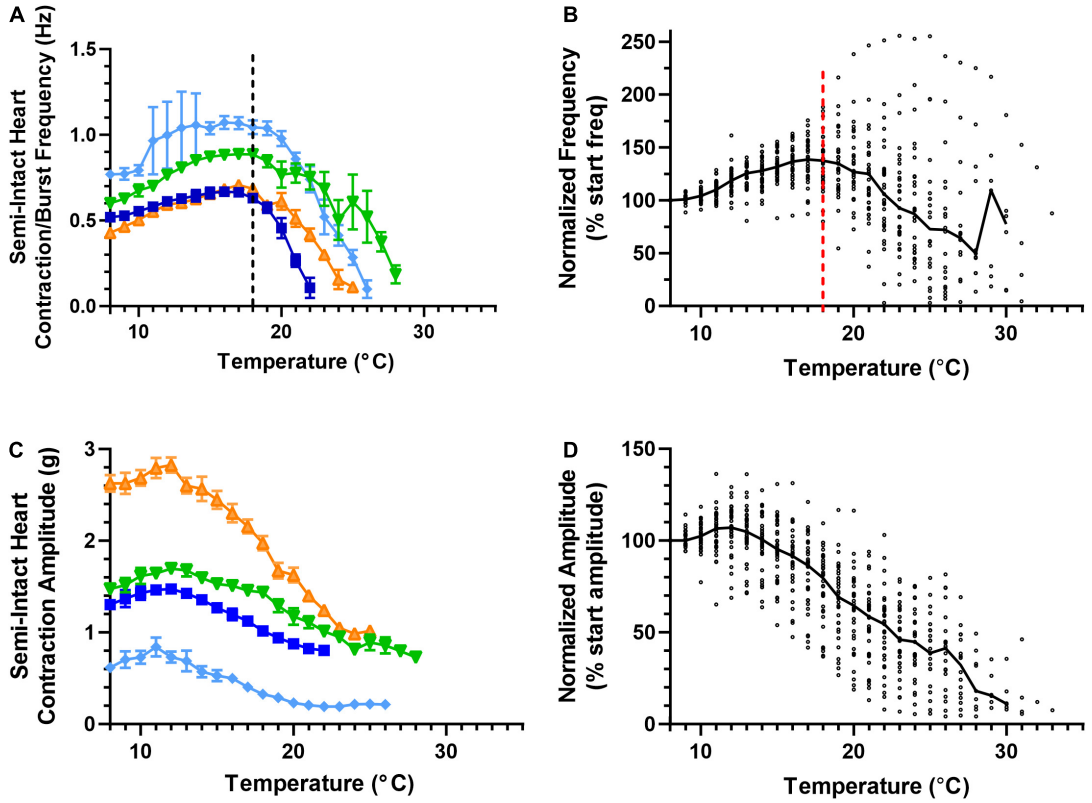

FIGURE 3
Cardiac neuromuscular system responses to an increasing temperature ramp: contraction frequency and amplitude. Values show data averaged in 1°C bins, with the data plotted at the center of each bin. **(A)** A plot of heart contraction frequency in response to a temperature ramp from 8°C to crash temperature for four semi-intact preparations (each shown in a different color). Note that at ~18°C (dashed line), contraction frequency began to decrease in each of these example preparations. **(B)** A plot of heart contraction frequency normalized to the contraction frequency at 8°C in response to a temperature ramp from 8°C to crash temperature for all semi-intact preparations. (*N* = 35 until the first preparation crashes at 19°C; *N* decreases from that temperature on). **(C)** Plot showing contraction amplitude (force, grams) as a function of temperature for the same four semi-intact preparations plotted in panel **(A)**. Note that contraction amplitude decreased as temperature was increased above ~12°C. **(D)** A plot of contraction amplitude as a function of temperature, with the contraction amplitude for each preparation at each temperature step normalized to the contraction amplitude at 8°C (*N* = 35 until the first preparation crashes at 19°C; *N* decreases from that temperature on). All data points in panels **(A,C)** show the mean ± SD for a given parameter at each temperature step. In panels **(B,D)**, the solid back line connects median normalized contraction frequency and amplitude, respectively, at each temperature step. Medians are omitted when $N \leq 5$.

whose contraction frequency was decreased by LNA. Because our sample size was small, we bootstrapped the data by pooling all values within each group (control vs. increased frequency and control vs. decreased frequency) and for each comparison, we randomly distributed the data (with replacement) into two groups and compared the newly generated groups with a Wilcoxon Sign Rank test. This process was repeated 10,000 times. All tests and bootstrapping were carried out in MATLAB (Mathworks, Nantucket, MA, USA).

When we compared the correlation between the change in crash temperature as a function of the change in heartbeat frequency between control and LNA conditions (Figure 10B), we used a Spearman rank correlation test. We used the same test to assess whether or not the contraction frequency in the control condition predicted the crash temperature of that preparation in LNA (Figure 10C), as well as to ask whether contraction frequency at baseline temperature predicted the crash temperature of that preparation in saline for a separate group of whole heart preparations (Figure 11). In both cases, analyses were carried out in MATLAB (Mathworks, Nantucket, MA, USA).

3. Results

3.1. The cardiac neuromuscular system maintains rhythmicity across a wide temperature range

We used two simultaneous approaches to examine how the cardiac neuromuscular system responds to changes in temperature in semi-intact preparations: (1) We recorded cardiac muscle contractions using a force transducer (Figure 1A, upper trace). In these recordings, each upward deflection corresponds to a single muscle contraction and each downward deflection corresponds to cardiac muscle relaxation. (2) We simultaneously monitored the bursts of action potentials produced by the CG neurons (Figure 1A, lower trace), using a suction electrode to record extracellularly from the CG nerve (Methods). These action potentials are generated by the five large cells (LCs; motor neurons). Rhythmicity in the LCs is coordinated largely by the four small cells (SCs; pacemaker neurons) and is maintained and stabilized by the recurrent synaptic

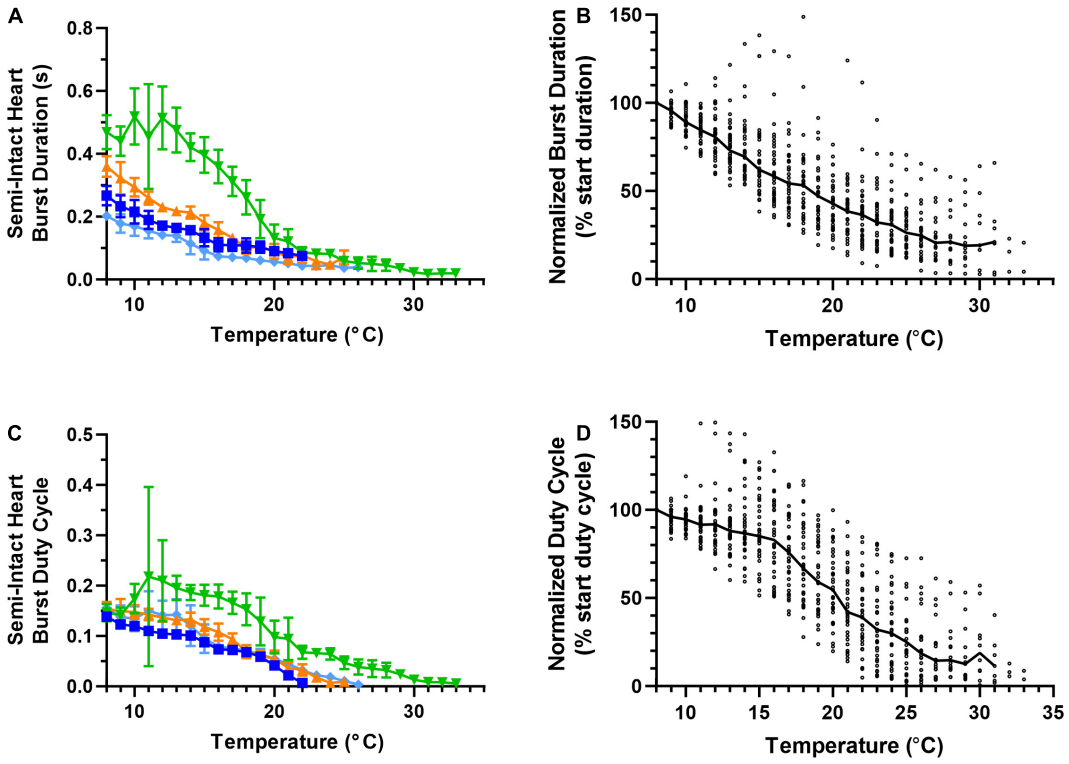

FIGURE 4
Responses of semi-intact cardiac neuromuscular system to an increasing temperature ramp: cardiac ganglion burst duration and duty cycle. Values show data averaged in 1°C bins, with the data plotted at the center of each bin. **(A)** A plot of cardiac ganglion burst duration within semi-intact hearts as a function of temperature for the same four semi-intact preparations in Figures 3A, C. CG burst duration decreases rapidly with temperature, and eventually stabilizes at a floor duration. **(B)** A plot of CG burst duration normalized to the duration at 8°C for all semi-intact preparations, showing the decrease in contraction duration across all temperatures (N = 35 until the first preparation crashes at 19°C; N decreases from that temperature on). **(C)** Plot of CG burst duty cycle as a function of temperature for the same four preparations plotted in panel **(A)**. CG burst duty cycle decreases across the entire range of temperatures tested. **(D)** A plot of CG burst duty cycle as a function of temperature, with the duty cycle for each preparation at each temperature step normalized to the burst duty cycle at 8°C (N = 35 until the first preparation crashes at 19°C; N decreases from that temperature on). Duty cycle decreases with increasing temperature over the entire range of temperatures. All data points in panels **(A,C)** show mean ± SD for a given parameter at each temperature step. In panels **(B,D)**, the solid back line connects median normalized burst duration and duty cycle, respectively at each temperature step. Medians are omitted when $N \leq 5$.

connections between these two groups of neurons (Figure 1C), as well as by some intrinsic properties of the LCs. Because the heart is dissected from the animal in these experiments and because an incision is made in the heart muscle in order to record from the CG, these preparations are referred to as "semi-intact."

Semi-intact preparations maintained rhythmic cardiac contractions as temperature was increased, until a critical temperature was reached. At this critical temperature, the muscles stopped contracting and the cardiac ganglion failed to generate rhythmic bursts of action potentials. So long as activity was recovered when temperature was decreased back into the permissible range, this loss of functional activity was called a "crash" (Tang et al., 2012; Rinberg et al., 2013). Figure 2 shows an example of this crash and recovery in a single preparation. Here we have plotted the instantaneous frequency and amplitude of each heart contraction as a function of time while temperature was being increased from ∼8°C to ∼25.5°C (the crash temperature for this preparation). While our results focus primarily on the effects of increasing temperature on this circuit-muscle effector system, it is important to note that the neuromuscular system did recover when temperature was decreased from the crash temperature, as is shown in Figure 2. In this example, the frequency and amplitude of the heart contractions initially increased as temperature was increased. This increase was followed by a decrease in both parameters as the temperature was increased to the crash point (∼25.5°C). Notably, the temperature dependencies of frequency and amplitude were not identical. In this preparation, for example, the decrease in amplitude started at ∼13°C, whereas frequency did not start to decrease until the temperature had reached ∼17°C. Decreasing temperature back to ∼8°C caused an approximately mirrored response for both frequency and amplitude. Although some differences can be observed, this may be due to a slower time course in increasing saline temperature compared to the faster decrease back to baseline temperature.

We measured four parameters as we increased temperature to the crash point in a set of semi-intact preparations (Methods). We measured the frequency of the heartbeat/CG bursts and heartbeat force of 35 hearts (Figure 3) and the motor neuron burst duration and duty cycle of 35 hearts (Figure 4). Thirty of the hearts recorded are in both data sets, but due to the varying qualities of recordings, the last 5 hearts in each group are from separate sets of five hearts each. Because there is a one-to-one relationship between a burst of action potentials from the CG and the subsequent heart contraction, burst frequency and contraction frequency are

synonymous (Figure 1A; see dashed line). They are thus depicted in a single plot. Although the baseline frequency and the details of the pattern of changes varied across individual preparations, as can be seen in the four example preparations shown in Figure 3A, the frequency initially increased with increasing temperature until approximately 18–19°C (mean peak frequency was recorded at 18.03 ± 2.88°C; $N = 35$), and then began to decrease until a critical temperature was reached and the preparations crashed. A similar pattern was observed across the population of hearts studied here. Figure 3B shows that as temperature was increased until each preparation crashed, median contraction frequency increased until ∼18°C, at which point median contraction frequency began to decrease. When temperature was increased beyond ∼26°C, the fraction of crashed preparations substantially increased (at 26°C, $N = 13/35$, at 28°C $N = 26/35$). Medians are not shown for temperatures at which five preparations or fewer remained in the testing set, i.e., for temperatures at or higher than that at which all but five of the preparations had crashed.

The force (measured here as contraction amplitude) generated by the heartbeat was measured at each temperature (Figure 3C); the example preparations plotted here show that contraction amplitude varied greatly across preparations. As was the case with frequency, heartbeat force began to decrease when temperature was increased beyond a certain temperature. However, this decline in force generally began at a lower temperature (declining above ∼12°C in most preparations). Previous studies show that a functional relationship exists between CG burst frequency and heartbeat amplitude (Mahadevan et al., 2004; Worden et al., 2006; Wiwatpanit et al., 2012; Williams et al., 2013). Although both frequency and amplitude eventually decreased as temperature was increased, the decrease in contraction frequency occurred at temperatures higher than the decrease in contraction force, as noted above (Figures 3A, B). This was true regardless of initial contraction strength, suggesting that either changes other than contraction frequency [e.g., duty cycle, which is an important component of the neuromuscular transform in the lobster cardiac neuromuscular system (Williams et al., 2013)] or changes at the periphery also play a role in the response to changing temperature.

Unlike heartbeat force and frequency (Figure 3), the duration of CG bursts (Figures 4A, B) decreased with each increased temperature step until around 24°C, at which point burst duration appears to asymptote, with a minimum burst duration being maintained until the preparations crashed. Interestingly, the decrease in duty cycle between 8°C and 16°C was gradual (∼10%; Figure 4D) relative to the increase in contraction frequency (∼40%; Figure 3A), indicating that the initial increase in contraction frequency was due to a simultaneous decrease in burst duration (Figure 4A) and interburst interval (not shown). As temperature was increased beyond ∼16°C, we observed a clear decrease in duty cycle (Figures 4C, D) along with burst duration (Figures 4A, B). However, between 13°C and 18°C, contraction frequency increased with increased temperature (Figures 3A, B), meaning that the observed decrease in burst duration (Figure 4A) was occurring at a slower rate than the decrease in duty cycle (Figure 4C). Between 25°C and 30°C, the decrease in burst duration began to asymptote (Figure 4B) along with duty cycle (Figure 4D). This explains why contraction frequency decreased in this warmer temperature range (Figures 3A, B). This is certainly the case at temperatures greater than ∼25°C, where burst duration is brief but stable (Figures 4A, B), and duty cycle and frequency continue to decrease until the crash temperature is reached (Figures 4C, D and Figures 3A, B, respectively). At temperatures greater than 30°C, too few preparations were still active to decipher any kind of trend.

3.2. The isolated CG crashes at a higher temperature than the semi-intact neuromuscular system

To better understand the biological processes that enable the cardiac neuromuscular system to maintain output across this wide range of temperatures, we asked how the temperature resilience of the isolated nervous system, which lacks any feedback input, compared to that of the semi-intact heart. Similar to the semi-intact experiments, the temperature of isolated CGs was stepped from ∼8°C to each preparation's critical temperature (Figure 5A). Across isolated CGs, we observed an increase in variability in burst frequency as temperature was increased. However, median burst frequency across preparations did not increase until temperature was increased above ∼17°C (Figure 5B). Interestingly, the isolated CGs maintained this trend of increasing cycle frequency with increased temperature until ∼22°C, before the cycle frequency began to decrease with increased temperature ($N = 25$). These isolated CGs were extracted from a subset of the same hearts as the semi-intact preparations (Figures 3, 4). Thus, it appears that the temperature dependencies of the processes governing cycle frequency in the intact neuromuscular system differ from those in the isolated CG (Figures 3A, B vs. Figures 5A, B). Although we measured the burst duration and duty cycle at each temperature step for each of the isolated CG preparations, when comparing these parameters, the isolated CGs did not substantially differ from the semi-intact preparations (data not shown).

Because the overall patterns of changes in CG activity were similar, but the temperatures at which the pattern changed appeared to differ between isolated CGs and non-isolated CGs within semi-intact preparations, we compared the crash temperatures of the non-isolated CGs to those of the isolated ganglia (Figure 6). After assessing the crash temperature in the semi-intact preparation, the CG was subsequently dissected out of the heart (Methods). In all but one preparation, the isolated CG crashed at a higher temperature than semi-intact heart from which it had been removed (Figure 6A, semi-intact vs. isolated CG; Wilcoxon Sign Rank test: $p < 0.001$, $N = 19$).

We initially postulated that the difference in crash temperatures in the two preparations might be due to some type of temperature adaptation, as we could not counter-balance the experimental order of each temperature ramp (i.e., we cannot re-insert a dissected nervous system back into the heart). To address this issue, we subjected 31 whole heart preparations to four sequential temperature ramps (Figure 6B). Although there were some differences in the crash temperatures with repeated ramps (Friedman test, $p = 0.008$, $N = 31$), these differences involved only the fourth ramp (Friedman/Dunn's multiple comparisons test: Ramp 1 vs. 4: $p = 0.047$; Ramp 3 vs. 4: $p = 0.030$, $N = 31$). That is, there were no changes in crash temperature between ramps 1, 2, and 3. Moreover, the crash temperature for Ramp 4 was lower than that of previous ramps, rather than higher, as would be expected if

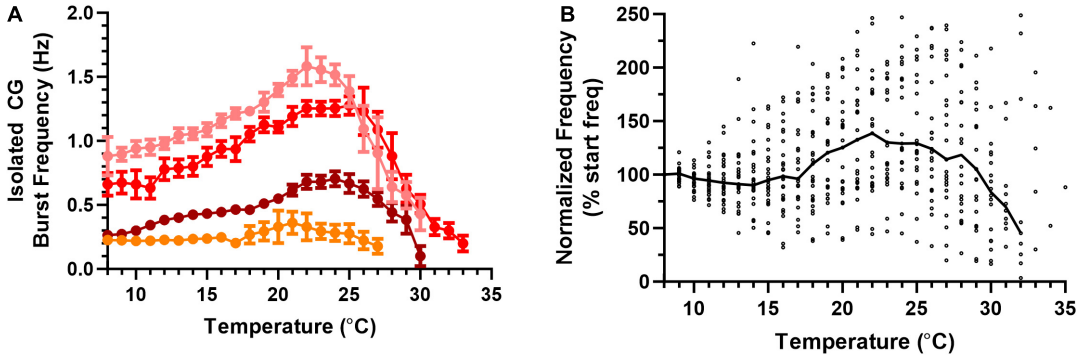

FIGURE 5
Frequency of bursts in an isolated cardiac ganglion increases, then decreases in response to an increasing temperature ramp. Values show data averaged in 1°C bins, with the data plotted at the center of each bin. **(A)** Plot of CG burst frequency as a function of temperature for four example preparations as temperature was increased from 8°C to crash temperature. Note that there no longer exists an inflection point in burst frequency at 18°C as was the case for contraction frequency. Although three of the preparations show clear increases followed by decreases in frequency, the change from increase to decrease occurred at different temperatures in each preparation. All data points show the mean ± SD for burst frequency at each temperature step. **(B)** Plot of normalized burst frequency as a function of temperature, with the burst frequency of each preparation at each temperature step normalized to the burst frequency at 8°C (N = 25 until the first preparation crashes at 20°C; N decreases from that temperature on, until N = 1 at 35°C). The solid back line connects median normalized burst frequency at each temperature step. Medians are omitted when $N \leq 5$.

the repeated heating were responsible for the difference in the crash temperatures of the ICG relative to the semi-intact heart.

There are a number of explanations that may address why the semi-intact cardiac neuromuscular system crashed at lower temperatures than the isolated CG: (1) At high temperatures (>30°C) the cardiac muscles may fail to contract even though the CG neurons are rhythmically producing action potential bursts. (2) The absence of NO feedback in the isolated CG may enable the ganglion to reach higher temperatures before crashing. For example, the nitric oxide (NO) production in the cardiac muscles that inhibits CG output (negative feedback pathway) may increase with increased temperature and inhibit CG action potentials prior to neuron crash point (i.e., the crash point observed in the isolated CG). (3) A non-intuitive change in the stretch feedback pathway may take place as a consequence of increased temperature. This last possibility is non-intuitive because stretch feedback most often produces excitatory drive (positive feedback) to the CG, such that muscle stretch promotes motor neuron activity. Therefore, the next several experiments detailed here address the hypotheses concerning the temperature tolerance of the cardiac muscles and NO feedback onto the CG neurons.

3.3. Semi-intact crashes are not due to muscle contraction failure

We first assessed whether the relatively cooler crash temperature observed in the semi-intact neuromuscular systems (Figure 6A) was in fact due to a failure of the cardiac muscle to contract at high temperatures (>20°C). For these experiments, we dissected out most of the CG from the heart (all neurons; Methods) while leaving a length of the anterior lateral nerve intact such that we could extracellularly stimulate the motor nerve *via* a suction electrode (Figure 1B; Methods). With this setup, we recorded the force generated by each cardiac muscle contraction in response to stimulation, which generated constant bursts of action potentials (frequency, duration, duty cycle). We stimulated the motor nerve at progressively increased temperatures in 1.5°C increments between baseline temperature (~8–9°C) and the crash temperature of that heart when previously tested in the semi-intact configuration.

Although endogenously the CG spontaneously produces bursts of action potentials continuously, we delivered our stimuli in bouts of 15 bursts, followed by a pause of 1 min; continual stimulation results in nerve failure within a relatively short time (Stevens et al., 2009). Because of this, we can see the patterns of facilitation and defacilitation that occurred with repeated stimuli. Although the dynamics of successive contractions differed across temperature, the muscles produced contractions in response to stimulation across the entire temperature range in all preparations.

For these experiments, we first assessed the crash temperature in each preparation before extracting the nervous system from the heart (Methods). After removing the CG from a given heart, we measured muscular responses to nerve stimulation at baseline and in response to a temperature ramp that rose to the previous crash temperature for that preparation. All heart muscles were able to contract in response to stimulation at the same temperature that the intact preparation crashed (N = 9). Therefore, crashes are not due to a failure of muscle contraction.

Figure 7A shows two example muscle tension recordings from the same preparation, one at 12.5°C and one at 26°C, to the same stimulus. For the responses recorded at 12.5°C (Figure 7A, top trace), contraction force increased noticeably over the first 4–5 stimuli. The remaining 10–11 stimuli in the train resulted in contractions that were more forceful but stabilized by the end of the train of stimuli. In contrast, at 26°C (Figure 7A, bottom trace), the largest muscle contraction was in response to the third stimulus; contraction force then decreased over the remainder of the train of stimuli.

Because this is the first study to examine the temperature dependence of facilitation and defacilitation in the cardiac nervous system of *Homarus*, and because these relationships are clearly different at low and high temperatures, we analyzed two aspects of

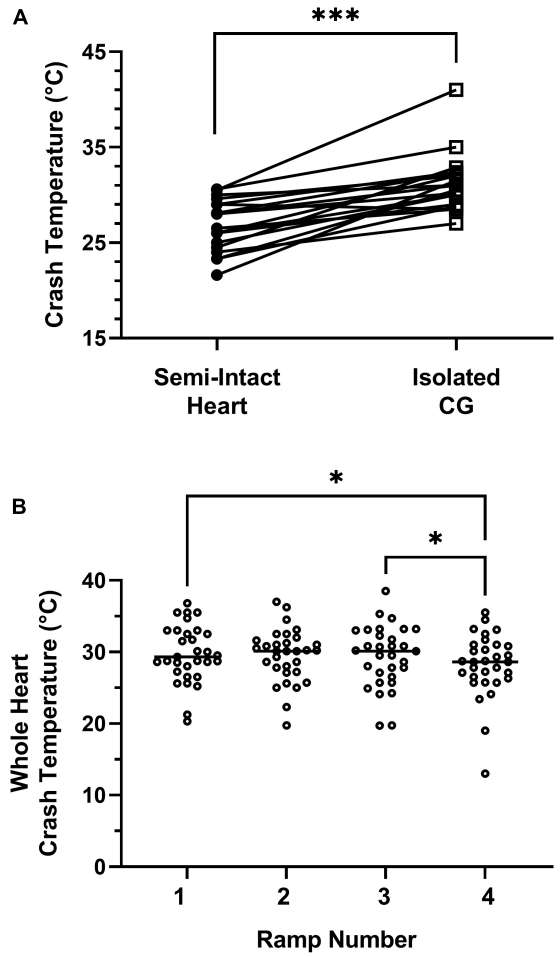

FIGURE 6
Isolated ganglia crash at a higher temperature than semi-intact preparations. **(A)** The crash temperatures of the isolated ganglia (ICG; 31.0°C; median) were higher than those of the semi-intact preparations (26.5°C; median); Wilcoxon Sign Rank test: $p < 0.001$; Shapiro–Wilks test for normality: Semi-intact heart, $p = 0.45$; ICG, $p = 0.005$; $N = 19$. **(B)** Crash temperature does not increase with repeated ramps, as seen in this comparison of four repeated temperature ramps in whole heart preparations. Although there were significant differences in crash temperature across hearts (Friedman repeated measures test: $p = 0.008$; $N = 31$), this reflected differences only between Ramps 1 and 4 (Dunn's multiple comparison test, $p = 0.047$; $N = 31$) and Ramps 3 and 4 (Dunn's multiple comparison test, $p = 0.03$; $N = 31$); Shapiro–Wilks test for normality: Ramp 1, $p = 0.44$; Ramp 2, $p = 0.52$; Ramp 3, $p = 0.97$; Ramp 4, $p = 0.01$; $N = 31$. In both of these cases, the median recorded for the later ramp, i.e., Ramp 4, was lower rather than higher than the median crash temperature of the earlier ramp. (Median for Ramp 1: 29.3°C; median for Ramp 3: 30.1°C; median for Ramp 4: 28.6°C). Bars in panel **(B)** indicate the median crash temperature. *Indicates $p < 0.05$; ***Indicates $p < 0.001$.

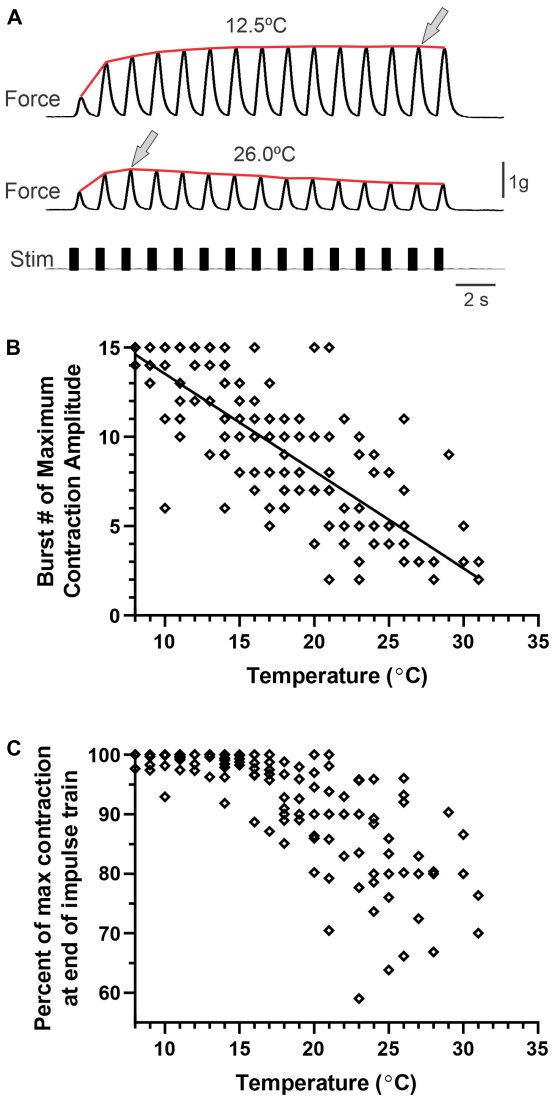

FIGURE 7
Cardiac muscle contractions persist at high temperatures, although facilitation is altered by temperature. **(A)** Example recordings of evoked muscle contractions at 12.5°C (top trace) and 26°C (middle trace) in response to exogenous nerve stimulation (lower trace). Arrows indicate the contraction of maximum amplitude in each recording. The red line shows the envelope of the contractions at each temperature. Both recordings are from the same preparation. **(B)** Plot of the burst number at which evoked contractions reach maximum amplitude for a train of stimulated contractions at each temperature (1.5°C increments) between 8°C and 31°C. Note that the contraction at which maximum amplitude is reached within the train of stimuli decreases with increased temperature ($R^2 = 0.63$, $p < 0.001$). **(C)** Contractions showed more defacilitation over the train of contractions at higher temperatures. Plot of the percentage of the maximum contraction amplitude that remained at the end of the train of stimuli [i.e., 100*(Amplitude last contraction/amplitude max contraction)]; $N = 9$.

the muscle facilitation/defacilitation relationship. First, to examine the temporal relationship of the facilitation vs. defacilitation of muscle contraction, we plotted the number of the stimulus (indexed to 1) that generated the maximum contraction amplitude for each temperature.

Each stimulus train generated fifteen stimuli (Figure 7A, stim. trace), so values on this plot are bounded between 1 and 15. As temperature was increased, the maximum contraction amplitude was reached earlier in the train of stimuli (Figure 7B); facilitation occurred over fewer stimuli, with contraction amplitude decreasing later in the train of repeated stimuli, as seen in the example in Figure 7A. Note that although the initial response amplitude in the example traces in Figure 7A was relatively small, this was not always the case. Second, to examine the extent to which

facilitation vs. defacilitation dominated the stimulus bout, we compared the ratio of response magnitude (force) between the last stimulus response in each stimulation train and the maximal response (Figure 7C). For example, the responses recorded at 12.5°C show that the smallest force generated occurred early in the stimulus train (i.e., 1st stimulus here), and the next to final stimulus generated the maximum force. In contrast, at 26°C, the third stimulus response was the largest, while the final response was one of the smallest. This is reflected in the plot shown in Figure 7C, where the ratio of maximum contraction to final contraction decreased as temperature was increased. At the higher temperatures, defacilitation dominated, especially later in the train of stimuli, whereas there was little or no defacilitation at the lower temperatures.

3.4. Nitric oxide decreases crash temperature in the isolated CG

We next assessed how the presence of NO affected the crash temperature of both the intact cardiac neuromuscular system (whole heart preparation) and the isolated CG. NO is synthesized in the cardiac muscle and then diffuses across neuron membranes to affect activity (Mahadevan et al., 2004). The addition of NO (*via* an NO donor) to the isolated CG usually decreases burst frequency by increasing the interburst interval (Mahadevan et al., 2004; Goy, 2005). Consistent with these observations, when we perfused an NO donor (PAPA NONOate) through the whole heart, we recorded a small (~10%) decrease in frequency (control saline: mean 0.502 ± 0.112 SD; PAPA NONOate: mean 0.455 ± 0.089 SD; paired *t*-test, $p = 0.04$, $N = 10$). However, we observed no change in crash temperature in the presence of PAPA NONOate (Figure 8A; paired *t*-test, $p = 0.4$, $N = 10$). In contrast, when we superfused an NO donor (SNAP) over the isolated ganglion, which, without the associated cardiac muscles, has no other source of NO, we observed a significant decrease in crash temperature (Figure 8B; paired *t*-test, $p = 0.015$, $N = 8$). NO application was sufficient to decrease the crash temperature in the isolated CG (Figure 8B), and it also decreased the CG crash temperatures into the same range observed for whole heart preparations (i.e., compare Figure 8B "SNAP" to Figure 8A "Control"; Independent Sample *t*-test: $p = 0.065$, $N = 8, 10$; Shapiro–Wilks test: $p = 0.69$, $N = 8$; $p = 0.63$, $N = 10$; Levene's test: $p = 0.9$, $N = 8, 10$). However, the magnitude of the difference between the crash temperature in the whole heart preparation and isolated CG (Figure 6A) and the magnitude of the difference between the crash temperature in control (saline) and SNAP (Figure 8B) was not significantly different (Independent Sample *t*-test; $p = 0.5$, $N = 8, 19$; Shapiro–Wilks test: $p = 0.29$, $N = 8$; $p = 0.38$, $N = 19$; Levene's test: $p = 0.035$, $N = 8, 19$).

Although different NO donors were used in the whole heart and in the isolated CG, we do not believe that using different NO donors affected our results. For each molecule of PAPA NONOate, two molecules of NO are released (Hrabie et al., 1993; Keefer et al., 1996). Because SNAP only dissociates NO with a 1:1 ratio (Singh et al., 1996), our effective concentrations of NO were 2×10^{-5} M using PAPA NONOate and 1×10^{-5} M using SNAP. Because the PAPA NONOate application did not have an effect on the whole heart crash temperature, it is unlikely that SNAP would affect the crash temperature.

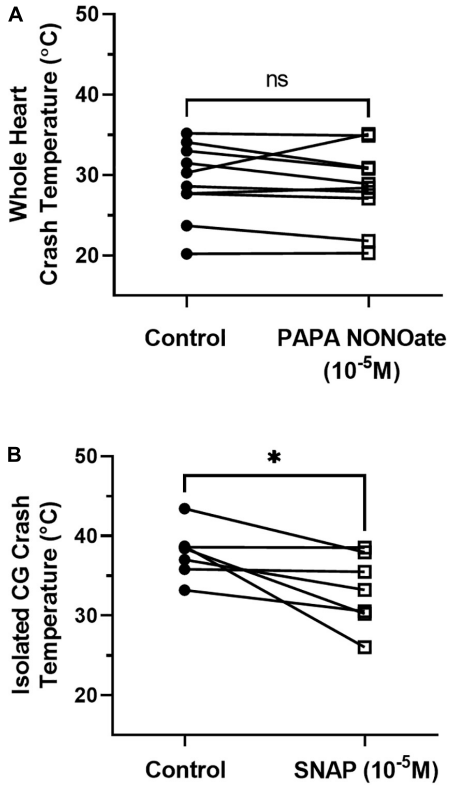

FIGURE 8
NO donors differently affect the crash temperature of whole heart and ICG preparations. **(A)** Plot of crash temperature for whole hearts perfused with normal saline compared to the same hearts perfused with saline and the NO donor PAPA NONOate (10^{-5} M). PAPA NONOate did not alter crash temperature; paired *t*-test: $p = 0.4$, $N = 10$; Shapiro–Wilks test: saline: $p = 0.69$, $N = 10$; NONOate: $p = 0.47$, $N = 10$. **(B)** Comparison of crash temperature between isolated cardiac ganglia superfused with normal saline and ganglia superfused with saline and the NO donor SNAP (10^{-5} M) within the same set of preparations. Preparations exposed to SNAP crashed at a lower temperature than controls; paired *t*-test, $p = 0.032$, $N = 7$; Shapiro–Wilks test: saline: $p = 0.49$, $N = 7$; SNAP: $p = 0.53$, $N = 7$. *Indicates $p < 0.05$, ns indicates not significant.

3.5. Blocking nitric oxide in the whole heart decreases crash temperature

Although the addition of NO to the isolated ganglion is sufficient to decrease the crash temperature of the isolated CG, we also wanted to test whether blocking NO synthesis in the cardiac muscles would increase the crash temperature of the whole heart preparation. To do this we perfused whole heart preparations with L-Nitroarginine (LNA) to block NO synthase activity.

As previously mentioned, NO typically decreases CG burst frequency and therefore heartbeat frequency. Blocking NOS should therefore result in an increase in heart rate. However, when LNA was perfused through the whole heart in a set of hearts

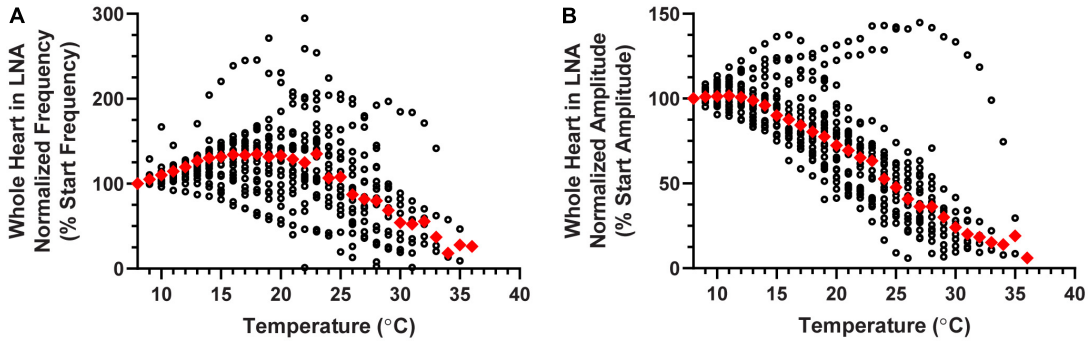

FIGURE 9
Whole heart responses to a temperature ramp in LNA. Plot of **(A)** normalized contraction frequency and **(B)** normalized contraction amplitude measured in the whole heart as a function of temperature during LNA perfusion. Contraction frequency **(A)** increases until about 20°C, at which point it begins to decrease with increased temperature. Contraction amplitude **(B)** began to decrease at temperatures greater than 13°C. Red triangles represent the median response at each temperature step for panels **(A,B)**.

that were not subjected to temperature ramps, we only observed such an increase in heart rate ∼50% of the time (increased heart rate: One-Sample Wilcoxon Sign-Rank test: $p < 0.001$, $N = 18$; decreased heart rate: One-Sample Wilcoxon Sign-Rank test: $p < 0.001$, $N = 12$; five preparations had a less than 5% deviation from control–too few to do statistics; data not shown). In a separate set of experiments, LNA was perfused through the whole heart while temperature was increased to crash point. Although LNA did change the baseline frequency in many of these preparations (see below), the patterns of change in both normalized contraction frequency (Figure 9A) and normalized contraction amplitude (Figure 9B) during temperature ramps were similar to the patterns recorded in response to temperature ramps during normal saline perfusion (Figures 3B, D). Specifically, contraction frequency initially increased as temperature was increased, then decreased until it reached crash point. Contraction amplitude was stable during the initial few temperature steps, then gradually decreased over the course of the temperature increase. As can be seen in Figure 9, there was some variability among preparations, but the median patterns were similar to those recorded in normal saline.

Similar to our previous findings, ∼30% of the hearts perfused with LNA showed an increase in heart rate, while the heart rate decreased or did not change in the remaining preparations. Interestingly, when LNA resulted in an increase in beat frequency, these hearts crashed at a higher temperature than they did during saline perfusion (Figures 10A, purple squares; Wilcoxon Sign-Rank test; $p = 0.047$, $N = 7$). Consistent with these results, we found that the opposite was true for the ∼40% of hearts from this experiment whose response to LNA was a decreased heart rate. These hearts crashed at a lower temperature compared to saline perfusion (Figure 10A, green triangles; Wilcoxon Sign-Rank test; $p = 0.016$, $N = 9$). Because these sample sizes are small, we bootstrapped each LNA response data set (increased frequency: $p = 0.018$; decreased frequency $p = 0.045$; Methods). The remaining 30% of hearts showed < 5% change in contraction frequency in response to LNA, and the crash temperature in LNA was not different from saline (Figure 10A, orange circles; Wilcoxon Sign-Rank test; $p = 0.56$, $N = 6$). Figure 10B plots the change in crash temperature as a function of change in heartbeat frequency in the presence of LNA compared to control saline (Spearman's Rank Correlation test: $\rho = 0.64$, $d = 3.74$, $p = 0.0013$, $N = 22$). Thus, LNA was able to extend the temperature tolerance in hearts that increase in heartbeat frequency when NO synthase is blocked, but it limited the temperature tolerance in preparations in which blocking NO synthase decreased the heart rate.

Figure 10A indirectly suggests that the crash temperature in control (saline) may predict the cardiac response to LNA. The control (saline) crash temperatures of most hearts in which beat frequency decreased in LNA were equivalent to the control crash temperatures of hearts in which LNA elicited an increase in beat frequency (Figure 10A, green triangles vs. purple squares) (independent sample t-test, $p = 0.061$, $N = 7, 9$; Shapiro–Wilks test: decreased freq. in LNA: $p = 0.2$, $N = 7$, increased freq. in LNA: $p = 0.5$, $N = 9$; Levene's test: $p = 0.82$, $N = 7, 9$). There was no correlation between saline (control) crash temperature and LNA crash temperature (Spearman's Rank Correlation test: $\rho = 0.53$, $d = 2.07$, $p = 0.062$, $N = 13$). Furthermore, there is no correlation between the initial heartbeat frequency at ∼8°C and the change in crash temperature in response to LNA (Figure 10C; Spearman's Rank Correlation test: $\rho = -0.25$, $d = -1.14$, $p = 0.26$, $N = 22$).

It is possible that the change in contraction frequency in response to LNA was due to the baseline contraction frequency (e.g., LNA decreased contraction frequency in preparations with a high initial frequency). However, there was no difference between the baseline contraction frequency in preparations in which LNA increased contraction frequency compared to preparations in which LNA decreased contraction frequency (Wilcoxon Mann–Whitney test: $p = 0.41$, $N = 7, 9$; data not shown).

3.6. Neuromodulation can bi-directionally affect functional temperature range of the nervous system

Our findings from Figure 10 indicate that there may exist a bi-directional effect on crash temperature such that modulation that

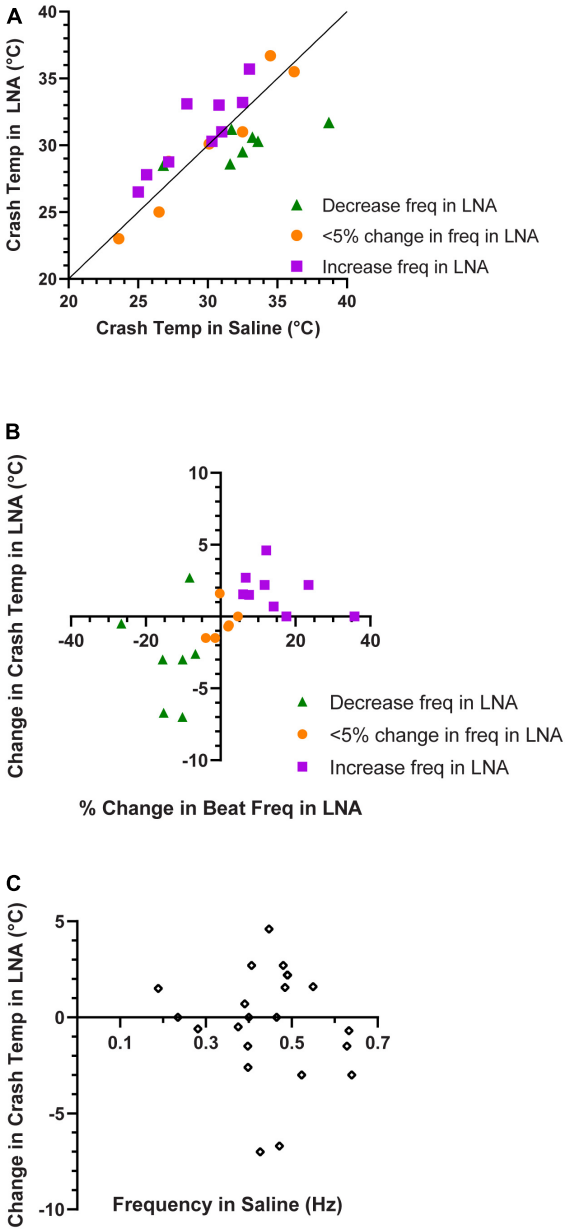

FIGURE 10
Contraction frequency in LNA correlates with crash temperature. **(A)** Comparison of crash temperatures between whole heart preparations perfused with saline vs. L-nitroarginine (LNA) for the same preparations. The unity line indicates the value at which crash temperature is identical in saline and LNA. Preparations in which LNA led to an increase in contraction frequency are shown as green triangles (Wilcoxon Sign-Rank test; $p = 0.047$, $N = 7$); those in which LNA did not change the contraction frequency are depicted as orange circles (Wilcoxon Sign-Rank test; $p = 0.56$, $N = 6$), and those in which LNA led to and a decrease in contraction frequency are shown as purple squares (Wilcoxon Sign-Rank test; $p = 0.016$, $N = 9$). Note that most of the preparations in which frequency decreased in LNA are above the line (increased crash temperature in LNA), while most of those in which frequency increased in LNA are below the line (decreased crash temperature in LNA). **(B)** Plot of whole heart crash temperature in LNA as a function of their percent change in contraction frequency. Spearman's Rank Correlation test: $\rho = 0.64$, $d = 3.74$, $p = 0.0013$, $N = 22$. **(C)** The change in crash temperature (LNA crash temperature−saline crash temperature) did not change as a function of the initial contraction frequency, Spearman's Rank Correlation test: $\rho = -0.25$, $d = -1.14$, $p = 0.26$, $N = 22$.

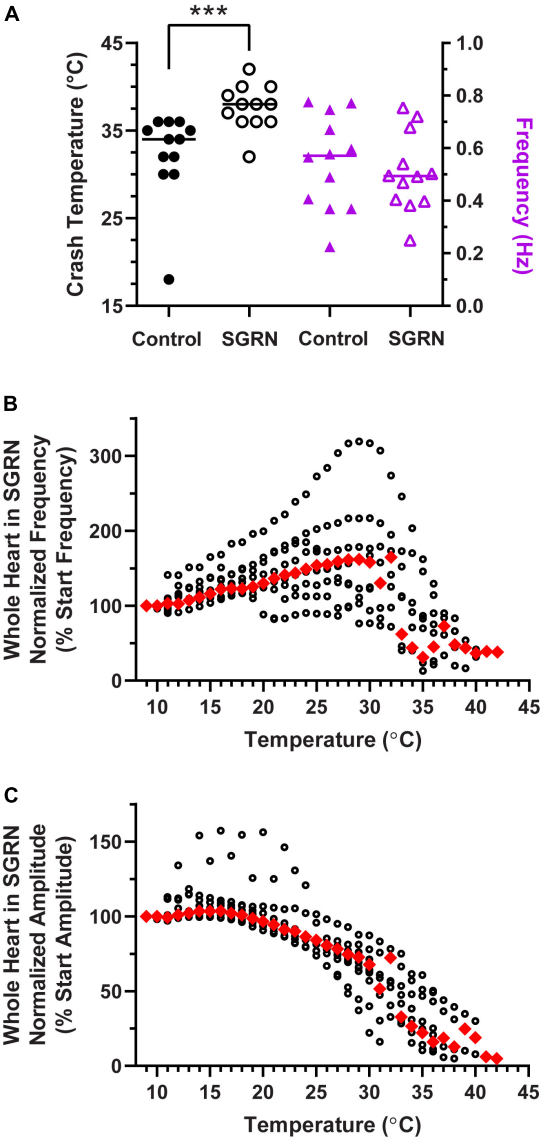

FIGURE 11
Modulation of the cardiac neuromuscular system by SGRN increases crash temperature. **(A)** Comparison of crash temperatures between whole heart preparations perfused with saline (34°C, median) vs. 10^{-8} M SGRN (38°C, median) in the same hearts. SGRN extended the temperature tolerance of these hearts (Wilcoxon test; $p = 0.0005$, $N = 12$). However, although SGRN generally excites cardiac activity, at this concentration, contraction frequency increased in only about half of the hearts, while it decreased in the other half, so that the average change in contraction frequency was not altered by SGRN [right y-axis; saline: 0.57 Hz, SGRN: 0.49 Hz (median frequencies); Wilcoxon test; $p = 0.47$, $N = 12$]. **(B)** Normalized whole heart contraction frequency as a function of temperature during SGRN perfusion. Note that contraction frequency increased until about 29°C, which is when preparations began to crash. **(C)** Normalized whole heart contraction amplitude as a function of temperature during SGRN perfusion. Contraction amplitude with increased temperature until ~19°C, at which point, it decreased until crash. Red triangles represent the median response at each temperature step for panels **(B,C)**. ***Indicates $p < 0.001$.

increases heartbeat frequency also increases the crash temperature and modulation that decreases heartbeat frequency, decreases the crash temperature. To test this hypothesis, we applied two different

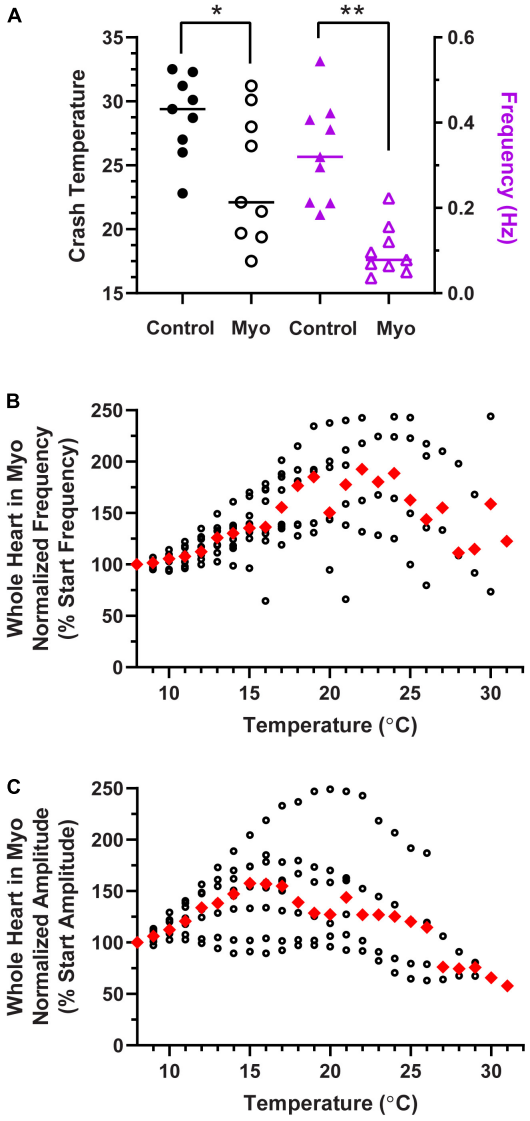

FIGURE 12
Modulation of the cardiac neuromuscular system by myosuppressin decreases crash temperature. **(A)** Comparison of crash temperatures between preparations perfused with saline (29.4°C, median) vs. 10^{-7} M myosuppressin (Myo; 22.1°C, median) in the same hearts. Myosuppressin decreased the temperature tolerance of these hearts (Wilcoxon Sign-Rank test: $p = 0.027$, $N = 9$). At the same time, contraction frequency (right y-axis) in all hearts decreased [saline: 0.32 Hz vs. myosuppressin: 0.08 Hz (median frequencies) Wilcoxon test; $p = 0.004$, $N = 9$]. **(B)** Normalized whole heart contraction frequency as a function of temperature during myosuppressin perfusion. Note that in myosuppressin, median contraction frequency initially increased, then decreased with increasing temperature, as is seen in other modulators, but the frequency never dropped below the initial frequency (100%) recorded at 8°C. **(C)** Normalized whole heart contraction amplitude as a function of temperature during myosuppressin perfusion. Contraction amplitude increased with increased temperature until ~17°C, at which point it decreased, but always remained above 50% of the initial contraction amplitude. Red triangles represent the median response at each temperature step for panels **(B,C)**. *Indicates $p < 0.05$; **Indicates $p < 0.01$.

feedforward neuromodulators to the whole heart preparation, one that is known to increase heartbeat frequency and one that decreases it.

To assess whether neuromodulators that increase heartbeat frequency could extend the temperature tolerance of the cardiac neuromuscular system, we perfused the FLRFamide-like neuropeptide SGRNFLRFamide (SGRN) through the whole heart while temperature was increased to crash. SGRN does in fact increase the temperature tolerance of the whole heart (Figure 11A; Wilcoxon Sign-Rank test; $p = 0.0005$, $N = 12$). However, the responses of lobster hearts to 10^{-8} M SGRN were highly variable (Figure 11A, purple triangles); in some hearts, 10^{-8} M SGRN increased contraction frequency, while in others, it decreased contraction frequency, as has been seen previously (Dickinson et al., 2015). Because of this, the mean frequency at baseline temperatures (8–10°C) did not change in these experiments (Figure 11A, purple triangles; Wilcoxon Sign-Rank test: $p = 0.47$, $N = 12$). This suggests that increased temperature resilience is not simply a function of change in contraction frequency but is instead a response to modulation that presumably increases neuron excitability. In this case, SGRN activates the modulator-activated, voltage-sensitive current I_{MI}, which is an inward current whose conductance increases across the voltage range in which cardiac neurons oscillate (Swensen and Marder, 2000; Dickinson et al., 2015). The increased excitability in response to SGRN is reflected here in the changes observed in normalized contraction frequency (Figure 11B) and normalized contraction amplitude (Figure 11C) as a function of temperature. Whole hearts perfused with SGRN increased in contraction frequency as temperature was increased until ~29°C, compared to an inflection point at about 18°C in saline (Figure 3B). Moreover, even though the median contraction frequency began to decrease at ~30°C, the median contraction frequency did not drop below 100% until preparations were nearing their crash temperatures (≥32°C). SGRN also extended the temperature range over which the normalized whole heart contraction amplitude remained ≥100% (~19°C, Figure 11B vs. ~14°C, Figure 3D).

Similarly, in a separate set of experiments, we perfused the neuromodulator myosuppressin through the whole heart preparation. Figure 12A shows that the crash temperature was significantly decreased by the presence of myosuppressin compared to saline (control) (Wilcoxon Sign-Rank test: $p = 0.027$, $N = 9$). Myosuppressin is a modulator that leads to large decreases in heartbeat frequency, as seen here (Figure 12A, purple triangles; Wilcoxon Sign-Rank test: $p = 0.004$, $N = 9$), and thus generally decreases excitability. Interestingly, when the hearts were exposed to temperature ramps in the presence of myosuppressin, we did not observe a consistent decrease in median normalized contraction frequency until ~25°C (Figure 12B), and even at that point, median contraction frequency never decreased below the initial frequency (Figure 12B, 100%). In fact, median frequency did not drop below 100% before the preparation crashed. Myosuppressin also typically increases the heartbeat contraction force (Stevens et al., 2009). This was also the case in our experiments when contraction amplitudes were compared at 11°C (mean ± SD 1.12 ± 0.46 g in saline vs. 1.6 ± 0.86 g in Myo; paired t-test: $p = 0.034$; Shapiro–Wilk test, $p = 0.96$ for saline and $p = 0.21$ for Myo; $N = 9$), but not at 9°C. In contrast to the patterns recorded in control saline and in other modulators, median normalized contraction amplitude increased with increased temperature until ~16°C (Figure 12C). At that temperature, it began to decrease. However, the median contraction amplitude never dropped below

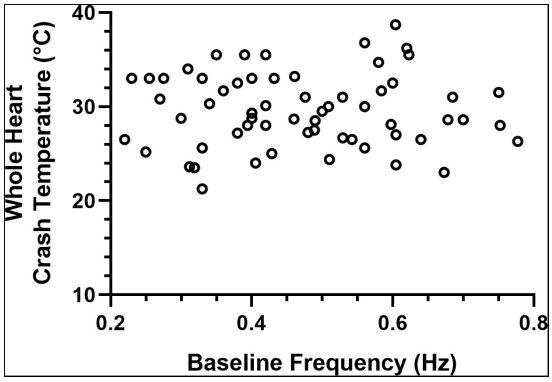

FIGURE 13
Whole heart crash temperature is not a function of initial contraction frequency. Plot of 63 hearts showing the temperature at which each heart crashed as a function of the baseline contraction frequency of that heart. There is no correlation between the crash temperature in the absence of a modulator (control) compared to the baseline (8–10°C) contraction frequency of each heart (Spearman Rank Correlation test: $\rho = 0.069$, $d = 0.54$, $p = 0.59$; $N = 63$).

50% of the initial median amplitude before crashing in the presence of myosuppressin. While the mechanisms underlying these responses to myosuppressin are not understood, they lay the groundwork for future experiments.

Together, these experiments show that for at least two neuromodulators, when modulation increases neuron excitability, the crash temperature was increased, and when modulation decreased neuron excitability, we conversely observed a decreased crash temperature.

3.7. Initial contraction frequency is not a predictor of crash temperature

Previous studies have shown that the effects of a modulator may be state-dependent, with the magnitude of the effect dependent on the baseline frequency of the pattern (Nusbaum and Marder, 1989). Because of this, and because some of the data presented here suggest the possibility that the initial contraction frequency may predict or determine the crash temperature of that cardiac neuromuscular system, we examined the relationship between contraction frequency at baseline temperature (8–10°C) and the crash temperature of a group of whole hearts. There was no correlation between baseline frequency and crash temperature, as seen in **Figure 13** (Spearman Rank Correlation test: $\rho = 0.069$, $d = 0.54$, $p = 0.59$; $N = 63$).

4. Discussion

4.1. Crash temperature changes with burst frequency

All neural circuits are subject to temperature fluctuation and must maintain function across that range. For some nervous systems, that range is homeostatically maintained within a few degrees and for others, that range maps onto temperature fluctuations in the environment, which can be quite large. The dynamics of changes to the whole heart function we observed in our study are similar to those seen previously in the same system (Camacho et al., 2006; Worden et al., 2006; Qadri et al., 2007). Worden et al. (2006) showed that stroke volume (contraction force) decreases with increased temperature and that the contraction frequency increased between 2°C to ∼16–18°C. Consequently, cardiac output did not change significantly between 2–20°C, though it began to decrease at 22°C. Here, we extended the upper range of temperatures tested to enable us to examine the resilience of hearts to increased temperature. As we predicted, based on earlier data from Worden et al. (2006), both contraction frequency and contraction force decreased at higher temperatures as we approached the crash temperature for each heart.

A number of studies have found that signaling molecules and feedback modulation play a role in maintaining circuit function even though the molecular kinetics of all cellular components are altered due to changes in temperature (Zhurov and Brezina, 2005; Hamilton et al., 2007; Biron et al., 2008; Tang et al., 2010; Thuma et al., 2013; Städele et al., 2015; Haddad and Marder, 2018; Takeishi et al., 2020; Städele and Stein, 2022). As such, we were particularly interested in examining the role of feedback in determining the crash temperature in this neuromuscular system. There are two feedback systems that are intrinsic to the lobster cardiac neuromuscular system. (1) Stretching of cardiac muscles during each contraction activates stretch-sensitive dendrites, resulting in a response that has generally been thought to be positive (i.e., increased stretch leads to increased contraction frequency). (2) The muscles contain NO synthase, which releases NO to negatively regulate the heartbeat (i.e., NO slows the frequency, which in turn results in a decrease in stroke volume; Mahadevan et al., 2004). These opposing feedback systems are thought to stabilize the heartbeat.

Because these feedback mechanisms appear to stabilize heart function, we anticipated that the whole heart would be more resilient to increases in temperature compared to the isolated CG, and thus the whole heart would exhibit a higher crash temperature than the isolated CG. However, as we show here, the crash temperature of the isolated CG is in fact significantly higher than that of the semi-intact heart. It is possible that creating the incision in the ventral side of the heart for the semi-intact heart (needed for extracellular recording of the CG, Methods) disrupts the stretch feedback pathway, resulting in minimal positive feedback. However, unpublished data suggest that opening the heart to record neuronal activity does not eliminate responses to stretch. Moreover, this experimental setup would not likely disrupt NO feedback.

Previous studies of temperature tolerance in the lobster heart postulated that the temperature dependence of heart rate arises largely from intrinsic properties of the CG neurons rather than from hormonal or cardio-regulatory neurons (Camacho et al., 2006; Worden et al., 2006). However, a more limited temperature range was used in those studies, and critical temperatures at which the neuromuscular system crashes were not evaluated. Nonetheless, our results are consistent with previous results (Worden et al., 2006), suggesting that there are temperature regulatory mechanisms intrinsic to the CG neurons, though it is likely that the temperature stability of the heart is also affected

by cardioregulatory inputs in the intact animal (i.e., modulation). Because the lobster heart is neurogenic, the heartbeat frequency is determined directly by the cycle frequency of the CG. However, it is worth noting that the CG is in turn extensively modulated. Both hormones and cardioregulatory fibers regulate the heartbeat in the intact animal, along with the two aforementioned feedback systems. These feedback systems are left intact in the isolated heart, and hormones can be perfused to assess their impact on cardiac physiology. Thus, we removed all of the modulatory inputs by isolating the CG. Rather than decreasing the temperature tolerance of the CG as predicted, we observed that the isolated CG was more temperature resilient than the semi-intact heart and crashed at a higher temperature. Because these experiments were carried out in the same preparations, we could directly compare the responses from the same CG both in the heart and when isolated from it.

4.2. Role of NO in determining crash temperature

The differences in crash temperature of the whole heart vs. the isolated CG led us to ask what role feedback plays in controlling the temperature resilience of the CG. Because we observed lower crash temperatures in the semi-intact heart compared to the isolated nervous systems, it seemed plausible that the relevant difference between the two preparations was the removal of negative feedback processes present in the intact system. NO release presumably occurs continuously, as it is released in response to muscle activity, and the muscles are the only known localization of NO synthase (Mahadevan et al., 2004). Furthermore, because increasing temperature increases the reaction rates of biological processes, NO production likely increases as temperature increases in the semi-intact preparations. It should be noted that in the lobster cardiac nervous system, NO does not activate the cGMP pathway described in vertebrate muscular systems (Goy, 2005). Therefore, while our findings pertaining to the influence of NO on a nervous system's temperature tolerance may not extrapolate to all NO pathways, it was interesting to find that at least two modulators that decrease neuron excitability also decreased the temperature tolerance of the nervous system.

We examined the role of NO in two ways: (1) applying NO to the isolated CGs and whole hearts using NO donors (PAPA NONOate and SNAP) and (2) blocking NO production in the whole heart using the nitric oxide synthase blocker L-nitroarginine (LNA). Because NO is released from the cardiac muscle in response to cardiac contractions, we would expect it to be present, at least at low levels, in most whole hearts. When we applied NO, using PAPA NONOate, to the whole heart we saw no change in crash temperatures compared to control (saline; **Figure 8A**). One possible explanation is a ceiling effect, in which concentrations of endogenously produced NO in most preparations were already sufficient such that additional NO did not affect the crash temperature. In contrast, NO was absent in the control saline applied to the isolated CGs (control condition); delivering exogenous NO, using SNAP, to these ganglia decreased the crash temperature in nearly all preparations. Although we applied different NO donors to the whole hearts than to the isolated ganglia, the major difference between these donors is the number of NO molecules released by each. Whereas PAPA NONOate releases two molecules of NO per donor molecule, SNAP donates only one molecule of NO. This means that NO concentrations would likely be higher in the whole hearts than in the isolated CGs.

In a second set of experiments, we blocked NO production in the whole hearts. Because adding NO suggested a ceiling effect of NO presence, we predicted that blocking NO would do two things: (1) increase contraction frequency by removing NO and (2) increase crash temperature if NO is sufficient to decrease crash temperature, as our SNAP data suggest. These were both observed in about half of the whole hearts in which we applied LNA. In those hearts in which LNA did indeed cause an increase in contraction frequency, as predicted based on Mahadevan et al. (2004), crash temperature also increased. Surprisingly, in about half of our hearts, LNA did not cause an increase, but actually resulted in a decreased contraction frequency. Although the mechanism that underlies such a decrease is not clear, it is striking that crash temperature in these preparations did not increase as expected, but instead decreased. These results suggest that positive regulators of excitability extend the temperature range of the heart, and that negative regulators of excitability limit the functional temperature range. This conclusion is corroborated by our experimental results in which exogenous modulators were perfused through the cardiac neuromuscular system.

4.3. Temperature robustness may be a function of neuron and circuit excitability

Ours is not the first study to assess whether neuromodulation alters the temperature resiliency of a nervous system (Zhurov and Brezina, 2005; Thuma et al., 2013; Städele et al., 2015; Haddad and Marder, 2018; Powell et al., 2021; Städele and Stein, 2022). Previous data show that activation of the modulator-activated, voltage-sensitive current (I_{MI}) can extend the temperature range of two other CPGs, the gastric mill and pyloric pattern generators of the stomatogastric system in lobsters and crabs (Städele et al., 2015; Haddad and Marder, 2018; Städele and Stein, 2022). I_{MI} voltage sensitivity is similar to that of the NMDA receptor, where membrane depolarization decreases the affinity for a Mg^{2+} ion to the channel pore (Golowasch and Marder, 1992). The I_{MI} peak current has been observed between −50 and −10 mV depending on cell type and the modulator used to activate it (Golowasch and Marder, 1992; Swensen and Marder, 2000; DeLong et al., 2009; Rodriguez et al., 2013; Gray and Golowasch, 2016). Importantly, I_{MI} currents increase at voltages more depolarized than resting potential, but well within the range of normal oscillations of these neurons, even in the absence of modulator. Because these currents have a negative conductance relationship between resting potential and approximately −10 mV, they can offset the increase in leak current associated with increased temperature (Städele et al., 2015). This may very well be of great importance in the CG, where all synaptic connections directly promote neuron activity (i.e., electrical synapses and excitatory chemical synapses). This is in slight contrast to the STG where intra-STG synapses are inhibitory, and neurons often rely on post-inhibitory rebound for rhythm maintenance. In the pyloric rhythm for instance, increases in leak currents are likely offset to some degree by increases in synaptic

conductance (Tang et al., 2010), which may help mitigate some deleterious effects of temperature increase.

Our data indicate that the temperature resilience of a nervous system may have less to do with the specific regulatory pathway influencing it and instead may rely on a more general rule: modulators that upregulate neural excitability increase resiliency and those that decrease excitability, decrease resiliency. This conclusion is supported by our final set of experiments: applying the peptide modulator SGRN, which activates the inward current I_{MI}, extended the temperature range tolerated by the whole heart, whereas myosuppressin, which decreases neuron excitability (Stevens et al., 2009), decreased the whole heart crash temperature. Although we did not directly assess changes in neuron excitability in response to SGRN, SGRN increases neuron/circuit output at lower concentrations (10^{-9} M; Dickinson et al., 2015) than those used here, which is indicative of increased excitability. While we did not exhaustively apply all regulatory peptides and hormones known to affect the cardiac neuromuscular system, many of the modulators that regulate the cardiac nervous system are thought to act on the same I_{MI} conductance (including SGRN) (Swensen and Marder, 2000, 2001). To our knowledge, this is the first set of experiments to examine the relationship between modulators that decrease neuron excitability (NO and myosuppressin) and temperature.

At the present time, the cellular mechanisms that decrease temperature resilience are entirely unknown. There are, however, a few possibilities that seem plausible. Due to the relatively fast response in the heart and isolated ganglion to NO (minutes timescale; Mahadevan et al., 2004), it is likely acting to modify ion channel conductance *via* second messenger signaling (i.e., phosphorylation of channels). Given that NO slows the CG burst frequency but does not alter burst duration, this could include, but is not limited to, upregulating potassium conductances that limit the cycle frequency (e.g., A-type potassium or calcium activated potassium). Prolonged potassium permeability would limit the ability for driver potentials to drive bursting by either decreasing membrane resistance or hyperpolarizing the membrane or both. It could also be the case that there is a down regulation of conductances that tend to decrease time between bursting by leading to slow membrane depolarization [e.g., a persistent sodium current (I_{NaP}) or the non-selective cation current (I_{CAN})]. Although the chloride reversal potential in these neurons is unclear, evidence suggests that E_{Cl} may be in the voltage range of neuron activity. If this is the case, NO may be acting on a chloride conductance.

4.4. Crash temperature depends on ocean temperature

Even within the same experimental preparation (e.g., isolated CG), crash temperature varied between different experimental groups. For example, the mean crash temperature shown in **Figure 6A** for those isolated CGs was different than the mean crash temperature for the isolated CGs shown in **Figure 8B**. Previous work has documented that crash temperature fluctuates with seasonality and ocean temperatures (Marder and Rue, 2021). This is unsurprising as all animals used in these studies are wild caught and their physiology reflects aspects of environmental adaptations beyond our control. In this case, animals caught in colder seasons, when the sea water is colder, typically exhibit a lower crash temperature than animals caught during warmer seasons (Owens, 2014; Marder and Rue, 2021). This is supported by experiments in which animals were maintained for a long period of time at specific acclimation temperatures (Camacho et al., 2006; Tang et al., 2012; Kushinsky et al., 2019; Oellermann et al., 2020). Results of these experiments show that acclimation temperature correlates with crash temperature. This phenomenon indicates that there are likely trade-offs in cell physiology that are temperature dependent. For instance, if it is energetically more expensive to maintain neuronal function in warm water, these processes may arrest during long periods in cold water temperatures.

Data from this study and others (Camacho et al., 2006; Hamilton et al., 2007; Tang et al., 2010; Tang et al., 2012; Thuma et al., 2013; Städele et al., 2015; Kushinsky et al., 2019; Oellermann et al., 2020; Marder and Rue, 2021; Powell et al., 2021; Städele and Stein, 2022) indicate that there are processes endogenous to at least these poikilothermic animals that enable their nervous systems to maintain functional output across a range of temperatures, including those that these organisms are routinely exposed to. However, it would not be surprising to find that these findings generalize across nervous systems. Although this study highlights two such processes (NO and myosuppressin) that decrease temperature robustness of the neuromuscular organ, most of the modulatory processes in the lobster heart act as positive regulators of neural and muscular activity (i.e., other circulating peptides and hormones) (Cruz-Bermudez and Marder, 2007; Christie et al., 2010). Even though it is likely that NO production increases with temperature increase, for the same reasons, it is likely that the production of these modulatory peptides also increases. Furthermore, there may exist evolutionary tradeoffs between the proportion of modulators present in a nervous system that decrease neuron excitability and the temperature tolerance of that system.

Data availability statement

The raw data supporting the conclusions of this article will be made available by the authors, without undue reservation.

Ethics statement

Ethical review and approval was not required for the study of animals in accordance with the local legislation and institutional requirements.

Author contributions

DP, EO, MB, PN, and PD contributed to the conception and design of the study. DP, EO, MB, MC, PN, EB, RJ, and PD conducted experiments and analyzed the data. DP and PD wrote the first draft of the manuscript. All authors contributed to manuscript revision, read, and approved the submitted version.

Funding

This work was funded by NIH award 8 P20 GMFigure3423-12 from NIGMS, NSF grants IOS-1121973, IOS-1354567, and IOS-1856433, the Maine Space Grant MERITS program, and the Henry L. and Grace Doherty Coastal Studies Research Fellowship at Bowdoin College.

Acknowledgments

We thank the following people for their assistance in setting up experiments and reading the manuscript: Sally Stronge, Hanna Renedo, and Evyn S. Dickinson.

Conflict of interest

The authors declare that the research was conducted in the absence of any commercial or financial relationships that could be construed as a potential conflict of interest.

Publisher's note

All claims expressed in this article are solely those of the authors and do not necessarily represent those of their affiliated organizations, or those of the publisher, the editors and the reviewers. Any product that may be evaluated in this article, or claim that may be made by its manufacturer, is not guaranteed or endorsed by the publisher.

References

Alonso, L. M., and Marder, E. (2020). Temperature compensation in a small rhythmic circuit. *Elife* 9:e55470. doi: 10.7554/eLife.55470

Beverly, M., Anbil, S., and Sengupta, P. (2011). Degeneracy and neuromodulation among thermosensory neurons contribute to robust thermosensory behaviors in *Caenorhabditis elegans*. *J. Neurosci.* 31, 11718–11727. doi: 10.1523/JNEUROSCI.1098-11.2011

Biron, D., Wasserman, S., Thomas, J. H., Samuel, A. D., and Sengupta, P. (2008). An olfactory neuron responds stochastically to temperature and modulates *Caenorhabditis elegans* thermotactic behavior. *Proc. Natl. Acad. Sci. U.S.A.* 105, 11002–11007. doi: 10.1073/pnas.0805004105

Busza, A., Murad, A., and Emery, P. (2007). Interactions between circadian neurons control temperature synchronization of *Drosophila* behavior. *J. Neurosci.* 27, 10722–10733. doi: 10.1523/JNEUROSCI.2479-07.2007

Camacho, J., Qadri, S. A., Wang, H., and Worden, M. K. (2006). Temperature acclimation alters cardiac performance in the lobster *Homarus americanus*. *J. Comp. Physiol. A Neuroethol. Sens. Neural Behav. Physiol.* 192, 1327–1334. doi: 10.1007/s00359006-0162-1

Cao, X. J., and Oertel, D. (2005). Temperature affects voltage-sensitive conductances differentially in octopus cells of the mammalian cochlear nucleus. *J. Neurophysiol.* 94, 821–832. doi: 10.1152/jn.01049.2004

Caplan, J. S., Williams, A. H., and Marder, E. (2014). Many parameter sets in a multicompartment model oscillator are robust to temperature perturbations. *J. Neurosci.* 34, 4963–4975. doi: 10.1523/JNEUROSCI.0280-14.2014

Carpenter, D. O. (1967). Temperature effects on pacemaker generation, membrane potential, and critical firing threshold in *Aplysia* neurons. *J. Gen. Physiol.* 50, 1469–1484. doi: 10.1085/jgp.50.6.1469

Chen, R., Jiang, X., Prieto Conaway, M. C., Mohtashemi, I., Hui, L., Viner, R., et al. (2010). Mass spectral analysis of neuropeptide expression and distribution in the nervous system of the lobster *Homarus americanus*. *J. Proteome Res.* 9, 818–832. doi: 10.1021/pr900736t

Cheng, Q., Sedlic, F., Pravdic, D., Bosnjak, Z. J., and Kwok, W. M. (2011). Biphasic effect of nitric oxide on the cardiac voltage-dependent anion channel. *FEBS Lett.* 585, 328–334. doi: 10.1016/j.febslet.2010.12.008

Christie, A. E., Stemmler, E. A., and Dickinson, P. S. (2010). Crustacean neuropeptides. *Cell. Mol. Life Sci.* 67, 4135–4169. doi: 10.1007/s00018-010-0482-8

Cooke, I. M. (2002). Reliable, responsive pacemaking and pattern generation with minimal cell numbers: The crustacean cardiac ganglion. *Biol. Bull.* 202, 108–136. doi: 10.2307/1543649

Cruz-Bermudez, N. D., and Marder, E. (2007). Multiple modulators act on the cardiac ganglion of the crab, *Cancer borealis*. *J. Exp. Biol.* 210, 2873–2884. doi: 10.1242/jeb.002949

DeLong, N. D., Kirby, M. S., Blitz, D. M., and Nusbaum, M. P. (2009). Parallel regulation of a modulator-activated current via distinct dynamics underlies comodulation of motor circuit output. *J. Neurosci.* 29, 12355–12367. doi: 10.1523/jneurosci.3079-09.2009

DeMaegd, M. L., and Stein, W. (2021). Neuropeptide modulation increases dendritic electrical spread to restore neuronal activity disrupted by temperature. *J. Neurosci.* 41, 7607–7622. doi: 10.1523/JNEUROSCI.0101-21.2021

Dickinson, E. S., Johnson, A. S., Ellers, O., and Dickinson, P. S. (2016). Forces generated during stretch in the heart of the lobster *Homarus americanus* are anisotropic and are altered by neuromodulators. *J. Exp. Biol.* 219(Pt 8), 1187–1202. doi: 10.1242/jeb.135657

Dickinson, P. S., Armstrong, M. K., Dickinson, E. S., Fernandez, R., Miller, A., Pong, S., et al. (2018). Three members of a peptide family are differentially distributed and elicit differential state-dependent responses in a pattern generator-effector system. *J. Neurophysiol.* 119, 1767–1781. doi: 10.1152/jn.00850.2017

Dickinson, P. S., Calkins, A., and Stevens, J. S. (2015). Related neuropeptides use different balances of unitary mechanisms to modulate the cardiac neuromuscular system in the American lobster, *Homarus americanus*. *J. Neurophysiol.* 113, 856–870. doi: 10.1152/jn.00585.2014

Fohlmeister, J. F., Cohen, E. D., and Newman, E. A. (2010). Mechanisms and distribution of ion channels in retinal ganglion cells: Using temperature as an independent variable. *J. Neurophysiol.* 103, 1357–1374. doi: 10.1152/jn.00123.2009

Foldes, F. F., Kuze, S., Vizi, E. S., and Deery, A. (1978). The influence of temperature on neuromuscular performance. *J. Neural Transm.* 43, 27–45. doi: 10.1007/BF02029017

Fry, F. E. (1958). Temperature compensation. *Annu. Rev. Physiol.* 20:207224.

Golowasch, J., and Marder, E. (1992). Proctolin activates an inward current whose voltage dependence is modified by extracellular Ca^{2+}. *J. Neurosci.* 12, 810–817. doi: 10.1523/JNEUROSCI.12-03-00810.1992

Goy, M. F. (2005). Nitric oxide: An inhibitory retrograde modulator in the crustacean heart. *Comp. Biochem. Physiol. Part A Mol. Integr. Physiol.* 142, 151–163. doi: 10.1016/j.cbpb.2005.05.050

Gray, M., and Golowasch, J. (2016). Voltage dependence of a neuromodulator-activated ionic current. *eNeuro* 3:ENEURO.0038-16.2016. doi: 10.1523/ENEURO.0038-16.2016

Haddad, S. A., and Marder, E. (2018). Circuit robustness to temperature perturbation is altered by neuromodulators. *Neuron* 100, 609–623.e603.

Hamilton, J. L., Edwards, C. R., Holt, S. R., and Worden, M. K. (2007). Temperature dependent modulation of lobster neuromuscular properties by serotonin. *J. Exp. Biol.* 210(Pt 6), 1025–1035. doi: 10.1242/jeb.02717

Harri, M., and Florey, E. (1977). The effects of temperature on a neuromuscular system of the crayfish, *Astacus leptodactylus*. *J. Comp. Physiol.* 117, 47–61.

Hazel, J. R., and Prosser, C. L. (1974). Molecular mechanisms of temperature compensation in poikilotherms. *Physiol. Rev.* 54, 620–677.

Hrabie, J. A., Klose, J. R., Wink, D. A., and Keefer, L. K. (1993). New nitric oxide-releasing zwitterions derived from polyamines. *J. Organic Chem.* 58, 1472–1476.

Junkins, M. S., Bagriantsev, S. N., and Gracheva, E. O. (2022). Towards understanding the neural origins of hibernation. *J. Exp. Biol.* 225:jeb229542. doi: 10.1242/jeb.229542

Kang, K., Panzano, V. C., Chang, E. C., Ni, L., Dainis, A. M., Jenkins, A. M., et al. (2011). Modulation of TRPA1 thermal sensitivity enables sensory discrimination in *Drosophila*. *Nature* 481, 76–80. doi: 10.1038/nature10715

Keefer, L. K., Nims, R. W., Davies, K. M., and Wink, D. A. (1996). "NONOates" (1substituted diazen-1-ium-1,2-diolates) as nitric oxide donors: Convenient nitric oxide dosage forms. *Methods Enzymol.* 268, 281–293. doi: 10.1016/s00766879(96)68030-6

Klöckner, U., Schiefer, A., and Isenberg, G. J. (1990). L-type Ca-channels: Similar Q10 of Ca-, Ba-and Na-conductance points to the importance of ion-channel interaction. *Pflugers Arch.* 415, 638–641. doi: 10.1007/BF02583518

Kushinsky, D., Morozova, E. O., and Marder, E. (2019). *In vivo* effects of temperature on the heart and pyloric rhythms in the crab Cancer borealis. *J. Exp. Biol.* 222(Pt 5):jeb199190. doi: 10.1242/jeb.199190

Ma, M., Chen, R., Sousa, G. L., Bors, E. K., Kwiatkowski, M. A., Goiney, C. C., et al. (2008). Mass spectral characterization of peptide transmitters/hormones in the nervous system and neuroendocrine organs of the American lobster *Homarus americanus*. *Gen. Comp. Endocrinol.* 156, 395–409. doi: 10.1016/j.ygcen.2008.01.009

Macdonald, J. A. (1981). Temperature compensation in the peripheral nervous system: Antarctic vs temperate poikilotherms. *J. Comp. Physiol.* 142, 411–418.

Mahadevan, A., Lappe, J., Rhyne, R. T., Cruz-Bermudez, N. D., Marder, E., and Goy, M. F. (2004). Nitric oxide inhibits the rate and strength of cardiac contractions in the lobster *Homarus americanus* by acting on the cardiac ganglion. *J. Neurosci.* 24, 2813–2824. doi: 10.1523/JNEUROSCI.3779-03.2004

Manning, J., and Pelletier, E. (2009). Environmental monitors on lobster traps (eMOLT): Long-term observations of New England's bottom-water temperatures. *J. Oper. Oceanogr.* 2, 25–33.

Marder, E., and Rue, M. C. P. (2021). From the neuroscience of individual variability to climate change. *J. Neurosci.* 41, 10213–10221.

Montgomery, J. C., and Macdonald, J. A. (1990). Effects of temperature on nervous system: Implications for behavioral performance. *Am. J. Physiol.* 259(2 Pt 2):R191196. doi: 10.1152/ajpregu.1990.259.2.R191

Moran, M. M., Xu, H., and Clapham, D. E. (2004). TRP ion channels in the nervous system. *Curr. Opin. Neurobiol.* 14, 362–369. doi: 10.1016/j.conb.2004.05.003

Mundim, K. C., Baraldi, S., Machado, H. G., and Vieira, F. M. (2020). Temperature coefficient (Q10) and its applications in biological systems: Beyond the Arrhenius theory. *J. Ecol. Model.* 431:109127.

Nusbaum, M. P., and Marder, E. (1989). A modulatory proctolin-containing neuron (MPN). II. State-dependent modulation of rhythmic motor activity. *J. Neurosci.* 9, 1600–1607. doi: 10.1523/JNEUROSCI.09-05-01600.1989

Oellermann, M., Hickey, A. J. R., Fitzgibbon, Q. P., and Smith, G. (2020). Thermal sensitivity links to cellular cardiac decline in three spiny lobsters. *Sci. Rep.* 10:202. doi: 10.1038/s41598-019-56794-0

O'Leary, T., and Marder, E. (2016). Temperature-robust neural function from activitydependent ion channel regulation. *Curr. Biol.* 26, 2935–2941. doi: 10.1016/j.cub.2016.08.061

Owens, E. A. (2014). The effects of temperature on the cardiac system of the American lobster, Homarus americanus. Brunswick, ME: Bowdoin College.

Powell, D., Haddad, S. A., Gorur-Shandilya, S., and Marder, E. (2021). Coupling between fast and slow oscillator circuits in *Cancer borealis* is temperature-compensated. *Elife* 10:e60454. doi: 10.7554/eLife.60454

Prosser, C. L., and Nelson, D. O. (1981). The role of nervous systems in temperature adaptation of poikilotherms. *Annu. Rev. Physiol.* 43, 281–300.

Qadri, S. A., Camacho, J., Wang, H., Taylor, J. R., Grosell, M., and Worden, M. K. (2007). Temperature and acid-base balance in the American lobster *Homarus americanus*. *J. Exp. Biol.* 210(Pt 7), 1245–1254. doi: 10.1242/jeb.02709

Racinais, S., and Oksa, J. (2010). Temperature and neuromuscular function. *Scand. J. Med. Sci. Sports* 20(Suppl. 3), 1–18. doi: 10.1111/j.1600-0838.2010.01204.x

Ratliff, J., Franci, A., Marder, E., and O'Leary, T. (2021). Neuronal oscillator robustness to multiple global perturbations. *Biophys J.* 120, 1454–1468. doi: 10.1016/j.bpj.2021.01.038

Reig, R., Mattia, M., Compte, A., Belmonte, C., and Sanchez-Vives, M. V. (2010). Temperature modulation of slow and fast cortical rhythms. *J. Neurophysiol.* 103, 1253–1261. doi: 10.1152/jn.00890.2009

Rinberg, A., Taylor, A. L., and Marder, E. (2013). The effects of temperature on the stability of a neuronal oscillator. *PLoS Comput. Biol.* 9:e1002857. doi: 10.1371/journal.pcbi.1002857

Robertson, R. M., and Money, T. G. (2012). Temperature and neuronal circuit function: Compensation, tuning and tolerance. *Curr. Opin. Neurobiol.* 22, 724–734. doi: 10.1016/j.conb.2012.01.008

Rodriguez, J. C., Blitz, D. M., and Nusbaum, M. P. (2013). Convergent rhythm generation from divergent cellular mechanisms. *J. Neurosci.* 33, 18047–18064. doi: 10.1523/JNEUROSCI.3217-13.2013

Ruf, T., and Geiser, F. (2015). Daily torpor and hibernation in birds and mammals. *Biol. Rev. Camb. Philos. Soc.* 90, 891–926. doi: 10.1111/brv.12137

Rutkove, S. B. (2001). Effects of temperature on neuromuscular electrophysiology. *Muscle Nerve* 24, 867–882. doi: 10.1002/mus.1084

Singh, R. J., Hogg, N., Joseph, J., and Kalyanaraman, B. (1996). Mechanism of nitric oxide release from S-nitrosothiols. *J. Biol. Chem.* 271, 18596–18603. doi: 10.1074/jbc.271.31.18596

Soofi, W., Goeritz, M. L., Kispersky, T. J., Prinz, A. A., Marder, E., and Stein, W. (2014). Phase maintenance in a rhythmic motor pattern during temperature changes *in vivo*. *J. Neurophysiol.* 111, 2603–2613. doi: 10.1152/jn.00906.2013

Srithiphaphirom, P., Lavallee, S., and Robertson, R. M. (2019). Rapid cold hardening and octopamine modulate chill tolerance in *Locusta migratoria*. *Comp. Biochem. Physiol. A Mol. Integr. Physiol.* 234, 28–35. doi: 10.1016/j.cbpa.2019.04.007

Städele, C., and Stein, W. (2022). Neuromodulation enables temperature robustness and coupling between fast and slow oscillator circuits. *Front. Cell. Neurosci.* 16:849160. doi: 10.3389/fncel.2022.849160

Städele, C., Heigele, S., and Stein, W. (2015). Neuromodulation to the rescue: Compensation of temperature-induced breakdown of rhythmic motor patterns via extrinsic neuromodulatory input. *PLoS Biol.* 13:e1002265. doi: 10.1371/journal.pbio.1002265

Stevens, J. S., Cashman, C. R., Smith, C. M., Beale, K. M., Towle, D. W., Christie, A. E., et al. (2009). The peptide hormone pQDLDHVFLRFamide (crustacean myosuppressin) modulates the *Homarus americanus* cardiac neuromuscular system at multiple sites. *J. Exp. Biol.* 212(Pt 24), 3961–3976. doi: 10.1242/jeb.035741

Swensen, A. M., and Marder, E. (2000). Multiple peptides converge to activate the same voltage-dependent current in a central pattern-generating circuit. *J. Neurosci.* 20, 6752–6759. doi: 10.1523/JNEUROSCI.20-18-06752.2000

Swensen, A. M., and Marder, E. (2001). Modulators with convergent cellular actions elicit distinct circuit outputs. *J. Neurosci.* 21, 4050–4058.

Takeishi, A., Yeon, J., Harris, N., Yang, W., and Sengupta, P. (2020). Feeding state functionally reconfigures a sensory circuit to drive thermosensory behavioral plasticity. *Elife* 9:e61167. doi: 10.7554/eLife.61167

Tang, L. S., Goeritz, M. L., Caplan, J. S., Taylor, A. L., Fisek, M., and Marder, E. (2010). Precise temperature compensation of phase in a rhythmic motor pattern. *PLoS Biol.* 8:e1000469. doi: 10.1371/journal.pbio.1000469

Tang, L. S., Taylor, A. L., Rinberg, A., and Marder, E. (2012). Robustness of a rhythmic circuit to short- and long-term temperature changes. *J. Neurosci.* 32:1007510085. doi: 10.1523/JNEUROSCI.1443-12.2012

Thuma, J. B., Hobbs, K. H., Burstein, H. J., Seiter, N. S., and Hooper, S. L. (2013). Temperature sensitivity of the pyloric neuromuscular system and its modulation by dopamine. *PLoS One* 8:e67930. doi: 10.1371/journal.pone.0067930

Versteven, M., Ernst, K. M., and Stanewsky, R. (2020). A robust and self-sustained peripheral circadian oscillator reveals differences in temperature compensation properties with central brain clocks. *iScience* 23:101388. doi: 10.1016/j.isci.2020.101388

Williams, A. H., Calkins, A., O'Leary, T., Symonds, R., Marder, E., and Dickinson, P. S. (2013). The neuromuscular transform of the lobster cardiac system explains the opposing effects of a neuromodulator on muscle output. *J. Neurosci.* 33, 16565–16575. doi: 10.1523/JNEUROSCI.2903-13.2013

Wiwatpanit, T., Powers, B., and Dickinson, P. S. (2012). Inter-animal variability in the effects of C-type allatostatin on the cardiac neuromuscular system in the lobster *Homarus americanus*. *J. Exp. Biol.* 215(Pt 13), 2308–2318. doi: 10.1242/jeb.069989

Worden, M. K., Clark, C. M., Conaway, M., and Qadri, S. A. (2006). Temperature dependence of cardiac performance in the lobster *Homarus americanus*. *J. Exp. Biol.* 209(Pt 6), 1024–1034.

Xu, H., and Robertson, R. (1994). Effects of temperature on properties of flight neurons in the locust. *J. Comp. Physiol. A* 175, 193–202.

Yang, F., and Zheng, J. (2014). High temperature sensitivity is intrinsic to voltage-gated potassium channels. *Elife* 3:e03255. doi: 10.7554/eLife.03255

Zečević, D., Levitan, H., and Pašić, M. (1985). Temperature acclimation: Influence on transient outward and inward currents in an identified neurone of *Helix pomatia*. *J. Exp. Biol.* 117, 369–388.

Zhurov, Y., and Brezina, V. (2005). Temperature compensation of neuromuscular modulation in *Aplysia*. *J. Neurophysiol.* 94, 3259–3277. doi: 10.1152/jn.00481.2005

frontiers | Frontiers in Neuroscience

TYPE Mini Review
PUBLISHED 17 March 2023
DOI 10.3389/fnins.2023.1154769

OPEN ACCESS

EDITED BY
Krista Todd,
Westminster College, United States

REVIEWED BY
Joshua Lillvis,
Janelia Research Campus, United States

*CORRESPONDENCE
Dawn M. Blitz
✉ blitzdm@miamioh.edu

SPECIALTY SECTION
This article was submitted to Neural Technology, a section of the journal Frontiers in Neuroscience

RECEIVED 31 January 2023
ACCEPTED 01 March 2023
PUBLISHED 17 March 2023

CITATION
Blitz DM (2023) Neural circuit regulation by identified modulatory projection neurons. *Front. Neurosci.* 17:1154769. doi: 10.3389/fnins.2023.1154769

Neural circuit regulation by identified modulatory projection neurons

Dawn M. Blitz*

Department of Biology and Center for Neuroscience, Miami University, Oxford, OH, United States

Rhythmic behaviors (e.g., walking, breathing, and chewing) are produced by central pattern generator (CPG) circuits. These circuits are highly dynamic due to a multitude of input they receive from hormones, sensory neurons, and modulatory projection neurons. Such inputs not only turn CPG circuits on and off, but they adjust their synaptic and cellular properties to select behaviorally relevant outputs that last from seconds to hours. Similar to the contributions of fully identified connectomes to establishing general principles of circuit function and flexibility, identified modulatory neurons have enabled key insights into neural circuit modulation. For instance, while bath-applying neuromodulators continues to be an important approach to studying neural circuit modulation, this approach does not always mimic the neural circuit response to neuronal release of the same modulator. There is additional complexity in the actions of neuronally-released modulators due to: (1) the prevalence of co-transmitters, (2) local- and long-distance feedback regulating the timing of (co-)release, and (3) differential regulation of co-transmitter release. Identifying the physiological stimuli (e.g., identified sensory neurons) that activate modulatory projection neurons has demonstrated multiple "modulatory codes" for selecting particular circuit outputs. In some cases, population coding occurs, and in others circuit output is determined by the firing pattern and rate of the modulatory projection neurons. The ability to perform electrophysiological recordings and manipulations of small populations of identified neurons at multiple levels of rhythmic motor systems remains an important approach for determining the cellular and synaptic mechanisms underlying the rapid adaptability of rhythmic neural circuits.

KEYWORDS

central pattern generator, neuropeptide, feedback, neuromodulation, neural circuit, modulatory projection neuron

1. Introduction

Rhythmic motor behaviors are generated by central nervous system (CNS) circuits called central pattern generators (CPGs) (Bucher et al., 2015). Although CPGs can produce rhythmic output without rhythmic input, modulatory input is often required to configure CPGs into an active state. Additionally, beyond simply turning on or off, CPGs are often "multifunctional," in that they produce different outputs to adapt to changes in the internal and external environments (Briggman and Kristan, 2008; Benjamin, 2012; Daur et al., 2016; Marder et al., 2022). In some cases, the source of modulation is intrinsic to the CPG and a necessary component of motor output (Katz, 1998). However, many sources originate

outside the CPG, including sensory inputs, hormones, and modulatory projection neurons (PNs), i.e., neurons which originate in higher order CNS regions and project to CPGs (Rosen et al., 1991; Briggman and Kristan, 2008; Nusbaum, 2008; Hsu and Bhandawat, 2016).

Small circuits, particularly those underlying rhythmic behaviors, with their identified neurons, have enabled many important insights into circuit function and plasticity (Calabrese et al., 2016; Cropper et al., 2018; Katz and Quinlan, 2019; Marder et al., 2022). Similar to the accessibility of identified circuit neurons, several invertebrate preparations also have relatively small populations of modulatory PNs which are accessible to electrophysiological approaches (Rosen et al., 1991; Heinrich, 2002; Mesce et al., 2008; Nusbaum, 2008). PN populations range from ∼20 pairs in crab and mollusk feeding systems to ∼200–500 pairs targeting the insect ventral nerve cord (Rosen et al., 1991; Coleman et al., 1992; Hsu and Bhandawat, 2016; Namiki et al., 2018). Comparable PN populations in vertebrates are typically larger, include heterogeneous types, and can be distributed across multiple nuclei (Garcia et al., 2011; Sharples et al., 2014; Ruder and Arber, 2019; Flaive et al., 2020). While technological advances are increasing the ability to control vertebrate neuron populations *in vitro* and *in vivo,* cellular-level experimental access to modulatory PNs and a fully described motor circuit connectome remains challenging in many vertebrate preparations (Kim et al., 2017; Leiras et al., 2022). Here, I will focus on lessons learned from several small, invertebrate motor systems, regarding the cellular mechanisms by which modulatory PNs alter CPG output, and how their activity is regulated. Much additional work on descending motor control, including fast activation of escape behaviors, and large-scale genetic approaches investigating insect descending neurons is beyond the scope of this article (Cande et al., 2018; Herberholz, 2022).

2. Modulatory projection neurons alter CPG output

2.1. Bath-application vs. neuronal-release

Early studies primarily using bath-applied neuromodulators, but also stimulation of identified modulatory PNs, demonstrated that there is considerable flexibility in the strength and pattern of neuronal activity, as well as in which CPG(s) the neurons are participating (Hooper and Marder, 1984; Kuhlman et al., 1985; Flamm and Harris-Warrick, 1986; Dickinson et al., 1990; Harris-Warrick and Marder, 1991; Ramirez and Pearson, 1991; Marder, 2012). Although bath-application continues to provide insights into circuit modulation, bath-applied modulator actions range from very similar to neuronally-released modulator, to only mimicking some effects, to having distinct, even opposite effects (Marder, 2012; Nusbaum et al., 2017). The small numbers and exceptional experimental access afforded by invertebrate modulatory neurons have revealed several explanations for distinctions between bath-applied and neuronally-released modulators. The crustacean stomatogastric nervous system (STNS), is particularly useful because the transmitters, intrinsic properties, and synaptic connections are identified for the ∼30 neurons comprising two feeding-related CPGs (pyloric, gastric mill) (**Figure 1A**; Marder and Bucher, 2007; Daur et al., 2016). Additionally, identified modulatory PNs are amenable to intra-somatic and intra-axonal recordings, and identification of their (co-)transmitter content allows for direct comparison of bath-applied vs. neuronally-released neuromodulators (**Figure 1A**; Nusbaum and Marder, 1989a; Coleman and Nusbaum, 1994; Stein, 2009; Kwiatkowski et al., 2013; Nusbaum et al., 2017).

2.2. Co-transmission

Modulatory CPG inputs, including PNs, use metabotropic receptors and second messenger signaling to alter intrinsic and synaptic properties of circuit neurons to select different outputs (Katz and Calin-Jageman, 2009; Nadim and Bucher, 2014). However, they often also use rapid ionotropic transmission. Co-transmission is ubiquitous and a likely contributor to distinctions between modulatory neuron activation and bath-application. Co-transmitter complements include neuropeptide plus classical and/or amine small molecule transmitters, or multiple small molecule transmitters (Nusbaum et al., 2017; Nässel, 2018; Trudeau and El Mestikawy, 2018; Svensson et al., 2019; Eiden et al., 2022). One or more neuropeptides plus a small molecule transmitter is common in modulatory PNs targeting CPGs (**Figure 1A**; Schlegel et al., 2016; Nusbaum et al., 2017; Nässel, 2018).

Neuropeptide and small molecule co-neurotransmitter actions range from varying degrees of convergence, to complementary, to entirely divergent (Thirumalai and Marder, 2002; Nusbaum et al., 2017; Nässel, 2018; Florman and Alkema, 2022). In the crab STNS, a modulatory PN (MCN5) switches the CPG neuron LPG from pyloric-only network participation to dual-network (pyloric plus gastric mill) activity *via* its neuropeptide Gly^1-SIFamide (**Figure 1B**; Fahoum and Blitz, 2021; Snyder and Blitz, 2022). However, bath applied Gly^1-SIFamide excites the pyloric CPG neuron LP, which inhibits LPG and prevents it from fully expressing dual-network activity. This Gly^1-SIFamide excitation of LP is opposite of MCN5 actions (**Figure 1B**; Fahoum and Blitz, 2021). MCN5-released Gly^1-SIFamide can elicit the switch in LPG activity due to co-released glutamate inhibiting the LP neuron that would otherwise interfere with LPG switching into dual-network activity (**Figure 1B**). Thus, ionotropic classical transmitter actions are essential for metabotropic neuropeptide actions to be fully expressed. Conversely, in *Aplysia* feeding, ionotropic actions are enhanced by metabotropic receptor-mediated co-transmitter actions. The feeding motor pattern activated by the modulatory PN CBI-2 changes over time, due to CBI-2 modulation of its cholinergic synaptic transmission onto feeding motor neurons (Koh et al., 2003). The time-dependent effects on the motor pattern and enhanced fast cholinergic synaptic transmission are mimicked by either of the CBI-2 peptide co-transmitters (CP2, FCAP). However, the cooperative peptide effects are distinct, with CP2 and FCAP increasing quantal content versus size, respectively (Koh et al., 2003). Intracellular recordings from identified modulatory PNs such as MCN5 and CBI-2, with identified co-transmitters, revealed co-transmitter cooperativity necessary for motor pattern selection that would be missed in bath-application studies.

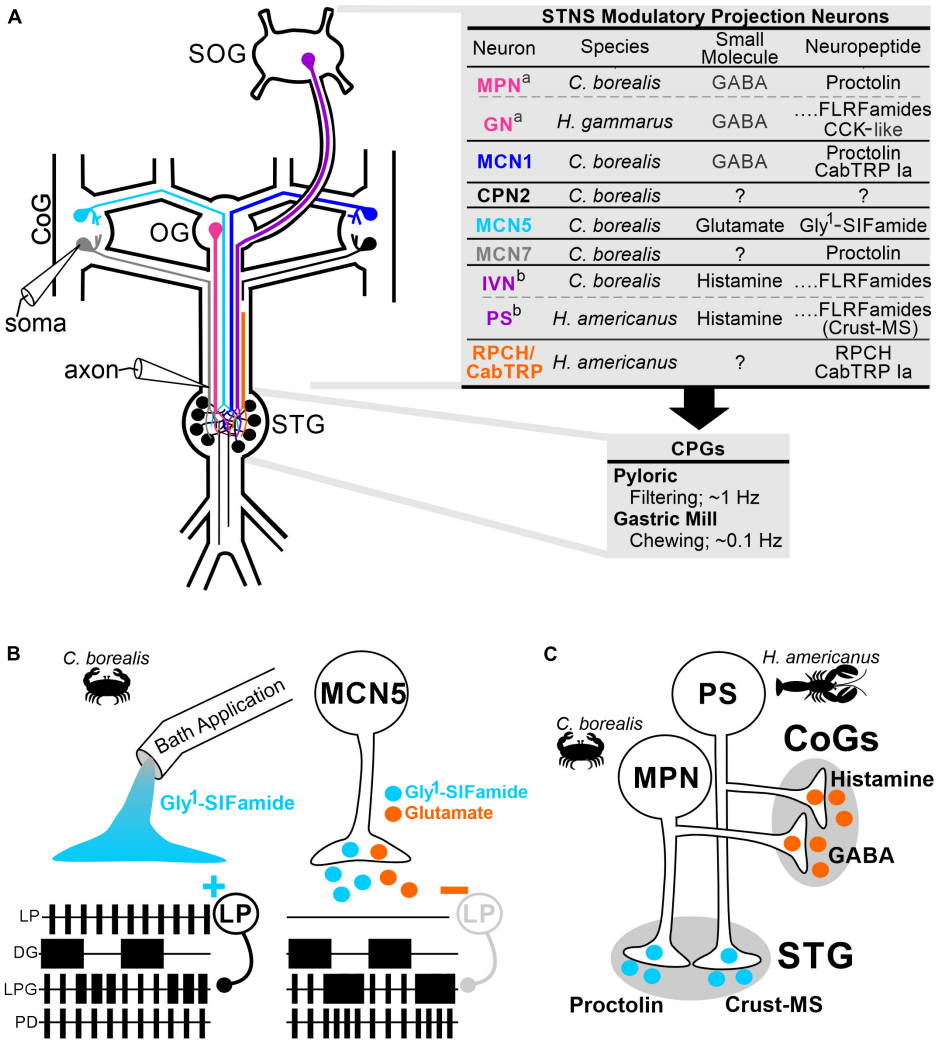

FIGURE 1
Identified modulatory projection neurons reveal cooperative and divergent actions contributing to distinctions between bath-applied and neuronally-released modulator. **(A)** The crustacean stomatogastric nervous system (STNS) includes the pyloric (food filtering, ~1 Hz) and gastric mill (food chewing, ~0.1 Hz) CPGs within the stomatogastric ganglion (STG). Modulatory PNs originating in the oesophageal (OG), the paired commissural ganglia (CoGs), and the supraoesophageal ganglion (SOG) project to and modulate the CPGs. Intracellular recordings of modulatory PNs can be made at the soma in the SOG, CoG, or OG, and axon terminals near the entrance to the STG (electrode symbols). Most modulatory PNs contain small molecule and neuropeptide co-transmitters as listed in the upper table. [a,b]Some analogous modulatory neurons in different species (lobster, *Homarus gammarus*, *H. americanus*; crab, *Cancer borealis*) contain the same co-transmitters, and others contain different complements. All PNs listed occur as pairs, either as a single copy in each CoG (MCN1/5/7, CPN2), or in the same location (OG: MPN/GN; SOG: IVN/PS), however they are drawn as single neurons for clarity. **(B)** Ionotropic co-transmitter actions are necessary for full expression of metabotropic actions. In *C. borealis,* the modulatory PN MCN5 elicits a motor pattern that includes dual-network activity in the LPG neuron (shorter duration, faster pyloric-timed bursts alternating with slower gastric mill-timed bursts). Pyloric network activity is evident in LP and PD neuron activity, gastric mill network activity is represented by DG neuron activity. Neuron activity is schematized as extracellular recordings with each box representing a burst of action potentials. Bath application of the MCN5 neuropeptide Gly^1-SIFamide mimics some but not all MCN5 actions. In particular, Gly^1-SIFamide excites the pyloric LP neuron (+) whereas MCN5 inhibits LP (−). The increased LP activity during Gly^1-SIFamide application inhibits the LPG neuron, preventing it from fully participating in the slower gastric mill network, note the extended duration LPG bursts alternating with DG that do not fully merge into a gastric mill-timed burst. MCN5 inhibits LP (gray) *via* its co-transmitter glutamate, which is essential for LPG to fully participate in the gastric mill network *via* Gly^1-SIFamide effects (Blitz et al., 2019; Fahoum and Blitz, 2021). **(C)** Spatially divergent co-transmitter actions occur in modulatory PNs in the STNS. The MPN and PS neurons use their peptide transmitters (proctolin and crust-MS, respectively) on pyloric and gastric mill CPGs in the STG, but their small molecule transmitters (GABA and histamine, respectively) in the CoGs. It is not known whether there is differential trafficking or other explanations for these segregated co-transmitter actions (Nusbaum and Marder, 1989a; Blitz and Nusbaum, 1999; Kwiatkowski et al., 2013). Species used in the referenced studies are indicted in each panel. Neuron/transmitter identification in panel **(A)**: (Nusbaum and Marder, 1989a; Coleman and Nusbaum, 1994; Norris et al., 1994, 1996; Blitz and Nusbaum, 1999; Blitz et al., 1999, 2019; Meyrand et al., 2000; Swensen et al., 2000; Thirumalai and Marder, 2002; Christie et al., 2004; Kwiatkowski et al., 2013; Fahoum and Blitz, 2021).

In some cases, neuropeptide and small molecule actions appear partially redundant. In the nematode *Caenorhabditis elegans,* serotonin or NLP-3 neuropeptide release from a modulatory PN is sufficient to activate egg-laying, however their combined actions elicit additional egg-laying. Further work is necessary to determine whether their actions converge onto the same targets (Brewer et al., 2019). Co-transmitters may converge onto the same cellular or even subcellular targets (Nadim and Bucher, 2014), however without

cellular-level access to the full CPG circuit, similar network level actions may hide cellular divergence. In *Aplysia* feeding, three neuropeptides released from modulatory neuron CBI-12, each have the same circuit level effect, shortening the protraction phase of an ingestive motor pattern (Jing and Weiss, 2005; Zhang et al., 2018). However, the peptides act on different CPG neurons to mediate the same circuit effect (Zhang et al., 2018). Such redundancy may ensure a particular adjustment to circuit output even when some targets are unresponsive.

2.3. Spatial segregation of co-transmitter actions

Divergent co-transmitter actions may result from spatial segregation. In the crustacean STNS, modulatory PNs (MPN, PS) each use their peptide transmitter on CPG neurons within the stomatogastric ganglion (STG), but their small molecule transmitters act at distinct arbors, in different ganglia [commissural ganglia (CoGs)] (**Figure 1C**; Nusbaum and Marder, 1989b; Blitz and Nusbaum, 1999; Kwiatkowski et al., 2013). Spatially distinct actions could occur due to distinct trafficking of transmitter vesicles, differential receptor expression on postsynaptic targets, or differential sensitivity of transmitter release to neuronal activity (Kueh and Jellies, 2012; Nusbaum et al., 2017; Cropper et al., 2018; Cifuentes and Morales, 2021). Where determined, the low end of physiological firing frequencies is sufficient to release both peptide and small molecule transmitters (Cropper et al., 2018). On a finer scale, peptidases can constrain the actions of neuronally-released peptides, enabling distinct effects even when released into the same densely overlapping neuropil regions (Christie et al., 1997; Blitz et al., 1999; Nusbaum, 2002; Wood and Nusbaum, 2002; Nässel, 2009). Although neuromodulators are often considered to act *via* relatively non-specific "volume transmission," it is becoming increasingly clear that there is also spatial constraint of neuromodulator actions (Disney and Higley, 2020; Liu et al., 2021; Nässel and Zandawala, 2022). Localization of reuptake and degradative machinery, and constrained release/receptor distributions beyond anatomically-defined synapses can limit the sphere of neuromodulator influence (Nusbaum, 2002; Disney and Higley, 2020; Liu et al., 2021; Eiden et al., 2022).

2.4. Local presynaptic feedback onto modulatory projection neurons

The ability to record from modulatory PN axon terminals revealed local presynaptic regulation of their transmission (Nusbaum, 1994). For example, rhythmic presynaptic inhibition from a circuit neuron onto modulatory PN terminals in the crab STNS and the subsequent waxing and waning of modulatory effects is essential to elicit a chewing pattern (Coleman et al., 1995). Further, the system is tuned such that this local feedback inhibition results in a more coordinated motor pattern when both PN copies are coactive compared to the same cumulative activity in a single PN copy (Colton et al., 2020). The presynaptic regulation occurs at terminals that are ~1–2 cm distant from the soma (**Figure 1A**) and due to electrotonic decay, is not present in somatic recordings and does not alter PN activity initiating in the PN ganglion of origin (Nusbaum et al., 1992; Coleman and Nusbaum, 1994; Coleman et al., 1995). Local synaptic input includes chemical transmission between circuit neurons and PNs and between PNs, plus extensive electrical coupling between circuit neurons and PN terminals (Perrins and Weiss, 1998; Hurwitz et al., 2005; Stein et al., 2007; Marder et al., 2017; Blitz et al., 2019). Local feedback actions may generally alter transmission, or be more specific, including decreasing chemical but not electrical transmission (Coleman et al., 1995), or decreasing peptide but not small molecule transmitter release (DeLong et al., 2009). Rhythmic presynaptic regulation from CPG elements can also cause modulatory PN actions to occur *via* distinct mechanisms (e.g., electrical vs. chemical transmission) during different phases of motor output (Coleman et al., 1995; Hurwitz et al., 2005). Long-distance synaptic feedback also regulates PN transmission, however through changes in PN activity (see Section "3.3. Long-distance CPG feedback"). While much continues to be learned from bath-application studies, studies discussed above provide a note of caution, as even co-transmitter bath application may not mimic neuronal release due to the lack of spatial and temporal control that occurs with neuronally-released neuromodulators.

3. Regulation of modulatory projection neuron activity

Modulatory PNs serve as a link between sensory and/or higher-order inputs, and the motor circuits responsible for behavior. Thus, understanding how PN activity is controlled is important to understanding how sensory information and higher-order decisions are converted to appropriate behavioral responses.

3.1. State-dependence

In vitro and *in vivo*, single modality sensory input can be sufficient to initiate relevant behaviors *via* activation of identified modulatory PNs (Willard, 1981; Rosen et al., 1991; Horn et al., 1999; Jing and Weiss, 2005; Hedrich et al., 2011). However, PN activity is often regulated by multiple sources. In particular, inputs relaying behavioral state information can alter PN sensitivity to other inputs during ongoing behaviors, or result in different behavioral versions, on multiple time scales (Kristan and Shaw, 1997; Staudacher, 2001; Beenhakker et al., 2007; Barrière et al., 2008; White et al., 2017; Ache et al., 2019; Cook and Nusbaum, 2021). State-dependent PN activity may be a consequence of inputs specifically targeting PNs, such as courtship-promoting neurons converging with visual input onto the *Drosophila* P9 PN, to elicit courtship locomotor behavior (Bidaye et al., 2020). Behavioral state can also be conveyed to PNs through broadly-acting hormones (Willard, 1981; Mesce and Pierce-Shimomura, 2010; Flood et al., 2013). In the medicinal leech, circulating serotonin increases with hunger, coincident with a decreased threshold for swimming. Although serotonin does not activate swim-activating cell 204, it modulates its intrinsic properties, making it easier for other inputs to activate this neuron and elicit swimming (Angstadt and Friesen, 1993; Kristan et al., 2005). Even if the responsiveness of a modulatory PN does not

change, the consequences of its activity may be state-dependent. The leech R3b1 PN elicits crawling or swimming, with the decision determined by the surrounding fluid level (Esch and Kristan, 2002). "Shallow water detector" sensory neurons appear to select motor output downstream from modulatory PNs, *via* actions on CPG neurons (**Figure 2A**). However, dopamine application biases the entire nervous system toward crawling and R3b1 only elicits crawling in this context (**Figure 2A**; Puhl et al., 2012), suggesting both PN- and CPG-level control of motor system state.

3.2. Long-lasting activity states

Inputs to modulatory PNs have rapid transient effects, *via* fast synaptic transmission, or trigger activity persisting beyond the stimulus duration, *via* slower metabotropic actions (Rosen et al., 1991; Beenhakker and Nusbaum, 2004; Kristan et al., 2005; Brodfuehrer et al., 2008; Benjamin, 2012). For long-lasting PN activation, a behavioral switch might require active termination of PN activity, such as a transient "stop" signal from a sensory pathway that triggers an incompatible behavior *via* other PNs (Esch and Kristan, 2002; Mesce and Pierce-Shimomura, 2010). Additionally, interactions between modulatory neurons, serving to either reinforce or suppress activity in other modulatory PNs, enables them to play important roles in maintaining or switching behavioral state. This includes inhibiting competing PNs to remove their drive of an alternative CPG, activating PNs which inhibit a competing CPG, or exciting complementary PNs (Blitz and Nusbaum, 1997, 1999; Crisp and Mesce, 2006; Wu et al., 2014; Pirger et al., 2021).

A persistent behavioral state can also occur without long-term PN activation, but instead due to the duration of PN modulatory actions. In *Aplysia* feeding, repeated CBI-2 stimulation progressively adapts CPG activity and improves behavioral output, due to second messenger accumulation in target CPG neurons (Cropper et al., 2017). As a result, the CPG is biased toward one output over another, which may stabilize the circuit when one behavior is more likely to be useful (Cropper et al., 2017). Different from this auto-regulation, in another mollusk, *Lymnaea*, the octopaminergic OC cells enhance CPG responses to other modulatory neurons for multiple motor pattern cycles (Benjamin, 2012). Thus, motor system state can be regulated directly at the PN level, or in circuit responsiveness to PNs, across multiple timescales.

3.3. Long-distance CPG feedback

Another source of regulation is synaptic feedback from CPG neurons to PNs, which results in PN firing being time-locked to circuit activity, including *in vivo* and in semi-intact preparations when PNs are activated by physiological stimuli (Gillette et al., 1978; Blitz and Nusbaum, 2008; Mesce et al., 2008; Hedrich et al., 2011; Blitz, 2017). A distinct case occurs in the stick insect *Carausius morosus* in which PN walking-timed activity is due to sensory feedback instead of CPG feedback (Stolz et al., 2019). Feedback to PNs contributes to inter-circuit coordination, duration of PN activity, and gating of other PN inputs (Wood et al., 2004; Antri et al., 2009; Kozlov et al., 2014). Additionally, feedback control of modulatory PN activity can be important for motor pattern selection (see Section "4.2. Activity code").

4. Motor pattern selection

4.1. Population code

Although experimentally-induced activation of an individual PN can elicit a motor pattern, physiological stimuli often activate more than one PN type (Coleman and Nusbaum, 1994; Esch and Kristan, 2002; Beenhakker and Nusbaum, 2004; Benjamin, 2012; Follmann et al., 2018; Fahoum and Blitz, 2021). This raises the possibility that the "modulatory code" for selecting a motor output is one in which different stimuli activate distinct PN subsets, resulting in a combinatorial "population code." Such a scenario occurs in several systems, and experimentally manipulating which PNs are active elicits switches between motor patterns (Kristan and Shaw, 1997; Combes et al., 1999; Kupfermann and Weiss, 2001; Hedrich et al., 2009; Guo et al., 2022). In *Aplysia* when the modulatory PN CBI-2 is active, repeated stimulations are necessary to elicit an ingestive pattern, which is persistent, but if CBI-2 and CBI-3 are both active, they immediately elicit an ingestive motor pattern without induction of a persistent state (Evans et al., 2021; **Figure 2B**). Thus, the population of modulatory neurons active can determine the pattern produced, and other aspects such as the dynamics of motor pattern selection.

4.2. Activity code

Quantitatively, modulatory PN firing rate can regulate motor output, although differences occur in network sensitivity (Kristan et al., 2005; Hedrich et al., 2011; Benjamin, 2012; Spencer and Blitz, 2016; Sakurai and Katz, 2019). Additionally, an "activity code," i.e., PN pattern and/or rate can encode qualitatively distinct motor patterns and behaviors. In *Drosophila* courtship, the same descending PN (aSP22) uses cumulative spike count, to elicit different behaviors in a sequential fashion. In this "ramp-to-threshold" mechanism, different behavioral components of courtship are generated as the aSP22 spike count crosses a series of thresholds (**Figure 2C**; McKellar et al., 2019). In the crab STNS, mechanosensory neurons and neuroendocrine cells each trigger long-lasting activation of two modulatory PNs (MCN1, CPN2) (Beenhakker and Nusbaum, 2004; Blitz et al., 2008). However, differential, long-lasting, modulation of CPG feedback in these two states results in distinct MCN1/CPN2 activity patterns and rates which encode different chewing behaviors, and different sensitivity to sensory feedback (**Figure 2D**; Beenhakker et al., 2007; Blitz and Nusbaum, 2008, 2012; Diehl et al., 2013; Blitz, 2017; White et al., 2017). The ability to manipulate feedback synapses onto small populations of identified modulatory neurons was essential for these insights into how CPG feedback to PNs contributes to motor pattern selection. Collectively, these examples illustrate that the same PNs can use an activity code to select motor outputs, instead of a population code of different PN subsets, with both

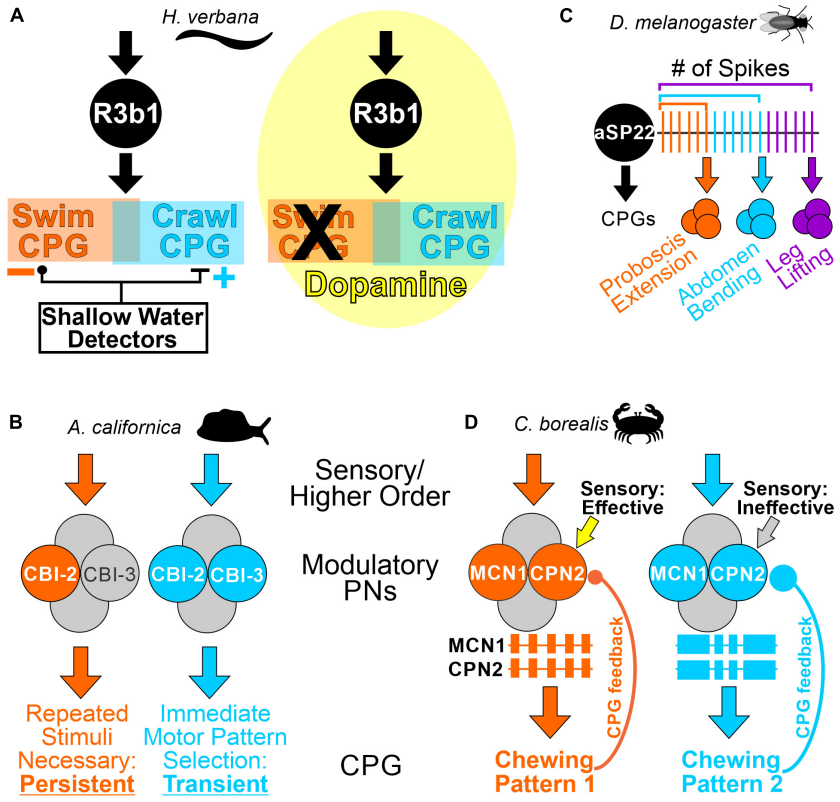

FIGURE 2
Motor pattern selection by modulatory PNs is state-dependent, and can be encoded in the population of active PNs, or in PN activity. **(A)** The effects of PN R3b1 are determined by environmental and internal conditions. *Left*, in an *in vitro* or semi-intact leech preparation, the R3b1 neuron elicits either swimming or crawling in response to the same input. The swim and crawl CPGs consist of partially overlapping neurons (orange and blue boxes). Fluid depth around the animal determines which locomotor pattern is selected. The proposed mechanism is that "shallow water detector" neurons provide inhibitory input to the swim CPG and excitatory input to the crawl CPG (Esch et al., 2002). *Right*, in the presence of dopamine (yellow cloud), the entire nervous system is biased toward crawling, and R3b1 only elicits crawling (Puhl et al., 2012). **(B)** Distinct subpopulations of activated PNs select feeding patterns with different dynamics. When the modulatory PN CBI-2 alone is activated, repeated stimulation is necessary to elicit an ingestive feeding pattern which persists for ~30 min. However, if CBI-2 and CBI-3 are co-activated, an ingestive feeding pattern is immediately selected, but it is a transient activation (Evans et al., 2021). **(C)** The same PN, aSP22, activates different CPGs and different behaviors based on a spike number code. In this "ramp-to-threshold" example, as an increasing number of action potentials crosses different thresholds, aSP22 progressively activates CPGs contributing to different aspects of courtship (McKellar et al., 2019). **(D)** In response to different stimuli, the modulatory PNs MCN1 and CPN2 elicit qualitatively different chewing patterns due to distinctions in their activity patterns and rates (Beenhakker and Nusbaum, 2004; Blitz et al., 2008; White and Nusbaum, 2011; Diehl et al., 2013). MCN1 and CPN2 activity is indicated as extracellular recordings, with each colored box representing a burst of action potentials (different firing rates are not represented in the schematics). The differences in their activity are due to different strengths of CPG feedback (CPG feedback terminal size (colored circles) is representative of relative CPG feedback strength) (Blitz, 2017). Additionally, proprioceptive sensory neurons regulate MCN1 and CPN2 activity in the "orange" state when CPG feedback is weak, but not in the "blue" state, when CPG feedback is stronger (Beenhakker et al., 2007; White et al., 2017). Species used in the referenced studies are indicated in the panels.

mechanisms possible even in the same system, albeit in distinct species (Beenhakker and Nusbaum, 2004; Blitz et al., 2008; Hedrich et al., 2009).

5. Conclusion

Cellular-level access to modulatory PNs at their somata and axon terminals, and their CPG neuron targets in several invertebrate preparations enabled insights into regulation of PN activity, strategies for selecting an appropriate motor pattern, and significant complexity in communication between modulatory PNs and their CPG targets. Invertebrate PNs and larger vertebrate populations similarly link sensory and higher-order processing with motor circuits, and many of the insights discussed have already, or likely will be found to extend to larger circuits (Dickinson, 2006; Sharples et al., 2014; Yang et al., 2020). Technological advances are enabling recording and manipulation of genetically identified populations in organisms with barriers to electrophysiological approaches (e.g., neuronal size, accessibility, population size). However invertebrate organisms remain important for determining how modulatory PNs regulate circuits at the cellular-level, *via* electrophysiological recordings and manipulations that remain difficult in larger systems. Given the rapidly developing techniques making investigation in larger systems more tractable, plus the application of genetic approaches to classic neurophysiologically-accessible model organisms (Kim et al., 2017; Northcutt et al., 2018, 2019; Devineni and Scaplen, 2022; Leiras et al., 2022), diverse models and approaches are expected to continue increasing our understanding of how

motor circuits rapidly adapt to the everchanging conditions in and around us.

Author contributions

DB wrote the first draft of the manuscript, revised the manuscript, read, and approved the final version.

Funding

Research in the author's lab was supported by the National Science Foundation (IOS-1755283) and the National Institute of Neurological Disorders and Stroke (R15-NS128619).

Acknowledgments

I thank Savanna-Rae H. Fahoum and Barathan Gnanabharathi for feedback on earlier versions of the manuscript and current and former students and colleagues for their participation in work reviewed here.

Conflict of interest

The author declares that the research was conducted in the absence of any commercial or financial relationships that could be construed as a potential conflict of interest.

Publisher's note

References

Ache, J. M., Namiki, S., Lee, A., Branson, K., and Card, G. M. (2019). State-dependent decoupling of sensory and motor circuits underlies behavioral flexibility in *Drosophila*. *Nat. Neurosci.* 22, 1132–1139. doi: 10.1038/S41593-019-0413-4

Angstadt, J. D., and Friesen, W. O. (1993). Modulation of swimming behavior in the medicinal leech. I. Effects of serotonin on the electrical properties of swim-gating cell 204. *J. Comp. Physiol. A* 172, 223–234. doi: 10.1007/BF00189398

Antri, M., Fénelon, K., and Dubuc, R. (2009). The contribution of synaptic inputs to sustained depolarizations in reticulospinal neurons. *J. Neurosci.* 29, 1140–1151. doi: 10.1523/JNEUROSCI.3073-08.2009

Barrière, G., Simmers, J., and Combes, D. (2008). Multiple mechanisms for integrating proprioceptive inputs that converge on the same motor pattern-generating network. *J. Neurosci.* 28, 8810–8820. doi: 10.1523/JNEUROSCI.2095-08.2008

Beenhakker, M. P., Kirby, M. S., and Nusbaum, M. P. (2007). Mechanosensory gating of proprioceptor input to modulatory projection neurons. *J. Neurosci.* 27, 14308–14316. doi: 10.1523/JNEUROSCI.4404-07.2007

Beenhakker, M. P., and Nusbaum, M. P. (2004). Mechanosensory activation of a motor circuit by coactivation of two projection neurons. *J. Neurosci.* 24, 6741–6750. doi: 10.1523/JNEUROSCI.1682-04.2004

Benjamin, P. R. (2012). Distributed network organization underlying feeding behavior in the mollusk Lymnaea. *Neural Syst. Circ.* 2:4. doi: 10.1186/2042-1001-2-4

Bidaye, S. S., Laturney, M., Chang, A. K., Liu, Y., Bockemühl, T., Büschges, A., et al. (2020). Two brain pathways initiate distinct forward walking programs in drosophila. *Neuron* 108, 469–485.e8. doi: 10.1016/J.NEURON.2020.07.032

Blitz, D. M. (2017). Circuit feedback increases activity level of a circuit input through interactions with intrinsic properties. *J. Neurophysiol.* 118, 949–963. doi: 10.1152/jn.00772.2016

Blitz, D. M., Christie, A. E., Coleman, M. J., Norris, B. J., Marder, E., and Nusbaum, M. P. (1999). Different proctolin neurons elicit distinct motor patterns from a multifunctional neuronal network. *J. Neurosci.* 19, 5449–5463. doi: 10.1523/jneurosci.19-13-05449.1999

Blitz, D. M., Christie, A. E., Cook, A. P., Dickinson, P. S., and Nusbaum, M. P. (2019). Similarities and differences in circuit responses to applied Gly^1-SIFamide and peptidergic (Gly^1 -SIFamide) neuron stimulation. *J. Neurophysiol.* 121, 950–972. doi: 10.1152/jn.00567.2018

Blitz, D. M., and Nusbaum, M. P. (1997). Motor pattern selection *via* inhibition of parallel pathways. *J. Neurosci.* 17, 4965–4975. doi: 10.1523/jneurosci.17-13-04965.1997

Blitz, D. M., and Nusbaum, M. P. (1999). Distinct functions for cotransmitters mediating motor pattern selection. *J. Neurosci.* 19, 6774–6783. doi: 10.1523/jneurosci.19-16-06774.1999

Blitz, D. M., and Nusbaum, M. P. (2008). State-dependent presynaptic inhibition regulates central pattern generator feedback to descending inputs. *J. Neurosci.* 28, 9564–9574. doi: 10.1523/JNEUROSCI.3011-08.2008

Blitz, D. M., and Nusbaum, M. P. (2012). Modulation of circuit feedback Specifies motor circuit output. *J. Neurosci.* 32, 9182–9193. doi: 10.1523/JNEUROSCI.1461-12.2012

Blitz, D. M., White, R. S., Saideman, S. R., Cook, A., Christie, A. E., Nadim, F., et al. (2008). A newly identified extrinsic input triggers a distinct gastric mill rhythm *via* activation of modulatory projection neurons. *J. Exp. Biol.* 211, 1000–1011. doi: 10.1242/jeb.015222

Brewer, J. C., Olson, A. C., Collins, K. M., and Koelle, M. R. (2019). Serotonin and neuropeptides are both released by the HSN command neuron to initiate *Caenorhabditis elegans* egg laying. *PLoS Genet.* 15:e1007896. doi: 10.1371/JOURNAL.PGEN.1007896

Briggman, K. L., and Kristan, W. B. (2008). Multifunctional pattern-generating circuits. *Annu. Rev. Neurosci.* 31, 271–294. doi: 10.1146/annurev.neuro.31.060407.125552

Brodfuehrer, P. D., McCormick, K., Tapyrik, L., Albano, A. M., and Graybeal, C. (2008). Activation of two forms of locomotion by a previously identified trigger interneuron for swimming in the medicinal leech. *Invert Neurosci.* 8, 31–39. doi: 10.1007/S10158-007-0064-0

Bucher, D., Haspel, G., Golowasch, J., and Nadim, F. (2015). Central pattern generators. *eLs* 1–12. doi: 10.1002/9780470015902.a0000032.pub2

Calabrese, R. L., Norris, B. J., and Wenning, A. (2016). The neural control of heartbeat in invertebrates. *Curr. Opin. Neurobiol.* 41, 68–77. doi: 10.1016/J.CONB.2016.08.004

Cande, J., Namiki, S., Qiu, J., Korff, W., Card, G. M., Shaevitz, J. W., et al. (2018). Optogenetic dissection of descending behavioral control in Drosophila. *Elife* 7:e34275. doi: 10.7554/ELIFE.34275

Christie, A. E., Baldwin, D. H., Marder, E., and Graubard, K. (1997). Organization of the stomatogastric neuropil of the crab, *Cancer borealis*, as revealed by modulator immunocytochemistry. *Cell Tissue Res.* 288, 135–148. doi: 10.1007/S004410050801

Christie, A. E., Stein, W., Quinlan, J. E., Beenhakker, M. P., Marder, E., and Nusbaum, M. P. (2004). Actions of a histaminergic/peptidergic projection neuron on rhythmic motor patterns in the stomatogastric nervous system of the crab *Cancer borealis*. *J. Comp. Neurol.* 469, 153–169. doi: 10.1002/CNE.11003

Cifuentes, F., and Morales, M. A. (2021). Functional implications of neurotransmitter segregation. *Front. Neural Circ.* 15:738516. doi: 10.3389/fncir.2021.738516

Coleman, M. J., Meyrand, P., and Nusbaum, M. P. (1995). A switch between two modes of synaptic transmission mediated by presynaptic inhibition. *Nature* 378, 502–505. doi: 10.1038/378502a0

Coleman, M. J., and Nusbaum, M. P. (1994). Functional consequences of compartmentalization of synaptic input. *J. Neurosci.* 14, 6544–6552. doi: 10.1523/JNEUROSCI.14-11-06544.1994

Coleman, M. J., Nusbaum, M. P., Cournil, I., and Claiborne, B. J. (1992). Distribution of modulatory inputs to the stomatogastric ganglion of the crab, *Cancer borealis*. *J. Comp. Neurol.* 325, 581–594. doi: 10.1002/CNE.903250410

Colton, G. F., Cook, A. P., and Nusbaum, M. P. (2020). Different microcircuit responses to comparable input from one versus both copies of an identified projection neuron. *J. Exp. Biol.* 223:jeb228114. doi: 10.1242/JEB.228114

Combes, D., Meyrand, P., and Simmers, J. (1999). Dynamic restructuring of a rhythmic motor program by a single mechanoreceptor neuron in lobster. *J. Neurosci.* 19, 3620–3628. doi: 10.1523/JNEUROSCI.19-09-03620.1999

Cook, A. P., and Nusbaum, M. P. (2021). Feeding state-dependent modulation of feeding-related motor patterns. *J. Neurophysiol.* 126, 1903–1924. doi: 10.1152/JN.00387.2021

Crisp, K. M., and Mesce, K. A. (2006). Beyond the central pattern generator: amine modulation of decision-making neural pathways descending from the brain of the medicinal leech. *J. Exp. Biol.* 209, 1746–1756. doi: 10.1242/JEB.02204

Cropper, E. C., Jing, J., Perkins, M. H., and Weiss, K. R. (2017). Use of the Aplysia feeding network to study repetition priming of an episodic behavior. *J. Neurophysiol.* 118, 1861–1870. doi: 10.1152/JN.00373.2017

Cropper, E. C., Jing, J., Vilim, F. S., Barry, M. A., and Weiss, K. R. (2018). Multifaceted expression of peptidergic modulation in the feeding system of *Aplysia*. *ACS Chem. Neurosci.* 9, 1917–1927. doi: 10.1021/ACSCHEMNEURO.7B00447

Daur, N., Nadim, F., and Bucher, D. (2016). The complexity of small circuits: the stomatogastric nervous system. *Curr. Opin. Neurobiol.* 41, 1–7. doi: 10.1016/J.CONB.2016.07.005

DeLong, N. D., Beenhakker, M. P., and Nusbaum, M. P. (2009). Presynaptic inhibition selectively weakens peptidergic cotransmission in a small motor system. *J. Neurophysiol.* 102, 3492–3504. doi: 10.1152/jn.00833.2009

Devineni, A. V., and Scaplen, K. M. (2022). Neural circuits underlying behavioral flexibility: insights from drosophila. *Front. Behav. Neurosci.* 15:821680. doi: 10.3389/FNBEH.2021.821680

Dickinson, P. S. (2006). Neuromodulation of central pattern generators in invertebrates and vertebrates. *Curr. Opin. Neurobiol.* 16, 604–614. doi: 10.1016/J.CONB.2006.10.007

Dickinson, P. S., Mecsas, C., and Marder, E. (1990). Neuropeptide fusion of two motor-pattern generator circuits. *Nature* 344, 155–158. doi: 10.1038/344155A0

Diehl, F., White, R. S., Stein, W., and Nusbaum, M. P. (2013). Motor circuit-specific burst patterns drive different muscle and behavior patterns. *J. Neurosci.* 33, 12013–12029. doi: 10.1523/JNEUROSCI.1060-13.2013

Disney, A. A., and Higley, M. J. (2020). Diverse spatiotemporal scales of cholinergic signaling in the neocortex. *J. Neurosci.* 40, 720–725. doi: 10.1523/JNEUROSCI.1306-19.2019

Eiden, L. E., Hernández, V. S., Jiang, S. Z., and Zhang, L. (2022). Neuropeptides and small-molecule amine transmitters: cooperative signaling in the nervous system. *Cell Mol. Life Sci.* 79:492. doi: 10.1007/S00018-022-04451-7

Esch, T., and Kristan, W. B. (2002). Decision-making in the leech nervous system. *Integr. Comp. Biol.* 42, 716–724.

Esch, T., Mesce, K. A., and Kristan, W. B. (2002). Evidence for sequential decision making in the medicinal leech. *J. Neurosci.* 22, 11045–11054. doi: 10.1523/JNEUROSCI.22-24-11045.2002

Evans, C. G., Barry, M. A., Jing, J., Perkins, M. H., Weiss, K. R., and Cropper, E. C. (2021). The complement of projection neurons activated determines the type of feeding motor program in *Aplysia*. *Front. Neural Circuits* 15:685222. doi: 10.3389/FNCIR.2021.685222

Fahoum, S. R. H., and Blitz, D. M. (2021). Neuronal switching between single- And dual-network activity *via* modulation of intrinsic membrane properties. *J. Neurosci.* 41, 7848–7863. doi: 10.1523/JNEUROSCI.0286-21.2021

Flaive, A., Fougère, M., van der Zouwen, C. I., and Ryczko, D. (2020). Serotonergic modulation of locomotor activity from basal vertebrates to mammals. *Front. Neural Circuits* 14:590299. doi: 10.3389/FNCIR.2020.590299

Flamm, R. E., and Harris-Warrick, R. M. (1986). Aminergic modulation in lobster stomatogastric ganglion. I. Effects on motor pattern and activity of neurons within the pyloric circuit. *J. Neurophysiol.* 55, 847–865. doi: 10.1152/JN.1986.55.5.847

Flood, T. F., Iguchi, S., Gorczyca, M., White, B., Ito, K., and Yoshihara, M. (2013). A single pair of interneurons commands the *Drosophila* feeding motor program. *Nature* 499, 83–87. doi: 10.1038/nature12208

Florman, J. T., and Alkema, M. J. (2022). Co-transmission of neuropeptides and monoamines choreograph the *C. elegans* escape response. *PLoS Genet.* 18:e1010091. doi: 10.1371/JOURNAL.PGEN.1010091

Follmann, R., Goldsmith, C. J., and Stein, W. (2018). Multimodal sensory information is represented by a combinatorial code in a sensorimotor system. *PLoS Biol.* 16:e2004527. doi: 10.1371/JOURNAL.PBIO.2004527

Garcia, A. J., Zanella, S., Koch, H., Doi, A., and Ramirez, J. M. (2011). Chapter 3–networks within networks: the neuronal control of breathing. *Prog. Brain Res.* 188, 31–50. doi: 10.1016/B978-0-444-53825-3.00008-5

Gillette, R., Kovac, M. P., and Davis, W. J. (1978). Command neurons in *Pleurobranchaea* receive synaptic feedback from the motor network they excite. *Science* 199, 798–801. doi: 10.1126/SCIENCE.622571

Guo, L., Zhang, N., and Simpson, J. H. (2022). Descending neurons coordinate anterior grooming behavior in *Drosophila*. *Curr. Biol.* 32, 823–833.e4. doi: 10.1016/J.CUB.2021.12.055

Harris-Warrick, R. M., and Marder, E. (1991). Modulation of neural networks for behavior. *Annu. Rev. Neurosci.* 14, 39–57. doi: 10.1146/ANNUREV.NE.14.030191.000351

Hedrich, U. B. S., Diehl, F., and Stein, W. (2011). Gastric and pyloric motor pattern control by a modulatory projection neuron in the intact crab *Cancer pagurus*. *J. Neurophysiol.* 105, 1671–1680. doi: 10.1152/JN.01105.2010

Hedrich, U. B. S., Smarandache, C. R., and Stein, W. (2009). Differential activation of projection neurons by two sensory pathways contributes to motor pattern selection. *J. Neurophysiol.* 102, 2866–2879. doi: 10.1152/jn.00618.2009

Heinrich, R. (2002). Impact of descending brain neurons on the control of stridulation, walking, and flight in orthoptera. *Microsc. Res. Tech.* 56, 292–301. doi: 10.1002/JEMT.10033

Herberholz, J. (2022). The giant escape neurons of crayfish: past discoveries and present opportunities. *Front. Physiol.* 13:1052354. doi: 10.3389/FPHYS.2022.1052354

Hooper, S. L., and Marder, E. (1984). Modulation of a central pattern generator by two neuropeptides, proctolin and FMRFamide. *Brain Res.* 305, 186–191. doi: 10.1016/0006-8993(84)91138-7

Horn, C. C., Benjamin, P. R., Weiss, K. R., and Kupfermann, I. (1999). Decrement of the response of a serotonergic modulatory neuron (the metacerebral cell) in *Aplysia*, during repeated presentation of appetitive (food) stimuli. *Neurosci. Lett.* 267, 161–164. doi: 10.1016/S0304-3940(99)00339-0

Hsu, C. T., and Bhandawat, V. (2016). Organization of descending neurons in *Drosophila melanogaster*. *Sci. Rep.* 6:20259. doi: 10.1038/SREP20259

Hurwitz, I., Susswein, A. J., and Weiss, K. R. (2005). Transforming tonic firing into a rhythmic output in the *Aplysia* feeding system: presynaptic inhibition of a command-like neuron by a CpG element. *J. Neurophysiol.* 93, 829–842. doi: 10.1152/JN.00559.2004

Jing, J., and Weiss, K. R. (2005). Generation of variants of a motor act in a modular and hierarchical motor network. *Curr. Biol.* 15, 1712–1721. doi: 10.1016/J.CUB.2005.08.051

Katz, P. S. (1998). Neuromodulation intrinsic to the central pattern generator for escape swimming in *Tritonia*. *Ann. N. Y. Acad. Sci.* 860, 181–188. doi: 10.1111/J.1749-6632.1998.TB09048.X

Katz, P. S., and Calin-Jageman, R. J. (2009). Neuromodulation. *Encycl. Neurosci.* 6, 497–503. doi: 10.1016/B978-008045046-9.01964-1

Katz, P. S., and Quinlan, P. D. (2019). The importance of identified neurons in gastropod molluscs to neuroscience. *Curr. Opin. Neurobiol.* 56, 1–7. doi: 10.1016/J.CONB.2018.10.009

Kim, L. H., Sharma, S., Sharples, S. A., Mayr, K. A., Kwok, C. H. T., and Whelan, P. J. (2017). Integration of descending command systems for the generation of context-specific locomotor behaviors. *Front. Neurosci.* 11:581. doi: 10.3389/FNINS.2017.00581

Koh, H. Y., Vilim, F. S., Jing, J., and Weiss, K. R. (2003). Two neuropeptides colocalized in a command-like neuron use distinct mechanisms to enhance its fast synaptic connection. *J. Neurophysiol.* 90, 2074–2079. doi: 10.1152/JN.00358.2003

Kozlov, A. K., Kardamakis, A. A., Kotaleski, J. H., and Grillner, S. (2014). Gating of steering signals through phasic modulation of reticulospinal neurons during locomotion. *Proc. Natl. Acad. Sci. U. S. A.* 111, 3591–3596. doi: 10.1073/PNAS.1401459111

Kristan, W. B., Calabrese, R. L., and Friesen, W. O. (2005). Neuronal control of leech behavior. *Prog. Neurobiol.* 76, 279–327. doi: 10.1016/J.PNEUROBIO.2005.09.004

Kristan, W. B., and Shaw, B. K. (1997). Population coding and behavioral choice. *Curr. Opin. Neurobiol.* 7, 826–831. doi: 10.1016/S0959-4388(97)80142-0

Kueh, D., and Jellies, J. A. (2012). Targeting a neuropeptide to discrete regions of the motor arborizations of a single neuron. *J. Exp. Biol.* 215, 2108–2116. doi: 10.1242/JEB.067603

Kuhlman, J. R., Li, C., and Calabrese, R. L. (1985). FMRF-amide-like substances in the leech. II. Bioactivity on the heartbeat system. *J. Neurosci.* 5, 2310–2317. doi: 10.1523/JNEUROSCI.05-09-02310.1985

Kupfermann, I., and Weiss, K. R. (2001). Motor program selection in simple model systems. *Curr. Opin. Neurobiol.* 11, 673–677. doi: 10.1016/S0959-4388(01)00267-7

Kwiatkowski, M. A., Gabranski, E. R., Huber, K. E., Chapline, M. C., Christie, A. E., and Dickinson, P. S. (2013). Coordination of distinct but interacting rhythmic

motor programs by a modulatory projection neuron using different co-transmitters in different ganglia. *J. Exp. Biol.* 216, 1827–1836. doi: 10.1242/JEB.082503

Leiras, R., Cregg, J. M., and Kiehn, O. (2022). Brainstem circuits for locomotion. *Annu. Rev. Neurosci.* 45, 63–85. doi: 10.1146/ANNUREV-NEURO-082321-025137

Liu, C., Goel, P., and Kaeser, P. S. (2021). Spatial and temporal scales of dopamine transmission. *Nat. Rev. Neurosci.* 22, 345–358. doi: 10.1038/S41583-021-00455-7

Marder, E. (2012). Neuromodulation of neuronal circuits: back to the future. *Neuron* 76, 1–11. doi: 10.1016/j.neuron.2012.09.010

Marder, E., and Bucher, D. (2007). Understanding circuit dynamics using the stomatogastric nervous system of lobsters and crabs. *Ann. Rev. Physiol.* 69, 291–316. doi: 10.1146/annurev.physiol.69.031905.161516

Marder, E., Gutierrez, G. J., and Nusbaum, M. P. (2017). Complicating connectomes: electrical coupling creates parallel pathways and degenerate circuit mechanisms. *Dev. Neurobiol.* 77, 597–609. doi: 10.1002/DNEU.22410

Marder, E., Kedia, S., and Morozova, E. O. (2022). New insights from small rhythmic circuits. *Curr. Opin. Neurobiol.* 76:102610. doi: 10.1016/J.CONB.2022.102610

McKellar, C. E., Lillvis, J. L., Bath, D. E., Fitzgerald, J. E., Cannon, J. G., Simpson, J. H., et al. (2019). Threshold-Based ordering of sequential actions during *Drosophila* courtship. *Curr. Biol.* 29, 426–434.e6. doi: 10.1016/J.CUB.2018.12.019

Mesce, K. A., Esch, T., and Kristan, W. B. (2008). Cellular substrates of action selection: a cluster of higher-order descending neurons shapes body posture and locomotion. *J. Comp. Physiol. A Neuroethol. Sens Neural Behav. Physiol.* 194, 469–481. doi: 10.1007/S00359-008-0319-1

Mesce, K. A., and Pierce-Shimomura, J. T. (2010). Shared strategies for behavioral switching: understanding how locomotor patterns are turned on and off. *Front. Behav. Neurosci.* 4:49. doi: 10.3389/FNBEH.2010.00049

Meyrand, P., Faumont, S., Simmers, J., Christie, A. E., and Nusbaum, M. P. (2000). Species-specific modulation of pattern-Generating circuits. *Eur. J. Neurosci.* 12, 2585–2596. doi: 10.1046/J.1460-9568.2000.00121.X

Nadim, F., and Bucher, D. (2014). Neuromodulation of neurons and synapses. *Curr. Opin. Neurobiol.* 29, 48–56. doi: 10.1016/j.conb.2014.05.003

Namiki, S., Dickinson, M. H., Wong, A. M., Korff, W., and Card, G. M. (2018). The functional organization of descending sensory-motor pathways in Drosophila. *Elife* 7:e34272. doi: 10.7554/ELIFE.34272

Nässel, D. R. (2009). Neuropeptide signaling near and far: how localized and timed is the action of neuropeptides in brain circuits? *Invert Neurosci.* 9, 57–75. doi: 10.1007/S10158-009-0090-1

Nässel, D. R. (2018). Substrates for neuronal cotransmission with neuropeptides and small molecule neurotransmitters in drosophila. *Front Cell Neurosci.* 12:83. doi: 10.3389/FNCEL.2018.00083/BIBTEX

Nässel, D. R., and Zandawala, M. (2022). Endocrine cybernetics: neuropeptides as molecular switches in behavioural decisions. *Open Biol.* 12:220174. doi: 10.1098/RSOB.220174

Norris, B. J., Coleman, M. J., and Nusbaum, M. P. (1994). Recruitment of a projection neuron determines gastric mill motor pattern selection in the stomatogastric nervous system of the crab, *Cancer borealis*. *J. Neurophysiol.* 72, 1451–1463. doi: 10.1152/JN.1994.72.4.1451

Norris, B. J., Coleman, M. J., and Nusbaum, M. P. (1996). Pyloric motor pattern modification by a newly identified projection neuron in the crab stomatogastric nervous system. *J. Neurophysiol.* 75, 97–108. doi: 10.1152/JN.1996.75.1.97

Northcutt, A. J., Fischer, E. K., Puhl, J. G., Mesce, K. A., and Schulz, D. J. (2018). An annotated CNS transcriptome of the medicinal leech, *Hirudo verbana*: De novo sequencing to characterize genes associated with nervous system activity. *PLoS One* 13:e0201206. doi: 10.1371/JOURNAL.PONE.0201206

Northcutt, A. J., Kick, D. R., Otopalik, A. G., Goetz, B. M., Harris, R. M., Santin, J. M., et al. (2019). Molecular profiling of single neurons of known identity in two ganglia from the crab *Cancer borealis*. *Proc. Natl. Acad. Sci. U. S. A.* 116, 26980–26990. doi: 10.1073/PNAS.1911413116

Nusbaum, M. P. (1994). Presynaptic control of neurones in pattern-generating networks. *Curr. Opin. Neurobiol.* 4, 909–914.

Nusbaum, M. P. (2002). Regulating peptidergic modulation of rhythmically active neural circuits. *Brain Behav. Evol.* 60, 378–387. doi: 10.1159/000067791

Nusbaum, M. P. (2008). "Modulatory projection neurons," in *Encyclopedia of Neuroscience*, eds M. D. Binder, N. Hirokawa and U. Windhorst (Berlin: Springer), 2385–2388. doi: 10.1007/978-3-540-29678-2_3538

Nusbaum, M. P., Blitz, D. M., and Marder, E. (2017). Functional consequences of neuropeptide and small-molecule co-transmission. *Nat. Rev. Neurosci.* 18, 389–403. doi: 10.1038/nrn.2017.56

Nusbaum, M. P., and Marder, E. (1989a). A modulatory proctolin-containing neuron (MPN). I. Identification and characterization. *J. Neurosci.* 9, 1591–1599. doi: 10.1523/JNEUROSCI.09-05-01591.1989

Nusbaum, M. P., and Marder, E. (1989b). A modulatory proctolin-containing neuron (MPN). II. State-dependent modulation of rhythmic motor activity. *J. Neurosci.* 9, 1600–1607. doi: 10.1523/JNEUROSCI.09-05-01600.1989

Nusbaum, M. P., Weimann, J. M., Golowasch, J., and Marder, E. (1992). Presynaptic control of modulatory fibers by their neural network targets. *J. Neurosci.* 12, 2706–2714. doi: 10.1523/JNEUROSCI.12-07-02706.1992

Perrins, R., and Weiss, K. R. (1998). Compartmentalization of information processing in an *Aplysia* feeding circuit interneuron through membrane properties and synaptic interactions. *J. Neurosci.* 18, 3977–3989. doi: 10.1523/JNEUROSCI.18-10-03977.1998

Pirger, Z., László, Z., Naskar, S., Crossley, M., O'Shea, M., Benjamin, P. R., et al. (2021). Interneuronal mechanisms for learning-induced switch in a sensory response that anticipates changes in behavioral outcomes. *Curr. Biol.* 31, 1754–1761.e3. doi: 10.1016/J.CUB.2021.01.072

Puhl, J. G., Masino, M. A., and Mesce, K. A. (2012). Necessary, sufficient and permissive: a single locomotor command neuron important for intersegmental coordination. *J. Neurosci.* 32, 17646–17657. doi: 10.1523/JNEUROSCI.2249-12.2012

Ramirez, J. M., and Pearson, K. G. (1991). Octopaminergic modulation of interneurons in the flight system of the locust. *J. Neurophysiol.* 66, 1522–1537. doi: 10.1152/JN.1991.66.5.1522

Rosen, S. C., Teyke, T., Miller, M. W., Weiss, K. R., and Kupfermann, I. (1991). Identification and characterization of cerebral-to-buccal interneurons implicated in the control of motor programs associated with feeding in *Aplysia*. *J. Neurosci.* 11, 3630–3655. doi: 10.1523/JNEUROSCI.11-11-03630.1991

Ruder, L., and Arber, S. (2019). Brainstem circuits controlling action diversification. *Annu. Rev. Neurosci.* 42, 485–504. doi: 10.1146/ANNUREV-NEURO-070918-050201

Sakurai, A., and Katz, P. S. (2019). Command or Obey? Homologous neurons differ in hierarchical position for the generation of homologous behaviors. *J. Neurosci.* 39, 6460–6471. doi: 10.1523/JNEUROSCI.3229-18.2019

Schlegel, P., Texada, M. J., Miroschnikow, A., Schoofs, A., Hückesfeld, S., Peters, M., et al. (2016). Synaptic transmission parallels neuromodulation in a central food-intake circuit. *Elife* 5:e16799. doi: 10.7554/ELIFE.16799

Sharples, S. A., Koblinger, K., Humphreys, J. M., and Whelan, P. J. (2014). Dopamine: a parallel pathway for the modulation of spinal locomotor networks. *Front. Neural Circuits* 8:55. doi: 10.3389/FNCIR.2014.00055

Snyder, R. R., and Blitz, D. M. (2022). Multiple intrinsic membrane properties are modulated in a switch from single- to dual-network activity. *J. Neurophysiol.* 128, 1181–1198. doi: 10.1152/JN.00337.2022

Spencer, R. M., and Blitz, D. M. (2016). Network feedback regulates motor output across a range of modulatory neuron activity. *J. Neurophysiol.* 115, 3249–3263. doi: 10.1152/jn.01112.2015

Staudacher, E. M. (2001). Sensory responses of descending brain neurons in the walking cricket, *Gryllus bimaculatus*. *J. Comp. Physiol. A* 187, 1–17. doi: 10.1007/S003590000171

Stein, W. (2009). Modulation of stomatogastric rhythms. *J. Comp. Physiol. A Neuroethol. Sens. Neural Behav. Physiol.* 195, 989–1009. doi: 10.1007/S00359-009-0483-Y

Stein, W., DeLong, N. D., Wood, D. E., and Nusbaum, M. P. (2007). Divergent co-transmitter actions underlie motor pattern activation by a modulatory projection neuron. *Eur. J. Neurosci.* 26, 1148–1165. doi: 10.1111/j.1460-9568.2007.05744.x

Stolz, T., Diesner, M., Neupert, S., Hess, M. E., Delgado-Betancourt, E., Pflüger, H. J., et al. (2019). Descending octopaminergic neurons modulate sensory-evoked activity of thoracic motor neurons in stick insects. *J. Neurophysiol.* 122, 2388–2413. doi: 10.1152/JN.00196.2019

Svensson, E., Apergis-Schoute, J., Burnstock, G., Nusbaum, M. P., Parker, D., and Schiöth, H. B. (2019). General principles of neuronal co-transmission: insights from multiple model systems. *Front. Neural Circuits* 12:117. doi: 10.3389/fncir.2018.00117

Swensen, A. M., Golowasch, J., Christie, A. E., Coleman, M. J., Nusbaum, M. P., and Marder, E. (2000). GABA and responses to GABA in the stomatogastric ganglion of the crab *Cancer borealis*. *J. Exp. Biol.* 203, 2075–2092. doi: 10.1242/JEB.203.14.2075

Thirumalai, V., and Marder, E. (2002). Colocalized neuropeptides activate a central pattern generator by acting on different circuit targets. *J. Neurosci.* 22, 1874–1882. doi: 10.1523/JNEUROSCI.22-05-01874.2002

Trudeau, L. E., and El Mestikawy, S. (2018). Glutamate cotransmission in cholinergic, GABAergic and monoamine systems: contrasts and commonalities. *Front. Neural Circuits* 12:113. doi: 10.3389/FNCIR.2018.00113/BIBTEX

White, R. S., and Nusbaum, M. P. (2011). The same core rhythm generator underlies different rhythmic motor patterns. *J. Neurosci.* 31, 11484–11494. doi: 10.1523/JNEUROSCI.1885-11.2011

White, R. S., Spencer, R. M., Nusbaum, M. P., and Blitz, D. M. (2017). State-dependent sensorimotor gating in a rhythmic motor system. *J. Neurophysiol.* 118, 2806–2818. doi: 10.1152/jn.00420.2017

Willard, A. L. (1981). Effects of serotonin on the generation of the motor program for swimming by the medicinal leech. *J. Neurosci.* 1, 936–944. doi: 10.1523/JNEUROSCI.01-09-00936.1981

Wood, D. E., Manor, Y., Nadim, F., and Nusbaum, M. P. (2004). Intercircuit control *via* rhythmic regulation of projection neuron activity. *J. Neurosci.* 24, 7455–7463. doi: 10.1523/JNEUROSCI.1840-04.2004

Wood, D. E., and Nusbaum, M. P. (2002). Extracellular peptidase activity tunes motor pattern modulation. *J. Neurosci.* 22, 4185–4195. doi: 10.1523/jneurosci.22-10-04185.2002

Wu, J. S., Wang, N., Siniscalchi, M. J., Perkins, M. H., Zheng, Y. T., Yu, W., et al. (2014). Complementary interactions between command-like interneurons that function to activate and specify motor programs. *J. Neurosci.* 34, 6510–6521. doi: 10.1523/JNEUROSCI.5094-13.2014

Yang, C. F., Kim, E. J., Callaway, E. M., and Feldman, J. L. (2020). Monosynaptic projections to excitatory and inhibitory prebötzinger complex neurons. *Front. Neuroanat.* 14:58. doi: 10.3389/FNANA.2020.00058

Zhang, G., Yuan, W. D., Vilim, F. S., Romanova, E. V., Yu, K., Yin, S. Y., et al. (2018). Newly identified Aplysia SPTR-gene family-derived peptides: localization and function. *ACS Chem. Neurosci.* 9, 2041–2053. doi: 10.1021/ACSCHEMNEURO.7B00513

frontiers | Frontiers in Neuroscience

TYPE Original Research
PUBLISHED 22 March 2023
DOI 10.3389/fnins.2023.1125433

OPEN ACCESS

EDITED BY
James Newcomb,
New England College, United States

REVIEWED BY
Thibaut Brunet,
Pasteur Institute, France
Josean Reyes-Rivera,
Pasteur Institute, France, in collaboration with reviewer TB
Rhanor Gillette,
University of Illinois Urbana-Champaign, United States

*CORRESPONDENCE
Leonid L. Moroz
✉ moroz@whitney.ufl.edu

SPECIALTY SECTION
This article was submitted to Neural Technology, a section of the journal Frontiers in Neuroscience

RECEIVED 16 December 2022
ACCEPTED 27 February 2023
PUBLISHED 22 March 2023

CITATION
Moroz LL, Mukherjee K and Romanova DY (2023) Nitric oxide signaling in ctenophores. *Front. Neurosci.* 17:1125433. doi: 10.3389/fnins.2023.1125433

Nitric oxide signaling in ctenophores

Leonid L. Moroz [1,2]*, Krishanu Mukherjee[2] and Daria Y. Romanova[3]

[1]Department of Neuroscience, McKnight Brain Institute, University of Florida, Gainesville, FL, United States, [2]The Whitney Laboratory for Marine Bioscience, University of Florida, St. Augustine, FL, United States, [3]Institute of Higher Nervous Activity and Neurophysiology of RAS, Moscow, Russia

Nitric oxide (NO) is one of the most ancient and versatile signal molecules across all domains of life. NO signaling might also play an essential role in the origin of animal organization. Yet, practically nothing is known about the distribution and functions of NO-dependent signaling pathways in representatives of early branching metazoans such as Ctenophora. Here, we explore the presence and organization of NO signaling components using *Mnemiopsis* and kin as essential reference species. We show that NO synthase (NOS) is present in at least eight ctenophore species, including *Euplokamis* and *Coeloplana*, representing the most basal ctenophore lineages. However, NOS could be secondarily lost in many other ctenophores, including *Pleurobrachia* and *Beroe*. In *Mnemiopsis leidyi*, NOS is present both in adult tissues and differentially expressed in later embryonic stages suggesting the involvement of NO in developmental mechanisms. Ctenophores also possess soluble guanylyl cyclases as potential NO receptors with weak but differential expression across tissues. Combined, these data indicate that the canonical NO-cGMP signaling pathways existed in the common ancestor of animals and could be involved in the control of morphogenesis, cilia activities, feeding and different behaviors.

KEYWORDS

***Mnemiopsis*, Ctenophora, nitric oxide synthase, guanylate cyclase, *Pleurobrachia*, nervous system evolution, Porifera, Placozoa**

Introduction

A free radical gas, nitric oxide (NO), is an evolutionary old and versatile signal molecule with a widespread distribution across all domains of life (Feelisch and Martin, 1995; Moroz and Kohn, 2011; Shepherd et al., 2022). NO can be synthesized by numerous non-enzymatic pathways (Moroz and Kohn, 2011) and enzymatically as parts of the nitrogen cycle and by NO synthases (NOS). NOSs were identified both in prokaryotes and eukaryotes. All NOSs catalyze the oxidation of L-arginine by molecular oxygen with several co-factors required for electron transfer from NADPH *via* FMN in the reductase domain to heme-/biopterin binding sites of the N-terminal oxygenase domain (Stuehr and Haque, 2019). Prokaryotic NOSs are usually truncated, often without the reductase part, and might contain additional subdomains (e.g., globin-like). Animal NOSs always have Ca^{2+}/calmodulin-binding domains that tightly control the electron transport and NO yield in response to environmental stimuli (Stuehr and Haque, 2019).

Eukaryotic type NOS was recently discovered in *Salpingoeca infusionum*, the representative of Choanoflagellata (Reyes-Rivera et al., 2022) – the sister group to Metazoa. In another choanoflagellate *Choanoeca flexa*, with prokaryotic-type NOS, NO application

induced contractions of colonies, providing a shift from feeding to swimming behaviors. Such an effect can be mediated by soluble guanylate cyclase (sGC), as in animals (Reyes-Rivera et al., 2022). These data and the presence of NOS in other eukaryotes suggest that the common ancestor of all animals might possess NOS-sGC signaling pathways. However, little is known about the distribution and functions of NO-mediated (nitrergic) signaling in early branching metazoans (Colasanti et al., 2010).

There are five major animal clades: Bilateria, Cnidaria, Placozoa, Porifera (sponges), and Ctenophora (comb jellies). The last four groups represent the earliest branching animal lineages, separated from Bilaterians more than 550 million years ago. These non-bilaterians are remarkably different in their bodyplans and tissue organizations. As a result, they are crucial to reconstruct the evolution and overall architecture of animal signaling pathways, including NO-dependent transmission. Yet only several papers deal with NO biology in Cnidaria and Porifera; and one publication discusses NO synthesis in placozoans (Moroz et al., 2020).

Ca-dependent and heat-stress-induced NO synthesis was reported in two species of desmosponges, *Axinella polypoides* and *Petrosia ficiformis* (Giovine et al., 2001). NADPH diaphorase histochemistry [a marker for NOS (Bredt et al., 1991; Moroz, 2000a)] showed specific localization of NOS activity in a particular network of dendritic cells in the sponge parenchyma (Giovine et al., 2001), but with unknown functions.

NO, and NOS control metamorphosis and symbiotic relationships in the desmosponge *Amphimedon* (Ueda et al., 2016; Hewitt and Degnan, 2022). There is growing evidence that NO can modulate body contractions and coordinated behaviors in freshwater sponges *Ephydatia muelleri* (Elliott and Leys, 2010), *Spongilla lacustris* (Musser et al., 2021), and the marine sponge *Tethya wilhelma* (Ellwanger and Nickel, 2006).

Similarly to sponges, NO signaling was implemented in cnidarian-algal symbioses (Perez and Weis, 2006; Safavi-Hemami et al., 2010; Hawkins and Davy, 2013), coral bleaching (Bouchard and Yamasaki, 2008), and apoptosis (Hawkins et al., 2013). In the hydroid polyp *Hydra*, non-neuronal NO/NOS is associated with regeneration (Colasanti et al., 2009) and feeding (Colasanti et al., 1995). Specific nitrergic neurons have been identified in tentacles of the hydromedusa *Aglantha digitale*, where the NO/cGMP pathway modulates the rhythmic swimming associated with feeding (Moroz et al., 2004). Multiples isoforms of NOSs present in the majority of sequenced cnidarian genomes, with evidence of endogenous enzymatic NO synthesis in this lineage (Morrall et al., 2000; Moroz et al., 2004; Kass-Simon and Pierobon, 2007; Cristino et al., 2008; Anctil, 2009; Colasanti et al., 2010).

The overall logic of NO signaling in early animals is still elusive. Nevertheless, both in sponges and cnidarians, we might expect tightly coupled interplays of morphogenic and behavioral functions mediated by NO, inherently linked to the ancestral feeding modes and innate immunity (Moroz, 2000b, 2001). Scattered comparative data point out that the volume transmission mediated by NO in nervous systems was a relatively later innovation in evolution, (Moroz et al., 2021). Unfortunately, no data are available about NOSs and NO signaling in ctenophores or comb-jellies with well-developed neuro-muscular organization across species (Norekian and Moroz, 2016, 2019a,b, 2020, 2021).

Ctenophora is one of the earliest branching lineages of metazoans with complex tissue and organ differentiations. All extant ctenophore species have well-developed neuronal and muscular systems, which might co-evolve independently (Moroz, 2015). The recently proposed most basal position of ctenophores (as the sister group to all other animals) is still highly debated (Whelan et al., 2015, 2017; Halanych et al., 2016; Telford et al., 2016; Laumer et al., 2019; Fernandez and Gabaldon, 2020; Kapli and Telford, 2020; Li et al., 2021; Redmond and McLysaght, 2021; Giacomelli et al., 2022). Nevertheless, the presence or absence of specific signaling pathways in the ctenophore lineage reshapes our general understanding of neuronal and animal evolution. NOS was not detected in the sequenced genome of *Pleurobrachia bachei* (Moroz et al., 2014), but we found a putative NOS in *Mnemiopsis leidyi* (Moroz and Kohn, 2016) by screening its sequenced genome (Moreland et al., 2020). Here, we further explore the presence and organization of NO signaling components using *Mnemiopsis* as essential reference species (Moreland et al., 2020).

Results and discussion

NOS phylogeny and derived NOS in ctenophores

Figure 1 shows the phyletic relationships among basal metazoan NOSs and several eukaryotic (e.g., Amoebozoa [*Physarum*], Fungi [*Aspergillus* and kin], and Ichthyosporea [*Sphaeroforma arctica*]) and prokaryotic outgroups. This tree confirms a highly derived nature of NOS in ctenophores, probably reflecting their accelerated evolution and a possible bottleneck in their paleontological history around the Permian extinction (Whelan et al., 2017). The tree also highlights several independent radiation events with duplication and triplication of NOSs in lineages leading to placozoans, cnidarians, and vertebrates [see also (Moroz et al., 2020)]. However, representative species from both Porifera and Ctenophora have only one NOS gene.

In addition to the sequenced ctenophore genomes (*Pleurobrachia bachei* and *Mnemiopsis leidyi*), we analyzed transcriptomes from 37 ctenophore species (Whelan et al., 2017). NOSs were found only in eight ctenophores, including six representatives of Lobata: *Mnemiopsis leidyi*, undescribed species of *Mnemiopsis* sp., and their sister species *Bolinopsis infundibulum* [the family Bolinopsidae], the venus girdle, *Cestum veneris* [Cestidae], *Ocyropsis crystallina* [Ocyropsidae], *Lobatolampea tetragona* [Lobatolampeidae]. Most interesting, NOS was found in *Euplokamis dunlapae* [Euplokamididae] and the benthic ctenophore *Coeloplana astericola* [Platyctenida, Coeloplanidae] – representatives of the first and second earliest branching lineages within the phylum Ctenophora (Moroz et al., 2014). In contrast, *Bolinopsis*, *Mnemiopsis, Cestum, Ocyropsis, Lobatolampea* belong to separate branches within a highly derived (and possibly polyphyletic) clade of Lobata (Whelan et al., 2017).

NOS-type sequences were not identified in more than two dozen transcriptomes from adult tissues and different developmental stages from *Pleurobrachia*. Moreover, NOS was not found in the recently sequenced genome of a closely related species *Hormiphora californica* [Pleurobrachiidae] (Schultz et al., 2021). These data suggest that the majority of sequenced so far ctenophore lineages (including Cydippida and Beroida) lost NOS

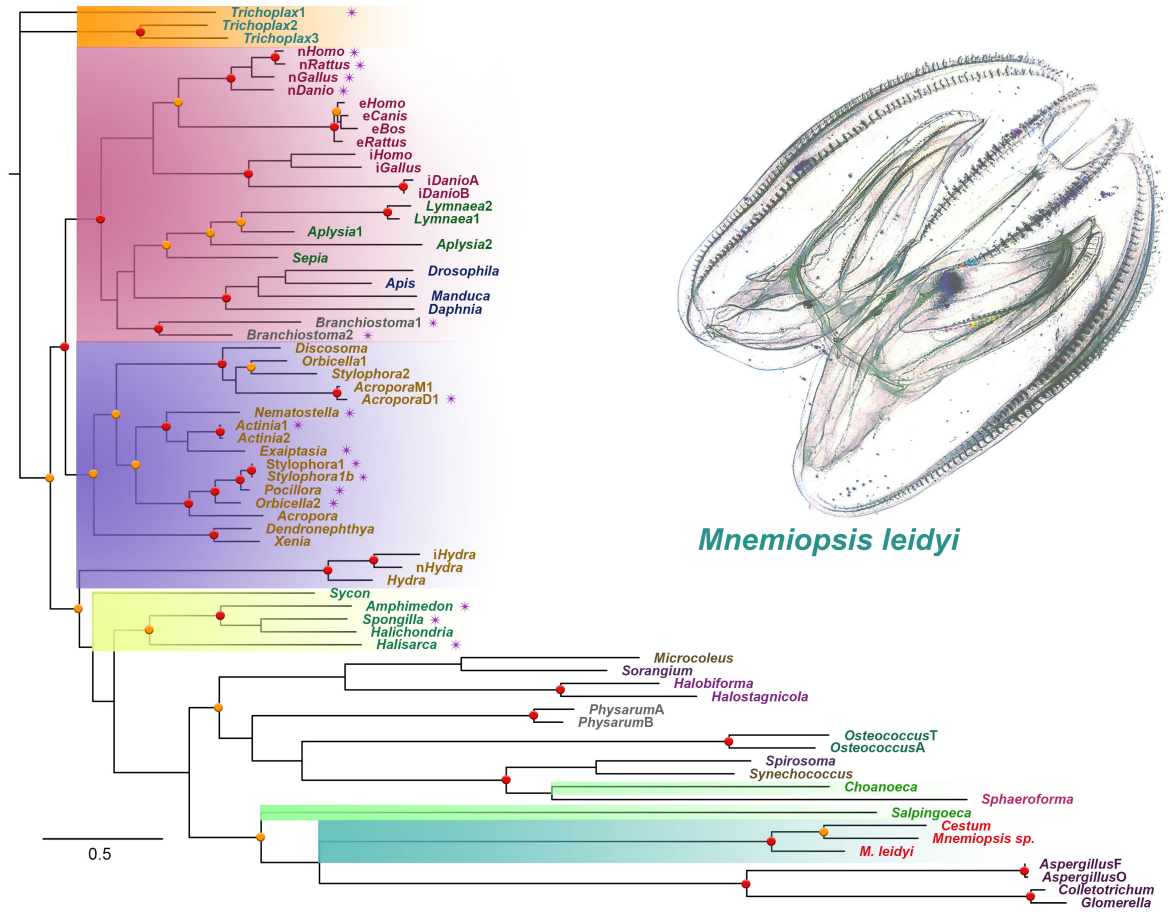

FIGURE 1
The phylogenetic tree of nitric oxide synthases (NOS) across different taxa, focusing on representative metazoan clades (ML analysis). Major taxons are highlighted: Ctenophora – aquamarine; Porifera – yellow; Placozoa – orange; Cnidaria – blue; Vertebrata/Bilateria – red; Choanoflagellata – bright green. The presence of PDZ domains is marked as purple stars near the species names. Bootstraps: red (90–100%) and orange (80–89%) dots.

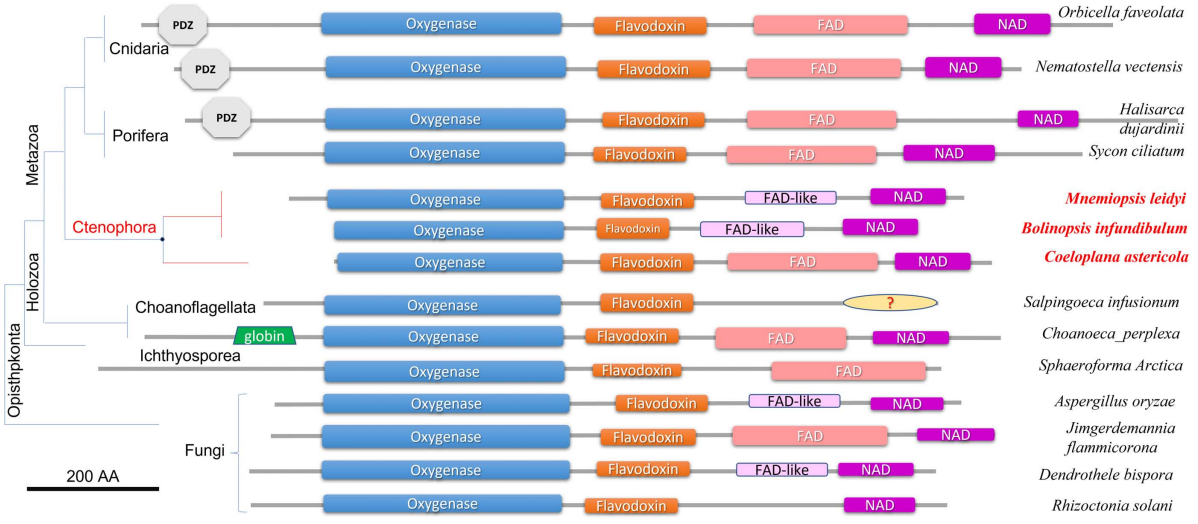

FIGURE 2
Domain organization of NOSs across eukaryotic phyla. All NOS are presented on the same scale, including the sizes of all domains and proteins. NOS oxygenase domain (Pfam NO_Synthase PF02898); Flavodoxin_1 (Pfam PF00258); FAD_binding_1 domain (Pfam PF00667); NAD_binding_1 (Pfam PF00175). NOSs include representatives of 3 metazoan phyla and 3 non-metazoan lineages with their respective phylogenetic relationships and species names. The references for each particular gene and/or their sequences with relevant GeneBank accession numbers are summarized in the Supplementary Table 1.

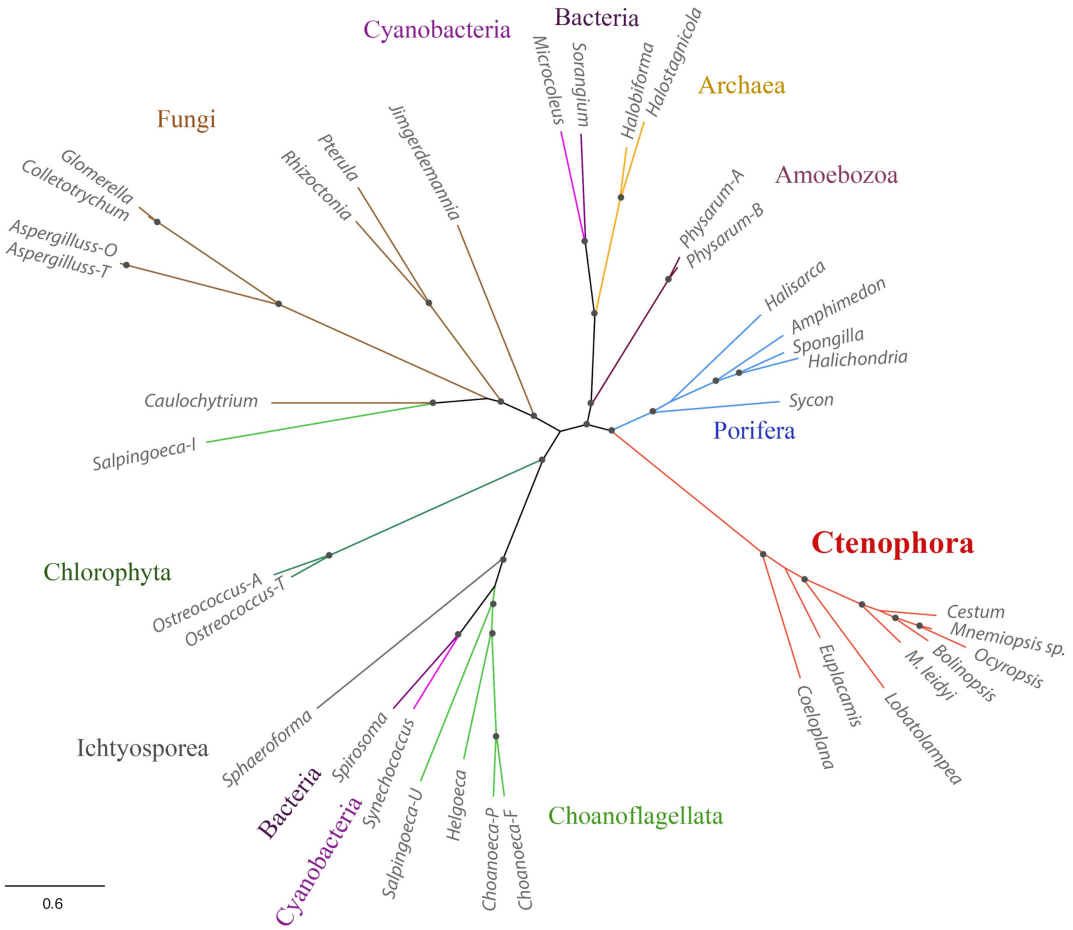

FIGURE 3
Phylogenetic relationships of NOSs in ctenophores, sponges, non-metazoan eukaryotes, and prokaryotes. The references for each particular gene and/or their sequences with relevant GeneBank accession numbers are summarized in the Supplementary Table 1.

from their common ancestors. This apparently massive loss of NOS in many representatives of Ctenophora is quite unusual compared to other phyla. For example, NOS was lost in some nematodes such as *C. elegans*, but for most animal lineages, NOS genes are well-preserved, despite enormous ecological and morphological diversifications.

Domain organization of NOS in ctenophores

Figure 2 illustrates the domain organization of NOS across species. The *Coeloplana*, *Bolinopsis,* and *Mnemiopsis* NOSs revealed the canonical basal domain architecture of this class of enzymes (Figure 2). At the same time, sequences from other ctenophore species were represented mainly by the oxygenase domain and were incomplete genes, which the nature of transcriptome datasets can explain. Thus, we used *M. leidyi* NOS (ML074215a) as the reference sequence for these types of enzymes in ctenophores.

At least three features distinguish ctenophore NOSs from many other species. First, both in *Bolinopsis* and its sister species *Mnemiopsis*, a critical for NOS function FAD domain is either highly derived or might need to be better recognized. Still, their NOSs perfectly preserved NAD-binding sites (Figure 2). With this architecture NOSs from *Bolinopsis* and *Mnemiopsis* are similar to eukaryotic NOSs from the choanoflagellate *Salpingoeca infusionum*, and some fungi such as *Aspergillus* (Ascomycota) and *Dendrothele* (Basidiomycota). Highly modified or derived FAD-binding domains in these species might affect complex or unusual electron transport mechanisms from NADPH to heme in NOS (Stuehr and Haque, 2019). Yet, such FAD-related ctenophore modifications are likely secondarily derived. The canonical FAD-binding region is well-conserved in the benthic ctenophore *Coeloplana* (Figure 2), which probably represents the ancestral condition for ctenophore NOSs.

Second, *Mnemiopsis leidyi* NOS lacks the PDZ domain, found in many NOSs from poriferans (desmosponges *Halisarca*, *Spongilla,* and *Amphimedon*, but not from the calcareous sponge *Sycon ciliatum*), Placozoa (*Trichoplax*), cnidarians (corals, sea anemones), and bilaterians/chordates (Figures 1, 2). PDZ domain is best studied in mammals and is responsible for anchoring neuronal NOSs in specific membrane compartments and protein complexes, facilitating more localized and spatial control of NO release and signaling in synapses (Brenman et al., 1996; Stricker et al., 1997; Jaffrey et al., 1998; Kim and Sheng, 2004;

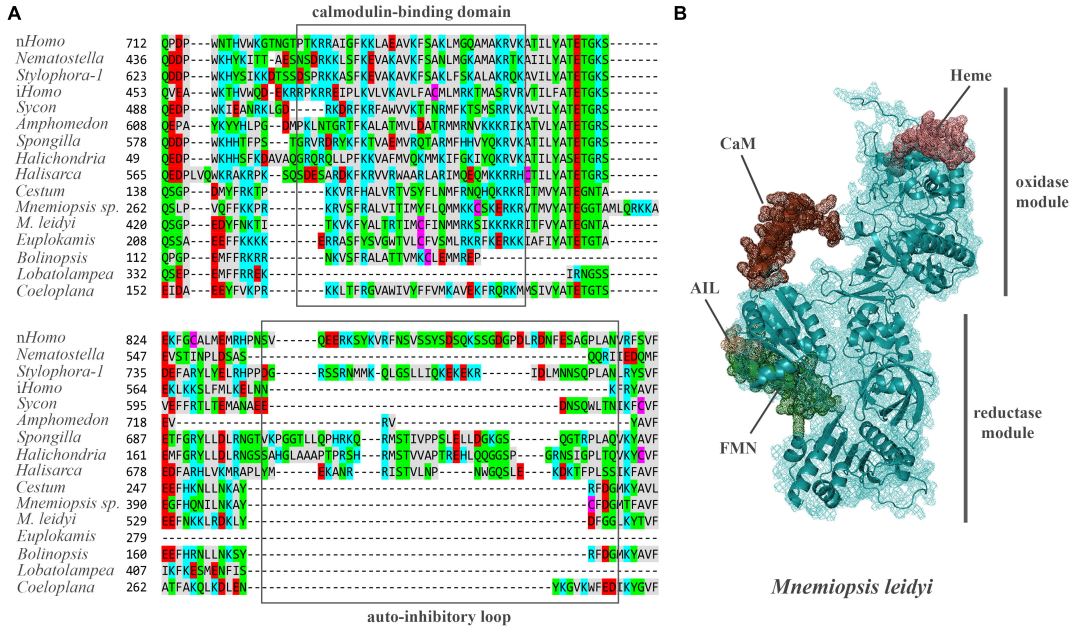

FIGURE 4
(A) The structure of auto-inhibitory loop and calmodulin-binding domains in NOSs. Amino acids (aa) are highlighted with different colors: red – polar negative charged aa; blue – polar positive charged aa; purple – cysteines; gray – hydrophobic aa; green – uncharged polar aa. **(B)** The predicted 3D structure of the NOS from *Mnemiopsis leidyi* with critical functional domains. Calmodulin (CaM) binding – brown, FMN – green, AIL – beige. The **Supplementary Table 1** summarizes the references for each particular gene and/or their sequences with relevant GeneBank accession numbers.

Feng and Zhang, 2009; Sheng et al., 2018; Murciano-Calles et al., 2020). Of note, PDZ NOSs were not found in non-metazoan eukaryotes and prokaryotes and can be viewed as animal innovation coupled with their morphological and signaling complexities.

Third, *Mnemiopsis leidyi* NOS is shorter or truncated than known cnidarian, poriferan, and placozoans NOSs. In this case, it is also superficially similar to non-metazoan NOSs. Yet ctenophore NOSs make a highly derived branch on the phylogenetic trees with different representations of species (**Figures 1**, **3**), suggesting an accelerated evolution within this group. A similar situation is also observed for choanoflagellates. Most choanoflagellate species apparently lose their NOSs from their common ancestor. The eukaryotic type of NOS is only preserved in one species, *Salpingoeca infusionum*, which is clustered with fungal NOSs (**Figure 3**) and lack some evolutionarily conserved regions, such as FAD- and NAD-binding (**Figure 2**). Other four choanoflagellate species had prokaryotic-type NOS [see (Reyes-Rivera et al., 2022) and **Figures 2**, **3**]; these NOS might be results of a horizontal gene transfer from cyanobacteria.

Mnemiopsis leidyi NOS (ML074215a) has a recognized Ca/Calmodulin-binding region coupling oxygenase and reductase domains as in all animal NOSs (**Figure 4**, see **Supplementary material** for alignment), suggesting calcium-calmodulin dependence. In mammals, transient activation of NOS by intracellular Ca^{2+} is controlled by the auto-inhibitory loop/inserts (Roman and Masters, 2006; Stuehr and Haque, 2019), without sequence similarities in neuronal and endothelial isoforms. In contrast, inducible Ca-independent NOS lacks this sequence motif (**Figure 4A**). Thus, activation of its expression is induced by bacterial liposaccharides as a component of the innate immune defense mechanisms. Interestingly, ctenophore NOSs also lack the autoinhibitory loops (**Figure 4A**), and their Ca-dependence, enzymology, and expression control must be experimentally characterized. Ca-dependences of NOS in sponges and cnidarians are also unknown. However, both poriferan and cnidarian NOSs show more remarkable overall sequence similarities with their bilaterian homologs.

Of note, we also found bacterial types of NOS in the *Mnemiopsis* microbiome (Mariita et al., 2021), suggesting both endogenous and exogenous sources of NO in ctenophores (e.g., from food or symbionts).

Soluble guanylyl cyclases as putative receptors of NO in ctenophores

As a free radical gas, NO can interact with most biological molecules, primarily targeting SH and tyrosine groups (Holguín-Peña et al., 2007). However, in animals including cnidarians, placozoans, and sponges, NO can specifically activate soluble guanylyl cyclases [sGC, members of the adenylate cyclase superfamily (Gancedo, 2013; Bassler et al., 2018)] by binding to its heme group, which leads to conformational changes and increase of cGMP synthesis (Krumenacker et al., 2004; Martin et al., 2005; Windsor and Thompson, 2008; Gunn et al., 2012; Montfort et al., 2017; Horst and Marletta, 2018; Horst et al., 2019; Kang et al., 2019). Three orthogroups of sGCs are present in humans.

The *Mnemiopsis* and *Pleurobrachia* genomes encode four and two sGCs, respectively (**Figure 5** and **Supplementary Figure 1**). These enzymes have the canonical heme NO binding domain and associated cyclase domain. Moreover, we also identified sGCs in

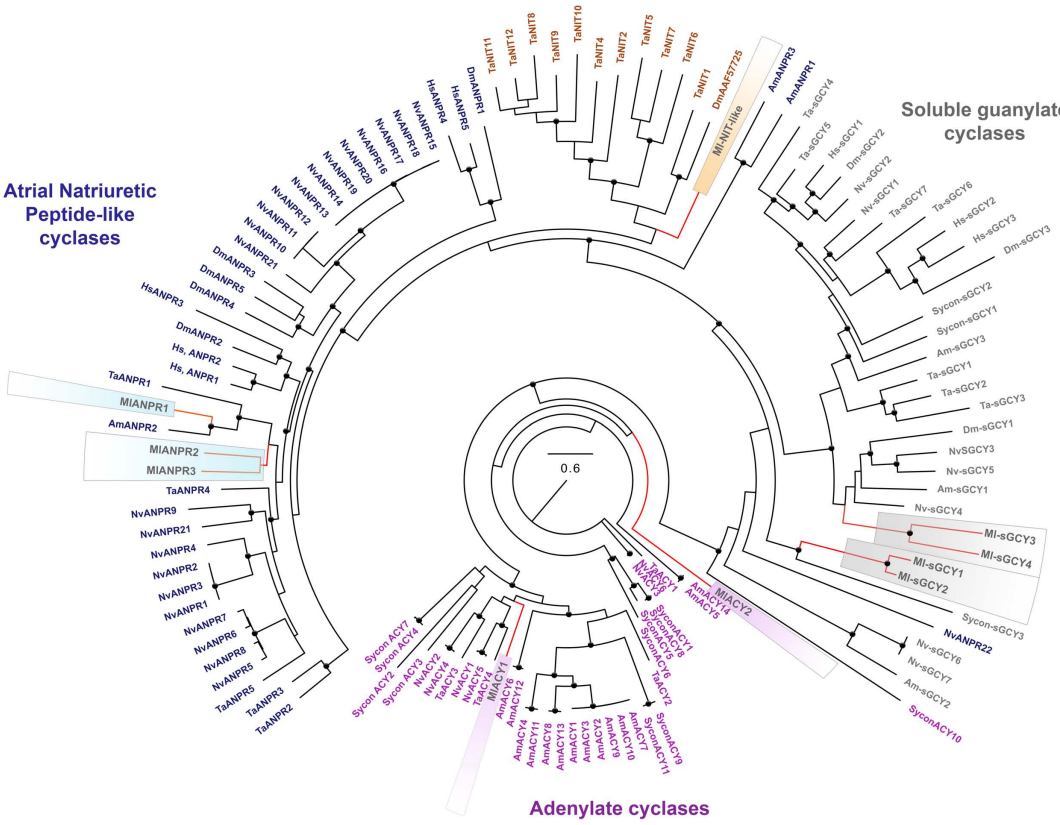

FIGURE 5
Phylogenomic ML analyses of cyclases across representative metazoans with the focus on *Mnemiopsis leidyi* and kin. Major classes of cyclases are highlighted by purple (adenylate cyclases), blue (ANPRs), brown (containing NIT-like domain cyclases), and gray (soluble guanylate cyclases). Bootstrap values are shown as black dots (90–100%). Genes of *M. leidyi* placed in color frames: purple (for ACYs), blue (for ANPRs), orange (for one putative NIT-like containing domain gene), gray (for sGCYs). The references for each particular gene and/or their sequences with relevant GeneBank accession numbers are summarized in the **Supplementary Table 1**.

several other ctenophore species with and without detectable NOS (**Supplementary Figure 1**). For example, there are four sGCs in the lobate *Ocyropsis* with NOS as in *Mnemiopsis*. In contrast, we have a reduced representation of sGCs in *Pleurobrachia* and other Cydippida and Beroida. Thus, the absence of NOS from the genomes does not exclude a possibility of NO signaling due to its non-enzymatic productions by different mechanisms (Moroz and Kohn, 2011) or from exogenous sources (environment, food, microbiomes, etc.).

Recent research also indicates that sGCs can be co-present with NOS in choanoflagellates, controlling swimming behaviors of colonies (Reyes-Rivera et al., 2022) and implying pre-metazoan origins of these signaling pathways. From this apparently simple ancestral condition, sGCs show lineage-specific radiations for many phyla, including 3 sGCs in sponges and humans, seven sGCs in placozoans and cnidarians (**Figure 5**).

In addition, ctenophores encode two other classes of membrane-bound cyclase candidates, such as a derived atrial natriuretic peptide receptor [ANPR] type group, probably involved in peptide sensing, and an enigmatic group of cyclases with NIT domains (**Figures 5**, **6**). *Mnemiopsis* has three orthologs of ANPR-like receptors with CYC/cGMP coupling.

Unique NIT (PF08376) domains (Oulavallickal et al., 2017), containing cyclases, were previously identified in *Trichoplax* (Moroz et al., 2020) as candidates for nitrite/nitrate sensors, similar to bacteria (Shu et al., 2003; Camargo et al., 2007). *Mnemiopsis* has one sequence (ML02033a) associated with the same cluster (**Figure 5**) but with a highly derived NIT-like region and unknown function.

Finally, *Mnemiopsis* has two adenylate cyclases (ML04963a, ML20918a) involved in the evolutionarily conserved cAMP signaling (**Figures 5**, **6**). Surprisingly, the genome screening indicates that cnidarians and sponges possess more adenylate cyclases (5-14) than ctenophores (**Figure 5**).

Expression NOS and putative functions of NO in ctenophores

Two groups of datasets provide initial estimates of the distribution of NOS and sGC expressions in *Mnemiopsis leidyi* (**Figures 7–9**): single cells data (scRNA-seq) from adult animals and transcriptomes (RNA-seq) of different embryonic and developmental stages (Levin et al., 2016).

According to the scRNA-seq datasets from 5,461 cells filtered as in Sebé-Pedrós et al. (2018), NOS was a relatively low-expressed gene, present in individual cells more or less randomly distributed in 15 clusters (out 41), including candidate clusters for some

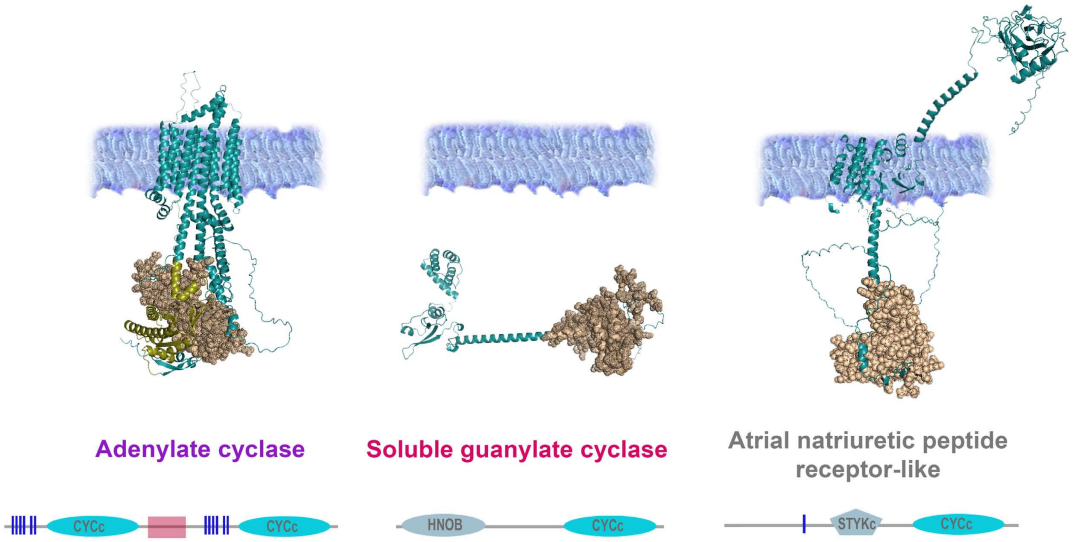

FIGURE 6
Organization of adenylate and guanylate cyclases in *Mnemiopsis leidyi*. Representative cyclases show notable structural differences: Adenylate cyclase anchor in the membrane with ten transmembrane regions and contain two intracellular catalytic CYCc domains; ANPR-like (atrial natriuretic peptide receptor-like) has the extracellular part (ANF-receptor) and two transmembrane domains, STYKc and CYCc domains are located in the intracellular space; soluble guanylate cyclase is located in the cytoplasm. All sequences were analyzed using SMART (Letunic and Bork, 2018; Letunic et al., 2021), NCBI Conserved Domain Search (Lu et al., 2020), and were built using AlphaFold2 (Jumper et al., 2021). The references for each particular gene and/or their sequences with relevant GeneBank accession numbers are summarized in the **Supplementary Table 1**.

secretory cells (recognized with neuropeptide markers identified for this species). We did not detect NOS expression in combs and photocytes.

Next, considering the low abundance of NOS-containing cells and low level of expression, we performed a similar analysis without any filtration with attempts to capture rare cell types. This analysis with 6,144 cells detects a very low level of NOS expression in 15 out of 24 clusters (**Figure 7**), including a few cells with NOS in tentacle-associated cells/tissues, as also shown with partition-based graph abstraction (PAGA) analysis (Wolf et al., 2019).

Among all identified cyclases, adenylate cyclases and ANP-like receptors with guanylyl cyclases are the most abundantly expressed (**Figure 9**). Their expression is detected in most cell types, including tentacles and putative neurons. Nevertheless, sGCs are also very weakly expressed, similar to NOS. In summary, a small number of sequenced cells and an extremely low level of detected NOS/sGC expression prevent making definite conclusions about cell type specificity that might employ this signaling pathway. In future studies, this ambitious task would require multi-color *in situ* hybridization and immunohistochemistry experiments. A limited number of ctenophore cell-specific molecular markers also prevent more detailed annotation of these scRNA-seq data.

RNA-seq data from development contain significantly deeper sequencing than single-cell datasets. During development, NOS (ML074215a) expression became noticeable starting with the 7th hour of post-fertilization (pft), and further increased at the 10th and 11th hours, and later decreased. Here, NOS expression was associated with the specification of tissues and formation of ctenophore-specific organs such as combs, the aboral organ, and components of the digestive systems [e.g., (Simmons et al., 2012; Fischer et al., 2014; Reitzel et al., 2016)]. Expression of sGC was also weak in development and partially corresponded to the same or later stages of development compared to NOS expression (**Supplementary Figure 2**).

We used fixative-resistance NADPH-diaphorase (NADPH-d) histochemistry as a reporter of NOS activity (Bredt et al., 1991; Moroz, 2000a) across phyla, from cnidarians to vertebrates (Bredt et al., 1991; Kurenni et al., 1995; Moroz et al., 2000, 2004; Giovine et al., 2001; Bishop et al., 2008; Moroz and Kohn, 2011). *Mnemiopsis* has extremely fragile tissues, often disintegrated during conventional fixation, highly limiting *in situ* hybridization experiments, requiring multiple steps. However, we managed to perform simpler NADPH-d protocols using larger (2–5 cm) adult animals (n = 6). The NADPH-d reactivity (putative NOS activity) is broadly distributed across tissues in *Mnemiopsis* (**Figure 10**), including cells in the aboral organ, polar fields, base of combs, auricles, and meridional canals regions, as well as putative sensory papillae around the body surface, and in components of the digestive system.

Furthermore, low expression levels do not imply the lack of functional role of NO-cGMP signaling because this pathway includes significant amplification cascades. Thus, we performed pilot pharmacological experiments to test the effects of NO on free-behaving animals (**Figure 11**).

Specifically, we used *Bolinopsis* as a model for these initial tests. Applications of the NO donor DEA/NO 2–20 μM (n = 8 for each concentration) resulted in the suppression of locomotion within the first 10–20 min, including reduction of long-term oscillations of swimming patterns, and eventually the suppression of swimming usually within 60–90 min (n = 8). Higher concentrations of the NO donor (20–200 μM) were apparently toxic, leading to a rapid arrest of locomotion and dissociation of animals (n = 8). Of note, applying the same concentrations to *Pleurobrachia* and *Beroe* did not result in such immediate toxic effects.

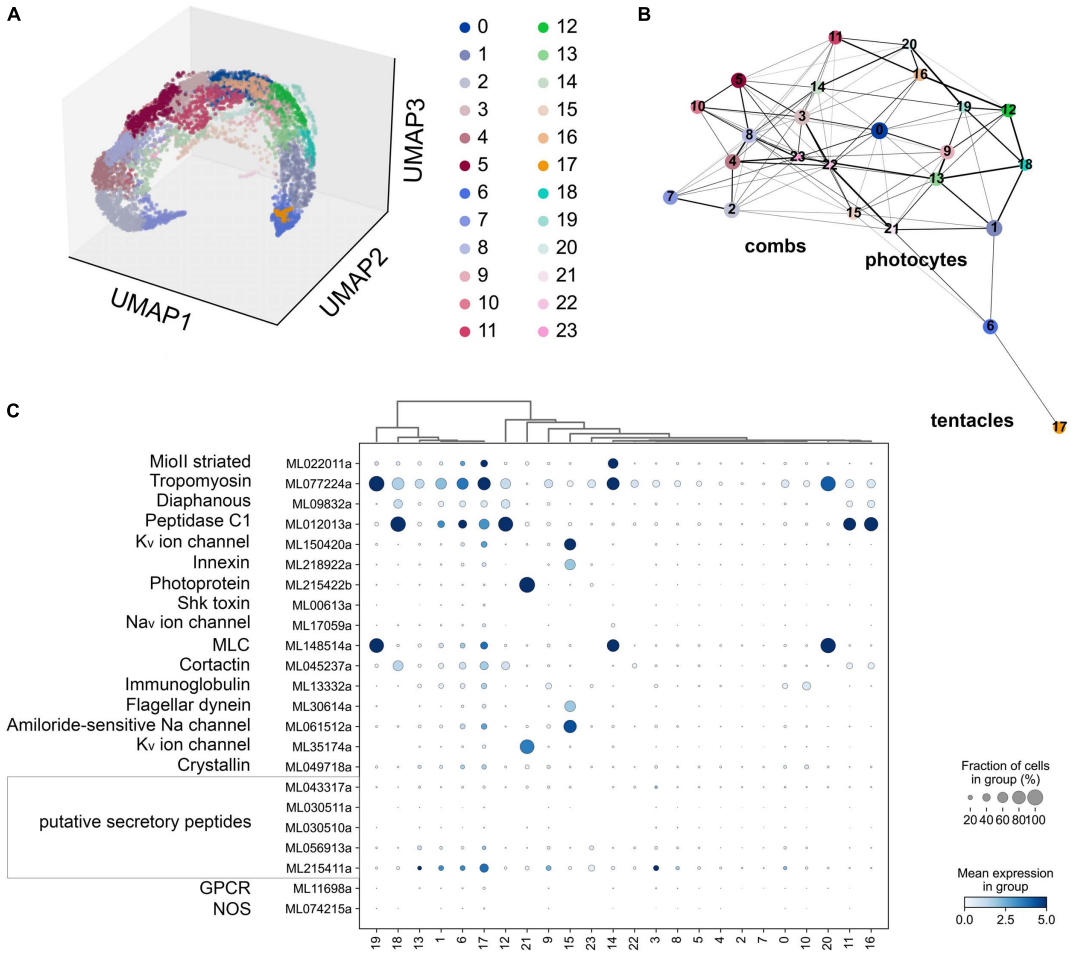

FIGURE 7
(A) The UMAP clustering for 6,144 cells of *Mnemiopsis leidyi* (Sebé-Pedrós et al., 2018) with 24 clusters. **(B)** The PAGA analysis placed clusters with connections based on their differential expressed genes. We found comb associated cluster (#15) using innexin, and flagellar dynein marker accordingly (Sebé-Pedrós et al., 2018). Photocyte's cluster (#21) can be recognized using such markers as photoprotein and potassium channel. The tentacle cluster #17 is placed separately; it contains both marker genes (secretory peptides, tropomyosin, potassium and sodium channels (Sebé-Pedrós et al., 2018)) and putative NOS expressing cells. **(C)** Dotplots highlights cluster-specific genes (Sebé-Pedrós et al., 2018; Burkhardt and Jékely, 2021).

Discussion: Conclusions and future directions

This manuscript outlines the first survey of NOS distribution and functions in ctenophores. The presence of NOS and intracellular NO receptors such as sGC in ctenophores are supported by molecular evidence. However, both comparative and, especially, functional aspects of NO-mediated signaling remain to be determined, and numerous components of NO/cGMP-mediated signaling can be a particular ctenophore lineage-specific. Conclusions are summarized below.

(1) NOS is present in ctenophores with the events of secondary gene loss across several species, primarily in cydippids, for yet unknown reasons.

(2) 2–4 sGCs are also present in ctenophores, with taxonomically broader distribution than NOSs, including their presence in species without NOS. These observations suggest the occurrence of other NO synthetic pathways [enzymatic and non-enzymatic (Moroz et al., 1998; Moroz and Kohn, 2011) and environmental sources of NO (e.g., from microbiota and symbiotic organisms)]. Of note, sGC can also sense CO and potentially other molecules (Feelisch and Martin, 1995; Moroz and Kohn, 2011; Stuehr and Haque, 2019; Shepherd et al., 2022).

(3) In *Mnemiopsis*, NOS and sGCs are expressed at later stages during embryogenesis, and this pathway might be associated with tissue and organ specification in ctenophore development.

(4) Although NO/sGC showed a relatively low expression level in adults, NO might be involved in both localized and systemic control of locomotion with cilia as one of the potential targets of this signaling (to be experimentally validated).

We would like to stress the importance of studying the non-neuronal and systemic functions of NO in ctenophores. NADPH-d did not reveal labeling of defined neuronal populations in mesoglea or subepithelial neural nets or particular comb areas where neurons were identified in previous studies (Moroz, 2015; Norekian and Moroz, 2016, 2019a,b, 2020, 2021). Although cells at the base of combs or ciliated plates in the auricles were NADPH-d positive, they are unlikely neurons. Similarly, the labelings in the aboral

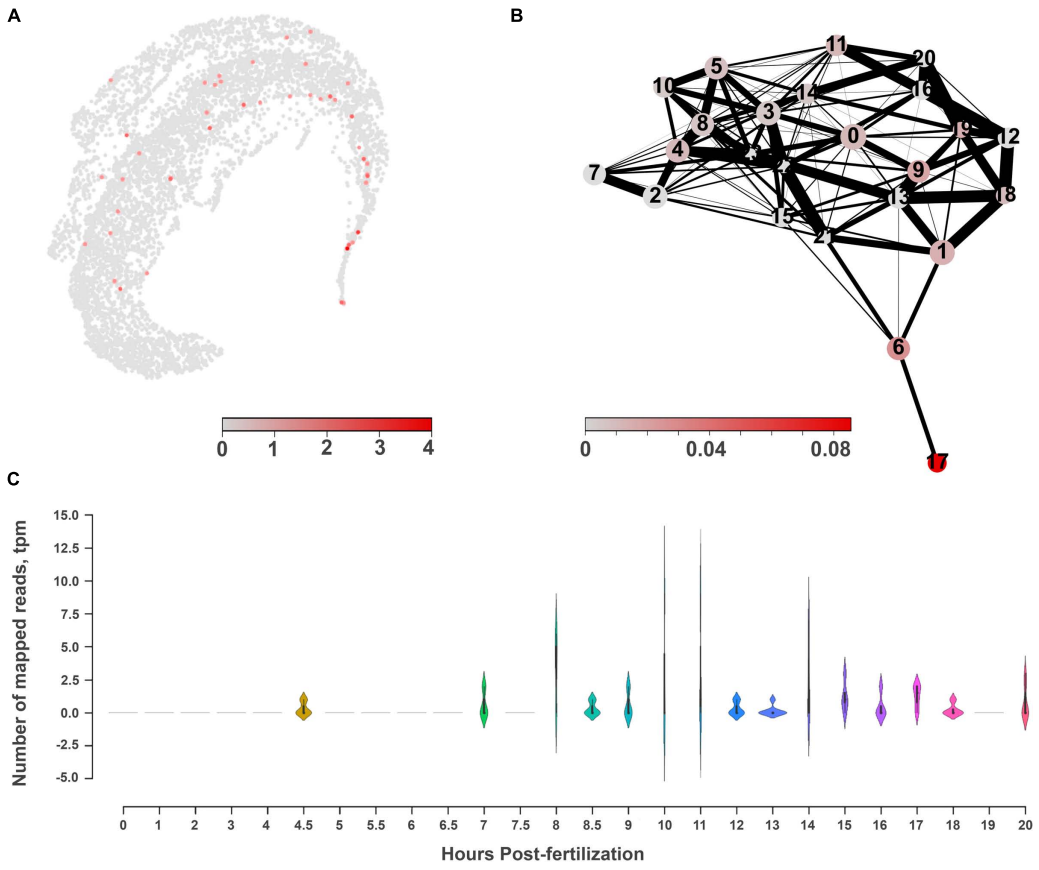

FIGURE 8
The molecular architecture and distribution of nitric oxide synthase (NOS) in *Mnemiopsis leidyi*. **(A)** The UMAP clustering for NOS shows a relatively diffuse distribution across several cell types with low expression levels. **(B)** PAGA analysis for NOS highlights its expression in cluster #17, which might belong to tentacles, according to the marker genes (Sebé-Pedrós et al., 2018). **(C)** RNA-seq profiling of NOS expression in development based on Levin et al. (2016), Moreland et al. (2020). NOS expression is detected after 7th hour of post-fertilization and is associated with the morphogenesis of major ctenophore organs.

organ (with the gravity sensor) and two other putative sensory structures (polar fields as well as papillae) do not convincingly occur in neurons.

These observations are consistent with our pilot findings about relatively small instant effects of NO on behaviors in two lobate ctenophores. In addition to *Bolinopsis*, we performed similar pilot pharmacological tests on *Mnemiopsis* using the same NO donor (DEA NO, 21 animals). Lower concentrations of NO donors (<1 μM, $n = 7$) had no noticeable effects; higher concentrations (>10–70 μM) moderately suppressed the ciliated locomotion and modulate muscle contractions.

Clearly, more systematic studies have to be performed using different NOS donors, inhibitors, and drugs affecting cGMP signaling using cilia, muscles, and secretory cells as effectors, to name a few. However, those observed and relatively "weak" effects of NO within short intervals of pharmacological testing (~30–60 min), together with the widespread distribution of putative NOS across multiple non-neuronal cells and tissues, suggest that NO-signaling in ctenophores might have been associated with more systemic functions. For example, assuming that NADPH-d reactivity in *Mnemiopsis* correlates with NOS activity [as in many other preparations (Bredt et al., 1991; Kurenni et al., 1995; Moroz et al., 2000, 2004; Giovine et al., 2001; Bishop et al., 2008; Moroz and Kohn, 2011)] with such broad distribution across cells and tissues, we anticipate potential roles of ctenophore NO-mediated signaling in development, differentiation, morphogenic processes, (neuro)plasticity, immunity, etc. – similar to a plethora of diverse NO functions described in bilaterians, including the vertebrate lineage.

In summary, the studies of NO signaling in ctenophores are in their infancy. Importantly to the field, we know little about NO synthesis, regulation, compartmentalization, and evolution within the group. As critical first steps and future directions, understanding the enzymology of NOS is needed due to its unusual structure. It would be essential to determine the Ca-dependence of ctenophore NOSs, control their expression, and characterize the pharmacology of NOS inhibition, providing tools for future research. Equally important would be the characterization of NOS expression both in development and in adults using *in situ* hybridization and immunohistochemistry, in addition to current observations with NADPH-d histochemistry. Finally, comparative physiological analyses of NO signaling in regulating reproduction, development, feeding, immunity, and complex behavioral integration are desirable.

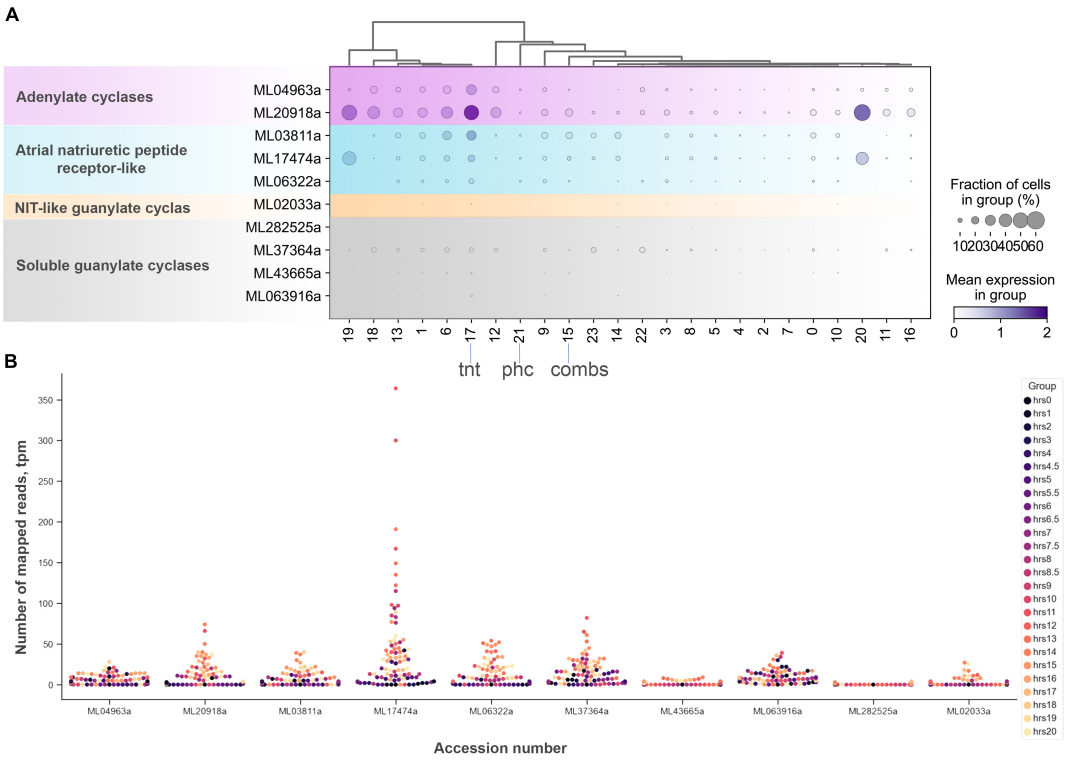

FIGURE 9
The diversity and expression of cyclase genes in *Mnemiopsis leidyi* based on scRNA-seq profiling (Sebé-Pedrós et al., 2018) (see text for details). **(A)** Dotplot analysis indicates that all cyclases are expressed in cluster #17 (tentacles) except one soluble guanylate cyclase (ML282525a). sGCY (ML37364a) has low expression levels in all cell clusters from an adult animal. However, the majority of sGCYs are expressed in developmental stages **(B)**. RNA-seq profiling of expression in development is based on Levin et al. (2016), Moreland et al. (2020). Post-fertilization hours are indicated as color dots on the right.

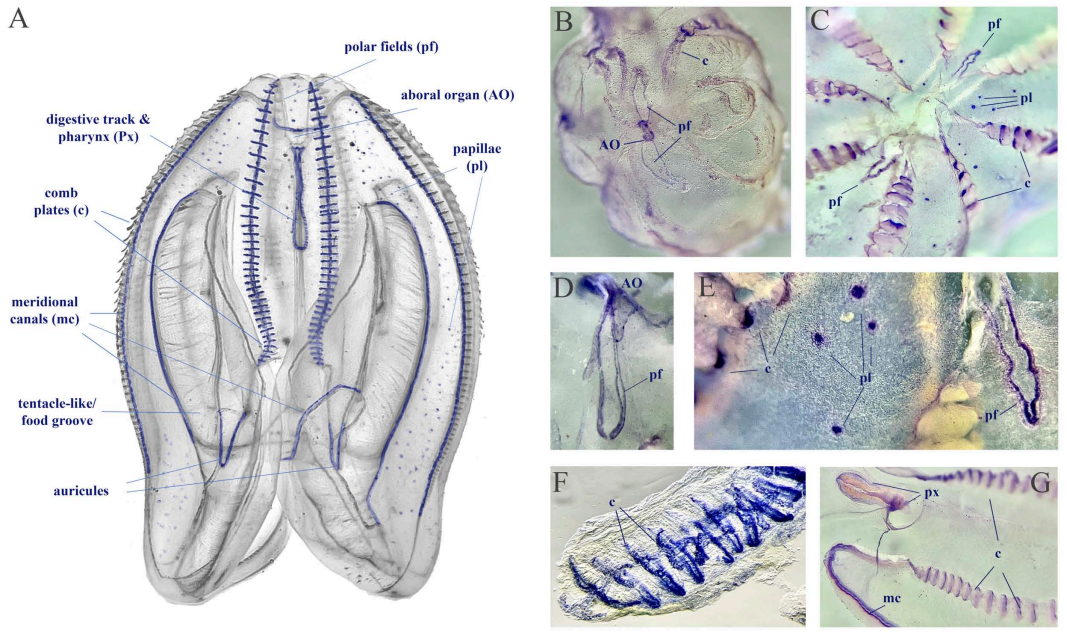

FIGURE 10
NADPH-diaphorase histochemistry in *Mnemiopsis leidyi*. **(A)** The distribution of putative NOS activity in *Mnemiopsis*. This schematics illustrate the regions with putative NOS, but not reflect quantitative estimates of tentative enzymatic activities. **(B,C)** Whole mount preparation with NADPH-d reactivity in the aboral organ (AO), the polar fields (pf), in comb plate areas (c), and papillae (pl). **(D–G)** Illustrated examples of NADPH-d reactivity across different structures, including the pharynx (px) and the meridional canal (mc) near the auricules (a feeding structure).

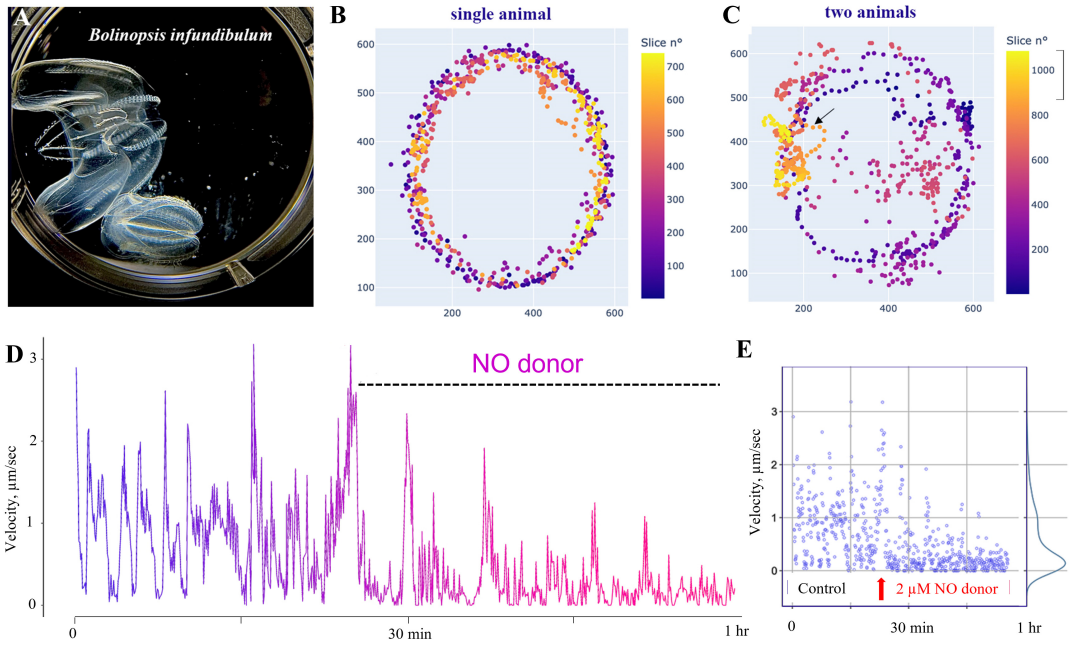

FIGURE 11
Nitric oxide suppresses swimming in *Bolinopsis*. **(A)** The photo of two *B. infundibulum* in an experimental Petri dish. **(B,C)** Velocity plots (color gradient at right) following the application of 2 µM of DEANO (NO donor). Illustrative tests on a single and two animals in the dish show a decrease of the speed of locomotion and travel distance following NO application. **(D)** Dynamic swimming shows oscillations in the velocity and gradual decay of locomotory speed in the presence of DEANO. **(E)** Velocity ranged from 0 to 3 in the control group, and these values gradually reduced to a nearly complete arrest of swimming in the experimental group of eight animals.

Materials and methods

We performed database searches for nitric oxide synthases (NOS) and soluble guanylyl cyclases (sGC) both in animals and non-metazoan organisms. All used NOS and sGC sequences and their sources are presented in **Supplementary Table 1**.

Protein domains were detected using Pfam (Mistry et al., 2021), UniProt (UniProt Consortium, 2010), SMART (Letunic and Bork, 2018; Letunic et al., 2021), and NCBI Conserved Domain Search (Lu et al., 2020). The reconstruction of 3D structures was based on PDB models using Phyre2 (Kelley et al., 2015), SWISS-MODEL (Waterhouse et al., 2018), and AlphaFold2 (Jumper et al., 2021). Three-dimensional structures were analyzed in PyMol (The PyMol Molecular Graphic System, Version 1.8.6.0 Schrodinger, LLC)[1,2].

NOS and sGC sequences were aligned with MAFFT v764 88, using the L-INS-i alignment algorithm with 1,000 iterations (Katoh et al., 2005). Phylogenomic ML analyses were performed by IQ-TREE ML ultrafast-bootstrap calculation (Trifinopoulos et al., 2016). The RAxML analyses of NOSs were made by a best-fit LG + F + I + G4 model, and for cyclases, we used a best-fit WAG + F + G4 model. Testing tree branches was done by SH-like aLRT with 1,000 replicates.

We screened publicly available transcriptomic (RNA-seq) datasets of 26 different development stages of *Mnemiopsis* (Levin et al., 2016) for NOS and sGC expression patterns. The original data were presented as TPM (log2(transcript per million (TPM)/100 + 1) and visualized using Pandas, matplotlib libraries in Python.

For analyses of cell-specific expression patters we used reference scRNA-seq data from adult *Mnemiopsis* (Sebé-Pedrós et al., 2018). Specifically, we visually inspected the distribution of genes, UMIs, and % mitochondrial genes across cells choosing a AnnData-file format with a final count matrix of 6,144 cells. We also fileted datasets and tested other criteria for removing cells, but we found that more stringent cutoffs yielded significantly different clustering results and eliminated low-expressed genes from the final visualization (including NOS and sGC-like genes). Standard guidelines for preprocessing, performing principal components analysis, normalization, and clustering were based on Satija et al. (2015).

We ranked differentially expressed genes in each cluster by Wilcoxon rank-sum (Mann–Whitney-U) test and *t*-test (Soneson and Robinson, 2018). As an alternative, we ranked genes using logistic regression (Ntranos et al., 2019). Initial annotation of clusters was based on previously suggested gene markers (Sebé-Pedrós et al., 2018). For visualization of gene expression and other variables, we used dotplots with a dendrogram implemented in Matplotlib, UMAP, and PAGA plottings.

Partition-based graph abstraction (PAGA) connectivity graphs were implemented in ScanPy, Python (Wolf et al., 2019) for mapping the expression for individual genes using Leiden algorithm as a base. Specifically, we employed PAGA to calculate connectivity between merged clusters, retaining all connections. For visualization purposes, we labeled strong edges thicker than others with the threshold 0.03. Finally, we placed the graph nodes on the median UMAP coordinates of the cells in the cluster to preserve the structure of the UMAP embedding and allow direct comparison between the PAGA graph and UMAP plots. To investigate expression changes along different paths in PAGA

1 https://www.schrodinger.com/products/pymol
2 https://pymol.org/2/

networks, we calculated diffusion maps and diffusion pseudotime as a proxy of the differentiation distance between all cells.

We used protocols described elsewhere in detail (Kurenni et al., 1995; Moroz, 2000a) for the visualization of NADPH-diaphorase histochemistry known as a marker for NOS activity (Bredt et al., 1991; Moroz, 2000a). Before staining, adult animals (2–5 cm) were fixed in 4% paraformaldehyde in seawater for 45–75 min at room temperature. The staining was also performed at room temperature, in the dark, for 2–5 h in the following solution: β-NADPH sodium salt (1 mM), and Nitro Blue Tetrazolium (0.5 mM) in 0.1 M Tris buffer (pH = 8.0). All reagents were from Sigma). Postfixation, embedding, and visualization were the same as described elsewhere (Moroz, 2000a; Giovine et al., 2001). Considering the highly fragile nature of ctenophore preparations, often dissociated during fixation, we processed different tissue segments separately, using care for all transfers of preparations. The data were obtained from NADPH-d labeling using six animals. The experiments were performed in the spring and summer of 2019–2021.

For behavioral assays, we used freshly collected *Bolinopsis infundibulum*. We used DEA NONOate (Diethylamine NONOate, Abcam, CAS Number 372965-00-9) as a nitric oxide donor. The time series for control behaviors and experimental tests were 30–60 min. We used Fiji/ImageJ and plugins (WRMTRCK, MTrack2) to track and calculate velocities, distances, and tracks. Post-analyses and visualization were done in Python environment (NumPy, Pandas, Matplotlib, SciPy).

Data availability statement

The datasets presented in this study can be found in online repositories. The names of the repository/repositories and accession number(s) can be found in this article/**Supplementary material**.

Author contributions

LM and DR designed the study. KM screened the genome datasets and 37 transcriptomes for the presence of NOS and cyclases. DR and KM was involved in the phylogenetic analyses. DR made 2D/3D protein modeling of NOS and cyclases, performed scRNA-seq and RNA-seq analyses, and involved in the behavioral analyses. LM performed the pharmacological and histochemical tests and wrote the manuscript. DR, KM, and LM confirmed the analyzed data. All authors reviewed and edited the manuscript.

Funding

This work was supported in part by the Human Frontiers Science Program (RGP0060/2017) and the National Science Foundation (1146575, 1557923, 1548121, and 1645219) grants to LM. Research reported in this publication was also supported in part by the National Institute of Neurological Disorders and Stroke of the National Institutes of Health under Award Number R01NS114491 (to LM).

Acknowledgments

We thank Drs. Arnau Sebe-Pedros and Amos Tanay for providing an original scRNA-seq dataset.

Conflict of interest

The authors declare that the research was conducted in the absence of any commercial or financial relationships that could be construed as a potential conflict of interest.

Publisher's note

All claims expressed in this article are solely those of the authors and do not necessarily represent those of their affiliated organizations, or those of the publisher, the editors and the reviewers. Any product that may be evaluated in this article, or claim that may be made by its manufacturer, is not guaranteed or endorsed by the publisher.

Author disclaimer

The content is solely the authors' responsibility and does not necessarily represent the official views of the National Institutes of Health and National Science Foundation.

Supplementary material

The Supplementary Material for this article can be found online at: https://www.frontiersin.org/articles/10.3389/fnins.2023.1125433/full#supplementary-material

SUPPLEMENTARY FIGURE 1
Diversification of soluble guanylyl cyclases (sGC) Ctenophora. The catalytic domain (~190aa) of the soluble guanylate, adenylate, and membrane-type receptor (MR) guanylyl cyclase proteins was used to reconstruct the maximum-likelihood (ML) based phylogenetic tree. Ctenophore soluble cyclases are clustered within three major clades —1/2, 3/4, and NIT-like. Both *Mnemiopsis leidyi* (Ml) and *Ocyropsis crystallina* (Oc) encode five copies of GC proteins, *Pleurobrachia bachei* (Pb) encodes three orthologs comprising one gene product under each cluster. *Pleurobrachia* soluble NIT-like cyclase gene encodes two copies of the catalytic domain shown as a and b. *Mnemiopsis* and *Pleurobrachia* genes are shown in bold font in dark and light blue color. Based on the ML tree membrane receptor type (ANP-like receptor), guanylyl cyclase can be classified under three groups. Both *Pleurobrachia bachei* (Pb) and *Mnemiopsis leidyi* (Ml) encode one gene under these three groups. Similarly, both Pb and Ml encode two genes of the adenylate cyclase family. However, both these species encode two copies of the catalytic domains labeled as a and b. Proteins under each group against all other ctenophore species were retrieved from the transcriptome datasets (Whelan et al., 2015, 2017). The catalytic domain used to build the tree is given in the **Supplementary Table 1**. Species names are shown in the figure as well as provided in the **Supplementary material**.

SUPPLEMENTARY FIGURE 2
Identifying cluster specific genes associated with NO-cGMP signaling in *Mnemiopsis leidyi* based on scRNA-seq data (Sebé-Pedrós et al., 2018) with filtration > 100 genes per cell. This filtration cutoff resulted produced 41 clusters (filtration *n* = 100, 5,461 cells). Without filtration, we produced 24 clusters with 6,144 cells (the main text and figures), and recognized digestive, epithelial, muscle, neuroid-type cells. However, here with the threshold *N* = 100, we lost cells with such low-expressed genes as NOS in tentacles and many cells expressing cyclase genes (see main text).

SUPPLEMENTARY FIGURE 3
RNA-seq expression profiling of NOS and different cyclases in *Mnemiopsis* development the calculated values are based on Levin et al. (2016), Moreland et al. (2020). Post-fertilization hours are indicated as color dots on the right.

SUPPLEMENTARY TABLE 1
Sequences of NOS and cyclases used for tree constructions and analyses.

SUPPLEMENTARY TABLE 2
Sequences of different cyclases identified in comparative ctenophore RNA-seq datasets.

SUPPLEMENTARY MATERIAL 1
Alignment of NOSs identified in ctenophores from RNA-seq datasets. All structural domains are marked.

SUPPLEMENTARY MATERIAL 2
Alignment of NOSs identified in ctenophores from RNA-seq datasets. All structural domains are marked.

References

Anctil, M. (2009). Chemical transmission in the sea anemone *Nematostella vectensis*: A genomic perspective. *Comp. Biochem. Physiol. Part D Genomics Proteomics* 4, 268–289. doi: 10.1016/j.cbd.2009.07.001

Bassler, J., Schultz, J. E., and Lupas, A. N. (2018). Adenylate cyclases: Receivers, transducers, and generators of signals. *Cell Signal.* 46, 135–144. doi: 10.1016/j.cellsig.2018.03.002

Bishop, C., Pires, A., Norby, S., Boudko, D., Moroz, L. L., and Hadfield, M. (2008). Analysis of nitric oxide-cyclic guanosine monophosphate signaling during metamorphosis of the nudibranch *Phestilla sibogae* Bergh (Gastropoda: Opisthobranchia). *Evol. Dev.* 10, 288–299. doi: 10.1111/j.1525-142X.2008.00238.x

Bouchard, J. N., and Yamasaki, H. (2008). Heat stress stimulates nitric oxide production in *Symbiodinium microadriaticum*: A possible linkage between nitric oxide and the coral bleaching phenomenon. *Plant Cell Physiol.* 49, 641–652. doi: 10.1093/pcp/pcn037

Bredt, D., Glatt, C., Hwang, P., Fotuhi, M., Dawson, T., and Snyder, S. (1991). Nitric oxide synthase protein and mRNA are discretely localized in neuronal populations of the mammalian CNS together with NADPH diaphorase. *Neuron* 7, 615–624. doi: 10.1016/0896-6273(91)90374-9

Brenman, J., Chao, D., Gee, S., McGee, A., Craven, S., Santillano, D., et al. (1996). Interaction of nitric oxide synthase with the postsynaptic density protein PSD-95 and alpha1-syntrophin mediated by PDZ domains. *Cell* 84, 757–767. doi: 10.1016/s0092-8674(00)81053-3

Burkhardt, P., and Jékely, G. (2021). Evolution of synapses and neurotransmitter systems: The divide-and-conquer model for early neural cell-type evolution. *Curr. Opin. Neurobiol.* 71, 127–138. doi: 10.1016/j.conb.2021.11.002

Camargo, A., Llamas, A., Schnell, R., Higuera, J., González-Ballester, D., Lefebvre, P., et al. (2007). Nitrate signaling by the regulatory gene NIT2 in *Chlamydomonas*. *Plant Cell.* 19, 3491–3503. doi: 10.1105/tpc.106.045922

Colasanti, M., Lauro, G. M., and Venturini, G. (1995). NO in *Hydra* feeding response. *Nature* 374:505. doi: 10.1038/374505a0

Colasanti, M., Mazzone, V., Mancinelli, L., Leone, S., and Venturini, G. (2009). Involvement of nitric oxide in the head regeneration of *Hydra vulgaris*. *Nitric Oxide* 21, 164–170. doi: 10.1016/j.niox.2009.07.003

Colasanti, M., Persichini, T., and Venturini, G. (2010). Nitric oxide pathway in lower metazoans. *Nitric Oxide* 23, 94–100. doi: 10.1016/j.niox.2010.05.286

Cristino, L., Guglielmotti, V., Cotugno, A., Musio, C., and Santillo, S. (2008). Nitric oxide signaling pathways at neural level in invertebrates: Functional implications in cnidarians. *Brain Res.* 1225, 17–25. doi: 10.1016/j.brainres.2008.04.056

Elliott, G. R., and Leys, S. P. (2010). Evidence for glutamate, GABA and NO in coordinating behaviour in the sponge, *Ephydatia muelleri* (Demospongiae, Spongillidae). *J. Exp. Biol.* 213, 2310–2321. doi: 10.1242/jeb.039859

Ellwanger, K., and Nickel, M. (2006). Neuroactive substances specifically modulate rhythmic body contractions in the nerveless metazoon *Tethya wilhelma* (Demospongiae, Porifera). *Front. Zool.* 3:7. doi: 10.1186/1742-9994-3-7

Feelisch, M., and Martin, J. F. (1995). The early role of nitric oxide in evolution. *Trends Ecol. Evol.* 10, 496–499. doi: 10.1016/s0169-5347(00)89206-x

Feng, W., and Zhang, M. (2009). Organization and dynamics of PDZ-domain-related supramodules in the postsynaptic density. *Nat. Rev. Neurosci.* 10, 87–99. doi: 10.1038/nrn2540

Fernandez, R., and Gabaldon, T. (2020). Gene gain and loss across the metazoan tree of life. *Nat. Ecol. Evol.* 4, 524–533. doi: 10.1038/s41559-019-1069-x

Fischer, A. H., Pang, K., Henry, J. Q., and Martindale, M. Q. (2014). A cleavage clock regulates features of lineage-specific differentiation in the development of a basal branching metazoan, the ctenophore *Mnemiopsis leidyi*. *Evodevo* 5:4. doi: 10.1186/2041-9139-5-4

Gancedo, J. (2013). Biological roles of cAMP: Variations on a theme in the different kingdoms of life. *Biol. Rev. Camb. Philos. Soc.* 88, 645–668. doi: 10.1111/brv.12020

Giacomelli, M., Rossi, M. E., Lozano-Fernandez, J., Feuda, R., and Pisani, D. (2022). Resolving tricky nodes in the tree of life through amino acid recoding. *iScience* 25:105594. doi: 10.1016/j.isci.2022.105594

Giovine, M., Pozzolini, M., Favre, A., Bavestrello, G., Cerrano, C., Ottaviani, F., et al. (2001). Heat stress-activated, calcium-dependent nitric oxide synthase in sponges. *Nitric Oxide* 5, 427–431. doi: 10.1006/niox.2001.0366

Gunn, A., Derbyshire, E. R., Marletta, M. A., and Britt, R. D. (2012). Conformationally distinct five-coordinate heme-NO complexes of soluble guanylate cyclase elucidated by multifrequency electron paramagnetic resonance (EPR). *Biochemistry* 51, 8384–8390. doi: 10.1021/bi300831m

Halanych, K. M., Whelan, N. V., Kocot, K. M., Kohn, A. B., and Moroz, L. L. (2016). Miscues misplace sponges. *Proc. Natl. Acad. Sci. U.S.A.* 113, E946–E947. doi: 10.1073/pnas.1525332113

Hawkins, T. D., and Davy, S. K. (2013). Nitric oxide and coral bleaching: Is peroxynitrite generation required for symbiosis collapse? *J. Exp. Biol.* 216, 3185–3188. doi: 10.1242/jeb.087510

Hawkins, T. D., Bradley, B. J., and Davy, S. K. (2013). Nitric oxide mediates coral bleaching through an apoptotic-like cell death pathway: Evidence from a model sea anemone-dinoflagellate symbiosis. *FASEB J.* 27, 4790–4798. doi: 10.1096/fj.13-235051

Hewitt, O., and Degnan, S. (2022). Distribution and diversity of ROS-generating enzymes across the animal kingdom, with a focus on sponges (Porifera). *BMC Biol.* 20:212. doi: 10.1186/s12915-022-01414-z

Holguín-Peña, R., Vázquez-Juárez, R., and Martínez-Soriano, J. (2007). First report of a 16SrI-B group phytoplasma associated with a yellows-type disease affecting tomato plants in the Baja California Peninsula of Mexico. *Plant Dis.* 91:328. doi: 10.1094/PDIS-91-3-0328B

Horst, B. G., and Marletta, M. A. (2018). Physiological activation and deactivation of soluble guanylate cyclase. *Nitric Oxide* 77, 65–74. doi: 10.1016/j.niox.2018.04.011

Horst, B., Yokom, A., Rosenberg, D., Morris, K., Hammel, M., Hurley, J., et al. (2019). Allosteric activation of the nitric oxide receptor soluble guanylate cyclase mapped by cryo-electron microscopy. *Elife.* 8:e50634. doi: 10.7554/eLife.50634

Jaffrey, S. R., Snowman, A. M., Eliasson, M. J., Cohen, N. A., and Snyder, S. H. (1998). CAPON: A protein associated with neuronal nitric oxide synthase that regulates its interactions with PSD95. *Neuron* 20, 115–124. doi: 10.1016/s0896-6273(00)80439-0

Jumper, J., Evans, R., Pritzel, A., Green, T., Figurnov, M., Ronneberger, O., et al. (2021). Highly accurate protein structure prediction with AlphaFold. *Nature* 596, 583–589. doi: 10.1038/s41586-021-03819-2

Kang, Y., Liu, R., Wu, J. X., and Chen, L. (2019). Structural insights into the mechanism of human soluble guanylate cyclase. *Nature* 574, 206–210. doi: 10.1038/s41586-019-1584-6

Kapli, P., and Telford, M. J. (2020). Topology-dependent asymmetry in systematic errors affects phylogenetic placement of Ctenophora and Xenacoelomorpha. *Sci. Adv.* 6:eabc5162. doi: 10.1126/sciadv.abc5162

Kass-Simon, G., and Pierobon, P. (2007). Cnidarian chemical neurotransmission, an updated overview. *Comp. Biochem. Physiol. A Mol. Integr. Physiol.* 146, 9–25. doi: 10.1016/j.cbpa.2006.09.008

Katoh, K., Kuma, K., Toh, H., and Miyata, T. (2005). MAFFT version 5: Improvement in accuracy of multiple sequence alignment. *Nucleic Acids Res.* 33, 511–518. doi: 10.1093/nar/gki198

Kelley, L. A., Mezulis, S., Yates, C. M., Wass, M. N., and Sternberg, M. J. (2015). The Phyre2 web portal for protein modeling, prediction and analysis. *Nat. Protoc.* 10, 845–858. doi: 10.1038/nprot.2015.053

Kim, E., and Sheng, M. (2004). PDZ domain proteins of synapses. *Nat. Rev. Neurosci.* 5, 771–781. doi: 10.1038/nrn1517

Krumenacker, J. S., Hanafy, K. A., and Murad, F. (2004). Regulation of nitric oxide and soluble guanylyl cyclase. *Brain Res. Bull.* 62, 505–515. doi: 10.1016/S0361-9230(03)00102-3

Kurenni, D., Thurlow, G., Turner, R., Moroz, L., Sharkey, K., and Barnes, S. (1995). Nitric oxide synthase in tiger salamander retina. *J. Comp. Neurol.* 361, 525–536. doi: 10.1002/cne.903610314

Laumer, C., Fernández, R., Lemer, S., Combosch, D., Kocot, K., Riesgo, A., et al. (2019). Revisiting metazoan phylogeny with genomic sampling of all phyla. *Proc. Biol. Sci.* 286:20190831. doi: 10.1098/rspb.2019.0831

Letunic, I., and Bork, P. (2018). 20 years of the SMART protein domain annotation resource. *Nucleic Acids Res.* 46, D493–D496. doi: 10.1093/nar/gkx922

Letunic, I., Khedkar, S., and Bork, P. (2021). SMART: Recent updates, new developments and status in 2020. *Nucleic Acids Res.* 49, D458–D460. doi: 10.1093/nar/gkaa937

Levin, M., Anavy, L., Cole, A., Winter, E., Mostov, N., Khair, S., et al. (2016). The mid-developmental transition and the evolution of animal body plans. *Nature* 531, 637–641. doi: 10.1038/nature16994

Li, Y., Shen, X. X., Evans, B., Dunn, C. W., and Rokas, A. (2021). Rooting the animal tree of life. *Mol. Biol. Evol.* 38, 4322–4333. doi: 10.1093/molbev/msab170

Lu, S., Wang, J., Chitsaz, F., Derbyshire, M., Geer, R., Gonzales, N., et al. (2020). CDD/SPARCLE: The conserved domain database in 2020. *Nucleic Acids Res.* 48, D265–D268. doi: 10.1093/nar/gkz991

Mariita, R. M., Hossain, M. J., and Moss, A. G. (2021). Comparative genomic analysis and characterization of *Staphylococcus* sp. AOAB, isolated from a notoriously invasive *Mnemiopsis leidyi* gut revealed multiple antibiotic resistance determinants. *bioRxiv* [Preprint]. doi: 10.1101/2021.01.11.426108

Martin, E., Berka, V., Tsai, A. L., and Murad, F. (2005). Soluble guanylyl cyclase: The nitric oxide receptor. *Methods Enzymol.* 396, 478–492. doi: 10.1016/S0076-6879(05)96040-0

Mistry, J., Chuguransky, S., Williams, L., Qureshi, M., Salazar, G., Sonnhammer, E., et al. (2021). Pfam: The protein families database in 2021. *Nucleic Acids Res.* 49, D412–D419. doi: 10.1093/nar/gkaa913

Montfort, W. R., Wales, J. A., and Weichsel, A. (2017). Structure and activation of soluble guanylyl cyclase, the nitric oxide sensor. *Antioxid. Redox Signal.* 26, 107–121. doi: 10.1089/ars.2016.6693

Moreland, R. T., Nguyen, A. D., Ryan, J. F., and Baxevanis, A. D. (2020). The *Mnemiopsis* genome project portal: Integrating new gene expression resources and improving data visualization. *Database* 2020:baaa029. doi: 10.1093/database/baaa029

Moroz, L. (2015). Convergent evolution of neural systems in ctenophores. *J. Exp. Biol.* 218(Pt 4), 598–611. doi: 10.1242/jeb.110692

Moroz, L. L. (2000a). Giant identified NO-releasing neurons and comparative histochemistry of putative nitrergic systems in gastropod molluscs. *Microsc. Res. Technol.* 49, 557–569. doi: 10.1002/1097-0029(20000615)49:6<557::AID-JEMT6>3.0.CO;2-S

Moroz, L. L. (2000b). "On the origin and early evolution of neuronal nitric oxide signaling: A comparative analysis," in *Nitric oxide and free radicals in peripheral neurotransmission*, ed. S. B. Kalsner (Basel: Birkhauser), 1–34.

Moroz, L. L. (2001). Gaseous transmission across time and species. *Am. Zool.* 41, 304–320.

Moroz, L. L., and Kohn, A. B. (2011). Parallel evolution of nitric oxide signaling: Diversity of synthesis and memory pathways. *Front. Biosci.* 16:2008–2051. doi: 10.2741/3837

Moroz, L. L., and Kohn, A. B. (2016). Independent origins of neurons and synapses: Insights from ctenophores. *Philos. Trans. R. Soc. Lond. B Biol. Sci.* 371:20150041. doi: 10.1098/rstb.2015.0041

Moroz, L. L., Meech, R. W., Sweedler, J. V., and Mackie, G. O. (2004). Nitric oxide regulates swimming in the jellyfish *Aglantha digitale*. *J. Comp. Neurol.* 471, 26–36. doi: 10.1002/cne.20023

Moroz, L. L., Norekian, T. P., Pirtle, T. J., Robertson, K. J., and Satterlie, R. A. (2000). Distribution of NADPH-diaphorase reactivity and effects of nitric oxide on feeding and locomotory circuitry in the pteropod mollusc, *Clione limacina*. *J. Comp. Neurol.* 427, 274–284.

Moroz, L. L., Romanova, D. Y., and Kohn, A. B. (2021). Neural versus alternative integrative systems: Molecular insights into origins of neurotransmitters. *Philos. Trans. R. Soc. Lond. B Biol. Sci.* 376:20190762. doi: 10.1098/rstb.2019.0762

Moroz, L., Kocot, K., Citarella, M., Dosung, S., Norekian, T., Povolotskaya, I., et al. (2014). The ctenophore genome and the evolutionary origins of neural systems. *Nature* 510, 109–114. doi: 10.1038/nature13400

Moroz, L., Norby, S., Cruz, L., Sweedler, J., Gillette, R., and Clarkson, R. (1998). Non-enzymatic production of nitric oxide (NO) from NO synthase inhibitors. *Biochem. Biophys. Res. Commun.* 253, 571–576. doi: 10.1006/bbrc.1998.9810

Moroz, L., Romanova, D., Nikitin, M., Sohn, D., Kohn, A., Neveu, E., et al. (2020). The diversification and lineage-specific expansion of nitric oxide signaling in Placozoa: Insights in the evolution of gaseous transmission. *Sci. Rep.* 10:13020. doi: 10.1038/s41598-020-69851-w

Morrall, C. E., Galloway, T. S., Trapido-Rosenthal, H. G., and Depledge, M. H. (2000). Characterisation of nitric oxide synthase activity in the tropical sea anemone *Aiptasia pallida*. *Comp. Biochem. Physiol. B Biochem. Mol. Biol.* 125, 483–491. doi: 10.1016/s0305-0491(00)00157-7

Murciano-Calles, J., Coello, A., Cámara-Artigas, A., and Martinez, J. (2020). PDZ/PDZ interaction between PSD-95 and nNOS neuronal proteins: A thermodynamic analysis of the PSD95-PDZ2/nNOS-PDZ interaction. *J. Mol. Recognit.* 33:e2826. doi: 10.1002/jmr.2826

Musser, J., Schippers, K., Nickel, M., Mizzon, G., Kohn, A., Pape, C., et al. (2021). Profiling cellular diversity in sponges informs animal cell type and nervous system evolution. *Science* 374, 717–723. doi: 10.1126/science.abj2949

Norekian, T. P., and Moroz, L. L. (2016). Development of neuromuscular organization in the ctenophore *Pleurobrachia bachei*. *J. Comp. Neurol.* 524, 136–151. doi: 10.1002/cne.23830

Norekian, T. P., and Moroz, L. L. (2019a). Neuromuscular organization of the ctenophore *Pleurobrachia bachei*. *J. Comp. Neurol.* 527, 406–436. doi: 10.1002/cne.24546

Norekian, T. P., and Moroz, L. L. (2019b). Neural system and receptor diversity in the ctenophore *Beroe abyssicola*. *J. Comp. Neurol.* 527, 1986–2008. doi: 10.1002/cne.24633

Norekian, T. P., and Moroz, L. L. (2020). Comparative neuroanatomy of ctenophores: Neural and muscular systems in *Euplokamis dunlapae* and related species. *J. Comp. Neurol.* 528, 481–501. doi: 10.1002/cne.24770

Norekian, T. P., and Moroz, L. L. (2021). Development of the nervous system in the early hatching larvae of the ctenophore *Mnemiopsis leidyi*. *J. Morphol.* 282, 1466–1477. doi: 10.1002/jmor.21398

Ntranos, V., Yi, L., Melsted, P., and Pachter, L. (2019). A discriminative learning approach to differential expression analysis for single-cell RNA-seq. *Nat. Methods* 16, 163–166. doi: 10.1038/s41592-018-0303-9

Oulavallickal, T., Brewster, J., McKellar, J., Fairhurst, M., Tenci, N., and Gerth, M. (2017). The *Pseudomonas syringae* pv. actinidiae chemoreceptor protein F (PscF) periplasmic sensor domain: Cloning, purification and X-ray crystallographic analysis. *Acta Crystallogr. F Struct. Biol. Commun.* 73(Pt 12), 701–705. doi: 10.1107/S2053230X17016831

Perez, S., and Weis, V. (2006). Nitric oxide and cnidarian bleaching: An eviction notice mediates breakdown of a symbiosis. *J. Exp. Biol.* 209(Pt 14), 2804–2810. doi: 10.1242/jeb.02309

Redmond, A. K., and McLysaght, A. (2021). Evidence for sponges as sister to all other animals from partitioned phylogenomics with mixture models and recoding. *Nat. Commun.* 12:1783. doi: 10.1038/s41467-021-22074-7

Reitzel, A. M., Pang, K., and Martindale, M. Q. (2016). Developmental expression of "germline"- and "sex determination"-related genes in the ctenophore *Mnemiopsis leidyi*. *Evodevo* 7:17. doi: 10.1186/s13227-016-0051-9

Reyes-Rivera, J., Wu, Y., Guthrie, B., Marletta, M., King, N., and Brunet, T. (2022). Nitric oxide signaling controls collective contractions in a colonial choanoflagellate. *Curr. Biol.* 32, 2539–2547.e5. doi: 10.1016/j.cub.2022.04.017

Roman, L. J., and Masters, B. S. (2006). Electron transfer by neuronal nitric-oxide synthase is regulated by concerted interaction of calmodulin and two intrinsic regulatory elements. *J. Biol. Chem.* 281, 23111–23118. doi: 10.1074/jbc.M603671200

Safavi-Hemami, H., Young, N. D., Doyle, J., Llewellyn, L., and Klueter, A. (2010). Characterisation of nitric oxide synthase in three cnidarian-dinoflagellate symbioses. *PLoS One* 5:e10379. doi: 10.1371/journal.pone.0010379

Satija, R., Farrell, J. A., Gennert, D., Schier, A. F., and Regev, A. (2015). Spatial reconstruction of single-cell gene expression data. *Nat. Biotechnol.* 33, 495–502. doi: 10.1038/nbt.3192

Schultz, D., Francis, W., McBroome, J., Christianson, L., Haddock, S., and Green, R. (2021). A chromosome-scale genome assembly and karyotype of the ctenophore *Hormiphora californensis*. *G3* 11:jkab302. doi: 10.1093/g3journal/jkab302

Sebé-Pedrós, A., Chomsky, E., Pang, K., Lara-Astiaso, D., Gaiti, F., Mukamel, Z., et al. (2018). Early metazoan cell type diversity and the evolution of multicellular gene regulation. *Nat. Ecol. Evol.* 2, 1176–1188. doi: 10.1038/s41559-018-0575-6

Sheng, N., Bemben, M., Díaz-Alonso, J., Tao, W., Shi, Y., and Nicoll, R. (2018). LTP requires postsynaptic PDZ-domain interactions with glutamate receptor/auxiliary protein complexes. *Proc. Natl. Acad. Sci. U.S.A.* 115, 3948–3953. doi: 10.1073/pnas.1800719115

Shepherd, M., Giordano, D., Verde, C., and Poole, R. K. (2022). The evolution of nitric oxide function: From reactivity in the prebiotic earth to examples of biological roles and therapeutic applications. *Antioxidants* 11:1222. doi: 10.3390/antiox11071222

Shu, C. J., Ulrich, L. E., and Zhulin, I. B. (2003). The NIT domain: A predicted nitrate-responsive module in bacterial sensory receptors. *Trends Biochem. Sci.* 28, 121–124. doi: 10.1016/S0968-0004(03)00032-X

Simmons, D. K., Pang, K., and Martindale, M. Q. (2012). Lim homeobox genes in the ctenophore *Mnemiopsis leidyi*: The evolution of neural cell type specification. *Evodevo* 3:2. doi: 10.1186/2041-9139-3-2

Soneson, C., and Robinson, M. D. (2018). Bias, robustness and scalability in single-cell differential expression analysis. *Nat. Methods* 15, 255–261. doi: 10.1038/nmeth.4612

Stricker, N., Christopherson, K., Yi, B., Schatz, P., Raab, R., Dawes, G., et al. (1997). PDZ domain of neuronal nitric oxide synthase recognizes novel C-terminal peptide sequences. *Nat. Biotechnol.* 15, 336–342. doi: 10.1038/nbt0497-336

Stuehr, D. J., and Haque, M. M. (2019). Nitric oxide synthase enzymology in the 20 years after the nobel prize. *Br. J. Pharmacol.* 176, 177–188. doi: 10.1111/bph.14533

Telford, M. J., Moroz, L. L., and Halanych, K. M. (2016). Evolution: A sisterly dispute. *Nature* 529, 286–287. doi: 10.1038/529286a

Trifinopoulos, J., Nguyen, L. T., von Haeseler, A., and Minh, B. Q. (2016). W-IQ-TREE: A fast online phylogenetic tool for maximum likelihood analysis. *Nucleic Acids Res.* 44, W232–W235. doi: 10.1093/nar/gkw256

Ueda, N., Richards, G., Degnan, B., Kranz, A., Adamska, M., Croll, R., et al. (2016). An ancient role for nitric oxide in regulating the animal pelagobenthic life cycle: Evidence from a marine sponge. *Sci. Rep*. 6:37546. doi: 10.1038/srep37546

UniProt Consortium (2010). The universal protein resource (UniProt) in 2010. *Nucleic Acids Res.* 38, D142–D148. doi: 10.1093/nar/gkp846

Waterhouse, A., Bertoni, M., Bienert, S., Studer, G., Tauriello, G., Gumienny, R., et al. (2018). SWISS-MODEL: Homology modelling of protein structures and complexes. *Nucleic Acids Res.* 46, W296–W303. doi: 10.1093/nar/gky427

Whelan, N. V., Kocot, K. M., Moroz, L. L., and Halanych, K. M. (2015). Error, signal, and the placement of Ctenophora sister to all other animals. *Proc. Natl. Acad. Sci. U.S.A.* 112, 5773–5778. doi: 10.1073/pnas.1503453112

Whelan, N., Kocot, K., Moroz, T., Mukherjee, K., Williams, P., Paulay, G., et al. (2017). Ctenophore relationships and their placement as the sister group to all other animals. *Nat. Ecol. Evol.* 1, 1737–1746. doi: 10.1038/s41559-017-0331-3

Windsor, L., and Thompson, S. (2008). Educating homeless youth in Texas: The McKinney-Vento homeless education assistance improvements act of 2001. *Educ. Real.* 33, 123–130.

Wolf, F., Hamey, F., Plass, M., Solana, J., Dahlin, J., Göttgens, B., et al. (2019). PAGA: Graph abstraction reconciles clustering with trajectory inference through a topology preserving map of single cells. *Genome Biol.* 20:59. doi: 10.1186/s13059-019-1663-x

frontiers | Frontiers in Neuroscience

TYPE Original Research
PUBLISHED 13 April 2023
DOI 10.3389/fnins.2023.1125624

OPEN ACCESS

EDITED BY
James Newcomb,
New England College,
United States

REVIEWED BY
Jian Jing,
Nanjing University,
China
Thomas Pirtle,
College of Idaho,
United States

*CORRESPONDENCE
Leonid L. Moroz
✉ moroz@whitney.ufl.edu

SPECIALTY SECTION
This article was submitted to Neural Technology, a section of the journal Frontiers in Neuroscience

RECEIVED 16 December 2022
ACCEPTED 10 March 2023
PUBLISHED 13 April 2023

CITATION
Nikitin MA, Romanova DY, Borman SI and Moroz LL (2023) Amino acids integrate behaviors in nerveless placozoans. *Front. Neurosci.* 17:1125624. doi: 10.3389/fnins.2023.1125624

Amino acids integrate behaviors in nerveless placozoans

Mikhail A. Nikitin[1], Daria Y. Romanova[2], Simkha I. Borman[3] and Leonid L. Moroz[4,5]*

[1]Belozersky Institute of Physico-Chemical Biology, Lomonosov Moscow State University, Moscow, Russia, [2]Institute of Higher Nervous Activity and Neurophysiology of RAS, Moscow, Russia, [3]Koltzov Institute of Developmental Biology Russian Academy of Sciences, Moscow, Russia, [4]Departments of Neuroscience and McKnight Brain Institute, University of Florida, Gainesville, FL, United States, [5]Whitney Laboratory for Marine Bioscience, University of Florida, St. Augustine, FL, United States

Placozoans are the simplest known free-living animals without recognized neurons and muscles but a complex behavioral repertoire. However, mechanisms and cellular bases of behavioral coordination are unknown. Here, using *Trichoplax adhaerens* as a model, we described 0.02–0.002Hz oscillations in locomotory and feeding patterns as evidence of complex multicellular integration; and showed their dependence on the endogenous secretion of signal molecules. Evolutionary conserved low-molecular-weight transmitters (glutamate, aspartate, glycine, GABA, and ATP) acted as coordinators of distinct locomotory and feeding patterns. Specifically, L-glutamate induced and partially mimicked endogenous feeding cycles, whereas glycine and GABA suppressed feeding. ATP-modified feeding is complex, first causing feeding-like cycles and then suppressing feeding. *Trichoplax* locomotion was modulated by glycine, GABA, and, surprisingly, by animals' own mucus trails. Mucus triples locomotory speed compared to clean substrates. Glycine and GABA increased the frequency of turns. The effects of the amino acids are likely mediated by numerous receptors (R), including those from ionotropic GluRs, metabotropic GluRs, and GABA-BR families. Eighty-five of these receptors are encoded in the *Trichoplax* genome, more than in any other animal sequenced. Phylogenetic reconstructions illuminate massive lineage-specific expansions of amino acid receptors in Placozoa, Cnidaria, and Porifera and parallel evolution of nutritional sensing. Furthermore, we view the integration of feeding behaviors in nerveless animals by amino acids as ancestral exaptations that pave the way for co-options of glutamate, glycine, GABA, and ATP as classical neurotransmitters in eumetazoans.

KEYWORDS

Placozoa, glutamate, GABA, ATP, evolution of nervous system, feeding, glycine, locomotion

Introduction

The nervous systems' origins are among the major evolutionary transitions in the history of life. During such transitions, the canonical, synaptically-wired nervous systems could be preceded by the so-called "volume transmission type integrative systems," composed of heterogeneous populations of secretory cells releasing signal molecules (Moroz, 2009, 2021). Volume transmission might lack speed and spatial localization of synaptic transmission, but in the Proterozoic world, without macroscopic predators, it could be sufficient for coordinating behaviors in early animals. The overall hypothesis is that signaling molecules, initially acquired

for volume transmission systems, later in evolution were co-opted as neurotransmitters and hormones (Moroz et al., 2021b). What are these signaling molecules, and how do they control behaviors in simplest animals?

Sponges (Porifera) and placozoans (Placozoa) are the two extant early-branching animal lineages, primarily lacking neurons, chemical, and electrical synapses but capable of complex and coordinated behaviors with about a dozen of cell types (Smith et al., 2014; Musser et al., 2021). Thus, both phyla are critical in deciphering mechanisms of neural evolution (Smith et al., 2015; Senatore et al., 2017; Moroz, 2018; Varoqueaux et al., 2018; Moroz and Romanova, 2021, 2022). Sponges are sedentary filtrators, while placozoans are highly motile, feed on macroscopic objects (bacterial and algal biofilms), and display various motor complexes, including exploratory and social behaviors (Ockshtein, 1987; Seravin, 1989; Smith et al., 2015; Senatore et al., 2017; Armon et al., 2018; Fortunato and Aktipis, 2019; Smith et al., 2019; Romanova et al., 2020a).

Therefore, we used *Trichoplax adhaerens* as the primary reference species to analyze the cellular bases of placozoan behaviors and focused on identifying individual intercellular signal molecules. The 3-layer cellular organization in Placozoa features functional asymmetry, underlying observed behavioral outcomes. The lower epithelium acts as the densely ciliated locomotory surface with a vertical orientation of digestive/secretory cells supporting feeding. In contrast, the upper contractive layer is more flattened and performs a defensive function against predators. The middle layer consists of more horizontally oriented so-called fiber cells with supposed integrative functions (Grell and Ruthmann, 1991; Smith et al., 2014; Romanova et al., 2021). Fiber cells and, perhaps, other smaller cells in the area form a meshwork of neural-like cell processes containing structures resembling secretory sites or exosomes (Hoshino et al., 2013; Smith et al., 2014; Romanova et al., 2021, 2022) Furthermore, microcavities between ventral and middle cell layers might contribute to the adsorption and sensing of metabolites (Moroz et al., 2021b).

Spaces between ventral epithelium and fiber cells might also contribute to the formation of a compartmentalized dynamic chemical microenvironment with a mixture of signal molecules, which can be both products of enzymatic digestion and specifically secreted molecules. Within this intercellular space, internally and locally secreted signal molecules could access different cellular targets supporting the integration of behaviors (Moroz et al., 2021b).

Thus, in the absence of canonical neurons and muscles, such simpler cellular architecture could facilitate volume transmission to be sufficient to coordinate local contractions, rapid ciliary beating, and even complex behaviors without synapses. However, the nature of signal molecules in Placozoa remains uncertain. In addition to several small peptides (Nikitin, 2015; Varoqueaux et al., 2018) low molecular weight transmitters such as nitric oxide (NO; Moroz et al., 2020a) and glycine (Romanova et al., 2020a) were implicated in coordinating behaviors.

Here, we test whether various amino acids (also acting as digestion products and more localized cell-specific release molecules) can control and integrate placozoan locomotion and feeding behaviors. Due to limited ethological observations, we first described *Trichoplax* behaviors with and without food substrates. Next, we characterized the action of glutamate and aspartate enantiomers, GABA, and glycine as one of the most abundant metabolites in *Trichoplax* (Moroz et al., 2020b). Finally, we tested the effects of ATP – the evolutionary ancient and critical component of synaptic/exocytosis vesicles, and purinergic transmission in general. The data indicate that *Trichoplax* can sense amino acids and suggest that different amino acids integrate behaviors in nerveless placozoans.

Materials and methods

Long-term culturing of placozoans

We used clonal cultures of *Trichoplax adhaerens* (Grell's strain H1, from the Red Sea). We maintained individuals in closed Petri dishes with artificial seawater (ASW, 35 ppm, pH 3–5 days), which was changed (70% of the total volume) every 3–5 days. At the same time, a suspension of the green alga *Tetraselmis marina* (WoRMS Aphia, ID 376158) was added to the culture dishes. We maintain placozoans at the constant temperature of 24 ^{0}C and natural light in environmental chambers (Romanova et al., 2022).

Behavioral experiments

We have routinely observed the relatively stereotyped feeding cycles with the green algae *Tetraselmis* or cyanobacteria *Oscillatoria* as food (Figure 1C).

However, on cyanobacteria *Oscillatoria,* animals can unexpectedly stop feeding and begin to glide around for several hours (Supplementary Figure S2). We could not reproduce these long gliding episodes or elucidate their factors. Therefore, only *Tetraselmis* biofilm has been used in pharmacological tests on feeding behavior (below). Nevertheless, we occasionally employed cyanobacterial biofilm for illustrative purposes of stereotyped patterns (Supplementary Videos S2, S9, S10) because of its uniform color and absence of carbonate sediments.

We have recorded 861 h of time-lapse video, usually recording 8–12 animals at once (over 8,000 animal hours). This dataset included 280 hours (h) of normal behavior (118 h on clean glass and 162 h on algal biofilms), 32 h of experiments with altered salt composition, 96 h with glutamate and aspartate, 278 h with GABA, 75 h with glycine, and 100 h with ATP.

Animal behavior was observed in small (52 mm) glass Petri dishes. Canon PowerShot SX100 camera in macro mode and Gphoto2 software was used for making time-lapse photo series of entire Petri dish with 10 or 30 s intervals. To increase contrast, the experimental Petri dish was installed on a wet black background and illuminated by a thin (3 mm) layer of light from all sides using a custom-made illumination device.

Abbreviations: ATP, adenosine triphosphate; ASW, artificial seawater; GABA, gamma-aminobutyric acid; GABA-BR, gamma-aminobutyric acid receptor type B; mGluR, metabotropic glutamate receptor; iGluR, ionotropic glutamate receptor; CaSR, extracellular calcium-sensing receptor; vGluT, vesicular glutamate transporter; vNuT, vesicular nucleotide transporter.

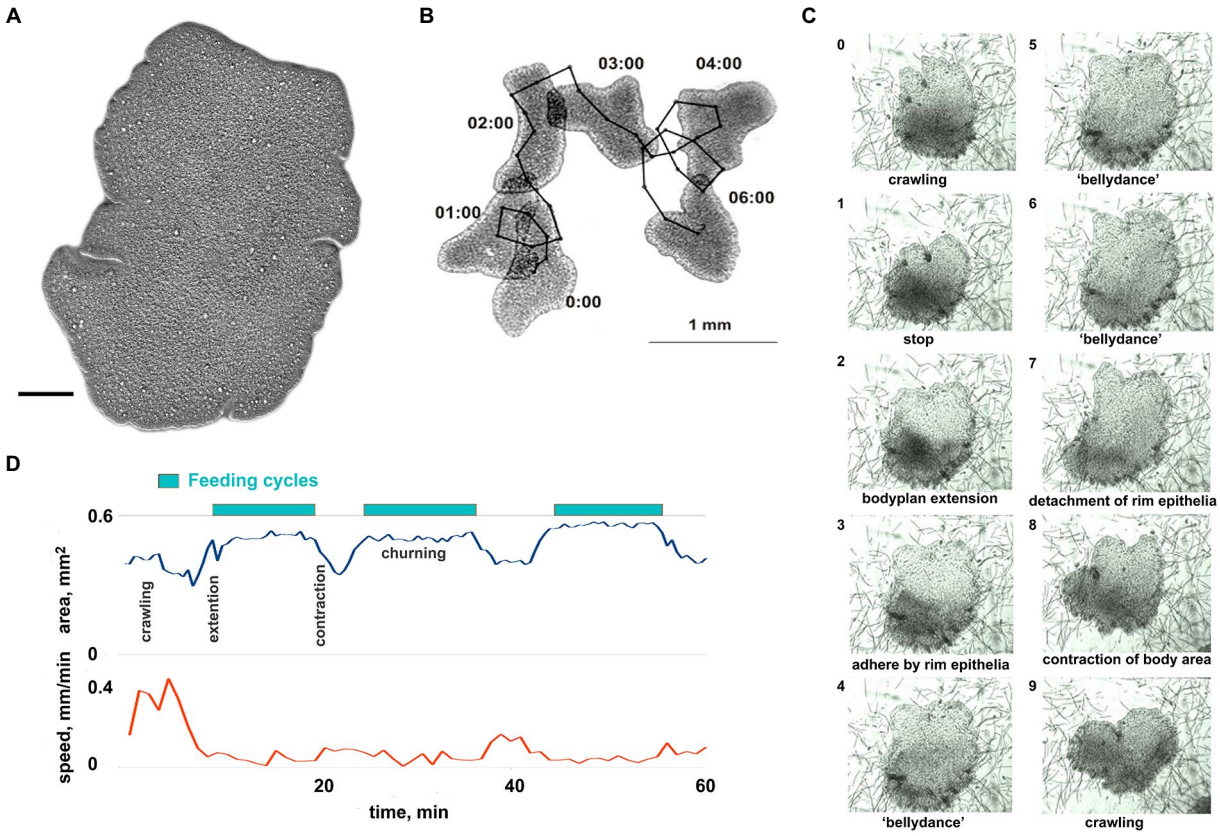

FIGURE 1
General overview of *Trichoplax* behavior. **(A)** *Trichoplax adhaerens* (photo) is a simple, irregularly shaped flat animal with three cell layers. Muscles, neurons, gastric cavities, or any organs are absent. Scale bar=0.1mm. **(B)** Example of *Trichoplax* movement and tracking. Superimposed images of an animal every 60s are shown. Black dots mark the positions of animal centroid every 10s. **(C)** The sequence of ten images shows the feeding cycle of *Trichoplax* on the cyanobacterial biofilm. Images were captured every minute. The animal ceases movement and expands at the beginning of each feeding cycle. The body edge is attached to a substrate, enzymes are secreted, and digested food is absorbed. Digestion is enhanced by churning movements of the central part of the animal. After a digested food is absorbed, the animal detaches its edges, contracts, and resumes movement. Each cycle takes approx. 10–20min. **(D)** The plot of the body area and crawling speed (mm/min) for representative animal feeding cycles on cyanobacterial biofilm. Body area increases at the beginning of each feeding cycle and decreases at the end of each cycle. Locomotion is suppressed during each feeding cycle.

Experimental animals were transferred from a cultural dish in the late exponential phase to a small clean Petri dish for 1 h. They transferred to a glass Petri dish for behavior ecording. 8–12 animals were filmed simultaneously in each experiment.

Experimental glass Petri dishes with algal biofilms were prepared for some experiments. Growing an algal biofilm from small inoculate invariably introduces numerous bright calcareous inclusions which interfere with time-lapse recording and video processing. For cyanobacteria, we placed 5–6 pieces of *Oscillatoria* biofilm (size ~ 1 mm) from cultural to experimental dish with clean ASW, waited 2–3 days for cyanobacterial filaments to spread across the dish, and gently removed residual pieces of transferred thick biofilm. After another 24 h, cyanobacteria spread to clean patches left after removing dense biofilm remnants, and fresh, uniformly thin biofilm was ready for experiments. For green algae biofilm, we scraped some *Tetraselmis* cells from a cultural dish with a pipette, transferred 200–300 µL of the cell suspension to a microcentrifuge tube, and waited for 1 min. After that, we gently moved most of the suspension (discarding the bottom 50 µL with calcareous sediment) to the experimental dish and waited for 1–2 h for algal cells to attach to the glass. All amino acids and ATP were from Sigma-Aldrich. Stock solutions were prepared for each experimental day.

Ca-free and high-Mg artificial seawater (ASW) recipes were based on the ASW recipe from Cold Springs Harbor Protocols (Seawater, 2012). Ca-free artificial seawater was prepared as follows: NaCl: 436 mM; $NaHCO_3$: 2 mM; KCl: 9 mM; $MgCl_2x6H_2O$: 23 mM; $MgSO_4x7H_2O$: 25.5 mM; dissolved in distilled water. For behavior experiments with low Ca^{2+} animals were initially recorded in ~1 ml drops of normal ASW (10 mM $CaCl_2$) and then 6X volume of Ca-free seawater was added to the final concentration of $CaCl_2$ 1.5 mM.

For behavior experiments with 200 mM $MgCl_2$ animals were initially recorded in normal ASW (48 mM $MgCl_2$) and then an equal volume of high-Mg seawater was added to a final concentration of $MgCl_2$ 200 mM. We have tested the effects of ASW with 200 mM $MgCl_2$ and appropriately decreased Na^+ (standard ASW contains 48 mM $MgCl_2$).

Analysis of behavior recordings

Time-lapse sequences of *Trichoplax* behavior were imported to the Fiji ImageJ program (Schindelin et al., 2012). Animal positions and paths were determined using the WrMtrck plugin (Nussbaum-Krammer et al., 2015). Illustrative videos were created from the same time-lapse photo series using Avidemux video editor[1].

Track data was analyzed in OpenOffice Calc (graphs, Welch *t*-test, straightness and turn angle calculation). There are several measures of animal path tortuosity described in the literature: Intensity of Habitat use (IU), Fractal D, MSD (Mean Squared Distance), Straightness (ST), and Sinuosity (SI; Benhamou, 2004; Almeida et al., 2010). In our data, path shape changes in different conditions were best captured by the simplest of these measures, the straightness index, which is just displacement (linear distance between start and finish) divided by path length. It takes values from 0 (closed loop) to 1 (straight path). We used 5-min and 60-min straightness in this work.

Feeding cycles were counted manually. Power spectral density was calculated using the Signal package from SciPy library (Virtanen et al., 2020) using a custom Python script.

Search and annotation of iGluR genes, alignment, and phylogenetic trees

We used the data from the sequenced genomes of animals deposited in GenBank and elsewhere (listed in Supplementary Table S2). The search for possible homologs was performed using sequence similarity methods (BLAST/DELTA BLAST) algorithm using all human iGluRs, mGluRs, GABA-Brs, and vGluTs from SwissProt database as initial queries. Protein sequences were aligned in MAFFT Online (Katoh et al., 2005, 2019).[2] Phylogenetic trees were inferred using either the Maximum Likelihood algorithm implemented in IQTREE 1.6.12 (Nguyen et al., 2015) with automatic choice of evolutionary models or the Bayesian algorithm in MrBayes 3.2.6 (Ronquist et al., 2012). Maximum Likelihood tree robustness was tested with 2000 ultrafast bootstrap replicates (Hoang et al., 2018). Trees were visualized and annotated in iTol WEB (Letunic and Bork, 2021).

Results

Native behavior of *Trichoplax adhaerens*

Search and feeding cycles as dominant behavioral patterns

Trichoplax behavior is substantially affected by substrate composition and food abundance, with relatively stereotyped feeding episodes. Without food, *Trichoplax* glides on ventral cilia without defined anterior end and constantly changing shape (Figures 1A,B; Supplementary Video S1). Its path is apparently chaotic and reminiscent of Brownian motion (Figure 1B). On suitable algal (*Tetraselmis*) or cyanobacteria (*Oscillatoria*) substrates, animals could move as little as 0.05 mm before the next feeding cycle, which is often initiated upon contact with microalgae (Smith et al., 2015; Senatore et al., 2017; Smith et al., 2019; Smith and Mayorova, 2019).

Each cycle takes approximately 10–20 min and begins with a locomotory pause, also associated with expanding the body surface area (Figures 1C,D; Supplementary Video S2). *Trichoplax* adhere to the substrate, secrete digestive enzymes on the surface below, and perform "churning" or swirl-like movements of the central area with body edges tightly attached. *Trichoplax* absorbs the contents of lysed algal cells during this period. After the 5–15 min absorption phase, animals detach their peripheral edges, decrease body surface area, and resume locomotion.

Long-term experiments show that feeding cycles on *Tetraselmis* biofilm are robust, stereotyped, and reproducible for 24–30 h. Therefore, *Tetraselmis* biofilm has been used in pharmacological tests on feeding and exploratory behavior (see below).

Low-frequency oscillations of *Trichoplax* behaviors

All tested animals showed spontaneous long-term oscillations of locomotory patterns under control conditions, even without algae or any other substrate. This is surprising because previous studies described *Trichoplax* locomotion as Brownian, which does not imply regular endogenous oscillations (see Discussion). We quantified this long-term rhythmicity, with a period of about 8 min, by power spectral density analysis using displacement parameters (Figures 2A,D). With 10-s interval displacement, the spectrum was nearly uniform (similar to white noise), while 1-min and especially 5-min displacement intervals showed an excess of low frequencies below 0.004 Hz (periods above 250 s).

Displacement can be expressed as the product of two values: path length and straightness (Figure 2B). Figure 2A shows that long-term oscillations in displacement were mirrored by the path straightness, whereas path length values were more constant (Figure 2A). Thus, fluctuations in displacement are associated with changes in turn patterns but not speed. In other words, *Trichoplax* locomotion is reminiscent of the "Viennese waltz," where "dancers" switch between straight motion and turn in one place (Supplementary Video S3).

Long-term recordings (24 h) also showed that locomotion speed increased over time. Locomotion was relatively slow during the first 2 h of their placement into experimental dishes (below 0.2 mm/min), gradually accelerating in the first 12 h. After that, the animal speed reached a plateau at about 0.4 mm/min (Figure 2E; Supplementary Video S4). The trajectory shapes did not change. We have hypothesized that the observed gradual increase in locomotion could be either mediated by animals' internal state (e.g., starvation level) or by changing environment (chemical composition of water and glass surface).

To choose between these possibilities, we have measured the locomotion of animals that were first starved for 24 h and then transferred to a new clean dish vs. animals moved a to a conditioned dish where other *Trichoplax* specimens were crawling for 24 h before tests. We also tried combinations of fresh

1 http://avidemux.sourceforge.net/

2 https://mafft.cbrc.jp/alignment/server/

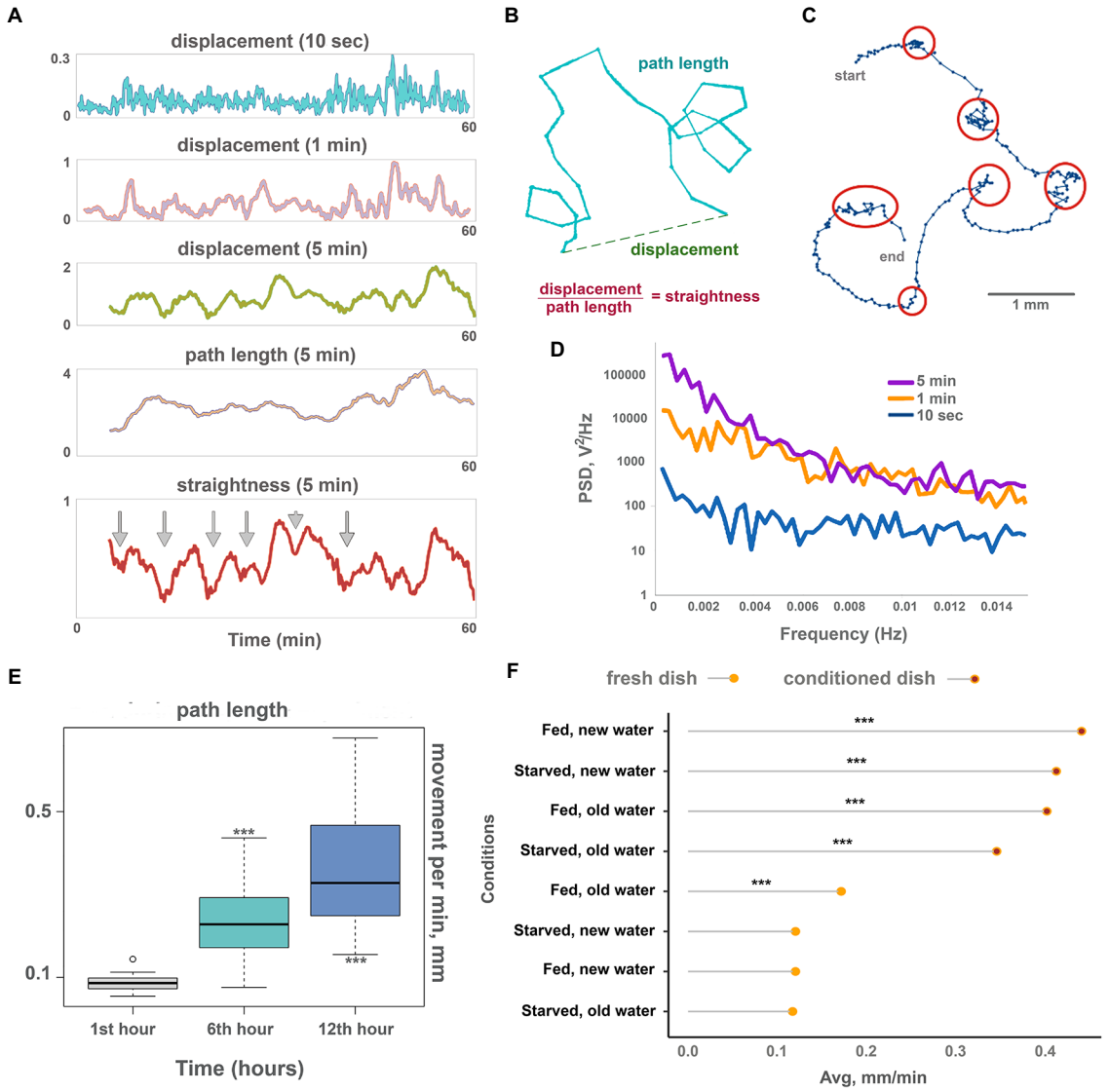

FIGURE 2
Oscillations and long-term dynamics during normal locomotion. **(A)** The plot of displacements (how far out of starting place an animal is located) of a single animal for 10s, 1min, and 5min periods, plus track length and track straightness (displacement/length ratio) for 5min periods observed for 60min on conditioned Petri dish. While 10-s displacements are chaotic, oscillations emerge in 1min and are clearly observed in 5min displacements. Larger scale oscillations of 5min displacement with a period of about 6–8min coincide with fluctuations of path straightness. The path length is more stable over time and does not show regular oscillations. Arrows denote chaotic "marking time" periods every 6–8min when track straightness is reduced. **(B)** Scheme showing displacement (how far out of an animal's starting position), path length, and straightness. **(C)** Track of the *Trichoplax* with dots marking an animal's positions every 10s, recorded for 40min—it is the same specimen as in **A**. Six periods of decreased locomotory speed (dense dots) are highlighted with red circles and correspond to straightness minima marked by arrows in **A**. Note that periods of decreased speed coincide with sharp turns of the track. See also Supplementary Videos S3. Animal size is about 0.5mm. **(D)** Plot of power spectral density (PSD) of 10s, 1min, and 5min displacements on conditioned Petri dish (average of 10 animals). PSD of 10-s displacements is nearly uniform (characteristic of white noise), while PSD of 1min and especially 5min displacements show pronounced low-frequency fluctuations (below 0.004Hz, or periods above 250s). **(E)** The speed of locomotion of the *Trichoplax* is gradually accelerated over 12h. Animal locomotion and tracks were recorded at 60-min intervals. Asterisks denote significant differences in the locomotion speed from initial observations during the 1st hour (Welch *t*-test, ***$p<0.001$) N animals=20. **(F)** Factors affecting the long-term acceleration of *Trichoplax adhaerens* on glass dish: animal starvation, water, and glass freshness. Data are presented as median±SD. $N=33, 36, 37, 34, 32, 35, 33, 35$. Locomotion is slow on a fresh glass dish and accelerated on the conditioned ("old") glass where placozoans (same or another specimen) crawled for 24h before. The speed of locomotion was recorded for 120min. Asterisks denote a significant difference in speed from the control condition (new dish, new water, well-fed animals; Welch *t*-test, ***$p<0.001$).

seawater on the conditioned dish, and conditioned seawater in a clean dish. To achieve this, we transferred seawater from the conditioned dish to the clean dish or gently poured fresh artificial seawater (ASW) into the emptied conditioned dish before placing the animals.

Combined, these experiments have shown that *Trichoplax* locomotion is significantly faster (about three times) on the conditioned surfaces compared to clean dishes, regardless of water freshness and animal starvation state (Figure 2F). These results suggest that the observed acceleration of locomotion over time is mediated by

changing substrate by animals. For example, it is well-known that *Trichoplax* can release mucus during locomotion (Mayorova et al., 2019) and accumulation of the mucus can increase the speed on the conditioned dishes.

Ca-dependent secretion of signal molecules can contribute to observed behavioral dynamics in placozoans

Low-frequency oscillations of feeding and locomotory patterns might be a result of complex intercellular chemical interactions (e.g., volume-type transmission) among different cell types in placozoans. In experiments on neural systems, polysynaptic inputs can be eliminated (or significantly suppressed) by high [Mg^{2+}] concentrations, where these ions, attracted to negatively charged phosphate residues of membrane phospholipids, caused functional membrane hyperpolarization and increased thresholds for generation of action potentials, depolarization-induced secretion and eventually chemical transmission in central and peripheral synapses (Del Castillo and Engbaek, 1954; Hutter and Kostial, 1954; Arossa et al., 2022). This phenomenon and seawater with high $MgCl_2$ concentration are widely used for anesthesia and relaxation of marine invertebrates (Arossa et al., 2022). Decreased concentrations of [Ca^{2+}] also suppress calcium-dependent exocytosis, including exocytosis of transmitters in all types of neurons and other secretory cells. Thus, if the integration of locomotory functions in *Trichoplax* is dependent on action potentials or calcium-dependent exocytosis, we can expect its disruption at high [Mg^{2+}] or low [Ca^{2+}] concentrations.

After adding ASW with 200 mM [Mg^{2+}] directional locomotion of *Trichoplax* gradually disappears. After 20 min in high [Mg^{2+}], animals only rotate and wobble in one place (Figures 3A,B; Supplementary Video S5). Low-frequency oscillations in displacement and straightness were decreased 5–10 times compared to the control, but the 5-min path is unchanged. In other words, cilia beating continued unchanged on the level of individual cells, but coordination between cells, required for coherent locomotory patterns, was wholly disrupted (Figure 3B). The decrease of [Ca^{2+}] concentration from normal 10 mM in the seawater to 1.5 mM had similar but faster effects (Figures 3A,B; Supplementary Video S6). Directional locomotion also stopped after 1 min in 1.5 mM [Ca^{2+}]; *Trichoplax* continued to turn and wobble in one place like in 200 mM [Mg^{2+}] (Figure 3B; Supplementary Video S6).

In summary, these experiments confirm the hypothesis that Ca-dependent secretion of signal molecules can contribute to observed low-frequency oscillations of behavior in placozoans.

Pharmacology of amino acids' signaling

L-/D-glutamate and L-/D-aspartate initiate feeding-like cycles even on a clean substrate

Enantiomers of glutamate (Glu) and aspartate (Asp) are among the most abundant metabolites in basal metazoans. However, their functional roles in these animals are elusive at this moment (Moroz et al., 2020b). In placozoans tested on a clean glass dish, both enantiomers of glutamate and aspartate induced reactions resembling feeding cycles on algal biofilms (Figures 4B,C; Supplementary Video S7). However, Glu- and Asp-induced cycles are shorter than natural feeding cycles (8–12 and 10–20 min/cycle, respectively), lack a churning phase, and their contraction phase is prolonged and incomplete. In a series of 3–4 Glu- or Asp-induced feeding-like cycles, the animal surface area increases from the first cycle to the next (Figure 4C).

The same type reduced feeding-like cycles without the churning phase are observed occasionally in clean glass dishes without any substances. 1–2 h after the addition of Glu or Asp., these cycles disappear, and animals continue normal locomotion.

Enantiomers of Glu and Asp had different behavioral effectiveness, increasing in order D-Glu → L-Asp → D-Asp → L-Glu. D-Glu is the least active of all; it induces 1.5–2 feeding-like cycles/h on average (Figure 4A). The effect of D-Glu is not dose-dependent in the tested range of concentrations from 0.1 to 3 mM (Figure 4A), and other isomers have dose-dependent effects (Figure 4A). The maximum possible effect, namely, animals continuously exhibiting feeding-like cycles (~4.5/h), is observed for ≥0.3 mM L-Glu, ≥1 mM D-Asp., and 3 mM L-Asp (Figure 4A).

A distinct effect was observed in the presence of 3 mM L-glutamate. *Trichoplax* expands and retains the same expanded shape for 2–3 h. During this time, animals exhibit elements of feeding-like cycles (stops and resuming locomotion, attachment, and detachment of edges) but do not perform contractions (Supplementary Video S8). After 2–3 h, animals folded into lumps, stopped moving, and then dissociated into separate cells, and die. 3 mM of L- and D-Asp or D-Glu did not show such adverse effects even after 24 h of incubation. Of note, no L-/D-glutamate and L-/D-aspartate initiate effects were observed when animals were already feeding on algae (data not shown).

ATP positively and negatively modulates feeding at different time scales

ATP and L-glutamate are the two major metabolites in the cytoplasm of most cells (Moroz et al., 2021a). They are released in media upon cell damage, could be sensed by other cells, and used to trigger defensive/regenerative or feeding responses. This injury-related sensing of L-glutamate and ATP could be exaptations for early neural signaling (Moroz et al., 2021b). Therefore, we tested *Trichoplax's* behavioral responses to ATP.

On the clean glass, the effect of ATP was very similar to glutamate but weaker. 3–5 min upon the addition of ATP, a series of 2–3 feeding-like cycles were observed (Figure 4A). These feeding-like cycles were shorter than naturally occurring feeding cycles on algal biofilms and lack the "churning" phase, the same as observed after L-glutamate addition. In contrast to Glu, these cycles ceased after about 1 h of incubation in ATP. After that, animals behaved similarly to controls (Figure 5B). Concentrations of 0.1 and 0.3 mM of ATP had the same magnitude of effects.

On the algal biofilm, the effects of ATP were more complex and prolonged. At first 1–2 h, feeding of *Trichoplax* was activated compared to control (unless they were not eating all the time before). But after 8–10 h of incubation with ATP, feeding was ceased almost entirely, while control animals continued to eat (Figure 5A). Similar long-term feeding suppression was observed for GABA (see below) but not for L-/D-glutamate, D-/L-aspartate.

Glycine and GABA suppress feeding cycles.

Glycine suppressed placozoan feeding on algal biofilms. This effect was relatively fast, on the order of 10–20 min (Figure 6A; Supplementary Video S9). Effect was dose-dependent: 0.1 mM glycine

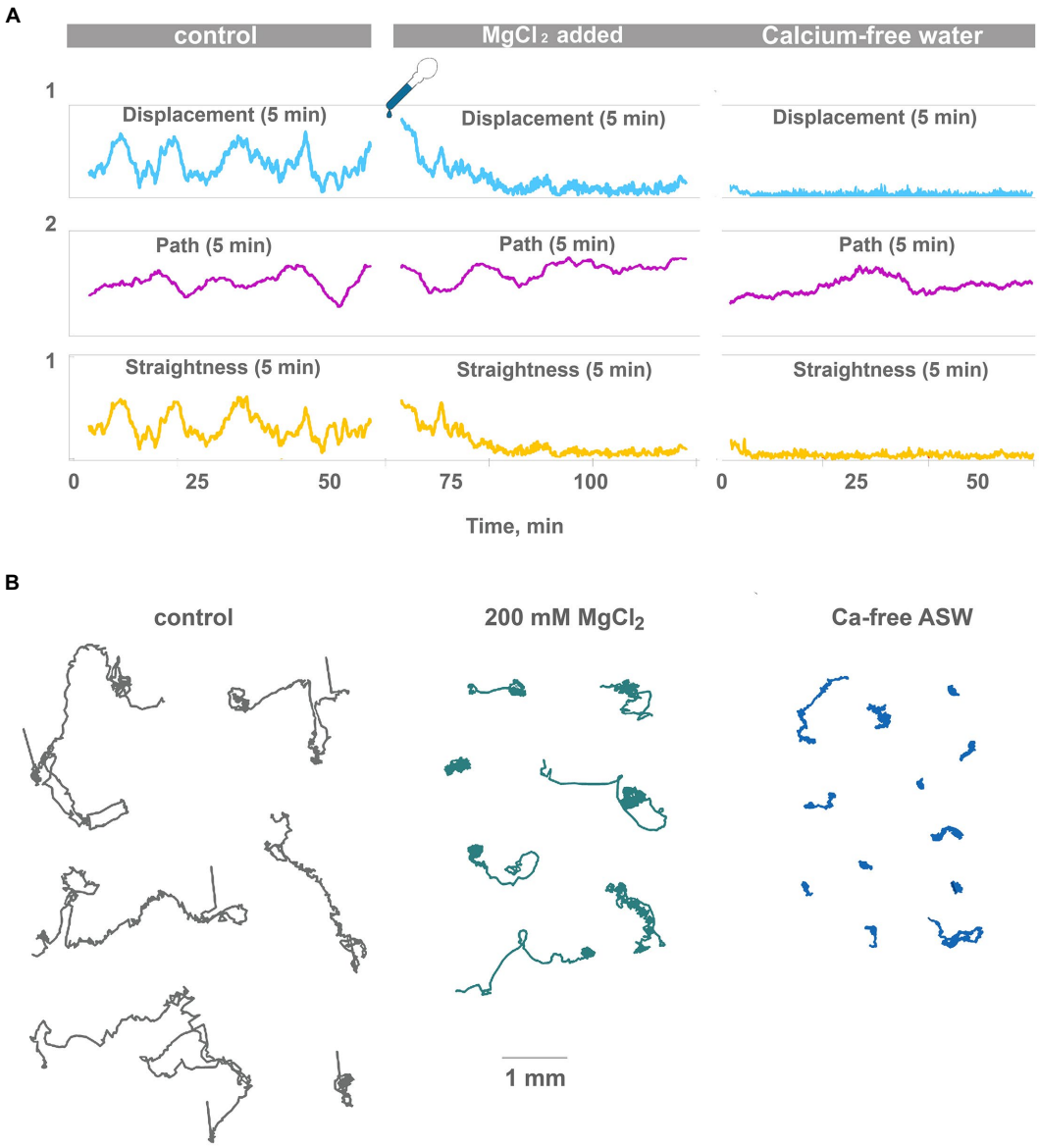

FIGURE 3
High Mg^{2+} or low Ca^{2+} disrupts coherent locomotion and oscillations. **(A)** Representative plot of displacement, track length, and track straightness (displacement/length ratio) for 5min periods for a single animal observed for 120min on a clean Petri dish in normal seawater and after the addition of 200mM $MgCl_2$ (corrected for osmolarity). Oscillations of straightness and displacement present in control conditions (compare Figure 2A) and gradually disappear after 20min in 200mM $MgCl_2$. However, the 5-min path is unchanged. Therefore, animals continue ciliated locomotion but lose the ability to maintain one direction. Representative plot of displacement, track length, and track straightness for 5min periods for single animal observed for 60min in low-Ca seawater. Displacement and straightness are close to zero immediately after a drop in Ca^{2+} concentration, but track length is similar to control. Coherent directed movement is quickly lost, compared to 20min transition period in 200mM $MgCl_2$. **(B)** Tracks of *Trichoplax* in normal seawater (45mMMg^{2+}, 10mM Ca^{2+} as control), after adding 200mM $MgCl_2$, and in low-Ca seawater (1mM Ca^{2+}), respectively. Tracks were recorded for 60min.

reduced the frequency of feeding cycles by 26%, 0.3 mM—by 86% (Figure 6B). Higher concentrations were not tested because toxicity was observed upon prolonged (24 h) exposure to 0.3 mM glycine. However, the effect of 1–2-h exposure to 0.3 mM glycine was reversible as animals resumed feeding at an average rate 15–30 min after glycine washout (data not shown).

Feeding was suppressed after prolonged incubation in GABA. Animals preincubated in 1 mM GABA for 20 h before relocation to algae showed 60% fewer feeding cycles per hour than average (Figures 6C,D). The dynamics were different if animals were incubated in GABA in a dish with algae. Feeding was normal in the first 2 h with GABA, suppressed between 3 and 6 h after GABA addition, and then recovering phase, reaching full recovery 14–16 h from GABA addition (Figure 6E; Supplementary Video S10). This difference in dynamics might result from form algae-meditated degradation of GABA.

Effects of amino acids on placozoan locomotion

GABA (0.3-1 mM) had a profound inhibitory effect on *Trichoplax* locomotion after long (6–24 h) incubation. Animal tracks became

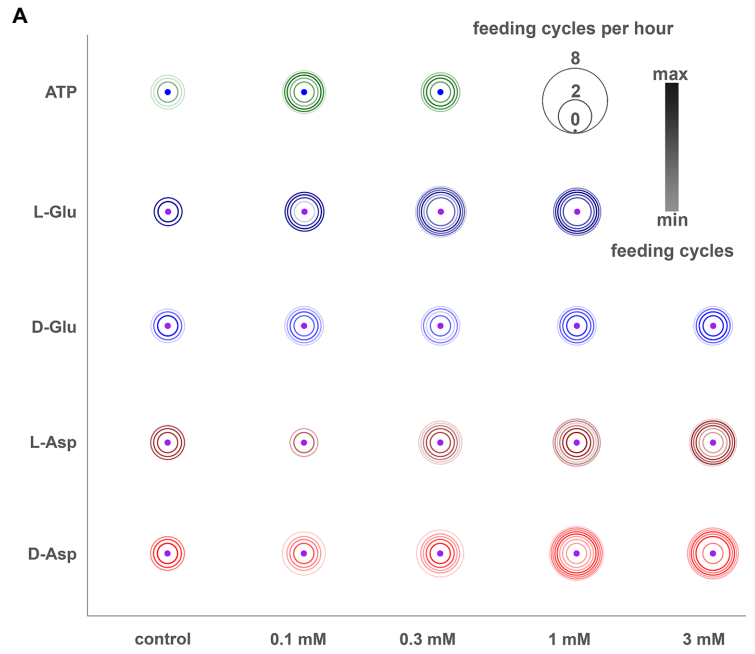

FIGURE 4
Glutamate, aspartate, and ATP induce reactions similar to feeding cycles on algal biofilm. **(A)** Bubble plot comparison of various ATP, L- and D-glutamate concentrations and L- and D-aspartate in inducing feeding-like cycles. Pharmacological activity decreases in the following order: L-Glu>D-Asp>L-Asp>D-Glu. Unlike other tested amino acids, the D-Glu response is not dose-dependent (the difference between adjacent concentrations is insignificant). Feeding cycles for 3mML-Glu are not shown because this concentration elicits prolonged (30–90min) arrest of locomotion and nearly permanent body expansion instead of regular 5–10min feeding cycles (see Supplementary Video S8). Scale: feeding cycles per hour, the color bar was normalized: black—max counts, light grey—min counts. **(B)** Diagram of feeding-like activity of *Trichoplax adhaerens* on the clean glass dish. In control, only a few occasional cycles are observed. After adding 1mML-glutamate, *Trichoplax* exhibit repeated feeding cycles similar but not identical to those observed on natural food substrates. **(C)** The plot of body area for representative animals feeding on cyanobacteria (light blue line) and clean glass upon addition of 0.3mML-Glu (dark blue line). Feeding-like cycles induced by L-Glu are shorter than natural feeding cycles (7–10min vs. 10–20min), lack a 'digestion phase' with churning movements (plateau on the area plot), and have a more extended body contraction phase. In glutamate-induced feeding-like cycles, body contraction is often incomplete, and body area increases over consecutive cycles.

extremely convoluted in the presence of GABA compared to the control (Figure 7A; Supplementary Video S11). Furthermore, slow oscillations of locomotory parameters (5 min displacement and straightness) with a period of about 6–10 min, observed in control testes, disappeared in the presence of GABA. Occasional 2–5 min long bursts of directed gliding were observed, interleaved with long turns and wobbling in one place (Figures 7D,E; 2 episodes of directed gliding in 120 min). Average track straightnesses were decreased from 0.27 to 0.12 after 12 h in 1 mM GABA on the clean dish (Figure 7C), and to a lesser extent on the conditioned dish (Supplementary Figure S1B). Suppression of directed gliding was partially similar to 200 mM Mg^{2+}.

The second effect of GABA on locomotion was a decreased average speed of animals on conditioned glass. If animals were placed on a conditioned dish with GABA, their average speed decreased twofold over 12 h (Figure 7B). On a clean dish with GABA, speed was uniformly low during the 24 h of recording (Supplementary Figure S1A), while in control, they accelerated from ~0.15 to ~0.5 mm/min in 12–20 h (Figure 1F).

Locomotion on clean glass was also subtly affected by glycine. The speed of animals' locomotion was unchanged (Figure 8C), but track shapes became more convoluted (Figure 8A; Supplementary Video S12). Quantitatively, the 5-min straightness index and 5-min path and displacement were not changed upon glycine addition; their long-term oscillations were not changed either. However, 60-min straightness was decreased significantly upon glycine addition. On the clean glass, 60 min straightness index (ST, see "Materials and methods") was 0.32 ± 0.16 (median ± SD) in control. After adding 0.1 mM glycine, 60-min ST decreased to 0.22 ± 0.09 (Figure 8B). This difference was statistically significant at $p < 0.01$. 0.3 mM of glycine caused a slightly weaker effect (ST = 0.24 ± 0.12, significantly different from the control at $p < 0.05$).

Molecular bases of amino acids' sensing in placozoans

Receptors

How and why observed effects of amino acids and ATP are mediated? We have analyzed the presence of receptors and relevant vesicular transporters involved in glutamatergic, GABAergic, and purinergic signaling within the *Trichoplax* genome (Srivastava et al., 2008). We have found 85 amino acid receptor genes, which encode14 ionotropic glutamate (iGluRs), 34 metabotropic glutamate-like (mGLuRs), and 37 metabotropic GABA-like (GABA-BRs) receptors (Supplementary Table S1). This is the richest repertoire of amino acid receptors among all analyzed animals, from sponges to humans. Humans have 25 amino receptors in these families (15 iGluR, 8 mGluR, and 2 GABA_BR), sponges *Amphimedon* and *Sycon*—0, 8, 21, and 1, 28,

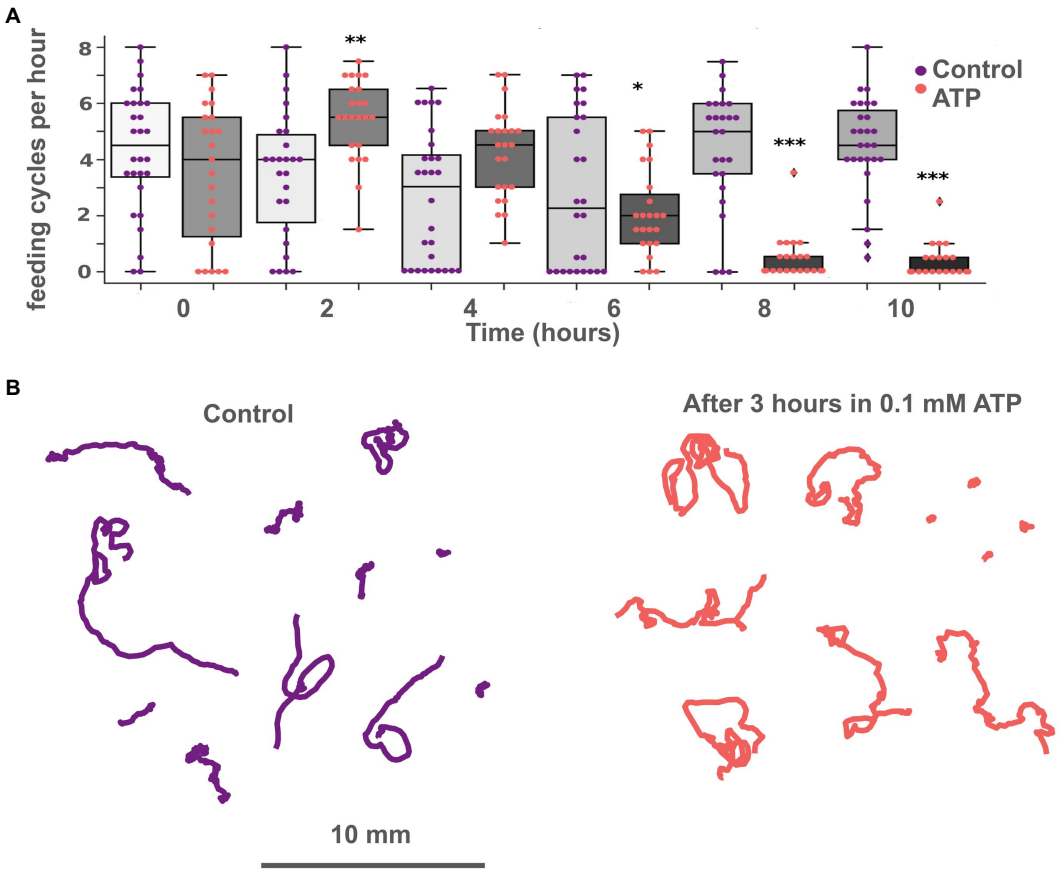

FIGURE 5
ATP exhibits long-term suppression of feeding and does not affect locomotion. **(A)** Bar chart of feeding activity of *Trichoplax* on green algae biofilms in normal conditions and with 0.1mM ATP. Adding ATP to the dish with green algae increases 'feeding' activity at first and decreases after 6h. In the experimental dish, ATP was added at 2h. Asterisks denote a significant difference in feeding activity from the control (Welch *t*-test, **p*<0.05, ***p*<0.01, ****p*<0.001). N animals=37 and 28 for ATP and control, respectively. **(B)** Tracks of animals incubated in 0.1mM ATP for 3h (right) and in control (left). No significant differences in track length, straightness, or displacement were found.

0, respectively. This is due to remarkable lineage-specific expansions of mGluRs, GABA-BRs, and Epsilon-type iGluRs in Placozoa. Ionotropic GABA-A and glycine receptor genes were not found in *Trichoplax* genome. Similar independent radiation events were found in the coral *Stylophora* and the hemichordate *Saccoglossus* (Figures 9–11; Supplementary Table S1). Ctenophores have an expansion of Epsilon iGluRs (lost in many bilaterian lineages) but very few metabotropic receptors. Homosclerid sponge *Oscarella* has an expansion of AKDF-type iGluRs but only single mGluR and GABA-BR. In contrast, in all analyzed species of demosponges and calcisponges (*Amphimedon*, *Ephydatia*, *Ircinia*, and *Sycon*), we noted a dramatic expansion of metabotropic receptors with a few cases of iGluRs (Figures 9–11; Supplementary Table S1).

Most analyzed *Trichoplax* receptors are not closely related to well-annotated mammalian receptor families. But *Trichoplax* does have one ortholog of GABA-BR1, two metabotropic glutamate-type receptors, and one encoding extracellular calcium-sensing receptors (Figures 10, 11; Supplementary Table S1).

All placozoan iGluRs belong either to Epsilon (10 members) or AKDF (4 members) families. On the phylogenetic tree (Figure 9; Supplementary Figure S3), one can see that placozoan AKDF receptors diverged in parallel with sponge and cnidarian clades and clustered with receptors from the calcareous sponge *Sycon*. This tree topology suggests the ancient radiation of AKDF receptors before major animal phyla diversification and reflects retaining this ancestral diversity in Placozoa.

Placozoan GABA-B receptors form seven independent clades across the phylogenetic tree and interleaved with multiple clades of cnidarian and hemichordate GABA-BRs (Figure 10; Supplementary Figure S4). This implies the rich ancestral diversity of GABA-B-like receptors that was lost in most Bilateria but preserved in hemichordates and basal metazoans.

Metabotropic glutamate-like receptors in Placozoa belong to four distinct clades (Figure 11). One is orthologous to molluscan mGluRs; three others are more related to extracellular calcium, taste, and vomeronasal receptors (Supplementary Figure S5).

Textbook glycine receptors are chloride-gated (inhibitory) members of the ionotropic pentameric Cys-loop receptor family. Cys-loop receptors are absent in the sequenced *Trichoplax* genome. However, glycine can act as a co-agonist of NMDA-type iGluRs (Ramos-Vicente et al., 2018) and was shown as the main ligand of two Epsilon-type excitatory iGluRs in Ctenophora and *Branchiostoma* (Alberstein et al., 2015; Ramos-Vicente et al., 2018). Therefore, some

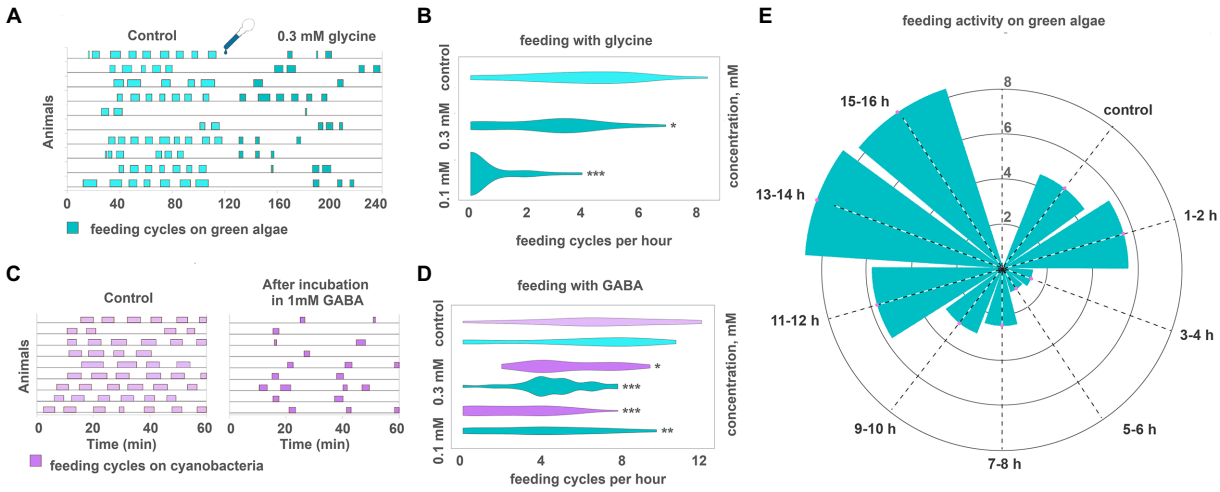

FIGURE 6
GABA and glycine modulate feeding cycles in *Trichoplax adhaerens*. **(A)** After adding 0.3mM glycine, the number, and frequency of feeding cycles on green algae biofilm reduced approximately threefold compared to the control. **(B)** The effect of glycine on feeding activity is dose-dependent. 0.1mM reduces the number of feeding cycles by 26%, 0.3mM—by 86%. Asterisks denote a significant difference in feeding activity from the control (Welch *t*-test, **p*<0.05, ****p*<0.001). N animals=65, 36, 29. **(C)** After 20h in 1mM GABA **(C**, right**)**, the number and frequency of feeding cycles reduced approximately threefold compared to the control [after 20h in pure artificial seawater (ASW)] **(C**, left**)**. In control, *Trichoplax* exhibit feeding cycles every 10–15min. **(D)** GABA decreased feeding activity on green algae and cyanobacterial biofilms in concentrations of 0.3 and 1mM. Asterisks denote a significant difference in feeding activity from the control (Welch *t*-test, **p*<0.05, ***p*<0.01, ****p*<0.001). N animals=80, 64, 27, 26, 47, 40. **(E)** After adding 0.3mM GABA, feeding activity decreased on the green algal mat (*T. marina*) after 1–2h from the starting point and recovered after 11–12h of incubation. N animals=10.

placozoan iGluRs can function as excitatory ionotropic glycine receptors.

ATP receptors are classified into ionotropic P2X and metabotropic P2Y (Abbracchio and Burnstock, 1994). P2X receptors were found in the *Trichoplax* genome (Srivastava et al., 2008) and localized immunohistochemically to fiber cells of the middle cell layer (Smith et al., 2014). Neither we nor Srivastava et al. (2008) were able to find any P2Y receptors in *Trichoplax*. Our phylogenetic analysis of P2X receptors (Figure 10) shows that all placozoans have two P2X genes most similar to their respective homologs from the sponge *Oscarella*. Cnidarians and sponges also have from 1 to 3 P2X receptors (Figure 12; Supplementary Table S1).

Transporters

Transmitters, such as amino acids and ATP, can be accumulated in secretory vesicles by specialized subfamilies of vesicular transporters. Vesicular transporters for both glutamate and ATP belong to the SLC17 family of membrane transporters together with sialic acid transporter (SLC17A5, also known as sialin), phosphate and urate transporters (SLC17A1-A4).

Figure 13 shows the phylogenetic tree of the SLC17 family with well-supported clades of vesicular glutamate transporters (vGluTs), sialins, and vesicular ATP transporters (vNuTs), as well as examples of lineage-specific radiation events. Placozoan SLC17 transporters form three clades belonging to vGluT, sialins, and the uncharacterized subfamily of ctenophore and sponge transporters. Therefore, *Trichoplax* does have a vesicular glutamate transporter and might utilize components of canonical glutamatergic transmission. VNuT clade contains predicted proteins from Porifera, Cnidaria, Bilateria, and the unicellular eukaryote *Capsaspora* (Figure 13). However, vNuT homologs were not found in *Trichoplax*, suggesting the loss of this type of transporter in the placozoan lineage.

In summary, we infer that vGluTs diverged in the common ancestor of (Placozoa+Cnidaria + Bilateria), while vNuTs have a deeper, pre-metazoan ancestry.

Discussion

Locomotion, feeding, and integrative systems in Placozoa

Here, we observed spontaneous oscillations in the locomotion of *Trichoplax adhaerens*. We also revealed the induction and modulation of endogenous locomotory and feeding cycles by transmitter candidates such as enantiomers of glutamate and aspartate, GABA, glycine, and ATP. The administration of each of these molecules resulted in induction or inhibition of well-coordinated behavioral responses suggesting that these are endogenous signal molecules. They might represent the cohort of signaling molecules, enabling behavioral integration in the common metazoan ancestor (Moroz et al., 2021b).

Integrative systems in biology express themselves in global electrical, chemical, and mechanical oscillations on the scale of the entire brain or organism (Hanson, 2021). These low-frequency electrical oscillations are often spontaneous (not caused by external stimuli), ubiquitously found in neural systems from *Hydra* to humans, and are also shown for higher plants, fungi, and bacterial biofilms (Hanson, 2021). Spontaneous mechanical and chemical oscillations are well-known as growth and development

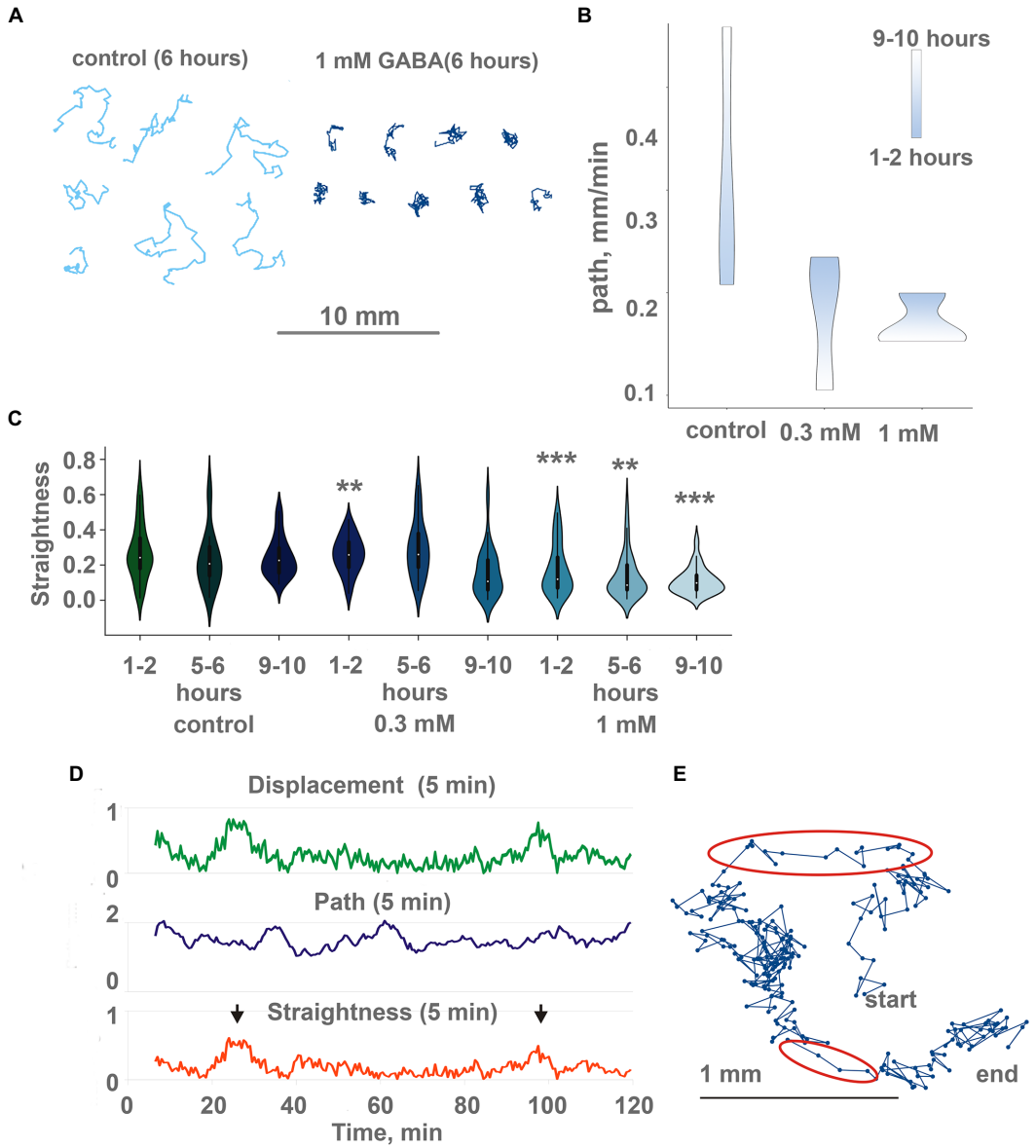

FIGURE 7
GABA modulate locomotion in *Trichoplax adhaerens*. **(A)** Tracks of animals incubated for 6h in 1mM GABA (right) and ASW (left). After GABA incubation, tracks are shorter and more squiggly compared to the control. Tracks were recorded for 60min. **(B)** in native conditions, animals show increasing path length through time (from starting point to the destination), the additional concentration of GABA (0.3 and 1mM) changes, and decreasing path. Individuals placed in the same locations for a long time (9–10h). Scale bar: blue—1-2h, white—9–10h. **(C)** During incubation with GABA, track straightness gradually decreases, while in control, it is unchanged. Asterisks denote a significant difference in track straightness from the control (Welch *t*-test, $^{**}p<0.01$, $^{***}p<0.001$). *N*=98, 50, 74, 29, 46, 69, 35, 44, 72. **(D)** Representative plot of displacement (green), track length (blue), and track straightness (red, displacement/length ratio) for 5min periods for a single animal observed for 120min on a conditioned Petri dish after 10h in 1mM GABA. Straightness and displacement are mostly low except for two periods at 25 and 100min (arrows). **(E)** Track of the same *Trichoplax* as in Figure 6D with dots marking positions every 10s, recorded for 120min. Two periods of nearly straight movement are highlighted with red ellipses and correspond to straightness maxima marked by arrows in Figure 6D. Compare with a track of control animal in Figure 2C.

regulation factors from hydrozoans to mammals (Tsiairis and Aulehla, 2016; Holmes et al., 2018; Marfenin and Dementyev, 2019).

In simpler animals like *Trichoplax*, analyses of mechanisms and integrative functions of such behavioral oscillations are important because placozoans lack chemical or electric synapses, gap junctions, pannexin, and connexin genes.

For example, the feeding cycle in placozoans includes coordinated changes in cilia beating, substrate adhesion, and body shape changes. Under the volume transmission hypothesis (Moroz et al., 2021b), we can expect the integrative function of established but dynamic chemical gradients (e.g., amino acids) in placozoans. Predicted chemical oscillations can be coupled to electrical signals and play a role in information processing (Romanova et al., 2020b). Mechanical integration is also possible as ultrafast contraction waves propagating across the placozoan body were observed (Armon et al., 2018).

Glutamate and ATP are among the most ancient signaling molecules in all life domains. They are abundant in cytoplasm, released to the extracellular medium upon cell rupture, and used

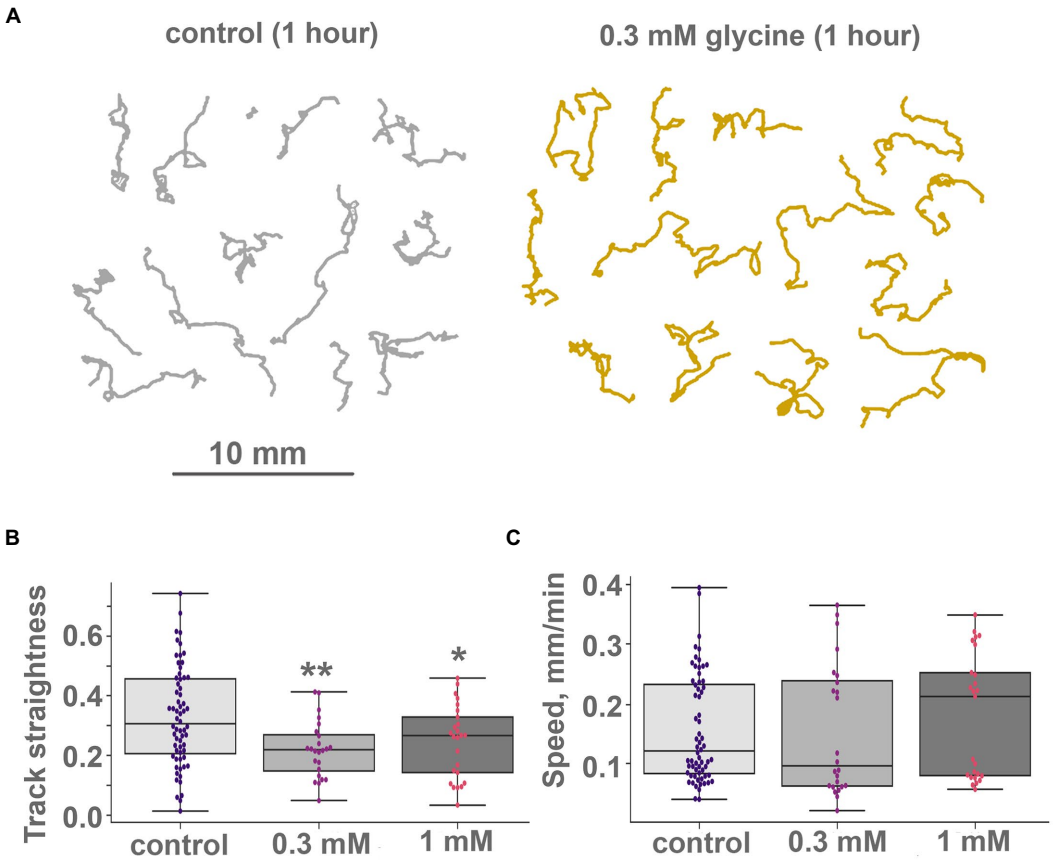

FIGURE 8
Glycine modulate locomotion in *Trichoplax adhaerens*. **(A)** Tracks of animals incubated for 1h in 0.3mM glycine (right) and ASW (left). After adding glycine, incubation tracks are squigglier than the control, but their length is unchanged. Tracks were recorded for 60min. **(B)** and **(C)** Glycine modulates turn patterns but does not affect locomotory speed. Diagrams of track straightness **(B)**, path length divided by distance between start and end) and crawling speed **(C)**, (mm/min) for the control, 0.1 and 0.3mM glycine. Glycine decreases track straightness but does not affect locomotion speed. Asterisks denote a significant difference in track straightness from the control (Welch *t*-test, *p<0.05, **p<0.01). All three speed values are not different (Welch *t*-test, value of p>0.05). N animals=64, 24, and 25, respectively.

as injury signals in a wide range of organisms, including plants and bacteria (Moroz et al., 2021b). GABA is a metabolite of glutamate pathways and is broadly utilized as a signaling molecule even in unicellular eukaryotes (Delmonte Corrado et al., 2002; Bucci et al., 2005). Here, we show that both pathways are involved in controlling feeding and locomotory patterns without overlapping functions, although the sources and cellular targets of glutamate/GABA release and action are currently unknown. The predicted sources could be primary extracellular such as products of extracellular digestion following its diffusion or selected uptake. However, specific glutamatergic or GABAergic cells might also exist. Such cells can selectively accumulate these molecules and release them endogenously or following selective stimuli. The co-existence of both scenarios is to be determined in future studies.

The genome of *Trichoplax adhaerens* encodes numerous components of predicted peptidergic, glutamatergic, GABAergic, purinergic (ATP), and nitric oxide-mediated transmission components (Srivastava et al., 2008; Moroz and Kohn, 2015; Moroz et al., 2020a,b, 2021b) but their spatial cellular distribution is also unknown. It was shown that secreted peptides could regulate some parts of the feeding cycle, some homologous to vertebrate endomorphins (Senatore et al., 2017; Varoqueaux et al., 2018) and peptidergic cells might also use certain amino acids as co-transmitters with canonical or novel regulatory release mechanisms. Some peptide-secreting cells are flask-shaped, have primary sensory cilia, and express secretory (exocytosis/presynaptic-like) components such as SNAP-25 and synaptobrevin (Smith et al., 2014).

We conclude that *Trichoplax* utilizes peptides (Senatore et al., 2017; Varoqueaux et al., 2018) and amino acids (our data) as endogenous signaling molecules. In the nervous systems of vertebrates and many invertebrates peptides exert slower effects *via* metabotropic receptors, while amino acids usually have faster postsynaptic actions mediated by ionotropic receptors (Greengard, 2001; Jing and Weiss, 2001; Nusbaum et al., 2001). This distinction is less evident in cnidarians and other invertebrates with a diverse set of peptide-gated ion channels of the DEG/ENAC family, which mediate fast signaling (Lingueglia et al., 1995; Grunder and Assmann, 2015; Schmidt et al., 2018). *Trichoplax* behavioral reactions are relatively slow, on the order of minutes, and ionotropic and metabotropic receptor-mediated effects are within the physiological range.

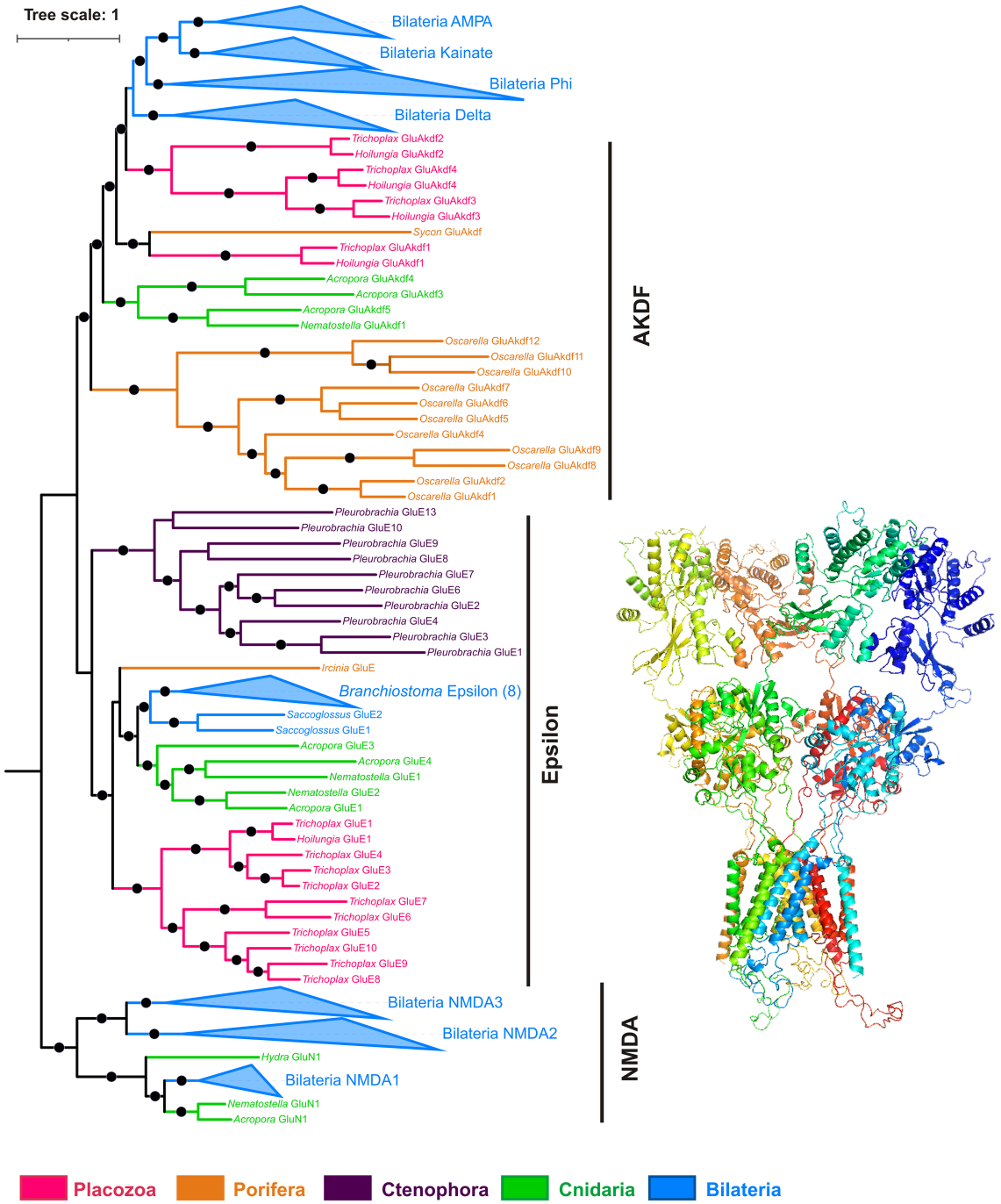

FIGURE 9
Phylogeny of ionotropic glutamate receptors (iGluRs). Bayesian phylogenetic tree of iGluRs has well-supported clades corresponding to most metazoan iGluR families (NMDA, AMPA, kainate, Delta, Phi, Epsilon), plus a paraphyletic group of AKDF-type receptors. *Trichoplax* has 14 iGluRs (4 AKDF and 10 Epsilon), and *Hoilungia* – has 5 iGluRs (4 AKDF and 1 Epsilon). Placozoan AKDF receptors split into two independent clades. Black dots mark highly supported nodes (Bayesian posterior probability >0.75). Full uncollapsed trees with numeric support values can be found in Supplementary Figure S3.

Baseline description of *Trichoplax* behavior

There are several descriptions of *Trichoplax* behavior in the existing literature (Okshtein, 1987; Seravin, 1989; Ueda et al., 1999; Heyland et al., 2014; Smith et al., 2015; Senatore et al., 2017; Fortunato and Aktipis, 2019; Smith et al., 2019). However, all papers before the 1990s used manual drawings or short photo sequences based on observations of a few animals and lacked statistical analysis. More recent articles (Smith and Mayorova, 2019) focused on shorter and smaller scales—several mm, compared to the 52 mm dish in our work. Only one paper reported video recording and statistical analysis of placozoan locomotion on a timescale of hours and spatial scale of over 10 mm (Ueda et al., 1999), but it does not present any tracks. It is based on an unknown (presumably small) number of observed animals.

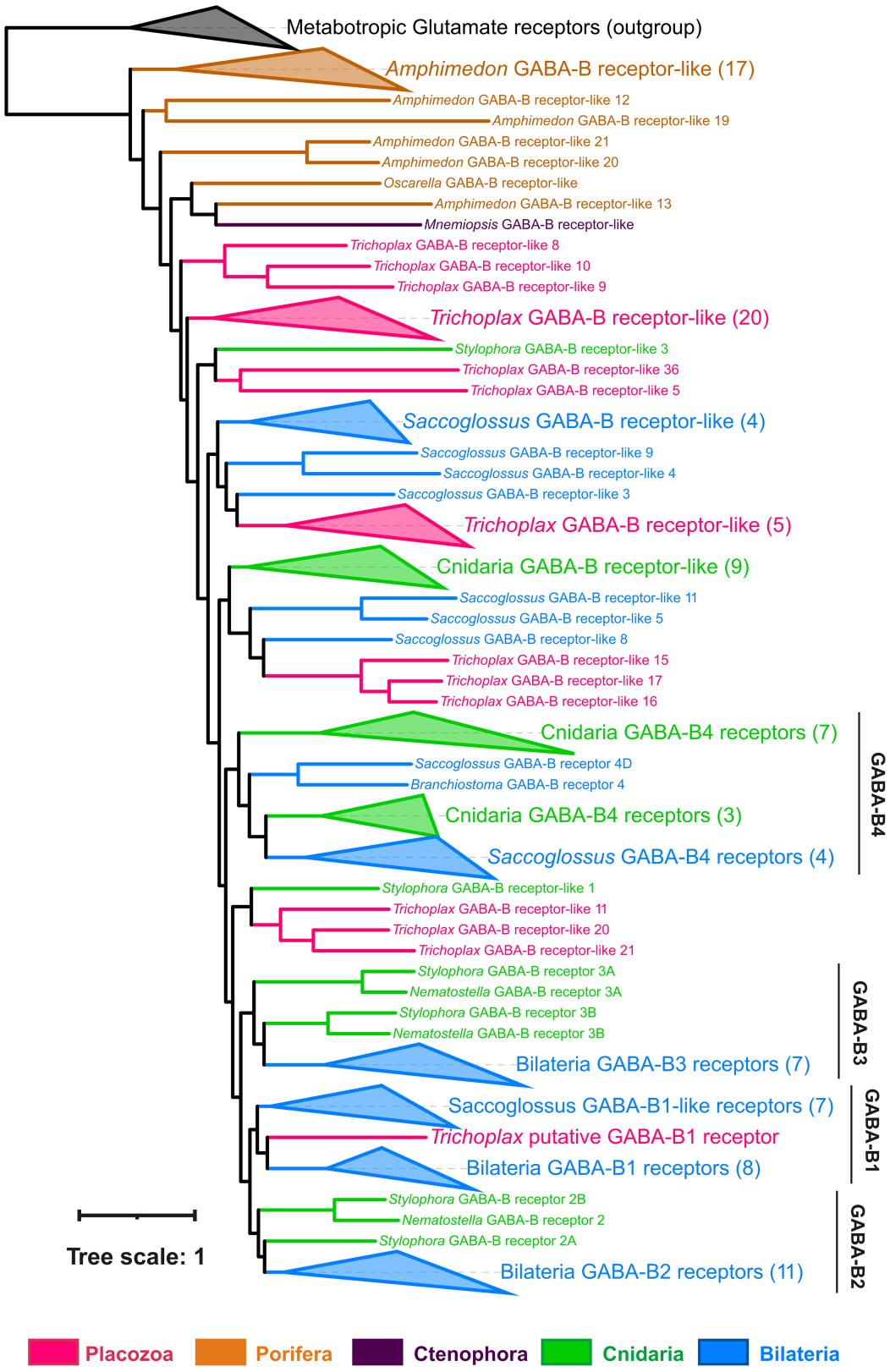

FIGURE 10
Phylogeny of GABA-B-like receptors: *Trichoplax* has 37 GABA-B-like receptors, more than any other analyzed species (Maximum likelihood phylogenetic tree). One placozoan receptor is orthologous to vertebrate GABA-BR1 and is the first candidate for sensing GABA. Placozoan GABA-B-like receptors form seven separate clades in the tree. Similarly, cnidarians and hemichordate *Saccoglossus* also have numerous GABA-B-like receptors (16 in *Stylophora*, 29 in *Saccoglossus*), comprising several different clades. This tree structure suggests high diversity of GABA-B-like receptors in basal metazoans and their subsequent loss in many bilaterian lineages. Black dots mark highly supported nodes (bootstrap support >0.75). Full uncollapsed trees with numeric support values can be found in Supplementary Figure S4.

We have recorded and digitized tracks for over 2,500 animal hours of normal placozoan behavior, testing at least 50 animals for each type of behavior and using long record times of up to 24 h. This is the most comprehensive analysis of normal placozoan behaviors performed so far (see also a recent preprint by Zhong et al. (2022) about a very detailed analysis of *Trichoplax* thermotaxis). Also, we made an effort to standardize animal conditions before testing by using only animals from the late exponential phase of culture growth. This approach helped to mitigate the poor reproducibility of placozoan behavior.

These efforts allowed us to observe the long-term dynamics of endogenous placozoan locomotion patterns: gradual acceleration of locomotion and its long-term oscillations. Gradual acceleration was observed when video recording was longer than 2 h and must be considered in all prolonged experiments with *Trichoplax*. These datasets also provide unique opportunities to study integrative systems of placozoans underlying long-term modulation of behaviors in the simplest free-living animals.

Locomotory and feeding oscillations and the integrative systems of Placozoa

Trichoplax, an animal without neurons, synapses, and muscles, exhibits the complex feeding cycle—a coordinated and stereotyped sequence of patterns leading to changes in cilia beating, body shape, cell adhesion, and secretion (Smith et al., 2015). The feeding cycle is activated by external stimuli (food), but it might also occur spontaneously due to endogenous center pattern generator activity phenomenologically similar to bilaterians and cnidarians. We also report endogenous oscillations in *Trichoplax*'s locomotory rhythm for directional motion and rotations.

High [Mg^{2+}] or low [Ca^{2+}] have abolished endogenous locomotory and feeding oscillations, suggesting the requirement for intercellular chemical communications for these behaviors. A high magnesium concentration causes stable hyperpolarization of cell membranes and suppresses action potentials. Low [Ca^{2+}] also decreases the evolutionarily conserved machinery of calcium-dependent exocytosis. These observations are consistent with the hypothesis of volume transmission as the ancestral integrative systems using electrochemical vesicular secretion (Moroz et al., 2021b).

Modulation of rhythmic patterns of the *Trichoplax* behavior by amino acid transmitters and ATP

L-glutamate is a versatile signal molecule in various organisms – from prokaryotes to bilaterians (Moroz et al., 2021a). D-aspartate is a co-agonist of NMDA-type glutamate receptors and was found in *Trichoplax* in sub-millimolar concentrations (Moroz et al., 2020b). D-glutamate also induced action potentials and muscle contraction in ctenophores (Moroz et al., 2014).

We have demonstrated that glutamate, aspartate, glycine, and GABA profoundly affect the locomotory and feeding patterns of the *Trichoplax*. L-glutamate (and, to less extent, aspartate isomers and D-glutamate) turn on the feeding-like behavior sequence even in the absence of food. Glycine and GABA have more subtle modulating effects. Glycine suppresses feeding on algae and increases curvature tracks on clean dishes. GABA suppresses feeding and locomotory rhythms and acts on orders for several hours.

Thus, GABA and glycine might act as antagonists of glutamate in regulating *Trichoplax* feeding behaviors. In mammalian CNS, glutamate is a predominant excitatory transmitter, while GABA and glycine—are primary inhibitory transmitters. The functional 'antagonism' of GABA and glutamate can be an ancient trait related to their metabolic relationships (Moroz et al., 2021a). GABA is synthesized from glutamate by glutamate decarboxylase. When the time-limited response to glutamate is desired, an antagonistic response to GABA is the simplest way to coordinate the overall outcome. The concerted action of these two transmitters forms a feed-forward loop (Alon, 2007).

L-Glutamate is a universal animal 'food' signal (Torii et al., 2013; Moroz et al., 2021a). It is not surprising that in *Trichoplax,* glutamate also invokes components of feeding-like behavior. It is interesting that a high concentration of L-glutamate (3 mM) caused irreversible body expansion in addition to other components of the feeding cycles (ciliary beating arrest, adhesion, and deadhesion). Enantiomers of aspartate do not show this effect in all tested concentrations. Such a situation may point to the dual role of L-glutamate in the placozoan feeding sequence: (1) initiation of feeding sequence, also caused by aspartate, and (2) regulation of body expansion and contraction, more associated with L-glutamate.

Comparison with the sponge integrative systems

Sponges (phylum Porifera) are sedentary filtrators. Their coordinated locomotory responses are limited to contractions of the osculum (water canal system opening), rhythmic contractions of the entire canal system, and "sneezing"—biphasic expansion and contraction of the whole body to remove the unwanted particles from canals (Leys, 2015). Most sponges are challenging to maintain in the lab, and most experimental data come from freshwater *Ephydatia muelleri* and marine *Tethya wilhelma*. *Tethya* responds with "sneeze" to glutamate, GABA, glycine, acetylcholine, serotonin, dopamine, cyclic AMP, caffeine, and nicotine (Ellwanger and Nickel, 2006; Ellwanger et al., 2007). In *Ephydatia*, glutamate stimulates "sneeze," while 0.1 mM GABA suppresses "sneeze" responses both to glutamate and mineral particles (Elliott and Leys, 2010). Mammalian mGluR antagonists AP3 and kynurenic acid inhibit 'sneeze' of *Ephydatia* in response to glutamate and mineral particles (Elliott and Leys, 2010), suggesting the involvement of mGluRs in the coordination of this reaction.

The role of action potentials and other electric processes in sponge coordination is unclear. An early study by Prosser (1967) has shown that contractions in marine sponges are regular in high extracellular potassium (100 mM) and even increase in amplitude in seawater with a complete exchange of sodium to potassium (450 mM). These high [K^{+}] concentrations cause stable membrane depolarization and complete blockade of action potentials. Therefore, desmosponges seem to coordinate body contraction without classical Na-dependent action potentials or have action potentials based on another set of ions.

In summary, we emphasize that glutamate causes coordinated behaviors in both sponges and placozoans. Effects of GABA are likely antagonistic to glutamate in *Trichoplax* and *Ephydatia* but synergistic in *Tethya*. Our data on the effects of high [Mg^{2+}] and low [Ca^{2+}] are compatible with the role of calcium-dependent exocytosis of signal molecules in integrating *Trichoplax* behaviors. However, the role of the Ca-dependent secretion of signal molecules in the coordination of sponge behavior is unknown.

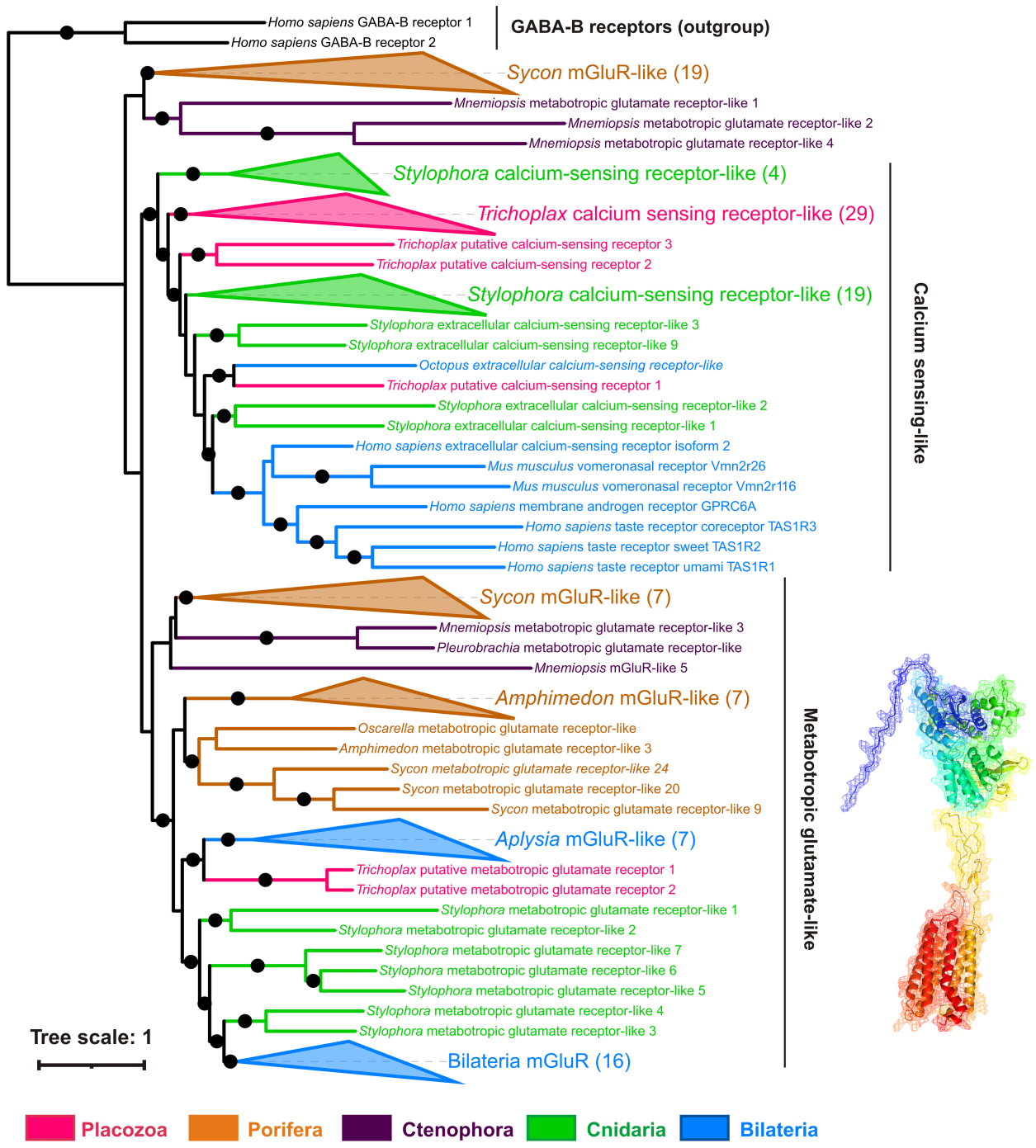

FIGURE 11
Phylogeny of metabotropic glutamate receptors (mGluRs): *Trichoplax* has 34 receptors of this highly diverse superfamily. Maximum likelihood tree shows mGluRs and related receptors such as extracellular calcium-sensing (CaSR), taste, and vomeronasal receptors. *Trichoplax* mGluR-related receptors form 4 separate clades in the tree. Two *Trichoplax* receptors are sisters to a clade of *Aplysia* mGluR-like receptors; the other three clades are more closely related to calcium-sensing, taste, and vomeronasal receptors. Similarly, cnidarians and calcisponge *Sycon* have numerous mGluR-like receptors (30 in *Stylophora*, 29 in *Sycon*), forming several clades. This tree structure suggests that the divergence of mGluRs and CaSR-like receptors predates the radiation of basal metazoan phyla. Black dots mark highly supported nodes (bootstrap support >0.75). Full uncollapsed trees with numeric support values can be found in Supplementary Figure S5.

Summary and perspectives

Our experiments provide initial information on the roles of glutamate, GABA, glycine, and ATP in integrating placozoan behaviors. This situation might represent the ancestral models of chemical integration, *via* volume transmission, in early metazoans without canonical neurons and synapses.

However, future experiments must be conducted by deciphering cellular bases of multiple behaviors to demonstrate the specific roles of these amino acids (and other signal molecules)

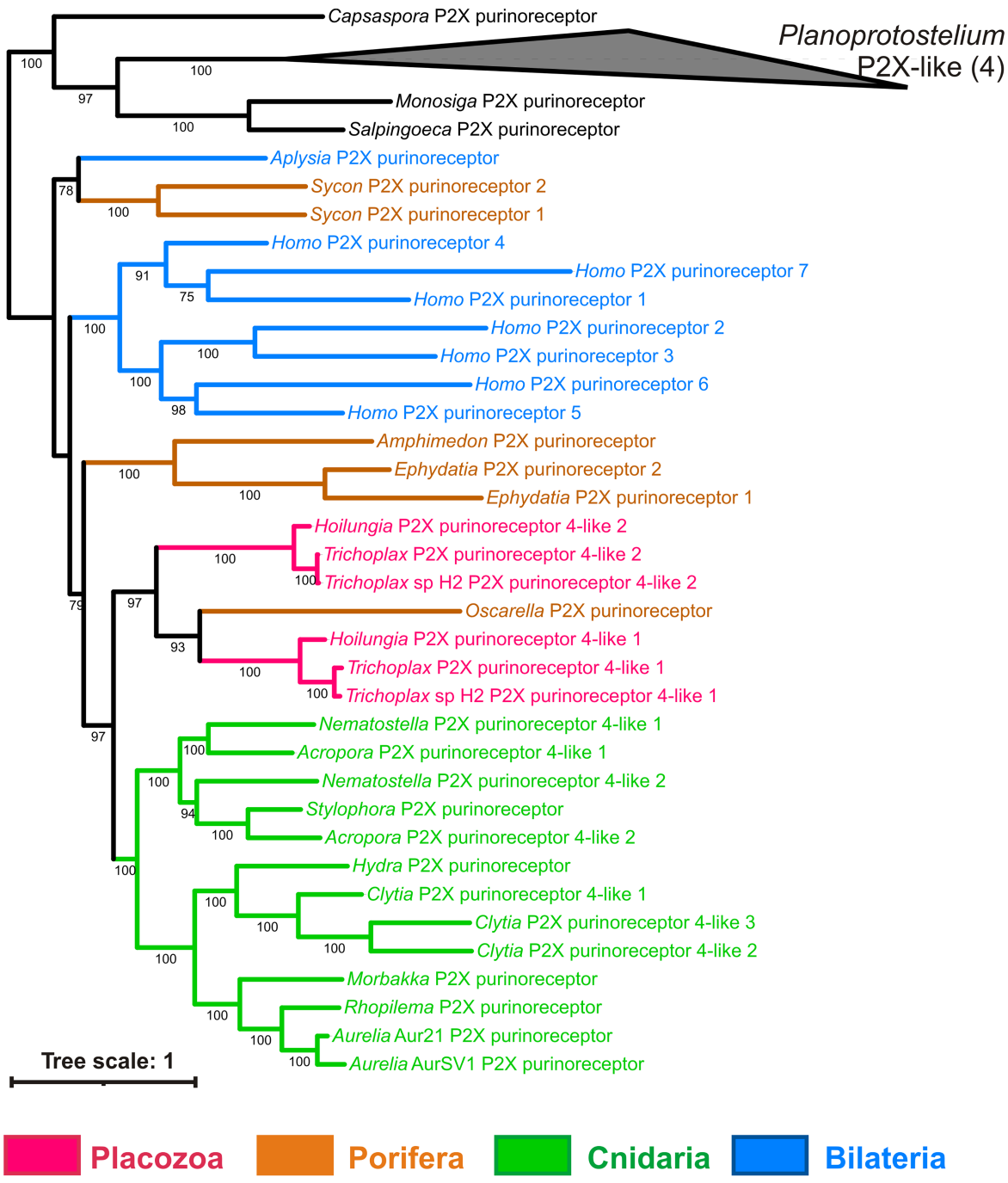

FIGURE 12
Bayesian phylogenetic tree of ionotropic purine (P2X) receptors. *Trichoplax* has 2 P2X receptors, and representatives of other invertebrate lineages have from 1 to 3 P2X receptors encoded in their genomes. Bayesian posterior probabilities of nodes (>0.5) are shown.

in Placozoa conclusively. The first priority is the unbiased identification of endogenous sources of glutamate, GABA, glycine, and ATP: the identification of specific cells and release mechanisms. In other words, we need to know the localization, quantitative secretion of these molecules, and the distribution of such hypothetical chemoconnectomes in the simplest free-living metazoans (Moroz et al., 2021b). The strategy can employ conventional approaches (e.g., single-cell RNA-seq, *in situ* hybridization to putative glutamate vesicular transporter mRNAs, immunocytochemistry, etc.). However, the predicted dynamic nature of numerous chemical gradients requires innovative components for real-time physiological measurements of

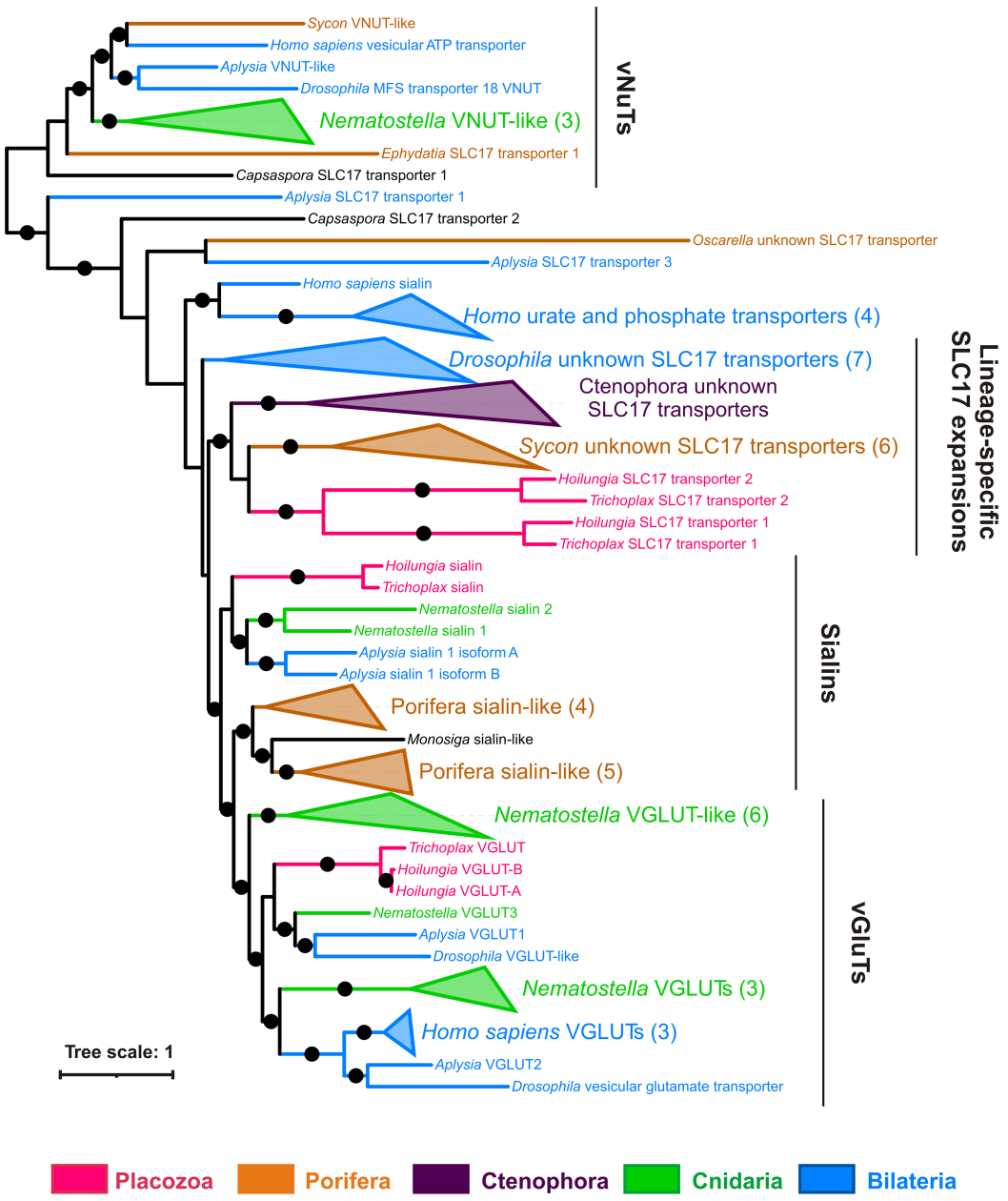

FIGURE 13
Trichoplax has a gene encoded putative vesicular glutamate transporter but no vesicular ATP transporters. Bayesian tree of vesicular glutamate and related transporters (SLC17 family) is shown. The superfamily of SLC17 transporters includes transmembrane carriers for various anions (phosphate, nucleotides, glutamate, and sialic acid). There are three well-defined clades of vesicular glutamate (vGluTs), sialins, and vesicular nucleotide (vNuT) transporters, plus several independent branches with lineage-specific expansions. Placozoan (*Trichoplax* and *Hoilungia*) transporters fall within vGluT and sialin clades, plus one separate clade of unknown substrate specificity. Full uncollapsed trees with numeric support values can be found in Supplementary Figure S6.

intercellular communications in placozoans, complemented with microchemical quantitative assays.

Data availability statement

The datasets presented in this study can be found in online repositories. The names of the repository/repositories and accession number(s) can be found in the article/Supplementary material.

Author contributions

MN, DR, and LM designed the study. MN and SB performed behavioral experiments, digitized animal tracks, and performed analyses of behavioral data. MN, LM, and SB identified genes encoding receptors and transporters and made phylogenetic trees. DR, MN, and LM made the figures and videos. MN, DR, and LM wrote the manuscript. All authors contributed to the article and approved the submitted version.

Funding

MN and SB were supported by the Russian Science Foundation grant (22-24-00566). LM was supported by HFSP, NSF, and NIH grants as well as private donors through UF Foundation.

Acknowledgments

This research was performed in 2014–2021, and the authors thank colleagues in our laboratories for the long-term support, facilities and fruitful discussions over years.

Conflict of interest

The authors declare that the research was conducted in the absence of any commercial or financial relationships that could be construed as a potential conflict of interest.

Publisher's note

All claims expressed in this article are solely those of the authors and do not necessarily represent those of their affiliated organizations, or those of the publisher, the editors and the reviewers. Any product that may be evaluated in this article, or claim that may be made by its manufacturer, is not guaranteed or endorsed by the publisher.

Supplementary material

The Supplementary material for this article can be found online at: https://www.frontiersin.org/articles/10.3389/fnins.2023.1125624/full#supplementary-material

SUPPLEMENTAL VIDEO S1
Normal locomotion of *Trichoplax adhaerens* on the clean glass. 10X magnification, 300X time-lapse. Seven animals are crawling freely. Tracks of four animals are shown in pink, blue, green, and yellow.

SUPPLEMENTARY VIDEO S2
Normal feeding of *Trichoplax* on cyanobacterial biofilm. 200X magnification, 300X time-lapse. One can see 6 feeding cycles in 42 minutes in real time.

SUPPLEMENTARY VIDEO S3
Normal locomotion of *Trichoplax* adhaerens, same specimen whose locomotion was plotted in Figures 2C,D. 10X magnification, 300X time-lapse. The animal track is shown in pink.

SUPPLEMENTARY VIDEO S4
Acceleration of normal locomotion over time. 10X magnification, 300X time-lapse. Animals glide on clean glass (first half of video) and after 12 hours.

SUPPLEMENTARY VIDEO S5
Effect of 200 mM $MgCl_2$ on locomotion. 10X magnification, 600X time-lapse. In control, animals crawl around. After adding MgCl2, animals gradually (~10 min) cease directed movements and stay in one place but continue to change shape.

SUPPLEMENTARY VIDEO S6
Effects of low Ca^{2+} concentration (<1.5 mM) on locomotion. 10X magnification, 600X time-lapse. In control, animals crawl around in small drops of seawater. After adding Ca-free seawater, animals immediately (<1min) cease directed movements and stay in one place but continue to change shape.

SUPPLEMENTARY VIDEO S7
Feeding-like cycles of *Trichoplax* induced by 0.1 mM L-glutamate in the absence of food. 80X magnification, 300X time-lapse. In control, the animal moves around on the glass, and a single feeding-like cycle is observed. After the addition of glutamate, a succession of four feeding-like cycles is induced.

SUPPLEMENTARY VIDEO S8
Effect of 3 mM L-glutamate: animal permanently expanded. One can see that upon the addition of 3mM L-Glu animal expands like at the beginning of the feeding cycle but never contracts back. 80X magnification, 300X time-lapse.

SUPPLEMENTARY VIDEO S9
Feeding suppression by 0.3 mM glycine. In the first half of the video, animals feed on cyanobacterial biofilm. After the addition of glycine, most of them stopped feeding and began to move around. 10X magnification, 600X time-lapse.

SUPPLEMENTAL VIDEO S10
Feeding suppression by 0.3 mM GABA. In control, animals feed on cyanobacterial biofilm. After 6 hours in 0.3 mM GABA, they quickly move around but barely stop to eat. 10X magnification, 600X time-lapse.

SUPPLEMENTARY VIDEO S11
Effects of 0.3 mM of GABA on locomotion. 10X magnification, 600X time-lapse. In control, animals crawl around. After 6 hours in 0.3 mM GABA, animals wobbled most of the time in one place and rarely changed position.

SUPPLEMENTARY VIDEO S12
Effects of 0.3 mM of glycine on locomotion. 10X magnification, 600X time-lapse. Tracks of four example animals are shown in pink (control) and blue (after glycine addition). After the addition of 0.3 mM glycine, animal tracks become more convoluted.

SUPPLEMENTARY TABLE S1
Sequences and accession numbers of proteins used for phylogenetic trees.

SUPPLEMENTARY TABLE S2
Source databases for protein sequences that were used in this paper.

SUPPLEMENTARY FIGURE 1
Effects of GABA on the locomotion of *Trichoplax* on a conditioned dish. **(A)** Animal locomotion on a clean dish is increased over time in control but slightly decreases during incubation with 0.3 or 1 mM GABA. Asterisks denote a significant difference in speed from the control (Welch *t*-test, *** - $p < 0.001$). N animals = 98, 50, 74, 29, 46, 69, 35, 44, and 72, respectively. **(B)**. Track straightness on a clean dish does not change over time in control but decreases during incubation with GABA (tracks become more convoluted). N animals are the same as in A.

SUPPLEMENTARY FIGURE 2
Comparison of feeding dynamics on green algae *Tetraselmis* and cyanobacteria *Oscillatoria*. After 12 hours, feeding on cyanobacteria is less active than on green algae, and the standard deviation of feeding activity is higher on cyanobacteria. N animals = 40 for green algae and 48 for cyanobacteria.

SUPPLEMENTARY FIGURE 3
Bayesian phylogenetic tree of ionotropic glutamate receptors. Numbers denote bayesian posterior probability near nodes. Analysis was run for 1.42 million generations, and convergence was checked with Tracer. Sequences were aligned using E-INS-i algorithm implemented in MAFFT online. Alignment consisted of 4071 positions, 1464 of them parsimony-informative.

SUPPLEMENTARY FIGURE 4
Maximum Likelihood phylogenetic tree of metabotropic glutamate and related receptors. Numbers denote ultrafast bootstrap support near nodes. Sequences were aligned using E-INS-i algorithm implemented in MAFFT online. Alignment consisted of 4071 positions, 1464 of them parsimony-informative.

SUPPLEMENTARY FIGURE 5
Maximum Likelihood phylogenetic tree of metabotropic GABA receptors. Numbers denote ultrafast bootstrap support near nodes. Sequences were aligned using E-INS-i algorithm implemented in MAFFT online. Alignment consisted of 5312 positions, 1376 of them parsimony-informative.

SUPPLEMENTARY FIGURE 6
Bayesian phylogenetic tree of vesicular glutamate and related transporters (SLC17 family). Numbers denote bayesian posterior probability near nodes. Analysis was run for 10 million generations, and convergence was checked with Tracer. Sequences were aligned using E-INS-i algorithm implemented in MAFFT online. Alignment consisted of 1036 positions, 603 of them parsimony-informative.

References

Abbracchio, M. P., and Burnstock, G. (1994). Purinoceptors: are there families of P2X and P2Y purinoceptors? *Pharmacol. Ther.* 64, 445–475. doi: 10.1016/0163-7258(94)00048-4

Alberstein, R., Grey, R., Zimmet, A., Simmons, D. K., and Mayer, M. L. (2015). Glycine activated ion channel subunits encoded by ctenophore glutamate receptor genes. *Proc. Natl. Acad. Sci. U. S. A.* 112, E6048–E6057. doi: 10.1073/pnas.1513771112

Almeida, P. J. A. L., Vieira, M. V., Kajin, M., Forero-Medina, G., and Rui Cerqueira, R. (2010). Indices of movement behaviour: conceptual background, effects of scale and location errors. *Zoologia* 27, 674–680. doi: 10.1590/S1984-46702010000500002

Alon, U. (2007). Network motifs: theory and experimental approaches. *Nat. Rev. Genet.* 8, 450–461. doi: 10.1038/nrg2102

Armon, S., Bull, M. S., Aranda-Diaz, A., and Prakash, M. (2018). Ultrafast epithelial contractions provide insights into contraction speed limits and tissue integrity. *Proc. Natl. Acad. Sci. U. S. A.* 115, E10333–E10341. doi: 10.1073/pnas.1802934115

Arossa, S., Klein, S. G., Parry, A. J., Aranda, M., and Duarte, C. M. (2022). Assessing magnesium chloride as a chemical for immobilization of a symbiotic jellyfish (*Cassiopea* sp.). *Front. Mar. Sci.* 9:632. doi: 10.3389/fmars.2022.870832

Benhamou, S. (2004). How to reliably estimate the tortuosity of an animal's path: straightness, sinuosity, or fractal dimension? *J. Theor. Biol.* 229, 209–220. doi: 10.1016/j.jtbi.2004.03.016

Bucci, G., Ramoino, P., Diaspro, A., and Usai, C. (2005). A role for GABAA receptors in the modulation of paramecium swimming behavior. *Neurosci. Lett.* 386, 179–183. doi: 10.1016/j.neulet.2005.06.006

Del Castillo, J., and Engbaek, L. (1954). The nature of the neuromuscular block produced by magnesium. *J. Physiol.* 124, 370–384. doi: 10.1113/jphysiol.1954.sp005114

Delmonte Corrado, M. U., Ognibene, M., Trielli, F., Politi, H., Passalacqua, M., and Falugi, C. (2002). Detection of molecules related to the GABAergic system in a single-cell eukaryote, *Paramecium primaurelia*. *Neurosci. Lett.* 329, 65–68. doi: 10.1016/S0304-3940(02)00579-7

Elliott, G. R., and Leys, S. P. (2010). Evidence for glutamate, GABA and NO in coordinating behaviour in the sponge, *Ephydatia muelleri* (Demospongiae, Spongillidae). *J. Exp. Biol.* 213, 2310–2321. doi: 10.1242/jeb.039859

Ellwanger, K., Eich, A., and Nickel, M. (2007). GABA and glutamate specifically induce contractions in the sponge *Tethya wilhelma*. *J. Comp. Physiol. A Neuroethol. Sens. Neural Behav. Physiol.* 193, 1–11. doi: 10.1007/s00359-006-0165-y

Ellwanger, K., and Nickel, M. (2006). Neuroactive substances specifically modulate rhythmic body contractions in the nerveless metazoon *Tethya wilhelma* (Demospongiae, Porifera). *Front. Zool.* 3:7. doi: 10.1186/1742-9994-3-7

Fortunato, A., and Aktipis, A. (2019). Social feeding behavior of *Trichoplax adhaerens*. *Front. Ecol. Evol.* 7:19. doi: 10.3389/fevo.2019.00019

Greengard, P. (2001). The neurobiology of slow synaptic transmission. *Science* 2, 1024–1030. doi: 10.1126/science.294.5544.1024

Grell, K. G., and Ruthmann, A. (1991). "Placozoa" in *Microscopic anatomy of invertebrates*. ed. F. W. Harrison (New York, NY: Wiley-Liss), 13–27.

Grunder, S., and Assmann, M. (2015). Peptide-gated ion channels and the simple nervous system of *Hydra*. *J Exp Biol. Feb* 15, 551–561. doi: 10.1242/jeb.111666

Hanson, A. (2021). Spontaneous electrical low-frequency oscillations: a possible role in hydra and all living systems. *Philos. Trans. R. Soc. Lond. Ser. B Biol. Sci.* 376:20190763. doi: 10.1098/rstb.2019.0763

Heyland, A., Croll, R., Goodall, S., Kranyak, J., and Wyeth, R. (2014). *Trichoplax adhaerens*, an enigmatic basal metazoan with potential. *Methods Mol. Biol.* 1128, 45–61. doi: 10.1007/978-1-62703-974-1_4

Hoang, D. T., Chernomor, O., Von Haeseler, A., Minh, B. Q., and Vinh, L. S. (2018). UFBoot2: improving the ultrafast bootstrap approximation. *Mol. Biol. Evol.* 35, 518–522. doi: 10.1093/molbev/msx281

Holmes, D. F., Yeung, C. C., Garva, R., Zindy, E., Taylor, S. H., Lu, Y., et al. (2018). Synchronized mechanical oscillations at the cell-matrix interface in the formation of tensile tissue. *Proc. Natl. Acad. Sci. U. S. A.* 115, E9288–E9297. doi: 10.1073/pnas.1801759115

Hoshino, D., Kirkbride, K. C., Costello, K., Clark, E. S., Sinha, S., Grega-Larson, N., et al. (2013). Exosome secretion is enhanced by invadopodia and drives invasive behavior. *Cell Rep.* 5, 1159–1168. doi: 10.1016/j.celrep.2013.10.050

Hutter, O. F., and Kostial, K. (1954). Effect of magnesium and calcium ions on the release of acetylcholine. *J. Physiol.* 124, 234–241. doi: 10.1113/jphysiol.1954.sp005102

Jing, J., and Weiss, K. R. (2001). Neural mechanisms of motor program switching in *Aplysia*. *J. Neurosci.* 21, 7349–7362. doi: 10.1523/JNEUROSCI.21-18-07349.2001

Katoh, K., Kuma, K., Toh, H., and Miyata, T. (2005). MAFFT version 5: improvement in accuracy of multiple sequence alignment. *Nucleic Acids Res.* 33, 511–518. doi: 10.1093/nar/gki198

Katoh, K., Rozewicki, J., and Yamada, K. D. (2019). MAFFT online service: multiple sequence alignment, interactive sequence choice and visualization. *Brief. Bioinform.* 20, 1160–1166. doi: 10.1093/bib/bbx108

Letunic, I., and Bork, P. (2021). Interactive tree of life (iTOL) v5: an online tool for phylogenetic tree display and annotation. *Nucleic Acids Res.* 49, W293–W296. doi: 10.1093/nar/gkab301

Leys, S. P. (2015). Elements of a 'nervous system' in sponges. *J. Exp. Biol.* 218, 581–591. doi: 10.1242/jeb.110817

Lingueglia, E., Champigny, G., Lazdunski, M., and Barbry, P. (1995). Cloning of the amiloride-sensitive FMRFamide peptide-gated sodium channel. *Nature* 14, 730–733.

Marfenin, N. N., and Dementyev, V. S. (2019). Longitudinal stolon pulsations in the colonial hydroid *Dynamena pumila* (Linnaeus, 1758). *Biol. Bull. Rev.* 9, 42–51. doi: 10.1134/S2079086419010043

Mayorova, T. D., Hammar, K., Winters, C. A., Reese, T. S., and Smith, C. L. (2019). The ventral epithelium of *Trichoplax adhaerens* deploys in distinct patterns cells that secrete digestive enzymes, mucus or diverse neuropeptides. *Biol Open* 8:bio045674. doi: 10.1242/bio.045674

Moroz, L. L. (2009). On the independent origins of complex brains and neurons. *Brain Behav. Evol.* 74, 177–190. doi: 10.1159/000258665

Moroz, L. L. (2018). NeuroSystematics and periodic system of neurons: model vs reference species at single-cell resolution. *ACS Chem. Neurosci.* 15, 1884–1903. doi: 10.1021/acschemneuro.8b00100

Moroz, L. L. (2021). Multiple origins of neurons from secretory cells. *Front. Cell Dev. Biol.* 9:669087. doi: 10.3389/fcell.2021.669087

Moroz, L. L., Kocot, K. M., Citarella, M. R., Dosung, S., Norekian, T. P., Povolotskaya, I. S., et al. (2014). The ctenophore genome and the evolutionary origins of neural systems. *Nature* 510, 109–114. doi: 10.1038/nature13400

Moroz, L. L., and Kohn, A. B. (2015). Unbiased view of synaptic and neuronal gene complement in ctenophores: are there Pan-neuronal and Pan-synaptic genes across Metazoa? *Integr. Comp. Biol.* 55, 1028–1049. doi: 10.1093/icb/icv104

Moroz, L. L., Nikitin, M. A., Policar, P. G., Kohn, A. B., and Romanova, D. Y. (2021a). Evolution of glutamatergic signaling and synapses. *Neuropharmacology* 199:108740. doi: 10.1016/j.neuropharm.2021.108740

Moroz, L. L., and Romanova, D. Y. (2021). Selective advantages of synapses in evolution. *Front. Cell Dev. Biol.* 9:726563. doi: 10.3389/fcell.2021.726563

Moroz, L. L., and Romanova, D. Y. (2022). Alternative neural systems: what is a neuron? (ctenophores, sponges and placozoans). *Front. Cell Dev. Biol.* 10:1071961. doi: 10.3389/fcell.2022.1071961

Moroz, L. L., Romanova, D. Y., and Kohn, A. B. (2021b). Neural versus alternative integrative systems: molecular insights into origins of neurotransmitters. *Philos. Trans. R. Soc. Lond. Ser. B Biol. Sci.* 376:20190762. doi: 10.1098/rstb.2019.0762

Moroz, L. L., Romanova, D. Y., Nikitin, M. A., Sohn, D., Kohn, A. B., Neveu, E., et al. (2020a). The diversification and lineage-specific expansion of nitric oxide signaling in Placozoa: insights in the evolution of gaseous transmission. *Sci. Rep.* 10:13020. doi: 10.1038/s41598-020-69851-w

Moroz, L. L., Sohn, D., Romanova, D. Y., and Kohn, A. B. (2020b). Microchemical identification of enantiomers in early-branching animals: lineage-specific diversification in the usage of D-glutamate and D-aspartate. *Biochem. Biophys. Res. Commun.* 527, 947–952. doi: 10.1016/j.bbrc.2020.04.135

Musser, J. M., Schippers, K. J., Nickel, M., Mizzon, G., Kohn, A. B., Pape, C., et al. (2021). Profiling cellular diversity in sponges informs animal cell type and nervous system evolution. *Science* 374, 717–723. doi: 10.1126/science.abj2949

Nguyen, L. T., Schmidt, H. A., Von Haeseler, A., and Minh, B. Q. (2015). IQ-TREE: a fast and effective stochastic algorithm for estimating maximum-likelihood phylogenies. *Mol. Biol. Evol.* 32, 268–274. doi: 10.1093/molbev/msu300

Nikitin, M. (2015). Bioinformatic prediction of *Trichoplax adhaerens* regulatory peptides. *Gen. Comp. Endocrinol.* 212, 145–155. doi: 10.1016/j.ygcen.2014.03.049

Nusbaum, M. P., Blitz, D. M., Swensen, A. M., Wood, D., and Marder, E. (2001). The roles of co-transmission in neural network modulation. *Trends Neurosci.* 24, 146–154. doi: 10.1016/S0166-2236(00)01723-9

Nussbaum-Krammer, C. I., Neto, M. F., Brielmann, R. M., Pedersen, J. S., and Morimoto, R. I. (2015). Investigating the spreading and toxicity of prion-like proteins using the metazoan model organism *C. elegans*. *J. Vis. Exp.* 52321:e52321. doi: 10.3791/52321

Okshtein, I. L. (1987). On the biology of *Trichoplax* sp. (Placozoa). *Zoological Zh.* 66, 325–338.

Prosser, L. C. (1967). Ionic analyses and effects of ions on contractions of sponge tissues. *Z. Vgl. Physiol.* 54, 109–120. doi: 10.1007/BF00298024

Ramos-Vicente, D., Ji, J., Gratacos-Batlle, E., Gou, G., Reig-Viader, R., Luis, J., et al. (2018). Metazoan evolution of glutamate receptors reveals unreported phylogenetic groups and divergent lineage-specific events. *eLife* 7:e35774. doi: 10.7554/eLife.35774

Romanova, D. Y., Heyland, A., Sohn, D., Kohn, A. B., Fasshauer, D., Varoqueaux, F., et al. (2020a). Glycine as a signaling molecule and chemoattractant in *Trichoplax*

(Placozoa): insights into the early evolution of neurotransmitters. *Neuroreport* 31, 490–497. doi: 10.1097/WNR.0000000000001436

Romanova, D. Y., Nikitin, M. A., Shchenkov, S. V., and Moroz, L. L. (2022). Expanding of life strategies in Placozoa: insights from long-term culturing of *Trichoplax* and *Hoilungia*. *Front. Cell Dev. Biol.* 10:823283. doi: 10.3389/fcell.2022.823283

Romanova, D. Y., Smirnov, I. V., Nikitin, M. A., Kohn, A. B., Borman, A. I., Malyshev, A. Y., et al. (2020b). Sodium action potentials in Placozoa: insights into behavioral integration and evolution of nerveless animals. *Biochem. Biophys. Res. Commun.* 532, 120–126. doi: 10.1016/j.bbrc.2020.08.020

Romanova, D. Y., Varoqueaux, F., Daraspe, J., Nikitin, M. A., Eitel, M., Fasshauer, D., et al. (2021). Hidden cell diversity in Placozoa: ultrastructural insights from *Hoilungia hongkongensis*. *Cell Tissue Res.* 385, 623–637. doi: 10.1007/s00441-021-03459-y

Ronquist, F., Teslenko, M., Van Der Mark, P., Ayres, D. L., Darling, A., Hohna, S., et al. (2012). MrBayes 3.2: efficient Bayesian phylogenetic inference and model choice across a large model space. *Syst. Biol.* 61, 539–542. doi: 10.1093/sysbio/sys029

Schindelin, J., Arganda-Carreras, I., Frise, E., Kaynig, V., Longair, M., Pietzsch, T., et al. (2012). Fiji: an open-source platform for biological-image analysis. *Nat. Methods* 9, 676–682. doi: 10.1038/nmeth.2019

Schmidt, A., Bauknecht, P., Williams, E. A., Augustinowski, K., Gründer, S., and Jékely, G. (2018). Dual signaling of Wamide myoinhibitory peptides through a peptide-gated channel and a GPCR in *Platynereis*. *FASEB J.* 32, 5338–5349. doi: 10.1096/fj.201800274R

Seawater, A. (2012). Artificial seawater. *Cold Spring Harb. Protoc.* doi: 10.1101/pdb.rec068270

Senatore, A., Reese, T. S., and Smith, C. L. (2017). Neuropeptidergic integration of behavior in *Trichoplax adhaerens*, an animal without synapses. *J. Exp. Biol.* 220, 3381–3390. doi: 10.1242/jeb.162396

Seravin, L. N. (1989). Orientation of invertebrates in three-dimensional space: 4. Reaction of turning from the dorsal side to the ventral one. *Zoological Zh.* 68, 18–28.

Smith, C. L., and Mayorova, T. D. (2019). Insights into the evolution of digestive systems from studies of *Trichoplax adhaerens*. *Cell Tissue Res.* 377, 353–367. doi: 10.1007/s00441-019-03057-z

Smith, C. L., Pivovarova, N., and Reese, T. S. (2015). Coordinated feeding behavior in Trichoplax, an animal without synapses. *PLoS One* 10:e0136098. doi: 10.1371/journal.pone.0136098

Smith, C. L., Reese, T. S., Govezensky, T., and Barrio, R. A. (2019). Coherent directed movement toward food modeled in *Trichoplax*, a ciliated animal lacking a nervous system. *Proc. Natl. Acad. Sci. U. S. A.* 116, 8901–8908. doi: 10.1073/pnas.1815655116

Smith, C. L., Varoqueaux, F., Kittelmann, M., Azzam, R. N., Cooper, B., Winters, C. A., et al. (2014). Novel cell types, neurosecretory cells, and body plan of the early-diverging metazoan *Trichoplax adhaerens*. *Curr. Biol.* 24, 1565–1572. doi: 10.1016/j.cub.2014.05.046

Srivastava, M., Begovic, E., Chapman, J., Putnam, N. H., Hellsten, U., Kawashima, T., et al. (2008). The *Trichoplax* genome and the nature of placozoans. *Nature* 454, 955–960. doi: 10.1038/nature07191

Torii, K., Uneyama, H., and Nakamura, E. (2013). Physiological roles of dietary glutamate signaling via gut-brain axis due to efficient digestion and absorption. *J. Gastroenterol.* 48, 442–451. doi: 10.1007/s00535-013-0778-1

Tsiairis, C. D., and Aulehla, A. (2016). Self-organization of embryonic genetic oscillators into spatiotemporal wave patterns. *Cells* 164, 656–667. doi: 10.1016/j.cell.2016.01.028

Ueda, T., Koya, S., and Maruyama, Y. K. (1999). Dynamic patterns in the locomotion and feeding behaviors by the placozoan *Trichoplax adhaerens*. *Biosystems* 54, 65–70. doi: 10.1016/S0303-2647(99)00066-0

Varoqueaux, F., Williams, E. A., Grandemange, S., Truscello, L., Kamm, K., Schierwater, B., et al. (2018). High cell diversity and complex peptidergic signaling underlie Placozoan behavior. *Curr. Biol.* 28:e3492, 3495–3501.e2. doi: 10.1016/j.cub.2018.08.067

Virtanen, P., Gommers, R., Oliphant, T. E., Haberland, M., Reddy, T., Cournapeau, D., et al. (2020). SciPy 1.0: fundamental algorithms for scientific computing in python. *Nat. Methods* 17, 261–272. doi: 10.1038/s41592-019-0686-2

Zhong, G., Kroo, L., and Prakash, M. (2022). Thermotaxis in an apolar, non-neuronal animal. *bioRxiv* [Epub ahead of preprint], pp. 2022–2008. doi: 10.1101/2022.08.19.504474

frontiers | Frontiers in Neuroscience

TYPE Original Research
PUBLISHED 19 May 2023
DOI 10.3389/fnins.2023.1160353

OPEN ACCESS

EDITED BY
Edgar Buhl,
University of Bristol, United Kingdom

REVIEWED BY
Sergio I. Hidalgo,
University of California, Davis, United States
Francois Rouyer,
Institut des Neurosciences Paris-Saclay, France

*CORRESPONDENCE
Todd C. Holmes
✉ tholmes@uci.edu

RECEIVED 07 February 2023
ACCEPTED 05 May 2023
PUBLISHED 19 May 2023

CITATION
Au DD, Liu JC, Park SJ, Nguyen TH, Dimalanta M, Foden AJ and Holmes TC (2023) *Drosophila* photoreceptor systems converge in arousal neurons and confer light responsive robustness.
Front. Neurosci. 17:1160353.
doi: 10.3389/fnins.2023.1160353

Drosophila photoreceptor systems converge in arousal neurons and confer light responsive robustness

David D. Au[1], Jenny C. Liu[1], Soo Jee Park[1], Thanh H. Nguyen[1], Mia Dimalanta[1], Alexander J. Foden[1] and Todd C. Holmes[1,2]*

[1]Department of Physiology and Biophysics, School of Medicine, University of California, Irvine, Irvine, CA, United States, [2]Center for Neural Circuit Mapping, School of Medicine, University of California, Irvine, Irvine, CA, United States

Lateral ventral neurons (LNvs) in the fly circadian neural circuit mediate behaviors other than clock resetting, including light-activated acute arousal. Converging sensory inputs often confer functional redundancy. The LNvs have three distinct light input pathways: (1) cell autonomously expressed cryptochrome (CRY), (2) rhodopsin 7 (Rh7), and (3) synaptic inputs from the eyes and other external photoreceptors that express opsins and CRY. We explored the relative photoelectrical and behavioral input contributions of these three photoreceptor systems to determine their functional impact in flies. Patch-clamp electrophysiology measuring light evoked firing frequency (FF) was performed on large LNvs (l-LNvs) in response to UV (365 nm), violet (405 nm), blue (450 nm), or red (635 nm) LED light stimulation, testing controls versus mutants that lack photoreceptor inputs *gl60j*, *cry-null*, *rh7-null*, and double mutant *gl60j-cry-null* flies. For UV, violet, and blue short wavelength light inputs, all photoreceptor mutants show significantly attenuated action potential FF responses measured in the l-LNv. In contrast, red light FF responses are only significantly attenuated in double mutant *gl60j-cry-null* flies. We used a light-pulse arousal assay to compare behavioral responses to UV, violet, blue and red light of control and light input mutants, measuring the awakening arousal response of flies during subjective nighttime at two different intensities to capture potential threshold differences (10 and 400 $\mu W/cm^2$). The light arousal behavioral results are similar to the electrophysiological results, showing significant attenuation of behavioral light responses for mutants compared to control. These results show that the different LNv convergent photoreceptor systems are integrated and together confer functional redundancy for light evoked behavioral arousal.

KEYWORDS

cryptochrome, external rhodopsin, internal rhodopsin-7, non-image forming vision, electrophysiology, light arousal behavior, *Drosophila melanogaster*, photoreceptor circuit

1. Introduction

Light provides sensory cues to many animals for navigating their environment. In insects like *Drosophila*, short-wavelength light has robust effects on visual behaviors, such as circadian entrainment, phototaxis, sleep/wake, and arousal that are mediated in part by non-image forming mechanisms based on two deep-brain photopigments: cryptochrome (CRY) and rhodopsin 7 (Rh7) (Stanewsky et al., 1998; Emery et al., 2000; Sheeba et al., 2008a; Kumar et al., 2012; Fogle et al., 2015; Baik et al., 2017, 2018, 2019b; Kistenpfennig et al., 2017; Ni et al., 2017; Senthilan et al., 2019). CRY is a light-sensitive photopigment that was initially identified in flies based on its role in light entraining fly circadian rhythm. CRY binds to TIMELESS (TIM) and PERIOD (PER) clock protein heteromultimeric complexes. Light-activated conformational changes of CRY's C-terminal tail initiates a degradation cascade of co-complexed clock protein TIM and PER, thus calibrating/resetting the transcription-translation loop circadian clock (Ceriani et al., 1999; Koh et al., 2006; Peschel et al., 2009). CRY photoactivation also depends on electron transfer between multiple tryptophan residues embedded within the structure that result in photoreduction of CRY's chromophore, flavin adenine dinucleotide (FAD) (Hoang et al., 2008; Zoltowski et al., 2011; Czarna et al., 2013; Levy et al., 2013; Vaidya et al., 2013; Lin et al., 2018; Baik et al., 2019a). CRY photoactivation also evokes robust increases in neuronal electrical excitability via redox coupled interactions with voltage-gated potassium channel beta subunits (Kvβ) hyperkinetic (Hk) (Fogle et al., 2011, 2015; Baik et al., 2017). Rh7 is a spectrally broad bistable photopigment with an absorbance peak around violet (∼400 nm) light and functions via a Gq/PLC (Gq class of G-proteins that couple to phospholipase C) phototransduction pathway (Ni et al., 2017; Sakai et al., 2017). While measurable using spectroscopic biophysical methods, functional Rh7 bistability is not fully explored at present. Both CRY and Rh7 are highly expressed in many of the neurons of the circadian/arousal neural circuit (Emery et al., 2000; Klarsfeld, 2004; Benito et al., 2008; Sheeba et al., 2008a; Yoshii et al., 2008; Fogle et al., 2011; Ni et al., 2017), including the lateral ventral neurons (LNvs), which use light input to tune many physiological and behavioral processes of the fly as noted above (Parisky et al., 2008; Shang et al., 2008; Sheeba et al., 2008a, 2010; Liu et al., 2014; Fogle et al., 2015; Muraro and Ceriani, 2015; Buhl et al., 2016; Potdar and Sheeba, 2018; Chaturvedi et al., 2022). Flies and other insects also navigate their environments using six external rhodopsin photoreceptors found in the compound eyes, the Hofbauer-Buchner (HB) eyelet, and the ocelli that contribute to image-forming and non-image forming visual processes. Together, six rhodopsin photopigments, rhodopsin 1-6 (Rh1-6), mediate a broad range of spectral sensitivity from UV to red (∼300–630 nm) light (Kirschfeld et al., 1978, 1977; Feiler et al., 1992; Salcedo et al., 1999; Sharkey et al., 2020). CRY and Rh7 are also expressed in these external photoreceptor structures, where they may play a role in modulating visual sensitivity gain control (Senthilan et al., 2019). Senthilan et al. (2019) find evidence for Rh7 mRNA expression in brain neurons that is approximately equivalent to Rh7 mRNA expression in eyes, and immunocytochemical staining of Rh7 in the eyes but not in brain neurons. In contrast, Ni et al. (2017) shows robust Rh7 immunocytochemical staining in brain neurons including the LNv. Thus, for this study we were particularly interested in seeing whether Rh7 mediates light responses in the l-LNv and the responses in the absence of CRY and eye photoreceptors. Previous work shows that circadian photoreception and light attraction/avoidance behaviors are coordinately regulated by all three cell-autonomous photoreceptive pathways (CRY, Rh7, external photoreceptors), which input to the LNvs, and provide functional redundancy for these important behaviors (Emery et al., 1998; Stanewsky et al., 1998; Helfrich-Förster et al., 2001, 2002; Malpel et al., 2002; Rieger et al., 2003; Klarsfeld, 2004; Veleri et al., 2007; Sheeba et al., 2008a; Kistenpfennig et al., 2012; Schlichting et al., 2014, 2015, 2016; Saint-Charles et al., 2016; Ni et al., 2017; Baik et al., 2018, 2019b; Lazopulo et al., 2019).

Most of the LNv light-activated arousal neurons express the circadian neuropeptide pigment-dispersing factor (PDF) and can be further categorized as small and large (s-LNvs and l-LNvs, respectively) that are each uniquely capable of transmitting light information that contribute to endogenous circadian timekeeping or wakefulness/arousal. Light-activated s-LNvs trigger the release of PDF to entrain dorsal neurons (DNs), lateral dorsal neurons (LNds), and other circadian pacemaker neurons, while l-LNvs receive inputs from CRY, Rh7, or the external photoreceptors to trigger PDF release in the accessory medulla (aME) to signal light information to s-LNvs, LNds, and other clock neurons (Helfrich-Förster et al., 2007; Cusumano et al., 2009; Yoshii et al., 2009, 2016; Guo et al., 2014; Eck et al., 2016; Schlichting et al., 2016). Additionally, l-LNvs exhibit both rapid and long-lasting excitatory electrophysiological events upon short-wavelength light exposure as marked by an increase in firing frequency (FF) and membrane depolarization lasting tens of seconds from stimulus onset (Sheeba et al., 2008b; Fogle et al., 2011, 2015; Baik et al., 2017, 2019a). This phenomenon is thought to be driven primarily by the CRY/Hk and Rh7 photoreceptor systems. However, l-LNvs also exhibit acute responses to red light (∼635 nm) that, albeit weaker, persist in a *cry-null* system (Baik et al., 2019a; Au et al., 2022). In terms of l-LNv photoexcitability, this suggests a possible input contribution from red-sensitive rhodopsin photopigments (Rh1 and Rh6) from the external photoreceptor structures or direct effects mediated by CRY and/or Rh7. While circadian photoentrainment is primarily modulated by CRY, flies are still able to entrain to light:dark (LD) cycles in a CRY-independent manner, also suggesting that light inputs to LNvs and the rest of the clock circuitry is mediated by external opsin-based photoreceptor structures and/or Rh7 (Ni et al., 2017, but see also Kistenpfennig et al., 2017). Further evidence suggests that different properties of light (intensity, exposure timing, spectral composition) recruit different photoreceptors for photoentrainment (Chatterjee et al., 2018) and light attraction/avoidance behaviors (Baik et al., 2019b). Anatomically, external photoreceptor structures project either directly into the aME or indirectly via lamina monopolar cells that project to the aME (Behnia and Desplan, 2015). It has been proposed that the aME acts as a central hub for parallel light input circuits from the external photoreceptor system to the clock circuit for photoentrainment (Li et al., 2018), but the extent of how all three photoreceptor systems functionally contribute to light evoked neuronal photoexcitation and behavioral arousal remain largely unknown.

Here, we comprehensively explore the functional contributions of the light input pathways from the three distinct external

and internal photoreceptor systems that activate LNvs electrical excitability and the relative contributions of these three distinct photoreceptor systems to the fly's arousal responses to UV, violet, blue, and red light stimuli. We employ the light-evoked whole-cell current clamp electrophysiology assay to measure l-LNvs responses to intensity matched UV, violet, blue, and red light, comparing control versus fly mutants that lack photoreceptor inputs *gl60j*, *cry-null*, *rh7-null*, and double mutant *gl60j-cry-null* flies. In a parallel set of studies, we use a light-pulse arousal assay to measure behavioral responses to intensity matched UV, violet, blue, and red light, measuring light-triggered wakefulness from sleep for controls and each fly mutant at two different levels of light intensity. We find that all photoreceptor systems functionally integrate in l-LNvs to enable light-evoked electrophysiological excitability. We find similarly that all light input channels contribute to arousal behavioral responses to light. Identifying a functional connection between each of the fly photoreceptor systems strengthens an emerging model that insect image-forming and non-image forming visual processes work together in a coordinate fashion to mediate complex light-evoked behaviors.

2. Materials and methods

2.1. Experimental animals

Our experimental flies were allowed *ad libitum* access to a standard food media consisting of yeast, cornmeal, and agar at 25 ± 1°C and 40–60% relative humidity in 12:12 h light:dark cycles during behavioral experiments. All flies used in the experiments are 3 to 4-day post-eclosion adult male flies. We obtained our *rh7-null*, *gl60j*, and *gl60j-cry-null* mutant flies through a prior collaboration with Craig Montell of UC Santa Barbara, and *cry-null* mutant flies from Amita Seghal of University of Pennsylvania. Once obtained, we crossed each photoreceptor mutant with a *pdfGAL4-p12c* driver line to drive expression of green fluorescent protein (GFP) in all PDF+ neurons in order to visualize l-LNvs for patch-clamp electrophysiology. The *p12c* line is a stable expression line that we previously developed in our lab to mark LNvs using GFP expression driven by *pdfGAL4*. Large lateral ventral neurons were identified by size, morphology, and anatomical positioning. Our wild-type control is the *pdfGAL4-p12c* driver line.

2.2. Light-evoked neuronal electrophysiology

We adapted our light-evoked potential electrophysiology assays established in Baik et al. (2019a) to measure adult male fly brain's large lateral ventral neuronal responses to various light stimuli. Our *ex vivo* brain preparations retain residual photoreceptor tissue from the compound eyes so as to avoid damaging the preparation and the input circuitry of the neurons we record from. This brain preparation closely follows the procedure outlined in Gu and O'Dowd (2006). Flies are dissected in an external recording solution comprised of the following components: 122 mM NaCl, 3 mM KCl, 1.8 mM $CaCl_2$, 0.8 mM $MgCl_2$, 5 mM glucose, 10 mM HEPES, and calibrated to a pH of 7.2 ± 0.02 and osmolarity of 250–255 mOsm. The internal recording solution is comprised of the following components: 102 mM Kgluconate, 17 mM NaCl, 0.085 mM $CaCl_2$, 1.7 mM $MgCl_2$ (hexahydrate), 8.5 mM HEPES, 0.94 mM EGTA, and is calibrated to a pH of 7.2 ± 0.02 and osmolarity of 232–235 mOsm. Our custom multichannel LED source (Prizmatix/Stanford Photonics, Palo Alto, CA, USA) is fitted onto an Olympus BX51 WI microscope and was used as our primary light source for light-evoked potential recordings. The LED are tuned to the following wavelengths of color: UV (365 nm), violet (405 nm), blue (450 nm), and red (635 nm), and all exposures were set to an intensity of 200 $\mu W/cm^2$ by use of a Newport 842-PE Power/Energy meter. Transistor-transistor-logic (TTL) triggered LEDs programmed by the data acquisition software, pClamp (molecular dynamics), enabled rapid on/off light stimuli with the following protocol: 50 s of dark for baseline recording, 5 s of colored-light stimulation, then 95 s of inter-pulse darkness for FF and membrane potential baseline recovery. We measure five continuously repeated sweeps per recording to allow for greater statistical confidence in our measurements, which are analyzed as follows: FF is determined by counting spikes per 10 s interval per 100 s sweep, then calculated as a FF ratio by the average number of spikes during lights on over the average number of spikes per 10 s interval pre-light stimulus. These ratios are averaged across the five repeated sweeps per recording for all samples of the same light-stimulus in the genotype set. This custom light-evoked potential protocol allows greater measurements for kinetically robust light-evoked effects in our samples.

2.3. Light-pulse arousal behavioral assay

Standard LD light pulse arousal assays were conducted from previously established and adapted protocols (Baik et al., 2017). The locomotor activity of individual flies was measured using the TriKinetics Locomotor Activity Monitoring System via infrared beam-crossing, recording total crosses in 1-min bins. Percentage activity and statistics were measured using Microsoft Excel. Custom LED fixtures were built using Waveform Lighting blue, violet, UV, and red LEDs with a narrow peak wavelength of 450, 405, 365, and 635 nm, respectively, and intensity-tuned to 10 $\mu W/cm^2$ and 400 $\mu W/cm^2$ for low and high intensity light exposures, respectively.

2.4. Quantification and statistical analysis

All reported values are represented as mean ± SEM. Values of *n* refer to the total number of experimental flies tested over all replicates of an experiment (minimum of three replicates). Firing frequency values are calculated as a ratio of spikes during the 5 s of lights on/average baseline firing rate binned in 10 s increments. Statistical tests were performed using Minitab, Matlab, and Microsoft Excel software. Statistical analysis began with performing an Anderson–Darling normality tests to determine normality of data. Variance was determined using F-tests for normally distributed data, then significance was determined using two-sample, one-tailed *t*-tests with alpha values of 0.5 before pairwise correction. Significance for non-normal data was determined by Mann-Whitney U-tests. Spike firing quantifications were performed using custom Matlab scripts and Clampfit software.

Multi-comparison tests leading to Type I error/false positives were mitigated by *p*-value adjustment based on false discovery rate (FDR, Benjamini and Hochberg, 1995). A standard FDR threshold of 0.1 was then implemented in order to indicate significance as an expected proportion of false positives that is no greater than 10%.

3. Results

3.1. Light excitation of arousal neurons to short-wavelength light relies on input coincident of multiple photoreceptor systems

Physiological and anatomical evidence indicates the convergence of multiple photoreceptor channels on the LNvs (Emery et al., 1998; Stanewsky et al., 1998; Helfrich-Förster et al., 2001, 2002; Malpel et al., 2002; Klarsfeld, 2004; Sheeba et al., 2008a; Schlichting et al., 2014, 2016; Behnia and Desplan, 2015; Ni et al., 2017; Chatterjee et al., 2018; Li et al., 2018; Baik et al., 2019b). CRY light activation is based successive redox reduction of its FAD starting at a base oxidized state with two absorption peaks corresponding to ultraviolet (UV, 365 nm) and blue (450 nm) light (Berndt et al., 2007; Bouly et al., 2007; Hoang et al., 2008). Higher reduction states of CRY confer light-evoked excitation by red light (635 nm) due to spectral absorption peak shifts. Light evoked redox transfer reactions mediated by FAD in CRY are transduced to changes in membrane potential and neuronal excitability through voltage gated potassium channel beta subunit, hyperkinetic (Sheeba et al., 2008b; Fogle et al., 2011, 2015; Baik et al., 2017). Rh7 exhibits a very broad absorption that peaks at violet light (405 nm) (Kistenpfennig et al., 2017; Ni et al., 2017). In order to test the relative contributions of different photoreceptor systems on l-LNv photoexcitability to short-wavelength light, we performed whole-cell current-clamp electrophysiology using 200 $\mu W/cm^2$ of UV (365 nm), violet (405 nm), and blue (450 nm) LED light. To test the contribution of each photoreceptor system to circadian/arousal neuronal photoexcitability to these short wavelengths, we measured the electrophysiological light responses of l-LNvs as a ratio of action potential FF during lights on/lights off, comparing control wild-type *p12c* with recordings of genetic knockouts *cry-null*, *rh7-null*, total external photoreceptor knockout *gl60j*, and a double-mutant *gl60j-cry-null* photoreceptor mutant flies using the whole-cell patch-clamp electrophysiology configuration. Recordings were performed on l-LNvs from each photoreceptor knockout group with 50 s of dark, 5 s exposures of 200 $\mu W/cm^2$ LED light for each wavelength of light, and 95 s of dark inter-pulse intervals in order to measure post-stimulus decay back to baseline. Each recording trace was repeated 5 times and FF ratios are reported as an average of all traces of all recordings for each group of parameters.

A total of 200 $\mu W/cm^2$ UV (365 nm) LED light evokes a robust 1.6-fold FF increase in recordings of *p12c* control l-LNvs (**Figure 1A** blue column). As expected, intensity matched UV light electrophysiological responses of l-LNvs are significantly attenuated in neurons recorded from *cry-null* fly brains (**Figure 1A**, blue column vs. green column) as 365 nm corresponds to one of the principal spectral absorption peaks for the base oxidized state of CRY. Intensity matched UV light electrophysiological responses of l-LNvs also are significantly attenuated to a similar degree in neurons recorded from *gl60j* and *rh7-null* fly brains (**Figure 1A**, blue column vs. red column and violet column, respectively). This indicates that opsin-based phototransduction in eyes/external photoreceptors and cell autonomously expressed Rh7 also contribute to the l-LNv electrophysiological responses to UV light. The UV photoresponse of the double mutant *gl60j-cry-null* is also significantly different from control *p12c* (**Figure 1A**, blue column vs. yellow column), in agreement with the attenuated UV light response trends measured from the single mutants *gl60j* and *cry-null*. Short term light exposure evokes long term subsequent increases in neuronal excitation in LNvs (Fogle et al., 2011, 2015; Baik et al., 2017, 2019a). In order to measure any lasting photoexcitatory effects post-stimulus, FF ratios for each knockout mutant are reported as 10 s intervals for 50 s post-stimulus: FF (10 s post-stimulus)/FF (baseline), FF (20 s post-stimulus)/FF (baseline), FF (30 s post-stimulus)/FF (baseline), FF (40 s post-stimulus)/FF (baseline), and FF (50 s post-stimulus)/FF (baseline). There are no significant increases in FF ratio post-stimulus when comparing *p12c* versus any of the knockout mutants (**Figures 1B–E**).

200 $\mu W/cm^2$ of violet (405 nm) LED light evokes 1.8-fold increases in FF in control *p12c* l-LNvs (**Figure 2A**, blue column). In contrast, intensity matched l-LNv violet light responses in FF are significantly attenuated in l-LNv recordings of *gl60j*, *rh7-null*, and double mutant *gl60j-cry-null* neurons (**Figure 2A**, blue column vs. red column, violet column, and yellow column, respectively). Unsurprisingly, *cry-null* violet light responses in FF are not significantly different from control as there is an absorption trough at 405 nm for CRY, but *cry-null* violet light responses are significantly higher compared to the *gl60j-cry-null* response (**Figure 2A**, green column vs. yellow column, respectively). Comparing the *gl60j* versus the double mutant *gl60j-cry-null* recordings of violet evoked changes in FF, this result suggests the l-LNvs responsiveness to violet light depends entirely on external and cell autonomous opsin-based photoreceptors. In comparison to control *p12c*, the post-stimulus FF ratio for violet light for each genotype (**Figures 2B–E**) shows significant increases up to 10 s post-stimulus for *gl60j* and *gl60j-cry-null* responses (**Figures 2B, D**, respectively), and up to 20 s for *rh7-null* responses (**Figure 2E**), but no significant increases for cry-null responses (**Figure 2C**).

Natively expressed CRY control *p12c* l-LNvs are robustly excited by blue light exposure, showing an almost a twofold increase in FF (**Figure 3A**, blue column), similar to results reported previously. Compared to *p12c* controls, the genetic absence of other photoreceptors/phototransducers including the *gl60j* mutation or *rh7-null* results in a significant attenuation of l-LNv responsiveness to blue light (**Figure 3A**, blue column vs. red column and violet column, respectively). Mutant *cry-null* show a significantly more attenuated response, as we have demonstrated previously (**Figure 3A**, blue column vs. green column). The double-mutant *gl60j-cry-null* exhibits the greatest attenuation of l-LNv responsiveness to blue light (**Figure 3A**, yellow column) suggesting a compounding effect from loss of photoreception from both systems. Blue light-responses are also long-lasting for the *p12c* control group compared to *gl60j* and *cry-null*, with *p12c* having a sustained FF ratio increase lasting up to 20 s post-stimulus (**Figures 3B, C**, respectively). In comparison to *rh7-null* and the double mutant *gl60j-cry-null*, the control blue light response persists for even longer, up to 30 s post-stimulus (**Figures 3D, E**, respectively).

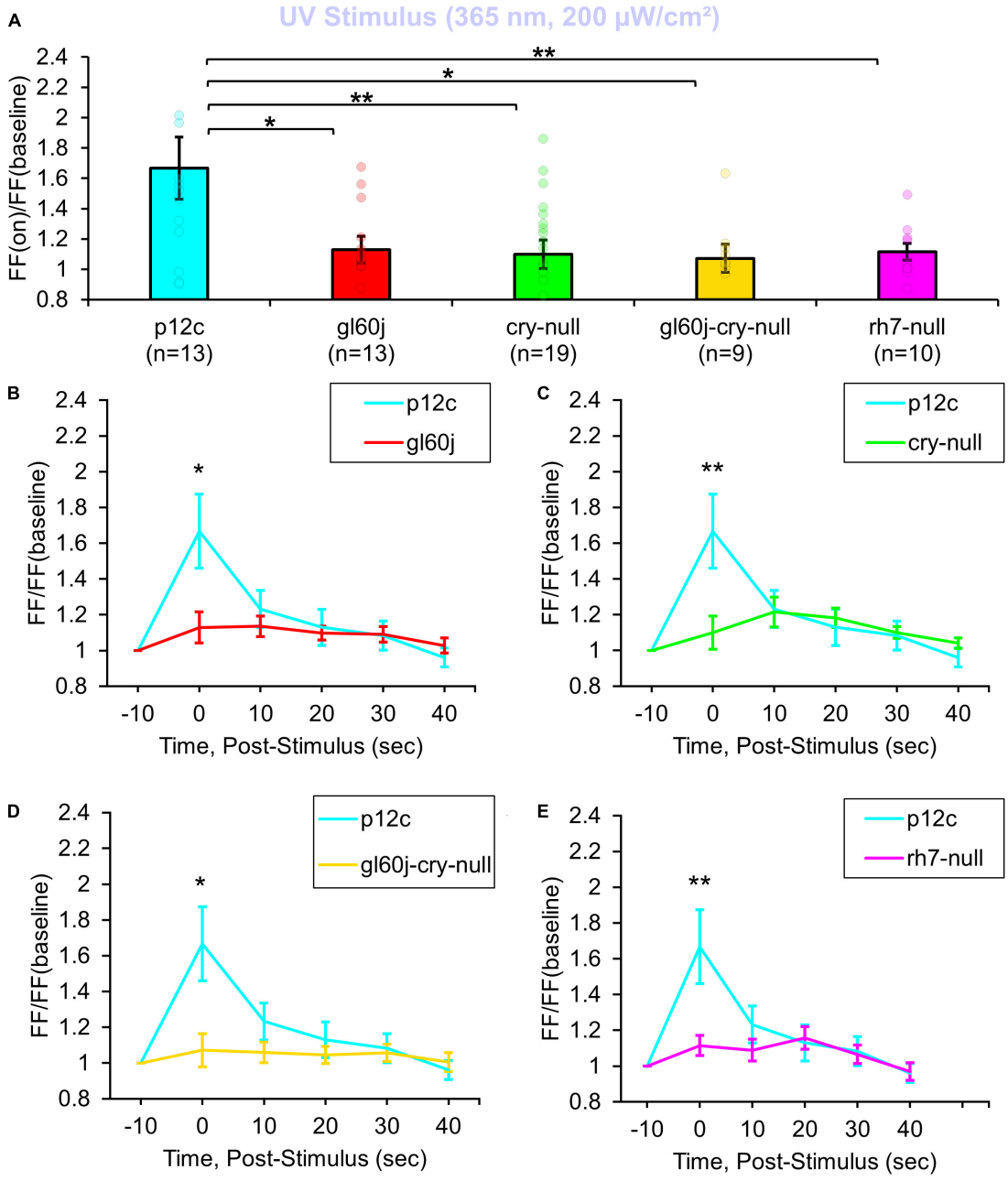

FIGURE 1
All photoreceptor mutants show an attenuated UV light firing frequency (FF) compared to native expressed *Drosophila* CRY. **(A)** Firing frequency response of *p12c* (blue column, n = 13) versus *gl60j* (red column, n = 13), *cry-null* (green column, n = 19), *gl60j-cry-null* (yellow column, n = 9), and *rh7-null* (violet column, n = 10) with 5 s UV (365 nm, 200 μW/cm^2) light stimulus. Post-stimulus FF response in 10 min bins for **(B)** *p12c* (blue trace) vs. *gl60j* (red trace), **(C)** *p12c* vs. *cry-null* (green trace), **(D)** *p12c* vs. *gl60j-cry-null* (yellow trace), and **(E)** *p12c* vs. *rh7-null* (violet trace). Data are plotted as average ± SEM. Pairwise comparison was analyzed using two-sample t-test with FDR adjustment. *$p < 0.1$ and **$p < 0.05$.

3.2. External photoreceptors and cryptochrome dually contribute to mediate red light excitability in primary arousal neurons

Multiple lines of evidence show that CRY also mediates acute red light responsiveness as measured by l-LNv electrophysiology (Baik et al., 2019a; Au et al., 2022). These surprising results suggest that CRY can be sufficiently reduced to reach long-wavelength light absorption *in vivo*. The only other known candidates for red light sensing in flies occur via red sensitive opsin-based photoreceptors expressed in the compound eyes including rhodopsin 1 and rhodopsin 6. Anatomical and physiological evidence suggest circumstantially that external photoreceptor systems directly input light information to the circadian/arousal neural circuits. Internally expressed Rh7 does contribute violet (405 nm) light sensing to l-LNvs, yet Rh7's contribution to

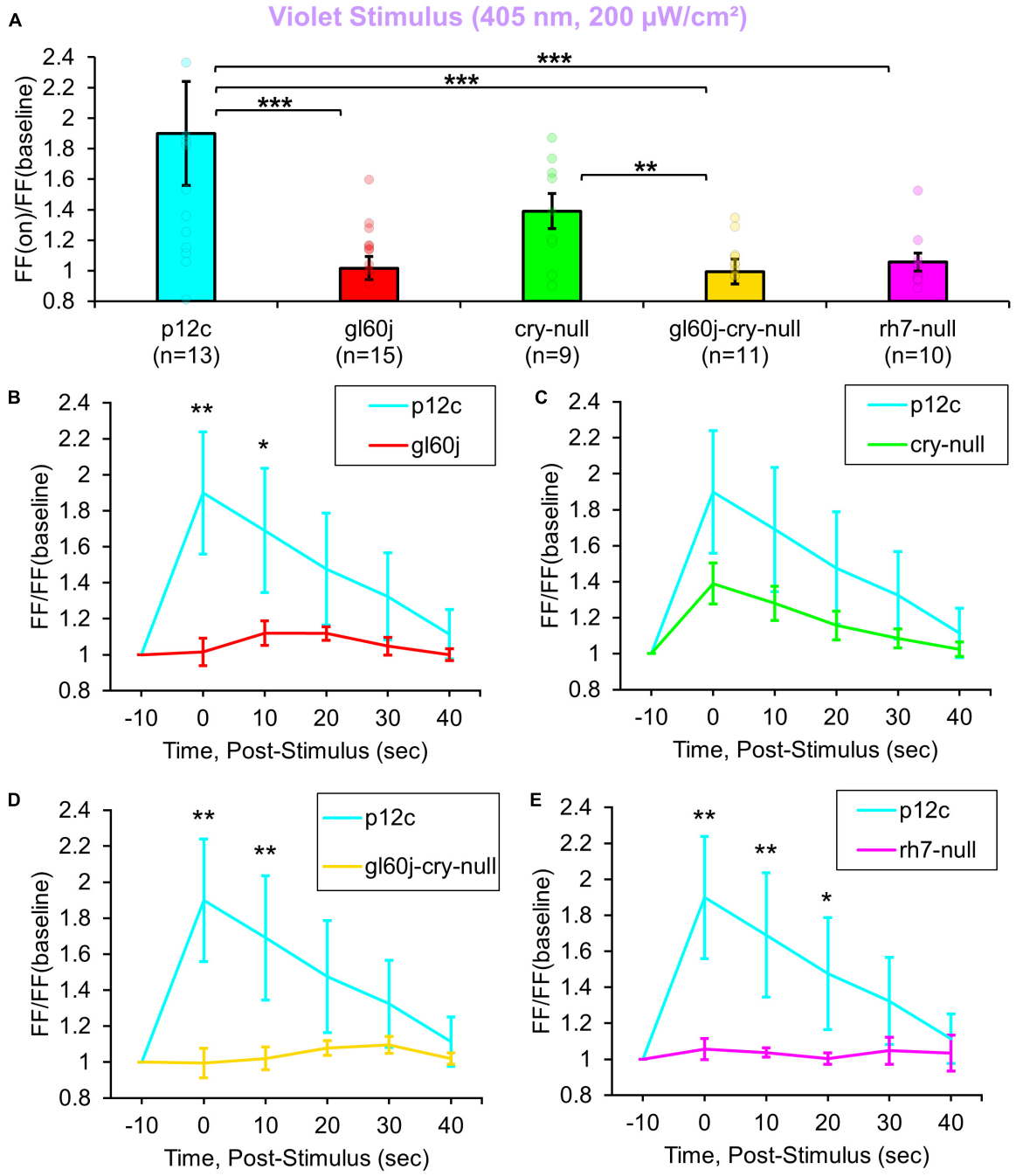

FIGURE 2
All photoreceptor mutants except *cry-null* show an attenuated violet light firing frequency (FF) compared to native expressed *Drosophila* CRY. **(A)** Firing frequency response of *p12c* (blue column, $n = 13$) versus *gl60j* (red column, $n = 15$), *cry-null* (green column, $n = 9$), *gl60j-cry-null* (yellow column, $n = 11$), and *rh7-null* (violet column, $n = 10$) with 5 s violet (405 nm, 200 μW/cm^2) light stimulus. Post-stimulus FF response in 10 min bins for **(B)** *p12c* (blue trace) vs. *gl60j* (red trace), **(C)** *p12c* vs. *cry-null* (green trace), **(D)** *p12c* vs. *gl60j-cry-null* (yellow trace), and **(E)** *p12c* vs. *rh7-null* (violet trace). Data are plotted as average ± SEM. Pairwise comparison was analyzed using two-sample *t*-test with FDR adjustment. *$p < 0.1$, **$p < 0.05$, ***$p < 0.01$.

l-LNv input to other wavelengths of light is largely unexplored. A total of 200 μW/cm^2 red light exposure evokes small but measurable acute increases in action potential FF in control *p12c* l-LNvs. In contrast, attenuated responses are measured in double knockout *gl60j-cry-null* l-LNvs (Figure 4A, blue column vs. yellow column). Red light evoked increases in FF quickly return to baseline firing within 10 s post-stimulus, indicating that l-LNv electrophysiological responses to red light are acute rather than long-lasting (Figure 4D, blue trace vs. yellow trace). Post-red stimulus plots for *gl60j*, *cry-null*, and *rh7-null* mutant groups show no significant differences in comparison to the *p12c* control (Figures 4B, C, E). A summary table of all genotypes FF responses (FF lights on/FF baseline no light) to light stimuli can be found on Table 1.

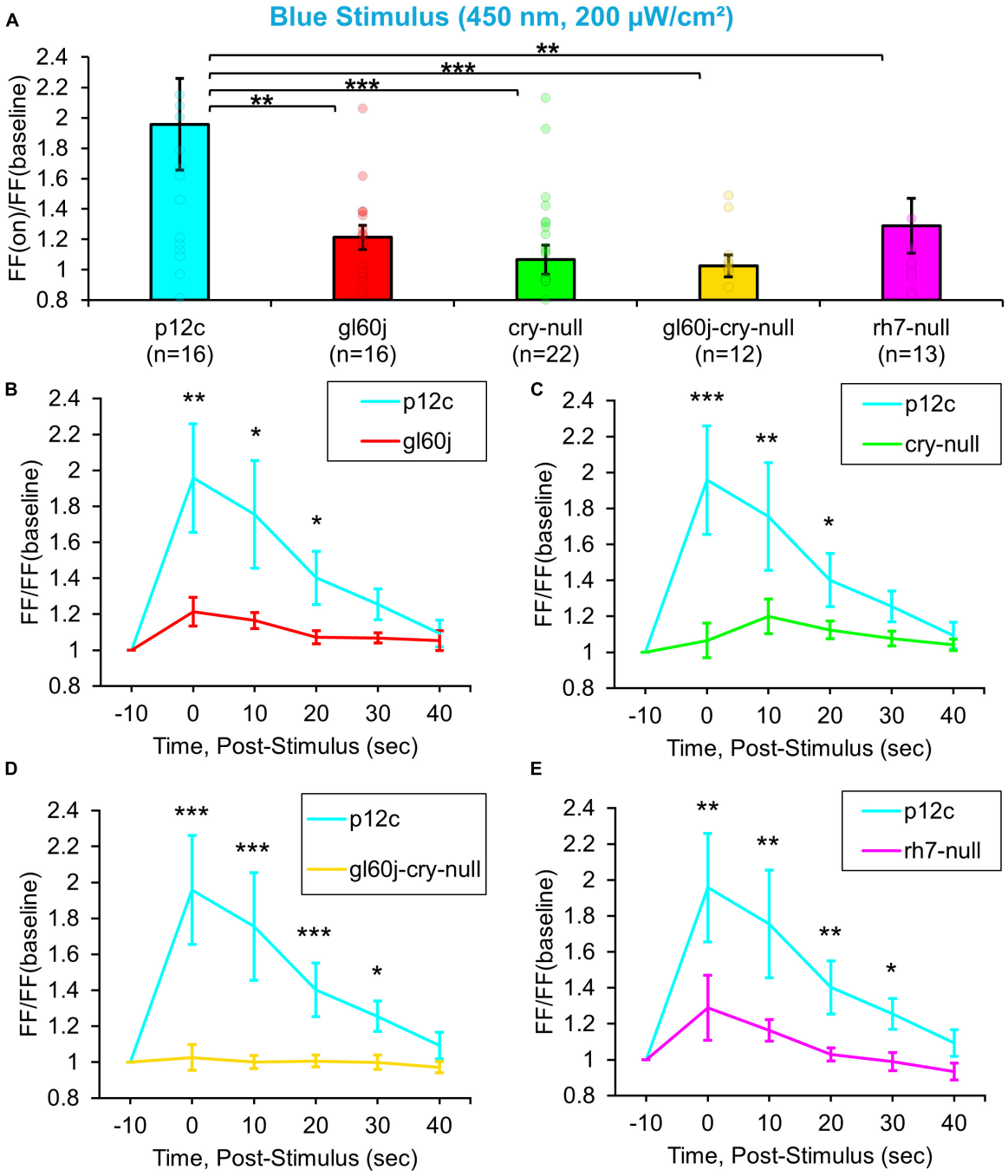

FIGURE 3
All photoreceptor mutants show an attenuated blue light firing frequency (FF) compared to native expressed *Drosophila* CRY. **(A)** Firing frequency response of *p12c* (blue column, $n = 16$) versus *gl60j* (red column, $n = 16$), *cry-null* (green column, $n = 22$), *gl60j-cry-null* (yellow column, $n = 12$), and *rh7-null* (violet column, $n = 13$) with 5 s blue (450 nm, 200 µW/cm^2) light stimulus. Post-stimulus FF response in 10 min bins for **(B)** *p12c* (blue trace) vs. *gl60j* (red trace), **(C)** *p12c* vs. *cry-null* (green trace), **(D)** *p12c* vs. *gl60j-cry-null* (yellow trace), and **(E)** *p12c* vs. *rh7-null* (violet trace). Data are plotted as average ± SEM. Pairwise comparison was analyzed using two-sample *t*-test with FDR adjustment. *$p < 0.1$, **$p < 0.05$, ***$p < 0.01$.

3.3. Light responses recorded from l-LNvs show no apparent time-of-day differences

Representative voltage traces with a 5 s baseline in dark, during the 5 s of 200 µW/cm^2 red, blue, violet, or UV light stimulation, and 50 s post-stimuli show the increase in FF and duration of sustained excitation for *p12c* (Figure 5, blue traces), *gl60j* (Figure 6, red traces), *cry-null* (Figure 7, green traces), *gl60j-cry-null* (Figure 8, yellow traces), and *rh7-null* (Figure 9, violet traces). The colored bars indicate onset of 5 s of 200 µW/cm^2 lights on and off during each recording. Most of the individual l-LNv recordings reveal predominately tonic action potential firing pattern, consistent with most other reports (Holmes et al., 2007; Cao and Nitabach, 2008;

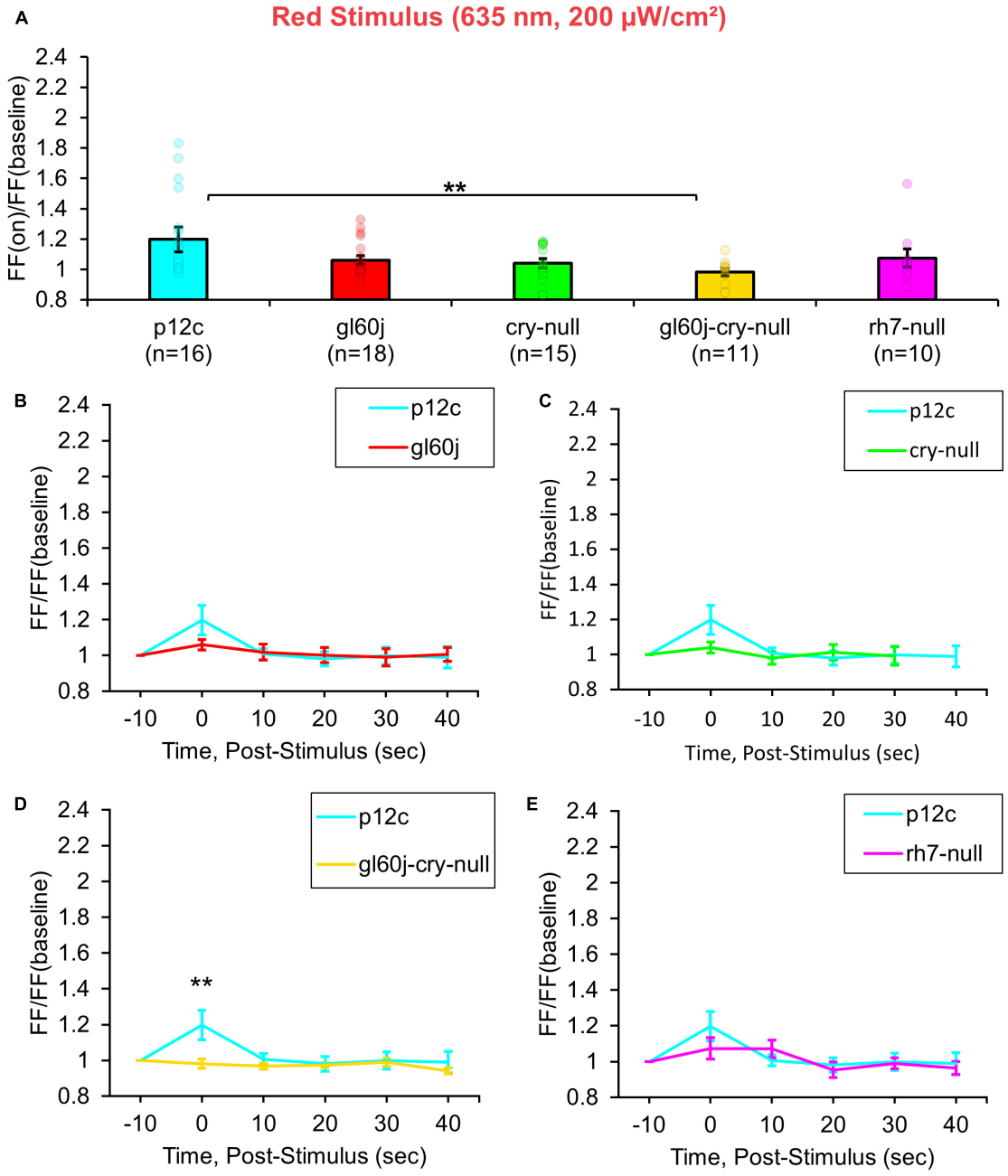

FIGURE 4
gl60j-cry-null photoreceptor mutants show an attenuated red light firing frequency (FF) compared to native expressed *Drosophila* CRY. **(A)** Firing frequency response of *p12c* (blue column, n = 16) versus *gl60j* (red column, n = 18), *cry-null* (green column, n = 15), *gl60j-cry-null* (yellow column, n = 11), and *rh7-null* (violet column, n = 10) with 5 s red (635 nm, 200 μW/cm^2) light stimulus. Post-stimulus FF response in 10 min bins for **(B)** *p12c* (blue trace) vs. *gl60j* (red trace), **(C)** *p12c* vs. *cry-null* (green trace), **(D)** *p12c* vs. *gl60j-cry-null* (yellow trace), and **(E)** *p12c* vs. *rh7-null* (violet trace). Data are plotted as average ± SEM. Pairwise comparison was analyzed using two-sample t-test with FDR adjustment. $^{**}p < 0.05$.

Sheeba et al., 2008b, 2010; McCarthy et al., 2011; Seluzicki et al., 2014; Flourakis and Allada, 2015; Flourakis et al., 2015; Fogle et al., 2015; Buhl et al., 2016, 2019; Baik et al., 2017, 2019a; Li et al., 2018; Smith et al., 2019; Au et al., 2022).

To determine if the absence of CRY or the internal and external rhodopsin photoreceptors alters the basal FF of l-LNvs, we plotted basal firing rates across the time of day of the recordings (Figure 10). Scatter plots for the *p12c* control and all photoreceptor mutants pre-exposed to UV, violet, blue, or red light (Figures 10A–D, respectively) show no discernable correlation to time-of-day of the recording and FF baseline. However, average FF baseline for each group plotted as a box and whisker plot shows significantly lower baseline FF for *gl60j* and *rh7-null* mutants compared to the control *p12c* (Figure 10E, approximate average of 4.2 Hz for *p12c*, blue box vs. 3.6 Hz for *gl60j*, red box and 2.4 Hz for *rh7-null*, violet box). The double knockout *gl60j-cry-null* had a significantly higher FF baseline than *gl60j* (Figure 10E, approximate average of 5.2 Hz for *gl60j-cry-null*, yellow box vs. red

TABLE 1 Summary of firing frequency ratio for each genotype against each color of light stimulus.

	UV	Violet	Blue	Red
p12c	1.667	1.899	1.958	1.197
gl60j	1.129	1.016	1.213	1.06
cry-null	1.099	1.39	1.066	1.04
gl60j-cry-null	1.328	0.994	1.026	0.981
rh7-null	1.115	1.056	1.289	1.074

Firing frequency responses (FF lights on/FF baseline no light) of *p12c*, *gl60j*, *cry-null*, *gl60j-cry-null*, and *rh7-null* for UV, violet, blue, and red (200 μW/cm^2 of 365, 405, 450, and 635 nm, respectively) light stimulus. The green shading represents larger FF light responses, while the white shading represents smaller FF light responses.

box) but recordings from this genotype tend to be more unstable as indicated by the wide range of measured FF. Similarly, *cry-null* baseline FF is significantly higher than *rh7-null* baseline FF (Figure 10E, approximate average of 3.9 Hz for *cry-null*, green box vs. violet box). To provide a clear of the data distribution, individually plotted points for each genotype can be found on Figure 10F. These results show that removal of any opsin-based photoreceptor system results in a decrease in l-LNv baseline FF in absence of light, thus opsin-based photoreceptors modulate baseline circadian/arousal neuronal firing.

3.4. Photoreceptor mutant fly light-evoked arousal responses during sleep are significantly attenuated but not abolished, similar to the l-LNvs photoexcitatory defects

Non-imaging forming vision in flies is primarily mediated by CRY and Rh7 photoreceptors expressed in the LNv subset of circadian/arousal neurons are responsible for acute light-mediated behaviors such as arousal as well as circadian entrainment. Fly light evoked arousal responses occur over a range of wavelengths from 365–635 nm and vary with intensity. Though primarily short-wavelength photodetectors, CRY and Rh7 may also exhibit sensitivities reaching longer wavelength orange-red colored light. External photoreceptors in the compound eyes, ocelli, and Hofbauer-Buchner eyelet of flies express a wide range of opsin-based photoreceptors that further equip the fly with image-forming visual photoreception spanning the UV and visible light spectrum. Visual neural circuits downstream of external photoreceptors appear to synapse in the accessory medulla in the fly brain in close proximity to LNv circadian/arousal neurons and appear to integrate with CRY and Rh7 non-image forming visual mechanisms to modulate circadian entrainment to light and phototaxis/photoavoidance (Klarsfeld, 2004; Veleri et al., 2007; Helfrich-Förster, 2020). Whether these external photoreceptors contribute excitatory light color-specific information to mediate behavioral arousal responses remains unclear. We measured the acute behavioral responses of *p12c* control flies and photoreceptor mutant flies (*gl60j*, *cry-null*, double mutant *gl60j-cry-null*, and *rh7-null*) to three 5-min pulses of low (10 μW/cm^2) or high (400 μW/cm^2) red (635 nm), blue (450 nm), violet (405 nm), or UV (365 nm) LED light during subjective nighttime at time points ZT18, ZT19, and ZT20 for three consecutive nights. Scatter plots show the average% of flies that awaken across the 3 days of experiment per each light-pulse with responses from the first, second, and third pulses spanning each cluster from left, middle, and right, respectively. Average fly arousal responses do not significantly differ between consecutive nights of experiment.

An average of nearly 85% of control *p12c* flies are aroused from sleep in response to low (10 μW/cm^2) intensity UV light (Figure 11A, light blue points). All photoreceptor mutants except *cry-null* exhibit significantly lower arousal responses to low intensity UV light pulses relative to *p12c* controls (Figure 11A), suggesting that the light intensity threshold for CRY activation is higher than that for opsins. The double mutant *gl60j-cry-null* shows the greatest response attenuation of light evoked arousal to low intensity UV light pulses compared to all other genotypes (Figure 11A, light yellow points). Notably, *gl60j-cry-nulls* do not show significantly attenuated response in l-LNv photoexcitability to UV light at 20 fold higher light stimulus intensity (Figures 1A, D), suggesting possible additional UV sensing mechanisms for fly arousal. All photoreceptor mutants except *cry-null* exhibit a loss of arousal sensitivity compared to *p12c* in response to higher intensity UV light pulses (Figure 11B). However, both *gl60j* and *gl60j-cry-null* flies show significantly attenuated higher intensity UV light arousal responses (Figure 11B, dark red points and dark yellow points, respectively) and double mutant *gl60j-cry-null* flies show significantly attenuated higher intensity UV light arousal responses relative to *gl60j* alone, indicating that CRY does contribute to UV light evoked arousal. Mutant *rh7-null* flies show the greatest degree of attenuation of higher intensity UV light arousal responses (Figure 11B, dark violet points and dark yellow points, respectively) and show significantly attenuated arousal responses to higher intensity UV light relative to *gl60j* (Figure 11B, dark violet points versus red points), *cry-null* (Figure 11B, dark violet points versus green points), and *gl60j-cry-null* (Figure 11B, dark violet points versus yellow points), underscoring the importance of Rh7 for UV light evoked arousal for this light intensity. This result is consistent with reports that Rh7 is a bistable broad range photopigment and is activated in the UV range (Ni et al., 2017; Sakai et al., 2017).

An average of approximately 85% of control *p12c* flies are aroused from sleep in response to low (10 μW/cm^2) intensity violet light (Figure 12A, light blue points). Low intensity violet light pulses evoke significantly lower arousal responses for all photoreceptor mutants compared to *p12c*, with *gl60j* and *gl60j-cry-null* showing the greatest attenuation of violet light evoked arousal (Figure 12A). Not surprisingly, *cry-null* alone shows the least attenuation of violet light evoked arousal as no redox state of CRY exhibits high absorption in the violet range of the spectra. Loss of Rh7 results in significant attenuation of the low intensity violet light response, but significantly less so relative to either *gl60j* or *gl60j-cry-null*. For high intensity violet light pulses, all photoreceptor mutants except *cry-null* flies show significantly attenuated arousal responses (Figure 12B), suggesting that the lack of CRY activation by violet light may mediate spectral differentiation for short-wavelength light arousal responses. Arousal of *rh7-null* flies is most significantly attenuated in response to high intensity violet light pulses (Figure 12B, dark violet points).

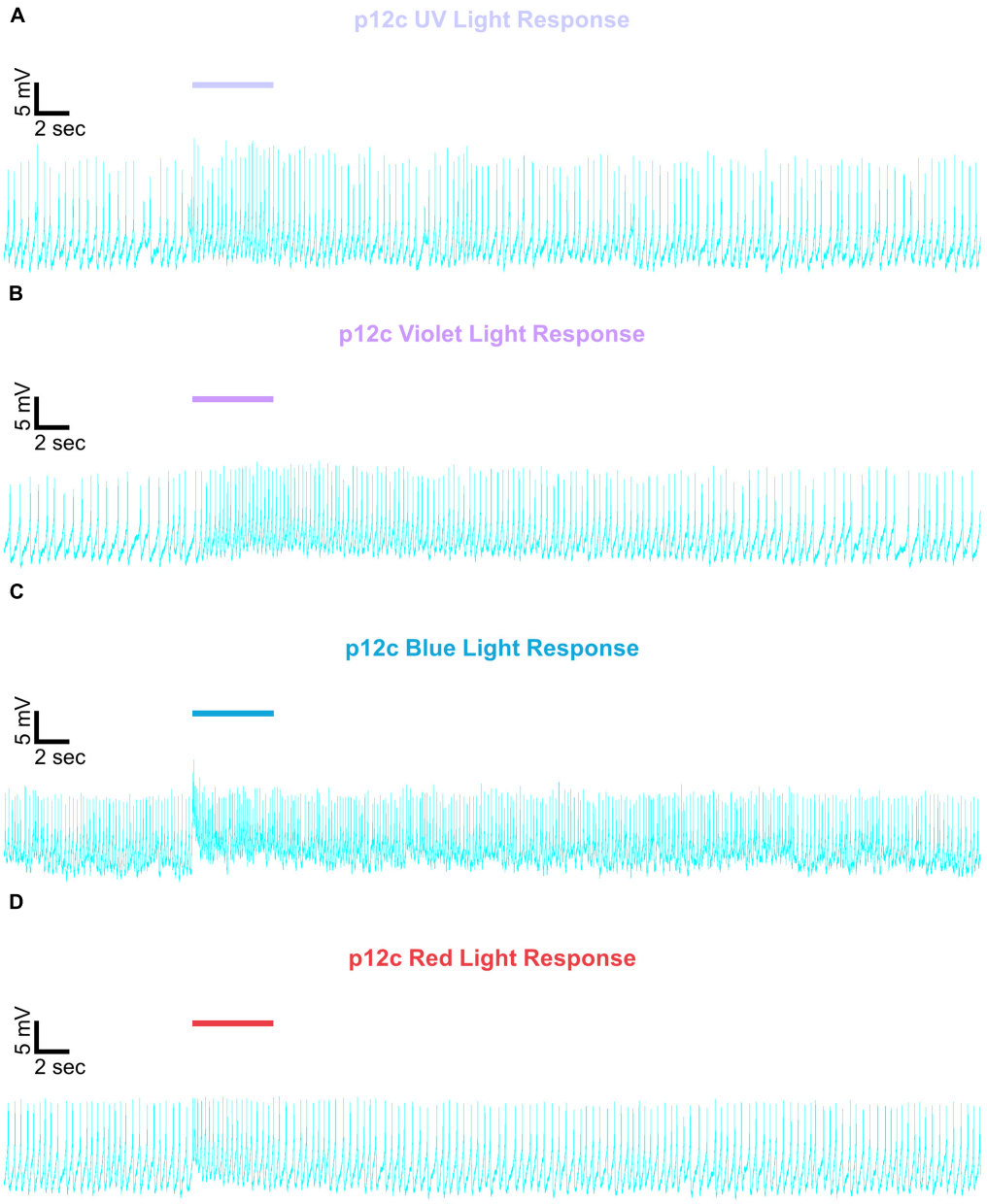

FIGURE 5
Representative voltage traces of l-LNvs electrophysiological responses to UV, violet, blue, and red light stimulus for native expressed *Drosophila* CRY. Representative voltage traces of the last 60 s of a patch-clamp recording of l-LNvs subjected to 5 s of **(A)** UV, **(B)** violet, **(C)** blue, and **(D)** red light stimulus for natively expressed *Drosophila* CRY, *p12c* (blue traces). Colored bars indicate 5 s of 200 $\mu W/cm^2$ light stimulus. Vertical scale bars represent 5 mV and horizontal scale bars represent 2 s.

On average, approximately 65% of *p12c* control flies are aroused in response to low intensity blue light while approximately 75% are aroused in response to high intensity blue light (Figures 13A, B). All photoreceptor mutants exhibit significantly attenuated arousal responses compared to *p12c* control flies for both low and high intensity blue light (Figures 13A, B). The trends for the degree of attenuation of blue light evoked arousal responses are very similar to those measured for l-LNv blue light evoked electrophysiological action potential firing (Figure 3). Both low and high intensity blue light evoked arousal responses show *rh7-null* flies have the most attenuated response (Figure 13A, light violet points; Figure 13B, dark violet points). Interestingly, compared to *gl60j* and *gl60j-cry-null* flies, *cry-null* flies exhibit significantly less arousal response attenuation to low intensity blue light pulses (Figure 13A, light green points) but significantly greater attenuation responses to high intensity blue light pulses (Figure 13B, dark green points) which may reflect higher threshold for CRY blue light activation relative to the blue light activation threshold for opsins.

On average, approximately 70% of *p12c* control flies are aroused in response to low intensity red light while less than 40% are aroused in response to high intensity red light (Figures 14A, B). Significantly fewer *gl60j*, *cry-null*, and *gl60j-cry-null* flies are

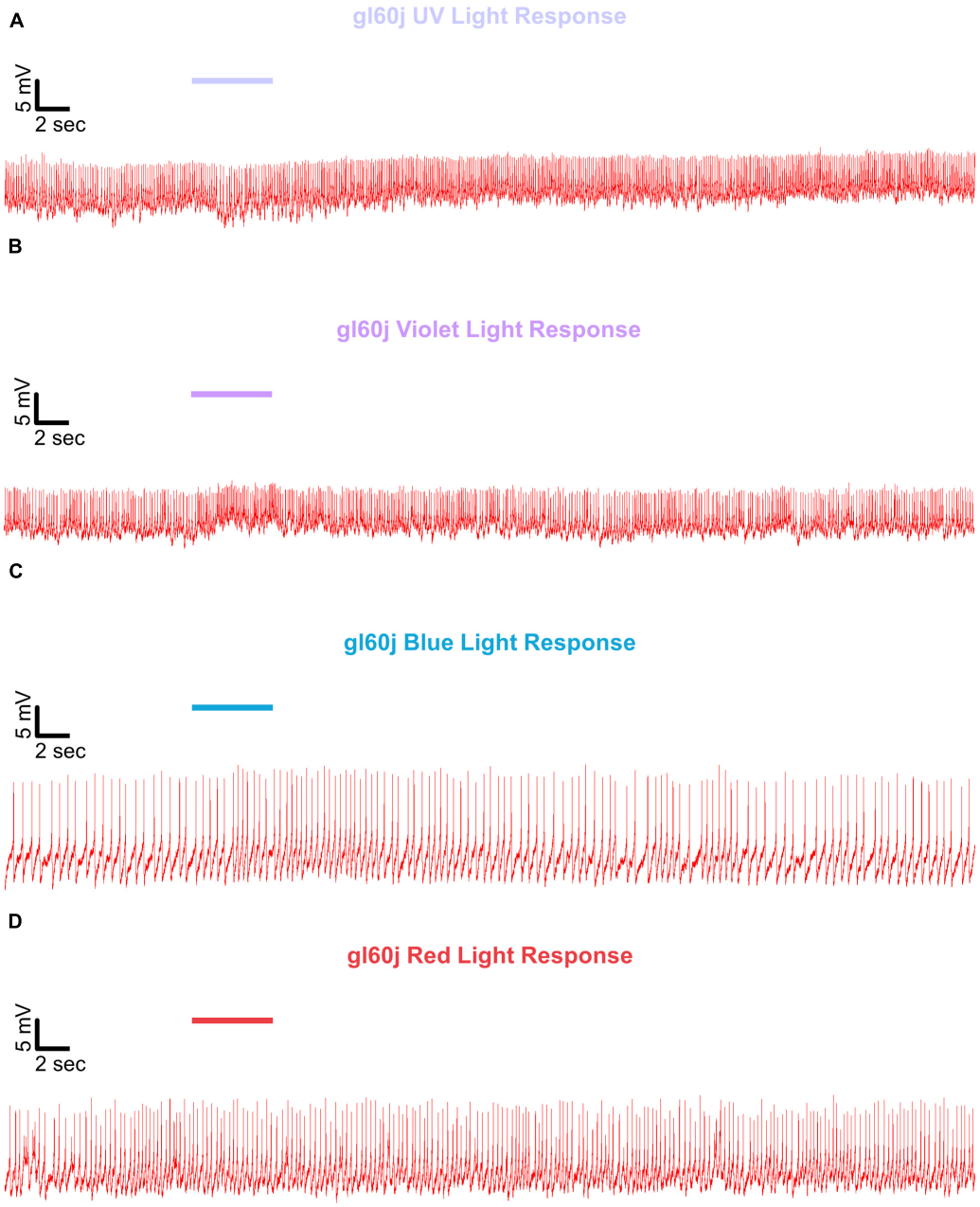

FIGURE 6
Representative voltage traces of l-LNvs electrophysiological responses to UV, violet, blue, and red light stimulus for *gl60j*. Representative voltage traces of the last 60 s of a patch-clamp recording of l-LNvs subjected to 5 s of **(A)** UV, **(B)** violet, **(C)** blue, and **(D)** red light stimulus for *gl60j* flies (red traces). Colored bars indicate 5 s of 200 $\mu W/cm^2$ light stimulus. Vertical scale bars represent 5 mV and horizontal scale bars represent 2 s.

aroused in response to low intensity red light relative to control (Figure 14A, light blue points vs. light red points, light green points, and light yellow points, respectively). Compared to *p12c* control flies, *rh7-null* flies do not significantly differ for low intensity red light pulse arousal responsiveness (Figures 14A, light blue points vs. light violet points). As the low intensity red light responses compared between *cry-null* and *gl60j-cry-null* flies do not significantly differ, external opsin-based photoreceptors appear to be the primary mediators of low intensity red light pulse arousal. High intensity red light evoked arousal response measurements further supports this (Figure 14B), as only *gl60j* (dark red points) and *gl60j-cry-null* (dark yellow points) flies are significantly less responsive compared to *p12c* controls (dark blue points).

The overall trend indicates that intensity matched short wavelength light more effectively arouses flies from sleep than long wavelength light. Curiously, for red light, significantly fewer flies are aroused by the higher intensity condition (Figure 15), while for blue light, significantly more flies respond to the higher intensity condition, except *cry-null* flies, which are effectively aroused for both intensity conditions (Figure 15). Violet light pulses also showed a similar trend, with all photoreceptor groups except *rh7-null* flies having an increase in arousal responsiveness to high

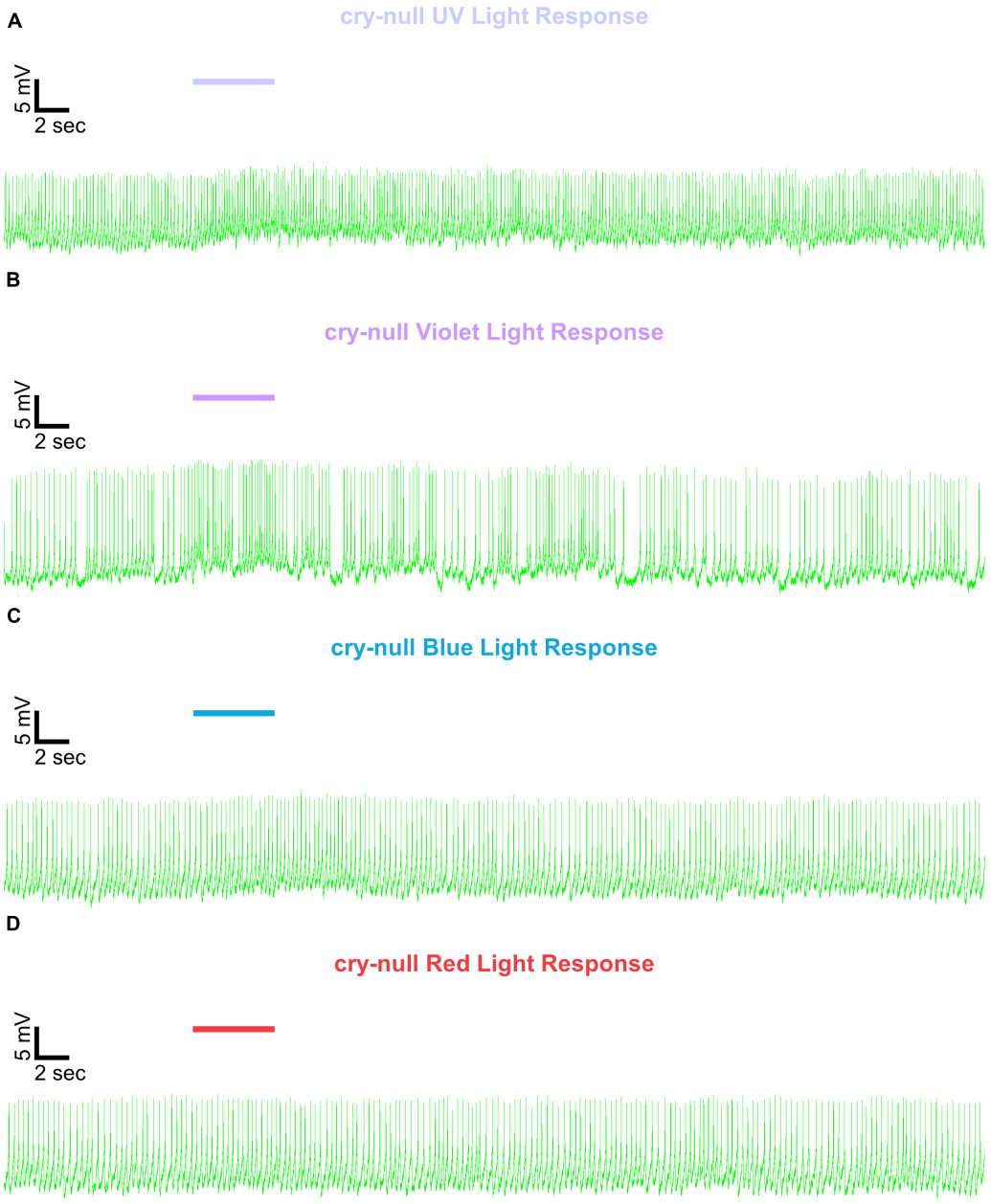

FIGURE 7
Representative voltage traces of l-LNvs electrophysiological responses to UV, violet, blue, and red light stimulus for *cry-null*. Representative voltage traces of the last 60 s of a patch-clamp recording of l-LNvs subjected to 5 s of **(A)** UV, **(B)** violet, **(C)** blue, and **(D)** red light stimulus for *cry-null* flies (green traces). Colored bars indicate 5 s of 200 $\mu W/cm^2$ light stimulus. Vertical scale bars represent 5 mV and horizontal scale bars represent 2 s.

intensity compared to low intensity violet light, while *rh7-null* flies significantly respond less to the high intensity condition compared to the low light intensity condition (Figure 15). A summary table of behavioral arousal responses to light pulse stimuli for all genotypes can be found on Table 2. Taken altogether, these results provide strong evidence of a multifaceted photoreceptor convergence system that inputs mechanistically distinct different channels of photic information to arousal neurons that correspond to different spectral wavelengths and different intensity-dependent light activation thresholds. Removal of any one of these photoreceptor systems results in a significant loss of l-LNv photoexcitability or downstream behavioral arousal, with partial remaining functionality indicating robustness through redundancy.

4. Discussion

Insects use a variety of sensory modalities to navigate their environments, including image forming and non-image forming vision. Remarkably, multiple critical light-driven behaviors are mediated through the clock gene expressing neural circuit in flies. In addition to regulating circadian behavior, this circuit also contributes to light activated behavioral arousal

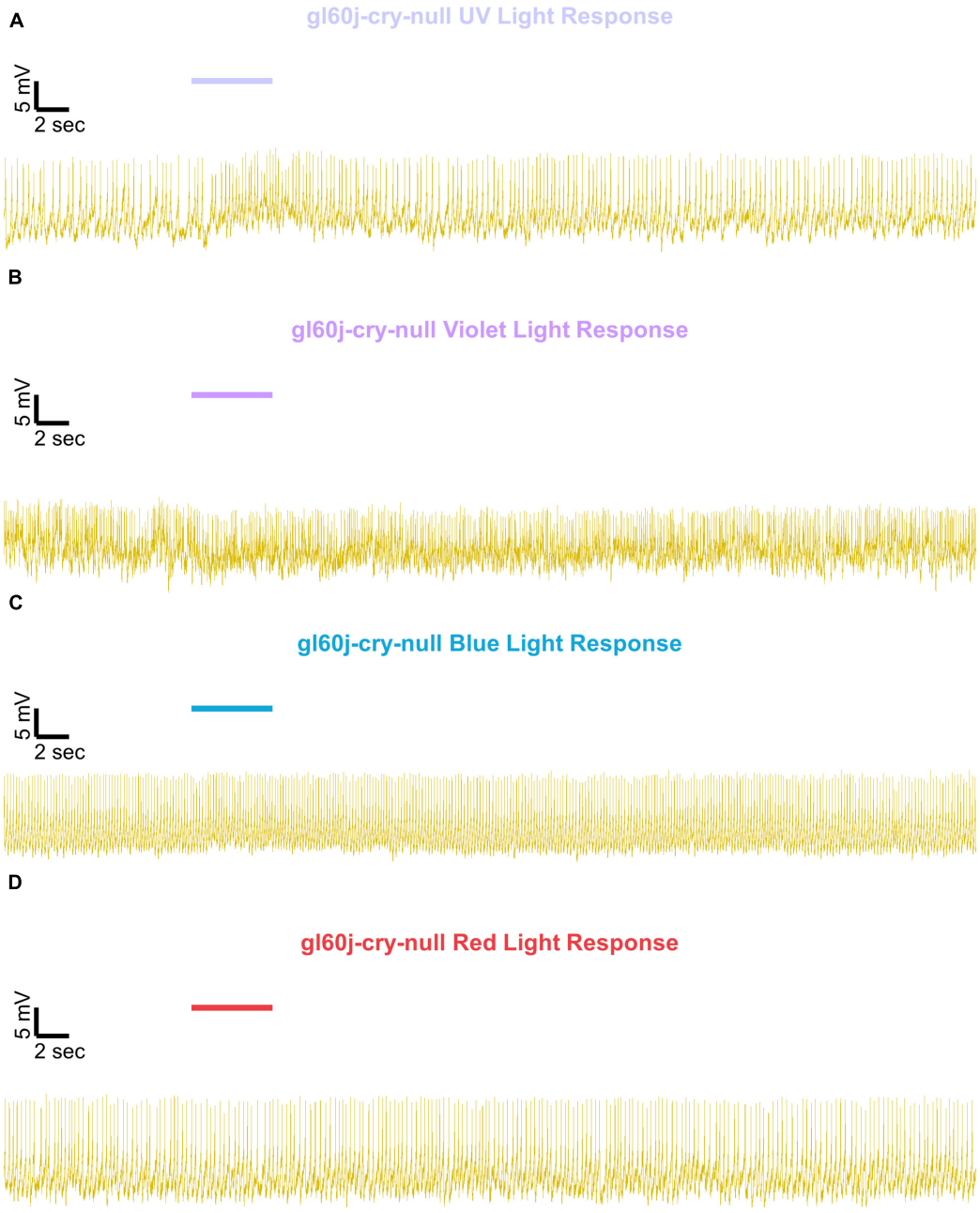

FIGURE 8
Representative voltage traces of l-LNvs electrophysiological responses to UV, violet, blue, and red light stimulus for *gl60j-cry-null*. Representative voltage traces of the last 60 s of a patch-clamp recording of l-LNvs subjected to 5 s of **(A)** UV, **(B)** violet, **(C)** blue, and **(D)** red light stimulus for *gl60j-cry-null* flies (yellow traces). Colored bars indicate 5 s of 200 $\mu W/cm^2$ light stimulus. Vertical scale bars represent 5 mV and horizontal scale bars represent 2 s.

and phototaxis/photoavoidance light choice behavior. The circuit localization of these functions suggest that these light evoked behaviors may be modulated by time of day. The integration of multiple photosensory inputs for behavioral responses to light suggests the importance of functional redundancy as well as higher level processing of complex light spectral and intensity features. Circadian photoentrainment appears to mediated through a combination of external rhodopsin photoreceptors in the eyes and HB eyelets, as well as deep-brain photopigments CRY and possibly Rh7 (Emery et al., 1998, 2000; Stanewsky et al., 1998; Helfrich-Förster et al., 2001, 2002; Malpel et al., 2002; Rieger et al., 2003; Klarsfeld, 2004; Veleri et al., 2007; Sheeba et al., 2008a; Schlichting et al., 2014, 2015, 2016; Saint-Charles et al., 2016; Ni et al., 2017; Senthilan et al., 2019). These mechanistically distinct photoreceptors detect differences in light intensity, spectral composition, and exposure time. While the role of CRY for circadian entrainment is widely accepted, Rh7's role is less clear (Kistenpfennig et al., 2017; Ni et al., 2017). Ni et al. (2017) show small but significant effects of Rh7 on circadian entrainment. Kistenpfennig et al. (2017) also show small but significant circadian

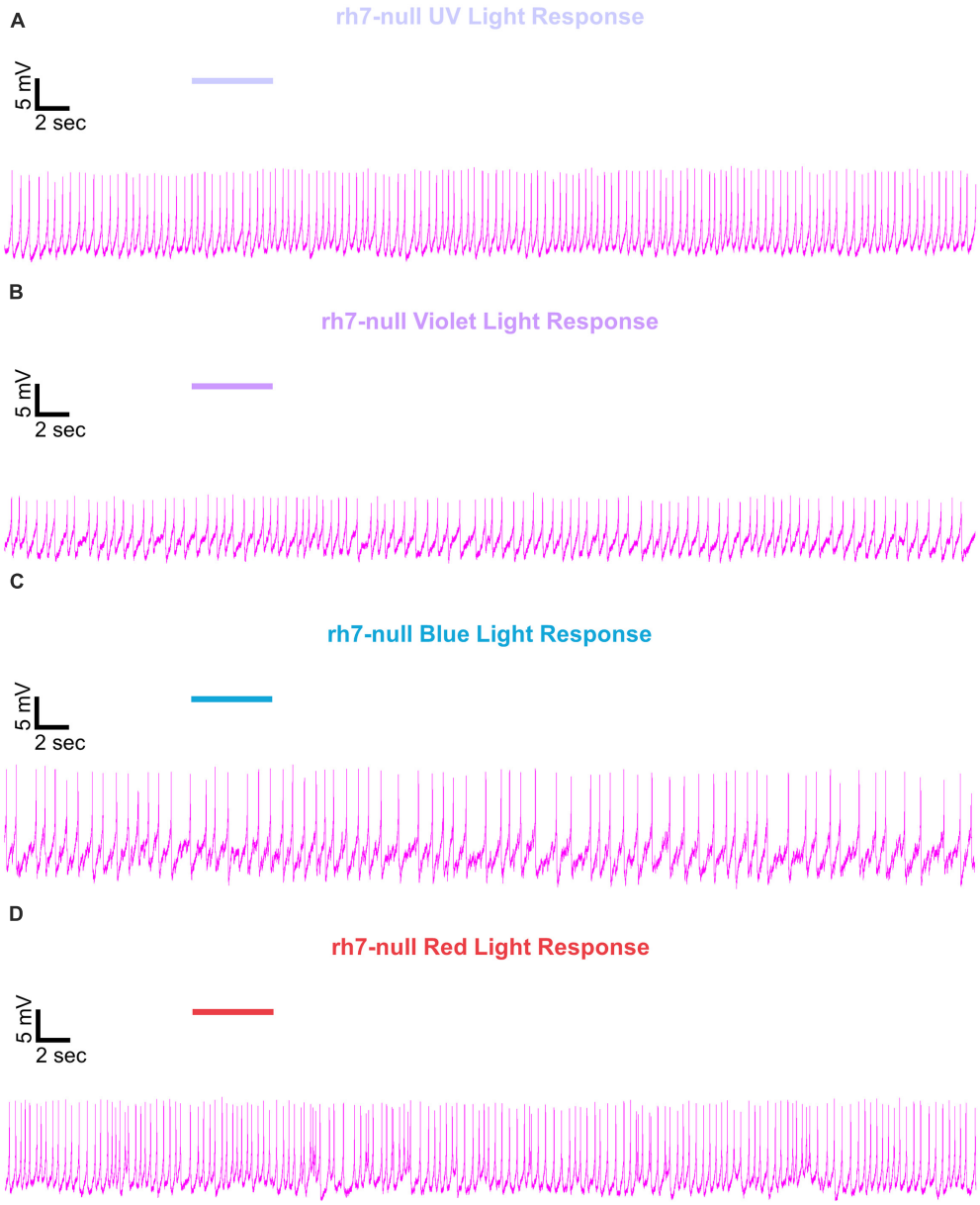

FIGURE 9
Representative voltage traces of l-LNvs electrophysiological responses to UV, violet, blue, and red light stimulus for *rh7-null*. Representative voltage traces of the last 60 s of a patch-clamp recording of l-LNvs subjected to 5 s of **(A)** UV, **(B)** violet, **(C)** blue, and **(D)** red light stimulus for *rh7-null* flies (violet traces). Colored bars indicate 5 s of 200 $\mu W/cm^2$ light stimulus. Vertical scale bars represent 5 mV and horizontal scale bars represent 2 s.

effects in *rh7-null* mutants, their abstract states "However, in blue light (470 nm), Rh7 (0) mutants needed significantly longer to synchronize than wild-type controls, suggesting that Rh7 is a blue light-sensitive photopigment with a minor contribution to circadian clock synchronization. In combination with mutants that lacked additionally cryptochrome-based and/or eye-based light input to the circadian clock, the absence of Rh7 provoked slightly stronger effects." The rich multiplicity of photosensory inputs suggests that these different input channels work together in a coordinated fashion, and likely extract sensory cues to determine precise time of day information. Such a system would allow further tuning of the circadian clock to respond to complex light cues that vary according to time of day, weather and season, particularly in the morning (Majercak et al., 1999; Chen et al., 2006; Bachleitner et al., 2007; Boothroyd et al., 2007; Picot et al., 2007; Stoleru et al., 2007; Vanin et al., 2012; Guo et al., 2014; Green et al., 2015; Breda et al., 2020). Other sensory modalities, such as temperature sensing also provide further cues. Similarly, light choice behavior, expressed as phototaxis versus photoavoidance, also relies on the combination of external rhodopsin photoreceptors in the eyes and HB eyelets and the deep-brain neuronal photopigments CRY and Rh7 (Heisenberg and Buchner, 1977; Miller et al., 1981; Gao et al., 2008; Yamaguchi et al., 2010; Schlichting et al., 2016; Baik et al., 2017, 2018). Recent work shows that light choice behavior varies by time of day and that the LNvs are a point of convergence for multiple light input channels that

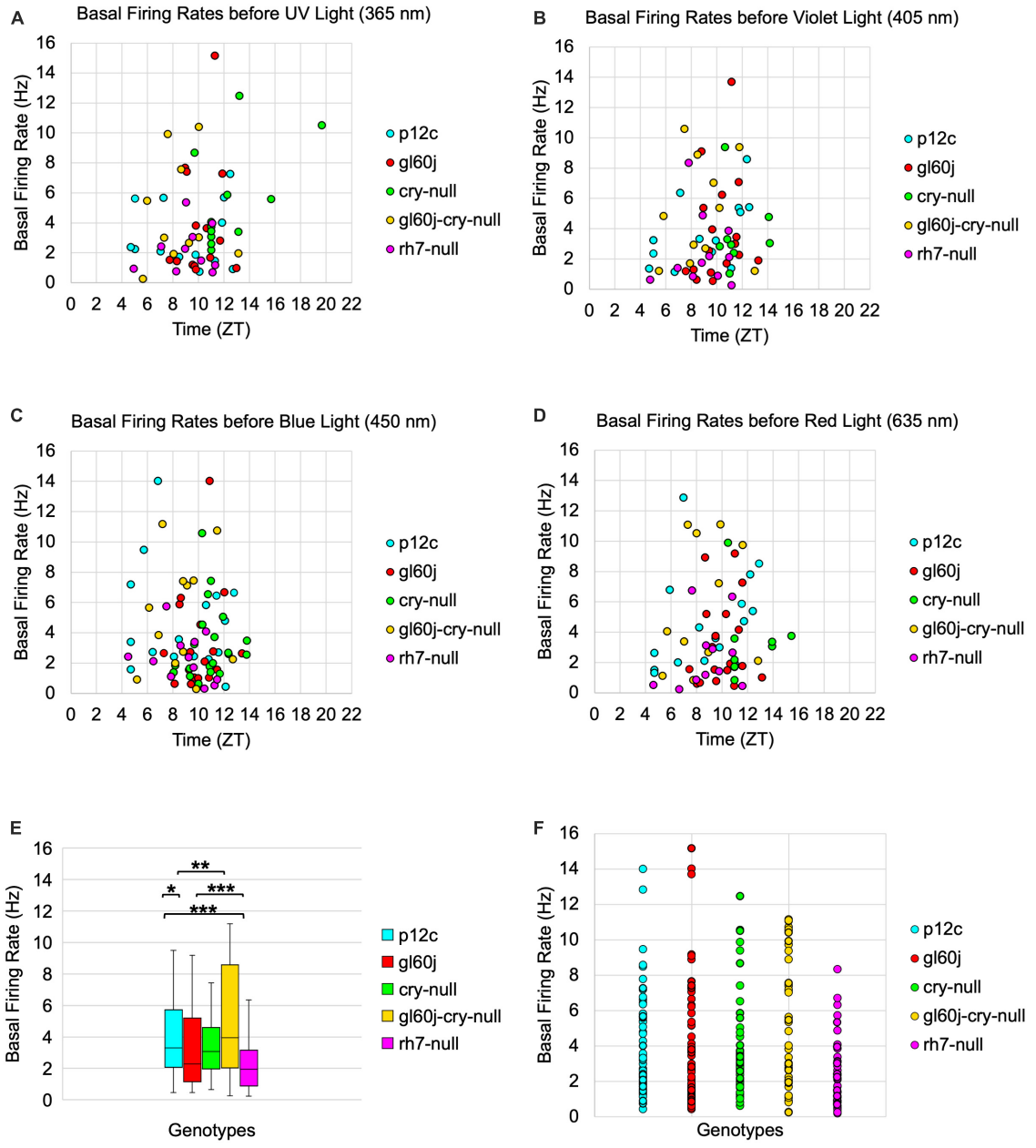

FIGURE 10
Basal firing rates are not equivalent across groups and there is no time-of-day dependent effect. Average basal firing rates of *p12c* (blue), *gl60j* (red), *cry-null* (green), *gl60j-cry-null* (yellow), and *rh7-null* (violet) before **(A)** UV, **(B)** violet, **(C)** blue, and **(D)** red light stimulus plotted against the relative time-of-day of each recording. **(E)** Box-and-whisker plot summary of the average basal firing rate for *p12c* [(n = 35) total, n (ZT0-12) = 30; n (ZT12-16) = 5], *gl60j* [(n = 22) total, n (ZT0-12) = 20; n (ZT12-16) = 2], *cry-null* [(n = 26) total, n (ZT0-12) = 14; n (ZT12-16) = 12], *gl60j-cry-null* [(n = 30) total, n (ZT0-12) = 22; n (ZT12-16) = 8], and *rh7-null* [(n = 30) total, n (ZT0-12) = 22; n (ZT12-16) = 8]. Median values are denoted by a solid black line within each box of the plot. **(F)** Individual data points for each genotype for all time points, showing the distribution of the data. Black *indicates FDR adjusted two-sample t-test $p \leq 0.01$ vs. *p12c*. Data are represented as a range of means in a sample set ± maximum and minimum values within the set. One significance symbol, $p \leq 0.1$; two significance symbols, $p \leq 0.05$; three significance symbols, $p \leq 0.01$.

modulate light choice behavior (Baik et al., 2019b). The LNvs, particularly the l-LNv also serve as light activated arousal neurons that are embedded within the circadian neural circuit (Parisky et al., 2008; Shang et al., 2008; Sheeba et al., 2008b; Chung et al., 2009; Kilman et al., 2009). Yet how LNv circadian/arousal neurons functionally integrate different photic inputs to behavioral light arousal responses remained incompletely understood. Based on this set of earlier findings, we were motivated to measure the relative input contributions to l-LNv light evoked electrical excitation and behavioral arousal.

Short wavelength light evoked electrical excitation of the l-LNvs is mediated through all three photoreceptor systems. Our previous work has shown that upon blue and UV exposure of l-LNvs, CRY-mediated phototransduction increases in membrane electrical activity via the potassium channel subunit hyperkinetic (HK), an NADH [Nicotinamide Adenine Dinucleotide (NAD) +

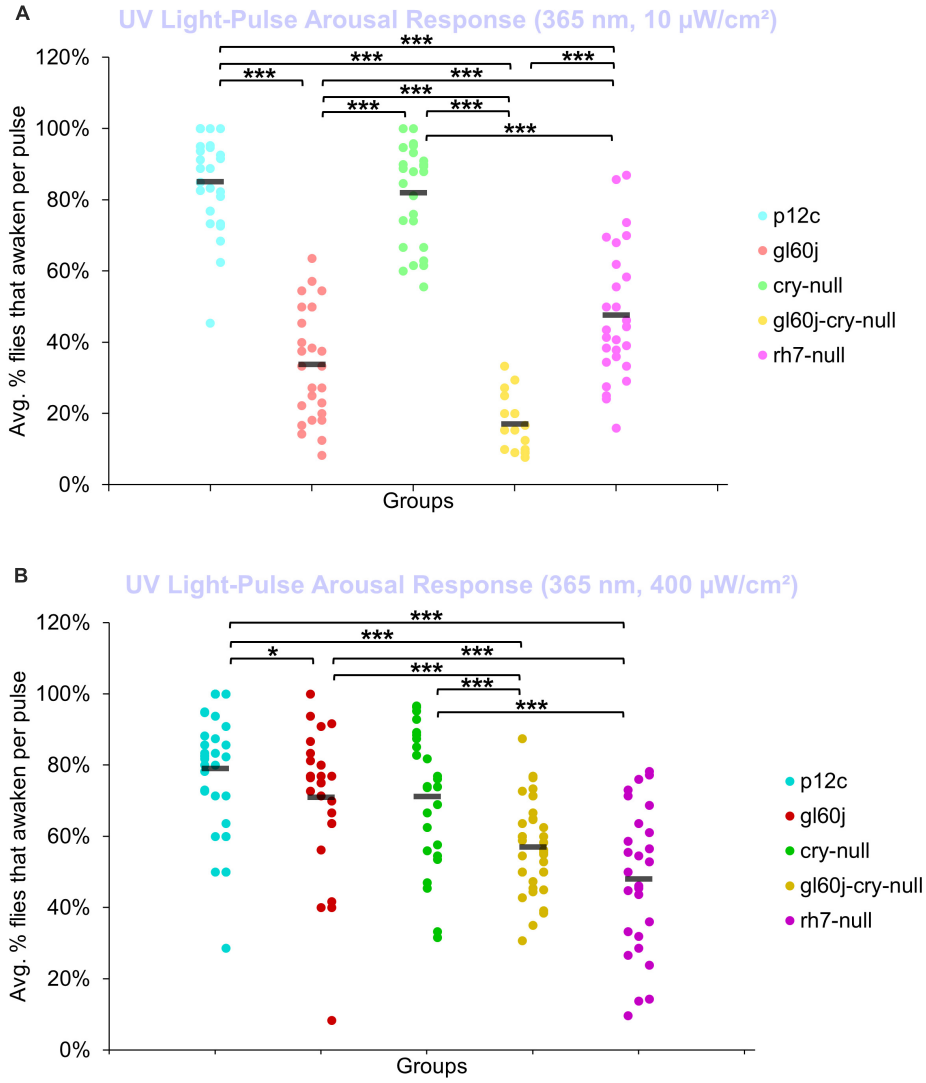

FIGURE 11
Low and high intensity UV light pulse arousal behavior is significantly attenuated in all photoreceptor mutants except *cry-null* compared to the control *p12c*. Three 5 min pulses of UV light were applied to flies during subjective nighttime (ZT18, ZT19, ZT20) for 3 days after 12:12 h LD entrainment to measure the arousal response of *p12c* (blue), *gl60j* (red), *cry-null* (green), *gl60j-cry-null* (yellow), and *rh7-null* (violet) flies for **(A)** low (10 $\mu W/cm^2$) and **(B)** high (400 $\mu W/cm^2$) light intensity. Scatter plots are grouped by average% of flies that awaken across the 3 days of light-pulse arousal experiment and separated as pulse 1 (left points for each group), pulse 2 (middle points for each group), and pulse 3 (right points for each group). Black bars indicate total average% flies that awaken across the 3 days and three pulses of light. Pairwise comparison was analyzed using two-sample *t*-test with FDR adjustment. *$p < 0.1$ and ***$p < 0.01$.

Hydrogen (H)] binding redox-sensor (Weng et al., 2006; Pan et al., 2008; Fogle et al., 2015). Using light-evoked electrophysiological assays that measure light evoked increases in action potential FF in positive control *w;pdfGAL4-p12c;* + flies, we record robust increases in FF following 5 s exposures of UV, blue, and violet light stimuli. By comparison, significantly attenuated short wavelength light responses relative to control are recorded most of the mutant photoreceptor knockout flies that lack either all external opsin-based photoreceptors (*gl60j*), or CRY (*cry-null*), Rh7 (*rh7-null*), and the double mutant *gl60j-cry-null.* Blue light stimulation evokes highly sustained FF increases for > 20 s before returning to baseline in controls. Blue light evoked sustained FF rates are significantly attenuated in each of mutant knockouts, showing that all three photosystems are critical for blue light sustained action potential firing rates. Violet light also evokes sustained action potential FF increases in controls, persisting for > 10 s, which are significantly attenuated in the mutant knockouts of photopigments that code for violet-sensitive rhodopsin-based phototransduction inputs (*gl60j*, *rh7-null*, and *gl60j-cry-null*). These results are consistent with previous findings that indicate CRY and Rh7 as the predominant blue and violet light internal photosensors, respectively, and show that external opsin driven photoreceptors also contribute additive/converging effects for blue and violet light sensing by the l-LNv. UV light exposure evokes significant, but less robust sustained increases in FF (< 10 s) in controls, which more rapidly return to baseline FF after the cessation of light. Short wavelength light evoked firing rate increases in l-LNvs are all significantly attenuated in *cry-null*, *gl60j* and *rh7-null* mutants and

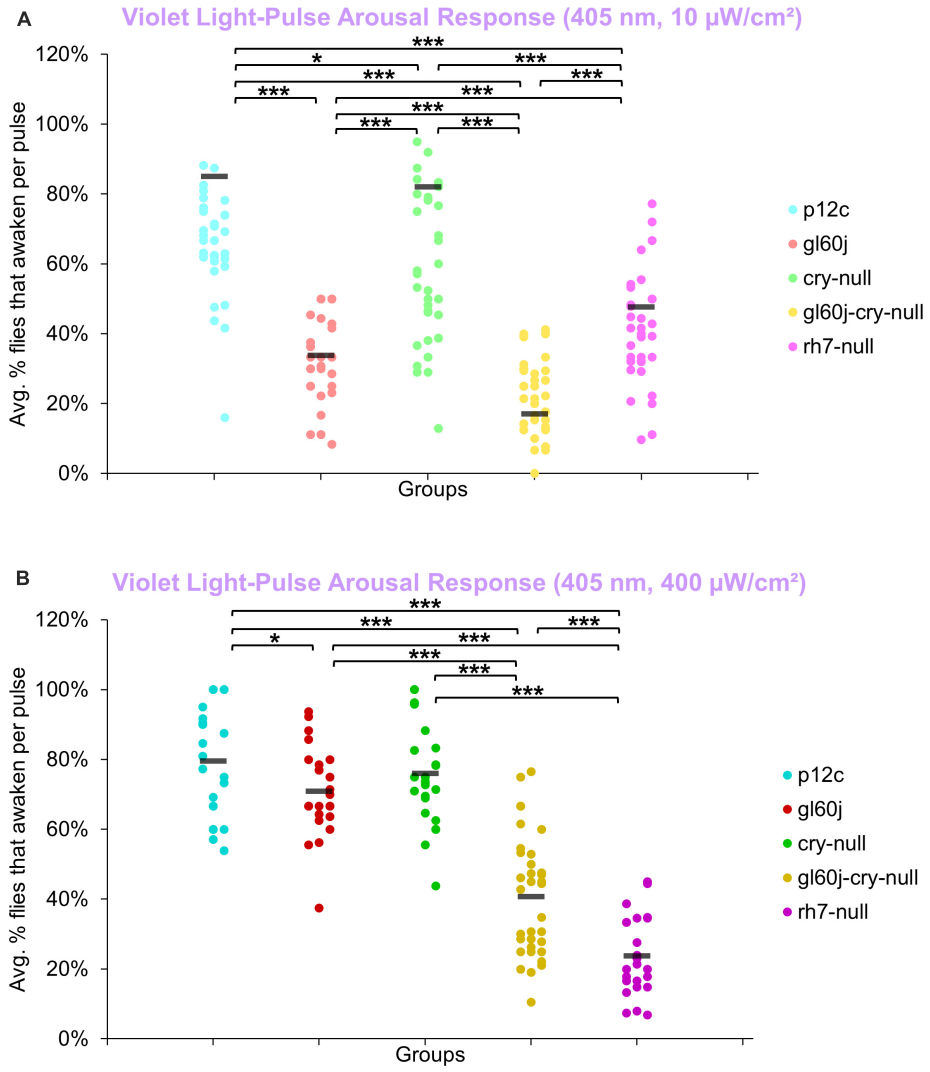

FIGURE 12
Violet light pulse arousal behavior is significantly attenuated in flies lacking Rh7 or external photoreceptors with low and high intensity light compared to the control *p12c*. Three 5 min pulses of violet light were applied to flies during subjective nighttime (ZT18, ZT19, ZT20) for 3 days after 12:12 h LD entrainment to measure the arousal response of *p12c* (blue), *gl60j* (red), *cry-null* (green), *gl60j-cry-null* (yellow), and *rh7-null* (violet) flies for **(A)** low (10 µW/cm^2) and **(B)** high (400 µW/cm^2) light intensity. Scatter plots are grouped by average% of flies that awaken across the 3 days of light-pulse arousal experiment and separated as pulse 1 (left points for each group), pulse 2 (middle points for each group), and pulse 3 (right points for each group). Black bars indicate total average% flies that awaken across the 3 days and three pulses of light. Pairwise comparison was analyzed using two-sample *t*-test with FDR adjustment. *$p < 0.1$ and ***$p < 0.01$.

double knockout *gl60j-cry-null* relative to control except for violet light and *cry-null* mutants, showing a remarkable convergence of light inputs. The results are consistent with the earlier finding that Rh7 is expressed in the LNv as shown by Ni et al. (2017). UV, violet and blue light evoked increases in l-LNvs are all significantly attenuated in double mutant knockout *gl60j-cry-null* flies that lack all eye structures and do not express CRY. This provides support for the most parsimonious interpretation that Rh7 is expressed and is functional in the l-LNvs. There remains a formal possibility that Rh7 is expressed in brain neurons other than the l-LNv that would have to provide very strong synaptic inputs to the l-LNv that are sufficient to mediate light evoked firing of the l-LNv—however, this scenario also requires that such hypothetical strongly synaptically connected neurons are not detectable either by anti-Rh7 immunocytochemistry as reported by Senthilan et al. (2019). Another interesting, understudied question is whether yet unknown inhibitory interactions occur between the different light input channels converging on the l-LNvs as shown by behavioral studies in Fogle et al. (2015). The composite photosensitivity of light input channels may be modulated by the presence or absence of other photic inputs. In future work, we would like to explore the possibility that there may be yet unknown inhibitory interactions occurring between the different light input channels converging on the l-LNvs.

In contrast to short wavelength light, red light evokes relatively weak but still measurable excitation in the l-LNvs. Furthermore, the short wavelength sustained light evoked responses recorded in the l-LNv are not observed for red light responses. Surprisingly, red photoexcitation of the l-LNvs is dually regulated by CRY and external photoreceptors as shown by the significant attenuation

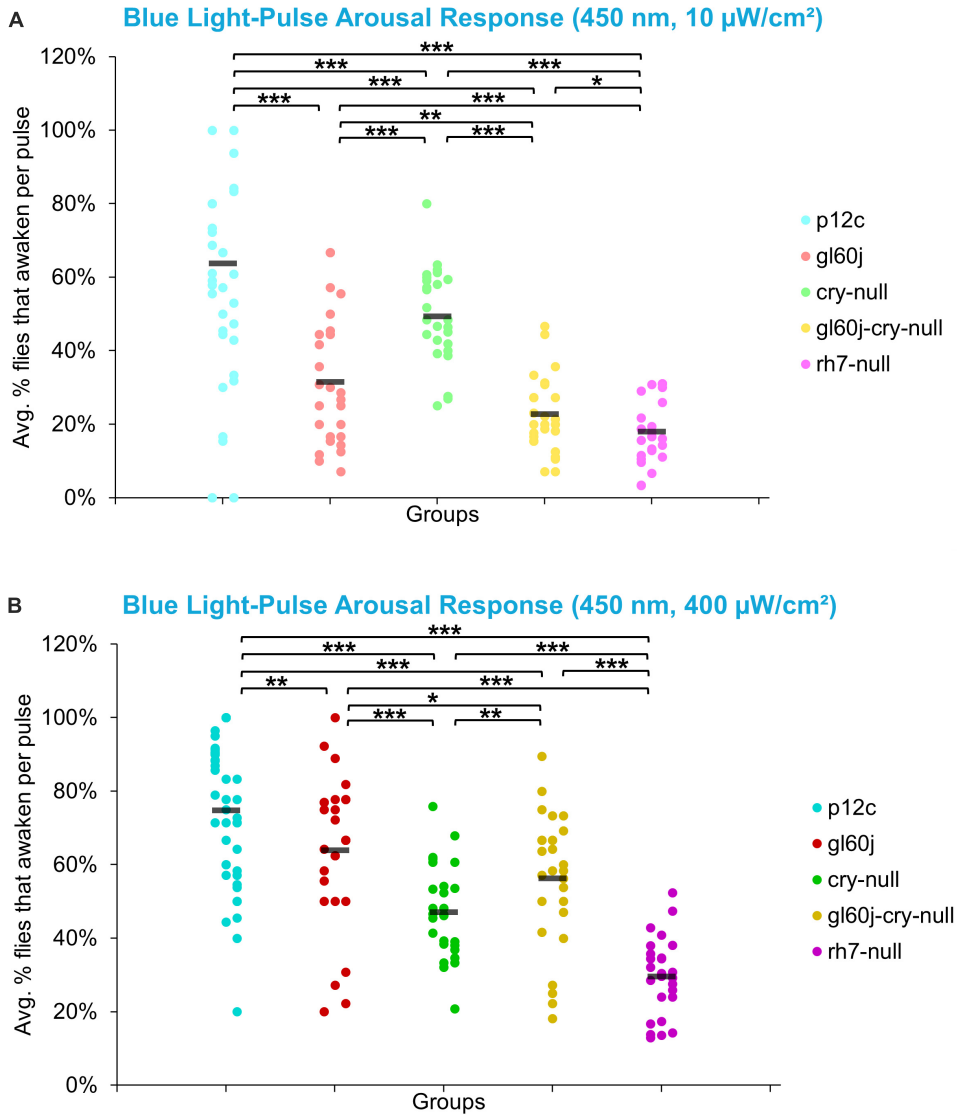

FIGURE 13
Low and high intensity blue light pulse arousal behavior is significantly attenuated in all photoreceptor mutants compared to the control *p12c*. Three 5 min pulses of blue light were applied to flies during subjective nighttime (ZT18, ZT19, ZT20) for 3 days after 12:12 h LD entrainment to measure the arousal response of *p12c* (blue), *gl60j* (red), *cry-null* (green), *gl60j-cry-null* (yellow), and *rh7-null* (violet) flies for **(A)** low (10 µW/cm^2) and **(B)** high (400 µW/cm^2) light intensity. Scatter plots are grouped by average% of flies that awaken across the 3 days of light-pulse arousal experiment and separated as pulse 1 (left points for each group), pulse 2 (middle points for each group), and pulse 3 (right points for each group). Black bars indicate total average% flies that awaken across the 3 days and three pulses of light. Pairwise comparison was analyzed using two-sample *t*-test with FDR adjustment. *$p < 0.1$, **$p < 0.05$, ***$p < 0.01$.

of red light evoked action potential firing in neurons double knockout *gl60j-cry-null* flies compared with controls. Earlier work also shows that red light evokes minimal FF changes during the red light pulse that are not as sustained as light evoked action potential post-stimulus probability of firing increases evoked by short wavelength light (Baik et al., 2019a; Au et al., 2022). Further, l-LNv red light excitability has been found to attenuate with treatment with an FAD functional inhibitor, Diphenyleneiodonium (DPI), with *cry-null* mutants, or with a partial loss-of-function CRY point mutant that disrupts FAD photoreduction (Baik et al., 2019a). In our most recent study, we transgenically expressed CRY1 from a nocturnal mosquito species, *Anopheles gambiae*, in a *cry-null Drosophila* background and found those l-LNvs exhibit an even greater electrophysiological sensitivity to red light (Au et al., 2022). Although spectral absorption analysis of CRY's FAD at oxidized and anionic semiquinone reduced states exhibit peak sensitivity primarily around blue and UV wavelengths, red wavelength sensitivity could occur if CRY expresses a biologically active neutral semiquinone FADH$^\bullet$ state. Altogether, external rhodopsins and CRY dually contribute to the l-LNv red light excitability in the present study, with previous work also supporting red light-excitatory CRY as an input to l-LNvs based on higher reduced states of FAD cycles. Additional experiments are required to dissect the exact external photoreceptive elements that provide red light signaling to l-LNvs and how they might interact with CRY and Rh7. Rh1 and Rh6 are likely candidates as they exhibit partial

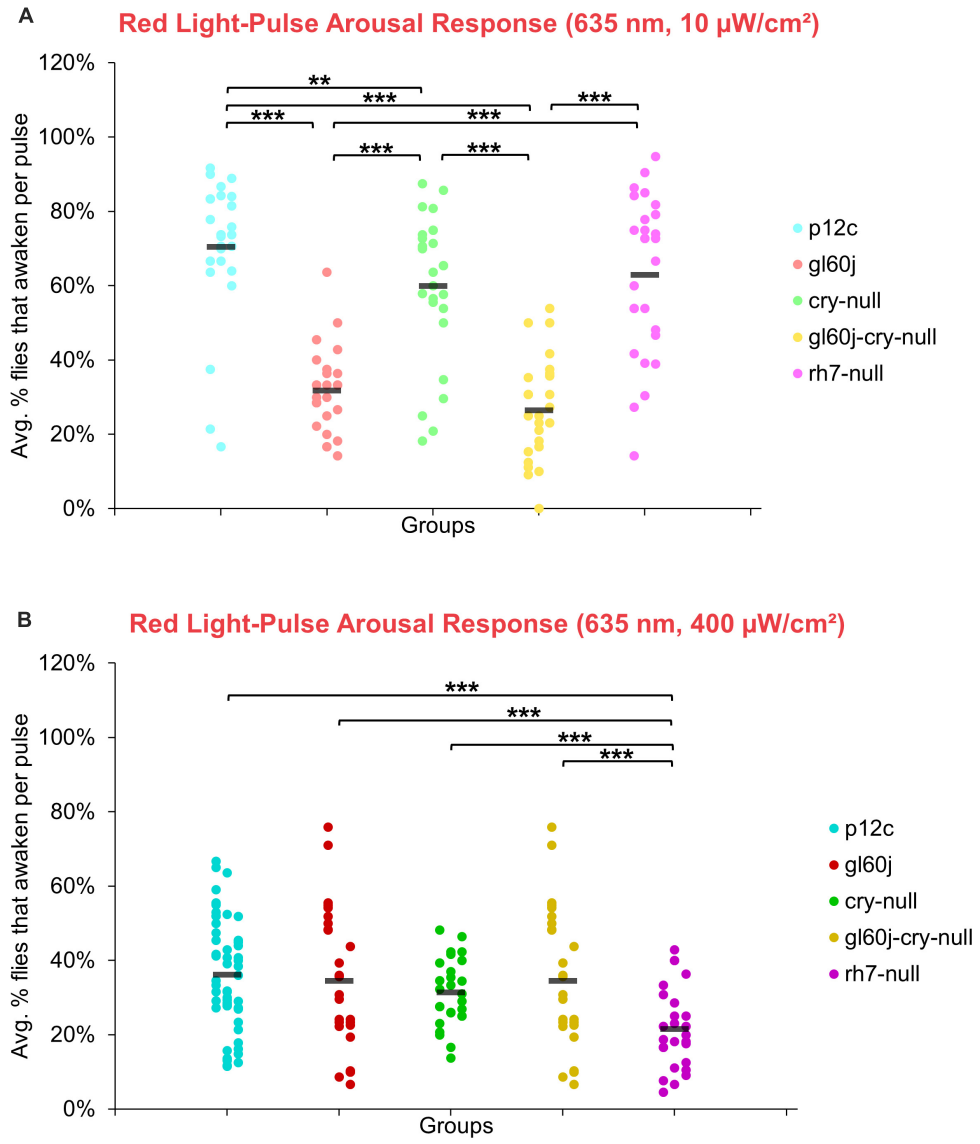

FIGURE 14
Red light pulse arousal behavior is significantly attenuated in flies lacking external photoreceptors at low and high light intensity compared to the control *p12c*. Three 5 min pulses of red light were applied to flies during subjective nighttime (ZT18, ZT19, ZT20) for 3 days after 12:12 h LD entrainment to measure the arousal response of *p12c* (blue), *gl60j* (red), *cry-null* (green), *gl60j-cry-null* (yellow), and *rh7-null* (violet) flies for **(A)** low (10 $\mu W/cm^2$) and **(B)** high (400 $\mu W/cm^2$) light intensity. Scatter plots are grouped by average% of flies that awaken across the 3 days of light-pulse arousal experiment and separated as pulse 1 (left points for each group), pulse 2 (middle points for each group), and pulse 3 (right points for each group). Black bars indicate total average% flies that awaken across the 3 days and three pulses of light. Pairwise comparison was analyzed using two-sample *t*-test with FDR adjustment. $^{**}p < 0.05$ and $^{***}p < 0.01$.

red light sensitivity and are expressed in photoreceptor cells that either directly or indirectly input to l-LNvs (Salcedo et al., 1999; Muraro and Ceriani, 2015; Schlichting et al., 2016).

We show representative firing records for each genotype tested and for each of the four light spectra employed in this study (UV, violet, blue and red). Consistent with most earlier publications, for our recordings, we observe predominantly tonic action potential firing in l-LNv recordings (Holmes et al., 2007; Cao and Nitabach, 2008; Sheeba et al., 2008b, 2010; McCarthy et al., 2011; Seluzicki et al., 2014; Flourakis and Allada, 2015; Flourakis et al., 2015; Fogle et al., 2015; Buhl et al., 2016, 2019; Baik et al., 2017, 2019a; Li et al., 2018; Smith et al., 2019; Au et al., 2022). Burst firing as the predominant firing mode in l-LNv has been reported by another group (Muraro and Ceriani, 2015; Fernandez-Chiappe et al., 2021). It remains unclear why different groups see different firing patterns in l-LNv recordings. The baseline firing rate of l-LNvs varies by time of day (Cao and Nitabach, 2008; Sheeba et al., 2008b). Based on anatomical location of the l-LNvs embedded within the circadian neural circuit, we considered the possibility that light evoked excitation of the l-LNvs is circadian regulated. However, our experiment is not formally set up to test this hypothesis. The data set does not cover all 24 h time points, the majority of recordings were performed during daytime on an approximately 12:12 LD cycle.

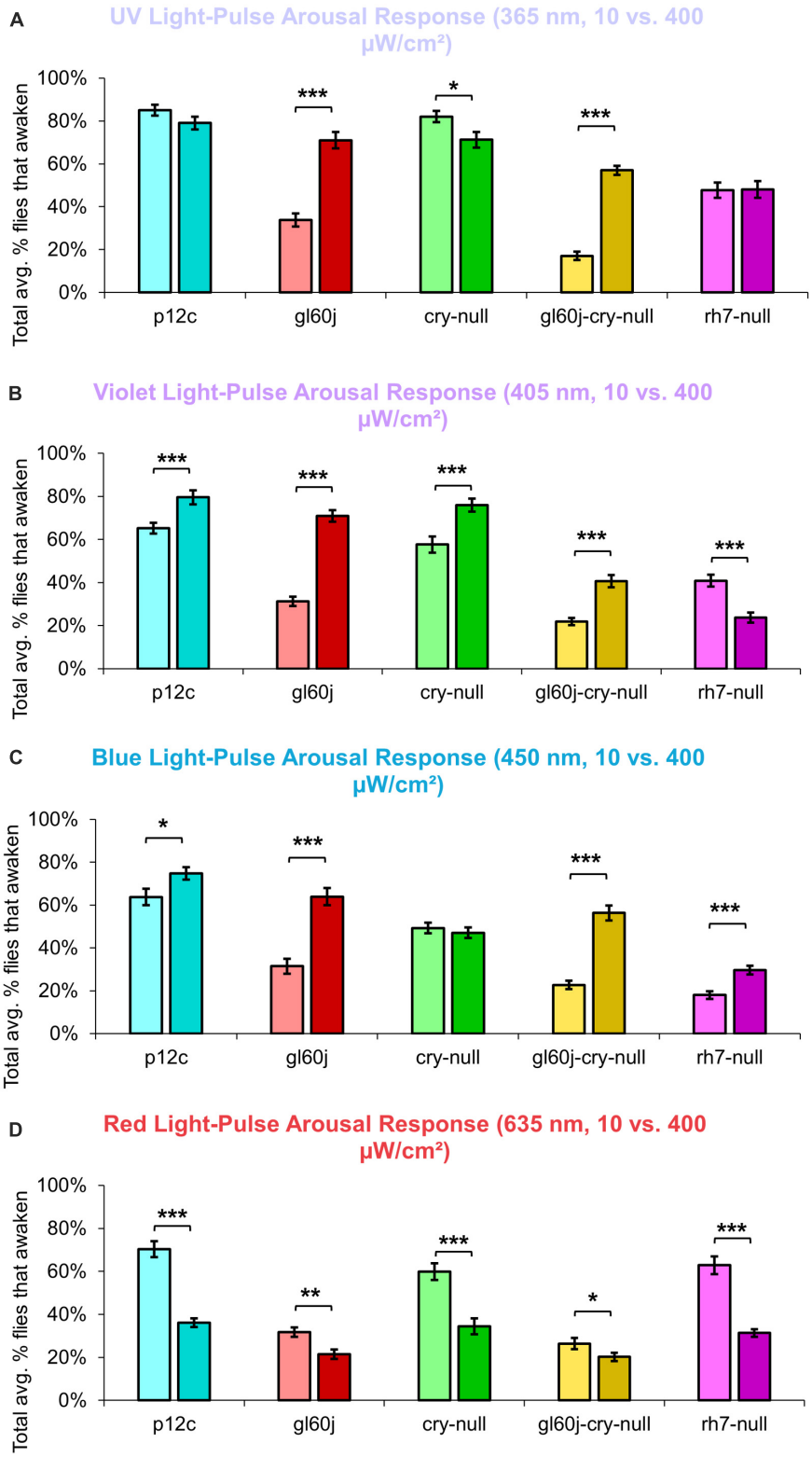

FIGURE 15
Pairwise summary comparison of light-pulse arousal between low and high intensity light. Light intensity comparison of total average% arousal response across 3 days and 3 pulses of light for *p12c* (lighter blue column, left, 10 μW/cm^2; darker blue column, right, 400 μW/cm^2), *gl60j* (light red, left, 10 μW/cm^2; dark red column, right, 400 μW/cm^2), *cry-null* (light green, left, 10 μW/cm^2; dark green column, right, 400 μW/cm^2), *gl60j-cry-null* (light yellow, left, 10 μW/cm^2; dark yellow column, right, 400 μW/cm^2), and *rh7-null* (light violet, left, 10 μW/cm^2; dark violet column, right, 400 μW/cm^2) flies for **(A)** UV, **(B)** violet, **(C)** blue, and **(D)** red light stimulus. Pairwise comparison was analyzed using two-sample *t*-test. *$p < 0.05$, **$p < 0.005$, ***$p < 0.001$.

TABLE 2 Summary of average% flies that awaken from light pulse arousal for each genotype against each color of light stimulus.

	Low intensity (10 μ W/cm^2)				High intensity (400 μ W/cm^2)			
	UV	Violet	Blue	Red	UV	Violet	Blue	Red
p12c	0.8503	0.6519	0.6375	0.7036	0.7905	0.7954	0.748	0.3611
gl60j	0.3379	0.3132	0.3147	0.317	0.7097	0.7091	0.6392	0.2145
cry-null	0.8199	0.5766	0.4928	0.5992	0.7119	0.7597	0.4706	0.3443
gl60j-cry-null	0.1705	0.2189	0.2268	0.2641	0.5701	0.4067	0.5631	0.2023
rh7-null	0.4767	0.4086	0.1794	0.6283	0.48	0.2372	0.2961	0.3132

Total average% flies that awaken from light pulse arousal responses of *p12c*, *gl60j*, *cry-null*, *gl60j-cry-null*, and *rh7-null* for UV, violet, blue, and red (365, 405, 450, and 635 nm, respectively) light stimulus. Left half of table represents the low intensity 10 μW/cm^2 light pulses, and the right half of the table represents the high intensity 400 μW/cm^2 light pulses. The green shading represents greater arousal responses, while the white shading represents smaller arousal responses.

Using this limited data set, we do not detect significant time-of-day basal firing rate differences. Our data at present does not indicate significant time-of-day effects for the l-LNv electrical light responses, but further testing is required. A previous study from another group testing this question more comprehensively shows differences in l-LNvs electrophysiological properties and their responses to light in daytime versus nighttime recordings (Buhl et al., 2016).

The l-LNvs contribute to different light regulated behaviors of the fly, including circadian behavior, light choice attraction/avoidance behavior and arousal behavior (Sheeba et al., 2008a; Yoshii et al., 2012; Fogle et al., 2015; Baik et al., 2017, 2018, Schlichting et al., 2016). CRY is the primary circadian photopigment in *Drosophila melanogaster* yet is not required to maintain light-dark entrainment, since the fly clock has been shown to directly entrain by inputs from rhodopsins in each of the external photoreceptor systems: compound eyes, HB eyelets, and ocelli (Rieger et al., 2003). Specifically, Rh1, Rh3, Rh4, and Rh6 mediate low-intensity light re-entrainment properties of the clock (Saint-Charles et al., 2016), while Rh5 mediates medium and high intensity light re-entrainment, though this may occur via a non-PLC phototransduction pathway (Szular et al., 2012; Ogueta et al., 2018). It is thought that Rh6 expressing photoreceptor cells in the eyes converge all inputs from the outer and inner receptor cells in order to mediate circadian entrainment (Schlichting et al., 2014; Ogueta et al., 2018; Alejevski et al., 2019), though the precise anatomical characterization to clock neurons from these photoreceptor cells remains elusive. However, even with the removal of CRY and NORPA, flies were observed to still respond and entrain to light, leading to the discovery of internally expressed rhodopsin 7, which was found to also contribute to small but significant changes in circadian light entrainment (Ni et al., 2017) and a "minor contribution to circadian clock synchronization" (Kistenpfennig et al., 2017).

Light choice attraction/avoidance behavior is mediated by multiple photic inputs from the eyes, CRY, and Rh7 (Zhao et al., 2003; Dolezelova et al., 2007; Yuan et al., 2007; Keene et al., 2011; Rakshit and Giebultowicz, 2013; Schlichting et al., 2016; Baik et al., 2017, 2018; Alonso San Alberto et al., 2022). Each of these photic input channels have distinct features based on light intensity, spectral composition, and light exposure time. Specifically, acute (minutes) high-intensity (400 μW/cm^2) and low-intensity (10 μW/cm^2) UV light attraction is primarily mediated by external rhodopsin photopigments while long-lasting (tens of seconds) high-intensity (400 μW/cm^2) UV light avoidance is primarily mediated by internal CRY and Rh7 photopigments.

In our present study, we provide evidence of multiple photic input integration for light arousal behavior. UV light-pulses show a significant attenuation in the arousal response of all rhodopsin-based phototransduction mutants (*gl60j*, *rh7-null*, and *gl60j-cry-null*) relative to controls for both low and high intensity lighting conditions, but not in *cry-null* mutant flies. Thus, fly arousal to UV light pulses is apparently opsin-dependent and CRY-independent. Unsurprisingly, violet light-pulses indicate the violet light-sensitive rhodopsins in the eyes and Rh7 as functional violet photosensors for violet light evoked arousal behavior. CRY appears to have a minor contribution for low-intensity violet light evoked arousal responses. Similarly, blue light evoked arousal responses depend on CRY and all rhodopsin photopigments (external and Rh7) for both low and high intensity blue light evoked arousal responses. These results suggest that functional redundancy is achieved by neutral integration of all three channels of photic input for blue light evoked arousal responses, while Rh7 activation may provide gain modulation for UV light evoked arousal responses. The average% of flies that awaken from low-intensity red light pulses is significantly attenuated relative to control with both the single knockout mutants *gl60j* and *cry-null*, as well as the double knockout mutants *gl60j-cry-null*. This finding closely matches the electrophysiological results for l-LNv electrophysiological recordings made from double knockout *gl60j-cry-null* flies. Surprisingly, with high-intensity red light pulses, the overall average% of flies that awaken are lower for all groups, and only *rh7-null* flies show significantly attenuated red light evoked arousal responses. This was a surprising observation that we believe suggests two possibilities: (1) the arousal neural circuit may have a detection threshold for red light that our 400 μW/cm^2 high-intensity red stimulus exceeds, and (2) Rh7 has the highest intensity detection threshold amongst the three photoreceptor systems, but still requires input from external rhodopsins and CRY to enable a proper red light pulse arousal response.

There is a strong relationship between circadian neuronal electrical activity and clock cycling (Nitabach et al., 2002, 2005; Nitabach, 2006). There are only a handful of publications that measure clock protein cycling at high temporal-spatial resolution (Shafer et al., 2002; Roberts et al., 2015; Nave et al., 2021), and only

a subset of those show the effects of 12:12 h light:dark cycles on the clock (Shafer et al., 2002; Nave et al., 2021). For clock driven behaviors, cryptochrome (CRY) is the primary circadian photoreceptor and mediates clock disruption by constant light, while eye light input is redundant to CRY (Helfrich-Förster et al., 2001; Nave et al., 2021). PER and TIM oscillations are highly synchronous across all major circadian neuronal subgroups in unshifted light schedules for 11 days. PER entry into the nucleus precedes TIM by about 3 h late at night (Shafer et al., 2002; Nave et al., 2021). A total of 3 h light phase delays followed several days later by 3 h light phase advances significantly dampens PER oscillator synchrony and rhythmicity in most circadian neurons during and after exposure. LNv clock protein oscillations are the first to desynchronize and the last to resynchronize following such light shifts, while the dorsal neuron group-3 (DN3s) within the circadian circuit increase their within-group synchrony in response to phase delay/phase advance light shifts. *In vivo*, alternating light shifts transiently disrupt sleep stability, and learning and memory processes, temporally coinciding with circuit desynchrony. The role of light shifts and subsequent clock circuit desynchrony is yet to be explored for other light evoked behaviors including light choice behavior and light evoked arousal.

Insect photobehaviors are evoked by many parameters of light, including intensity, spectral composition, and exposure time. Circadian photoentrainment and light attraction/avoidance behaviors function through the integration of multiple photic inputs. We provide additional evidence of a functional integration between these multiple sensory systems that converge input in l-LNvs to mediate neuronal photoexcitation and behavioral light arousal. Understanding how such complex light-evoked behaviors may allow us to target specific photoreceptor systems for more effective behavioral manipulations, which would lead a promising direction toward novel insect vector-control strategies (Grant et al., 1970; Chandler et al., 1976; Doukas and Payne, 2007).

Data availability statement

The original contributions presented in this study are included in the article/supplementary material, further inquiries can be directed to the corresponding author.

Author contributions

DA and TH designed the research, wrote, reviewed, and edited the manuscript. DA, JL, SP, MD, AF, and TN performed the research and analyzed the data. All authors contributed to the article and approved the submitted version.

Funding

This study was funded by the NIH National Institute of General Medical Sciences grants R35 GM127102 (TH) and F31 GM140592 (DA).

Acknowledgments

We thank the Francesco Tombola, Kevin Beier, and Brian Zoltowski for helpful discussions; Lisa Baik, Amita Seghal, Patrick Emery, and Craig Montell for research support; Parrish Powell for lab managerial support; and Janita Parpana, Lillian Li, Consuelo Barajas, Duke Park, and Terri Warren for administrative support.

Conflict of interest

The authors declare that the research was conducted in the absence of any commercial or financial relationships that could be construed as a potential conflict of interest.

Publisher's note

All claims expressed in this article are solely those of the authors and do not necessarily represent those of their affiliated organizations, or those of the publisher, the editors and the reviewers. Any product that may be evaluated in this article, or claim that may be made by its manufacturer, is not guaranteed or endorsed by the publisher.

References

Alejevski, F., Saint-Charles, A., Michard-Vanhée, C., Martin, B., Galant, S., Vasiliauskas, D., et al. (2019). The HisCl1 histamine receptor acts in photoreceptors to synchronize *Drosophila* behavioral rhythms with light-dark cycles. *Nat. Commun.* 10:252. doi: 10.1038/s41467-018-08116-7

Alonso San Alberto, D., Rusch, C., Zhan, Y., Straw, A. D., Montell, C., and Riffell, J. A. (2022). The olfactory gating of visual preferences to human skin and visible spectra in mosquitoes. *Nat. Commun.* 13:555. doi: 10.1038/s41467-022-28195-x

Au, D. D., Foden, A. J., Park, S. J., Nguyen, T. H., Liu, J. C., Tran, M. D., et al. (2022). Mosquito cryptochromes expressed in *Drosophila* confer species-specific behavioral light responses. *Curr. Biol.* 32, 3731–3744.e4. doi: 10.1016/j.cub.2022.07.021

Bachleitner, W., Kempinger, L., Wülbeck, C., Rieger, D., and Helfrich-Förster, C. (2007). Moonlight shifts the endogenous clock of *Drosophila melanogaster*. *Proc. Natl. Acad. Sci. U.S.A.* 104, 3538–3543. doi: 10.1073/pnas.0606870104

Baik, L. S., Recinos, Y., Chevez, J. A., Au, D. D., and Holmes, T. C. (2019b). Multiple phototransduction inputs integrate to mediate UV light-evoked avoidance/attraction behavior in *Drosophila*. *J. Biol. Rhythms* 34, 391–400. doi: 10.1177/0748730419847339

Baik, L. S., Au, D. D., Nave, C., Foden, A. J., Enrriquez-Villalva, W. K., and Holmes, T. C. (2019a). Distinct mechanisms of *Drosophila* CRYPTOCHROME-mediated light-evoked membrane depolarization and in vivo clock resetting. *Proc. Natl. Acad. Sci. U.S.A.* 116, 23339–23344. doi: 10.1073/pnas.1905023116

Baik, L. S., Fogle, K. J., Roberts, L., Galschiodt, A. M., Chevez, J. A., Recinos, Y., et al. (2017). CRYPTOCHROME mediates behavioral executive choice in response to UV light. *Proc. Natl. Acad. Sci. U.S.A.* 114, 776–781. doi: 10.1073/pnas.1607989114

Baik, L. S., Recinos, Y., Chevez, J. A., and Holmes, T. C. (2018). Circadian modulation of light-evoked avoidance/attraction behavior in *Drosophila*. *PLoS One* 13:e0201927. doi: 10.1371/journal.pone.0201927

Behnia, R., and Desplan, C. (2015). Visual circuits in flies: Beginning to see the whole picture. *Curr. Opin. Neurobiol.* 34, 125–132. doi: 10.1016/j.conb.2015.03.010

Benito, J., Houl, J. H., Roman, G. W., and Hardin, P. E. (2008). The blue-light photoreceptor CRYPTOCHROME is expressed in a subset of circadian oscillator neurons in the *Drosophila* CNS. *J. Biol. Rhythms* 23, 296–307. doi: 10.1177/0748730408318588

Benjamini, Y., and Hochberg, Y. (1995). Controlling the false discovery rate: A practical and powerful approach to multiple testing. *J. R. Stat. Soc. Ser. B Methodol.* 57, 289–300. doi: 10.1111/j.2517-6161.1995.tb02031.x

Berndt, A., Kottke, T., Breitkreuz, H., Dvorsky, R., Hennig, S., Alexander, M., et al. (2007). A novel photoreaction mechanism for the circadian blue light photoreceptor drosophila cryptochrome. *J. Biol. Chem.* 282, 13011–13021. doi: 10.1074/jbc.M608872200

Boothroyd, C. E., Wijnen, H., Naef, F., Saez, L., and Young, M. W. (2007). Integration of light and temperature in the regulation of circadian gene expression in *Drosophila*. *PLoS Genet.* 3:e54. doi: 10.1371/journal.pgen.0030054

Bouly, J.-P., Schleicher, E., Dionisio-Sese, M., Vandenbussche, F., Van Der Straeten, D., Bakrim, N., et al. (2007). Cryptochrome blue light photoreceptors are activated through interconversion of flavin redox states. *J. Biol. Chem.* 282, 9383–9391. doi: 10.1074/jbc.M609842200

Breda, C., Rosato, E., and Kyriacou, C. P. (2020). Norpa signalling and the seasonal circadian locomotor phenotype in *Drosophila*. *Biology* 9:130. doi: 10.3390/biology9060130

Buhl, E., Bradlaugh, A., Ogueta, M., Chen, K.-F., Stanewsky, R., and Hodge, J. J. (2016). Quasimodo mediates daily and acute light effects on *Drosophila* clock neuron excitability. *Proc. Natl. Acad. Sci. U.S.A.* 113, 13486–13491. doi: 10.1073/pnas.1606547113

Buhl, E., Higham, J. P., and Hodge, J. J. L. (2019). Alzheimer's disease-associated tau alters *Drosophila* circadian activity, sleep and clock neuron electrophysiology. *Neurobiol. Dis.* 130:104507. doi: 10.1016/j.nbd.2019.104507

Cao, G., and Nitabach, M. N. (2008). Circadian control of membrane excitability in *Drosophila* melanogaster lateral ventral clock neurons. *J. Neurosci.* 28, 6493–6501. doi: 10.1523/JNEUROSCI.1503-08.2008

Ceriani, M. F., Darlington, T. K., Staknis, D., Más, P., Petti, A. A., Weitz, C. J., et al. (1999). Light-dependent sequestration of TIMELESS by CRYPTOCHROME. *Science* 285, 553–556. doi: 10.1126/science.285.5427.553

Chandler, J. A., Hill, M. N., and Highton, R. B. (1976). The use of light traps for long-term surveillance of mosquitoes of epidemiological importance on the Kano Plain, Kenya. *East Afr. Med. J.* 53, 596–600.

Chatterjee, A., Lamaze, A., De, J., Mena, W., Chélot, E., Martin, B., et al. (2018). Reconfiguration of a multi-oscillator network by light in the *Drosophila* circadian clock. *Curr. Biol.* 28, 2007–2017.e4. doi: 10.1016/j.cub.2018.04.064

Chaturvedi, R., Stork, T., Yuan, C., Freeman, M. R., and Emery, P. (2022). Astrocytic GABA transporter controls sleep by modulating GABAergic signaling in *Drosophila* circadian neurons. *Curr. Biol.* 32, 1895–1908.e5. doi: 10.1016/j.cub.2022.02.066

Chen, W.-F., Majercak, J., and Edery, I. (2006). Clock-gated photic stimulation of timeless expression at cold temperatures and seasonal adaptation in *Drosophila*. *J. Biol. Rhythms* 21, 256–271. doi: 10.1177/0748730406289306

Chung, B. Y., Kilman, V. L., Keath, J. R., Pitman, J. L., and Allada, R. (2009). The GABAA receptor RDL acts in peptidergic PDF neurons to promote sleep in *Drosophila*. *Curr. Biol.* 19, 386–390. doi: 10.1016/j.cub.2009.01.040

Cusumano, P., Klarsfeld, A., Chélot, E., Picot, M., Richier, B., and Rouyer, F. (2009). PDF-modulated visual inputs and cryptochrome define diurnal behavior in *Drosophila*. *Nat. Neurosci.* 12, 1431–1437. doi: 10.1038/nn.2429

Czarna, A., Berndt, A., Singh, H. R., Grudziecki, A., Ladurner, A. G., Timinszky, G., et al. (2013). Structures of *Drosophila* cryptochrome and mouse cryptochrome1 provide insight into circadian function. *Cell* 153, 1394–1405. doi: 10.1016/j.cell.2013.05.011

Dolezelova, E., Dolezel, D., and Hall, J. C. (2007). Rhythm defects caused by newly engineered null mutations in *Drosophila*'s *cryptochrome* Gene. *Genetics* 177, 329–345. doi: 10.1534/genetics.107.076513

Doukas, D., and Payne, C. C. (2007). The use of ultraviolet-blocking films in insect pest management in the UK; effects on naturally occurring arthropod pest and natural enemy populations in a protected cucumber crop. *Ann. Appl. Biol.* 151, 221–231. doi: 10.1111/j.1744-7348.2007.00169.x

Eck, S., Helfrich-Förster, C., and Rieger, D. (2016). The timed depolarization of morning and evening oscillators phase shifts the circadian clock of *Drosophila*. *J. Biol. Rhythms* 31, 428–442. doi: 10.1177/0748730416651363

Emery, P., So, W. V., Kaneko, M., Hall, J. C., and Rosbash, M. (1998). CRY, a *Drosophila* clock and light-regulated cryptochrome, is a major contributor to circadian rhythm resetting and photosensitivity. *Cell* 95, 669–679. doi: 10.1016/S0092-8674(00)81637-2

Emery, P., Stanewsky, R., Helfrich-Förster, C., Emery-Le, M., Hall, J. C., and Rosbash, M. (2000). *Drosophila* CRY is a deep brain circadian photoreceptor. *Neuron* 26, 493–504. doi: 10.1016/S0896-6273(00)81181-2

Feiler, R., Bjornson, R., Kirschfeld, K., Mismer, D., Rubin, G., Smith, D., et al. (1992). Ectopic expression of ultraviolet-rhodopsins in the blue photoreceptor cells of *Drosophila*: Visual physiology and photochemistry of transgenic animals. *J. Neurosci.* 12, 3862–3868. doi: 10.1523/JNEUROSCI.12-10-03862.1992

Fernandez-Chiappe, F., Frenkel, L., Colque, C. C., Ricciuti, A., Hahm, B., Cerredo, K., et al. (2021). High-frequency neuronal bursting is essential for circadian and sleep behaviors in *Drosophila*. *J. Neurosci.* 41, 689–710. doi: 10.1523/JNEUROSCI.2322-20.2020

Flourakis, M., and Allada, R. (2015). "Patch-clamp electrophysiology in *Drosophila* circadian pacemaker neurons," in *Methods in Enzymology*, ed. A. Sehgal (Amsterdam: Elsevier), 23–44. doi: 10.1016/bs.mie.2014.10.005

Flourakis, M., Kula-Eversole, E., Hutchison, A. L., Han, T. H., Aranda, K., Moose, D. L., et al. (2015). A conserved bicycle model for circadian clock control of membrane excitability. *Cell* 162, 836–848. doi: 10.1016/j.cell.2015.07.036

Fogle, K. J., Baik, L. S., Houl, J. H., Tran, T. T., Roberts, L., Dahm, N. A., et al. (2015). CRYPTOCHROME-mediated phototransduction by modulation of the potassium ion channel β-subunit redox sensor. *Proc. Natl. Acad. Sci. U.S.A.* 112, 2245–2250. doi: 10.1073/pnas.1416586112

Fogle, K. J., Parson, K. G., Dahm, N. A., and Holmes, T. C. (2011). CRYPTOCHROME is a blue-light sensor that regulates neuronal firing rate. *Science* 331, 1409–1413. doi: 10.1126/science.1199702

Gao, S., Takemura, S., Ting, C.-Y., Huang, S., Lu, Z., Luan, H., et al. (2008). The neural substrate of spectral preference in *Drosophila*. *Neuron* 60, 328–342. doi: 10.1016/j.neuron.2008.08.010

Grant, G. G., Carmichael, A. G., Smith, C. N., and Brown, A. W. A. (1970). Autochemosterilization of the southern house mosquito by means of a modified light trap. *J. Econ. Entomol.* 63, 648–650. doi: 10.1093/jee/63.2.648

Green, E. W., O'Callaghan, E. K., Hansen, C. N., Bastianello, S., Bhutani, S., Vanin, S., et al. (2015). *Drosophila* circadian rhythms in seminatural environments: Summer afternoon component is not an artifact and requires TrpA1 channels. *Proc. Natl. Acad. Sci. U.S.A.* 112, 8702–8707. doi: 10.1073/pnas.1506093112

Gu, H., and O'Dowd, D. K. (2006). Cholinergic synaptic transmission in adult *Drosophila* kenyon cells *in situ*. *J. Neurosci.* 26, 265–272. doi: 10.1523/JNEUROSCI.4109-05.2006

Guo, F., Cerullo, I., Chen, X., and Rosbash, M. (2014). PDF neuron firing phase-shifts key circadian activity neurons in *Drosophila*. *Elife* 3:e02780. doi: 10.7554/eLife.02780

Heisenberg, M., and Buchner, E. (1977). The role of retinula cell types in visual behavior of *Drosophila* melanogaster. *J. Comp. Physiol. A* 117, 127–162. doi: 10.1007/BF00612784

Helfrich-Förster, C. (2020). Light input pathways to the circadian clock of insects with an emphasis on the fruit fly *Drosophila* melanogaster. *J. Comp. Physiol. A* 206, 259–272. doi: 10.1007/s00359-019-01379-5

Helfrich-Förster, C., Edwards, T., Yasuyama, K., Wisotzki, B., Schneuwly, S., Stanewsky, R., et al. (2002). The extraretinal eyelet of *Drosophila*: Development, ultrastructure, and putative circadian function. *J. Neurosci.* 22, 9255–9266. doi: 10.1523/JNEUROSCI.22-21-09255.2002

Helfrich-Förster, C., Winter, C., Hofbauer, A., Hall, J. C., and Stanewsky, R. (2001). The circadian clock of fruit flies is blind after elimination of all known photoreceptors. *Neuron* 30, 249–261. doi: 10.1016/S0896-6273(01)00277-X

Helfrich-Förster, C., Yoshii, T., Wülbeck, C., Grieshaber, E., Rieger, D., Bachleitner, W., et al. (2007). The lateral and dorsal neurons of *Drosophila melanogaster*: New insights about their morphology and function. *Cold Spring Harb. Symp. Quant. Biol.* 72, 517–525. doi: 10.1101/sqb.2007.72.063

Hoang, N., Schleicher, E., Kacprzak, S., Bouly, J.-P., Picot, M., Wu, W., et al. (2008). Human and *Drosophila* cryptochromes are light activated by flavin photoreduction in living cells. *PLoS Biol.* 6:e160. doi: 10.1371/journal.pbio.0060160

Holmes, T., Sheeba, V., Mizrak, D., Rubovszky, B., and Dahdal, D. (2007). "Circuit-breaking and behavioral analysis by molecular genetic manipulation of neural activity in *Drosophila*," in *Invertebrate Neurobiology*, eds G. North and R. Greenspan (Cold Spring Harbor, NY: Cold Spring Harbor Laboratory Press), 49, 19–52.

Keene, A. C., Mazzoni, E. O., Zhen, J., Younger, M. A., Yamaguchi, S., Blau, J., et al. (2011). Distinct visual pathways mediate *Drosophila* larval light avoidance and circadian clock entrainment. *J. Neurosci.* 31, 6527–6534. doi: 10.1523/JNEUROSCI.6165-10.2011

Kilman, V. L., Zhang, L., Meissner, R.-A., Burg, E., and Allada, R. (2009). Perturbing dynamin reveals potent effects on the *Drosophila* circadian clock. *PLoS One* 4:e5235. doi: 10.1371/journal.pone.0005235

Kirschfeld, K., Feiler, R., and Franceschini, N. (1978). A photostable pigment within the rhabdomere of fly photoreceptors no. 7. *J. Comp. Physiol. A* 125, 275–284. doi: 10.1007/BF00656606

Kirschfeld, K., Franceschini, N., and Minke, B. (1977). Evidence for a sensitising pigment in fly photoreceptors. *Nature* 269, 386–390. doi: 10.1038/269386a0

Kistenpfennig, C., Grebler, R., Ogueta, M., Hermann-Luibl, C., Schlichting, M., Stanewsky, R., et al. (2017). A new rhodopsin influences light-dependent daily activity patterns of fruit flies. *J. Biol. Rhythms* 32, 406–422. doi: 10.1177/0748730417721826

Kistenpfennig, C., Hirsh, J., Yoshii, T., and Helfrich-Förster, C. (2012). Phase-shifting the fruit fly clock without cryptochrome. *J. Biol. Rhythms* 27, 117–125. doi: 10.1177/0748730411434390

Klarsfeld, A. (2004). Novel features of cryptochrome-mediated photoreception in the brain circadian clock of *Drosophila*. *J. Neurosci.* 24, 1468–1477. doi: 10.1523/JNEUROSCI.3661-03.2004

Koh, K., Zheng, X., and Sehgal, A. (2006). JETLAG resets the *Drosophila* circadian clock by promoting light-induced degradation of TIMELESS. *Science* 312, 1809–1812. doi: 10.1126/science.1124951

Kumar, S., Chen, D., and Sehgal, A. (2012). Dopamine acts through cryptochrome to promote acute arousal in *Drosophila*. *Genes Dev.* 26, 1224–1234. doi: 10.1101/gad.186338.111

Lazopulo, S., Lazopulo, A., Baker, J. D., and Syed, S. (2019). Daytime colour preference in *Drosophila* depends on the circadian clock and TRP channels. *Nature* 574, 108–111. doi: 10.1038/s41586-019-1571-y

Levy, C., Zoltowski, B. D., Jones, A. R., Vaidya, A. T., Top, D., Widom, J., et al. (2013). Updated structure of *Drosophila* cryptochrome. *Nature* 495, E3–E4. doi: 10.1038/nature11995

Li, M.-T., Cao, L.-H., Xiao, N., Tang, M., Deng, B., Yang, T., et al. (2018). Hub-organized parallel circuits of central circadian pacemaker neurons for visual photoentrainment in *Drosophila*. *Nat. Commun.* 9:4247. doi: 10.1038/s41467-018-06506-5

Lin, C., Top, D., Manahan, C. C., Young, M. W., and Crane, B. R. (2018). Circadian clock activity of cryptochrome relies on tryptophan-mediated photoreduction. *Proc. Natl. Acad. Sci. U.S.A.* 115, 3822–3827. doi: 10.1073/pnas.1719376115

Liu, S., Lamaze, A., Liu, Q., Tabuchi, M., Yang, Y., Fowler, M., et al. (2014). WIDE AWAKE mediates the circadian timing of sleep onset. *Neuron* 82, 151–166. doi: 10.1016/j.neuron.2014.01.040

Majercak, J., Sidote, D., Hardin, P. E., and Edery, I. (1999). How a circadian clock adapts to seasonal decreases in temperature and day length. *Neuron* 24, 219–230. doi: 10.1016/S0896-6273(00)80834-X

Malpel, S., Klarsfeld, A., and Rouyer, F. (2002). Larval optic nerve and adult extra-retinal photoreceptors sequentially associate with clock neurons during *Drosophila* brain development. *Development* 129, 1443–1453. doi: 10.1242/dev.129.6.1443

McCarthy, E. V., Wu, Y., Decarvalho, T., Brandt, C., Cao, G., and Nitabach, M. N. (2011). Synchronized bilateral synaptic inputs to *Drosophila* melanogaster neuropeptidergic rest/arousal neurons. *J. Neurosci.* 31, 8181–8193. doi: 10.1523/JNEUROSCI.2017-10.2011

Miller, G. V., Hansen, K. N., and Stark, W. S. (1981). Phototaxis in *Drosophila*: R1–6 input and interaction among ocellar and compound eye receptors. *J. Insect Physiol.* 27, 813–819. doi: 10.1016/0022-1910(81)90073-1

Muraro, N. I., and Ceriani, M. F. (2015). Acetylcholine from visual circuits modulates the activity of arousal neurons in *Drosophila*. *J. Neurosci.* 35, 16315–16327. doi: 10.1523/JNEUROSCI.1571-15.2015

Nave, C., Roberts, L., Hwu, P., Estrella, J. D., Vo, T. C., Nguyen, T. H., et al. (2021). Weekend light shifts evoke persistent *Drosophila* circadian neural network desynchrony. *J. Neurosci.* 41, 5173–5189. doi: 10.1523/JNEUROSCI.3074-19.2021

Ni, J. D., Baik, L. S., Holmes, T. C., and Montell, C. (2017). A rhodopsin in the brain functions in circadian photoentrainment in *Drosophila*. *Nature* 545, 340–344. doi: 10.1038/nature22325

Nitabach, M. N. (2006). Electrical hyperexcitation of lateral ventral pacemaker neurons desynchronizes downstream circadian oscillators in the fly circadian circuit and induces multiple behavioral periods. *J. Neurosci.* 26, 479–489. doi: 10.1523/JNEUROSCI.3915-05.2006

Nitabach, M. N., Holmes, T. C., and Blau, J. (2005). Membranes, ions, and clocks: Testing the Njus–Sulzman–Hastings model of the circadian oscillator. *Methods Enzymol.* 393, 682–693. doi: 10.1016/S0076-6879(05)93036-X

Nitabach, M. N., Llamas, D. A., Thompson, I. J., Collins, K. A., and Holmes, T. C., (2002). Phosphorylation-dependent and phosphorylation-independent modes of modulation of shaker family voltage-gated potassium channels by SRC family protein tyrosine kinases. *J. Neurosci.* 22, 7913–7922. doi: 10.1523/JNEUROSCI.22-18-07913.2002

Ogueta, M., Hardie, R. C., and Stanewsky, R. (2018). Non-canonical phototransduction mediates synchronization of the *Drosophila* melanogaster circadian clock and retinal light responses. *Curr. Biol.* 28, 1725–1735.e3. doi: 10.1016/j.cub.2018.04.016

Pan, Y., Weng, J., Cao, Y., Bhosle, R. C., and Zhou, M. (2008). Functional Coupling between the Kv1.1 Channel and Aldoketoreductase Kvβ1. *J. Biol. Chem.* 283, 8634–8642. doi: 10.1074/jbc.M709304200

Parisky, K. M., Agosto, J., Pulver, S. R., Shang, Y., Kuklin, E., Hodge, J. J. L., et al. (2008). PDF cells are a GABA-responsive wake-promoting component of the *Drosophila* sleep circuit. *Neuron* 60, 672–682. doi: 10.1016/j.neuron.2008.10.042

Peschel, N., Chen, K. F., Szabo, G., and Stanewsky, R. (2009). Light-dependent interactions between the *Drosophila* circadian clock factors cryptochrome, jetlag, and timeless. *Curr. Biol.* 19, 241–247. doi: 10.1016/j.cub.2008.12.042

Picot, M., Cusumano, P., Klarsfeld, A., Ueda, R., and Rouyer, F. (2007). Light activates output from evening neurons and inhibits output from morning neurons in the *Drosophila* circadian clock. *PLoS Biol.* 5:e315. doi: 10.1371/journal.pbio.0050315

Potdar, S., and Sheeba, V. (2018). Wakefulness is promoted during day time by PDFR signalling to dopaminergic neurons in *Drosophila* melanogaster. *eNeuro* 5, ENEURO.129-18.2018. doi: 10.1523/ENEURO.0129-18.2018

Rakshit, K., and Giebultowicz, J. M. (2013). Cryptochrome restores dampened circadian rhythms and promotes healthspan in aging *Drosophila*. *Aging Cell* 12, 752–762. doi: 10.1111/acel.12100

Rieger, D., Stanewsky, R., and Helfrich-Förster, C. (2003). Cryptochrome, compound eyes, hofbauer-buchner eyelets, and ocelli play different roles in the entrainment and masking pathway of the locomotor activity rhythm in the fruit fly *Drosophila* melanogaster. *J. Biol. Rhythms* 18, 377–391. doi: 10.1177/0748730403256997

Roberts, L., Leise, T. L., Noguchi, T., Galschiodt, A. M., Houl, J. H., Welsh, D. K., et al. (2015). Light evokes rapid circadian network oscillator desynchrony followed by gradual phase retuning of synchrony. *Curr. Biol.* 25, 858–867. doi: 10.1016/j.cub.2015.01.056

Saint-Charles, A., Michard-Vanhée, C., Alejevski, F., Chélot, E., Boivin, A., and Rouyer, F. (2016). Four of the six *Drosophila* rhodopsin-expressing photoreceptors can mediate circadian entrainment in low light: Rhodopsin-dependent clock synchronization. *J. Comp. Neurol.* 524, 2828–2844. doi: 10.1002/cne.23994

Sakai, K., Tsutsui, K., Yamashita, T., Iwabe, N., Takahashi, K., Wada, A., et al. (2017). *Drosophila* melanogaster rhodopsin Rh7 is a UV-to-visible light sensor with an extraordinarily broad absorption spectrum. *Sci. Rep.* 7:7349. doi: 10.1038/s41598-017-07461-9

Salcedo, E., Huber, A., Henrich, S., Chadwell, L. V., Chou, W.-H., Paulsen, R., et al. (1999). Blue- and green-absorbing visual pigments of *Drosophila*: Ectopic expression and physiological characterization of the R8 photoreceptor cell-specific Rh5 and Rh6 rhodopsins. *J. Neurosci.* 19, 10716–10726. doi: 10.1523/JNEUROSCI.19-24-10716.1999

Schlichting, M., Grebler, R., Peschel, N., Yoshii, T., and Helfrich-Förster, C. (2014). Moonlight detection by *Drosophila* 's endogenous clock depends on multiple photopigments in the compound eyes. *J. Biol. Rhythms* 29, 75–86. doi: 10.1177/0748730413520428

Schlichting, M., Menegazzi, P., and Helfrich-Förster, C. (2015). Normal vision can compensate for the loss of the circadian clock. *Proc. R. Soc. B Biol. Sci.* 282:20151846. doi: 10.1098/rspb.2015.1846

Schlichting, M., Menegazzi, P., Lelito, K. R., Yao, Z., Buhl, E., Dalla Benetta, E., et al. (2016). A neural network underlying circadian entrainment and photoperiodic adjustment of sleep and activity in *Drosophila*. *J. Neurosci.* 36, 9084–9096. doi: 10.1523/JNEUROSCI.0992-16.2016

Seluzicki, A., Flourakis, M., Kula-Eversole, E., Zhang, L., Kilman, V., and Allada, R. (2014). Dual PDF signaling pathways reset clocks via TIMELESS and acutely excite target neurons to control circadian behavior. *PLoS Biol.* 12:e1001810. doi: 10.1371/journal.pbio.1001810

Senthilan, P. R., Grebler, R., Reinhard, N., Rieger, D., and Helfrich-Förster, C. (2019). Role of rhodopsins as circadian photoreceptors in the *Drosophila* melanogaster. *Biology* 8:6. doi: 10.3390/biology8010006

Shafer, O. T., Rosbash, M., and Truman, J. W. (2002). Sequential nuclear accumulation of the clock proteins period and timeless in the pacemaker neurons of *Drosophila* melanogaster. *J. Neurosci.* 22, 5946–5954. doi: 10.1523/JNEUROSCI.22-14-05946.2002

Shang, Y., Griffith, L. C., and Rosbash, M. (2008). Light-arousal and circadian photoreception circuits intersect at the large PDF cells of the *Drosophila* brain. *Proc. Natl. Acad. Sci. U.S.A.* 105, 19587–19594. doi: 10.1073/pnas.0809577105

Sharkey, C. R., Blanco, J., Leibowitz, M. M., Pinto-Benito, D., and Wardill, T. J. (2020). The spectral sensitivity of *Drosophila* photoreceptors. *Sci. Rep.* 10:18242. doi: 10.1038/s41598-020-74742-1

Sheeba, V., Fogle, K. J., and Holmes, T. C. (2010). Persistence of morning anticipation behavior and high amplitude morning startle response following functional loss of small ventral lateral neurons in *Drosophila*. *PLoS One* 5:e11628. doi: 10.1371/journal.pone.0011628

Sheeba, V., Fogle, K. J., Kaneko, M., Rashid, S., Chou, Y.-T., Sharma, V. K., et al. (2008a). Large ventral lateral neurons modulate arousal and sleep in *Drosophila*. *Curr. Biol.* 18, 1537–1545. doi: 10.1016/j.cub.2008.08.033

Sheeba, V., Gu, H., Sharma, V. K., O'Dowd, D. K., and Holmes, T. C. (2008b). Circadian- and light-dependent regulation of resting membrane potential and spontaneous action potential firing of *Drosophila* circadian pacemaker neurons. *J. Neurophysiol.* 99, 976–988. doi: 10.1152/jn.00930.2007

Smith, P., Buhl, E., Tsaneva-Atanasova, K., and Hodge, J. J. L. (2019). Shaw and Shal voltage-gated potassium channels mediate circadian changes in *Drosophila* clock neuron excitability. *J. Physiol.* 597, 5707–5722. doi: 10.1113/JP278826

Stanewsky, R., Kaneko, M., Emery, P., Beretta, B., Wager-Smith, K., Kay, S. A., et al. (1998). The cryb mutation identifies cryptochrome as a circadian photoreceptor in *Drosophila*. *Cell* 95, 681–692. doi: 10.1016/S0092-8674(00)81638-4

Stoleru, D., Nawathean, P., Fernández, M. P., Menet, J. S., Ceriani, M. F., and Rosbash, M. (2007). The *Drosophila* circadian network is a seasonal timer. *Cell* 129, 207–219. doi: 10.1016/j.cell.2007.02.038

Szular, J., Sehadova, H., Gentile, C., Szabo, G., Chou, W.-H., Britt, S. G., et al. (2012). *Rhodopsin 5* – and *Rhodopsin 6* –mediated clock synchronization in *Drosophila melanogaster* is independent of retinal phospholipase C-β signaling. *J. Biol. Rhythms* 27, 25–36. doi: 10.1177/0748730411431673

Vaidya, A. T., Top, D., Manahan, C. C., Tokuda, J. M., Zhang, S., Pollack, L., et al. (2013). Flavin reduction activates *Drosophila* cryptochrome. *Proc. Natl. Acad. Sci. U.S.A.* 110, 20455–20460. doi: 10.1073/pnas.1313336110

Vanin, S., Bhutani, S., Montelli, S., Menegazzi, P., Green, E. W., Pegoraro, M., et al. (2012). Unexpected features of *Drosophila* circadian behavioural rhythms under natural conditions. *Nature* 484, 371–375. doi: 10.1038/nature10991

Veleri, S., Rieger, D., Helfrich-Förster, C., and Stanewsky, R. (2007). Hofbauer-Buchner eyelet affects circadian photosensitivity and coordinates TIM and PER expression in *Drosophila* clock neurons. *J. Biol. Rhythms* 22, 29–42. doi: 10.1177/0748730406295754

Weng, J., Cao, Y., Moss, N., and Zhou, M. (2006). Modulation of voltage-dependent shaker family potassium channels by an aldo-keto reductase. *J. Biol. Chem.* 281, 15194–15200. doi: 10.1074/jbc.M513809200

Yamaguchi, S., Desplan, C., and Heisenberg, M. (2010). Contribution of photoreceptor subtypes to spectral wavelength preference in *Drosophila*. *Proc. Natl. Acad. Sci. U.S.A.* 107, 5634–5639. doi: 10.1073/pnas.0809398107

Yoshii, T., Hermann-Luibl, C., and Helfrich-Förster, C. (2016). Circadian light-input pathways in *Drosophila*. *Commun. Integr. Biol.* 9:e1102805. doi: 10.1080/19420889.2015.1102805

Yoshii, T., Rieger, D., and Helfrich-Förster, C. (2012). Two clocks in the brain: an update of the morning and evening oscillator model in *Drosophila*. *Prog. Brain Res.* 199, 59–82. doi: 10.1016/B978-0-444-59427-3.00027-7

Yoshii, T., Todo, T., Wülbeck, C., Stanewsky, R., and Helfrich-Förster, C. (2008). Cryptochrome is present in the compound eyes and a subset of *Drosophila*'s clock neurons. *J. Comp. Neurol.* 508, 952–966. doi: 10.1002/cne.21702

Yoshii, T., Wulbeck, C., Sehadova, H., Veleri, S., Bichler, D., Stanewsky, R., et al. (2009). The neuropeptide pigment-dispersing factor adjusts period and phase of *Drosophila*'s clock. *J. Neurosci.* 29, 2597–2610. doi: 10.1523/JNEUROSCI.5439-08.2009

Yuan, Q., Metterville, D., Briscoe, A. D., and Reppert, S. M. (2007). Insect cryptochromes: Gene duplication and loss define diverse ways to construct insect circadian clocks. *Mol. Biol. Evol.* 24, 948–955. doi: 10.1093/molbev/msm011

Zhao, J., Kilman, V. L., Keegan, K. P., Peng, Y., Emery, P., Rosbash, M., et al. (2003). *Drosophila* clock can generate ectopic circadian clocks. *Cell* 113, 755–766. doi: 10.1016/S0092-8674(03)00400-8

Zoltowski, B. D., Vaidya, A. T., Top, D., Widom, J., Young, M. W., and Crane, B. R. (2011). Structure of full-length *Drosophila* cryptochrome. *Nature* 480, 396–399. doi: 10.1038/nature10618

frontiers | Frontiers in Neuroscience

TYPE Original Research
PUBLISHED 22 May 2023
DOI 10.3389/fnins.2023.1154549

OPEN ACCESS

EDITED BY
Krista Todd,
Westminster College, United States

REVIEWED BY
Dawn M. Blitz,
Miami University, United States
Gennady Cymbalyuk,
Georgia State University, United States

*CORRESPONDENCE
Astrid A. Prinz
✉ astrid.prinz@emory.edu
Stefan R. Pulver
✉ sp96@st-andrews.ac.uk

†These authors have contributed equally to this work

RECEIVED 31 January 2023
ACCEPTED 21 April 2023
PUBLISHED 22 May 2023

CITATION
Megwa OF, Pascual LM, Günay C, Pulver SR and Prinz AA (2023) Temporal dynamics of Na/K pump mediated memory traces: insights from conductance-based models of *Drosophila* neurons.
Front. Neurosci. 17:1154549.
doi: 10.3389/fnins.2023.1154549

Temporal dynamics of Na/K pump mediated memory traces: insights from conductance-based models of *Drosophila* neurons

Obinna F. Megwa[1], Leila May Pascual[1], Cengiz Günay[2], Stefan R. Pulver[3]*† and Astrid A. Prinz[1]*†

[1]Department of Biology, Emory University, Atlanta, GA, United States, [2]School of Science and Technology, Georgia Gwinnett College, Lawrenceville, GA, United States, [3]School of Psychology and Neuroscience, University of St Andrews, St Andrews, United Kingdom

Sodium potassium ATPases (Na/K pumps) mediate long-lasting, dynamic cellular memories that can last tens of seconds. The mechanisms controlling the dynamics of this type of cellular memory are not well understood and can be counterintuitive. Here, we use computational modeling to examine how Na/K pumps and the ion concentration dynamics they influence shape cellular excitability. In a *Drosophila* larval motor neuron model, we incorporate a Na/K pump, a dynamic intracellular Na^+ concentration, and a dynamic Na^+ reversal potential. We probe neuronal excitability with a variety of stimuli, including step currents, ramp currents, and zap currents, then monitor the sub- and suprathreshold voltage responses on a range of time scales. We find that the interactions of a Na^+-dependent pump current with a dynamic Na^+ concentration and reversal potential endow the neuron with rich response properties that are absent when the role of the pump is reduced to the maintenance of constant ion concentration gradients. In particular, these dynamic pump-Na^+ interactions contribute to spike rate adaptation and result in long-lasting excitability changes after spiking and even after sub-threshold voltage fluctuations on multiple time scales. We further show that modulation of pump properties can profoundly alter a neuron's spontaneous activity and response to stimuli by providing a mechanism for bursting oscillations. Our work has implications for experimental studies and computational modeling of the role of Na/K pumps in neuronal activity, information processing in neural circuits, and the neural control of animal behavior.

KEYWORDS

***Drosophila* larvae, motor neuron, sodium potassium pump, intrinsic excitability, sodium equilibrium potential**

Introduction

Sodium potassium ATPases (Na/K pumps) are ubiquitous components of neuronal membranes. They use ATP to pump Na^+ out of neurons and K^+ into neurons against their respective concentration gradients, and play a critical role in maintaining the resting membrane potential of neurons (reviewed in Kaplan, 2002). There is a growing realization that in addition to playing this housekeeping role, Na/K pumps also play surprisingly dynamic roles in regulating cellular excitability. In particular, Na/K pumps mediate long-lasting membrane afterhyperpolarizations (AHPs) in response to stimulus-induced high spiking activity. These

AHPs can provide a neuronal memory of previous activity than can last tens of seconds (reviewed in Picton et al., 2017b). Pump mediated AHPs were first characterized in invertebrate neurons (Scuri et al., 2007; Pulver and Griffith, 2010) but have now been found in *Xenopus* (Zhang and Sillar, 2012) and mouse spinal neurons (Picton et al., 2017a).

In all species studied to date, the fundamental mechanisms of Na/K pump mediated AHPs appear remarkably conserved. High frequency bouts of spiking in neurons trigger long-lasting outward currents with little or no conductance changes for tens of seconds. These long-lasting hyperpolarizations are subject to neuromodulation (Picton et al., 2017a; Hachoumi et al., 2022) and interact with voltage gated ionic conductances to shape neuronal intrinsic properties (Pulver and Griffith, 2010; Picton et al., 2018). Despite this growing awareness of Na/K pumps as dynamic players in tuning cellular excitability within neural circuit components, our understanding of how specific Na/K pump properties shape intrinsic properties generally and the relationships between spiking and AHP properties remains relatively fragmented. This is in part due to a lack of pharmacological or genetic tools for precisely manipulating specific pump properties and difficulty of experimentally controlling and monitoring intra- and extracellular Na^+ and K^+ concentrations while also maintaining physiologically realistic conditions for the neurons under study.

Neuroscience researchers have increasingly turned to computational modeling of Na/K pumps to circumvent challenges associated with studying pumps in experimental preparations. In multiple model systems, Hodgkin-Huxley-type model neurons that incorporate both voltage-gated conductances and Na/K pump currents have been developed. This has revealed how Na/K pump currents contribute to rhythm and pattern generation in motor systems (Ellingson et al., 2021), intrinsic excitability in vertebrate neurons (Forrest et al., 2012), how pump currents mediate effects of neuromodulators (Forrest et al., 2012), and how pumps contribute to signal propagation through multi-compartment models (Scuri et al., 2007; Ellingson et al., 2021). Computational modeling in several neuronal cell types has also highlighted the importance of considering the dynamics of intracellular sodium concentration and its interactions with sodium-dependent pumps when examining neuronal dynamics, in particular on long time scales (Kueh et al., 2016; Zylbertal et al., 2017a,b; Sharples et al., 2021).

Multiple studies have anecdotally noted the presence of pump mediated effects on motor neuron excitability on multiple time scales, but exactly how specific pump parameters simultaneously shape intrinsic properties in motor neurons on both short (ms-s) and long (s-min) time scales remain relatively poorly understood. Paradoxically, Na/K pump activity is often described and modeled without the use of any explicit time constants. This raises the interesting question of how long-lasting cellular events such as AHPs can be generated by instantaneous cellular processes. Overall, understanding how pump functional properties and the cellular ion concentration dynamics they contribute to shape excitability has relevance for human health, given that multiple human disorders are thought to arise from anomalous Na/K pump activity (reviewed in Holm and Lykke-Hartmann, 2016, and in Isaksen and Lykke-Hartmann, 2016).

Creating computational models of pump activity that can be deployed within the context of a genetically tractable model organism has value added, because the resulting models can then be coupled with genetic manipulations of cellular and circuit activity (Pulver and Griffith, 2010). Here, we model Na/K pump activity in a Hodgkin-Huxley-type model based on a model of a motor neuron in *Drosophila* larvae, a system with an unsurpassed genetic toolkit. Our aim was to reveal conserved principles governing how modulation of specific Na/K pump functional properties shapes neuronal excitability on both short (ms-s) and longer (s-min) time scales. We deliberately chose to use a highly streamlined model with as few conductances as possible to maximize our ability to directly interpret effects of pump activity and generate a knowledgebase relevant across multiple species. We find that Na/K pumps have complex and often counterintuitive effects on intrinsic excitability, dynamics, and cellular memory. Systematic exploration of the effects of modulating pump functional properties highlights the necessity of considering Na/K pump and Na reversal potential dynamics when interpreting the effects of experimental manipulations of cellular excitability and neural circuit function. This work provides insight and guidance for analogous work in vertebrate model organisms while also contributing to the groundwork for computational modeling in a genetically tractable invertebrate species.

Methods and materials

Model neuron

We used a single compartment model neuron (Figure 1A) modified from Gunay et al. (2015) for all simulations. In this model, membrane potential V is governed by:

$$\frac{dV}{dt} = -\frac{1}{C}\left(I_{NaT} + I_{NaP} + I_{Naleak} + I_{Kf} + I_{Ks} + I_{Kleak} + I_{pump} - I_{inj}\right) \quad (1)$$

where C is the membrane capacitance (4.0 pF). The transient sodium current I_{NaT}, the persistent sodium current I_{NaP}, two potassium currents with fast (I_{Kf}) and slow (Peters et al., 2018) voltage-dependent gating dynamics, and sodium and potassium leak currents I_{Naleak} and I_{Kleak} are given by:

$$I_{NaT} = g_{NaT} * m_{NaT}^3 * h_{NaT} * \left(V - E_{Na}\right)$$

$$I_{NaP} = g_{NaP} * m_{NaP} * \left(V - E_{Na}\right)$$

$$I_{Naleak} = g_{Naleak} * \left(V - E_{Na}\right)$$

$$I_{Kf} = g_{Ks} * m_{Kf}^4 * \left(0.95 * h_{Kf1} + 0.05 * h_{Kf2}\right) * \left(V - E_K\right)$$

$$I_{Ks} = g_{Ks} * n_{Ks}^4 * \left(V - E_K\right)$$

$$I_{Kleak} = g_{Kleak} * \left(V - E_K\right)$$

where g_{NaT} (100.0 nS), g_{NaP} (0.80 nS), g_{Naleak} (1.2 nS), g_{Kf} (15.1 nS), g_{Ks} (50.0 nS), and g_{Kleak} (3.75 nS) are the maximal conductances for the respective currents. E_{Na} is the sodium reversal potential (defined below), E_K (−80.0 mV) is the potassium reversal potential, and the dynamic activation and inactivation variables are given by:

$$\frac{d}{dt}m_{NaT} = \frac{m_{NaT\infty} - m_{NaT}}{\tau_{mNaT}}$$

$$\frac{d}{dt}h_{NaT} = \frac{h_{NaT\infty} - h_{NaT}}{\tau_{hNaT}}$$

$$\frac{d}{dt}m_{NaP} = \frac{m_{NaP\infty} - m_{NaP}}{\tau_{mNaP}}$$

$$\frac{d}{dt}m_{Kf} = \frac{m_{Kf\infty} - m_{Kf}}{\tau_{mKf}}$$

$$\frac{d}{dt}h_{Kf1} = \frac{h_{Kf1\infty} - h_{Kf1}}{\tau_{hKf}}$$

$$\frac{d}{dt}h_{Kf2} = \frac{h_{Kf2\infty} - h_{Kf2}}{116}$$

$$\frac{d}{dt}n_{Ks} = \frac{n_{Ks\infty} - n_{Ks}}{\tau_{nKs}}$$

with voltage dependences and time constants

$$m_{NaT\infty} = \frac{1}{1+\exp\left(\frac{V+29.13}{-8.922}\right)}$$

$$\tau_{mNaT} = 3.861 - \frac{3.434}{1+\exp\left(\frac{V+51.35}{-5.98}\right)}$$

$$h_{NaT\infty} = \frac{1}{1+\exp\left(\frac{V+40.0}{6.048}\right)}$$

$$\tau_{hNaT} = 2.834 - \frac{2.371}{1+\exp\left(\frac{V+2.19}{-2.641}\right)}$$

$$m_{NaP\infty} = \frac{1}{1+\exp\left(\frac{V+48.77}{-3.68}\right)}$$

$$\tau_{NaP} = 1$$

$$m_{Kf\infty} = \frac{1}{1+\exp\left(\frac{V+17.55}{-7.27}\right)}$$

$$\tau_{Kf} = 1.94 + \frac{2.66}{1+\exp\left(\frac{V-8.12}{7.96}\right)}$$

$$h_{Kf1\infty} = \frac{1}{1+\exp\left(\frac{V+45.0}{6.0}\right)}$$

$$h_{Kf2\infty} = \frac{1}{1+\exp\left(\frac{V+44.2}{1.5}\right)}$$

$$\tau_{hKf} = 1.79 + \frac{515.8}{1+\exp\left(\frac{V+147.4}{-28.66}\right)}$$

$$m_{nKs\infty} = \frac{1}{1+\exp\left(\frac{V+12.85}{-19.91}\right)}$$

$$\tau_{nKs} = 2.03 + \frac{1.96}{1+\exp\left(\frac{V-29.83}{3.32}\right)}$$

In the equations above, all times are in units of ms, all voltages are in units of mV.

The Na/K pump model is modified from Kueh et al. (2016). The current I_{pump} is given by:

$$I_{pump} = I_{pumpmax} * \frac{1}{1+\exp\left(\frac{NaH - \left[Na^+\right]}{NaS}\right)} \quad (2)$$

where $I_{pumpmax}$ is the maximal pump current when the pump is fully activated, NaH is the sodium concentration at which the pump current is half-activated, and NaS is a factor that determines the steepness and range of the sodium concentration dependence of pump activation. Eq. 2 specifies a simple sigmoidal dependence of pump activation and pump current magnitude on intracellular sodium concentration as illustrated in Figure 1B (Kueh et al., 2016). Unless otherwise specified, the default values for the three pump parameters used here are $I_{pumpmax}$ = 75 pA, NaH = 40 mM, and NaS = 10 mM. Note that Eq. 2 does not contain an explicit time constant of pump activation, rather, pump current activation follows changes in $[Na^+]$ instantaneously.

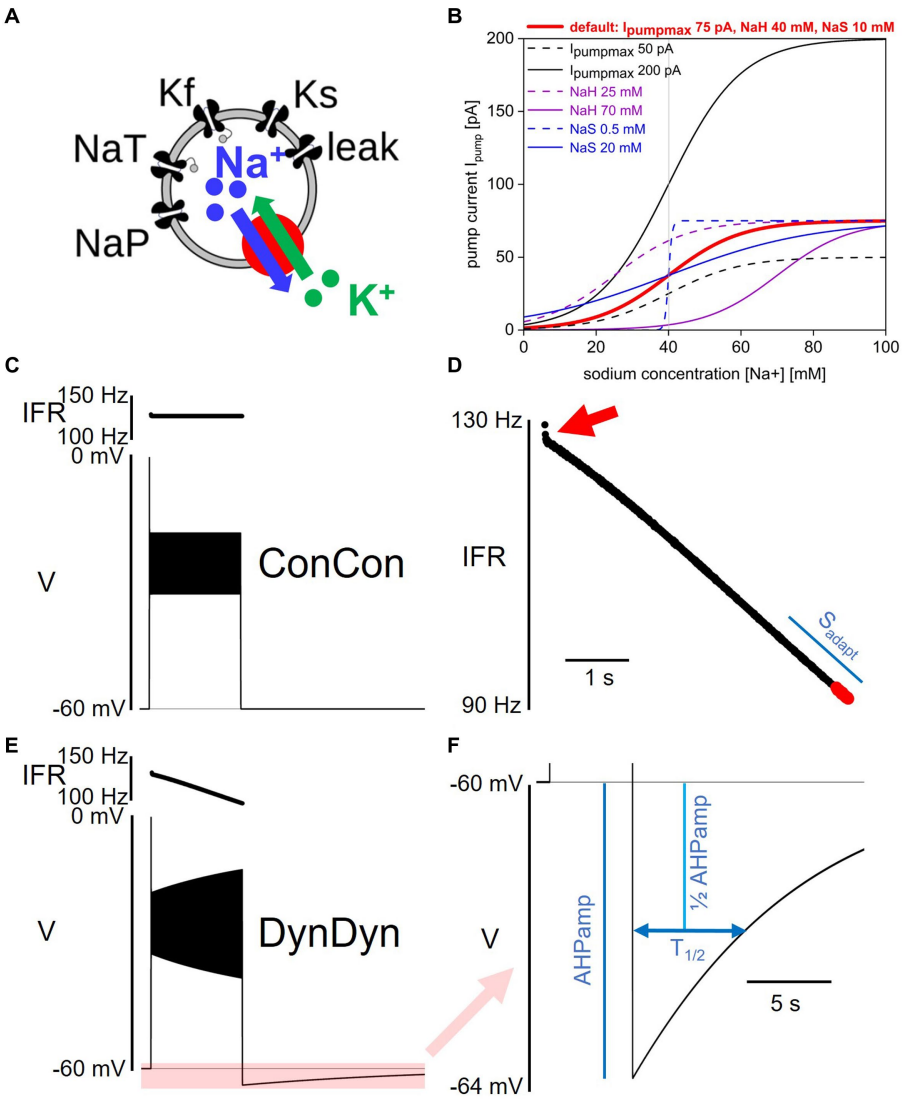

FIGURE 1
Model and pump properties, pump effects on spiking and after-hyperpolarization. **(A)** Schematic of model structure. **(B)** Dependence of Na/K pump current I_{pump} on intracellular sodium concentration [Na^+] and pump parameters $I_{pumpmax}$, NaH, and NaS. Red solid line shows pump activation curve with default pump parameters as listed at top, red. Other curves show pump activation curve for minimum (dashed) and maximum (solid) values of $I_{pumpmax}$ (black), NaH (purple), and NaS (blue) explored in Figure 7. Gray vertical line indicates resting sodium concentration of model with default pump parameters. **(C)** Voltage response of model ConCon with constant [Na^+] and E_{Na} to 5 s injection of 50 pA stimulus current. Insert above voltage trace shows instantaneous firing rate. **(D)** Expanded view of instantaneous firing rate IFR in DynDyn model, from panel **(E)**. Adaptation slope (s_{adapt}) is indicated in blue and calculated based on trajectory of IFR in final periods of spiking (red dots, see Methods). Red arrow indicates initial rapid spike rate adaptation. **(E)** Same as panel **(C)**, but for model version DynDyn with dynamic [Na^+] and E_{Na}. Note constant IFR in ConCon, **(C)**, and adapting IFR in DynDyn, **(E)**. Shaded pink box in panel **(E)** corresponds to expanded view of AHP in panel **(F)**. **(F)** Expanded view of DynDyn AHP, from panel **(E)**. Definitions of AHP amplitude (AHPamp) and AHP half duration ($T_{1/2}$) are illustrated in blue. Thin horizontal black lines in panels **(C,E,F)** indicate resting membrane potential.

Together with the pump current I_{pump}, the sodium currents I_{NaT}, I_{NaP}, and I_{Naleak} in this model alter the intracellular sodium concentration [Na^+] via:

$$\frac{d\left[Na^+\right]}{dt} = -\frac{I_{NaT} + I_{NaP} + I_{Naleak} + 3 * I_{pump}}{F * Vol} \quad (3)$$

from its default value of [Na^+] = 40.08 mM. Here, Vol = 549 μm^3 = 0.549 pL is the volume of a shell under the neuronal membrane. In this shell, the sodium concentration is considered under the influence of sodium currents entering and exiting the cell. The factor 3 multiplying the pump current accounts for the fact that each pump cycle extrudes three sodium ions and imports two potassium ions, corresponding to extrusion of three sodium ions for every net electrical charge change. Given the momentary intracellular sodium concentration [Na^+] and a constant extracellular sodium concentration of 135 mM, the momentary sodium reversal potential E_{Na} driving Na^+ fluxes through the membrane conductances is calculated according to the Nernst equation assuming a temperature of 25°C.

To tease apart the roles of pump current, dynamic [Na^+], and dynamic E_{Na} in neuronal excitability and memory, we introduced two switches in the model: a concentration switch that allows toggling the intracellular sodium concentration [Na^+] between being constant at 40.08 mM versus being dynamic according to Eq. 3, and a reversal potential switch that allows toggling the sodium reversal potential E_{Na} between being constant at 31.2 mV (the Nernst potential corresponding to [Na^+] = 40.08 mM) versus being dynamic according to the Nernst equation and the momentary value of [Na^+]. These switches allow separating the direct effects of a time-varying intracellular sodium concentration from the indirect, electrical effects of the accompanying changes in sodium reversal potential E_{Na}, which sets the driving force ($V-E_{Na}$) for sodium flux through membrane channels. Where indicated in text and figures, model versions ConCon, DynCon, and DynDyn correspond to: version ConCon—[Na^+] constant, E_{Na} constant; version DynCon—[Na^+] dynamic, E_{Na} constant; and version DynDyn—[Na^+] dynamic, E_{Na} dynamic.

Measures of spiking activity and AHP features

We used several measures to quantify the spiking activity of model responses to step current injections of 5 s duration. Initial and final instantaneous firing rates IFR_{ini} and IFR_{fin} during the 5 s injection were calculated by taking the inverse of the first and last interspike intervals, respectively. Additionally, the rate of change in spike frequency was quantified as the slope s_{adapt} of the IFR profile at the end of the step current injection. Spike rate adaptation slope s_{adapt} was determined by taking the last 19 IFR values, separating them into two groups of 9, and averaging those two groups, while leaving off the very last IFR value (which in some simulations was invalid because the last spike was truncated by the step current injection ending mid-spike). The difference between the two IFR group averages, divided by the time difference between the middle spikes in each group of 9, is the adaptation slope s_{adapt} in units of Hz/s (see Figure 1D for illustration). The rationale for this descriptor of spike rate adaptation, s_{adapt}, is explained in the Results section, below.

The after-hyperpolarization amplitude (AHPamp) was determined by taking the lowest voltage value after the end of the injection minus the pre-injection voltage. The after-hyperpolarization half duration ($T_{1/2}$) was determined by finding the time after the end of the injection at which the AHP had decayed to 50% of the AHPamp value (see Figure 1F).

Zap currents

The zap current injection was adopted from Tohidi and Nadim (2009). The zap current is given by:

$$I_{zap} = I_{zapmax} * \left(0.5 + 0.5 * \cos\left(2\pi f_{zap} t + \pi\right)\right).$$

where I_{zapmax} is the maximum zap current amplitude, and f_{zap} is the exponentially increasing and decreasing zap frequency. For the acceleration portion of the zap, given f_{zap} is by:

$$f_{zap} = \frac{f_0}{\lambda t}\left(\exp(\lambda t) - 1\right)$$

where f_0 (0.1 Hz) is the minimum zap frequency, and t is time since the start of the acceleration portion of the zap injection. For the deceleration portion, the f_{zap} used is the mirror image (in time) of the acceleration f_{zap} function.

Lambda (λ) is the exponential rising factor given by:

$$\lambda = \ln\frac{f_{max}}{f_0} * \frac{1}{\tau_{zap1/2}}$$

where f_{max} (5.0 Hz) is the maximum zap frequency, and $\tau_{zap1/2}$ (20 s) is half the total zap duration (acceleration and deceleration portions combined).

Model implementation and code availability

The model was implemented in Python (version 3.9). Differential equations were solved numerically using the fourth order Runge-Kutta algorithm ODEint available in the SciPy Python library, with absolute and relative tolerances set to 1.49012e-8 and 1e-10, respectively. Voltage trace analysis such as spike detection, calculations of instantaneous firing rate, s_{adapt}, and measurement of AHPamp and $T_{1/2}$, were implemented directly in the simulation code and executed at run-time. Simulation results were exported from the simulation code and imported into Origin 2022b (OriginLabs) for further analysis and plotting. All code is freely available on ModelDB at http://modeldb.yale.edu/267620.

Results

Na/K pump, dynamic sodium concentration and reversal potential added to basic model neuron

To examine the effects of Na/K pumps and intracellular sodium dynamics on the electrical activity and excitability of neurons, we incorporated a pump model and dynamic sodium concentration and reversal potential into a single-compartment, conductance-based neuron model. While the model neuron is loosely based on the electrical behavior of fly larval motoneurons and is a modified version of a previously published model, it does not include all the voltage-gated conductances known to be present in larval neurons (Lin et al., 2012; Gunay et al., 2015). Our intent was rather to study the effects of Na/K pumps and their parameters and dynamics using a basic pump model in a basic model neuron, so that we could assess the effects of modulating pump currents with as few confounds as possible and so that our findings may be applicable across a range of neuron types and neural systems that contain pumps. This approach complements studies on the other end of the scale of neuronal model complexity that examine the effects of pumps and sodium dynamics in multi-compartment models of specific neuron types with multiple

membrane conductances and complex ion diffusion, buffering, and binding dynamics (Zylbertal et al., 2017a).

Briefly, our simplified model neuron contains two Na^+ membrane currents, a transient sodium current I_{NaT} and a persistent sodium current I_{Nap}, two K^+ membrane currents with fast (I_{Kf}) and slow (Peters et al., 2018) voltage dependent gating dynamics, and a membrane leak current with a Na^+ and a K^+ component (Figure 1A). The equations governing the voltage-dependent dynamics of these currents and the model neuron's membrane potential V are specified in the Methods section.

To this baseline model, we added a pump current I_{pump} whose activation depends on the intracellular sodium concentration $[Na^+]$ with the three parameters $I_{pumpmax}$ (the maximal pump current when the pump is fully activated), NaH (the sodium concentration at which the pump current is half-activated), and NaS (a factor that determines the range and steepness of the sodium concentration dependence of pump activation; Figure 1B). We further replaced the previously static intracellular sodium concentration $[Na^+]$ by a dynamic concentration variable influenced by sodium influx through the sodium membrane currents I_{NaT}, I_{NaL}, and I_{Naleak}, and by sodium ion extrusion via the pump current. In contrast to more elaborate models of Na/K pumps and intracellular $[Na^+]$ dynamics (see for example, Zylbertal et al., 2017a), Eqs. 2, 3, which describe pump activation and $[Na^+]$ dynamics, do not include any explicit activation time constants, buffering, or chemical reaction rate constants.

Addition of the pump current with default values of the three pump parameters of $I_{pumpmax} = 75$ pA, NaH = 40 mM, and NaS = 10 mM, combined with making the intracellular sodium concentration $[Na^+]$ and the sodium reversal potential E_{Na} dynamic, produced a silent (not spontaneously spiking or bursting) resting state of the model in which the pump is approximately half activated. This baseline activation can be thought of as the 'housekeeping' component of the pump's activity, which balances the ongoing sodium influx in the resting state (primarily through the sodium component of the membrane leak conductance) to maintain a stable sodium concentration at rest. This particular resting state positions the $[Na^+]/E_{Na}$/pump dynamic system in the steepest part of the pump's $[Na^+]$-dependent activation curve with default pump parameters (bold red in Figure 1B), making it maximally sensitive to changes in $[Na^+]$ when the neuron is perturbed out of its resting state. However, our exploration of pump parameter space shows that our results are qualitatively similar and robust to pump parameter variations over wide ranges, and thus not idiosyncratic to this particular parameter combination and resting state.

Addition of the pump and of dynamic $[Na^+]$ and E_{Na} substantially altered the model's spiking activity in response to step current injections (details below) and produced long-lasting (on the order of tens of seconds) afterhyperpolarizations (AHPs, Figure 1E). These AHPs show qualitative similarities to AHPs observed in larval Drosophila motor neurons and many other neuron types (Picton et al., 2017b).

Effects of pump activity on spiking

We characterized how pump properties and dynamic $[Na^+]$ and E_{Na} affect spiking activity by applying a variety of stimulus types to the model neuron, the simplest (and most frequently used in electrophysiology experiments) being the injection of step currents. To quantify spiking activity during step current injections, we focused on three descriptive measures: the initial instantaneous firing rate IFR_{ini} at the beginning of step current injection, the final instantaneous firing rate IFR_{fin} at the end of a 5 s step current injection, and the slope of spike rate adaptation s_{adapt}. How these measures are defined is described in the Methods section and in Figures 1D,F. In particular, we chose the slope s_{adapt} at the end of the instantaneous firing rate trajectory as a descriptor of the degree of firing rate adaptation because the instantaneous firing rate trajectories we observed in all model versions tended to have approximately linear shape over most of the 5 s current injection (see IFR profiles in Figures 1–3) that would be poorly characterized by other functions, such as an exponential fit.

Figure 2 quantifies these measures of spiking activity in response to step current injections of 5 s duration and of various amplitudes by comparing three model versions: version ConCon—which has constant values of $[Na^+]$ and E_{Na}; version DynCon—in which $[Na^+]$ is dynamic, but E_{Na} is held constant; and version DynDyn—in which both $[Na^+]$ and E_{Na} are dynamic.

Note that because in living neurons, $[Na^+]$ and E_{Na} are directly linked through the Nernst equation, model version DynCon (in which $[Na^+]$ and E_{Na} are uncoupled) is an artificial construct, primarily intended to distinguish the effects of dynamic sodium concentration from the effects of dynamic changes in reversal potential (as we proceed to do in Figure 3) in a way that would not be possible in electrophysiology experiments, but is possible in a computational model. However, model version DynCon could also be interpreted as a simple, single-compartment proxy for a spatially extended neuron in which local changes in $[Na^+]$ that influence Na/K pumps in one location in the cell are spatially uncoupled from changes in E_{Na} that affect sodium influx through voltage-gated membrane channels in another location. Similarly, model version ConCon, in which neither $[Na^+]$ nor E_{Na} are allowed to vary, could be taken as a model of a patch-clamped neuron in which the intracellular ion concentrations are completely dominated by the large reservoir of patch pipette solution, and thus unable to vary. While spatial control of the intracellular milieu is rarely this complete in patch clamp experiments, considering this extreme case (implemented in ConCon) can be informative for the interpretation of experiments with partial control of the intracellular ion concentrations.

Note that comparison to a fourth model version in which the pump is entirely removed by setting $I_{pumpmax} = 0$ would not be physiologically meaningful in our simple model. In the absence of additional cellular mechanisms (Zylbertal et al., 2017a) that could help maintain sodium concentration, sodium reversal potential, and resting membrane potential, removing the pump entirely would lead to an unphysiological state in our simple model.

In all three model versions, ConCon, DynCon, and DynDyn, injection current amplitude was varied over a wide range, 0–100 pA, for Figure 2. For clarity, results from injection current levels that were either subthreshold (no spiking, at the low end of the injection current range) or produced depolarization block during part or all of the 5 s injection duration (at the high end of the injection current range) were omitted from Figure 2.

Initial firing rates at the beginning of step current injections of various amplitudes were virtually identical in model versions ConCon (black), DynCon (blue), and DynDyn (Carballo-Pacheco et al., 2019), as Figure 2A indicates. This reflects that the resting values of $[Na^+]$ and

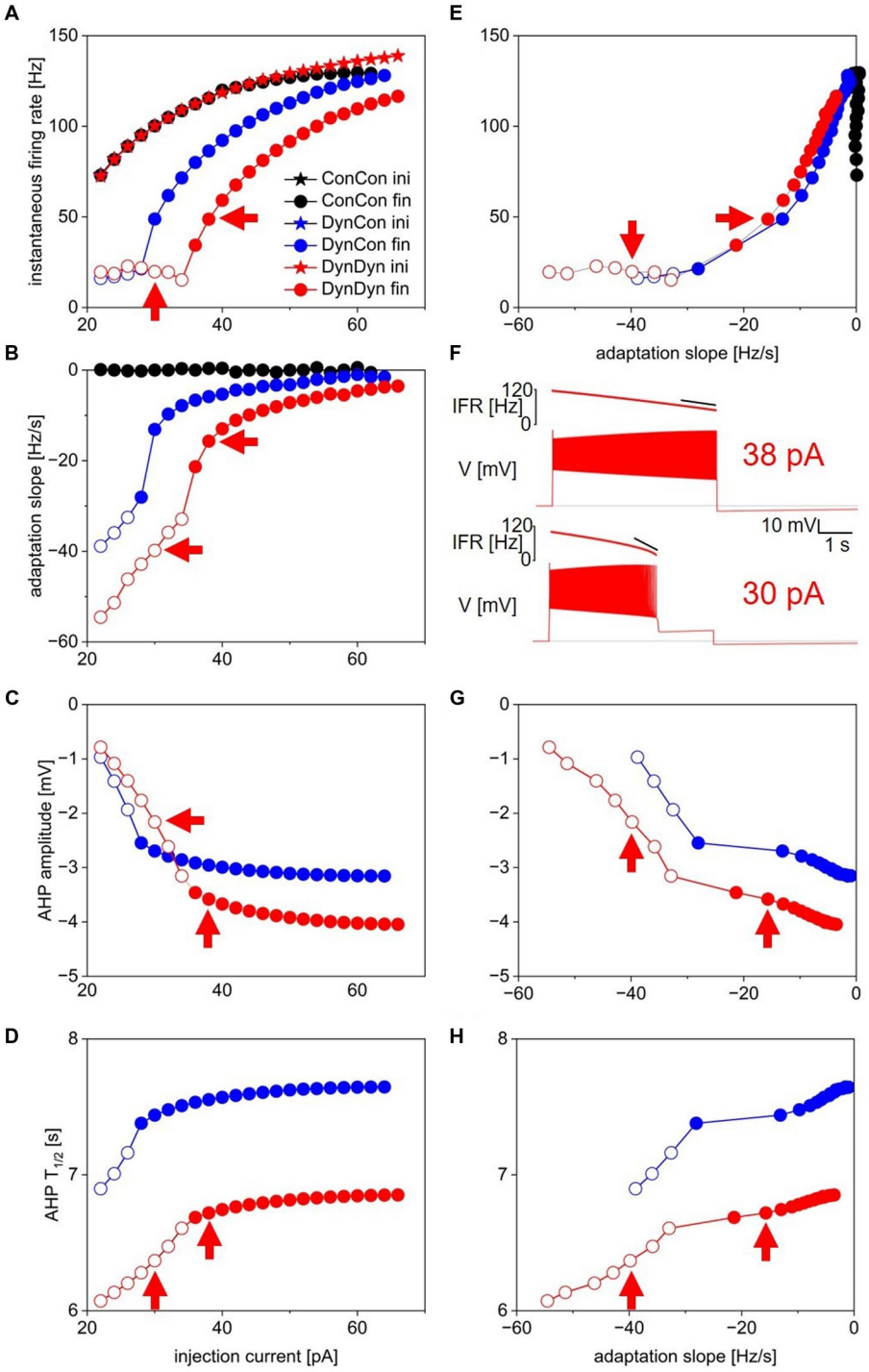

FIGURE 2
Measures of spiking activity and AHP dynamics in three model versions. **(A)** Initial (stars) and final (circles) instantaneous firing rate as a function of injection current in model versions with constant $[Na^+]$ and E_{Na} (ConCon, black), with dynamic $[Na^+]$ but constant E_{Na} (DynCon, blue), or with dynamic $[Na^+]$ and E_{Na} (DynDyn, red). Because initial IFR is almost identical in all three model versions, blue and black stars are occluded by red stars. Situations in which spiking stops before end of current injection in models DynCon and DynDyn are indicated by open circles. Red arrows indicate datapoints corresponding to traces in 2F. **(B)** Adaptation slope (s_{adapt}) as a function of injection current. Color scheme same as in 2A, and throughout figure. **(C)** AHP amplitude as a function of injection current. **(D)** AHP half-duration $T_{1/2}$ as a function of injection current. Model version ConCon omitted from panels **(C,D)** because of lack of AHP. **(E)** Same as panel **(A)**, but plotted against s_{adapt}. **(F)** Example voltage traces showing full and incomplete spiking in DynDyn model for 38 pA (Kay and Stopfer, 2006) and 30 pA (bottom) injection currents, corresponding datapoints indicated by red arrows in all other panels. Black horizontal lines show pre-injection resting potential of −60mV. Instantaneous firing rate (IFR) is shown above voltage trace, with diagonal black lines indicating s_{adapt}, which is −15.7 Hz/s for 38 pA injection (Kay and Stopfer, 2006) and −39.8 Hz/s for 30 pA injection (bottom). **(G)** Same as 2C, but plotted against s_{adapt}. **(H)** Same as 2D, but plotted against s_{adapt}.

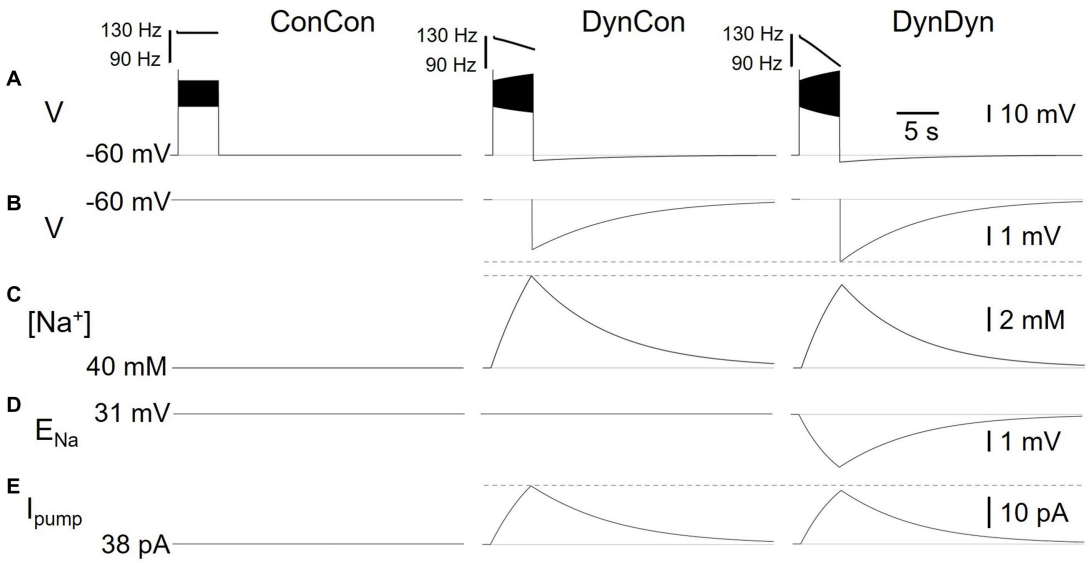

FIGURE 3
Effects of dynamic pump on spiking and AHP in model versions ConCon (left), DynCon (Peters et al., 2018), and DynDyn (Palmer et al., 2021). **(A)** Membrane potential V in response to 5 s, 50 pA current injection. Inserts above voltage traces show instantaneous firing rate IFR. **(B)** Membrane potential V at expanded vertical scale to show AHP. **(C)** Dynamics of intracellular sodium concentration [Na^+] in the three model variants **(D)** Sodium reversal potential $E_{Na,}$ in all variants. **(E)** Pump current I_{pump} in variants. Dashed gray lines in panels **(B,C,E)** are inserted to facilitate comparison between DynCon and DynDyn.

E_{Na} in versions ConCon and DynCon were chosen to match the resting values that establish themselves in simulations of DynDyn after any numerical initialization artifact has decayed away. The three model versions thus are identical in their resting state—and therefore also in their firing rate immediately after the onset of current injection—and any differences only emerge after perturbation out of the resting state, in this case via step current injection.

In response to strong step current injection, spiking in all three model versions exhibits initial rapid spike rate adaptation over a few tens of ms (corresponding to a few spikes), as evident in the instantaneous firing rate profiles displayed in Figure 3A, and indicated in Figure 1D (red arrow). After this initial rapid adaptation, model version ConCon shows no further spike rate adaptation, whereas version DynCon shows intermediate and version DynDyn shows strong spike rate adaptation on the timescale of seconds (Figures 2A,B, inserts in 3A). Both versions with dynamic [Na^+], DynCon and DynDyn, also exhibit a gradually increasing spike amplitude (in contrast to the constant spike amplitude in version ConCon).

While spiking in version DynDyn is continuous for the entire 5 s current injection when the injection current is above 35 pA, injection currents below 35 pA in version DynDyn produce spiking that ceases prematurely before the 5 s stimulus current ends (see Figure 2F, bottom for an example), because I_{pump} gradually increases during initial spiking activity, and eventually overwhelms the depolarizing injection current and inward membrane currents and suppresses further spiking despite ongoing stimulation. Similar premature termination of spiking also occurs in model DynCon, albeit at lower injection currents (below 28 pA, see open blue circles in Figure 2B). Notably, when spiking prematurely terminates in both DynCon and DynDyn, it does so once a similar final firing rate IFR_{fin} is reached, regardless of injection current—see open blue and red circles in Figure 2A, all are around 20 Hz. Interactions of pump currents with a dynamic intracellular sodium concentration and reversal potential thus appear to impose a limit on the maximal firing rate sustainable in a neuron, unless the injection current is so large that it dominates the membrane potential dynamics and forces the neuron to continue spiking despite high pump current activation. This effect of a dynamic pump/[Na^+]/E_{Na} system could be interpreted as neuroprotective, in that it could potentially prevent overexcitation, exceedingly rapid spiking, and the accompanying risk of excitotoxity. Such a potentially protective effect is entirely absent in model version ConCon, where spiking at very high rates continues as long as a depolarizing injection current is provided (Figure 2A).

Figure 2 shows that addition of the Na/K pump with dynamic [Na^+] and E_{Na} enriches neuronal spiking dynamics by adding slow spike rate adaptation and diversifying the nature of the spiking response to current steps. This addition transforms uniform spiking at a constant rate when the pump is merely a constant "housekeeper" of sodium concentration, to a variable duration spiking response with spike rate adaptation when dynamic pump effects on sodium concentration and reversal potential are considered.

Effects of pump on AHP features

Besides showing the effects of the pump and sodium concentration dynamics on spiking activity during step current stimulation, Figure 2 also illustrates dynamic pump effects on the AHP. We use two simple measures, the afterhyperpolarization amplitude (AHPamp) and half-duration ($T_{1/2}$), as defined in the Methods section and illustrated in Figure 1F. While additional characterizations of the afterhyperpolarization, such as mathematical functions fitted to the AHP shape, could provide further information, AHPamp and $T_{1/2}$ characterize basic features of AHP shape in condensed form.

Model version ConCon (black in Figure 2) exhibits no AHP, whereas versions DynCon and DynDyn have long-lasting AHPs with membrane potential troughs dipping to −3.2 mV and −4.0 mV below resting membrane potential, respectively, for the larger depolarizing current injections (Figure 2C). These AHPs last for several tens of seconds, despite the absence of an explicit long time constant in the equations governing pump activation and sodium concentration dynamics (Eqs. 2, 3 in Methods section). The AHP amplitude in model version DynDyn is larger than the AHP in version DynCon; this indicates that indirect electrical effects of pump-mediated sodium concentration changes via changes in sodium reversal potential E_{Na} can play an important role in how ion pumps shape cellular activity and memory.

The AHP in model DynDyn has a larger amplitude than that in DynCon (Figure 2C), but is also somewhat shorter, with half durations $T_{1/2}$ in the range of 6–7 s, compared to $T_{1/2}$ values in the 7–8 s range for version DynCon (Figure 2D). The AHP in DynDyn is therefore more "pointy" (less shallow) than in DynCon.

Relationship of AHP features to preceding spiking activity

The range of step current amplitudes explored in Figure 2 influences both features of the spiking response and features of the subsequent AHP. Previous experimental investigation of spiking, pump current, and AHP dynamics in fly larval motoneurons indicates that Na/K pump mediated AHPs can serve as spiking activity integrators and thus may constitute a form of cellular memory (Pulver and Griffith, 2010). To determine what kind and amount of information about preceding spiking might be contained in features of the AHP, we examined the relationships between spiking features IFR_{fin} and s_{adapt}, and AHP features AHPamp and $T_{1/2}$ (Figures 2E,G,H). In the following description and analysis of this comparison, we focus on the range of injection current amplitudes for which spiking continues for the entire duration of the 5 s step current injection (filled circles in Figures 2E,G,H), to avoid the complexities inherent in lower level injection current simulations for which spiking terminates prematurely at different times for different levels of current injection (open circles in the same figures).

Interestingly, in both model versions DynCon (blue) and DynDyn (Carballo-Pacheco et al., 2019), we found close to linear four-way relationships between IFR_{fin}, s_{adapt}, AHPamp, and $T_{1/2}$, with more vigorous firing at stimulus offset and more pronounced spike rate adaptation corresponding to a deeper and longer-lasting AHP as the injection current was increased. In both models, features of the afterhyperpolarization therefore reflect information not only about the number of preceding spikes but also the dynamics of spiking. In contrast, the absence of an AHP in the ConCon model version means that just fractions of a second after vigorous spiking activity, any "memory" of it in the form of persistent ion concentration changes and membrane hyperpolarization is lost if $[Na^+]$ and E_{Na} are not dynamic.

Mechanisms underlying effects of pump activity

To investigate the electrical and Na^+ concentration-related mechanisms producing and shaping the pump's effects on spiking activity and longer time scale AHP features, we examined the time courses of multiple underlying dynamic variables in the model in addition to the membrane potential V, and for the same three model versions introduced in Figure 2. Figure 3 shows the dynamics of sodium concentration, reversal, and pump current in response to 5 s, 50 pA rectangular current pulses.

Intracellular $[Na^+]$ levels, while held constant in ConCon (Figure 3C, left), increase during spiking activity in DynCon (Figure 3C, middle) and DynDyn (Figure 3C, right) due to increased Na^+ influx through the voltage-gated sodium channels underlying I_{NaT} and I_{NaP}, which open during action potential firing. In both model versions, elevated $[Na^+]$ requires several tens of seconds to return back to baseline, far outlasting the spiking activity. The sodium concentration increase during stimulation is slightly smaller in DynDyn compared to DynCon. This is because the sodium driving force driving Na^+ through the membrane conductances g_{NaT}, g_{NaP}, and g_{Naleak} is smaller in DynDyn, because in that model version, the sodium reversal potential E_{Na} is dynamic according to the Nernst equation, and is thus reduced during the $[Na^+]$ increase caused by spiking (Figure 3D).

Because the $[Na^+]$ increase is slightly smaller in DynDyn compared to DynCon, the pump is also slightly less activated, leading to a lower peak pump current at the end of spiking activity in DynDyn compared to DynCon (Figure 3E). Counter-intuitively, this smaller pump current nonetheless corresponds to a larger AHP amplitude in DynDyn compared to DynCon (−3.9 mV compared to −3.1 mV, Figure 3B). This is again explained by the reduced sodium driving force at the end of and immediately after current injection. The AHP is the result of a net hyperpolarizing current that in our simple neuron model arises from the balance of hyperpolarizing, outward currents I_{Kf}, I_{Ks}, I_{Kleak}, and I_{pump}, and depolarizing, inward currents I_{NaT}, I_{NaP}, and I_{Naleak}, with the three latter smaller in DynDyn compared to DynCon because of the reduced value of E_{Na}. The inward/outward current balance is therefore shifted more in favor of a net outward current in DynDyn compared to DynCon, which explains the deeper AHP.

Considering the inward/outward balance is also instructive when thinking about ion fluxes, not just electrical currents. The sodium membrane currents I_{NaT}, I_{NaP}, and I_{Naleak} provide avenues for sodium to flow into the cell and increase $[Na^+]$, which is counter-balanced by the pump reducing $[Na^+]$. In our model, for default pump parameters as well as a wide range of other pump parameters, this balance is strongly in favor of sodium influx and $[Na^+]$ increase during spiking, when the voltage-gated channels underlying I_{NaT}, I_{NaP} are open. In contrast, after spiking has ended and these channels close, the inward and outward sodium fluxes are nearly balanced, resulting in only a small net extrusion of sodium that takes tens of seconds to return the elevated intracellular sodium concentration to its baseline resting value (Figure 3C). This is the mechanism through which a $[Na^+]$-dependent pump whose activation follows changes in $[Na^+]$ instantaneously, without an explicit time constant in Eq. 2, can nonetheless lead to a long-lasting memory trace in the form of elevated $[Na^+]$ and the accompanying AHP.

Although the differences in $[Na^+]$, E_{Na}, AHP features, and Na/K pump dynamics between model versions DynCon and DynDyn appear modest in Figures 3B–E, the impact on spiking activity of holding the sodium reversal potential E_{Na} constant (model DynCon) as opposed to allowing it to vary with varying sodium concentration $[Na^+]$ (model DynDyn) is substantial. This is illustrated by the much

stronger spike rate adaptation in DynDyn compared to DynCon (see steeper slope of IFR profile in Figure 3A, right compared to middle, and Figures 2A,B). It is therefore important to consider E_{Na} as a dynamic variable when modeling the role of Na/K pumps in neuronal activity, and when interpreting corresponding experimental data.

Na/K pump effects on neuronal excitability and functional range: test pulses

Figures 2 and 3 illustrate the effects of Na/K pumps and dynamic vs. constant $[Na^+]$ and E_{Na} on neuronal spiking activity and AHP features in response to step current injections. To investigate further how pumps affect neuronal excitability on multiple timescales, we simulated responses to several additional stimulation protocols designed to assess the extent to which the long-lasting dynamics of the $[Na^+]/E_{Na}/I_{pump}$ system shape fast spiking, and vice versa.

In a first set of experiments, we assessed for how long pump-mediated cellular memories persist. We delivered a short 200 ms, 22 pA test pulse to the model to probe its baseline excitability, then delivered a 50 pA, 5 s current stimulus to elicit spiking (Figure 4). Afterward, at different time points during the course of the resulting AHP, we delivered the same short test pulse a second time in separate simulations that were executed independently, but that are overlaid in time in Figure 4B in different colors. For each test pulse individually, we examined the voltage response and measured the number of spikes fired during the 200 ms test pulse (Figure 4D) and the time-to-first-spike (T_1) after test pulse onset (Figure 4E) as basic indicators of excitability. Figure 4A shows traces from simulation runs in which the test pulse was delivered immediately after the AHP trough (1 s delay, red), immediately before and after the response transitioned from sub-threshold depolarization to spike firing (orange and green, 35 and 36 s delays, respectively), and immediately before and after the response reached the same number of spikes (eight) as the pre-stimulus test pulse response (blue and black, 51 and 52 s delays, with seven vs. eight spikes, respectively). Note that even when the number of spikes in response to the test current pulse and the time-to-first-spike have returned to pre-stimulus values, subtle differences remain between the voltage response at that time (52 s after the end of the main stimulus) and the pre-stimulus voltage response—compare for example the amplitudes of the last spikes in the two black traces in Figure 4A. It takes several more tens of seconds for the post-stimulus test pulse response to become indistinguishable from the pre-stimulus response. In addition, we confirmed that isolated test pulses given at the same extended time (e.g., 52 s) in the absence of the 5 s AHP generating stimulus elicited spiking responses that were identical to the initial response (data not shown). This indicates that pump activation and changes in $[Na^+]$ and E_{Na} during the spiking activity caused by the main 5 s stimulus affect cellular excitability even more than a minute after the end of the stimulation, at a time when the AHP

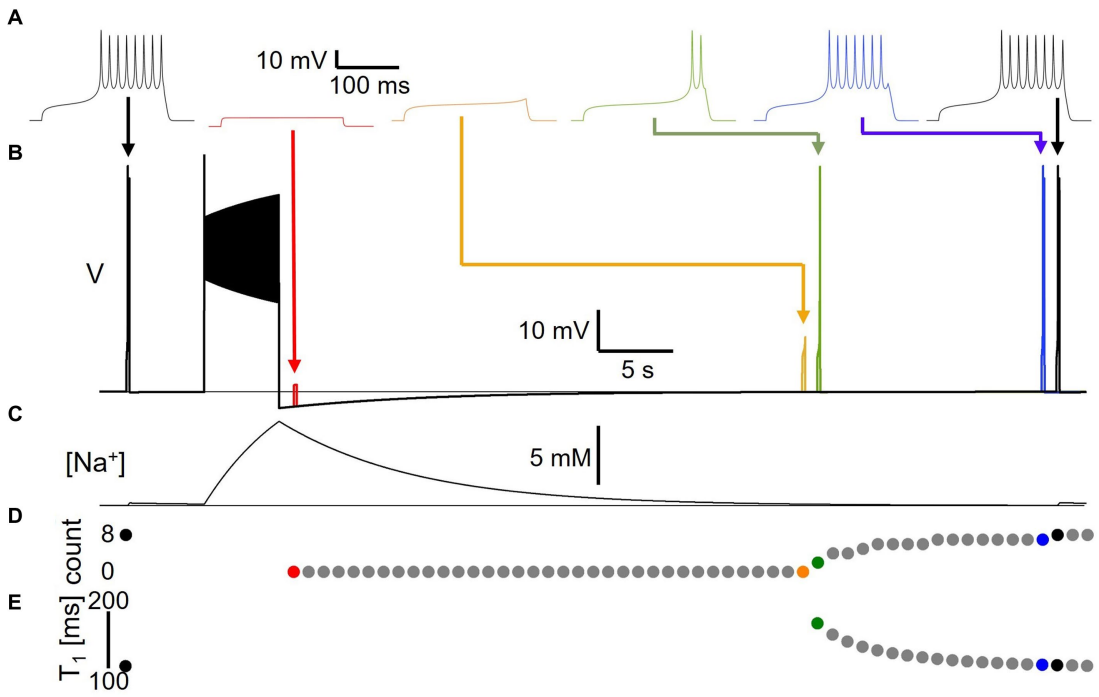

FIGURE 4
Long-lasting excitability changes following Na/K pump activation by spiking activity. **(A)** Voltage responses to 22 pA, 200 ms test pulses delivered to model version DynDyn—from left to right—before (black), and 1 s (Carballo-Pacheco et al., 2019), 35 s (orange), 36 s (green), 51 s (blue) and 52 s (black) after a 50 pA, 5 s stimulus to generate spiking and a long-lasting AHP. Arrows indicate timing of test pulses in panel **(B)**. **(B)** Superimposed simulations of individual test pulse responses and response to spike-inducing stimulus. Color code as in panel **(A)**. **(C)** Sodium concentration during simulation with test pulses delivered pre-stimulus and 52 s after stimulus, corresponding to black traces in panels **(A,B)**. **(D)** Number of spikes elicited by test pulses delivered before and once a second after main stimulus, in separate trials. **(E)** Time-to-first-spike T_1 from test pulse onset as a function of test pulse delay after main stimulus. Note that changes in excitability are present after AHP has finished and model has returned to original resting membrane potential.

(Figure 4B) and the accompanying change in intracellular sodium concentration (Figure 4C) appear at first glance to have returned to baseline, and in an electrophysiology experiment might be smaller than typical levels of recording noise.

Na/K pump effects on neuronal excitability and functional range: ramp currents

In a next set of experiments, we simulated ramps of injection current on different time scales, a stimulus protocol frequently used in electrophysiology to probe neuronal input–output relationships and dynamic properties. We simulated fast (2 s total duration) and slower (10 s total duration and 40 s total duration) bidirectional ramps of injection current from 0 to 70 pA, then back to 0 pA. The peak injected current of 70 pA was chosen as it is in the range of injection current for which model versions ConCon and DynDyn transition from spiking for the full duration of a 5 s step current injection, to depolarization block for part, or for all of the 5 s step current duration (Figure 2A).

Figure 5 shows the stimulus currents, voltage responses, and instantaneous firing rates as a function of momentary injection current for bidirectional ramps simulated in model versions ConCon (Figures 5A,D) and DynDyn (Figures 5B,E). The plots of instantaneous firing rate against momentary injection current in Figures 5D,E show clear firing hysteresis for slow and fast ramps in both model versions (i.e., with constant $[Na^+]$ and E_{Na} in ConCon, and dynamic $[Na^+]$ and E_{Na} in DynDyn). However, in ConCon spiking hysteresis only occurs in the form of spiking resuming at a lower injection current on the down ramp compared to the current at which spiking stopped on the up ramp, but not in terms of the instantaneous firing rate as a function of momentary injection current. In contrast, in the model version with dynamic $[Na^+]$ and E_{Na}, IFR is consistently lower on the downward ramp compared to the upward ramp at the same momentary value of injection current, and this becomes more and more apparent with longer ramps. This is attributable to the activation of pump current as sodium accumulates intracellularly due to acceleration of spiking activity during the upward ramp; sodium levels then remain elevated and the pump current remains activated during the downward ramp, which sharply curtails spiking. Because the slower ramp stimuli allow more time for sodium to accumulate and the pump to be activated, the instantaneous firing rate at the same level of momentary injection current is consistently lower in the slowest ramp (blue in Figure 5E) than in the fastest ramp (Carballo-Pacheco et al., 2019).

Notably, the presence of a dynamic $[Na^+]/E_{Na}$/pump system in the DynDyn model version reduced or prevented the depolarization block experienced by the ConCon version for injection currents near the peak of the bidirectional ramp, while also increasing the amount of current required to sustain spiking on the downward ramp, regardless of ramp speed (compare Figures 5A,B,D,E). Thus, sodium concentration and reversal potential dynamics altered the dynamic range of the model neuron, and "rescued" it from depolarization block and spike amplitude attenuation, while making it less responsive to lower levels of injection current on the downward ramp.

Overall, Figure 5 shows that spiking dynamics in the DynDyn model are richer than in the ConCon model, with instantaneous firing rate reflecting not only the momentary level of injection current, but the previous history of injection current and spiking response experienced by the neuron. Notably, this richness is readily apparent with longer slower ramps, but less evident with shorter faster ramps. This finding could be taken into consideration when designing

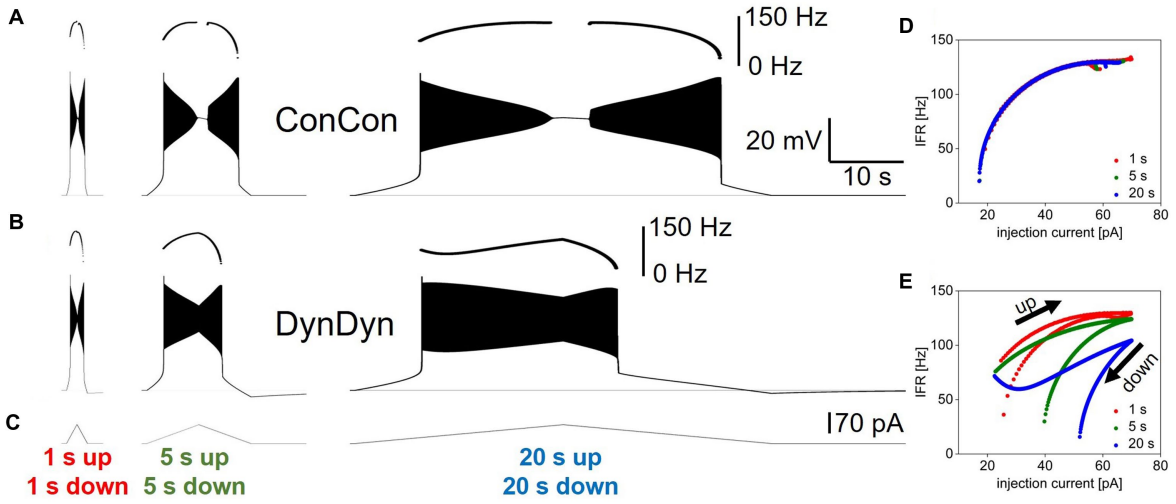

FIGURE 5
Influence of dynamic $[Na^+]/E_{Na}$/pump system on neuronal response to ramp currents. **(A)** Voltage response of model version ConCon to ramp currents with ramp up and ramp down durations of 1 s (left), 5 s (Peters et al., 2018), and 20 s (Palmer et al., 2021), and 70 pA peak amplitude. Inserts above voltage traces show instantaneous firing rate IFR. **(B)** Same for model version DynDyn. **(C)** Injected ramp currents. **(D)** Instantaneous firing rate from panel **(A)** (ConCon) as a function of momentary injection current for 1s ramps (Carballo-Pacheco et al., 2019), 5 s ramps (green), and 20 s ramps (blue). **(E)** Same for firing rates from panel **(B)** (DynDyn). Note similarities in response to fast ramps in panels **(A,B)** and increased divergence in IFR trajectory and hysteresis as duration of ramp increases.

experimental stimulus protocols to probe slow dynamics in neuronal activity, in particular when the role of pumps is being investigated.

Na/K pump effects on neuronal excitability and functional range: zap currents

In a third set of experiments, we explored how pump currents and sodium and reversal dynamics shape responses to rhythmic current pulses of accelerating and decelerating frequency, termed 'zap' currents (Hutcheon and Yarom, 2000; Tseng and Nadim, 2010). This type of stimulus is highly relevant physiologically as larval motor neurons are typically recruited into rhythmic bursting through a range of frequencies (Pulver et al., 2015). We simulated sinusoidal, oscillating current injections that started with a 10 s cycle period (0.1 Hz frequency) and sped up to a cycle period of 200 ms (5 Hz frequency) over the course of 20 s with an exponential frequency profile (for details, see Methods section). Once cycle period reached 100 ms, the oscillations then returned to a 10 s cycle period over 20 s. Figure 6 shows the zap current (Figure 6D) and the corresponding voltage responses (Figures 6A–C) of model versions ConCon (left) and DynDyn (Palmer et al., 2021).

A zap current of 30.5 pA amplitude evoked a supra-threshold voltage response in both model versions ConCon and DynDyn, with spikes occurring for every injected current peak, even up to the highest zap frequency, although at the fastest zap frequencies injected into DynDyn (middle of the voltage trace and IFR plot in Figure 6A, right) the model fired only a single spike per current peak, resulting in an instantaneous firing rate that tracked the zap frequency around its 5 Hz maximum in the middle of the zap injection. Consistent with the spike frequency-reducing effects of dynamic $[Na^+]$ and E_{Na} in Figures 2, 3, 5, spike frequencies in response to zap current injection were also lower in DynDyn compared to ConCon throughout the zap simulation (see IFR plots in Figure 6A).

The overall activity profile of model version ConCon in both voltage and IFR is largely symmetric, showing very similar responses to the same zap frequencies in the two halves of the zap injection, whereas DynDyn responses to the same zap frequency in the deceleration half of the zap differed from the acceleration half—note for example the reduced burst duration and lower peak of the IFR profile in DynDyn in response to the last zap current peak compared to the first zap current peak in Figure 6A, right. This indicates that with dynamic $[Na^+]$ and E_{Na} the neuron's activity depends on its previous spiking history, whereas with constant $[Na^+]$ and E_{Na} it does not.

A zap current of 21.6 pA amplitude evoked a sub-threshold (non-spiking) voltage response in both model versions (Figure 6C), with relatively minor differences between the voltage responses. These differences primarily consisted of a slightly reduced voltage amplitude (first voltage peak of −51.5 mV in DynDyn compared to −49.9 mV in ConCon, see horizontal gray lines in Figure 6C) and a very small (<1 mV) AHP in DynDyn after the zap injection that is absent in ConCon.

Such subtle differences in sub-threshold voltage response would appear to have little effect on neuronal activity. However, the voltage responses to a zap current of 22.0 pA shown in Figure 6B reveal that even subthreshold voltage changes sculpted by a dynamic $[Na^+]/E_{Na}/I_{pump}$ system can affect neuronal spiking response and endow a neuron with a long-lasting memory for not only supra-threshold, spiking activity, but also sub-threshold inputs and voltage fluctuations. This is evident in Figure 6B, right, where model version DynDyn responds to the first peak of the injected zap current with a brief burst of spikes, but fails to spike in response to the corresponding last current peak at the end of the zap injection, resulting in asymmetry of the spiking response to the symmetric zap current. The subthreshold voltage fluctuations that occur between the first and last current peaks, by slightly activating the Na/K pump and changing $[Na^+]$ and E_{Na}, have therefore left a memory trace that is reflected in DynDyn's failure to spike in response to the last current peak.

Overall, our zap exploration of the effects of dynamic reversal and pump currents has revealed that pump currents shape how neurons respond to current injections on both fast and slow time scales.

Systematic exploration of pump parameter space

Dynamic pump currents clearly generate a diversity of outputs in response to current stimuli. In Figures 1–6, we used a fixed set of pump parameters, $I_{pumpmax}$ = 75 pA, NaH = 40 mM, NaS = 10 mM. How does modulating those parameters further shape spiking on short and long time scales in response to step current pulses? Our streamlined computational model enabled with relatively few cellular components allowed us to systematically vary all pump parameters and examine how each sculpts excitability. Figure 7 shows how key features of spiking and AHPs depend on $I_{pumpmax}$, NaH and NaR. For each column in the figure, one of the parameters (left column—$I_{pumpmax}$, middle—NaH, right—NaS) was varied over a physiologically meaningful range while the other two parameters were held at their default values. A step current of 50 pA amplitude and 5 s duration (same as in Figure 3) was simulated for each parameter combination, and spiking activity and AHP features were analyzed and plotted in Figure 7.

The ranges over which each parameter was varied were chosen as follows: $I_{pumpmax}$—lower bound set to 50 pA because $I_{pumpmax}$ < 50 pA led to resting states with unphysiologically high $[Na^+]$ and low E_{Na}; upper bound set to 200 pA because most effects of increasing $I_{pumpmax}$ on spiking dynamics and AHP features appeared to saturate in that range. NaH—lower bound of 25 mM chosen because NaH < 25 mM led to depolarization block during part or all of the 5 s current injection; upper bound of NaH = 70 mM because NaH > 70 mM caused premature termination of spiking (as in Figure 2F, bottom) despite ongoing current injection. NaS varied all the way down to 0.5 mM, which corresponds to an extremely steep pump current dependence on $[Na^+]$ (see dashed blue curve in Figure 1B), and up to 20 mM, where most effects of increasing NaS on spiking dynamics and AHP features appeared to saturate. The pump activation curves corresponding to the lower and upper bounds of these explored ranges are illustrated in Figure 1B in black for $I_{pumpmax}$, purple for NaH, and blue for NaS.

Overall, the response of the model with dynamic $[Na^+]$ and E_{Na} (DynDyn) to step 5 s, 50 pA current injection did not qualitatively change over the parameter ranges covered in Figure 7, and consisted of spiking with spike rate adaptation for the duration of the stimulus injection, followed by a long-lasting (tens of seconds) AHP of several mV amplitude. Our model version DynDyn with our chosen default pump parameter set (indicated by blue dots in Figure 7) is therefore representative of a wide range of pump parameters.

The results in Figure 7 can be considered from two perspectives: (1) Which pump parameters primarily control a given feature of

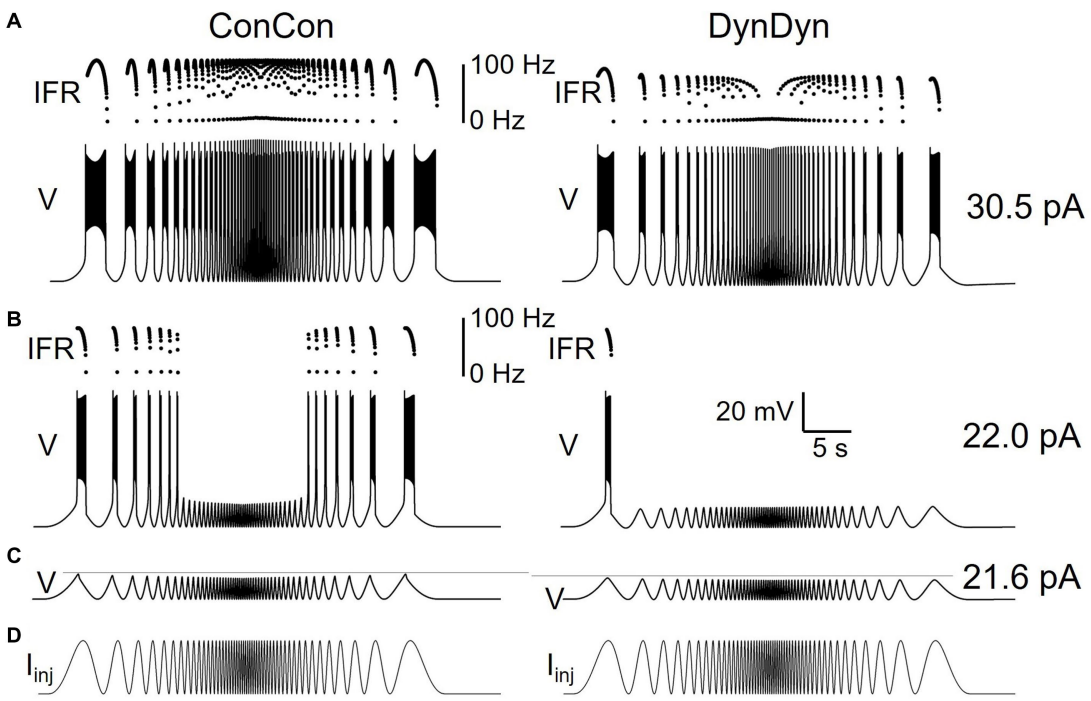

FIGURE 6
Dynamic $[Na^+]/E_{Na}/I_{pump}$ system shapes neuronal response to oscillatory inputs of different frequencies. **(A)** Voltage response of model versions ConCon (left) and DynDyn (Palmer et al., 2021) to a 'zap' injection current (described in Results section) of 30.5 pA amplitude and frequencies sweeping from 0.1 to 5 Hz and back over a total duration of 40 s. Dots above voltage trace show instantaneous firing rate. **(B)** Same as panel **(A)** but for 22.0 pA zap current amplitude. **(C)** Voltage responses of ConCon (left) and DynDyn to 21.6 pA zap current. Horizontal gray lines included for ease of amplitude comparison, aligned to first voltage peak in each trace. Voltage and time scales in panel **(B)** (Palmer et al., 2021) apply to panels **(A,B,C)**. **(D)** Injected zap current time course showing increasing and decreasing stimulus frequency. Same time course was used in panels **(A,B,C)**, but scaled vertically by current amplitudes given at right of panels **(A,B,C)**, respectively.

spiking or AHP? (2) Which spiking and AHP features does a given pump parameter control?

Figure 7A indicates that the instantaneous firing rate at the beginning and end of the 5 s current injection is influenced to a limited extent by the maximal pump current $I_{pumpmax}$ and the slope factor NaS over most of their explored range, whereas the sodium concentration NaH of pump half-activation influences the firing rate more strongly, with higher values of NaH leading to lower spike rates. This seemingly counter-intuitive effect is explained by higher NaH leading to lower pump activation in the resting state, which results in higher resting $[Na^+]$ and correspondingly lower $E_{Na,}$ and an overall hyperpolarization of the model compared to the DynDyn model with default pump parameters. This more hyperpolarized state results in lower firing rates, all compared to default pump parameters.

The slope of spike rate adaptation s_{adapt} (Figure 7B) is also almost independent of all three pump parameters over a wide range, except for very large values of NaH (which produce steeply negative spike rate adaptation slopes), and very small values of NaS (which produce less spike rate adaptation). This latter effect occurs because the very steep dependence of pump activation on $[Na^+]$ for small values of NaS means that sodium influx due to a few spikes can rapidly activate the pump at the beginning of the 5 s injection, leaving little room for further pump activation and spike rate adaptation toward the end of the 5 s injection, where s_{adapt} is measured.

The influence of all three pump parameters on AHP amplitude and half-duration $T_{1/2}$ (Figures 7C,D) is monotonic and straightforward. AHPs are deeper (more negative values of AHPamp, Figure 7C) for larger $I_{pumpmax}$ (because the pump is stronger), lower values of NaH (because the pump is activated at lower sodium concentrations), and lower values of NaS (because the pump activates over a narrower range of concentrations). In all three cases (three columns in Figure 7), larger AHP amplitudes (more negative values in Figure 7C) go along with shorter AHP half-durations (Figure 7D). This means that all three parameters can tune the AHP between a deep and pointy shape and a long and shallow shape, albeit the influence of NaH on $T_{1/2}$ is relatively modest (Figure 7D, middle).

Taken together, our results illustrate that—at least in our simple neuron and pump model—pump parameters can vary widely while resulting in the same qualitative model behavior. Our results will therefore likely generalize to more complex pump and neuron models. Features of spiking and AHP, such as IFR, spike rate adaptation, and AHP amplitude, duration, and shape, are controlled by the interaction of all dynamic pump parameters, rather than one pump parameter controlling one activity or AHP feature independently. Our model therefore predicts that neuromodulation of pump currents or genetic alterations of pump proteins that affect the pump's dependence on a dynamic intracellular sodium concentration can have complex and at times counter-intuitive effects that can be understood with the help of computational modeling.

Modulation of pump properties shapes diversity of neuronal activity patterns

While manually sampling and exploring pump parameter space, we encountered a variety of pump parameter combinations that produced diverse activity patterns beyond our default model's silence in the absence of current injection, and spiking response to 5 s current injection (Figures 2–4) or ramp or zap current injections (Figure 5). While a comprehensive exploration of the entire three-dimensional parameter space spanned by $I_{pumpmax}$, NaH, and NaS is beyond the scope of this paper, Figure 8 illustrates examples of such different neuronal dynamics. Note that the examples in Figure 8 differ only in their three pump parameters, but have otherwise identical membrane conductance amplitudes and voltage-dependent dynamics, the same as our default DynDyn model.

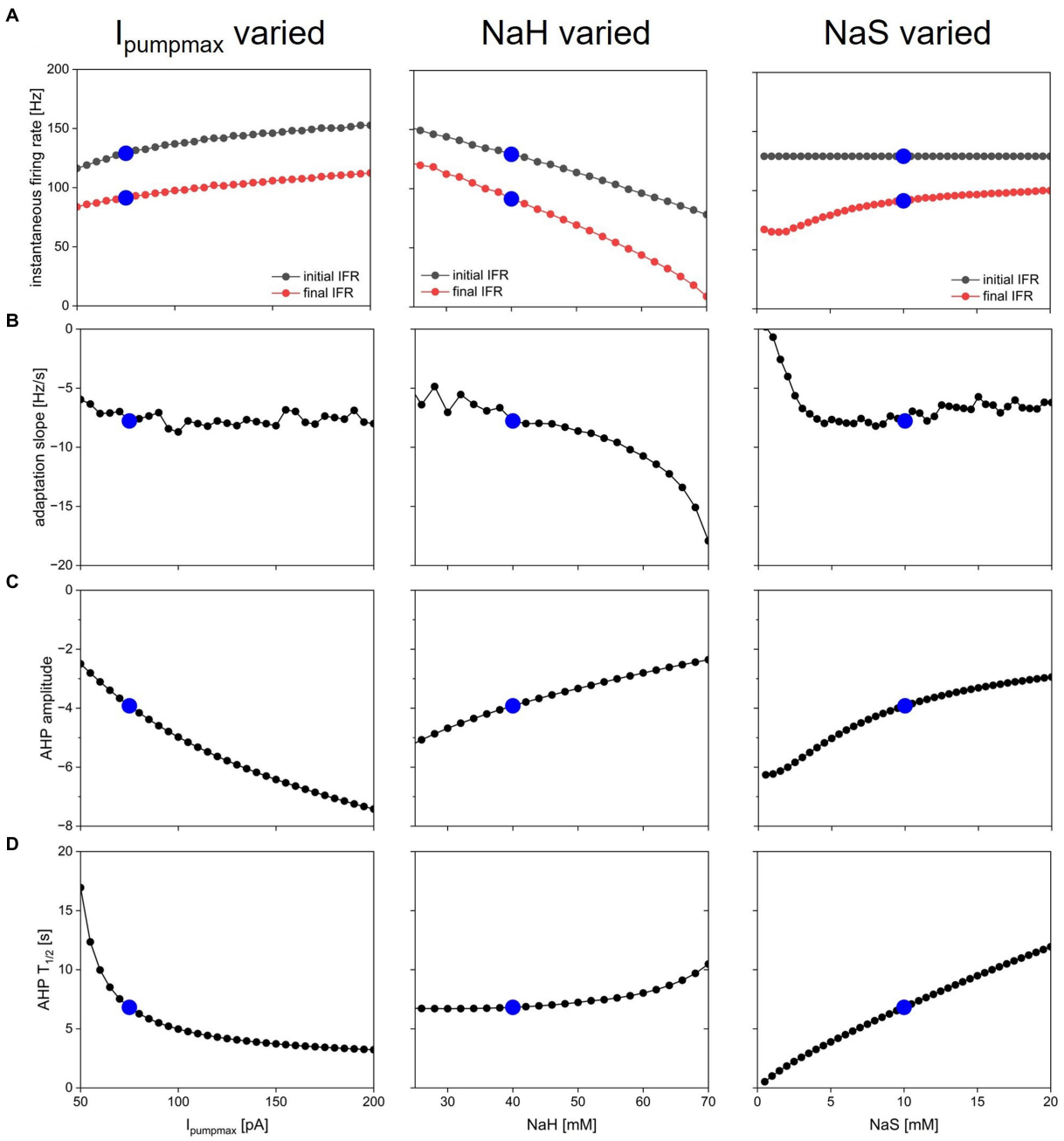

FIGURE 7
Dependence of spiking activity and AHP features on pump parameters. Each column shows variation of one pump parameter while keeping the other two at default value. Parameters varied were maximal pump current $I_{pumpmax}$ (left column), sodium concentration NaH of pump half-activation (Peters et al., 2018), and slope factor NaS of pump sodium-dependence (Palmer et al., 2021). Blue dots show default value in each panel. **(A)** Initial (black) and final (Carballo-Pacheco et al., 2019) instantaneous firing rate in response to a step current injection of 50 pA amplitude and 5 s duration (same stimulus as in Figure 3). **(B)** Spike rate adaptation slope s_{adapt} from same simulations. **(C)** AHP amplitude. **(D)** AHP half duration.

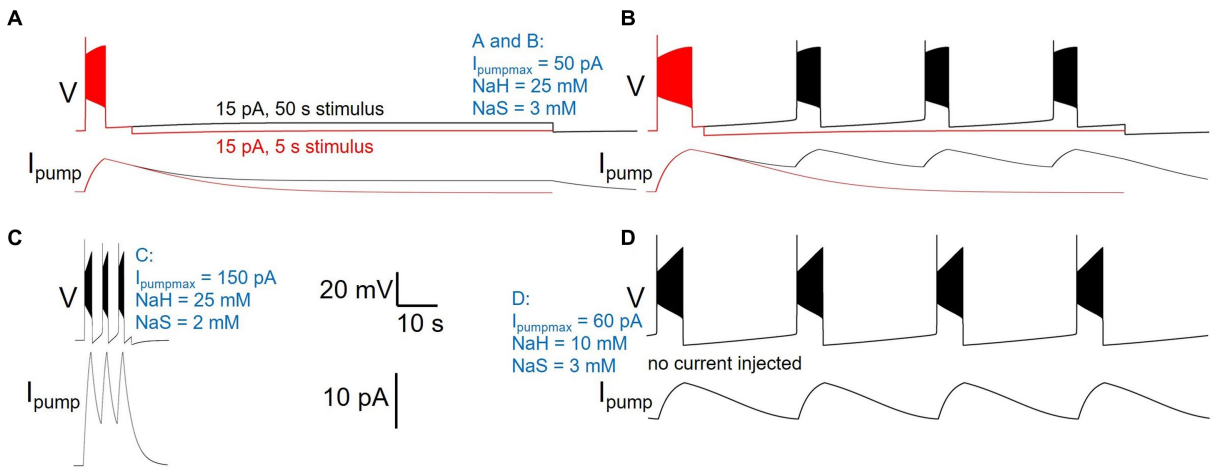

FIGURE 8
Different pump parameters produce a variety of activity types. Four examples of model version DynDyn with pump parameters varied (given in blue), but all other model parameters identical. **(A)** Pump parameters $I_{pumpmax}$ = 50 pA, NaH = 25 mM, NaS = 3 mM produce premature termination of spiking in response to 15 pA, 5 s current injection (Carballo-Pacheco et al., 2019). Spiking does not resume when 15 pA is continued for 50 s (black). Top: voltage; bottom: pump current. **(B)** In response to 20 pA, 5 s current injection, same pump parameters as in panel **(A)** also produce premature spike termination (Carballo-Pacheco et al., 2019), but 50 s injection reveals repetitive bursting with 13.73 s burst period, 2.51 s burst duration, and 0.18 duty cycle (black). **(C)** Pump parameters $I_{pumpmax}$ = 150 pA, NaH = 25 mM, NaS = 2 mM produce repetitive bursting with 1.69 s burst period, 0.57 s burst duration, and 0.33 duty cycle in response to 15 pA, 5 s current injection. **(D)** With pump parameters $I_{pumpmax}$ = 60 pA, NaH = 10 mM, NaS = 3 mM, the model neuron becomes an endogenous burster in the absence of current injection, with 14.9 s burst period, 2.8 s burst duration, and 0.19 duty cycle. Same scale bars (bottom center of figure) apply to panels **(A–D)**.

Many pump parameter combinations produce continuous spiking in response to a step current injection of sufficient amplitude, as in Figures 2–4, but for a subset of pump parameter combinations we explored, spiking terminates before the end of 5 s stimuli of low current amplitude, as described above and shown in Figure 8A, where continuation of the stimulus current for 50 s reveals no further spiking, but a slightly depolarized silent state. In contrast, the same pump parameter combination (parameter values listed in Figure 8 caption, and in blue in the figure) enters a repetitive bursting regime when the injection current is slightly increased, from 15 to 20 pA (Figure 8B). We observed repetitive bursting in response to constant, small current injection for multiple pump parameter combinations, with burst periods, burst durations, and duty cycles (burst duration divided by burst period) covering wide ranges—Figure 8C shows an example of a pump parameter set that produces bursting on a much shorter time scale compared to that in Figure 8B. Finally, for some combinations of pump parameters, the DynDyn model neuron was transformed from a silent neuron in the absence of current injection, to an endogenously bursting neuron with oscillations of membrane potential and the $[Na^+]/E_{Na}/I_{pump}$ system even without current injection (Figure 8D). A simple Na/K pump model in the context of a basic model neuron, as we explored here, can therefore endow the neuron with oscillatory properties on various time scales. This demonstrates that pump currents and dynamics of $[Na^+]$ and E_{Na} can substantially contribute to the richness of neuronal activity and response properties.

Discussion

Here, we explore how modulation of Na/K pump activity sculpts intrinsic properties in a conductance-based model of an invertebrate motor neuron. We find that long-lasting AHPs following spike trains can be generated in a model neuron in which Na/K pump activity is modeled by a single type of Na/K pump that is dependent on a dynamically varying internal sodium concentration and a dynamically changing E_{Na} (model version DynDyn, Figure 3). AHPs can also be generated in models in which intracellular sodium is dynamic but E_{Na} is fixed (DynCon, Figure 3). We found that modeling E_{Na} as a dynamic variable can have profound effects on neuronal excitability. Strikingly, DynDyn models showed strong apparent spike frequency adaptation in response to current pulses. They also showed strong hysteresis in response to ramp up/ramp down stimuli, whereas ConCon models (with constant internal sodium and E_{Na}) showed largely symmetric responses and very limited hysteresis (Figure 5). Similarly, DynDyn models showed asymmetric responses to oscillatory stimulation with oscillation frequencies accelerating and decelerating over a wide range (Figure 6). This suggests that dynamic E_{Na} could play a key supporting role in spike frequency adaptation and in encoding sodium pump mediated cellular memory in a variety of neuron types.

E_{Na} is widely considered to be a static parameter in neurons and is often modeled as such (Prinz et al., 2004; Catterall et al., 2012; Gunay et al., 2015). Traditional intracellular recording techniques by their nature tend to clamp or stabilize ionic concentrations inside and outside cells. In order to record from cells, it is necessary to expose them to relatively large volumes of physiological saline, and in some cases to largely dialyze out their internal solution, with patch pipette solutions. These recording conditions may impede a neuron's activity to influence ionic concentrations sufficiently to affect E_{Na}. In the animal however, where extracellular spaces are restricted by glial wrapping (Flanagan et al., 2018), cellular activity could conceivably shape ionic concentrations sufficiently to

modulate E_{Na}. Indeed multiple studies have used sodium sensitive dyes to show that bursts of activity in neurons and glia and even in cardiac cells can generate changes in intracellular sodium that could conceivably shift E_{Na} to a similar degree as seen in our model (Levi et al., 1997; Gulledge et al., 2013; Gerkau et al., 2019; Felix et al., 2020). Further, intracellular sodium gradients have been shown to change substantially over developmental time in the vertebrate nervous system (Lindsly et al., 2017). Our modeling suggests that dynamic E_{Na} could enrich cellular memory mechanisms. This raises the interesting (and unnerving) possibility that whole-cell recording techniques may be masking important and potentially highly conserved E_{Na} based intrinsic memory mechanisms in neurons. Hodgkin-Huxley type neuron models increasingly include simulations of intracellular and even extracellular ion concentrations, which enable researchers to explore how dynamically changing equilibrium potentials could shape excitability (Florence et al., 2009; Zylbertal et al., 2015, 2017a; Saetra et al., 2021). Non-invasive methods for optically measuring voltage could enable more detailed experiment study of processes that depend on dynamic E_{Na} and other equilibrium potentials (Miyazaki and Ross, 2015; Abdelfattah et al., 2019; Xie et al., 2021). However, voltage imaging methods may also increasingly generate results that conflict with or diverge from those obtained using traditional electrophysiological methods. Presence or absence of dynamic equilibrium potentials across preparations, and details of the recording technique used (sharp electrode vs. whole cell vs. perforated patch), could help explain these divergences.

Pump currents, together with the dynamics of intracellular sodium concentration and reversal potential, produce a long slow AHP that is evident in the membrane potential measured in electrophysiology experiments. Previous work has demonstrated how this long-lasting hyperpolarization allows cells to retain a memory of previous spiking through de-inactivation of voltage gated I_A channels (Pulver and Griffith, 2010). But our results suggest that beyond what is typically considered the duration of the AHP—at a time after vigorous activity when the measured membrane potential has returned to within a fraction of 1 mV of the resting membrane potential—the consequence of a dynamic $[Na^+]/E_{Na}$/pump system can still silently shape neuronal excitability (Figure 4). These dynamics therefore create a window of 'silent' cellular memory for previous electrical activity that extends well beyond the experimentally obvious AHP. In our model, this memory mechanism arises solely from subtle lingering elevations of the sodium concentration that are only gradually returned to baseline because of the closely balanced interactions between inward sodium flux through membrane conductances, and outward sodium ion movement via the pump. This long-lasting biochemical integrator would be effectively invisible to noisy experimental voltage recording, but could shape responses to synaptic inputs in unpredictable ways. Optical imaging of sodium within neurons is a way to resolve whether these subtle events are present in living neurons, and explore how they interact with signaling molecules generated in neurons with more complex mixtures of ion channels and exchangers (Miyazaki and Ross, 2015; Zylbertal et al., 2015; Meyer et al., 2022).

The slow dynamics of $[Na^+]$ and E_{Na} influenced by Na/K pump action can furthermore shape the responses of a neuron to oscillatory inputs (Figure 6). Surprisingly, these dynamics can encode memories not just for prior spiking activity, but also for subthreshold membrane potential oscillations on a variety of time scales. Motor systems—particularly those of invertebrates—often operate on the time scale of seconds or tens of seconds and employ not only spike-mediated, but also graded synaptic transmission, in which transmitter release is dependent on subthreshold membrane potential fluctuations (Prinz et al., 2003; Ivanov and Calabrese, 2006a,b). Previous work has characterized how pump currents can mediate memory of spiking and how neuromodulators sculpt those memories (Hachoumi et al., 2022). Our results suggest that pump-based cellular memory could have further profound effects on motor systems because it can shape motor neuron recruitment patterns in a manner that is dependent on both prior spiking and subthreshold activity of the motor system, as well as its neuromodulatory state.

Pump properties can also generate what appears at first to be a relatively simple spike frequency adaptation; but upon further investigation it is actually a manifestation of a slow bursting mechanism (Figure 8). Whether or not this bursting mechanism is apparent on any given time scale will be determined in part by the combination of sodium pump parameters in a given cell and the experimental protocols used for measuring excitability. Previous work has demonstrated how Na/K pumps can interact with hyperpolarization-activated currents I_h to generate episodic bursting in vertebrate spinal cord (Sharples et al., 2021) and leech heartbeat generator (Kueh et al., 2016). Extensive work in cardiac physiology has also demonstrated a key role for Na/K pumps in myogenic rhythms (reviewed in McDonough et al., 2002). Our results demonstrate that a simpler bursting mechanism is also possible in which depolarizations lead to bursts of spikes that trigger sodium influx. This then shifts E_{Na} and activates an outward current which hyperpolarizes neurons, and restarts a cycle. Similar bursting and oscillations with involvement of the Na/K pump current have previously been described in another simple Hodgkin-Huxley-type model and analyzed using a dynamical systems approach to separate the fast (spiking) time scale from a slow time scale arising from pump contributions to ion concentration changes (Barreto and Cressman, 2011). Bursting with pump involvement has further been noted in more complex individual neurons and in small circuits of more complex neurons with pumps and additional synaptic dynamics (Zylbertal et al., 2017b), or as arising from the interaction of pump-supported intrinsic dynamics and network connectivity (Zylbertal et al., 2017b). In our model, bursting occurs in the absence of membrane currents that typically support bursting dynamics, such as the hyperpolarization-activated current I_h, or oscillations on the basis of calcium currents and the calcium-dependent potassium current I_{KCa}. Pump-supported oscillation cycles can be remarkably long (i.e., tens of seconds, Figure 8) and therefore could be playing important evolutionarily conserved roles in generating oscillations underlying longer time scale rhythmic activities like sleep (Tabuchi et al., 2018) and mating (Wagenaar et al., 2010). Indeed, sodium dependent mechanisms are thought to contribute to 'infra-slow' oscillations in vertebrate olfactory neurons (Wagenaar et al., 2010; Zylbertal et al., 2017b).

Our exploration of pump parameter space suggests that in addition to affecting the responsiveness of a neuron to inputs, pump properties can also qualitatively change the spontaneous activity produced by a neuron. This includes the transformation of silent neurons (that spike or

burst only in response to inputs), into endogenously spiking or bursting neurons via moderate changes to the dependence of pump activation on the intracellular sodium concentration (Figure 8). Many invertebrate motor circuits are composed of both types of neurons, silent "follower" neurons as well as endogenously oscillating "pacemaker" neurons (reviewed in Marder and Calabrese, 1996; Marder et al., 2022). Furthermore, the same neurons that act as motor neurons and control muscles can also act as interneurons and participate in pattern generation based on their oscillatory and response properties. Modifying pump properties that affect these neurons' excitability and responsiveness, for example through neuromodulation, could therefore provide mechanisms to sculpt rhythm generation with pumps playing roles that go beyond simple cellular housekeeping.

Studies of invertebrate neural circuits have consistently demonstrated a core principle: to understand how a circuit generates outputs, it is critical to measure the dynamics of synaptic transmission and the dynamic intrinsic properties of individual neurons within a circuit. The dynamics of synaptic transmission and voltage-gated ionic conductances in identified neurons within circuits have been well explored in multiple systems (reviewed in Marder and Calabrese, 1996; Marder et al., 2022). However, the dynamics of Na/K pump currents are less well understood. Given that Na/K pumps are highly conserved across all animal phyla, and play fundamental roles in shaping excitability, it makes sense to establish knowledgebases for understanding how dynamics of pump activity influence intrinsic properties of neurons, which, in turn, shape neural circuit activity. Genetically tractable invertebrate nervous systems such as the *Drosophila* larval locomotor system, in combination with computational modeling, provide attractive vehicles for crawling into this space.

Data availability statement

The original contributions presented in the study are included in the article/supplementary material, further inquiries can be directed to the corresponding authors.

Author contributions

OM, LP, and CG designed, conducted, and analyzed experiments and contributed to manuscript writing. SP and AP designed and analyzed the experiments and wrote the manuscript. All authors contributed to the article and approved the submitted version.

Funding

This work was supported by a Royal Society Research Grant to SP (RG150108), Collaborative Research Grant funding by the Halle Institute for Global Research at Emory University and university of St Andrews to SP and AP, a Wellcome Trust Seed Award to SP (105621/Z/14/Z), a Emory Computational Neuroscience Fellowship stipend to OM, support from Emory University's Graduate Division of Biological and Biomedical Sciences and from the George W. Woodruff Fellowship for LP, and VPASA Seed Grant funding at Georgia Gwinnett College awarded to CG.

Acknowledgments

The authors thank Ben Orli-Nathanson, Julius Jonaitis, and Lindsay Hexter for their valuable contributions during the initial phases of this project. We would like to thank Eve Marder, Leslie Griffith, Don Katz, and the Brandeis University Neuroscience Program for supporting inspirational work on invertebrate and vertebrate neural circuits, and for the Brandeis community's steadfast commitment to training and mentoring young scientists over many decades.

Conflict of interest

The authors declare that the research was conducted in the absence of any commercial or financial relationships that could be construed as a potential conflict of interest.

Publisher's note

References

Abdelfattah, A. S., Kawashima, T., Singh, A., Novak, O., Liu, H., Shuai, Y., et al. (2019). Bright and photostable chemigenetic indicators for extended in vivo voltage imaging. *Science* 365, 699–704. doi: 10.1126/science.aav6416

Barreto, E., and Cressman, J. R. (2011). Ion concentration dynamics as a mechanism for neuronal bursting. *J. Biol. Phys.* 37, 361–373. doi: 10.1007/s10867-010-9212-6

Carballo-Pacheco, M., Desponds, J., Gavrilchenko, T., Mayer, A., Prizak, R., Reddy, G., et al. (2019). Receptor crosstalk improves concentration sensing of multiple ligands. *Phys. Rev. E* 99:022423. doi: 10.1103/PhysRevE.99.022423

Catterall, W. A., Raman, I. M., Robinson, H. P., Sejnowski, T. J., and Paulsen, O. (2012). The Hodgkin-Huxley heritage: from channels to circuits. *J. Neurosci.* 32, 14064–14073. doi: 10.1523/JNEUROSCI.3403-12.2012

Ellingson, P. J., Barnett, W. H., Kueh, D., Vargas, A., Calabrese, R. L., and Cymbalyuk, G. S. (2021). Comodulation of h- and Na(+)/K(+) pump currents expands the range of functional bursting in a central pattern generator by navigating between dysfunctional regimes. *J. Neurosci.* 41, 6468–6483. doi: 10.1523/JNEUROSCI.0158-21.2021

Felix, L., Delekate, A., Petzold, G. C., and Rose, C. R. (2020). Sodium fluctuations in astroglia and their potential impact on astrocyte function. *Front. Physiol.* 11:871. doi: 10.3389/fphys.2020.00871

Flanagan, B., Mcdaid, L., Wade, J., Wong-Lin, K., and Harkin, J. (2018). A computational study of astrocytic glutamate influence on post-synaptic neuronal excitability. *PLoS Comput. Biol.* 14:e1006040. doi: 10.1371/journal.pcbi.1006040

Florence, G., Dahlem, M. A., Almeida, A. C., Bassani, J. W., and Kurths, J. (2009). The role of extracellular potassium dynamics in the different stages of ictal bursting and spreading depression: a computational study. *J. Theor. Biol.* 258, 219–228. doi: 10.1016/j.jtbi.2009.01.032

Forrest, M. D., Wall, M. J., Press, D. A., and Feng, J. (2012). The sodium-potassium pump controls the intrinsic firing of the cerebellar Purkinje neuron. *PLoS One* 7:e51169. doi: 10.1371/journal.pone.0051169

Gerkau, N. J., Lerchundi, R., Nelson, J. S. E., Lantermann, M., Meyer, J., Hirrlinger, J., et al. (2019). Relation between activity-induced intracellular sodium transients and Atp dynamics in mouse hippocampal neurons. *J. Physiol.* 597, 5687–5705. doi: 10.1113/JP278658

Gulledge, A. T., Dasari, S., Onoue, K., Stephens, E. K., Hasse, J. M., and Avesar, D. (2013). A sodium-pump-mediated afterhyperpolarization in pyramidal neurons. *J. Neurosci.* 33, 13025–13041. doi: 10.1523/JNEUROSCI.0220-13.2013

Gunay, C., Sieling, F. H., Dharmar, L., Lin, W. H., Wolfram, V., Marley, R., et al. (2015). Distal spike initiation zone location estimation by morphological simulation of ionic current filtering demonstrated in a novel model of an identified Drosophila motoneuron. *PLoS Comput. Biol.* 11:e1004189. doi: 10.1371/journal.pcbi.1004189

Hachoumi, L., Rensner, R., Richmond, C., Picton, L., Zhang, H., and Sillar, K. T. (2022). Bimodal modulation of short-term motor memory via dynamic sodium pumps in a vertebrate spinal cord. *Curr. Biol.* 32, 1038–1048.e2. doi: 10.1016/j.cub.2022.01.012

Holm, T. H., and Lykke-Hartmann, K. (2016). Insights into the pathology of the α3 Na+/K+-atpase ion pump in neurological disorders; lessons from animal models. *Front. Physiol.* 7:209. doi: 10.3389/fphys.2016.00209

Hutcheon, B., and Yarom, Y. (2000). Resonance, oscillation and the intrinsic frequency preferences of neurons. *Trends Neurosci.* 23, 216–222. doi: 10.1016/S0166-2236(00)01547-2

Isaksen, T. J., and Lykke-Hartmann, K. (2016). Insights into the pathology of the α2-Na+/K+-atpase in neurological disorders; lessons from animal models. *Front. Physiol.* 7:161. doi: 10.3389/fphys.2016.00161

Ivanov, A. I., and Calabrese, R. L. (2006a). Graded inhibitory synaptic transmission between leech interneurons: assessing the roles of two kinetically distinct low-threshold Ca currents. *J. Neurophysiol.* 96, 218–234. doi: 10.1152/jn.01093.2005

Ivanov, A. I., and Calabrese, R. L. (2006b). Spike-mediated and graded inhibitory synaptic transmission between leech interneurons: evidence for shared release sites. *J. Neurophysiol.* 96, 235–251. doi: 10.1152/jn.01094.2005

Kaplan, J. H. (2002). Biochemistry of Na,K-Atpase. *Annu. Rev. Biochem.* 71, 511–535. doi: 10.1146/annurev.biochem.71.102201.141218

Kay, L. M., and Stopfer, M. (2006). Information processing in the olfactory systems of insects and vertebrates. *Semin. Cell Dev. Biol.* 17, 433–442. doi: 10.1016/j.semcdb.2006.04.012

Kueh, D., Barnett, W. H., Cymbalyuk, G. S., and Calabrese, R. L. (2016). Na(+)/K(+) pump interacts with the h-current to control bursting activity in central pattern generator neurons of leeches. *Elife* 5:e19322. doi: 10.7554/eLife.19322

Levi, A. J., Dalton, G. R., Hancox, J. C., Mitcheson, J. S., Issberner, J., Bates, J. A., et al. (1997). Role of intracellular sodium overload in the genesis of cardiac arrhythmias. *J. Cardiovasc. Electrophysiol.* 8, 700–721. doi: 10.1111/j.1540-8167.1997.tb01834.x

Lin, W. H., Gunay, C., Marley, R., Prinz, A. A., and Baines, R. A. (2012). Activity-dependent alternative splicing increases persistent sodium current and promotes seizure. *J. Neurosci.* 32, 7267–7277. doi: 10.1523/JNEUROSCI.6042-11.2012

Lindsly, C., Gonzalez-Islas, C., and Wenner, P. (2017). Elevated intracellular Na(+) concentrations in developing spinal neurons. *J. Neurochem.* 140, 755–765. doi: 10.1111/jnc.13936

Marder, E., and Calabrese, R. L. (1996). Principles of rhythmic motor pattern generation. *Physiol. Rev.* 76, 687–717. doi: 10.1152/physrev.1996.76.3.687

Marder, E., Kedia, S., and Morozova, E. O. (2022). New insights from small rhythmic circuits. *Curr. Opin. Neurobiol.* 76:102610. doi: 10.1016/j.conb.2022.102610

Mcdonough, A. A., Velotta, J. B., Schwinger, R. H., Philipson, K. D., and Farley, R. A. (2002). The cardiac sodium pump: structure and function. *Basic Res. Cardiol.* 97, 119–124. doi: 10.1007/s003950200024

Meyer, D. J., Diaz-Garcia, C. M., Nathwani, N., Rahman, M., and Yellen, G. (2022). The Na(+)/K(+) pump dominates control of glycolysis in hippocampal dentate granule cells. *Elife* 11:e81645. doi: 10.7554/eLife.81645

Miyazaki, K., and Ross, W. N. (2015). Simultaneous sodium and calcium imaging from dendrites and axons. *eNeuro* 2, 1–10. doi: 10.1523/ENEURO.0092-15.2015

Palmer, S. E., Wright, B. D., Doupe, A. J., and Kao, M. H. (2021). Variable but not random: temporal pattern coding in a songbird brain area necessary for song modification. *J. Neurophysiol.* 125, 540–555. doi: 10.1152/jn.00034.2019

Peters, D. M., Fridriksson, J., Stewart, J. C., Richardson, J. D., Rorden, C., Bonilha, L., et al. (2018). Cortical disconnection of the ipsilesional primary motor cortex is associated with gait speed and upper extremity motor impairment in chronic left hemispheric stroke. *Hum. Brain Mapp.* 39, 120–132. doi: 10.1002/hbm.23829

Picton, L. D., Nascimento, F., Broadhead, M. J., Sillar, K. T., and Miles, G. B. (2017a). Sodium pumps mediate activity-dependent changes in mammalian motor networks. *J. Neurosci.* 37, 906–921. doi: 10.1523/JNEUROSCI.2005-16.2016

Picton, L. D., Sillar, K. T., and Zhang, H. Y. (2018). Control of xenopus tadpole locomotion via selective expression of Ih in excitatory interneurons. *Curr. Biol.* 28, 3911–3923. e2. doi: 10.1016/j.cub.2018.10.048

Picton, L. D., Zhang, H., and Sillar, K. T. (2017b). Sodium pump regulation of locomotor control circuits. *J. Neurophysiol.* 118, 1070–1081. doi: 10.1152/jn.00066.2017

Prinz, A. A., Bucher, D., and Marder, E. (2004). Similar network activity from disparate circuit parameters. *Nat. Neurosci.* 7, 1345–1352. doi: 10.1038/nn1352

Prinz, A. A., Thirumalai, V., and Marder, E. (2003). The functional consequences of changes in the strength and duration of synaptic inputs to oscillatory neurons. *J. Neurosci.* 23, 943–954. doi: 10.1523/JNEUROSCI.23-03-00943.2003

Pulver, S. R., Bayley, T. G., Taylor, A. L., Berni, J., Bate, M., and Hedwig, B. (2015). Imaging fictive locomotor patterns in larval Drosophila. *J. Neurophysiol.* 114, 2564–2577. doi: 10.1152/jn.00731.2015

Pulver, S. R., and Griffith, L. C. (2010). Spike integration and cellular memory in a rhythmic network from Na+/K+ pump current dynamics. *Nat. Neurosci.* 13, 53–59. doi: 10.1038/nn.2444

Saetra, M. J., Einevoll, G. T., and Halnes, G. (2021). An electrodiffusive neuron-extracellular-glia model for exploring the genesis of slow potentials in the brain. *PLoS Comput. Biol.* 17:e1008143. doi: 10.1371/journal.pcbi.1008143

Scuri, R., Lombardo, P., Cataldo, E., Ristori, C., and Brunelli, M. (2007). Inhibition of Na+/K+ atpase potentiates synaptic transmission in tactile sensory neurons of the leech. *Eur. J. Neurosci.* 25, 159–167. doi: 10.1111/j.1460-9568.2006.05257.x

Sharples, S. A., Parker, J., Vargas, A., Milla-Cruz, J. J., Lognon, A. P., Cheng, N., et al. (2021). Contributions of h- and Na(+)/K(+) pump currents to the generation of episodic and continuous rhythmic activities. *Front. Cell. Neurosci.* 15:715427. doi: 10.3389/fncel.2021.715427

Tabuchi, M., Monaco, J. D., Duan, G., Bell, B., Liu, S., Liu, Q., et al. (2018). Clock-generated temporal codes determine synaptic plasticity to control sleep. *Cells* 175, 1213–1227.e18. doi: 10.1016/j.cell.2018.09.016

Tohidi, V., and Nadim, F. (2009). Membrane resonance in bursting pacemaker neurons of an oscillatory network is correlated with network frequency. *J. Neurosci.* 29, 6427–6435. doi: 10.1523/JNEUROSCI.0545-09.2009

Tseng, H. A., and Nadim, F. (2010). The membrane potential waveform of bursting pacemaker neurons is a predictor of their preferred frequency and the network cycle frequency. *J. Neurosci.* 30, 10809–10819. doi: 10.1523/JNEUROSCI.1818-10.2010

Wagenaar, D. A., Hamilton, M. S., Huang, T., Kristan, W. B., and French, K. A. (2010). A hormone-activated central pattern generator for courtship. *Curr. Biol.* 20, 487–495. doi: 10.1016/j.cub.2010.02.027

Xie, M. E., Adam, Y., Fan, L. Z., Bohm, U. L., Kinsella, I., Zhou, D., et al. (2021). High-fidelity estimates of spikes and subthreshold waveforms from 1-photon voltage imaging in vivo. *Cell Rep.* 35:108954. doi: 10.1016/j.celrep.2021.108954

Zhang, H. Y., and Sillar, K. T. (2012). Short-term memory of motor network performance via activity-dependent potentiation of Na+/K+ pump function. *Curr. Biol.* 22, 526–531. doi: 10.1016/j.cub.2012.01.058

Zylbertal, A., Kahan, A., Ben-Shaul, Y., Yarom, Y., and Wagner, S. (2015). Prolonged intracellular Na+ dynamics govern electrical activity in accessory olfactory bulb mitral cells. *PLoS Biol.* 13:e1002319. doi: 10.1371/journal.pbio.1002319

Zylbertal, A., Yarom, Y., and Wagner, S. (2017a). The slow dynamics of intracellular sodium concentration increase the time window of neuronal integration: a simulation study. *Front. Comput. Neurosci.* 11:85. doi: 10.3389/fncom.2017.00085

Zylbertal, A., Yarom, Y., and Wagner, S. (2017b). Synchronous infra-slow bursting in the mouse accessory olfactory bulb emerge from interplay between intrinsic neuronal dynamics and network connectivity. *J. Neurosci.* 37, 2656–2672. doi: 10.1523/JNEUROSCI.3107-16.2017

frontiers | Frontiers in Neuroscience

TYPE Brief Research Report
PUBLISHED 02 June 2023
DOI 10.3389/fnins.2023.1125476

OPEN ACCESS

EDITED BY
James Newcomb,
New England College, United States

REVIEWED BY
Kei Jokura,
University of Exeter, United Kingdom
Maria Sachkova,
University of Bergen, Norway

*CORRESPONDENCE
Leonid L. Moroz
✉ moroz@whitney.ufl.edu

†These authors have contributed equally to this work

RECEIVED 16 December 2022
ACCEPTED 03 May 2023
PUBLISHED 02 June 2023

CITATION
Norekian TP and Moroz LL (2023) Recording cilia activity in ctenophores: effects of nitric oxide and low molecular weight transmitters. *Front. Neurosci.* 17:1125476. doi: 10.3389/fnins.2023.1125476

Recording cilia activity in ctenophores: effects of nitric oxide and low molecular weight transmitters

Tigran P. Norekian[1,2†] and Leonid L. Moroz[1,3*†]

[1]Whitney Laboratory for Marine Bioscience, University of Florida, St. Augustine, FL, United States, [2]Friday Harbor Laboratories, University of Washington, Friday Harbor, WA, United States, [3]Departments of Neuroscience and McKnight, Brain Institute, University of Florida, Gainesville, FL, United States

Cilia are the major effectors in Ctenophores, but very little is known about their transmitter control and integration. Here, we present a simple protocol to monitor and quantify cilia activity and provide evidence for polysynaptic control of cilia coordination in ctenophores. We also screened the effects of several classical bilaterian neurotransmitters (acetylcholine, dopamine, L-DOPA, serotonin, octopamine, histamine, gamma-aminobutyric acid (GABA), L-aspartate, L-glutamate, glycine), neuropeptide (FMRFamide), and nitric oxide (NO) on cilia beating in *Pleurobrachia bachei* and *Bolinopsis infundibulum*. NO and FMRFamide produced noticeable inhibitory effects on cilia activity, whereas other tested transmitters were ineffective. These findings further suggest that ctenophore-specific neuropeptides could be major candidates for signal molecules controlling cilia activity in representatives of this early-branching metazoan lineage.

KEYWORDS

Ctenophora, electrophysiology, behavior, neuropeptides, nitric oxide, Pleurobrachia, Bolinopsis, Mnemiopsis

Introduction

The phylum Ctenophora represents descendants of the earliest animal group, sister to the rest of Metazoa (e.g., Moroz et al., 2014; Whelan et al., 2017; Li et al., 2021; Schultz et al., 2023). Ctenophores or comb jellies have the largest cilia in the animal kingdom, primarily used for complex locomotion in most species within this phylum. Moreover, cilia contribute to the majority of functions and behaviors of ctenophores (Tamm, 1982; Tamm, 2014). One primary example is ctene rows, which consist of the large mechanically fused swim cilia (ctene plates) used by ctenophores to move in the water column. The coordination of multiple behaviors in ctenophores is controlled by variations in the activity of swim cilia, and these mechanisms were under intensive investigation (Tamm and Tamm, 1981; Tamm, 1983, 1984; Nakamura and Tamm, 1985; Moss and Tamm, 1986, 1987; Tamm, 1988; Tamm and Tamm, 1988; Tamm and Terasaki, 1994).

Although cilia are the main effectors in ctenophores, with presumed neuronal control and different subtypes of synapses detected by electron microscopy (Hernandez-Nicaise, 1991; Burkhardt et al., 2023), little is known about synaptic regulation and neurotransmitters controlling cilia movement. Initial identification of glutamate as a small signal molecule and neurotransmitter candidate in ctenophores (Moroz et al., 2014, 2020b, 2021) targeted muscular systems. Still, in early experiments, glutamate did not change cilia beating (Moroz et al., 2014), and some ionotropic glutamate receptors were sensitive to glycine (Alberstein et al., 2015; Yu et al., 2016).

It was proposed that neural systems evolved independently in ctenophores by developing a unique molecular and structural organization (Moroz, 2014; Dabe et al., 2015; Kohn et al., 2015; Moroz, 2015; Moroz and Kohn, 2015; Whelan et al., 2015), including a subset of ctenophore-specific secretory peptides that could act as signal molecules (Moroz, 2014; Moroz et al., 2014; Moroz, 2021). Multiple candidates were identified in *Pleurobrachia* and *Mnemiopsis* (Moroz et al., 2014; Moroz and Kohn, 2016). The recent genome-wide and mass spectroscopy survey further expanded the list of secretory peptide candidates and identified some (neuro)peptides involved in the control of cilia beating in juvenile *Mnemiopsis* (Sachkova et al., 2021) and *Bolinopsis* (Hayakawa et al., 2022). However, cellular bases of ctenophore behavior are unknown.

Quantitative recording of cilia activity in ctenophores is equally essential for behavioral and functional analyses in both juvenile and adult animals. First, we described a simple protocol successfully used to quantify the frequency of cilia beating in ctenophores. This protocol can be practical for screening and investigating the physiological roles of different transmitters. Second, we provided initial evidence of (i) polysynaptic control of cilia coordination using chemical transmission, (ii) confirmed negative results of classical bilaterian neurotransmitter action on cilia, and (iii) showed a potential regulatory role of the gaseous molecule, nitric oxide (NO), in cilia beating.

Materials and methods

Large, 1-to-2 cm, *Pleurobrachia bachei* and medium-size, 3-to-4 cm, *Bolinopsis infundibulum* [the updated valid name for this species is currently *Bolinopsis microptera* (Johnson et al., 2023)] were collected from the dock at Friday Harbor Laboratories, University of Washington, in the Pacific Northwest. The animals were tightly pinned to a Sylgard-coated Petri dish (World Precision Instruments, Sylgard Silicone Elastomer, SYLG184) with small steel insect pins to prevent all body movements other than cilia beating. Most animals were used as whole-mount preparations without dissection. However, the larger animals (>2 cm *Pleurobrachia* and 4 cm *Bolinopsis*) were dissected, and parts of a body wall with 2–3 cilia rows were pinned the same way to the Petri dish. Prior to dissection, freshly caught animals were incubated in high magnesium seawater (300 mM $MgCl_2$ added to filtered seawater at a 1:1 ratio) for about 15 min. After dissection, the preparation was washed several times in a regular seawater for over 10 min before the experiment started.

The Petri dish was placed in a standard electrophysiological rig on a recording platform and connected to the Ag/AgCl reference electrode. We used glass microelectrodes (borosilicate glass micropipettes for intracellular recording from World Precision Instruments – standard glass capillaries 2 mm diameter with a thin filament, 1B200F-4), filled with 3 M potassium acetate to record cilia beating. The sharp microelectrodes were pulled using Microelectrode Puller (Sutter Instruments, Flaming/Brown Micropipette Puller P-97). The original resistance of sharp microelectrodes (made for intracellular recordings) was around 30 MΩ. A narrow strip of thin paper was used to carefully touch the tip of the electrode to break off the most fragile sharp end. The resulting electrode was more stable to further mechanical contact and had a resistance of 5–15 MΩ. Electrodes with very low resistances (below 1 MΩ) and wider tips were unsuitable. The electrodes were then connected to the micromanipulators (Warner Instruments, Standard Manual Control Micromanipulators, MM-33) and the intracellular amplifiers (Neuroprobe 1,600, A-M Systems).

With the help of micromanipulators and under visual control via a dissecting microscope (Nikon stereoscopic microscope SMZ-10A), the tip of the electrode was carefully placed next to the cilia combs so that during cilia beating, cilia were touching the end of the electrode (Figure 1A). This physical contact created a brief electrical signal picked up by amplifiers and recorded on paper and in digital form using Gould Recorder (WindoGraf 980). Thus, each cilia beat was translated into a fast electrical spike. Combining electrophysiology with microscopy, we observed a one-to-one relationship between a cilia strike and a recorded electrical signal/spike, which allowed a digital recording of cilia beat frequency. It is important to note that this technique did not allow quantification of cilia beating amplitude and forces – only the frequency. It was crucial for stable recording to have the ctenophore body wall tightly pinned to the Sylgard-coated Petri dish, with no movements except cilia beating.

Most recordings were conducted in freshly filtered seawater. We used high $MgCl_2$ seawater only to suppress chemical/synaptic transmission and excitability in particular experiments described in the results. Muscle contractions were not a problem for cilia recording in tightly pinned preparations. Only in some very active *Bolinopsis* specimens a temporary withdrawal of the entire cilia row inside the body sometimes did interrupt the continuous cilia recording.

To test the possible role of different neurotransmitter candidates in cilia control, we applied them to the recording dish using a graduated 1 mL pipette attached to a long, small-diameter tube. The final concentrations were calculated from the known volume of injected solution and the known volume of the recording dish.

The following candidates for signal molecules were used in these experiments: GABA, acetylcholine, serotonin, glutamate, dopamine, histamine, glycine, aspartate, octopamine, FMRFamide, and two donors of nitric oxide (NOC-9 [6-(2-Hydroxy-1-methyl-2-nitrosohydrazino)-N-methyl-1-hexanamine], diethylamine NONOate [DEA NO or Diethylammonium (Z)-1-(N,N-diethylamino)diazen-1-ium-1,2-diolate], see details in (Maragos et al., 1991; Keefer et al., 1996; Braga et al., 2009; Li et al., 2020). All chemicals were obtained from Sigma. Specifically, we used the following concentrations on both *Pleurobrachia bachei* and *Bolinopsis infundibulum*. Gamma-aminobutyric acid (GABA), total semi-intact preparations $n = 6$, at concentrations: 0.1 mM, 0.2 mM and 0.5 mM (4 independent tests for each concentration– no effect); Acetylcholine (ACh), $n = 5$, at concentrations: 0.1 mM, 0.2 mM, 0.5 mM and (2 independent tests for each concentration – no effect); Serotonin (5-HT), $n = 5$ preparations, at concentrations: 0.1 mM and 0.5 mM (2 independent tests for each concentration – no effect); L-Glutamate, $n = 3$ preparations, at concentrations: 0.5 mM and 0.2 mM (2 independent tests for each concentration – no effect); Dopamine (DA), $n = 3$, at concentrations: 0.1 mM, 0.2 mM and 0.4 mM (3 independent tests for each concentration – no effect); L-DOPA (DA precursor); once at 0.5 mM – no effect; Histamine, $n = 3$; at concentrations: 0.5 mM, 0.4 mM and 0.1 mM (3 independent tests for each concentration – no effect); Glycine, $n = 2$; at concentrations: 0.4 mM, and 0.2 mM (2 independent tests for each concentration – no effect); L-Aspartate, $n = 2$, 0.5 mM and 0.2 mM (2 independent tests for each concentration – no effect); Octopamine, $n = 2$, 0.4 mM and 0.2 mM (2 independent tests for each concentration – no effect); FMRFamide, $n = 8$ preparations at concentrations: 0.2 mM and 0.1 mM (3–5 independent tests for each concentration – suppression of complex patterns of cilia activity in

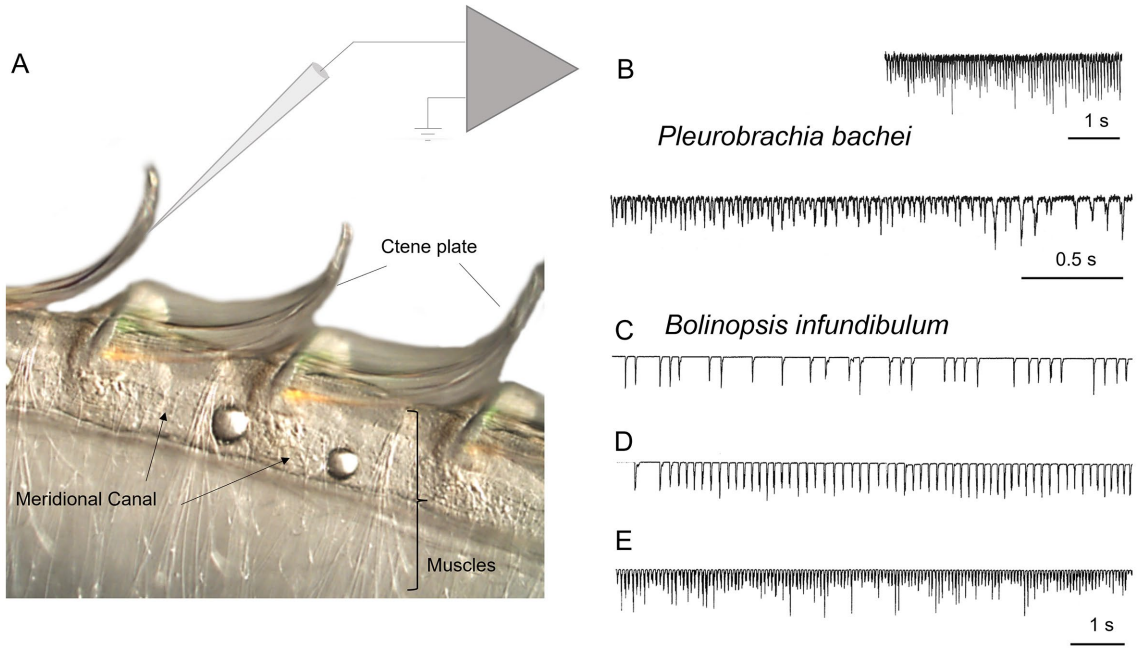

FIGURE 1
Recording cilia activity in *Bolinopsis* and *Pleurobrachia*. **(A)** Schematic diagram showing the position of a recording microelectrode near comb plates in *Bolinopsis* (see text for details). Illustrative examples of cilia beating recording in *Pleurobrachia* **(B)** and *Bolinopsis* **(C–E)**.

combs). Effects of NO donors: NOC-9, $n = 5$, at 0.1 mM and 0.2 mM (3 independent tests for each concentration –inhibition of comb's cilia beating); Diethylamine NONOate, $n = 13$ at subsequent 0.02 mM, 0.06 mM, 0.1 mM, and 0.2 mM in seawater, and $n = 3$ in high MgCl2 (3 independent tests for each condition – inhibition of comb's cilia beating). Details about NO donors and FMRFamide are described in the result section.

To understand whether the possible effect was direct on the cilia cells or indirect via potential interneurons and due to chemical transmission, 'chemical isolation' was used by bathing the preparation in high Mg^{2+} saline for 5–15 min (333 mM $MgCl_2$ was added to filtered seawater at a 1:1 ratio). Elevated magnesium chloride solution suppresses synaptic chemical transmission and is widely used in comparative neurobiology (Del Castillo and Engbaek, 1954; Hutter and Kostial, 1954). All solutions were prepared immediately before use. In all experiments, we checked the effect of a candidate neurotransmitter on the frequency of cilia beating and the occurrence and intensity of bursts. The cilia beating was compared before transmitter application, after application for about 5–30 min, and then after washing in seawater for about 5–15 min (the entire volume of the experimental chamber was replaced by fresh seawater at least 5 times).

Immunohistochemical labeling was performed as described elsewhere using anti-FMRFamide antibody (Cat # AB15348, Sigma-Aldrich). See details about the protocol and *Pleurobrachia* neuroanatomy (Norekian and Moroz, 2019a, 2020).

Results and discussion

In semi-intact preparations, patterns of cilia beating in *Pleurobrachia* were variable, with periods of bursts and inhibitory episodes (Figure 2). Such activity might represent intact behaviors in free-moving *Pleurobrachia* as an ambush predator. In contrast, *Bolinopsis* had more regular cilia beating with fewer activity patterns (Figures 1C–E), also reminiscent of its free-moving behavior. The maximum cilia beat frequency recorded during high-intensity bursting was around 40 Hz in *Pleurobrachia* and 20 Hz in *Bolinopsis* (Figures 1B,E).

The irregular patterns of cilia activity were eliminated in the presence of a high concentration of Mg^{2+}, known to suppress synaptic inputs (Del Castillo and Engbaek, 1954; Hutter and Kostial, 1954). The effect of high Mg^{2+} solution was a regular uniform cilia beating without any high-frequency bursts or inhibitory episodes, which was quickly washed out by rinses in regular seawater to restore the initial patterned activity (Figure 3). These findings indicate the presence of multifaceted regulatory chemical inputs and likely neuronal/secretory control of cilia, which was anticipated from ultrastructural data and neuro-ciliary synapses (Hernandez-Nicaise, 1991).

Cilia excitatory and cilia inhibitory transmitters are unknown for most ctenophore species. A few neuropeptides have been recently identified in *Mnemiopsis leidyi* (Sachkova et al., 2021) and *Bolinopsis* (Hayakawa et al., 2022) as putative signal molecules controlling ciliated locomotion in these species. We performed pharmacological screening of low molecular weight transmitter candidates in our ctenophore preparations. The effects of different signal molecules on cilia beating were similar in *Pleurobrachia* and *Bolinopsis*: no observable effects on the application of selected low molecular weight transmitters and inhibitory action of FMRFamide and nitric oxide donors (see below). Our screening showed an apparent lack of involvement of bilaterian neurotransmitters in the ctenophore cilia activity.

Previous pharmacological and electrophysiological tests were consistent with the hypothesis that L-glutamate could be a

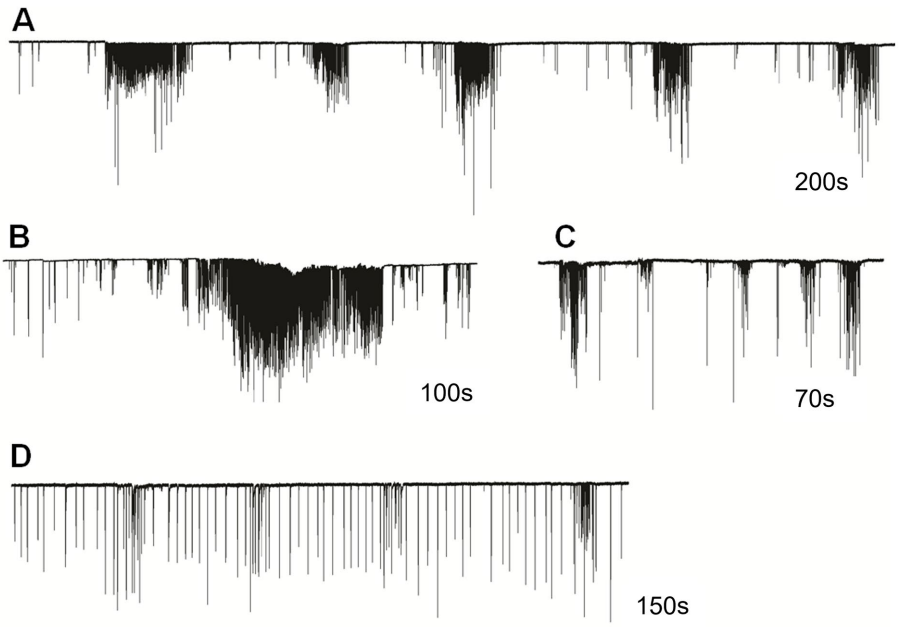

FIGURE 2
Cilia beating in *Pleurobrachia bachei* was very variable and complex, similar to intact behaviors in free-moving animals. For example, **(A)** regular episodes of high-frequency bursting with periods of inhibition between them, **(B)** long-duration powerful bursts of comb cilia strikes, **(C)** irregular unstructured bursting of cilia movements, **(D)** regular cilia beating with possible brief episodes of acceleration. Numbers under all traces show the duration of recordings.

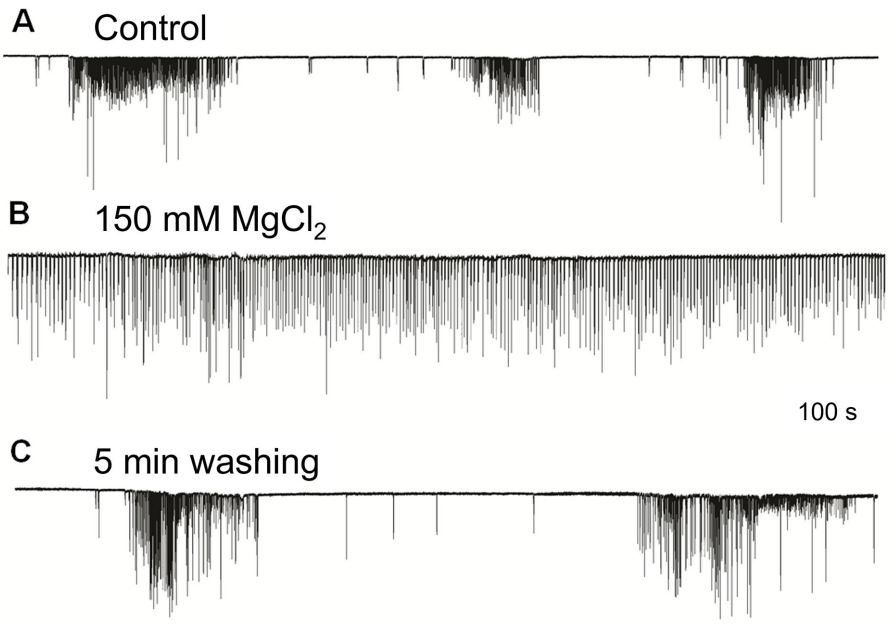

FIGURE 3
High Mg^{2+} seawater **(B)** blocked complex patterns of cilia activity [**(A)** – control], suggesting that synaptic inputs initiated high-frequency bursting and inhibition episodes. The regular unvarying cilia beating in high Mg^{2+} solution **(B)** was removed by washing in normal seawater, fully restoring **(C)** previously observed episodes of bursting and inhibition. Numbers under all traces show the time of recordings.

neuromuscular transmitter in ctenophores because of its higher efficiency in inducing muscle contractions than D-glutamate and L-aspartate (Moroz et al., 2014). However, neither L-glutamate, L-aspartate, nor any other bilaterian amino acid-derived neurotransmitters tested here (glycine, GABA, acetylcholine, serotonin, dopamine, octopamine, and histamine) could noticeably change the frequency of cilia beating in *Pleurobrachia* and *Bolinopsis* in concentrations up to 0.5 mM (see methods). These observations

also support the hypothesis that acetylcholine and monoamines are bilaterian innovations (Moroz and Kohn, 2015; Moroz et al., 2021).

Modeling peptidergic signaling

The first neural systems might have mainly been peptidergic (Moroz, 2009, 2021). Peptidergic signaling can significantly affect interneuronal communication in ctenophores (Moroz et al., 2014; Sachkova et al., 2021; Hayakawa et al., 2022). *Pleurobrachia* and *Mnemiopsis* genomes do not encode FMRFamide (Moroz and Kohn, 2016). However, this versatile tetrapeptide might be used as a tool to mimic the action of some other endogenous short neuropeptides. Specifically, these peptides have different conformational states (Edison et al., 1999; Espinoza et al., 2000; Dossey et al., 2006) with affinity to various receptors because they are short. When the complete list of endogenous peptides is not determined precisely (as in ctenophores), RFamide related peptides can be efficiently used as a model for initial screening for the presence of peptidergic neurons and their actions. This approach was applied here as a part of screening for modulatory action on cilia activity in *Pleurobrachia*.

FMRFamide had an apparent inhibitory effect on high-frequency bursts of activity in cilia (Figure 4). In 10–20 s after application, the frequency of cilia beating in bursts was reduced, and the appearance of bursts was also decreased. The whole effect could be observed within 1–2 min. Of note, there was no effect of FMRFamide in high Mg^{2+} seawater (Figure 5, $n = 2$). It suggests that the observed action of FMRFamide was indirect and polysynaptic.

Because FMRFamide and other short peptides have confirmation dynamic in solutions (Edison et al., 1999; Espinoza et al., 2000; Dossey et al., 2006), we also assumed they might be cross-reactive with many endogenous peptides. We tested this situation using immunohistochemistry and revealed a distinct subset of peptidergic neurons, not reported previously (Jager et al., 2011; Norekian and Moroz, 2016, 2019, 2020). This is consistent with an observation that RFamide immunoreactivity was also detected in specific cells of the polar field in *Pleurobrachia* (Figure 6). These potentially chemoreceptive cells might use short neuropeptides as afferent components of neural circuits controlling locomotion via still-unknown interneurons and motoneurons.

Modeling nitrergic signaling

Nitric oxide (NO) is an ancient and versatile signal molecule (Moroz and Kohn, 2011), recently proposed as a transmitter candidate in ctenophores (Moroz and Kohn, 2016; Moroz et al., 2023). In contrast to classical transmitters, the application of NO donors (NOC-9 and Diethylamine NONOate, 0.02–0.2 mM) caused inhibition of comb cilia beating both in *Pleurobrachia* and *Bolinopsis* with a complete arrest of cilia activity in most cases at higher concentrations, 100 μM and above (Figure 7). The effect developed slowly over 1–2 min after NO-donor solution applications [half-life of NO release is reached 10–15 min after diluting the NO-donors in the seawater (Maragos et al., 1991; Keefer et al., 1996; Li et al., 2020)]. This inhibitory effect was always reversible and was washed out in the seawater with a complete restoration of pre-application activity in about 5 min. Of note, this inhibitory action of NO donors persisted in high Mg^{2+} seawater, suggesting the direct action of NO on the cilia in combs (Figure 8).

Our results imply that endogenous or environmental NO suppresses the cilia beating in ctenophores. Gaseous NO is one of the

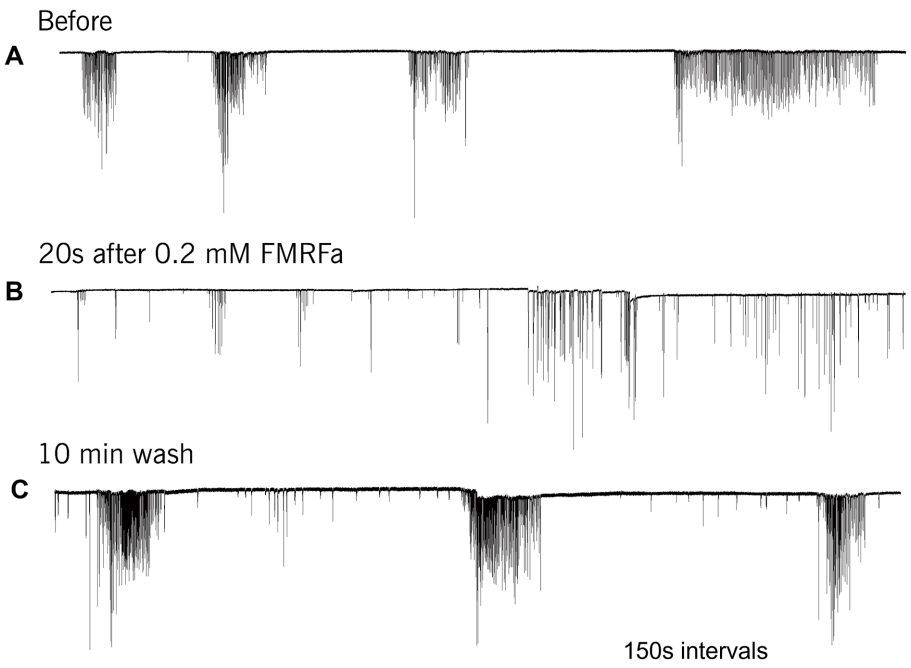

FIGURE 4
In *Pleurobrachia* FMRFamide reversibly inhibited the intensity of cilia bursting activity, repressing or even eliminating the occurrence of bursts, significantly weakening the degree of cilia acceleration in the remaining bursts **(A–C)**. Numbers under all traces show the time of recordings.

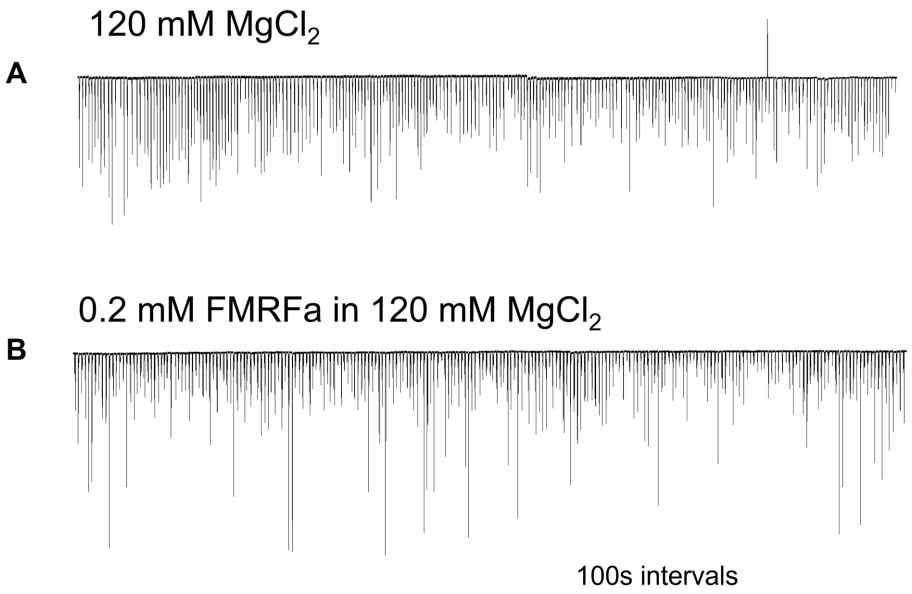

FIGURE 5
In high Mg^{2+} seawater, which blocked the variable bursting activity of *Pleurobrachia* cilia **(A)**, FMRFamide did not demonstrate any noticeable effect on locomotory cilia **(B)**, suggesting that its target was not comb's cilia themselves but an external source controlling inputs to ciliated cells. Numbers under the traces show the time of recordings.

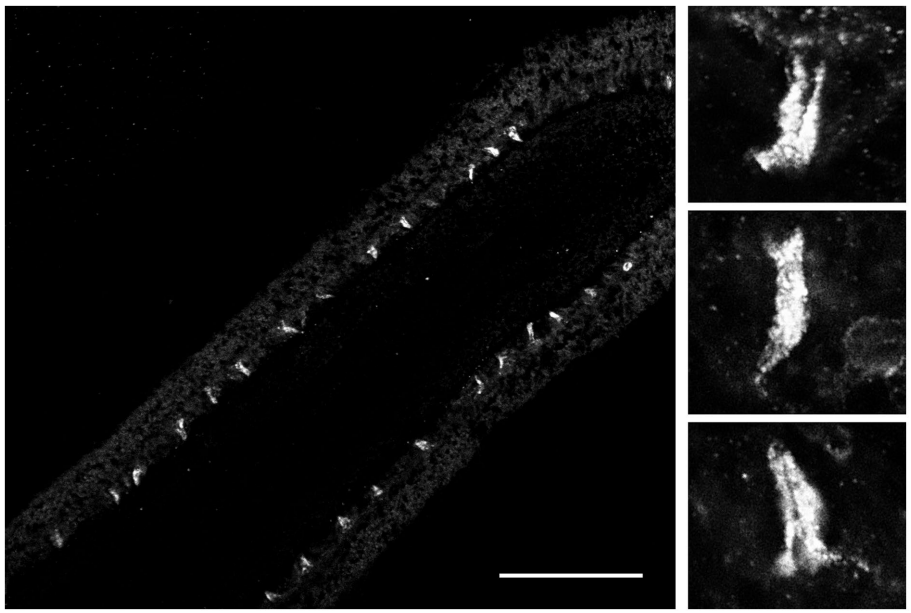

FIGURE 6
FMRF-like immunoreactivity in the polar field, a putative chemosensory organ of *Pleurobrachia bachei*. The left image shows regularly positioned stained putative chemoreceptive cells at lower magnification. Scale bar – 100 μm. Images on the right show the same cells are at higher magnification. See details about the protocol and *Pleurobrachia* neuroanatomy (Norekian and Moroz, 2019a, 2020).

smallest and most diffusible signal molecules, with multiple non-enzymatic and enzymatic synthetic pathways, including nitric oxide synthase (NOS) in both host cells and microbiome (Moroz and Kohn, 2011). Interestingly, the screening of the sequenced genome in *Pleurobrachia* and several transcriptomes from this species did not recover any NOS-like enzymes (Moroz et al., 2014). However, NOS was detected in basal and more derived species of ctenophores, such as *Mnemiopsis leidyi* (Moroz and Kohn, 2016; Moroz et al., 2020a) and *Bolinopsis* (Moroz et al., 2023). These comparative analyses illustrate the mosaic nature of NOS distribution within the phylum Ctenophora and provide evidence for the secondary loss of NOS in *Pleurobrachia* from the common ancestor of ctenophores (Moroz et al., 2023). However, *Pleurobrachia* has soluble guanylyl cyclases and possibly other receptors for NO, which might sense this molecule from

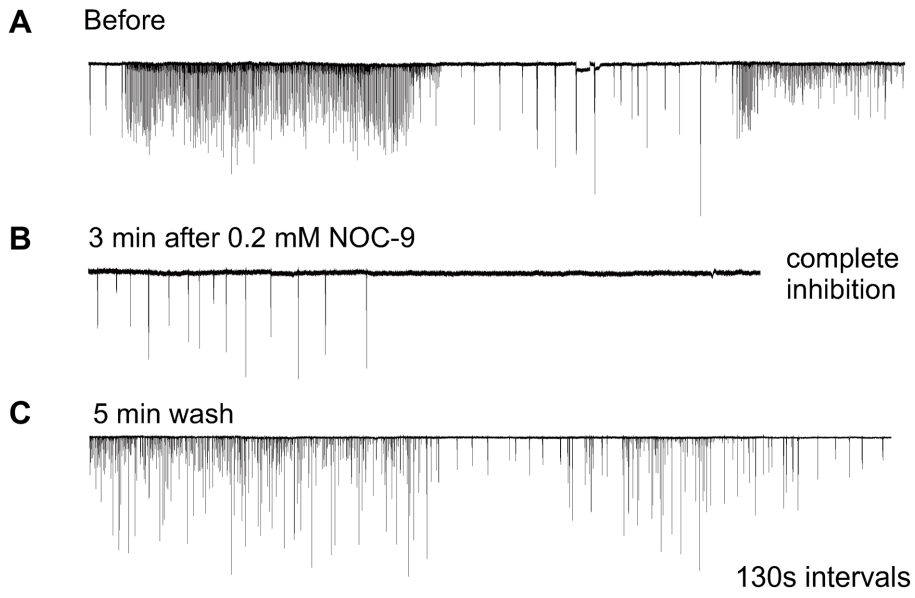

FIGURE 7
Nitric Oxide (NO) donors, such as NOC-9, reversibly suppressed cilia beating, completely inhibiting cilia movements in *Pleurobrachia* **(A,B)**. This effect was reversible, and cilia beating was restored within 5min of washing **(C)**. Numbers under all traces show the time of recordings.

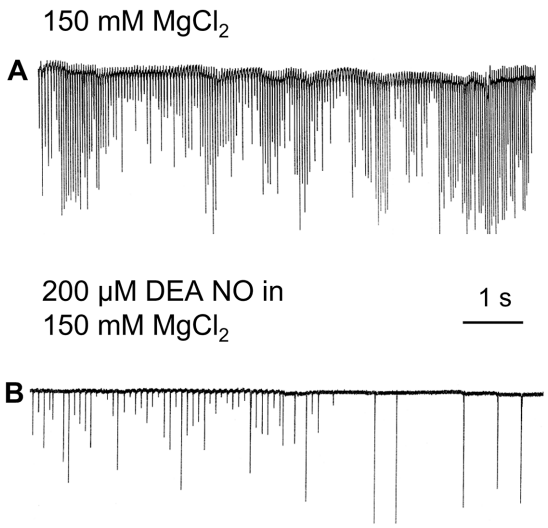

FIGURE 8
In high Mg^{2+} seawater, which blocked variable synaptic inputs and chemical transmission **(A)**, Nitric Oxide (NO) donors noticeably inhibited cilia beating in *Pleurobrachia* **(B)**, suggesting that NO targets can be comb's cilia themselves.

alternative endogenous and exogenous sources (e.g., microbiomes and/or food).

Conclusion and future directions

Ctenophores is the earliest lineage of metazoans (Whelan et al., 2015, 2017; Li et al., 2021; Schultz et al., 2023), central to understanding the origins and fundamental principles of animal organization. The life of ctenophores is entirely based on cilia, with dozens of populations of ciliated cells (Tamm, 1982; Hernandez-Nicaise, 1991; Tamm, 2014; Norekian and Moroz, 2019b). As a result, multi-transmitter control of cilia activity is paramount to ctenophore organization and behaviors.

NO-cilia interactions can be one of the ancient signaling pathways in the evolution of animals, but this is a little investigated direction, with no comparative data (Saternos and Aboualaiwi, 2018). Thus, it would be essential to identify both sources and mechanisms of the action of NO on cilia in different ecological groups of ctenophores. Experiments on other ctenophore species are imperative because of the mosaic distribution of NOS across species, with examples of secondary loss of this enzyme in many lineages (Moroz et al., 2023).

Second, the observed suppression of complex ciliary patterns by $MgCl_2$ indicates the significance of steady-state chemical transmission in generating ctenophore behaviors. This experiment is important because of the recently discovered syncytial organization of five ctenophore neurons in the subepithelial nerve net of early developmental stages of *Mnemiopsis* (Burkhardt et al., 2023). The finding might be interpreted as support for the widespread role of non-synaptic and non-chemical transmission in ctenophores (Dunn, 2023). However, the majority of neurons in ctenophores and external control of cilia activities are likely mediated by chemical transmission. Specifically, distinct ctenophore neural systems can employ well-recognized synapses already detected by electron microscopy (Hernandez-Nicaise, 1991; Burkhardt et al., 2023) and volume-type intercellular transmission (Moroz et al., 2021) mediated by small peptides, nitric oxide and, perhaps, additional low molecular weight messengers to be determined in future studies.

The precise balance and complementary contributions of different transmitter mechanisms in ctenophores are the areas of exciting discoveries essential for fundamental neuroscience and deciphering the evolution of alternative integrative systems across basal metazoan lineages (Jekely, 2021; Moroz et al., 2021; Moroz and Romanova, 2022; Moroz et al., 2004; Nikitin et al., 2023).

In conclusion, we would like to add that both *Pleurobrachia* and *Bolinopsis* (but especially *Pleurobrachia*) have complicated cilia activity

patterns, including high-frequency bursts, periods of inhibition, and more regular activity. Some of these are reported in illustrative figures. Those patterns and frequencies could also be different across animals and maybe also depend on the age, size, reproductive, and nutrition status of wild animals collected in nature. The overall scope of ctenophore behaviors is comparable to bilaterian animals and is currently understudied. We understood that more detailed and systematic future analysis might reveal some subtle modulatory effects of various chemical signals (neuronal-derived and non-neuronal transmitters), which is the subject of future, more detailed studies. Considering the variability of animals and their states, we anticipate that this direction would include future analysis of hundreds of individuals. The proposed protocol is one of the first steps in this direction to be expanded and correlated with detailed and complex behaviors of intact free-swimming animals in natural habitats.

Data availability statement

The raw data supporting the conclusions of this article will be made available by the authors, without undue reservation.

Author contributions

TPN and LLM designed the study, jointly performed experiments, wrote the manuscript, reviewed, and edited the manuscript. All authors contributed to the article and approved the submitted version.

Funding

This work was supported in part by the Human Frontiers Science Program (RGP0060/2017) and National Science Foundation (1146575, 1557923, 1548121 and 1645219) grants to LLM. Research reported in this publication was also supported in part by the National Institute of Neurological Disorders and Stroke of the National Institutes of Health under Award Number R01NS114491 (to LM). The content is solely the authors' responsibility and does not necessarily represent the official views of the National Institutes of Health.

Conflict of interest

The authors declare that the research was conducted in the absence of any commercial or financial relationships that could be construed as a potential conflict of interest.

Publisher's note

All claims expressed in this article are solely those of the authors and do not necessarily represent those of their affiliated organizations, or those of the publisher, the editors and the reviewers. Any product that may be evaluated in this article, or claim that may be made by its manufacturer, is not guaranteed or endorsed by the publisher.

References

Alberstein, R., Grey, R., Zimmet, A., Simmons, D. K., and Mayer, M. L. (2015). Glycine activated ion channel subunits encoded by ctenophore glutamate receptor genes. *Proc. Natl. Acad. Sci. U. S. A.* 112, E6048–E6057. doi: 10.1073/pnas.1513771112

Braga, A. A., Aguiar, D. C., and Guimaraes, F. S. (2009). NOC-9, a selective nitric oxide donor, induces flight reactions in the dorsolateral periaqueductal gray of rats by activating soluble guanylate cyclase. *Neurosci. Lett.* 459, 79–83. doi: 10.1016/j.neulet.2009.05.009

Burkhardt, P., Colgren, J., Medhus, A., Digel, L., Naumann, B., Soto-Angel, J. J., et al. (2023). Syncytial nerve net in a ctenophore adds insights on the evolution of nervous systems. *Science* 380, 293–297. doi: 10.1126/science.ade5645

Dabe, E. C., Sanford, R. S., Kohn, A. B., Bobkova, Y., and Moroz, L. L. (2015). DNA methylation in basal metazoans: insights from ctenophores. *Integr. Comp. Biol.* 55, 1096–1110. doi: 10.1093/icb/icv086

Del Castillo, J., and Engbaek, L. (1954). The nature of the neuromuscular block produced by magnesium. *J. Physiol.* 124, 370–384. doi: 10.1113/jphysiol.1954.sp005114

Dossey, A. T., Reale, V., Chatwin, H., Zachariah, C., Debono, M., Evans, P. D., et al. (2006). NMR analysis of *Caenorhabditis elegans* FLP-18 neuropeptides: implications for NPR-1 activation. *Biochemistry* 45, 7586–7597. doi: 10.1021/bi0603928

Dunn, C. (2023). Neurons that connect without synapses. *Science* 380, 241–242. doi: 10.1126/science.adh0542

Edison, A. S., Espinoza, E., and Zachariah, C. (1999). Conformational ensembles: the role of neuropeptide structures in receptor binding. *J. Neurosci.* 19, 6318–6326. doi: 10.1523/JNEUROSCI.19-15-06318.1999

Espinoza, E., Carrigan, M., Thomas, S. G., Shaw, G., and Edison, A. S. (2000). A statistical view of FMRFamide neuropeptide diversity. *Mol. Neurobiol.* 21, 35–56. doi: 10.1385/MN:21:1-2:035

Hayakawa, E., Guzman, C., Horiguchi, O., Kawano, C., Shiraishi, A., Mohri, K., et al. (2022). Mass spectrometry of short peptides reveals common features of metazoan peptidergic neurons. *Nat. Ecol. Evol.* 6, 1438–1448. doi: 10.1038/s41559-022-01835-7

Hernandez-Nicaise, M.-L. (1991). "Ctenophora" in *Microscopic Anatomy of Invertebrates: Placozoa, Porifera, Cnidaria, and Ctenophora*. eds. F. W. F. W. Harrison and J. A. Westfall (New York: Wiley), 359–418.

Hutter, O. F., and Kostial, K. (1954). Effect of magnesium and calcium ions on the release of acetylcholine. *J. Physiol.* 124, 234–241. doi: 10.1113/jphysiol.1954.sp005102

Jager, M., Chiori, R., Alié, A., Dayraud, C., Quéinnec, E., and Manuel, M. (2011). New insights on ctenophore neural anatomy: immunofluorescence study in *Pleurobrachia pileus* (Müller, 1776). *J. Exp. Zool. B Mol. Dev. Evol.* 316B, 171–187. doi: 10.1002/jez.b.21386

Jekely, G. (2021). The chemical brain hypothesis for the origin of nervous systems. *Philos. Trans. R. Soc. Lond. Ser. B Biol. Sci.* 376:20190761. doi: 10.1098/rstb.2019.0761

Johnson, S. B., Winnikoff, J. R., Schultz, D. T., Christianson, L. M., Patry, W. L., Mills, C. E., et al. (2022). Speciation of pelagic zooplankton: Invisible boundaries can drive isolation of oceanic ctenophores. *Front Genet* 13:970314. doi: 10.3389/fgene.2022.970314

Keefer, L. K., Nims, R. W., Davies, K. M., and Wink, D. A. (1996). "NONOates" (1-substituted diazen-1-ium-1,2-diolates) as nitric oxide donors: convenient nitric oxide dosage forms. *Methods Enzymol.* 268, 281–293. doi: 10.1016/s0076-6879(96)68030-6

Kohn, A. B., Sanford, R. S., Yoshida, M. A., and Moroz, L. L. (2015). Parallel evolution and lineage-specific expansion of RNA editing in ctenophores. *Integr. Comp. Biol.* 55, 1111–1120. doi: 10.1093/icb/icv065

Li, B., Ming, Y., Liu, Y., Xing, H., Fu, R., Li, Z., et al. (2020). Recent developments in pharmacological effect, mechanism and application Prospect of Diazeniumdiolates. *Front. Pharmacol.* 11:923. doi: 10.3389/fphar.2020.00923

Li, Y., Shen, X. X., Evans, B., Dunn, C. W., and Rokas, A. (2021). Rooting the animal tree of life. *Mol. Biol. Evol.* 38, 4322–4333. doi: 10.1093/molbev/msab170

Maragos, C. M., Morley, D., Wink, D. A., Dunams, T. M., Saavedra, J. E., Hoffman, A., et al. (1991). Complexes of.NO with nucleophiles as agents for the controlled biological release of nitric oxide. Vasorelaxant effects. *J. Med. Chem.* 34, 3242–3247. doi: 10.1021/jm00115a013

Moroz, L. L. (2009). On the independent origins of complex brains and neurons. *Brain Behav. Evol.* 74, 177–190. doi: 10.1159/000258665

Moroz, L. L. (2014). The genealogy of genealogy of neurons. *Commun. Integr. Biol.* 7:e993269. doi: 10.4161/19420889.2014.993269

Moroz, L. L. (2015). Convergent evolution of neural systems in ctenophores. *J. Exp. Biol.* 218, 598–611. doi: 10.1242/jeb.110692

Moroz, L. L. (2021). Multiple origins of neurons from secretory cells. *Front. Cell Dev. Biol.* 9:669087. doi: 10.3389/fcell.2021.669087

Moroz, L. L., Kocot, K. M., Citarella, M. R., Dosung, S., Norekian, T. P., Povolotskaya, I. S., et al. (2014). The ctenophore genome and the evolutionary origins of neural systems. *Nature* 510, 109–114. doi: 10.1038/nature13400

Moroz, L. L., and Kohn, A. B. (2011). Parallel evolution of nitric oxide signaling: diversity of synthesis and memory pathways. *Front. Biosci. (Landmark Ed)* 16, 2008–2051. doi: 10.2741/3837

Moroz, L. L., and Kohn, A. B. (2015). Unbiased view of synaptic and neuronal gene complement in ctenophores: are there Pan-neuronal and Pan-synaptic genes across Metazoa? *Integr. Comp. Biol.* 55, icv104–icv1049. doi: 10.1093/icb/icv104

Moroz, L. L., and Kohn, A. B. (2016). Independent origins of neurons and synapses: insights from ctenophores. *Philos. Trans. R. Soc. Lond. Ser. B Biol. Sci.* 371:20150041. doi: 10.1098/rstb.2015.0041

Moroz, L. L., Meech, R. W., Sweedler, J. V., and Mackie, G. O. (2004). Nitric oxide regulates swimming in the jellyfish Aglantha digitale. *J Comp Neurol* 471, 26–36. doi: 10.1002/cne.20023

Moroz, L. L., Mukherjee, K., and Romanova, D. Y. (2023). Nitric oxide signaling in ctenophores. *Front. Neurosci.* 17:1125433. doi: 10.3389/fnins.2023.1125433

Moroz, L. L., and Romanova, D. Y. (2022). Alternative neural systems: what is a neuron? (ctenophores, sponges and placozoans). *Front. Cell Dev. Biol.* 10:1071961. doi: 10.3389/fcell.2022.1071961

Moroz, L. L., Romanova, D. Y., and Kohn, A. B. (2021). Neural versus alternative integrative systems: molecular insights into origins of neurotransmitters. *Philos. Trans. R. Soc. Lond. Ser. B Biol. Sci.* 376:20190762. doi: 10.1098/rstb.2019.0762

Moroz, L. L., Romanova, D. Y., Nikitin, M. A., Sohn, D., Kohn, A. B., Neveu, E., et al. (2020a). The diversification and lineage-specific expansion of nitric oxide signaling in Placozoa: insights in the evolution of gaseous transmission. *Sci. Rep.* 10:13020. doi: 10.1038/s41598-020-69851-w

Moroz, L. L., Sohn, D., Romanova, D. Y., and Kohn, A. B. (2020b). Microchemical identification of enantiomers in early-branching animals: lineage-specific diversification in the usage of D-glutamate and D-aspartate. *Biochem. Biophys. Res. Commun.* 527, 947–952. doi: 10.1016/j.bbrc.2020.04.135

Moss, A. G., and Tamm, S. L. (1986). Electrophysiological control of ciliary motor responses in the ctenophore *Pleurobrachia*. *J. Comp. Physiol. A* 158, 311–330. doi: 10.1007/BF00603615

Moss, A. G., and Tamm, S. L. (1987). A calcium regenerative potential controlling ciliary reversal is propagated along the length of ctenophore comb plates. *Proc. Natl. Acad. Sci. U. S. A.* 84, 6476–6480. doi: 10.1073/pnas.84.18.6476

Nakamura, S., and Tamm, S. L. (1985). Calcium control of ciliary reversal in ionophore-treated and ATP-reactivated comb plates of ctenophores. *J. Cell Biol.* 100, 1447–1454. doi: 10.1083/jcb.100.5.1447

Nikitin, M. A., Romanova, D. Y., Borman, S. I., and Moroz, L. L. (2023). Amino acids integrate behaviors in nerveless placozoans. *Front. Neurosci.* 17, 1–21. doi: 10.3389/fnins.2023.1125624

Norekian, T. P., and Moroz, L. L. (2016). Development of neuromuscular organization in the ctenophore *Pleurobrachia bachei*. *J. Comp. Neurol.* 524, 136–151. doi: 10.1002/cne.23830

Norekian, T. P., and Moroz, L. L. (2019a). Neuromuscular organization of the ctenophore *Pleurobrachia bachei*. *J. Comp. Neurol.* 527, 406–436. doi: 10.1002/cne.24546

Norekian, T. P., and Moroz, L. L. (2019b). Neural system and receptor diversity in the ctenophore Beroe abyssicola. *J Comp Neurol* 527, 1986–2008. doi: 10.1002/cne.24633

Norekian, T. P., and Moroz, L. L. (2020). Comparative neuroanatomy of ctenophores: neural and muscular systems in *Euplokamis dunlapae* and related species. *J. Comp. Neurol.* 528, 481–501. doi: 10.1002/cne.24770

Sachkova, M. Y., Nordmann, E. L., Soto-Angel, J. J., Meeda, Y., Gorski, B., Naumann, B., et al. (2021). Neuropeptide repertoire and 3D anatomy of the ctenophore nervous system. *Curr. Biol.* 31:e5276, 5274–5285.e6. doi: 10.1016/j.cub.2021.09.005

Saternos, H. C., and Aboualaiwi, W. A. (2018). Signaling interplay between primary cilia and nitric oxide: a mini review. *Nitric Oxide* 80, 108–112. doi: 10.1016/j.niox.2018.08.003

Schultz, D. T., Haddock, S. H. D., Bredeson, J. V., Green, R. E., Simakov, O., and Rokhsar, D. S. (2023). Ancient gene linkages support ctenophores as sister to other animals. *Nature*. doi: 10.1038/s41586-023-05936-6

Tamm, S. L. (1982). "Ctenophora" in *Electrical conduction and behavior in simple invertebrates* (Oxford: Clarendon Press), 266–358.

Tamm, S. L. (1983). Motility and mechanosensitivity of macrocilia in the ctenophore Beroe. *Nature* 305, 430–433. doi: 10.1038/305430a0

Tamm, S. L. (1984). Mechanical synchronization of ciliary beating within comb plates of ctenophores. *J. Exp. Biol.* 113, 401–408. doi: 10.1242/jeb.113.1.401

Tamm, S. L. (1988). Calcium activation of macrocilia in the ctenophore *Beroe*. *J. Comp. Physiol. A* 163, 23–31. doi: 10.1007/BF00611993

Tamm, S. L. (2014). Cilia and the life of ctenophores. *Invertebr. Biol.* 133, 1–46. doi: 10.1111/ivb.12042

Tamm, S. L., and Tamm, S. (1981). Ciliary reversal without rotation of axonemal structures in ctenophore comb plates. *J. Cell Biol.* 89, 495–509. doi: 10.1083/jcb.89.3.495

Tamm, S. L., and Tamm, S. (1988). Development of macrociliary cells in *Beroe*. II. Formation of macrocilia. *J. Cell Sci.* 89, 81–95. doi: 10.1242/jcs.89.1.81

Tamm, S. L., and Terasaki, M. (1994). Visualization of calcium transients controlling orientation of ciliary beat. *J. Cell Biol.* 125, 1127–1135. doi: 10.1083/jcb.125.5.1127

Whelan, N. V., Kocot, K. M., Moroz, L. L., and Halanych, K. M. (2015). Error, signal, and the placement of Ctenophora sister to all other animals. *Proc. Natl. Acad. Sci. U. S. A.* 112, 5773–5778. doi: 10.1073/pnas.1503453112

Whelan, N. V., Kocot, K. M., Moroz, T. P., Mukherjee, K., Williams, P., Paulay, G., et al. (2017). Ctenophore relationships and their placement as the sister group to all other animals. *Nat. Ecol. Evol.* 1, 1737–1746. doi: 10.1038/s41559-017-0331-3

Yu, A., Alberstein, R., Thomas, A., Zimmet, A., Grey, R., Mayer, M. L., et al. (2016). Molecular lock regulates binding of glycine to a primitive NMDA receptor. *Proc. Natl. Acad. Sci. U. S. A.* 113, E6786–E6795. doi: 10.1073/pnas.1607010113

frontiers | Frontiers in Physiology

TYPE Hypothesis and Theory
PUBLISHED 03 October 2023
DOI 10.3389/fphys.2023.1263453

OPEN ACCESS

EDITED BY
James Newcomb,
New England College, United States

REVIEWED BY
Angelique Christine Paulk,
Massachusetts General Hospital and Harvard Medical School, United States
Akira Sakurai,
Georgia State University, United States

*CORRESPONDENCE
Rhanor Gillette,
rhanor@illinois.edu

RECEIVED 19 July 2023
ACCEPTED 12 September 2023
PUBLISHED 03 October 2023

CITATION
Gribkova ED, Lee CA, Brown JW, Cui J, Liu Y, Norekian T and Gillette R (2023), A common modular design of nervous systems originating in soft-bodied invertebrates.
Front. Physiol. 14:1263453.
doi: 10.3389/fphys.2023.1263453

A common modular design of nervous systems originating in soft-bodied invertebrates

Ekaterina D. Gribkova[1], Colin A. Lee[2], Jeffrey W. Brown[3], Jilai Cui[2], Yichen Liu[4], Tigran Norekian[5] and Rhanor Gillette[2,4]*

[1]Coordinated Science Laboratory, University of Illinois at Urbana-Champaign, Urbana, IL, United States, [2]Neuroscience Program, University of Illinois at Urbana-Champaign, Urbana, IL, United States, [3]Stanson Toshok Center for Brain Function and Repair, Rosalind Franklin University of Medicine and Science, North Chicago, IL, United States, [4]Department of Molecular & Integrative Physiology, University of Illinois at Urbana-Champaign, Urbana, IL, United States, [5]Whitney Laboratory for Marine Biosciences, University of Florida, St. Augustine, FL, United States

Nervous systems of vertebrates and invertebrates show a common modular theme in the flow of information for cost-benefit decisions. Sensory inputs are incentivized by integrating stimulus qualities with motivation and memory to affect appetitive state, a system of homeostatic drives, and labelled for directionality. Appetitive state determines action responses from a repertory of possibles and transmits the decision to a premotor system that frames the selected action in motor arousal and appropriate postural and locomotion commands. These commands are then sent to the primary motor pattern generators controlling the motorneurons, with feedback at each stage. In the vertebrates, these stages are mediated by forebrain pallial derivatives for incentive and directionality (olfactory bulb, cerebral cortex, pallial amygdala, *etc.*) interacting with hypothalamus (homeostasis, motivation, and reward) for action selection in the forebrain basal ganglia, the mid/hindbrain reticular formation as a premotor translator for posture, locomotion, and arousal state, and the spinal cord and cranial nuclei as primary motor pattern generators. Gastropods, like the predatory sea slug *Pleurobranchaea californica*, show a similar organization but with differences that suggest how complex brains evolved from an ancestral soft-bodied bilaterian along with segmentation, jointed skeletons, and complex exteroceptors. Their premotor feeding network combines functions of hypothalamus and basal ganglia for homeostasis, motivation, presumed reward, and action selection for stimulus approach or avoidance. In *Pleurobranchaea*, the premotor analogy to the vertebrate reticular formation is the bilateral "A-cluster" of cerebral ganglion neurons that controls posture, locomotion, and serotonergic motor arousal. The A-cluster transmits motor commands to the pedal ganglia analogs of the spinal cord, for primary patterned motor output. Apparent pallial precursors are not immediately evident in *Pleurobranchaea*'s central nervous system, but a notable candidate is a subepithelial nerve net in the peripheral head region that integrates chemotactile stimuli for incentive and directionality. Evolutionary centralization of its computational functions may have led to the olfaction-derived pallial forebrain in the ancestor's vertebrate descendants and their analogs in arthropods and annelids.

KEYWORDS

evolution, homology, analogy, pallium, reticular system, *Pleurobranchaea*

Introduction

Did the general neural organization of decision and action selection precede or follow the evolution of complex body form and behavior? We argue that despite broad differences in complexity (detail) of brain and body, soft-bodied invertebrates like gastropods even with primitive, incompletely centralized brains show a blueprint for a modular organization of the nervous system similar to vertebrates, although simpler in detail. Vertebrates, insects, and polychaete annelids likely evolved segmentation and articulated skeletons with jointed appendages independently (Mullins et al., 2011; Hochner, 2013; Katz, 2016). These acquisitions are adaptations for speed and agility beyond what is easily gotten by a soft body. The skeletal joints allow local sensory-motor regulation of segmental musculature, and sensory monitoring of joint angles for incorporating into central motor templates. Vertebrates and insects share analogous modular designs for computational functions that mediate decision, spatial mapping, and motivation (Loesel and Heuer, 2010; Tosches and Arendt, 2013; Holland, 2016). Such functions may have originated in the ancestral bilaterian with simpler anatomy and behavior or could have evolved independently multiple times. The above lineages each have more complicated body forms than the expected urbilaterian ancestor (Hejnol and Martindale, 2008).

For comparative analysis, it is useful to examine circuits in organisms more like the expected common ancestor. It is pertinent that a simple sea slug, with primitive ciliary locomotion and lacking segmentation and appendages, has modular design in neuronal network coordination similar to vertebrates for posture, locomotion, and general arousal. Thus, the general scheme controlling locomotion and posture could have preceded the evolution of segmented bodies and articulated appendages. Could then the neuronal circuitry of cost-benefit decision and action selection be also analogous, and possibly homologous in origin, among the phyla?

We previously discussed the evolution of the nervous system and developed hypotheses on the nature of the nervous system in the common urbilaterian ancestor (Gillette and Brown, 2015). As the ancestor is unavailable, we took a classic comparative approach. We used the sea slug *Pleurobranchaea californica* as a model system whose nervous system and behavior have been examined and are likely relatively close to the ancestor's (Figure 1). The nervous system and behavior are also known in more detail than for many other animal systems, particularly with respect to mechanisms for decision-making, and are amenable to the comparative approach. Moreover, there is much useful information on brain and behavior of related gastropods. Among other model systems available, information on the brains and behaviors of vertebrate animals has been amassed over more than a century by thousands of researchers. Thus, we may compare markedly distant lineages that split over 500 Myr ago into protostome and deuterostome by examining functional analogies in brain and behavior.

Comparisons of functional analogies in brain and behavior of the streamlined *Pleurobranchaea* with the rather more complex vertebrates may show commonalities interpretable in terms of direct or parallel evolution. Gastropods like *Pleurobranchaea* boast systems that may be closer in brain, body, and behavior to the simple common ancestor than the more complex, segmented vertebrates, insects, and polychaete annelids with jointed appendages. The former lack complicating segmentation and jointed skeletons with appendages and many of them locomote primitively by myriads of cilia paddling their way through secreted mucus, as expected of the common ancestor. Moreover, especially for the opisthobranch sea slugs like *Pleurobranchaea*, their soft bodies and behaviors are quite simple, and they are hermaphroditic with minimal investment in offspring care, thereby further reducing neural complexities of animals with two different sexes that may brood their young.

Pleurobranchaea shows simple reward-based learning for approach or avoidance of prey (Noboa and Gillette, 2013). Their behavior and neuronal circuitry are characterized well enough to generate computational simulations which express cost-benefit decisions in autonomous agents with efficient, reward-based mechanisms for stimulus valuations. The algorithms used reproduce the basic modular functions of nervous systems as treated here (Brown et al., 2018; Gribkova et al., 2020).

Thus, a fuller answer to the nature and origin of complexity in human brain and behavior can begin to be sought in the simplicity of

FIGURE 1
Pleurobranchaea californica, head shot. The chemotactile oral veil is flared above the mouth. The oral veil papillae and the lateral tentacles have ciliated chemotactile receptors that feed into a peripheral subepithelial network to mediate incentive and stimulus location. Photo by Fred Zwicky.

our very early ancestors. We may safely assume that the problems faced by the ancestors were basically the same as they are today, and that their nervous systems were designed by natural selection to generate appropriate behavioral algorithms. The threefold basic imperatives of life are: 1) acquisition of resources; 2) defense; and 3) reproduction. These three constraints of behavioral design are largely interconnected and interdependent. Even single cells may follow this design, where biochemical pathways do the computations of an integrating nervous system, connecting sensors to motor pathways for movement and secretion. We annotate these constraints briefly, below, and then continue on to document the organization of simple and complex nervous systems in resolving the imperatives.

Acquisition of resources

The essential resource is energy, which underlies the abilities for defense and reproduction. More complicated faces of this basic resource come from derived characters aimed at maximizing and conserving energy, like shelter, clothing, and storage in fatty tissues. Even social characters such as attention to status and reputation, play, and aggression intimately involve the economics of energy. Other resources are the chemical building blocks of cells: amino acids, fats, carbohydrates, and water.

Defense

Once life evolved to a point where it could acquire energy and use it in reproduction, strong selective forces would have had it evolve mechanisms to keep from losing it, such as a cell membrane (which then involved a whole new set of problems resulting in the evolution of ion pumps). Once organisms had developed to conserve energy, they became treasure troves to some that devised ways to break into their stores and use them for themselves. This would have been an early manifestation of predation.

Reproduction

As early cells devised asexual and sexual ways of reproduction, impelled by the obvious selective forces excluding nonreproductive cells, reproductive predators evolved to hijack their mechanisms, becoming intracellular parasites, and perhaps degenerating from free-living cells to viruses (Forterre, 2006). Thus, the three design constraints are inextricably intertwined.

For most animal species that have been observed in detail, the cost-benefit decisions employed to solve the problems of acquisition, defense, and reproduction integrate internal state, sensory input, and memory. This holds for vertebrates, insects, and gastropod mollusks (see Gillette et al., 2000; Clore et al., 2021). The dynamic changes in internal state for motivation, in varying sensory input, and in memory plasticity may lead to a broad spectrum of cost-benefit responses tailored to each situation. There are sufficient data presently to compare the neural architectures that support such decision-making. First, we would like to review the functional modules of the vertebrate nervous system, then compare them with analogs in the sea slug.

In each of these functions there is a modular design for the flow of information from stimulus to response: incentive-directionality; reward expectation; approach-avoidance decision; decision implementation in motor response.

Vertebrate nervous systems

A modular organization of the mammalian nervous system, in terms of interacting subsystems, has been long recognized both anatomically, physiologically, and computationally (Arbib, 2007).

Hypothalamus

Nutrition, thermoregulation, hydration, and social behaviors like sex and parental care are homeostatic drives founded in the hypothalamus, whose neural activity represents appetitive state and biases behavioral choices for the different goals. Nutritional state is fairly well understood. In vertebrates, nutritional state is closely monitored by hypothalamic neurons sensitive to serum glucose, digestive hormones, and hormonal indicators of fat and glycogen storage. Motivation, in terms of hunger/satiation, regulates exploration after food resources or avoidance of such activity. Moreover, the hypothalamic circuits and hormones that mediate hunger and satiety appropriately regulate the sensitivity of the reward system (Cassidy and Tong, 2017).

Basal ganglia

Action selection for cost-benefit decisions is determined by the basal ganglia, which integrate sensory incentives weighed with motivation-related reward and memory of experience (Turner and Desmurget, 2010). The basal ganglia have access to cortical areas with memories laden with positive and negative affect related to context and can compare possible costs and benefits of potential decisions. Final summation leads to selection of motor actions that essentially represent approach or avoidance of a predicted situation. The decision outputs are sent to premotor areas in the reticular system of the brainstem that extends from the upper part of the midbrain to the lower part of the medulla. Important dopaminergic and serotonergic modulatory inputs to the basal ganglia come from the substantia nigra compacta and raphe nuclei, respectively, for reward and arousal.

Reticular formation and spinal cord

Premotor patterning networks in the hindbrain reticular system are disinhibited by basal ganglia inputs to form premotor commands configured for the selected motor actions. From the reticular formation the commands for locomotion and posture descend to the spinal cord to be translated into direct motor action by the segmental pattern generators. The reticular system has critical roles in maintaining arousal state in behavioral and motor systems through ascending pathways to the forebrain and descending pathways to the spinal cord via the reticulospinal tracts. The raphe nuclei of the reticular system are critical serotonergic

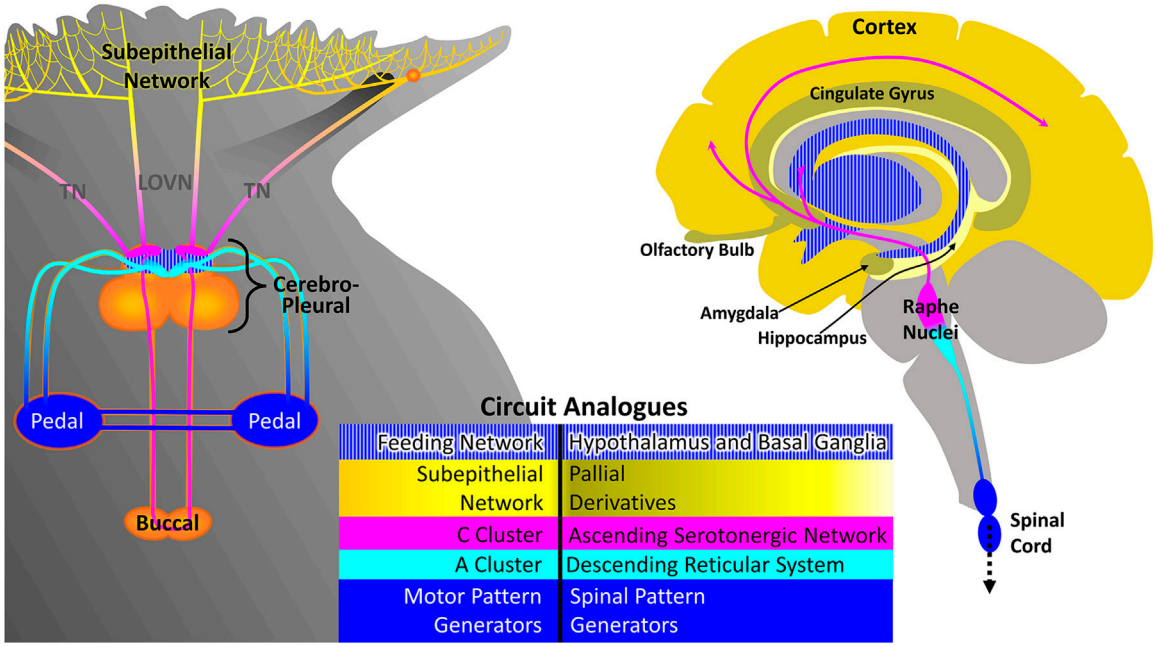

FIGURE 2
Proposed analogs of *Pleurobranchaea californica* and vertebrate central nervous systems, as represented by the human brain and spinal cord. The feeding network (blue striped) in the cerebral lobes of the cerebropleural ganglion combines homeostatic functions of the vertebrate hypothalamus in motivation and decisive action selection of the basal ganglia. The C-cluster (magenta) is functionally analogous to the serotonergic portions of the vertebrate ascending reticular system. The A cluster (cyan) is functionally analogous to the vertebrate reticular system, projecting to pattern generators in the pedal ganglion, which are in turn analogous to the mammalian spinal cord in final motor pattern output. The serotonergic cells of the A-cluster are analogous to the serotonergic cells of the descending raphe nuclei. The chemotactile sensory subepithelial network (yellow) of *Pleurobranchaea* is proposed as resembling an ancestral precursor to pallial derivatives of the ancient olfactory system in evolution, such as the olfactory bulb, neocortex, hippocampus, basal ganglia, amygdaloid complex and others.

sources for modulation of mood, reward, and arousal (Teissier et al., 2015; Venkatraman et al., 2017). Ascending fibers from the anterior raphe nuclei innervate the basal ganglia and other forebrain derivatives, and descending fibers from the posterior nuclei innervate the spinal cord pattern generators and sensory pathways.

The spinal cord is segmented, and the coupled spinal pattern generators' final outputs are through their motorneurons. Spinal pattern generators receive direct feedback from muscle and tendon stretch receptors and from descending inputs that can smooth coordination and aid adaptation of motor pattern to uneven terrain (Rossignol et al., 2006).

Pallial derivatives

Olfactory bulb, cortex, pallial amygdala, and other pallial structures are thought to have evolved as elaborations of the olfactory system, with the addition of more sensory inputs from complex exteroceptors such as mediate vision, audition, proprioception, and taste (Reiner et al., 1998; Redgrave et al., 1999; Smeets et al., 2000; Aboitiz et al., 2003; Grillner et al., 2013; Aboitiz and Montiel, 2015; Jacobs, 2023). Functionally, these structures interact with each other and the subpallial striatum to integrate reward, motivation, affect, and memory to compute incentive for decision making and to place it in physical context with directional information. The motor cortex apparently only appeared in evolution with mammals and is not treated further here.

Analogs in the Gastropod's nervous system

Comparison of the gastropod decision-making system, represented by *Pleurobranchaea*, with vertebrates' finds general similarities in organization (Figure 2) However, a major exception regarding vertebrate forebrain is discussed below. Mainly, they differ in complexity of detail related to the elaborate bodies and exteroceptors of the vertebrates. Previous work described neuronal circuitry underlying cost-benefit and approach-avoidance decisions in *Pleurobranchaea*'s foraging (Jing and Gillette, 2000; Gillette and Jing, 2001; Yafremava et al., 2007; Hirayama et al., 2012; Hirayama and Gillette, 2012; Brown, 2014). These circuits share functional analogies with the vertebrate striatum and hypothalamus in that they express homeostatic state and instruct goal-directed action selection (Gillette and Brown, 2015), with the analogies extending to coordination of locomotion in goal-directed behavior. Thus, a cluster of neurons, the A-cluster, works analogously to the reticular system for posture, locomotion, and arousal (Lee et al., 2023), and a peripheral neuronal network may serve functions of forebrain pallial derivatives for incentive and simple place-coding. Of the several ganglia of Pleurobranchaea's central nervous system (CNS), the cerebropleural ganglion contains the circuits in its cerebral lobes that function analogously to the combined basal ganglia-hypothalamus and the reticular system. Sensory input to the ganglion is integrated with motivation and memory to decide actions. These decisions descend to pattern

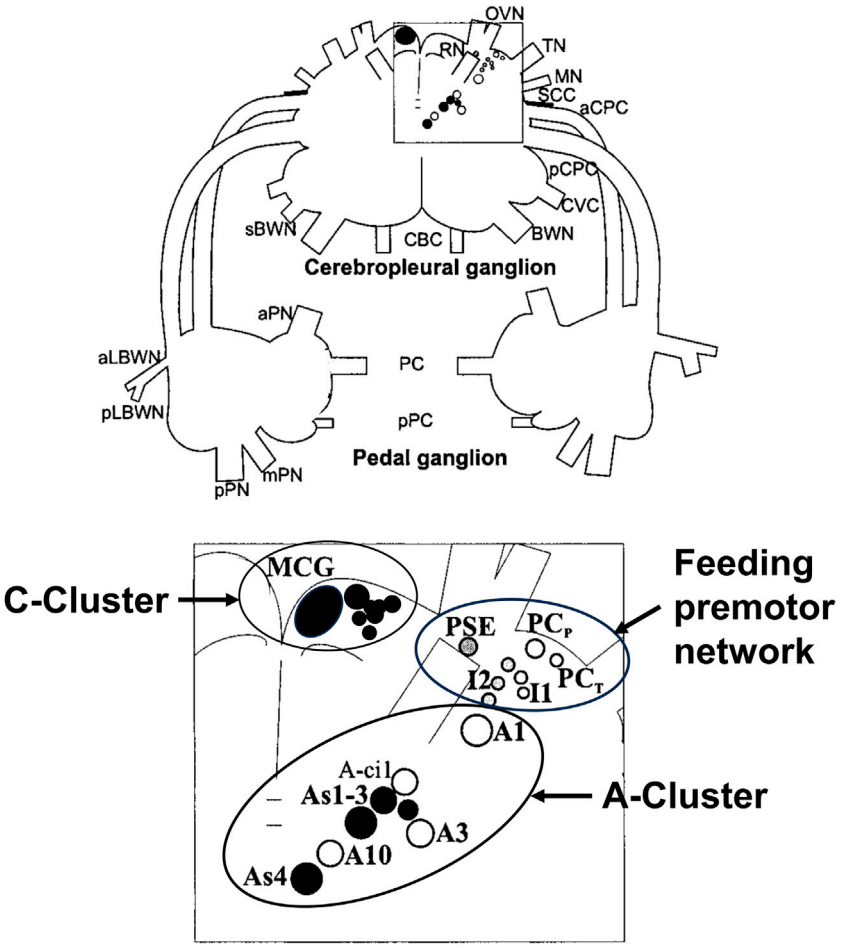

FIGURE 3
Drawing of the dorsal surface of the cerebropleural and pedal ganglia showing identified neuronal somata of networks for the feeding network, the A-Cluster for posture, locomotion, and motor arousal, and the serotonergic C-Cluster. Filled circles show serotonin immunoreactive somata. The somata are bilaterally symmetrical, but only shown unilaterally. Abbreviations: MCG, metacerebral giant neuron; PCP, phasic paracerebral interneuron; PSE, polysynaptic excitor of the PCP; PCT, tonic paracerebral interneuron; I1, I2, Interneurons 1; and 2, Interneuron 2; BWN, body wall nerve; sBWN, small body wall nerve; CBC, cerebrobuccal connective; aCPC, anterior cerebropedal connective; pCPC, posterior cerebropedal connective; CVC, cerebrovisceral connective; MN, mouth nerve; OVN, oral veil nerve; RN, rhinophore nerve; SCC, subcerebral commissure; TN, tentacle nerve; aLBWN, anterior lateral body wall nerve; pLBWN, posterior lateral body wall nerve; PC, pedal commissure; pPC, parapedal commissure; aPN, anterior pedal nerve; mPN, medial pedal nerve; and pPN, posterior pedal nerve.

generators in the pedal ganglia, which themselves have functions analogous to the vertebrate spinal cord in final patterning of direct motor output (Figure 2). A significant difference may be that *Pleurobranchaea*'s basal ganglia analog has only the direct neural pathway output integrating sensation, internal state, and memory, and lacks the explicit comparison of potential costs and benefits afforded by the indirect pathway originating in the vertebrate striatum, as may the insects (Strausfeld and Hirth, 2013).

Cerebral lobes: feeding network

The distributed feeding motor network combines the homeostatic functions of the hypothalamus in motivation and the basal ganglia in decisive action selection. Hunger/satiety is represented in the excitation state and neuronal activity configuration of the feeding network (Hirayama et al., 2012; Hirayama and Gillette, 2012; Hirayama et al., 2014). Sensory input incentivized by memory summates with the neuronal representation of motivation to bring the network towards or away from exploring a stimulus. In cost-benefit decisions for approach-avoidance, hungry animals approach food odors, but when satiated they turn away from them. The feeding network excitation state sets the thresholds for active feeding, which can vary a million-fold between ravenous hunger and logy satiation (Davis and Gillette, 1978; London and Gillette, 1986; Hirayama et al., 2014). Incentivized input to the feeding network may be mediated by dopaminergic afferents from chemotactile areas (Kabotyanski et al., 2000; Brown et al., 2018), which may well include the effects of learned preference and avoidance (Elliott and Susswein, 2002). The functions of *Pleurobranchaea*'s homeostatic feeding network in action selection are located in the subpallial basal ganglia of the vertebrate, however still under the influence of the hypothalamus analog of the feeding network. Thus, in evolution the computations

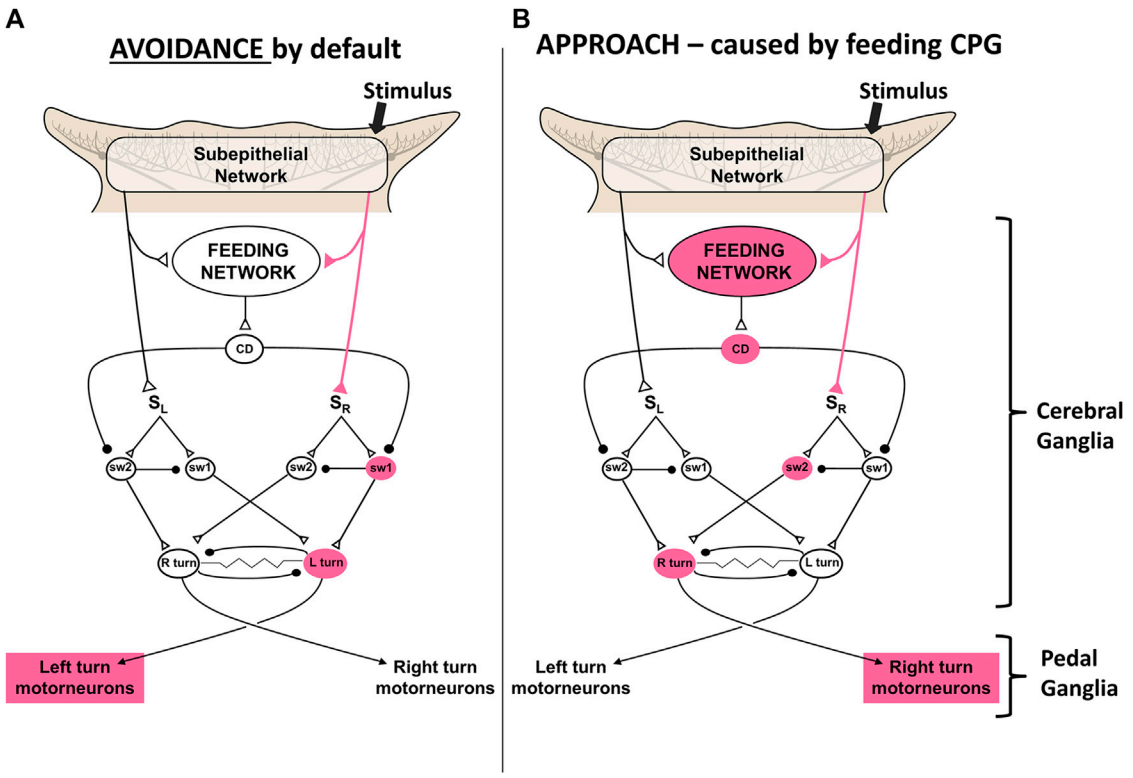

FIGURE 4
A simplest model for control of the turn by excitation state of the feeding motor network. A simple neuronal switch mechanism under control of corollary discharge from the CPG mediating feeding is postulated. **(A)** When the activity of the feeding network is low, sensory inputs from the oral veil drive avoidance turns away from the site of the stimulus. **(B)** Increased activity of the network, through hunger or greater sensory stimulation, changes the avoidance response to an approach-turn toward the stimulus by a postulated disinhibitory mechanism that shifts activity to the contralateral side of the turn motor network. Figure modified from Gillette and Brown (2015).

of homeostasis and action selection may have been either separated to different modules in evolution in the vertebrates or joined in the feeding network of gastropods.

Figure 3 shows a map of the neurons of the premotor feeding network, the A-cluster that controls posture and locomotion with its serotonergic As1-4 interneurons, and the anterior serotonergic C-cluster to which we will refer below.

Action selections by the feeding network are quite simple choices between approach and avoidance of stimuli, and whether to locomote or not. Avoidance turns are the default responses to sensory stimuli in the absence of feeding network excitation. Higher activity in the feeding network converts the turn responses to approach, possibly by shunting sensory input to the turn network from one side to the other (Gillette et al., 2000; Hirayama and Gillette, 2012; Brown, 2014; Hirayama et al., 2014). Thus, partly satiated animals actively avoid weaker feeding stimuli and approach stronger ones. Active feeding causes inhibition of the premotor neurons that mediate turning and locomotion, which prevents the animal from overrunning its prey before finishing the meal. Figure 4 shows a simplest model based on synaptic disinhibition routing excitation to the opposite side of the turn motor network, reflecting similar downstream disinhibitory mechanisms by the basal ganglia in action selection.

Cerebral lobes: reticular system analog

A-cluster

In *Pleurobranchaea*, the analog of the vertebrate reticular formation lies in a bilaterally paired group of neurons, the A-cluster (Jing and Gillette, 1999; Jing and Gillette, 2000; Lee et al., 2023), posterior to the feeding network neurons in the cerebral lobes. A-cluster homologs are also found in other gastropods (Sudlow et al., 1998; Popescu and Frost, 2002; Jing et al., 2008; Jing et al., 2009). The A-cluster was first recognized in a search for the premotor pattern generator for the escape swim. This search was correctly based on a presumption that the swim network would incorporate the neurons of the turn network, which could be studied for approach-avoidance decisions. Thus, it was eventually found that the A-cluster in different states of coordination mediates the escape swim, approach-avoidance turns, crawling locomotion, and likely righting behavior (Jing and Gillette, 1995; Jing and Gillette, 1999; Jing and Gillette, 2000; Jing and Gillette, 2003). Thus, A-cluster neurons are concerned with different aspects of posture and locomotion, very similar to the functions of the reticular system. The major differences in complexity can be simply related to control of a soft body vs. an articulated, skeletonized body.

Moreover, as for the raphe nuclei of the reticular formation, the behavioral functions of the A cluster are critically dependent on a serotonergic network. The four bilaterally paired serotonergic As1-4 neurons lie at the core of the A-cluster and provide the neuromodulatory drive to swimming, turning, and crawling locomotion. They are interconnected both chemically by serotonergic synapses and electrically, and fire in different patterns with the different motor outputs. Unlike the concentrated localization of the ~7 raphe nuclei in the vertebrate brain, serotonergic neurons of the gastropod brain are dispersed within and among the ganglia, lying within motor pattern generators like the A-cluster and the As1-4 cells and the feeding network and the C-cluster, where they drive motor arousal (Jing and Gillette, 2003; Gillette, 2006). However, their interconnections allow activity in one group to contribute to the arousal of another and thereby its motor network. If the serotonergic neurons of the gastropod were indeed homologous to those of the vertebrate raphe nuclei, it could mean either that the serotonergic neurons became concentrated in vertebrates or that they dispersed in the mollusks (Gillette, 2006).

Like the posterior raphe nuclei, the serotonergic As1-4 neurons send descending innervation to the pedal ganglia analogs of the spinal pattern generators to drive crawling locomotion and approach-avoidance turns in different states of coordination (Jing and Gillette, 2003; Lee et al., 2023). They are also chemically coupled to the serotonergic neurons of the feeding motor network. In coordination with other identified neurons of the A cluster, they sustain the swimming escape response episode (Jing and Gillette, 1999). Thus, their actions are obligatory to the actions of posture and locomotion mediated by the A-cluster analog of the reticular activating system.

C-cluster

The serotonergic C-cluster neurons and the metacerebral giant neurons of the cerebral ganglia lobes innervate the feeding motor network and the peripheral sensory neuronal network. They are functionally analogous to the serotonergic portions of the vertebrate ascending reticular formation (Figure 2), which innervates the hypothalamus, basal ganglia, and other pallial derivatives. The C-clusters of 12+ neurons each and the metacerebral giant neurons lie anteriorly in the cerebral lobes and are both electrically and chemically coupled (Gillette and Davis, 1977; Jing and Gillette, 2000). They are embedded in the feeding network where during the active feeding cycle they receive alternating synaptic excitation and inhibition during the retraction and protraction (swallowing and biting) phases of the feeding apparatus, respectively (Gillette and Davis, 1977). The C-cluster cells richly innervate the cerebral ganglia lobes and send axons to the periphery to innervate the subepithelial network (see below) of the chemotactile oral veil (Moroz et al., 1997), where ongoing work indicates that serotonin promotes sensory gain. The paired metacerebral neurons provide neuromodulatory input to the buccal ganglion's feeding central pattern generator (CPG), but the majority of its outputs are peripheral: to the esophagus/crop, the musculature of the buccal mass, and the chemosensory mouth area (Gillette, 1991). Serotonergic modulation of the feeding network sets the basal excitation state and lowers the thresholds for both the approach turn and active feeding (Hirayama and Gillette, 2012; Hirayama et al., 2014). Serotonergic modulation of sensory gain in the gastropod peripheral nervous system may contribute to incentivization of stimuli and conceivably also contributes to attentional mechanisms and odor/taste learning.

Pedal ganglia–spinal cord analogs

Like the vertebrate spinal cord, the gastropod pedal ganglia mediate the larger part of direct motor patterning for posture and locomotion. They receive descending commands, including neuromodulatory serotonergic input, from the A-cluster in *Pleurobranchaea*, to express the motor outputs of approach and avoidance turns, escape swimming, body withdrawal, and locomotion. They correspond to the subesophageal ganglia of other ecdysozoans like the arthropods and annelids, which partially serially segment in development to form the ventral nerve cords, themselves similar to vertebrate spinal cord in development and molecular signatures (Vergara et al., 2017).

Subepithelial network–potentially like the ancestral pallial precursor?

The pallial circuitry of the vertebrate brain is largely concerned with processing incentive on the basis of stimulus qualities, motivation, reward experience (hedonic affect), and memory, and with directional information for stimuli. *Pleurobranchaea* has no such central neuronal module that has yet been identified. However, there is a peripheral, subepithelial network (SeN) of interneurons postsynaptic to the primary receptors for chemotactile stimuli in the oral veil that does perform simple functions of incentivizing stimuli and estimating their directional location (Figure 2). Thus, it is quite possible that the origin of the telencephalic derivatives of the ancient olfactory system in evolution–the olfactory bulb, cortex, hippocampus, basal ganglia, amygdaloid complex and the others–may have lain in a peripheral SeN processing incentive and directionality like that in the oral veil of *Pleurobranchaea*, which became centralized and enhanced with the evolving body complexities of segmentation and jointed skeletons.

Olfaction is among the most primitive of senses (Cuschieri, 1976). Elaboration of olfactory systems and associated structures for odor learning is closely tied to the emergence of pallial structures. Directional olfaction may have formed the basis for the evolution of memory organization in the bilaterian brain, with hippocampal-like structures used for mapping and encoding the spatial distributions of novel odorants (Jacobs, 2012; 2023). Further, the olfactory system is the only sensory system that bypasses the thalamus, a structure for multi-modal sensory relay; instead, the olfactory bulb projects directly to amygdala and piriform cortex, which are important for emotion and memory (Kay and Sherman, 2007; Jacobs, 2023). Like the olfactory bulb, the SeN of *Pleurobranchaea* is notably dopaminergic and is richly innervated by the serotonergic neurons of the C-cluster.

The primary olfactory centers in vertebrate and insect brains seem to have similar neuronal types, sensory coding mechanisms, coherent oscillatory activity, and organization, including dense olfactory projections to structures critical for memory: vertebrate hippocampus and insect mushroom bodies (Strausfeld and Hildebrand, 1999; Tomer et al., 2010). Some gastropods share similar features, including presence of glomeruli and coherent oscillations in procerebral lobes of pulmonate mollusks, which are important for odor learning (Gelperin, 1999; Kay, 2015).

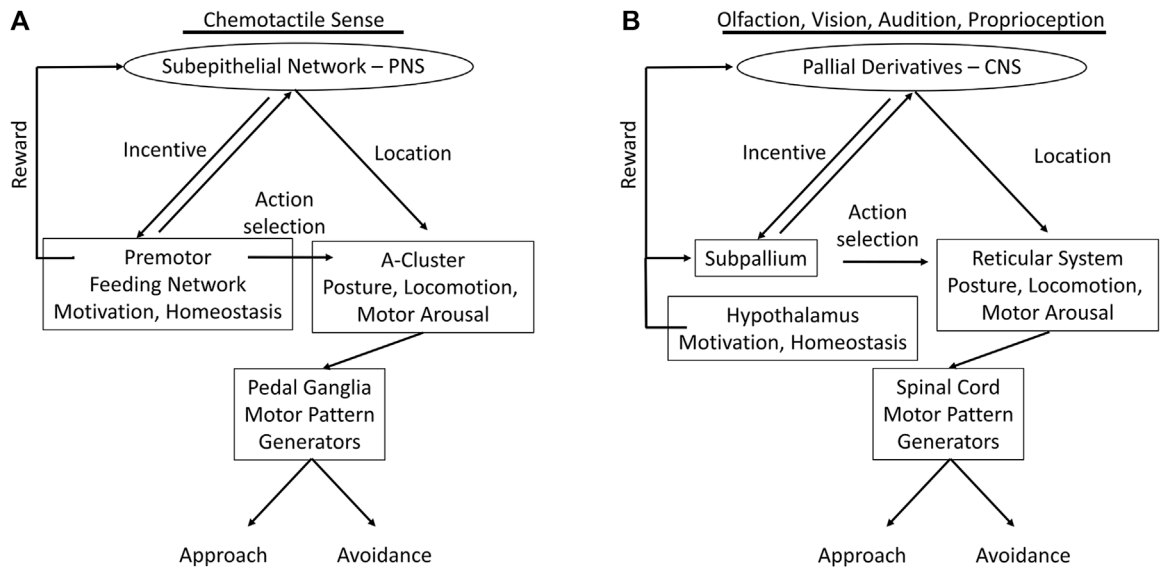

FIGURE 5
Functional analogs in nervous systems of *Pleurobranchaea* **(A)** and vertebrates **(B)**; comparing the flow of information from sensory input to motor output. In the vertebrates the incentive and directionality functions of the gastropod subepithelial network are centralized and markedly enhanced in pallial cortex (entorhinal, hippocampal, *etc.*) for vision, audition, and posture. Action selection for approach-avoidance decisions in the vertebrates, which in *Pleurobranchaea* is the province of the feeding network, is separated to the subpallial basal ganglia. The motivational and homeostatic functions of the *Pleurobranchaea* feeding network are retained by the vertebrate hypothalamus. The multifunctional premotor network in the A-cluster neurons of *Pleurobranchaea* is analogous to the vertebrate reticular formation, framing action decisions in terms of motor arousal, posture, and locomotion. The pedal ganglia and spinal cord receive motor commands from the premotor networks and express the primary motor patterns.

In *Pleurobranchaea*, while there is no clear analogue to mushroom bodies or procerebral lobes, learning and mapping of olfactory stimuli are supported by the oral veil SeN. Computations in the SeN allow *Pleurobranchaea* to map locations of environmental stimuli relative to its body. The cell bodies whose axons carry the location information have central cell bodies (unpublished observations). This somatotopic map of stimulus location and distribution over a target area can provide a template for directed motor reaction, and further, it offers a potential evolutionary substrate type for place coding, contextual memory and spatial memory, as seen in arthropod mushroom and ellipsoid bodies, and vertebrate hippocampus (Devaud et al., 2015; Eichenbaum, 2017).

The SeN suggests insights into the evolution of learning and memory circuits by its nature as an extensive interconnected sensory network with dopaminergic elements that also receives prominent central serotonergic innervation. The interactions of dopamine and serotonin are notable in other systems for supporting hetero-associative reward feedback underlying attention and short- and long-term memory. A basic form of associative learning is classical conditioning, where a neutral stimulus is paired with a biologically potent stimulus, such as food, reward, or even pain, to elicit a conditioned response. The simplest of associative memory systems that can support classical conditioning must have circuitry that handles at least two different kinds of input, such as a sensory signal and motor feedback signal, or a sensory signal paired with a reward feedback signal (e.g., Hawkins et al., 1998). Second-order conditioning involves the associative pairing of a neutral stimulus with an already conditioned (previously neutral) stimulus, to elicit a conditioned response (Brogden, 1939). Circuitry for second-order conditioning must therefore contain a neuron or set of neurons that responds to both types of neutral stimuli.

Thus, the higher in complexity a memory system is, the more intermediate circuitry it must have between neurons that respond to sensory input and those that receive reward or motor feedback. This is particularly apparent in systems capable of sequence learning and spatial memory, such as mammalian hippocampus and octopus' vertical lobe, which have both extensive auto-associative and hetero-associative architectures. The SeN expresses potential precursors to these associative architectures as it consists of an extensive interconnected sensory network that also receives intricate serotonergic innervation, which could well provide hetero-associative reward feedback.

Spatial learning demands neuronal circuitry that can associate the order and strength of sequentially encountered stimuli, with their connectivity influenced by reward. In principle, this does not look complicated. Such learning may have been selected for in evolution in motile opportunists for efficiently exploiting particular territories, and for homing to a safe refuge when not foraging. While the nomadic and homeless *Pleurobranchaea* most likely lack spatial learning, they provide an interesting example of a potential neuronal precursor for more context-dependent substrates of associative learning. In particular, the *Pleurobranchaea* SeN is well-positioned for associatively pairing specific odor and reward stimuli, and it may even support pairing of the *location* of the specific olfactory stimulus relative to its body with reward feedback. This possible encoding of additional context, i.e., the somatotopic stimulus location, may enable the simple short-term working odor

memory that may aid *Pleurobranchaea* in navigating its olfactory environment (Yafremava and Gillette, 2011). A recurrent inhibitory network was proposed as a simple averaging computation of stimulus loci for motor targeting (Yafremava and Gillette, 2011). Moreover, the serotonergic innervation of the SeN by the C-cluster cells could well provide a mechanism for working memory, attention, and long-term memory through heterosynaptic facilitation.

Conclusion

We have summarized marked analogies between the complex vertebrate systems, and to some degree those of insects, with the nervous systems of gastropods much simpler in body form and behavior. Figure 5 recapitulates the functional analogies, possible homologies and/or convergences, between the nervous systems of the gastropod *Pleurobranchaea* and vertebrates.

The evolved neural complexities of the vertebrates and insects may be largely ascribed to their segmentation and jointed skeletons, which lend them speed and agility through ability to monitor body posture for motor planning, to more functional equilibrium organs, and to their high resolution exteroceptors for vision, vibration, and electroreception in some cases. However, we are able to describe a similar modular organization of the nervous system in the gastropod *Pleurobranchaea*, though so much simpler in body form and behavior, with many fewer neurons, and even incomplete centralization of the CNS. Figure 5 summarizes the analogous neural modules between *Pleurobranchaea* and vertebrates that mediate action selection and reward as feeding network/basal ganglia and hypothalamus. The analogies for posture, locomotion, and motor arousal are the neuron group A-cluster/reticular system of the mid-to-hindbrain. For the serotonergic raphe nuclei of the vertebrate reticular system, the *Pleurobranchaea* analogy is a distributed serotonergic network with ascending and descending projections, and for primary motor pattern generation, the spinal cord is analogous to the *Pleurobranchaea* pedal ganglia.

Finally, we introduced the SeN as a simplest analog of the pallial derivatives (olfactory bulb, cortex, *etc.*). The SeN receives interconnected input from primary sensory receptors to compute incentive from stimulus qualities and to estimate the averaged stimulus source direction (place) for directed motor response. Its final output targets are at the feeding network, where it sums with appetitive state, and at the turn motor network in the A cluster, where it sets the moment-to-moment amplitude of the approach-avoidance turn. The computations of incentive and stimulus location lend the SeN qualities which could have been precursor to the more detailed computations of the vertebrate forebrain for incentive, for the computations of more complicated place codes of more environmental stimuli transduced by complex eyes and ears, and for the eventual evolution of more complex cognitive ability in episodic memory for signatures in space and time.

In the vertebrates, these stages are mediated by pallial derivatives for incentive (olfactory bulb, cerebral cortex, amygdala, &c) interacting with hypothalamus (motivation and reward) for action selection. The reticular formation acts as a premotor translator for posture, locomotion, and arousal state, and the spinal cord and cranial nuclei as primary motor pattern generators.

Finally, our work here may contribute to an answer to whether the modular organizations of vertebrate and arthropod brains evolved independently or were inherited and embellished from a soft-bodied, unsegmented bilaterian ancestor. The marked similarities observed in gastropods are consistent with a common inheritance and may invite future comparative molecular and developmental analyses to cast further light on this compelling question.

Data availability statement

The original contributions presented in the study are included in the article/Supplementary Material, further inquiries can be directed to the corresponding author.

Author contributions

EG: Conceptualization, Writing–original draft, Writing–review and editing. CL: Conceptualization, Writing–original draft, Writing–review and editing, Investigation. JB: Data curation, Writing–review and editing, Investigation. JC: Data curation, Investigation, Writing–review and editing. YL: Data curation, Investigation, Writing–review and editing. TN: Data curation, Investigation, Writing–review and editing. RG: Conceptualization, Funding acquisition, Writing–original draft.

Funding

The author(s) declare financial support was received for the research, authorship, and/or publication of this article. This work was supported by Office of Naval Research Grant N00014-19-1-2373. TN was also supported in part by the grants from the National Science Foundation (1557923) and the National Institute of Neurological Disorders and Stroke (R01NS114491) to Leonid Moroz.

Conflict of interest

The authors declare that the research was conducted in the absence of any commercial or financial relationships that could be construed as a potential conflict of interest.

Publisher's note

References

Aboitiz, F., and Montiel, J. F. (2015). Olfaction, navigation, and the origin of isocortex. *Front. Neurosci.* 9, 402. doi:10.3389/fnins.2015.00402

Aboitiz, F., Morales, D., and Montiel, J. (2003). The evolutionary origin of the mammalian isocortex: towards an integrated developmental and functional approach. *Behav. Brain Sci.* 26 (5), 535–552. doi:10.1017/s0140525x03000128

Arbib, M. A. (2007). Modular models of brain function. *Scholarpedia* 2 (3), 1869. doi:10.4249/scholarpedia.1869

Brogden, W. (1939). Higher order conditioning. *Am. J. Psychol.* 52, 579–591. doi:10.2307/1416470

Brown, J. W. (2014). *Reciprocal interactions between feeding and turning motor networks mediate foraging decisions in a predatory sea-slug*. PhD thesis. Champaign: University of Illinois at Urbana-Champaign.

Brown, J. W., Schaub, B. M., Klusas, B. L., Tran, A. X., Duman, A. J., Haney, S. J., et al. (2018). A role for dopamine in the peripheral sensory processing of a gastropod mollusc. *PLOS One* 13 (12), e0208891. doi:10.1371/journal.pone.0208891

Cassidy, R. M., and Tong, Q. (2017). Hunger and satiety gauge reward sensitivity. *Front. Endocrinol.* 8, 104. doi:10.3389/fendo.2017.00104

Clore, G. L., Proffitt, D. R., and Zadra, J. R. (2021). "Feeling, seeing, and liking: how bodily resources inform perception and emotion," in *Handbook of embodied psychology* (Berlin, Germany: Springer), 43–64.

Cuschieri, A. (1976). Functional anatomy of olfactory sense organs. *St. Luke's Hosp. Gazette* 11 (2), 98–106.

Davis, W. J., and Gillette, R. (1978). Neural correlate of behavioral plasticity in command neurons of Pleurobranchaea. *Science* 199 (4330), 801–804. doi:10.1126/science.622572

Devaud, J.-M., Papouin, T., Carcaud, J., Sandoz, J.-C., Grünewald, B., and Giurfa, M. (2015). Neural substrate for higher-order learning in an insect: mushroom bodies are necessary for configural discriminations. *Proc. Natl. Acad. Sci.* 112 (43), E5854–E5862. doi:10.1073/pnas.1508422112

Eichenbaum, H. (2017). The role of the hippocampus in navigation is memory. *J. Neurophysiology* 117 (4), 1785–1796. doi:10.1152/jn.00005.2017

Elliott, C., and Susswein, A. (2002). Comparative neuroethology of feeding control in molluscs. *J. Exp. Biol.* 205 (7), 877–896. doi:10.1242/jeb.205.7.877

Forterre, P. (2006). The origin of viruses and their possible roles in major evolutionary transitions. *Virus Res.* 117 (1), 5–16. doi:10.1016/j.virusres.2006.01.010

Gelperin, A. (1999). Oscillatory dynamics and information processing in olfactory systems. *J. Exp. Biol.* 202 (14), 1855–1864. doi:10.1242/jeb.202.14.1855

Gillette, R., and Brown, J. W. (2015). The sea slug, *Pleurobranchaea californica*: A signpost species in the evolution of complex nervous systems and behavior. *Integr. Comp. Biol.* 55 (6), 1058–1069. doi:10.1093/icb/icv081

Gillette, R., and Davis, W. J. (1977). The role of the metacerebral giant neuron in the feeding behavior of Pleurobranchaea. *J. Comp. Physiology* 116 (2), 129–159. doi:10.1007/bf00605400

Gillette, R. (2006). Evolution and function in serotonergic systems. *Integr. Comp. Biol.* 46 (6), 838–846. doi:10.1093/icb/icl024

Gillette, R., Huang, R.-C., Hatcher, N., and Moroz, L. L. (2000). Cost-benefit analysis potential in feeding behavior of a predatory snail by integration of hunger, taste, and pain. *Proc. Natl. Acad. Sci.* 97 (7), 3585–3590. doi:10.1073/pnas.97.7.3585

Gillette, R., and Jing, J. (2001). The role of the escape swim motor network in the organization of behavioral hierarchy and arousal in Pleurobranchaea. *Am. Zoologist* 41 (4), 983–992. doi:10.1093/icb/41.4.983

Gillette, R. (1991). On the significance of neuronal giantism in gastropods. *Biol. Bull.* 180 (2), 234–240. doi:10.2307/1542393

Gribkova, E. D., Catanho, M., and Gillette, R. (2020). Simple aesthetic sense and addiction emerge in neural relations of cost-benefit decision in foraging. *Sci. Rep.* 10, 9627. doi:10.1038/s41598-020-66465-0

Grillner, S., Robertson, B., and Stephenson-Jones, M. (2013). The evolutionary origin of the vertebrate basal ganglia and its role in action selection. *J. Physiol.* 591 (22), 5425–5431. doi:10.1113/jphysiol.2012.246660

Hawkins, R. D., Greene, W., and Kandel, E. R. (1998). Classical conditioning, differential conditioning, and second-order conditioning of the Aplysia gill-withdrawal reflex in a simplified mantle organ preparation. *Behav. Neurosci.* 112 (3), 636–645. doi:10.1037//0735-7044.112.3.636

Hejnol, A., and Martindale, M. Q. (2008). Acoel development indicates the independent evolution of the bilaterian mouth and anus. *Nature* 456 (7220), 382–386. doi:10.1038/nature07309

Hirayama, K., Catanho, M., Brown, J. W., and Gillette, R. (2012). A core circuit module for cost/benefit decision. *Front. Neurosci.* 6, 123. doi:10.3389/fnins.2012.00123

Hirayama, K., and Gillette, R. (2012). A neuronal network switch for approach/avoidance toggled by appetitive state. *Curr. Biol.* 22 (2), 118–123. doi:10.1016/j.cub.2011.10.055

Hirayama, K., Moroz, L. L., Hatcher, N. G., and Gillette, R. (2014). Neuromodulatory control of a goal-directed decision. *PLOS One* 9 (7), e102240. doi:10.1371/journal.pone.0102240

Hochner, B. (2013). How nervous systems evolve in relation to their embodiment: what we can learn from octopuses and other molluscs. *Brain, Behav. Evol.* 82 (1), 19–30. doi:10.1159/000353419

Holland, L. Z. (2016). Tunicates. *Curr. Biol.* 26 (4), R146–R152. doi:10.1016/j.cub.2015.12.024

Jacobs, L. F. (2012). From chemotaxis to the cognitive map: the function of olfaction. *Proc. Natl. Acad. Sci.* 109 (1), 10693–10700. doi:10.1073/pnas.1201880109

Jacobs, L. F. (2023). The PROUST hypothesis: the embodiment of olfactory cognition. *Anim. Cogn.* 26 (1), 59–72. doi:10.1007/s10071-022-01734-1

Jing, J., and Gillette, R. (1999). Central pattern generator for escape swimming in the notaspid sea slug Pleurobranchaea californica. *J. Neurophysiology* 81 (2), 654–667. doi:10.1152/jn.1999.81.2.654

Jing, J., and Gillette, R. (2003). Directional avoidance turns encoded by single interneurons and sustained by multifunctional serotonergic cells. *J. Neurosci.* 23 (7), 3039–3051. doi:10.1523/JNEUROSCI.23-07-03039.2003

Jing, J., and Gillette, R. (2000). Escape swim network interneurons have diverse roles in behavioral switching and putative arousal in Pleurobranchaea. *J. Neurophysiology* 83 (3), 1346–1355. doi:10.1152/jn.2000.83.3.1346

Jing, J., and Gillette, R. (1995). Neuronal elements that mediate escape swimming and suppress feeding behavior in the predatory sea slug Pleurobranchaea. *J. Neurophysiology* 74 (5), 1900–1910. doi:10.1152/jn.1995.74.5.1900

Jing, J., Gillette, R., and Weiss, K. R. (2009). Evolving concepts of arousal: insights from simple model systems. *Rev. Neurosci.* 20, 405–427. doi:10.1515/revneuro.2009.20.5-6.405

Jing, J., Vilim, F. S., Cropper, E. C., and Weiss, K. R. (2008). Neural analog of arousal: persistent conditional activation of a feeding modulator by serotonergic initiators of locomotion. *J. Neurosci.* 28 (47), 12349–12361. doi:10.1523/JNEUROSCI.3855-08.2008

Kabotyanski, E. A., Baxter, D. A., Cushman, S. J., and Byrne, J. H. (2000). Modulation of fictive feeding by dopamine and serotonin in Aplysia. *J. Neurophysiology* 83 (1), 374–392. doi:10.1152/jn.2000.83.1.374

Katz, P. S. (2016). Phylogenetic plasticity in the evolution of molluscan neural circuits. *Curr. Opin. Neurobiol.* 41, 8–16. doi:10.1016/j.conb.2016.07.004

Kay, L. M. (2015). Olfactory system oscillations across phyla. *Curr. Opin. Neurobiol.* 31, 141–147. doi:10.1016/j.conb.2014.10.004

Kay, L. M., and Sherman, S. M. (2007). An argument for an olfactory thalamus. *Trends Neurosci.* 30 (2), 47–53. doi:10.1016/j.tins.2006.11.007

Lee, C. A., Brown, J. W., and Gillette, R. (2023). Coordination of locomotion by serotonergic neurons in the predatory gastropod Pleurobranchaea californica. *J. Neurosci.* 43 (20), 3647–3657. doi:10.1523/JNEUROSCI.1386-22.2023

Loesel, R., and Heuer, C. M. (2010). The mushroom bodies–prominent brain centres of arthropods and annelids with enigmatic evolutionary origin. *Acta Zool.* 91 (1), 29–34. doi:10.1111/j.1463-6395.2009.00422.x

London, J. A., and Gillette, R. (1986). Mechanism for food avoidance learning in the central pattern generator of feeding behavior of Pleurobranchae californica. *Proc. Natl. Acad. Sci.* 83 (11), 4058–4062. doi:10.1073/pnas.83.11.4058

Moroz, L. L., Sudlow, L. C., Jing, J., and Gillette, R. (1997). Serotonin-immunoreactivity in peripheral tissues of the opisthobranch molluscs *Pleurobranchaea californica* and *Tritonia diomedea*. *J. Comp. Neurology* 382 (2), 176–188. doi:10.1002/(sici)1096-9861(19970602)382:2<176:aid-cne3>3.0.co;2-0

Mullins, O. J., Hackett, J. T., Buchanan, J. T., and Friesen, W. O. (2011). Neuronal control of swimming behavior: comparison of vertebrate and invertebrate model systems. *Prog. Neurobiol.* 93 (2), 244–269. doi:10.1016/j.pneurobio.2010.11.001

Noboa, V., and Gillette, R. (2013). Selective prey avoidance learning in the predatory sea-slug *Pleurobranchaea californica*. *J. Exp. Biol.* 216, 3231–3236. doi:10.1242/jeb.079384

Popescu, I. R., and Frost, W. N. (2002). Highly dissimilar behaviors mediated by a multifunctional network in the marine mollusk Tritonia diomedea. *J. Neurosci.* 22 (5), 1985–1993. doi:10.1523/JNEUROSCI.22-05-01985.2002

Redgrave, P., Prescott, T. J., and Gurney, K. (1999). The basal ganglia: a vertebrate solution to the selection problem? *Neuroscience* 89, 1009–1023. doi:10.1016/S0306-4522(98)00319-4

Reiner, A., Medina, L., and Veenman, C. L. (1998). Structural and functional evolution of the basal ganglia in vertebrates. *Brain Res. Rev.* 28 (3), 235–285. doi:10.1016/s0165-0173(98)00016-2

Rossignol, S., Dubuc, R., and Gossard, J.-P. (2006). Dynamic sensorimotor interactions in locomotion. *Physiol. Rev.* 86 (1), 89–154. doi:10.1152/physrev.00028.2005

Smeets, W. J., Marin, O., and Gonzalez, A. (2000). Evolution of the basal ganglia: new perspectives through a comparative approach. *J. Anat.* 196 (4), 501–517. doi:10.1046/j.1469-7580.2000.19640501.x

Strausfeld, N. J., and Hildebrand, J. G. (1999). Olfactory systems: common design, uncommon origins? *Curr. Opin. Neurobiol.* 9 (5), 634–639. doi:10.1016/S0959-4388(99)00019-7

Strausfeld, N. J., and Hirth, F. (2013). Deep homology of arthropod central complex and vertebrate basal ganglia. *Science* 340 (6129), 157–161. doi:10.1126/science.1231828

Sudlow, L. C., Jing, J., Moroz, L. L., and Gillette, R. (1998). Serotonin immunoreactivity in the central nervous system of the marine molluscs *Pleurobranchaea californica* and *Tritonia diomedea*. *J. Comp. Neurology* 395 (4), 466–480. doi:10.1002/(sici)1096-9861(19980615)395:4<466:aid-cne4>3.0.co;2-#

Teissier, A., Chemiakine, A., Inbar, B., Bagchi, S., Ray, R. S., Palmiter, R. D., et al. (2015). Activity of raphé serotonergic neurons controls emotional behaviors. *Cell Rep.* 13 (9), 1965–1976. doi:10.1016/j.celrep.2015.10.061

Tomer, R., Denes, A. S., Tessmar-Raible, K., and Arendt, D. (2010). Profiling by image registration reveals common origin of annelid mushroom bodies and vertebrate pallium. *Cell* 142 (5), 800–809. doi:10.1016/j.cell.2010.07.043

Tosches, M. A., and Arendt, D. (2013). The bilaterian forebrain: an evolutionary chimaera. *Curr. Opin. Neurobiol.* 23 (6), 1080–1089. doi:10.1016/j.conb.2013.09.005

Turner, R. S., and Desmurget, M. (2010). Basal ganglia contributions to motor control: a vigorous tutor. *Curr. Opin. Neurobiol.* 20 (6), 704–716. doi:10.1016/j.conb.2010.08.022

Venkatraman, A., Edlow, B. L., and Immordino-Yang, M. H. (2017). The brainstem in emotion: a review. *Front. Neuroanat.* 11, 15. doi:10.3389/fnana.2017.00015

Vergara, H. M., Bertucci, P. Y., Hantz, P., Tosches, M. A., Achim, K., Vopalensky, P., et al. (2017). Whole-organism cellular gene-expression atlas reveals conserved cell types in the ventral nerve cord of *Platynereis dumerilii*. *Proc. Natl. Acad. Sci. U. S. A.* 114 (23), 5878–5885. doi:10.1073/pnas.1610602114

Yafremava, L. S., Anthony, C. W., Lane, L., Campbell, J. K., and Gillette, R. (2007). Orienting and avoidance turning are precisely computed by the predatory sea-slug Pleurobranchaea californica McFarland. *J. Exp. Biol.* 210 (4), 561–569. doi:10.1242/jeb.02697

Yafremava, L. S., and Gillette, R. (2011). Putative lateral inhibition in sensory processing for directional turns. *J. Neurophysiology* 105 (6), 2885–2890. doi:10.1152/jn.00124.2011

Frontiers in Neuroscience

Provides a holistic understanding of brain function from genes to behavior

Part of the most cited neuroscience journal series which explores the brain - from the new eras of causation and anatomical neurosciences to neuroeconomics and neuroenergetics.

Discover the latest Research Topics

See more →

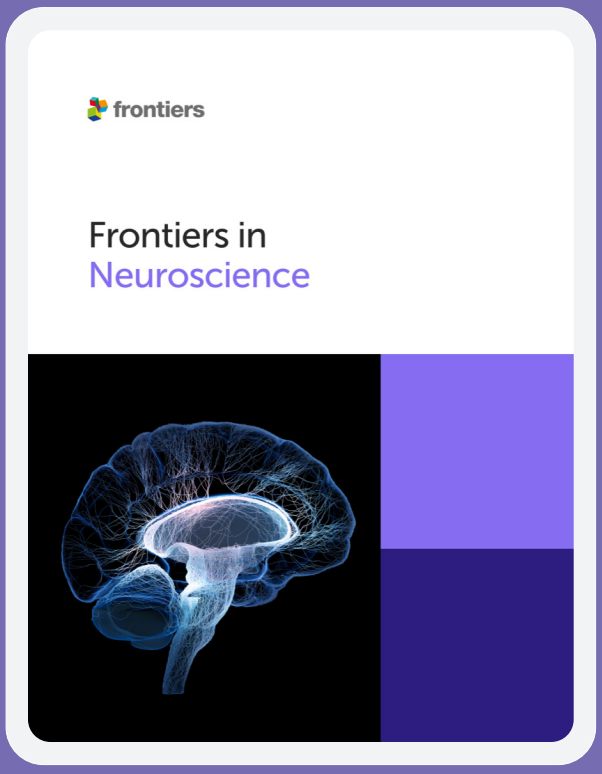

Frontiers

Avenue du Tribunal-Fédéral 34
1005 Lausanne, Switzerland
frontiersin.org

Contact us

+41 (0)21 510 17 00
frontiersin.org/about/contact